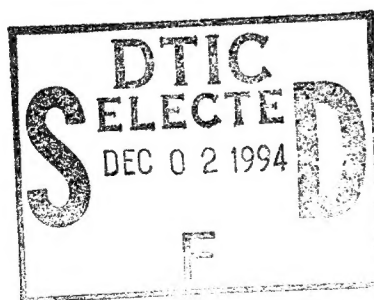
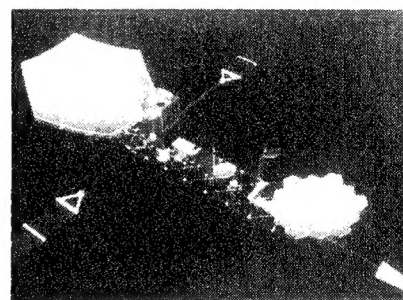
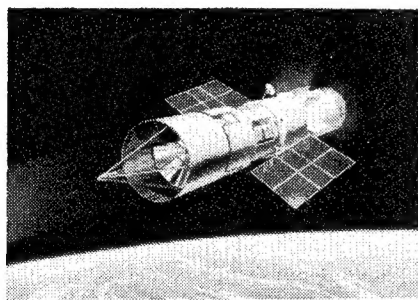
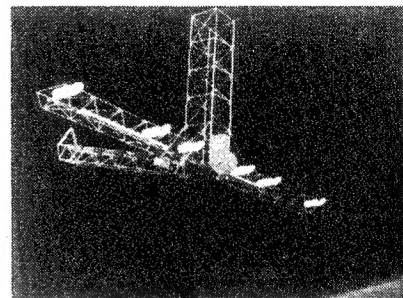
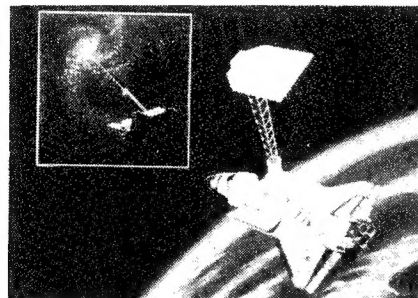


Fifth NASA/DoD Controls-Structures Interaction Technology Conference



*Proceedings of a conference held in
Lake Tahoe, Nevada
March 3-5, 1992*

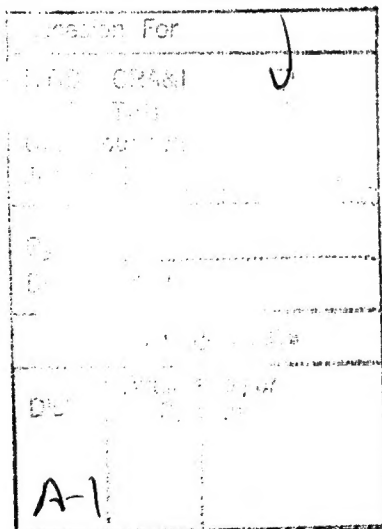
This document has been approved
for public release and sale; its
distribution is unlimited.

NASA

19941128 040

Fifth NASA/DoD Controls-Structures Interaction Technology Conference

Compiled by
Jerry R. Newsom
NASA Langley Research Center
Hampton, Virginia



Proceedings of a conference sponsored by the
National Aeronautics and Space Administration,
Washington, D.C., and the Department of Defense,
Washington, D.C., and held in
Lake Tahoe, Nevada
March 3-5, 1992



National Aeronautics and
Space Administration
Office of Management
Scientific and Technical
Information Program

1993

PREFACE

The National Aeronautics and Space Administration (NASA) and the Department of Defense (DoD) are actively involved in the development of a validated technology data base in the area of controls-structures interaction (CSI) for flexible spacecraft. The development of this technology is essential to the efficient and confident development of future spacecraft to meet stringent goals in performance and cost. Both NASA and DoD have programs in CSI, structural dynamics, and controls. The activities of these programs provide a systematic approach to address technology voids through development and validation of analytical tools, extensive ground testing of representative structures, and future in-space experiments for verification of analysis and ground test methods.

In order to promote timely dissemination of technical information acquired in these programs, the NASA Langley Research Center and the Wright Laboratory alternately sponsor a conference to report to industry, academia, and government agencies on the current status of controls-structures interaction technology. This publication is a compilation of the papers presented at the fifth NASA/DoD CSI Technology Conference.

The use of trade names or manufacturers in this publication does not constitute an official endorsement of such products or manufacturers, either expressed or implied, by the National Aeronautics and Space Administration.

Jerry R. Newsom
Technical Program Chairman

CONTENTS

Preface	iii
Attendees	ix

Part 1

SESSION I

Chairman: Henry B. Waites
Co-Chairman: Capt. Ted Doederlein

The Mini-Mast CSI Testbed: Lessons Learned	3
S. E. Tanner, W. K. Belvin, L. G. Horta, and R. S. Pappa	
Model Reduction for the Dynamics and Control of Large Structural Systems Via Neural Network Processing Direct Numerical Optimization	25
Georges A. Bécus and Alistair K. Chan	
Physical Insight into the Simultaneous Optimization of Structure and Control	35
Robert N. Jacques and David W. Miller	
Smart Patch Piezoceramic Actuator Issues	47
S. F. Griffin, K. K. Denoyer, and B. J. Yost	
A Numerical Approach to Controller Design for the Aces Facility	65
W. Garth Frazier and R. Dennis Irwin	
Model Reduction Results for Flexible Space Structures	79
Trevor Williams and Masoud Mostarshedi	
An Application of the Observer/Kalman Filter Identification (OKID) Technique to Hubble Flight Data	97
Jer-Nan Juang, Lucas G. Horta, W. Keith Belvin, John Sharkey, and Frank H. Bauer	

SESSION II

Chairman: Jerome Pearson
Co-Chairman: James Fanson

Micro-Precision Control/Structure Interaction Technology for Large Optical Space Systems	115
Samuel W. Sirlin and Robert A. Laskin	
Static and Dynamic Characteristics of a Piezoceramic Strut	133
Brett Pokines, W. Keith Belvin, and Daniel J. Inman	
System Identification and Structural Control on the JPL Phase B Testbed	141
Cheng-Chih Chu, John F. O'Brien, and Boris J. Lurie	
The Development and Testing of the Lens Antenna Deployment Demonstration (LADD) Test Article	153
Mark L. Pugh, Robert J. Denton Jr., and Timothy J. Strange	

Integrated Design of the CSI Evolutionary Structure: A Verification of the Design Methodology	161
P. G. Maghami, S. M. Joshi, K. B. Elliot, and J. E. Walz	
Control/Structure Interaction During Space Station Freedom-Orbiter Berthing	181
T. Hua, E. Kubiak, Yeongching Lin, M. Kilby, and J. Mapar	

POSTER SESSION

Integrated Modeling of Advanced Optical Systems	207
Hugh C. Briggs, Laura Needels, and B. Martin Levine	
A Comparison of Refined Models for Flexible Subassemblies	215
Suzanne Weaver Smith and David C. Zimmerman	
The JPL Phase B Interferometer Testbed	231
Daniel Eldred and Mike O'Neal	
Design, Analysis and Testing of High Frequency Passively Damped Struts	239
Y. C. Yiu, Porter Davis, Kevin Napolitano, and Rory Ninneman	
A Comparison of Viscoelastic Damping Models	251
Joseph C. Slater, W. Keith Belvin, and Daniel J. Inman	
Structural Control Sensors for the Cases GTF	263
H. W. Davis and A. P. Buckley	
SSF Loads and Controllability During Assembly	277
C. R. Larson, S. Ghofranian, and E. Fujii	
Evaluation of Inertial Devices for the Control of Large, Flexible, Space-Based Telerobotic Arms	289
Raymond C. Montgomery, Sean Kenny, Dave Ghosh, and Joram Shenhar	
A Darwinian Approach to Control-Structure Design	303
David C. Zimmerman	

SESSION III

Chairman: Robert A. Laskin
Co-Chairman: Richard Martin

CSI Flight Computer System and Experimental Test Results	317
D. W. Sparks, Jr., F. Peri, Jr., and P. Schuler	
Optical Pathlength Control on the JPL Phase B Interferometer Testbed	343
John Spanos and Zahidul Rahman	
Dynamic Test Results for the Cases Ground Experiment	359
Angelia P. Buckley, Alan F. Patterson, and Victoria L. Jones	
Results of the Advanced Space Structures Technology Research Experiments (ASTREX) Hardware and Control Development	367
1Lt. Derek F. Cossey	

Design Optimization of the JPL Phase B Testbed	373
M. Milman, M. Salama, M. Wette, and C. Chu	
Piezoelectric Devices for Vibration Suppression: Modeling and Application to a Truss Structure	393
C. C. Won, D. W. Sparks, W. K. Belvin, and J. L. Sulla	

Part 2*

SESSION IV	
Chairman: Kevin Slimak	
Co-Chairman: William L. Grantham	
CSI Related Dynamics and Control Issues in Space Robotics	415
Eric Schmitz and Madison Ramey	
Optimization for Efficient Structure-Control Systems	435
Hayrani Öz and Narendra S. Khot	
C-Side: The Control-Structure Interaction Demonstration Experiment	455
James B. Mohl and Hugh W. Davis	
An Explicit Solution to the Optimal LQG Problem for Flexible Structures With Collocated Rate Sensors	475
A. V. Balakrishnan	
A Synopsis of Test Results and Knowledge Gained From the Phase-0 CSI Evolutionary Model	489
W. Keith Belvin, Kenny B. Elliott, and Lucas G. Horta	
Controls-Structures-Interaction Dynamics During RCS Control of the Orbiter/SRMS/SSF Configuration	509
J. A. Schliesing and L. S. Shieh	
Model Reduction in Integrated Controls-Structures Design	529
P. G. Maghami and S. P. Kenny	
The Middeck Active Control Experiment (MACE)	551
David W. Miller, Raymond B. Sepe, Daniel Rey, Erik Saarmaa, and Edward F. Crawley	
SESSION V	
Chairman: Brantley R. Hanks	
Co-Chairman: Capt. Chuck Sherwin	
CSI/MMC Studies for Improving Jitter Performance for Large Multi-Payload Platforms	569
John Chionchio and Michael Garnek	
Precision Slew/Settle Technologies for Flexible Spacecraft	617
R. A. Manning and V. A. Spector	

*Part 2 is presented under separate cover.

Average-Cost Based Robust Structural Control	639
Nesbitt W. Hagood	
Modal Characterization of the ASCIE Segmented Optics Test Bed: New Algorithms and Experimental Results	665
Alain Carrier and Jean-Noel Aubrun	
Active Suspension Design for a Large Space Structure Ground Test Facility	707
Thomas Lange and Clemens Schlegel	
Modeling, System Identification, and Control of ASTREX	727
N. S. Abhyankar, J. Ramakrishnan, and K. W. Byun	
Analysis, Design, and Testing of a Low Cost, Direct Force Command Linear Proof Mass Actuator for Structural Control	751
G. L. Slater, Stuart Shelley, and Mark Jacobson	
CSI Flight Experiment Projects of the Naval Research Laboratory	763
Shalom Fisher	

ATTENDEES

Nandu S. Abhyankar
Bus. Phone: 805-275-5526
Dynacs Engineering Company
C/O OLAC PL/STS
Edwards AFB, CA 93523-5000

Scott Adams
Bus. Phone: 215-531-5199
General Electric
751 Vandenburg Road
King of Prussia, PA 19406

Gregory S. Agnes
Bus. Phone: 513-255-5236 X408
Wright Laboratory
WL/FIBGC
WPAFB, OH 45433

Dr. James J. Allen
Bus. Phone: 505-844-6764
Sandia National Laboratories
Structural Dynamics Division, 1434
Albuquerque, NM 87185

Dr. Willard W. Anderson
Bus. Phone: 804-864-1718
NASA Langley Research Center
Mail Stop 479
Hampton, VA 23665-5225

Peter M. Bainum
Bus. Phone: 202-806-6612
Howard University
Dept. of Mechanical Engineering
2300 6th Street, NW
Washington, DC 20059

Prof. A. V. Balakrishnan
Bus. Phone: 310-825-2180
University of California at LA
Electrical Engineering Department
Engr. IV Bldg., room 56-125B
UCLA (Mail Code #159410)
Los Angeles, CA 90024

Dr. Michael F. Barrett
Bus. Phone: 612-782-7286
Honeywell SRC
3660 Technology Drive
Minneapolis, MN 55418

Bob Bauer
Bus. Phone: 602-561-3257
Honeywell
P. O. Box 52199
Phoenix, AZ 85072-2199

Victor M. Beazel
Bus. Phone: 805-275-5798
USAF
OLAC PL/STS
Edwards AFB, CA 93523-5000

Dr. Georges A. Becus
Bus. Phone: 513-556-3222
University of Cincinnati
AsE/EM Department
Mail Location #70
Cincinnati, OH 45221-0070

Dr. W. Keith Belvin
Bus. Phone: 804-864-4319
NASA Langley Research Center
Mail Stop 230
Hampton, VA 23665-5225

Dr. Peter L. Bender
Bus. Phone: 303-492-6793
University of Colorado
Joint Institute for Laboratory Astro.
Campus Box 440
Boulder, CO 80309

Dr. Andrew S. Bicos
Bus. Phone: 714-896-1534
McDonnell Douglas Space Systems Co.
5301 Bolsa Avenue
M/S A3-Y857-13-3
Huntington Beach, CA 92647

Ross M. Blankinship
Bus. Phone: 505-262-2626
Lockheed Missiles and Space Company
1601 Randolph Road, SE, Suite 210 S
Albuquerque, NM 87106

Dr. Bob J. Boan
Bus. Phone: 407-729-7133
Harris Corporation
P. O. Box 94000
Melbourne, FL 32902

Ed B. Bokhour
Bus. Phone: 617-868-8086
Payload Systems Inc.
270 Third Street
Cambridge, MA 02142

Dr. John Breakwell
Bus. Phone: 408-743-7806
Lockheed Missiles & Space Company
P. O. Box 3504
Sunnyvale, CA 94088-3504

Dr. Hugh C. Briggs
Bus. Phone: 818-354-8192
Jet Propulsion Laboratory
Mail Stop T1710
4800 Oak Grove Drive
Pasadena, CA 91109

Patsy Brito
Bus. Phone:
USAF
Kirtland AFB, NM 87117

Ms. Angie Bukley
Bus. Phone: 205-544-0054
NASA Marshall Space Flight Center
Mail Stop ED12
Huntsville, AL 35812

Thomas F. Burns
Bus. Phone:
U. S. Government
13126 Thornapple Place
Herndon, VA 22071

Dr. Alain C. Carrier
Bus. Phone: 415-424-2735
Lockheed Missiles & Space Co., Inc.
3251 Hanover Street
Building 281, Org. 92-30
Palo Alto, CA 94304-1191

Cheng-Chih Chu
Bus. Phone: 818-354-7457
Jet Propulsion Laboratory
Mail Stop 198-326
4800 Oak Grove Drive
Pasadena, CA 91109

Lt. Derek F. Cossey
Bus. Phone: 805-275-5350
Phillips Laboratory - USAF - AFSC
OLAC PL/STSS
Edwards AFB, CA 93523-5000

Prof. Roy R. Craig, Jr.
Bus. Phone: 512-471-4172
University of Texas at Austin
ASE-EM Department
Austin, TX 78712-1085

Dr. Edward F. Crawley
Bus. Phone: 617-253-7510
Massachusetts Inst. of Technology
Building 37-351
77 Massachusetts Avenue
Cambridge, MA 02139

Dr. J. F. Creedon
Bus. Phone: 804-864-6033
NASA Langley Research Center
Mail Stop 113
Hampton, VA 23665-5225

Darby A. Davis
Bus. Phone: 408-743-1206
Lockheed Missiles and Space Company
1111 Lockheed Way
O/77-50 B/551
Sunnyvale, CA 94089-3504

Hugh W. Davis
Bus. Phone: 303-939-4022
Ball Electro-Optics/Cryogenics Div.
P. O. Box 1062
Boulder, CO 80306

L. Porter Davis
Bus. Phone: 602-561-3483
Honeywell, Inc. Satellite Systems Div
19019 N. 59th Avenue
Glendale, AZ 85308-9650

William M. Day
Bus. Phone: 205-922-7574
McDonnell Douglas Space Systems Co.
Mail Stop 15A1
689 Discovery Drive
Huntsville, AL 35806

Geoffrey S. Dean
Bus. Phone: 504-257-2454
Martin Marietta Manned Space System
P. O. Box 29304
Department 3041
New Orleans, LA 70189

Martha E. Demeo
Bus. Phone: 804-864-8045
Vigyan, Inc.
NASA Langley Research Center
Mail Stop 298
Hampton, VA 23665-5225

Keith K. Denoyer
Bus. Phone: 805-275-6187
USAF
Phillips Laboratory
OLAC PL/VTSS
Edwards AFB, CA 93523-5000

Robert J. Denton, Jr.
Bus. Phone: 315-330-4441
USAF/Rome Laboratory
OCDS
Griffiss AFB, NY 13441-5700

John W. Dettmer
Bus. Phone:
Lockheed Missiles and Space Company
1601 Randolph Road, SE
Suite 210 South
Albuquerque, NM 87119

Ted A. Doederlein
Bus. Phone: 805-275-5483
Air Force
OLAC PL/STSS
Edwards AFB, CA 93523

Daniel B. Eldred
Bus. Phone: 818-354-6519
Jet Propulsion Laboratory
Mail Stop 198-326
4800 Oak Grove Drive
Pasadena, CA 91109

Dr. Kenny B. Elliott
Bus. Phone: 804-864-4359
NASA Langley Research Center
Mail Stop 230
Hampton, VA 23665-5225

Andy M. Engelhardt
Bus. Phone: 602-561-3482
Honeywell, Inc.
P. O. Box 52199
Phoenix, AZ 85072-2199

Dr. James L. Fanson
Bus. Phone: 818-354-7014
Jet Propulsion Laboratory
Mail Stop 157-316
4800 Oak Grove Drive
Pasadena, CA 91109

Clarence J. Fennell
Bus. Phone: 505-846-4703
Phillips Laboratory
PL/VTS
Kirtland AFB, NM 87117-6008

Dr. Shalom "Mike" Fisher
Bus. Phone: 202-767-3914
Naval Research Laboratory
Code 8240.1
Washington, DC 20375-5000

Anthony Fontana
Bus. Phone: 804-864-6491
NASA Langley Research Center
Mail Stop 298
Hampton, VA 23665-5225

Eugene R. Fosness
Bus. Phone: 505-846-1338
Phillips Laboratory
PL/VTSA
Kirtland AFB, NM 87117-6008

Rodney Galloway
Bus. Phone: 505-846-1338
Phillips Laboratory
PL/VTSA
Kirtland AFB, NM 87117-6008

Dr. Joseph F. Garibotti
Bus. Phone: 714-545-8825
Ketema
Advanced Materials Group
3611 South Harbor Boulevard
Suite 225
Santa Ana, CA 92704-6928

Michael Garnek
Bus. Phone: 215-354-3827
General Electric Company
Astro Space Division
P. O. Box 8555, Bldg 100, M4018
Philadelphia, PA 19101

Margaret N. Giesecking
Bus. Phone: 804-864-6493
NASA Langley Research Center
Mail Stop 298
Hampton, VA 23665-5225

Ray E. Gogan
Bus. Phone: 407-727-6293
Harris Corporation
P. O. Box 94000
Melbourne, FL 32902

Stephen C. Gould
Bus. Phone: 505-846-1338
Phillips Laboratory
PL/VTSA
Kirtland AFB, NM 87117-6008

Joel Greenstein
Bus. Phone: 407-352-3700
Coleman Research Corporation
5950 Lakehurst Drive
Orlando, FL 32819

Steven F. Griffin
Bus. Phone: 805-275-5304
USAF
OLAC PL/STSS
Edwards AFB, CA 93523

Angel Garnica
Bus. Phone: 818-354-1903
Jet Propulsion Laboratory
4800 Oak Grove Drive
Mail Stop 158/224
Pasadena, CA 91109

Michael G. Gilbert
Bus. Phone: 804-864-2839
NASA Langley Research Center
Mail Stop 297
Hampton, VA 23665-5225

A. Ernesto (Ernie) Golan
Bus. Phone: 714-531-7340
Consultant
11069 Sudith Avenue
Fountain Valley, CA 92708

William L. Grantham
Bus. Phone: 804-864-6494
NASA Langley Research Center
Mail Stop 298
Hampton, VA 23665-5225

Joseph W. Gregory
Bus. Phone: 804-864-4358
Lockheed Engineering and Sciences
NASA Langley Research Center
Mail Stop 230
Hampton, VA 23665-5225

Marc Gronet
Bus. Phone: 408-756-5673
Lockheed Missiles and Space Company
ORG/6N-24, Bldg 579
1111 Lockheed Way
Sunnyvale, CA 94089-3504

Sandeep Gupta
Bus. Phone: 804-864-4054
Vigyan, Inc.
NASA Langley Research Center
Mail Stop 230
Hampton, VA 23665-5225

Dr. Fred Y. Hadaegh
Bus. Phone: 818-354-8777
Jet Propulsion Laboratory
Mail Code 198-318
4800 Oak Grove Drive
Pasadena, CA 91109

Nesbitt W. Hagood
Bus. Phone: 617-253-2738
Massachusetts Inst. of Technology
77 Massachusetts Avenue
Room 33-313
Cambridge, MA 02139

Mike Hagopian
Bus. Phone: 301-286-7854
NASA Goddard Space Flight Center
Mail Code 716.5
Greenbelt, MD 20771

Brian J. Hamilton
Bus. Phone: 602-561-3554
Honeywell
P. O. Box 52199, Mail Stop 2P9
Phoenix, AZ 85072-2199

Brantley Hanks
Bus. Phone: 804-864-4322
NASA Langley Research Center
Mail Stop 297
Hampton, VA 23665-5225

Robert J. Hayduk
Bus. Phone: 202-453-2962
NASA Headquarters
Code RM
Washington, DC 20546

John M. Hedgepeth
Bus. Phone: 805-569-1344
Astro Aerospace Corporation
202 E. Pedregosa Street
Santa Barbara, CA 93101

John Higgins
Bus. Phone: 505-846-1338
Phillips Laboratory
PL/VTSA
Kirtland AFB, NM 87117-6008

Lucas G. Horta
Bus. Phone: 804-864-4352
NASA Langley Research Center
Mail Stop 230
Hampton, VA 23665-5225

J. Warren Hoskins
Bus. Phone: 408-742-6560
Lockheed Missiles and Space Company
P. O. Box 3504
B/551, D/77-50
Sunnyvale, CA 94088-3504

Stuart Hsu
Bus. Phone: 602-561-3485
Honeywell, Inc.
P. O. Box 52199
Phoenix, AZ 85072

Tuyen Hua
Bus. Phone: 713-483-8296
NASA Johnson Space Center
Mail Code EG2
Houston, TX 77058

Daniel J. Inman
Bus. Phone: 716-636-2733
State Univ. of New York at Buffalo
Department of Mech. and Aero.
Buffalo, NY 14260

A. Dean Jacot
Bus. Phone: 206-773-8629
Boeing Aerospace Company
P.O. Box 3999, MS 82-23
Seattle, WA 98124

Robert N. Jacques
Bus. Phone: 617-253-3267
Massachusetts Inst. of Technology
77 Massachusetts Avenue
Room 37-391
Cambridge, MA 02139

Bruce G. Johnson
Bus. Phone: 617-661-0540 x207
SatCon Technology Corporation
12 Emily Street
Cambridge, MA 02139-4507

Conor D. Johnson
Bus. Phone: 415-494-7351
CSA Engineering, Inc.
2850 W. Bayshore Road
Palo Alto, CA 94306-3843

Victoria L. Jones
Bus. Phone: 205-882-2650
Logicon Control Dynamics
600 Blvd. S., Suite 304
Huntsville, AL 35802

Dr. Jer-Nan Juang
Bus. Phone: 804-864-4351
NASA Langley Research Center
Mail Stop 297
Hampton, VA 23665-5225

Prof. John L. Junkins
Bus. Phone: 409-845-3912
Texas A&M University
Aerospace Engineering Department
Room 701 Bright Building
College Station, TX 77843-3141

Claude R. Keckler
Bus. Phone: 804-864-1716
NASA Langley Research Center
Mail Stop 479
Hampton, VA 23665-5225

Sean P. Kenny
Bus. Phone: 804-864-6612
NASA Langley Research Center
Mail Stop 230
Hampton, VA 23665-5225

Dr. Farshad Khorrami
Bus. Phone: 718-260-3227
Polytechnic University
Dept. of Electrical Engineering
Six Metrotech Center
Brooklyn, NY 11201

Dr. Narendra S. Khot
Bus. Phone: 513-255-6992
WL/FIBRA
WPAFB, OH 45433-6553

Jim A. King
Bus. Phone: 407-727-2140
Harris Corporation
Government Aerospace Systems Div.
Mail Stop 22/4847
P. O. Box 94000
Melbourne, FL 32902

Andy Kissil
Bus. Phone: 818-354-8479
Jet Propulsion Laboratory
Building 157-410
4800 Oak Grove Drive
Pasadena, CA 91109

Robert L. Kittyle
Bus. Phone: 719-472-4088
USAF
HQ USAFA/DFAS
USAF Academy, CO 80840

Roy E. Klusendorf
Bus. Phone: 805-684-6641
Astro Aerospace Corporation
6384 Via Real
Carpinteria, CA 93013-2920

Timothy Kreitinger
Bus. Phone: 505-846-1338
Phillips Laboratory
PL/VTSA
Kirtland AFB, NM 87117-6008

Thomas J. H. Lange
Bus. Phone: 49-8153-28-1177
DLR/GSOC
Munchnerstr. 20
D-8031 Oberpeffenhofen
GERMANY

Charles R. Larson
Bus. Phone: 310-922-2031
Rockwell International
Mail Stop AD88
12214 Lakewood Boulevard
Downey, CA 90241

Robert W. Lashlee, Jr.
Bus. Phone: 314-341-6172
USAF
UMR Rolla MO
1105 Joyce Avenue
Rolla, MO 65401

Dr. Robert A. Laskin
Bus. Phone: 818-354-5086
Jet Propulsion Laboratory
Mail Stop 198-326
4800 Oak Grove Drive
Pasadena, CA 91109

James P. Lauffer
Bus. Phone: 505-844-5176
Sandia National Laboratories
Org. 2743
P. O. Box 5800
Albuquerque, NM 87185

Marie B. Levine-West
Bus. Phone: 818-354-6273
Jet Propulsion Laboratory
4800 Oak Grove Drive
Mail Stop 157-316
Pasadena, CA 91109

Dr. Kyong B. Lim
Bus. Phone: 804-864-4342
NASA Langley Research Center
Mail Stop 161
Hampton, VA 23665-5225

Chiang Lin
Bus. Phone: 713-333-7061
Lockheed Engineering & Science
2400 NASA Road 1
Houston, TX 77058-3799

Yeongching Lin
Bus. Phone: 333-8502
Dynacs Engineering Co., Inc.
1110 NASA Road One, Suite 650
Houston, TX 77058

Doug Looze
Bus. Phone: 413-545-0973
University of Massachusetts
Dpt of Electrical and Computer Eng
Amherst, MA 01003

Boris J. Lurie
Bus. Phone: 818-354-3690
Jet Propulsion Laboratory
4800 Oak Grove Drive
Mail Stop 198/326
Pasadena, CA 91109

Lt. John R. Mackaman
Bus. Phone: 513-255-5236 X406
Wright Laboratory, USAF
WL/FIBG
WPAFB, OH 45433-6553

H. Bruce Mackay
Bus. Phone: 619-458-4702
SAIC
4161 Campus Point Court
San Diego, CA 92121

Dr. Peiman G. Maghami
Bus. Phone: 804-864-4039
NASA Langley Research Center
Mail Stop 230
Hampton, VA 23665-5225

Richard M. Martin
Bus. Phone: 805-275-5354
USAF
OLAC PL/STS
Edwards AFB, CA 93523-5000

David R. Martinez
Bus. Phone: 505-844-1457
Sandia National Laboratories
Org. 1434
P. O. Box 5800
Albuquerque, NM 87185

Mark D. McLaren
Bus. Phone: 415-852-4767
Space Systems/LORAL
Mail Stop G76
3825 Fabian Way
Palo Alto, CA 94303

Dr. David W. Miller
Bus. Phone: 617-253-3288
Massachusetts Inst. of Technology
Space Engineering Research Center
Room 37-371
70 Vassar Street
Cambridge, MA 02139

Mark H. Milman
Bus. Phone: 818-354-3627
Jet Propulsion Laboratory
Mail Stop 198-326
4800 Oak Grove Drive
Pasadena, CA 91109

Michael G. Moeller
Bus. Phone: 407-729-7141
Harris Corporation
Gov. Aerospace & Systems Division
P. O. Box 94000, MS 19-4737
Melbourne, FL 32902

Dr. Raymond C. Montgomery
Bus. Phone: 804-864-6615
NASA Langley Research Center
Mail Stop 161
Hampton, VA 23665-5225

Dr. Ibrahaim A. Murra
Bus. Phone: 416-790-2800X4787
SPAR Aerospace Limited
9445 Airport Road
Brampton, Ontario
CANADA L6S4J3

Gregory W. Neat
Bus. Phone: 818-354-0584
Jet Propulsion Laboratory
Mail Stop 198-326
4800 Oak Grove Drive
Pasadena, CA 91109

R. Rory Ninneman
Bus. Phone: 505-846-4699
Phillips Laboratory
PL/VTSA
Kirtland, NM 87117-6008

Jerrel R. Mitchell
Bus. Phone: 614-593-1566
Ohio University
Stocker Center 327
Athens, OH 45701

James B. Mohl
Bus. Phone: 303-939-5064
Ball Space Systems Division
Mail Stop CO-10B
P. O. Box 1062
Boulder, CO 80306-1062

R. Jorge Montoya
Bus. Phone: 919-541-6807
Research Triangle Institute
P. O. Box 12194
Research Triangle Park, NC 27709

James J. Murray
Bus. Phone: 703-834-3796
General Electric
924 Riva Ridge Drive
Great Falls, VA 22066-1619

Jerry R. Newsom
Bus. Phone: 804-864-6488
NASA Langley Research Center
Mail Stop 298
Hampton, VA 23665-5225

John F. O'Brian
Bus. Phone: 818-354-1250
Jet Propulsion Laboratory
4800 Oak Grove Drive
Pasadena, CA 91109

Robert P. O'Donnell
Bus. Phone: 703-385-0723
MRT, Inc.
10455 White Granite Drive
Oakton, VA 22124

Hayrani Oz
Bus. Phone: 614-292-3843
Ohio State University
Bolz Hall
2036 Neil Avenue Mall, Rm 328
Columbus, OH 43210

Dr. Eric K. Parsons
Bus. Phone: 415-424-2654
Lockheed Missiles & Space Co., Inc.
Research and Development
Department 92-30, Building 281
3251 Hanover Street
Palo Alto, CA 94304-1191

Janet Perrault
Bus. Phone: 805-275-5219
USAF
OLAC PL/STS
Edwards AFB, CA 93523-5000

Jerome Pearson
Bus. Phone: 513-255-6622
Wright Laboratory
WL/FIBG
WPAFB, OH 45433-6553

Doug J. Phillips
Bus. Phone: 407-727-6239
Harris Corporation
P. O. Box 94000
Melbourne, FL 32901

Lee D. Peterson
Bus. Phone: 303-492-1743
University of Colorado
Campus Box 429
Boulder, CO 80309-0429

Tom Pollock
Bus. Phone: 409-845-1686
Texas A&M University
Aerospace Engineering
College Station, TX 77843-3141

Brett J. Pokines
Bus. Phone: 716-636-2199
State Univ. of New York at Buffalo
Mechanical & Aerospace Engineering
1012 Furnus Hall
Amherst, NY 14260

Karim S. Qassim
Bus. Phone: 505-846-4704
Phillips Laboratory
PL/VTSA
Kirtland AFB, NM 87117-6008

Dr. Douglas B. Price
Bus. Phone: 804-864-6605
NASA Langley Research Center
Mail Stop 161
Hampton, VA 23665-5225

Ralph W. Quan
Bus. Phone: 719-472-3122
United States Air Force Academy
Frank J. Seiler Lab, USAFA
Colorado Springs, CO 80840

Zahidul H. Rahman
Bus. Phone: 818-354-3659
Jet Propulsion Laboratory
4800 Oak Grove Drive
Mail Stop 157-316
Pasadena, CA 91109

Dr. Kenneth E. Richards, Jr.
Bus. Phone: 303-971-9376
Martin Marietta Astronautics
P. O. Box (MS H4330)
Denver, CO 80201

Linda B. Rowell
Bus. Phone: 804-864-1718
NASA Langley Research Center
Mail Stop 479
Hampton, VA 23665-5225

Celeste M. Satter
Bus. Phone: 818-354-9246
Jet Propulsion Laboratory
Mail Stop 157-410
4800 Oak Grove Drive
Pasadena, CA 91109

Dr. Eric Schmitz
Bus. Phone: 303-971-2732
Martin Marietta Civil Space & Comm.
MS 4372
P. O. Box 179
Denver, CO 80201

Kendall W. Sherman
Bus. Phone: 804-864-6488
NASA Langley Research Center
Mail Stop 298
Hampton, VA 23665-5225

Prof. Vittal S. Rao
Bus. Phone: 314-341-6371
University of Missouri-Rolla
Intelligent Systems Center
Rolla, MO 65401

John M. Richardson
Bus. Phone: 505-846-4693
Phillips Laboratory
PL/VTSA
Kirtland AFB, NM 87117-6008

Chris A. Sandridge
Bus. Phone: 804-864-2816
Lockheed Engineering & Sciences Co.
NASA Langley Research Center
Mail Stop 230
Hampton, VA 23665-5225

Ian R. Scarle
Bus. Phone: 206-773-2046
Boeing Defense & Space Group
P. O. Box 3999
Mail Stop 82-97
Seattle, WA 98124

Sherman Seltzer
Bus. Phone: 205-379-3428
Consultant
2786 Hurricane Road
New Market, AL 35761

Samuel W. Sirlin
Bus. Phone: 818-354-8484
Jet Propulsion Laboratory
Mail Stop 198-326
4800 Oak Grove Drive
Pasadena, CA 91109

Joseph C. Slater
Bus. Phone: 716-636-3977
State Univ. of New York at Buffalo
Mechanical & Aerospace Engineering
Buffalo, NY 14260

Andrew J. Smith
Bus. Phone: 505-846-4706
Phillips Laboratory
PL/VTSA
Kirtland AFB, NM 87117-6008

Dr. Suzanne W. Smith
Bus. Phone: 606-257-4584
University of Kentucky
Dept. of Engineering Mechanics
467 Anderson Hall
Lexington, KY 40506-0046

Monty J. Smith
Bus. Phone: 805-275-5348
DOD Phillips Laboratory
Lancaster, CA 93536

Rudeen Smith-Taylor
Bus. Phone: 804-864-6490
NASA Langley Research Center
Mail Stop 298
Hampton, VA 23665-5225

Rose Marie Snow
Bus. Phone: 513-255-5200 X251
Wright Laboratory
WL/FIBG
WPAFB, OH 45433-6553

John T. Spanos
Bus. Phone: 818-354-6572
Jet Propulsion Laboratory
Mail Stop 198-326
4800 Oak Grove Drive
Pasadena, CA 91109

Dean W. Sparks, Jr.
Bus. Phone: 804-864-4349
NASA Langley Research Center
Mail Stop 230
Hampton, VA 23665-5225

Dr. Victor A. Spector
Bus. Phone: 310-814-6304
TRW Inc.
R9/2181
One Space Park
Redondo Beach, CA 90278

Captain Daniel J. Stech
Bus. Phone: 719-472-3122
FJSRL/NA
USAF Academy, CO 80840-6528

Tzu-Jeng Su
Bus. Phone: 804-864-4395
NASA Langley Research Center - NRC
National Research Council
Mail Stop 230
Hampton, VA 23665-5225

John Sudey, Jr.
Bus. Phone: 301-286-8908
NASA Goddard Space Flight Center
Mail Code 716.0
Greenbelt, MD 20771

Jeff L. Sulla
Bus. Phone: 804-864-4348
Lockheed Engineering & Sciences Co.
NASA Langley Research Center
Mail Stop 230
Hampton, VA 23665-5225

Lee F. Sword
Bus. Phone: 818-354-1908
Jet Propulsion Laboratory
4800 Oak Grove Drive
Mail Stop 158-224
Pasadena, CA 91109

George A. Tan
Bus. Phone: 804-864-6621
Lockheed Engineering & Sciences Co.
NASA Langley Research Center
Mail Stop 161
Hampton, VA 23665-5225

Ms. Sharon E. Tanner
Bus. Phone: 804-864-4353
NASA Langley Research Center
Mail Stop 230
Hampton, VA 23665-5225

Lawrence W. Taylor, Jr.
Bus. Phone: 804-864-4040
NASA Langley Research Center
Mail Stop 489
Hampton, VA 23665-5225

Nimfa C. Teneza
Bus. Phone: 202-404-8338
Naval Research Laboratory
Code 8240
Washington, DC 20375-5000

Dr. A. Fernando Tolivar
Bus. Phone: 818-354-6215
Jet Propulsion Laboratory
4800 Oak Grove Drive
MS 198-330
Pasadena, CA 91109

Dr. John J. Tracy
Bus. Phone: 714-896-1534
McDonnell Douglas Space Systems Co.
5301 Bolsa Avenue
Mail Station A3-Y857-13/3
Huntington Beach, CA 92647

Dr. Hubert Troidl
Bus. Phone: 089/6088-3905
IABG
Department TRV
Einsteinstrabe 20
D-8012 Ottobrunn
GERMANY

Ben K. Wada
Bus. Phone: 818-354-3600
Jet Propulsion Laboratory
Mail Stop 157-507
4800 Oak Grove Drive
Pasadena, CA 91109

Dr. Henry B. Waites
Bus. Phone: 205-544-1441
NASA Marshall Space Flight Center
Mail Stop ED12
MSFC, AL 35812

J. M. (Mel) Waldman
Bus. Phone: 408-756-4498
Lockheed Missiles and Space Company
P. O. Box 3504
Building 579, Organization 6N-24
Sunnyvale, CA 94088-3504

David W. Walsh
Bus. Phone: 602-561-4116
Honeywell
P. O. Box 52199
Phoenix AZ 85072-2199

James F. Walton
Bus. Phone: 518-785-2477
Mechanical Technology Incorporated
968 Albany Shaker Road
Latham, NY 12110

Dr. Shyh J. (Don) Wang
Bus. Phone: 818-354-7288
Jet Propulsion Laboratory
Mail Stop TR1711
4800 Oak Grove Drive
Pasadena, CA 91109

Donald C. Washburn
Bus. Phone: 505-846-1338
Phillips Laboratory
PL/VTSA
Kirtland AFB, NM 87117-6008

Major Steven G. Webb
Bus. Phone: 719-472-2196
USAF Academy
HQ USAFA/DFEM
USAF Academy, CO 80840-5000

Mark S. Webster
Bus. Phone: 818-354-1212
Jet Propulsion Laboratory
4800 Oak Grove Drive
Mail Stop 157-316
Pasadena, CA 91109

Edward V. White
Bus. Phone: 314-232-1479
McDonnell Douglas Missile Systems
Mail Code 3064275
P. O. Box 516
Saint Louis, MO 63166

Dr. Trevor Williams
Bus. Phone: 513-556-3221
University of Cincinnati
Dept. of Aero. Eng. & Eng. Mechanics
ML 70
Cincinnati, OH 45221

Chin (John) Won
Bus. Phone: 804-864-8225
Lockheed Engineering and Sciences
NASA Langley Research Center
Mail Stop 230
Hampton, VA 23665-5225

Stanley E. Woodard
Bus. Phone: 804-864-4053
NASA Langley Research Center
Mail Stop 230
Hampton, VA 23665-5225

Shih-Chin Wu
Bus. Phone: 804-864-4355
Lockheed Engineering & Sciences Co.
NASA Langley Research Center
Mail Stop 230
Hampton, VA 23665-5225

Spencer T. Wu
Bus. Phone: 202-767-6962
AFOSR
Bolling AFB
Washington, DC 20332-6448

Y. C. Yiu
Bus. Phone: 408-742-4048
Lockheed Missiles & Space Co., Inc.
1111 Lockheed Way
B/551, O/7750
Sunnyvale, CA 94089-3504

Joseph S.C. Yuan
Bus. Phone: 416-745-9682X6763
SPAR Aerospace Limited
1700 Ormont Drive
Weston, Ontario
CANADA M9L2W7

Brad J. Yost
Bus. Phone: 805-275-5304
Wyle Laboratories
OLAC PL/VTSS E
Edwards AFB, CA 93523-5000

Dr. David C. Zimmerman
Bus. Phone: 904-392-6229
University of Florida
231 Aerospace Building
Gainesville, FL 32611

Total Number of Attendees: 184

PART 1

SESSION I

Chairman: Henry B. Waites
Marshall Space Flight Center
Huntsville, Alabama

Co-Chairman: Capt. Ted Doederlein
Phillips Laboratory
Edwards AFB, California

The Mini-Mast CSI Testbed: Lessons Learned

S.E. Tanner, W.K. Belvin, L.G. Horta and R.S. Pappa

NASA Langley Research Center

Abstract

The Mini-Mast testbed was one of the first large scale Controls-Structure-Interaction (CSI) systems used to evaluate state-of-the-art methodology in flexible structure control.[1] Now that all the testing at Langley Research Center has been completed, a look back is warranted to evaluate the program. This paper describes some of the experiences and technology development studies by NASA, university, and industry investigators. Lessons learned are presented from three categories: the testbed development, control methods, and the operation of a guest investigator program. It is shown how structural safety margins provided a realistic environment to simulate on-orbit CSI research, even though they also reduced the research flexibility afforded to investigators. The limited dynamic coupling between the bending and torsion modes of the cantilevered test article resulted in highly successful SISO and MIMO controllers. However, until accurate models were obtained for the torque wheel actuators, sensors, filters, and the structure itself, most controllers were unstable. Controls research from this testbed should be applicable to cantilevered appendages of future large space structures.

Lessons Learned: Controls Methods

Just as modeling played a key role in readying the testbed for guest investigators' use, it also was the first consideration for controls designers. The finite element model developed by NASA to represent the structural dynamics of the truss structure was found to be adequate for accurately predicting the low- frequency dynamics of the flexible test article. However, the best dynamic representation of the full system was obtained from experimentally identified models. Models based on system identification could include the dynamics of actuators and sensors and the computational delays within the system, in addition to the structural dynamics of the truss. Whether the application was controls implementation or failure detection, identified models were found to be preferable over FEM-based models for capturing system level dynamics.

With its decoupled dynamics, the Mini-Mast testbed could be controlled with classical single-input single-output (SISO) techniques. This success emphasized the potential of controlling some appendages on future space platforms via simple classical techniques. The simplicity of parameterization with the classical methods has the distinct advantage of providing physical insight into the system being controlled.

Modern controls techniques were also successful in providing substantial amounts of damping to the system's response. These multi-input multi-output (MIMO) designs share a common difficulty, however. The parameterization via weighting matrices lacks the physical insight provided by classical SISO techniques, making a priori performance predictions difficult. In fact, while in theory the parameters for modern MIMO controllers would encompass the control-space of any SISO controller, no modern controller was developed that could match the performance of an SISO constant gain feedback controller which was most effective in controlling the Mini-Mast first torsion mode.

Design Models

- FEM based models proved to be adequate for structural dynamics representation
- System ID models provide best dynamic representation of system (actuators/structure/sensors/computational delay)

Classical

- SISO design viable for systems with decoupled dynamics
- Simplicity of parameterization provides physical insight

Modern

- MIMO designs were successful in providing damping
- Difficult to prescribe performance a priori with weighting matrices (parameterization)
- Torsion mode controlled "best" by SISO constant gain feedback

Guest Investigator Studies

University and industry researchers applied a wide variety of techniques to the Mini-Mast testbed, as shown in this figure which highlights the methodology applied by each guest investigator who used the facility. A synopsis of the guest investigators' work with Mini-Mast, as well as their work at a second CSI facility, can be found in Ref. 1. In addition, numerous publications have been completed by individual investigators, providing more detailed reporting of their work. A listing of their publications on research with Mini-Mast is provided in the references.[4-19]

Five teams who used the Mini-Mast facility conducted controls experiments and one worked with failure detection and isolation applied to both sensors and actuators. Four groups designed controllers based on the NASTRAN finite element model developed by NASA. Two groups developed their own modal models of the testbed, but only one group used its experimentally derived model for controls design. Both classical and modern control theories were employed in creating SISO and MIMO controllers.

<u>Institution (Principal Investigator)</u>	<u>Methodology</u>
MIT (Wally Vander Velde)	Failure Detection and Isolation Methods
Arizona State University (Bong Wie)	Classical Theory with Disturbance Rejection, using collocated and noncollocated Sensors
Harris Corporation (Dave Hyland)	Maximum Entropy Optimal Projection; and Decentralized Hierarchical Control
CalTech (John Doyle) (Gary Balas)	H_{∞} and μ -Synthesis, with Additive and Multiplicative Uncertainties
University of Cincinnati (Randy Alleman) (Gary Slater)	System Identification; and Multivariable Positivity Control Design
Purdue University (Bob Skelton)	System identification using Q-Markov, Modal Cost Analysis, and Multivariable Control Design

Generic Controls Software

To minimize phase distortion, fast controller update commands are needed to digitally implement controllers designed using continuous time synthesis procedures. The "real-time" computer chosen for the Mini-Mast testbed was an existing CYBER-175 used at LaRC for aircraft flight simulation. However, software for this computer was not configured for typical linear state space controllers, so new software was developed for this application. The software was written to accommodate real-time implementation of any linear time invariant controller design; hence the term generic software is used.

The generic software is one of the key benefits derived from the Mini-Mast program. The FORTRAN program permits both system identification and vibration suppression experiments. Various excitation, filtering, controls, bias removal and data file generation software were developed, with the capability of using each function in either an open- or closed-loop mode of testing. A crucial part of the code was the limit-checking software required to prevent excessive response of the structure. This was necessary for the Mini-Mast testbed since relatively small displacements or twist angles could have resulted in buckling of the truss members.

The CYBER-175 could execute the control code at an update rate which was adequate for the research objectives of Mini-Mast. For example, it had an update rate of 80 Hz for a 40-state controller with 6 inputs and 3 outputs.

- **Implemented on existing CYBER-175**
- **Generic software developed to accommodate:**
 - Any linear time-invariant controller design
 - System ID and vibration suppression
 - Open- or closed-loop mode of testing
 - Excitation, filtering, bias removal, and
 - data file generation
Limit checking software included
- **Adequate update rate**
 - **(80 Hz update rate for a 40-state controller with 6 inputs and 3 outputs)**

CSI Pathfinder Testbed

Even as the CSI program was just beginning, it was clear that application of controls theory to realistic hardware would play an essential role in advancing CSI technology. A need was identified for a pathfinder CSI research program for early investigation of flexible space structure control. The rapid development and implementation of the Mini-Mast testbed fulfilled this need during the time period when other more complex testbeds were being developed. Three constraints were imposed by the overall objective: (1) that, wherever possible, the testbed emulate physical characteristics of future space structures or space structure components; (2) that the testbed operation be sufficiently flexible to accommodate multiple researchers with varied experiment objectives; (3) and that the testbed be brought on-line quickly. The last constraint resulted in the use of existing equipment that could be brought together to form the testbed. Existing sensors and actuators were incorporated, and software was developed so that the flight simulation computer at NASA Langley Research Center (LaRC) could be used as a real-time controls computer. Even the test article was an existing space-quality truss, called Mini-Mast, which had been used in a previous program.

Objective

Develop and implement a pathfinder CSI research test program for early investigation of flexible space structure control

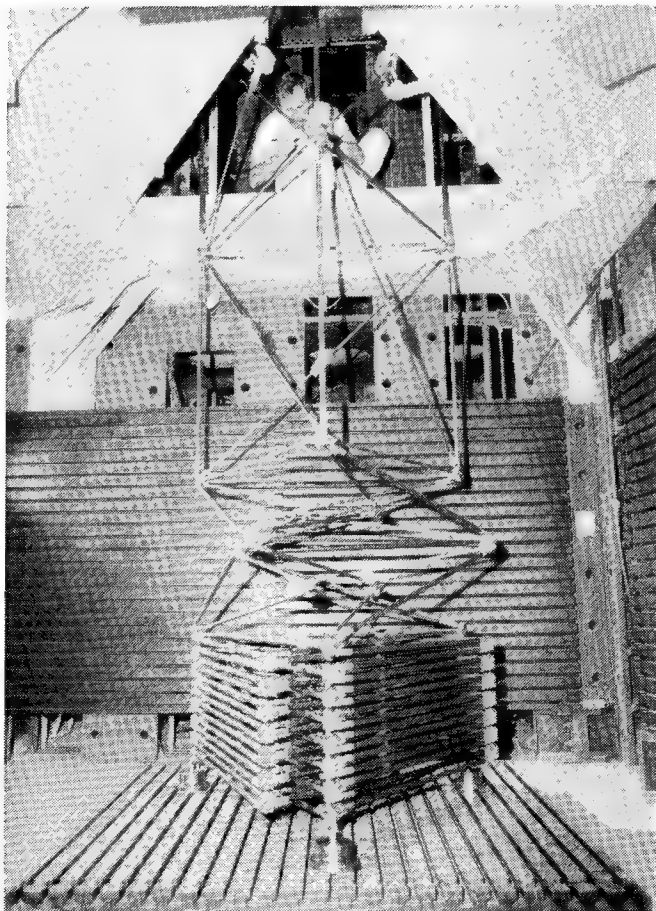
Constraints

- Emulate space component physical characteristics where possible**
- Provide for multiple experiment objectives and multiple researchers**
- Bring the CSI testbed on-line quickly**

Deployable Composite Truss

The truss structure, made of graphite epoxy tubes and titanium joints, extends from approximately 3 feet in a stowed configuration to approximately 65 feet when fully deployed. Both longeron members (parallel to the truss longitudinal axis) and diagonal members (in the face plane) have pinned connections to allow their rotation during deployment. Batten members, forming the triangular cross section, were fixed rigidly to the corner-body joints.

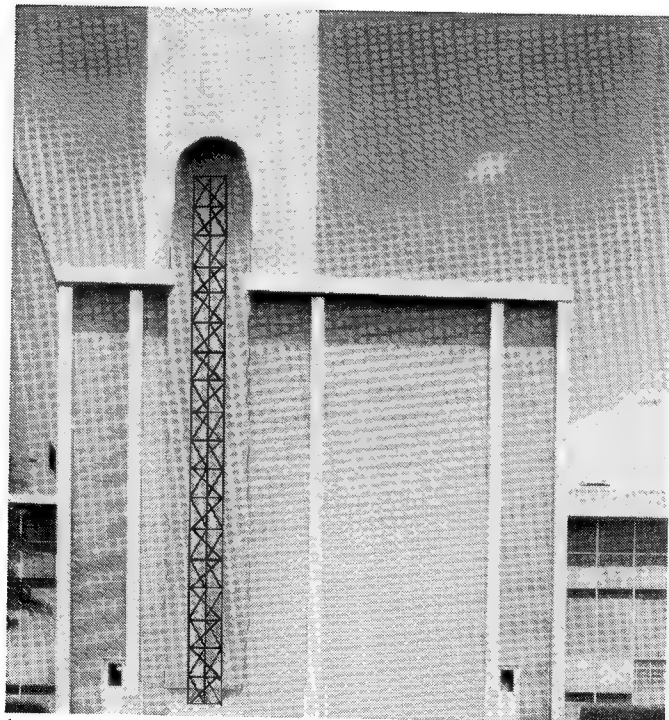
Diagonal members were also hinged to allow their folding during retraction and storage. These heavy hinges create clusters of localized bending modes, with 108 local modes between the system's pair of second bending modes at approximately 6.5 Hz and the second torsion mode at approximately 22 Hz. It is important to note that the diagonal modes do not involve the bending of only a single diagonal, but rather show localized displacements along the entire length of the structure and thus contribute to the testbed's complexity. The problem of clustered local modes is anticipated for future large space structures, such as clusters of solar array modes with Space Station Freedom.



Mini-Mast Structure

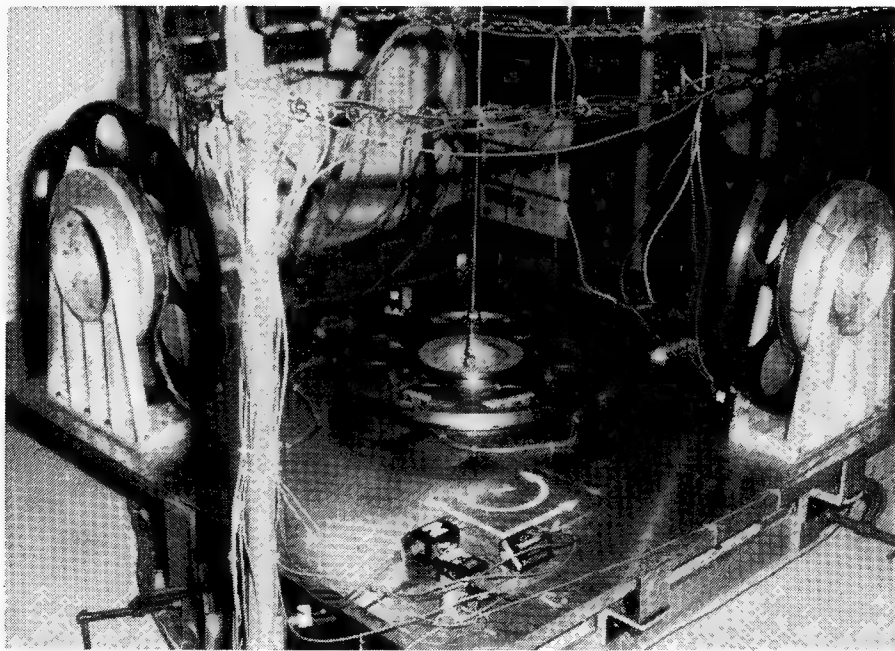
Mini-Mast was an existing 65 foot long deployable/retractable truss which was available for research purposes at the time of the testbed development. This prototype structure was one of the first flight-quality deployable space structures ever tested on the ground. In its cantilevered configuration in the tower of Building 1293B at NASA LaRC, the dynamic response of the truss was dominated by low frequency vibrational modes.[2] The pair of first bending modes of the structure was at approximately 0.86 Hz. Five target modes identified for control purposes were all below 10 Hz. They were the pair of first bending modes, the first torsional mode, and the pair of second bending modes. A full discussion of the dynamic characteristics of the structure and the validated finite element model can be found in Reference 3.

The truss was already instrumented with noncontacting displacement sensors mounted to the tower along the truss length. While the truss was used as the flexible-body structure for the pathfinder CSI testbed, external locks were in place on the diagonal truss member hinges to ensure they could not open during testbed operation.



Torque Wheel Actuators

The torque wheels, shown mounted on the tip plate prior to its installation on Mini-Mast, are angular momentum actuators used to impart control (or excitation) moments to the tip of the cantilevered truss. Oriented along three orthogonal axes and weighing approximately 80 pounds each, the actuators provided ample control authority in the frequency range of interest. The actuators are comprised of two sections, the center hub where the motor resides and a 24 in. diameter annular ring connected to the hub. The motor is a permanent magnet motor with a rated 50 ft-lbs peak torque at 50 volts and 9.6 amps. The wheel motor is driven by a high power, high frequency switching amplifier.



Introduction

Future space missions will most likely include large, flexible structures with high precision performance requirements. Control engineers and structural dynamicists will need to work together in an integrated effort to meet these requirements. Toward this purpose, NASA developed the multidisciplinary Controls-Structures-Interaction (CSI) Program to aid in the development and validation of CSI technology. Industry and university researchers are included through the Guest Investigator (GI) Program, providing participants the opportunity to validate experimentally CSI methodology on ground-test hardware and thereby improve the understanding of the practical performance characteristics of promising active-vibration-control techniques which may be applied to future space structures.

The Mini-Mast testbed at NASA Langley Research Center (LaRC) was one of two testbeds used in the first phase of the GI Program. Objectives of the testbed and testbed constraints will be discussed. A brief description of the testbed is presented, highlighting its major components and their modeling. Development of generic controls software, a significant benefit of this program, is discussed.

The structural safety margins and operational procedures created a realistic environment for space flight applications, but one that necessarily limited the research flexibility of guest investigators. Those guest investigators will be identified, together with the major topics they studied. Finally, recommendations will be presented in the form of lessons learned in three categories: the testbed development (including hardware, modeling and simulation) and software development; the control methods, covering design models as well as both classical and modern techniques; and the operation of a guest investigator program.

Outline

- **Objective**
- **Testbed Hardware/Modeling**
- **Generic Controls Software**
- **Operational Procedures**
- **Guest Investigator Studies**
- **Recommendations/Summary**

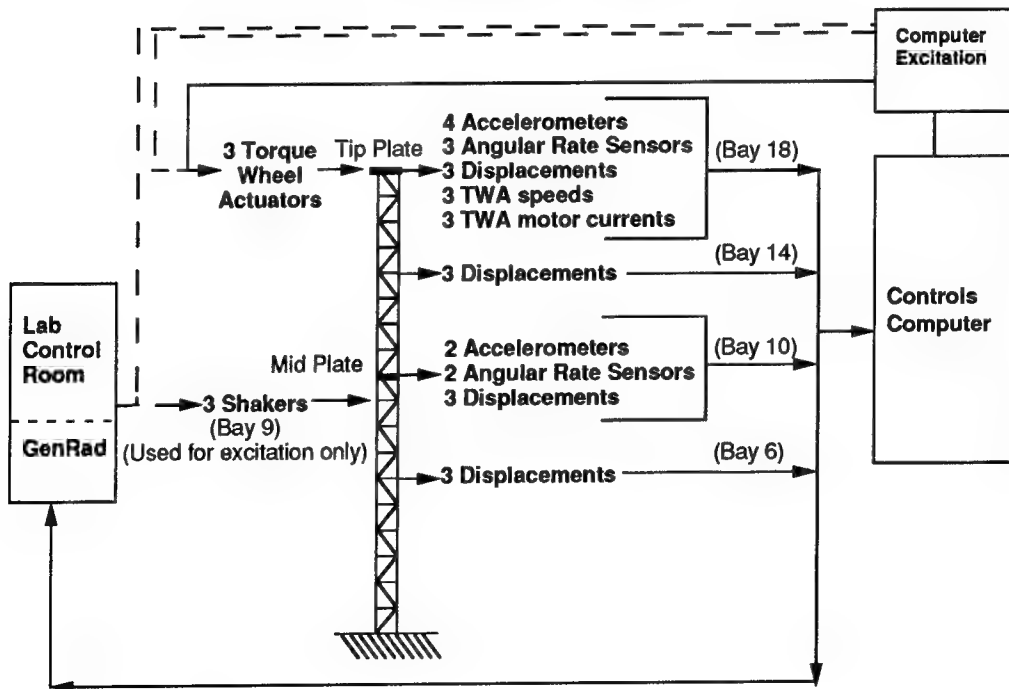
Mini-Mast Testbed Schematic

A schematic of the Mini-Mast testbed shows the integrated cantilevered truss with instrumentation linked via fiber optic cables to a real-time computer for excitation and control. The second computer connected to the system (GenRad) was used for post-processing data. Three torque wheel actuators, mounted on the tip platform, were the only control effectors available through the GI program. Measurement sensors for wheel speed and actuator motor currents were also included. Excitation of the truss structure could be performed with the torque wheels or with shakers that were available at Bay 9 of the 18-bay truss. Shaker excitation could be initiated by either the controls computer or the laboratory computer.

Accelerometers and rate gyros were mounted on two platforms, one at the tip and the other near the mid-span of the truss, at Bay 10. Early in the program, five rate gyros were available--three at the tip-plate and two at the mid-plate. However, equipment failures reduced that number to one before the two year program was completed. At the end of the program, only one rate gyro was available. The surviving rate gyro was located on the tip plate measuring torsion about the longitudinal axis.

Noncontacting displacement sensors were distributed along the length of the truss, at each vertex of the triangular cross-section. These sensors were mounted to the tower along side the truss, thus providing absolute displacement measurements of the truss with respect to the tower. Displacement measurements from Bays 6, 10, 14, and 18 were linked to the computers and thus could be used for controls feedback if selected by guest investigators.

Mini-Mast Testbed



Mini-Mast Testbed Development

The flight quality truss added realism to the Mini-Mast CSI testbed, in line with the constraint that physical characteristics of future space structure components be emulated whenever possible. To ready the structure for use as a CSI testbed, equipment mounting platforms were added together with acceleration and rate sensors. Two equipment mounting platforms were designed, built and installed, one at the tip (Bay 18) and one near the midspan of the truss length (Bay 10). Existing servo accelerometers and rate gyro sensors were installed on the platforms, linked via fiber optic cables to an existing real-time computer. Torque wheel actuators, designed and built under a previous research program, were also included in the new testbed.

Mini-Mast Testbed Overview

- **Used available flight-quality truss**
- **Added equipment mounting platforms**
- **Installed existing actuators and sensors**
- **Linked signals to existing real-time computer**

Torque Wheel Actuators Characteristics

Initially the actuators operated in a current mode, i.e., voltage commands proportional to the current flowing to the motor. In this mode, modeling of the torque wheel dynamics should have reduced to a determination of a torque constant while the wheel was operating without feedback compensation. However, nonlinearities in the actuators made such simple models inaccurate. Proper characterization of the torque wheel dynamics was critical because the actuators were capable of buckling truss members. Ultimately, the nonlinearities led to modifications of the actuators that reduced their nonlinear response.

To minimize nonlinearities and facilitate modeling, feedback was introduced from a friction driven tachometer attached to the wheel. Using rate feedback, nonlinear effects were reduced significantly. In particular, the amplitude dependence of the transfer function was minimized, allowing the same model to be used at different excitation levels. With the local feedback loop in place, a second-order torque wheel model provided good agreement between the analytic predictions and experimentally derived measurements. This model, which was now a representation of the closed-loop torque wheel dynamics, was accurate for most of the test operating conditions.

Torque Wheel Actuators

- **Characteristics:**
 - Weigh 80 lbs. each
 - Provide 50 ft-lbs peak load
 - Nonlinear response
- **Local feedback loop added**
 - Linearized actuators
 - Facilitated modeling
- **2nd-order model provided good agreement**

Important Considerations of the Truss Structure

Some joint nonlinearities are present in the structure, causing both modal damping and modal frequency to increase with decreasing displacement amplitudes. Such nonlinearities add realism to the controls problem.

Dynamic coupling between torsion and bending modes is anticipated with CSI problems and future large space structures. Mini-Mast has limited coupling between the bending and torsion modes, and thus, research from this testbed is most applicable to beam-like structures such as cantilevered appendages on space platforms. In fact, the significant decoupling of the vibration modes allowed good closed-loop controls performance with single-input, single-output (SISO) controllers.

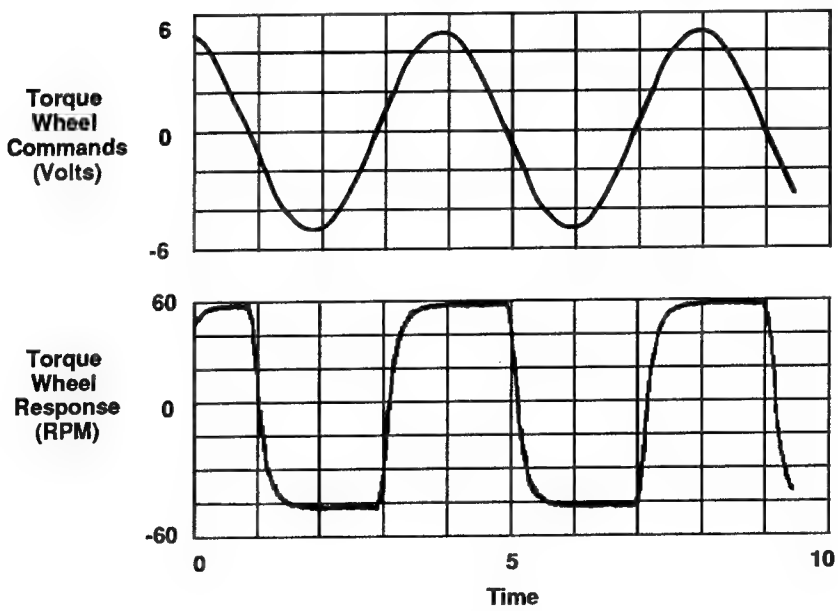
A safety concern resulted from the high compressive stresses at the base of the structure due to the vertical cantilevered configuration. These stresses could break the brittle graphite-epoxy truss members, and no replacement parts were available. Consequently, strict operational limitations were necessary to protect the structure; specifically, tip displacements were limited to 0.3 inches and tip rotations were limited to 0.15 degrees.

- **Realistic joints and nonlinearities**
- **Limited bending/torsion coupling**
- **Stress constraints resulted in strict operational limits on controls**

Torque Wheel Actuator Nonlinearities

Modeling the actuators was very difficult due to nonlinearities such as static/dynamic friction and impedance variations due to temperature changes. In addition, speed and current saturation limits were both frequency dependent. This figure shows the torque wheel actuator input commands in volts and actuator response in rpm during a typical test before any modifications were made to the actuators. The commanded sine wave was not reproduced due both to saturation and to the nonlinearities present in the devices. The amplitude dependence of the frequency response functions is not demonstrated in this figure. Attempts to experimentally determine some of the nonlinear parameters failed to produce an analytical model which would be accurate throughout the operating range of interest.

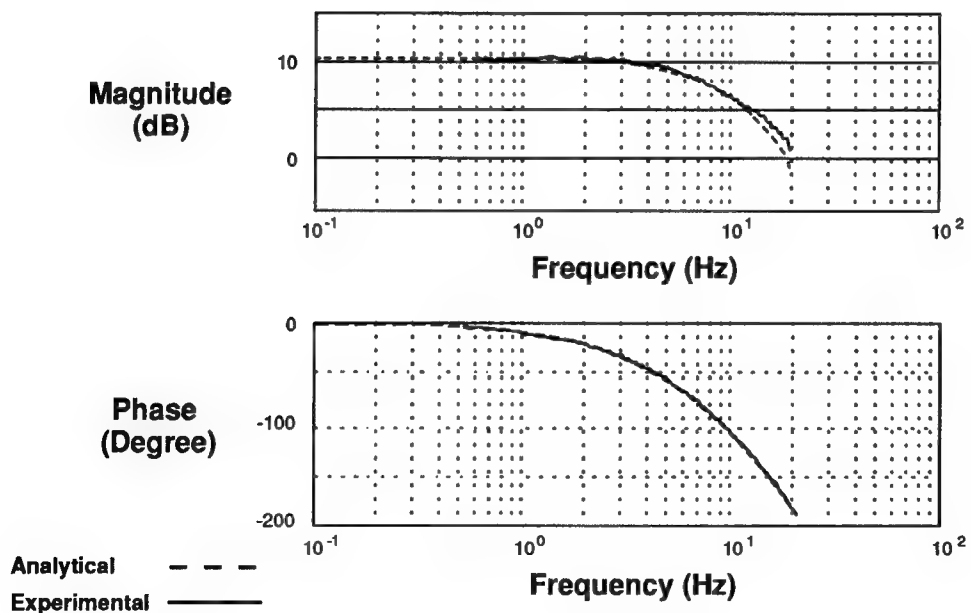
Torque Wheel Actuator Nonlinear Characteristics



Analytical Models of the Torque Wheel Actuators

Once the local feedback loop was created for each of the torque wheel actuators, parameters were experimentally obtained to create a second- order torque wheel model for use in subsequent analyses. This model, now a representation of the closed-loop torque wheel dynamics, was accurate for most of the test operating conditions. This figure compares the experimentally determined transfer function for one of the torque wheels, shown in the solid line, and its second order analytical model developed from experimental parameters, shown in the dashed line. The agreement between the transfer functions is sufficient for control purposes on the Mini-Mast testbed.

Torque Wheel Actuator Dynamics with Local Feedback Loop

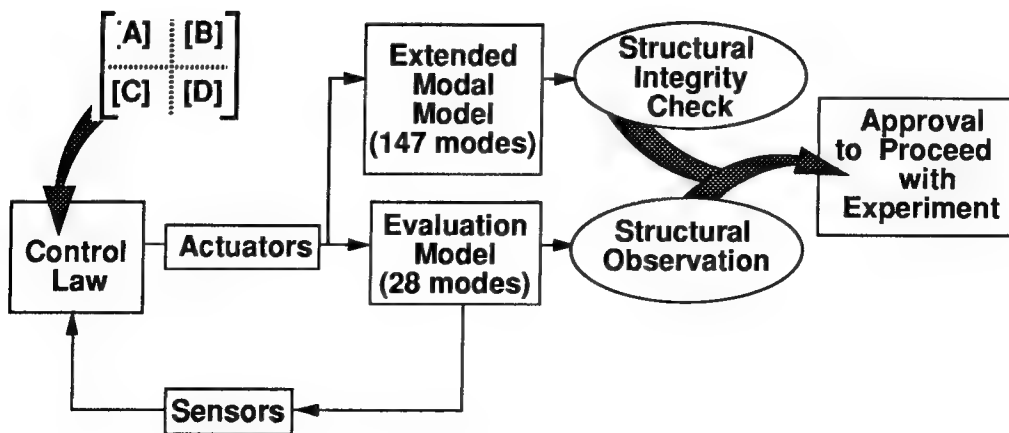


Pre-Test Approval Process

Through analysis, member loads were found to be sensitive not only to the amplitude of excitation and control commands but also to the relative phase between the shaker excitations and the actuator control moments. Therefore, in the absence of a reliable load measurement, a pretest approval process was instigated, as shown in this figure, to estimate the worst case loading on critical longeron and diagonal members.

Actuator and shaker time histories were created during closed-loop simulations, using a 28-mode evaluation model to represent the structural dynamics. Loads verification was accomplished by applying these load time histories in an open-loop transient analysis to a high fidelity finite element structural model comprised of 147 modes between 0 and 100 Hz.[3] The calculation of transient member loads was performed using a modal acceleration technique for improved accuracy. A conservative approach was again used in determining the worst-case single load: the maximum bending moment of any member in the truss was combined with the maximum axial load of any member, and these loads were assumed to act at the same time on a single member.

The time required for the loads calculation meant that each controller had to be submitted to the loads analysis group well before the controller could be implemented in the laboratory. The operational constraints imposed by the high stresses prevented changes to the controller by the researcher during testing, which is realistic for flight applications. Researchers were not able to immediately test the numerous "What if?" questions that arose; the investigation of unpredicted events that occurred while testing had to be delayed until additional loads analysis could be completed for the desired control law changes. However, on occasions during the GI program, small variations in control laws were permitted without additional simulation.



Lessons Learned: Testbed Development

A significant strength of the CSI program lies in the application of theory to actual, realistic hardware, thus eliminating the simplifying assumptions that can be made with purely analytical studies and requiring a certain degree of robustness in any control design. This may be the program's main contribution in advancing the respective control theories.

Operational constraints and requirements for thorough simulation of all control laws prior to implementation on the testbed added realism to the program but also limited the research flexibility afforded to the guest investigators. In addition, such constraints placed a strong emphasis on scheduling work to meet required deadlines.

Other hardware observations include the need for ample spares for key equipment. Specifically with respect to rate gyro sensors, the program experienced high rates of failure. Four of the five rate gyros failed within the two year program. Initially, the rate gyros were considered essential for low frequency control feedback sensors. However, the servo accelerometers proved to be viable feedback sensors in the 0.5-10 Hz frequency range. The high reliability and the inertial measurement available with accelerometers make them suitable for primary flexible-body control sensors.

The analysis and simulation efforts provided additional lessons during the testbed development. First, developing good mathematical models early in any test program is essential. In addition, extensive testing and model verification is an integral part of model development. For example, early torque wheel models were inadequate to cover the full range of actuator operation; ultimately, a local feedback loop was added to the actuators to make the devices more linear. As another example, while early analytical models of Mini-Mast structural dynamics were in good agreement with the preliminary experimental models, a more thorough analysis of the experimental data resulted in frequency shifts of up to 30 percent in higher modes. More extensive early studies might have allowed less stringent safety or operational constraints for protecting the test article.

Adopting a single tool for transferring control laws, dynamics models, or experimental data among program participants proved to be a strong benefit to the program, decreasing the potential for miscommunication. In addition, development of the generic software package for controls implementation has already been noted as a significant accomplishment of the program.

Hardware

- Application to realistic hardware provides crucial key to full development of CSI technology
- Real spacecraft operational constraints
 - Affect scheduling
 - Limit research flexibility
 - Require prioritizing
- Ample spares necessary for key equipment
- Accelerometers proved to be viable low frequency control sensors

Analysis & Simulation

- Develop good mathematical models early
- All participants should use a common modeling tool
- Generic software format proved valuable

Lessons Learned: Guest Investigator Program

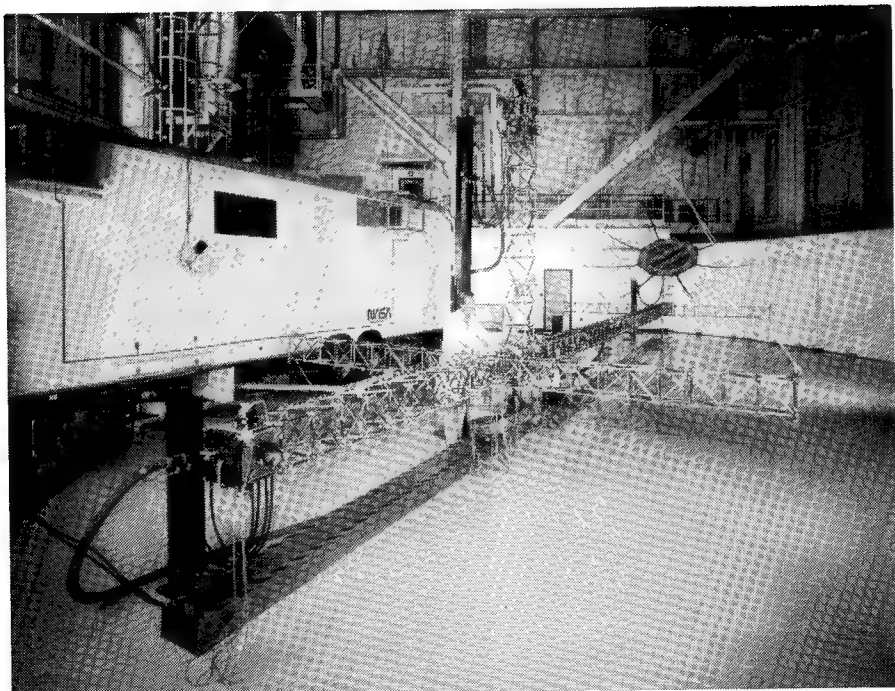
Some general observations can be made for the GI program as a whole. While miscommunications are likely to be a part of any human endeavor, they could be decreased by use of a well-controlled interface document. Rigorously abiding by established naming conventions for sensors, actuators, filters, and analytical models would prevent confusion. Including the date in the names of analytical models would ensure that all program participants were using the latest version of a given model. (This was particularly a problem early in the GI program when the torque wheel actuator models were changing frequently.) A standardized format for test plans could also be defined in such an interface document. Changes to test plans should only be accepted in written format; verbal changes are most likely to cause errors. Finally, the document should identify a single contact person for each outside researcher, a function established in the GI program through NASA technical monitors.

Considerable freedom was given to guest investigators using the Mini-Mast testbed. They determined their own research objectives, selected the method(s) they wished to apply, and determined which sensors and actuators to use. These freedoms, however, formed the basis for several concerns which could be addressed in future programs. First, by not focusing the group on a single objective, the ability was lost to compare the inherent value of various control methodologies. In addition, investigators were more likely to concentrate on controller performance while sacrificing a more generic application of the methodology.

- **Well-controlled interface documentation is critical but it limits experiment freedom**
- **Tendency to demonstrate successful controllers without exploring boundaries of the methodology**
- **Target performance objectives would allow comparison of methodologies**

Summary

The many lessons learned through the Mini-Mast testbed development and the associated guest investigator program have since been applied to new CSI testbeds, such as the CSI Evolutionary Model shown in this photograph. The necessity of applying theory to realistic hardware will continue to be emphasized throughout the CSI programs, advancing the technology to meet future challenges in large space structures.



References

1. Smith-Taylor, R. and Tanner, S.: *The Controls-Structures Interaction Guest Investigator Program - An Overview and Phase 1 Experimental Results*, NASA TM L-17052, January 1992.
2. Tanner, S. E., et.al.: *Mini-Mast CSI Testbed User's Guide*, NASA TM 102630, December 1991.
3. Stockwell, A. E; Perez, S. E; and Pappa, R. S.: *Integrated Modeling and Analysis of a Space-Truss Article*, NASA TM 102615, March 1990.
4. Van Schalkwyk, C. M. and Vander Velde, W. E.: Failure Detection and Isolation on the Mini-Mast Using Generalized Parity Relations. Presentation at the 2nd USAF/NASA Workshop on System Identification and Health Monitoring of Precision Space Structures, California Institute of Technology, Pasadena, California, March 27-29, 1990.
5. Vander Velde, W. E.: Monitoring the Health of Control System Components. Presentation at the US-Japan Workshop on Smart/Intelligent Materials and Systems, Honolulu, March 19-23, 1990.
6. Vander Velde, W. E. and Van Schalkwyk, C. M.: Failure Detection and Isolation Experiments with the Langley Mini-Mast. Proceedings of the American Control Conference, San Diego, May 23-25, 1990.
7. Webster, M. S.: The On-Orbit Identification of Nonlinear Systems. Presentation at the 2nd USAF/NASA Workshop on System Identification and Health Monitoring of Precision Space Structures, California Institute of Technology, Pasadena, California, March 27-29, 1990.
8. Webster, M. S. and Vander Velde, W. E.: Modeling Beam-Like Space Trusses with Nonlinear Joints. Presentation at the 32nd Structures, Structural Dynamics and Materials Conference, Baltimore, April 8-10, 1991.
9. Webster, M. S. and Vander Velde, W. E.: Application of a Robust Linear Control Design to a Truss Structure with Nonlinear Joints. Presentation at the 1991 AIAA Guidance, Navigation and Controls Conference, New Orleans, August 12-14, 1991.
10. Wie, B.: Active Vibration Control Synthesis for the COFS-I. *Journal of Guidance, Control and Dynamics*, Vol. 11, No. 6, 1988, pp. 271-276.
11. Wie, B. and Bernstein, D.: Benchmark Problems for Robust Control Design. Proceedings of the American Control Conference, San Diego, May 23-25, 1990, pp. 961-962.
12. Wie, B. and Gonzalez, M.: Control Synthesis for Flexible Space Structures Excited by Persistent Disturbances. *Journal of Guidance, Control, and Dynamics*, Vol. 15, No. 1, 1992. (Also, proceedings of AIAA Guidance, Navigation and Control Conference, August 1990, pp. 1022-1031.)
13. Wie, B., Horta, L., and Sulla, J.: Active Vibration Control Synthesis and Experiment for the Mini-Mast. *Journal of Guidance, Control and Dynamics*, Vol. 14, No. 4, 1991, pp. 778-784. (Also, proceedings of the American Control Conference, May 1990, pp 1428-1434.)
14. Collins, E. G., Jr., et. al.: Experimental Results in Active Control of the Mini-Mast and ACES Structures. *Proceedings of the Winter Annual Meeting of the ASME: Control for Aerospace Systems*, DSC-Vol 35, December 1991, pp. 27-34.
15. Collins, E. G., Jr. et. al. *High Performance, Accelerometer-Based Control of the Mini-MAST Structure at Langley Research Center*, NASA CR 4377, May 1991.
16. Balas, G. J. and Doyle, J.C.: Robustness and Performance Tradeoffs in Control Design for Flexible Structures. *Proceedings of the 29th IEEE Controls and Dynamics Conference*, Honolulu, December 1990.

17. Balas, Gary J., Young, Peter, and Doyle, John C.: The Process of Control Design for the NASA Langley Minimast Structure. *Proceedings of the American Control Conference*, Boston, June 26-28, 1991, Vol. 1, pp. 562-567.
18. Bosse, Albert and Slater, Gary: Digital Implementation of Vibration Suppression Controllers for LSS. Presented at the 8th VPISU Symposium on Dynamics and Control of Large Structures, Blacksburg, Virginia, May 1991.
19. Hsieh, C., Kim, J., and Skelton, R. E.: Closed Loop Lab Tests of NASA's Mini-MAST. *Proceedings of the 1990 American Control Conference*, San Diego May 1990, pp. 1441-1444.

**MODEL REDUCTION FOR THE DYNAMICS AND CONTROL OF LARGE
STRUCTURAL SYSTEMS VIA NEURAL NETWORK PROCESSING
DIRECT NUMERICAL OPTIMIZATION¹**

Georges A. Bécus and Alistair K. Chan
Aerospace Engineering and Engineering Mechanics
University of Cincinnati
Cincinnati, OH

ABSTRACT

Three neural network processing approaches in a direct numerical optimization model reduction scheme are proposed and investigated.

INTRODUCTION

Large structural systems, such as large space structures, offer new challenges to both structural dynamicists and control engineers. One such challenge is that of dimensionality. Indeed these distributed parameter systems can be modeled either by infinite dimensional mathematical models (typically partial differential equations) or by high dimensional discrete models (typically finite element models) often exhibiting thousands of vibrational modes usually closely spaced and with little, if any, damping. Clearly, some form of model reduction is in order, especially for the control engineer who can actively control but a few of the modes using system identification based on a limited number of sensors. Inasmuch as the amount of "control spillover" (in which the control inputs excite the neglected dynamics) and/or "observation spillover" (where neglected dynamics affect system identification) is to a large extent determined by the choice of a particular reduced model (RM), the way in which this model reduction is carried out is often critical.

Different techniques to obtain RM's have been proposed by various authors. While they are based on the same philosophy of retaining only those modes which play a significant role, they differ in the way the roles of the modes are quantified. Among these techniques we mention: (i) Modal Truncation; (ii) Balanced Controller Reduction; (iii) Component Cost Analysis; (iv) Optimal Projection Conditions; (v) Energy Based Model Reduction (also referred to as Modal Performance Tracking); (vi) Subsystem Balancing. (See [1] for references on methods (ii-iv), [2] and the references therein for method (v) and [3] for (vi).)

Model reduction can also be viewed as providing an answer to the question: What are the $m < n$ linear combinations of the $n \leq \infty$ states of the full model which best describe the behavior of the system? The various techniques only differ in the way "best" is defined. As such, model reduction is an optimization

¹ The work of both authors was supported in part by NASA-Lewis Research Center under Grant NAG3-1174.

problem. In fact, most model reduction schemes first attempt to find an analytical solution to the optimization problem, using necessary optimality conditions to obtain one or several equations to be satisfied by the solution and which can then be solved in an iterative numerical scheme. Viewed in this light, most currently available model reduction schemes suffer from three shortcomings: (i) they are restricted to optimality criteria for which a (partial) analytical solution to the optimization problem can be found, (ii) being based on necessary conditions, they cannot guarantee that the solution so obtained is the actual optimum sought, and (iii) the iterative numerical construction of the solution can be a formidable task. Recently, to alleviate the above shortcomings, we proposed to carry model reduction by direct numerical solution of the optimization problem [4]. In this paper we propose and investigate the use of neural network processing methods to carry out this direct optimization. First we review the direct numerical optimization approach proposed in [4].

DIRECT NUMERICAL OPTIMIZATION METHOD

Consider the n -th order linear time-invariant state space model of a large structural system

$$\dot{\mathbf{x}} = \mathbf{A} \mathbf{x} + \mathbf{B} \mathbf{u} \quad (1a)$$

$$\mathbf{y} = \mathbf{C} \mathbf{x} . \quad (1b)$$

Here \mathbf{x} , \mathbf{u} and \mathbf{y} are the n , r and p -dimensional state, input and output vectors respectively, \mathbf{A} , \mathbf{B} , and \mathbf{C} are constant matrices of appropriate dimensions and the system is assumed to be completely controllable. Model reduction consists of finding a model of order $m < n$

$$\dot{\mathbf{x}}_m = \mathbf{A}_m \mathbf{x}_m + \mathbf{B}_m \mathbf{u} \quad (2a)$$

$$\mathbf{y}_m = \mathbf{C}_m \mathbf{x}_m . \quad (2b)$$

Here \mathbf{x}_m and \mathbf{y}_m are m and p -dimensional state and output vectors, while \mathbf{A}_m , \mathbf{B}_m and \mathbf{C}_m are constant matrices of appropriate dimensions, which "best approximates" the full order model (1a,b).

In this paper, as in [4], we restrict ourselves to model reduction schemes based on an integral-square-error performance index (in particular to the optimal projection method of Hyland and Bernstein), [1,5], but the methodology is applicable to other schemes as well. We are thus interested in determining matrices \mathbf{A}_m , \mathbf{B}_m and \mathbf{C}_m which minimize

$$J(\mathbf{A}_m, \mathbf{B}_m, \mathbf{C}_m) = \lim_{t \rightarrow \infty} \mathbf{E}[(\mathbf{y} - \mathbf{y}_m)^T \mathbf{R}(\mathbf{y} - \mathbf{y}_m)] \quad (3)$$

when \mathbf{u} is white noise with intensity \mathbf{V} . In (3) $\mathbf{E}[\cdot]$ denotes expected value and \mathbf{R} is a positive definite weighting matrix.

Introducing the augmented system of order $n+m$

$$\dot{\mathbf{x}}_a = \mathbf{A}_a \mathbf{x}_a + \mathbf{B}_a \mathbf{u} \quad (4a)$$

$$\mathbf{y}_a = \mathbf{C}_a \mathbf{x}_a, \quad (4b)$$

where

$$\mathbf{x}_a = \begin{bmatrix} \mathbf{x} \\ \mathbf{x}_m \end{bmatrix}, \quad \mathbf{y}_a = \mathbf{y} - \mathbf{y}_m, \quad \mathbf{A}_a = \begin{bmatrix} \mathbf{A} & \mathbf{0} \\ \mathbf{0} & \mathbf{A}_m \end{bmatrix}, \quad \mathbf{B}_a = \begin{bmatrix} \mathbf{B} \\ \mathbf{B}_m \end{bmatrix}, \quad \mathbf{C}_a = [\mathbf{C} \ -\mathbf{C}_m], \quad (5)$$

the optimality criterion (3) is written as

$$J(\mathbf{A}_m, \mathbf{B}_m, \mathbf{C}_m) = \lim_{t \rightarrow \infty} E[\mathbf{y}_a^T \mathbf{R} \mathbf{y}_a] = \text{tr}[\mathbf{Q}_a \mathbf{R}_a] \quad (6)$$

where \mathbf{Q}_a is the positive semidefinite solution of the Lyapunov equation

$$\mathbf{0} = \mathbf{A}_a \mathbf{Q}_a + \mathbf{Q}_a \mathbf{A}_a^T + \mathbf{B}_a \mathbf{V} \mathbf{B}_a^T \quad (7)$$

and

$$\mathbf{R}_a = \mathbf{C}_a \mathbf{R} \mathbf{C}_a^T. \quad (8)$$

The model reduction problem has been recast as the optimization problem:

$$\min \text{tr}[\mathbf{Q}_a \mathbf{R}_a] \quad (9)$$

$$\text{subject to} \quad \mathbf{0} = \mathbf{A}_a \mathbf{Q}_a + \mathbf{Q}_a \mathbf{A}_a^T + \mathbf{B}_a \mathbf{V} \mathbf{B}_a^T. \quad (7)$$

Similar results hold for other integral-square-error performance indices (see [6] for example).

Introducing the partition

$$\mathbf{Q}_a = \begin{bmatrix} \mathbf{Q}_1 & \mathbf{Q}_2 \\ \mathbf{Q}_2^T & \mathbf{Q}_m \end{bmatrix}, \quad (10)$$

compatible with partitions (5), the constraint (7) is decomposed as

$$\mathbf{0} = \mathbf{A} \mathbf{Q}_1 + \mathbf{Q}_1 \mathbf{A}^T + \mathbf{B} \mathbf{V} \mathbf{B}^T \quad (11a)$$

$$\mathbf{0} = \mathbf{A} \mathbf{Q}_2 + \mathbf{Q}_2 \mathbf{A}_m^T + \mathbf{B} \mathbf{V} \mathbf{B}_m^T \quad (11b)$$

$$\mathbf{0} = \mathbf{A}_m \mathbf{Q}_m + \mathbf{Q}_m \mathbf{A}_m^T + \mathbf{B}_m \mathbf{V} \mathbf{B}_m^T. \quad (11c)$$

Note, from (11a), that \mathbf{Q}_1 is completely determined from knowledge of the full model. Thus expanding the

objective function in (9) and neglecting the constant term involving \mathbf{Q}_1 , the optimization problem (9,7) is rewritten as

$$\min \{ \text{tr}[\mathbf{Q}_m \mathbf{C}_m^T \mathbf{R} \mathbf{C}_m] - 2 \text{tr}[\mathbf{Q}_2^T \mathbf{C}^T \mathbf{R} \mathbf{C}_m] \} \quad (12)$$

$$\text{subject to} \quad \mathbf{0} = \mathbf{A} \mathbf{Q}_2 + \mathbf{Q}_2 \mathbf{A}_m^T + \mathbf{B} \mathbf{V} \mathbf{B}_m^T \quad (11b)$$

$$\mathbf{0} = \mathbf{A}_m \mathbf{Q}_m + \mathbf{Q}_m \mathbf{A}_m^T + \mathbf{B}_m \mathbf{V} \mathbf{B}_m^T . \quad (11c)$$

Note that all of the above manipulations were aimed at transforming the statement of the optimization problem and not at obtaining a (partial) solution. Thus, this approach does indeed alleviate the first two of the shortcomings mentioned earlier since it is not restricted to particular optimality criteria (although it was illustrated here for a particular one), and it is guaranteed to yield at least a local minimum. In addition, we can choose the numerical optimization scheme which is best adapted to the particular optimization problem which the RM must satisfy. In [4] some promising preliminary results for a classic and somewhat pathological example [5,7] and the use of a generalized reduced gradient algorithm [8] were presented. Here we investigate the feasibility of using neural network processing methods to solve the optimization problem (9,7) or (12,11b,c). Improving the computational efficiency for large problems through massive parallelization is the motivation for using these methods, thus alleviating the third shortcoming.

NEURAL NETWORK PROCESSING METHOD

The neural network processing method is an extension of the Hopfield neural network model [9] which has been successfully used to solve combinatorial optimization problems such as the Travelling Salesman problem. Developed by W. Jeffrey and R. Rosner to solve a class of ill posed inverse problems, the neural network processing method [10] is a reformulation of the Hopfield model. Our aim is to apply this methodology to the model reduction problem. We begin with some details of the method.

Consider a network, possibly modeled by analog electronic components, the energy E of which at any time can be expressed as a quadratic function of its state \mathbf{x} as

$$E(\mathbf{x}) = -\mathbf{x} \mathbf{W} \mathbf{x} + 2\mathbf{T}^T \mathbf{x} . \quad (13)$$

$E(\mathbf{x})$ can be regarded as the objective function in an optimization problem for which \mathbf{x} is the design variable. Matrix \mathbf{W} and vector \mathbf{T} are constant valued and arise from the mapping of the optimization problem into the above format.

The change in the energy function resulting from a discrete step, i.e. a change Δx_k in a single element x_k of \mathbf{x} , can be shown to be given as

$$\Delta E_k = (-2 \mathbf{w}_k \mathbf{x} + 2 \mathbf{T}_k - \mathbf{w}_{kk} \Delta x_k) \Delta x_k \quad (14)$$

where $\Delta x_k = \lambda_k (-2 w_k x + 2 T_k)$, w_k being the k -th row of W , w_{kk} the k,k -th element of W , T_k the k -th element of T and λ_k the step size for Δx_k . The parallel processing capabilities come into play here since all the elements of x can be changed simultaneously, increasing the computational speed.

We now continue changing x in this manner until $\Delta E_k = 0$ for all k . The state so obtained represents a minimum energy state. By adjusting the size of λ_k we can show that $\Delta E_k \leq 0$ for all Δx_k . Since we can reduce equation (14) to

$$\Delta E_k = \left(\frac{1}{\lambda_k} - w_{kk} \right) (\Delta x_k)^2, \quad (15)$$

then $\Delta E_k = 0$ when $\frac{1}{\lambda_k} \leq w_{kk}$ for $\lambda_k < 0$.

Hopfield and Tank [9] showed that the stable state reached is a minimum for the optimization problem. Jeffrey and Rosner [10] extended this formulation by allowing for higher order (i.e. non quadratic) terms to be included in the energy function when necessary. The details of their formulation, being similar to the analysis just presented, are not given here.

Note that the neural network processing method of Jeffrey and Rosner is restricted to unconstrained optimization problems. Before applying it to the model reduction application at hand, the constrained optimization problem (9,7) or (12,11b,c) must first be recast as an unconstrained one. We now present three ways in which this can be accomplished: first a penalty function approach, then by solving the problem as a sequence of unconstrained problems in a multi-stage approach, and finally a substitution approach in which the constraint equation is solved and substituted into the objective function.

PENALTY FUNCTION APPROACH

The penalty function approach incorporates all of the constraints into the energy function via penalty terms. The problem becomes an unconstrained problem for the penalty function. This is accomplished in two steps:

1. The equality constraints (7) or (11b,c) are incorporated into the energy function to create a modified Lagrangian or penalty function [11], that is:

$$E(x) = F(x) + \sum_{i,j} [\phi h_{ij}^2(x) + \gamma l_{ij} h_{ij}(x)] \quad (16)$$

where $F(x)$ is the objective function of the constrained problem ($\text{tr}[Q_a R_a]$ or $\{\text{tr}[Q_m C_m^T R C_m] - 2\text{tr}[Q_2^T C^T R C_m]\}$ for the problem at hand), ϕ and γ are penalty parameters, l_{ij} are Lagrange multipliers and

h_{ij} is the i,j -th element of the equality constraint.

2. The underlying inequality constraint $Q_a \geq 0$ is enforced by factoring Q_a as the product of an upper triangular matrix M_a , partitioned as

$$M_a = \begin{bmatrix} M_1 & M_2 \\ 0 & M_m \end{bmatrix}, \quad (17)$$

and its transpose. In (17) M_1 and M_m are upper triangular matrices such that $Q_2 = M_2 M_m^T$ and $Q_m = M_m M_m^T$. These are substituted into the energy function so that the vector of design variables x is made up of (i) elements of A_m , (ii) elements of B_m , (iii) elements of M_2 , (iv) non zero (i.e. upper triangular) elements of M_m , and (iv). l_{ij} the Lagrange multipliers.

The Modified Differential Multiplier Method (MDMM), proposed by Platt [12] for use in neural network processing, is then used to solve the problem. This essentially amounts to applying gradient ascent on the Lagrange multipliers while applying gradient descent on all of the other design variables.

MULTI-STAGE APPROACH

The multi stage approach is loosely based on a model reduction algorithm proposed by Wilson [13]. It is simply the following algorithm:

1. Pick initial guesses for matrices A_m and B_m .
2. Calculate Q_2 and Q_m .
3. Minimize the objective function using the neural network processing method with elements of B_m as the only design variables.
4. Update the A_m matrix using $A_m = Q_m^{-1} Q_2^T A Q_2 Q_m^{-T}$. (This is analogous to the necessary condition for an optimum used by Wilson [13].)
5. Go to step 2 until the objective function stops changing from iteration to iteration

Note that in this approach, the minimization problem of step 3 is an unconstrained problem. Thus the model reduction problem is solved as a sequence of unconstrained optimization problems.

SUBSTITUTION APPROACH

In the substitution approach the Q_2 and Q_m matrices, as solutions of (11b,c), are functions of A_m and B_m which are substituted in the objective function of (12) to yield an unconstrained problem where the elements of A_m and B_m are the only design variables. Neural network processing is then used with the energy function $E = \text{tr}[Q_m(A_m, B_m) C_m^T R C_m] - 2 \text{tr}[Q_2(A_m, B_m) C^T R C_m]$.

RESULTS

In all examples considered we assumed that actuators and sensors were collocated so that $B = C^T$ and $B_m = C_m^{-T}$, and, without loss of generality, that R and V are identity matrices of appropriate dimensions.

All three methods presented solved only problems of a very limited scope: all methods were able to solve very small real eigenvalue problems, but all showed an inability to solve problems of a practical size and nature. For example all three methods yielded an optimal solution for the following very simple problem considered in [4] (and given here with its solution)

$$A = \begin{bmatrix} -.005 & -.99 \\ .99 & -5000 \end{bmatrix}, \quad B = \begin{bmatrix} 1 \\ 100 \end{bmatrix}, \quad A_m = [-4998.1], \quad B_m = [100.0], \quad \text{obj} = -10004.0.$$

The point of interest of this example is that some model reduction techniques yield a solution corresponding to a maximum rather than the minimum [5,7].

a. Penalty Function Approach

The penalty function approach exhibited poor performance in solving model reduction problems. It was able to solve problems in which the original A matrix was 4×4 and the reduced matrix A_m was 2×2 ; however, this was the largest problem that we were able to solve using this method. The encouraging fact is that the method did yield good, possibly optimal, solutions to a few small problems with complex eigenvalues. For example the following problem (given here with its solution) was solved successfully

$$A = \begin{bmatrix} -.1 & -10 & 0 & 0 \\ 10 & -.1 & 0 & 0 \\ 0 & 0 & -.5 & -15 \\ 0 & 0 & 15 & -.5 \end{bmatrix}, \quad B = \begin{bmatrix} 1 \\ 3 \\ -2 \\ 3 \end{bmatrix}, \quad A_m = \begin{bmatrix} -.124 & -10.075 \\ 9.924 & -.0794 \end{bmatrix}, \quad B_m = \begin{bmatrix} -2.867 \\ -1.392 \end{bmatrix}, \quad \text{obj} = -253.4.$$

Difficulties with this approach were due to a lack of good guiding principles in setting step size and penalty parameters, a slow convergence, and an apparent large number of local minima.

b. Multi Stage Approach

The multi stage approach exhibited a slightly different behavior. Since the traditional optimization portion of the algorithm which was carried out using neural network processing involved a much smaller problem, the method was able to solve overall larger problems. However, the approach would not solve problems with complex eigenvalues but would successfully solve problems with strictly real eigenvalues. The maximum size of these models were 6 inputs, 6 outputs with 16×16 \mathbf{A} matrices. As problems with strictly real eigenvalues have little practical application, this approach was abandoned.

c. Substitution Approach

The substitution approach presented basically the same difficulties as the penalty approach. Although it successfully solved the example given in the penalty function approach subsection above, yielding the same solution, it showed limitations in that it was unable to solve problems with \mathbf{A} matrices bigger than 4×4 .

CONCLUDING REMARKS

The results obtained so far have not lived up to our expectations when we embarked on this investigation. In all fairness it must be pointed out that the difficulties encountered do not appear to be a result of the neural network processing approach. Parallel investigations using a standard optimization software package [8] were also disappointing. The difficulty appears to stem from the fact that the objective function has apparently a large number of local minima. In particular, it appears that any reasonable starting point is a local minimum!

A positive result in our lack of success in solving practical sized problems is the development of a type of modal cost analysis based on the objective function developed for the optimization methods. In this method we transform the system matrices such that the \mathbf{A} matrix has 2×2 blocks on the main diagonal, each block corresponding to a mode of the structural system, and the \mathbf{B} matrix is consistent with these new coordinates. Next we calculate the objective function for each 2×2 system individually. The objective values for all of the individual (1 mode) reduced models are sorted and the lowest ones are retained. At this time we have not put enough time into this approach to make any firm statement about the quality and cost of these solutions. However preliminary results are encouraging. We have reduced models with \mathbf{A} matrices up to 168×168 (the JPL/AFAL experiment structure) down to \mathbf{A}_m matrices of 108×108 yielding excellent results when looking at the time response characteristics. We are now looking into this method in more detail to see if this approach can be used to obtain directly or aid us in finding optimal reduced models. Results will be reported elsewhere as they become available.

REFERENCES

1. Hyland, D.C., "Comparison of Various Controller-Reduction Methods: Suboptimal versus Optimal Projection," **AIAA Paper 84-1033**, 1984.
2. Béclus, G.A. and Cheng, C.W., "Energy Methods for Model Reduction in the Dynamics and Control of Large Structural Systems," **Proc. 3rd Int. Conf. Recent Adv. Structural Dyn.**, Southampton, U.K., 901-910, 1988.
3. Williams, T. and Mostarshedi, M., "Model Reduction Results for Flexible Space Structures," **5th NASA/DoD CSI Tech. Conf., NASA CP- 3177**, 1992.
4. Béclus, G.A., "Direct Numerical Optimization Methods for Model Reduction in the Dynamics and Control of Large Structural Systems," **3rd AF/NASA Symp. Recent Adv. Multidisc. Anal. and Optim.**, San Francisco, CA, 1990.
5. Hyland, D.C. and Bernstein, D.S., "The Optimal Projection Equations for Model Reduction and the Relationships Among the Methods of Wilson, Skelton, and Moore," **IEEE Trans. Aut. Con.**, AC-30, 1201-1211, 1985.
6. Bryson, A.E. Jr. and Carrier, A., "Second order algorithm for optimal model order reduction," **J. Guid. Cont. Dyn.**, 13, 887-892, 1990.
7. Kabamba, P.T., "Balanced gains and their significance for balanced model reduction," **IEEE Trans. Aut. Con.**, AC-30, 690-693, 1985.
8. Lasdon, L.S. and Waren, A.D., **GRG2 User's Guide**, Univ. of Texas at Austin, 1982.
9. J. J. Hopfield & D. W. Tank, "Neural Computations of Decisions in Optimization Problems," **Biological Cybernetics**, 52, pp. 141-152, 1985.
10. Jeffrey, W. and R. Rosner, "Optimization Algorithms: Simulated Annealing and Neural Network Processing," **The Astrophysical Journal**, 310, 473-481, 1986.
11. Reklaitis, G. V., A. Ravindran, and K. M. Ragsdell, **Engineering Optimization Methods and Applications**, Wiley and Sons, NY, 1983.
12. Platt, J. C. & A. H. Barr, "Constrained Differential Optimization," in Anderson, Dana Z. (ed.), **Neural Information Processing Systems**, 612-621. American Institute of Physics, NY, 1988.
13. Wilson, D. A., "Optimum solution of Model-Reduction Problem," **Proc. IEE**, 117, 1161-1165, 1970.

Physical Insight into the Simultaneous Optimization of Structure and Control

Robert N. Jacques and David W. Miller
Space Engineering Research Center
Massachusetts Institute of Technology

Abstract

Recent trends in spacecraft design which yield larger structures with more stringent performance requirements place many flexible modes of the structure within the bandwidth of active controllers. The resulting complications to the spacecraft design make it highly desirable to understand the impact of structural changes on an optimally controlled structure. This work uses low order structural models with optimal \mathcal{H}_2 and \mathcal{H}_∞ controllers to develop some basic insight into this problem. This insight concentrates on several basic approaches to improving controlled performance and how these approaches interact in determining the optimal designs. A numerical example is presented to demonstrate how this insight can be generalized to more complex problems.

1 Introduction

Traditionally, control and structure subsystems in spacecraft have been designed separately. This was an efficient approach when the required bandwidth of rigid body controllers was well below the frequencies of the flexible modes of the structure. Recently however, increasing size in spacecraft structural designs has resulted in ever decreasing frequencies for flexible modes, while more stringent pointing and alignment requirements have resulted in control designs of increasing bandwidth. The net result is that several to many flexible modes of a spacecraft structure can lie within the bandwidth of onboard controllers. The strong interaction of structure and control that arises from this makes simultaneous design of these two subsystems highly desirable.

One approach to this problem can be called numerical control/structure optimization [1]. In this method, one first selects a basic structural and control design (e.g. a ten bay truss with full state feedback). Several structural parameters (e.g. truss member thicknesses) and control gains are designated as design variables and a dynamic performance metric is formulated. A numerical algorithm is then employed to search over the space of allowable designs for a particular one which optimizes a dynamic performance metric with a suitable constraint on the overall mass or size of the structure.

The Achilles Heel of this approach lies in the lack of physical insight yielded by the numerical solution. This insight is crucial in designing any controlled structure, including one which will ultimately be designed numerically. A good understanding of how changes in the structure influence controlled performance is essential in formulating the optimization problem to be solved numerically. Physical insight will hopefully lead to a wise, rather than arbitrary, selection of the design variables. Otherwise selection of design variables can place design objectives at odds and thereby yield a needlessly compromised solution.

One can envision four basic ways that a change to the structure of a spacecraft can alter its controlled performance. First, it can alter the way that disturbances influence the dynamics of the structure (disturbability). Second, it can affect the influence of control actuators (controllability). Third, it can change the way in which the dynamics of the structure appear in the performance metric (observability). And finally, it can change the frequencies and damping ratios of the structure. These different qualities of the structure; controllability, disturbability, observability, frequency and damping; are defined here as the structure's *modal properties*.

It should be noted that there is also a fifth way that one can alter the performance of a controlled structure, and that concerns changes which affect the robustness of the controllers. However, this is beyond the scope of this work. The next section describes the basic mathematical controlled structure problem and formulates a low order problem (typical section) useful in studying how a controlled structure's modal properties interact to produce dynamic performance.

2 Problem Description and Typical Section

A general linear structure can be described by the equation of motion:

$$\begin{aligned} M(\alpha)\ddot{r} + D(\alpha)\dot{r} + K(\alpha)r &= F(\alpha)u + G(\alpha)v \\ y &= N(\alpha)r \end{aligned} \quad (1)$$

where r is a vector of physical displacements on the structure, y is a vector of displacements (either physical or modal) to be controlled, u is a vector of control forces, and v is a vector of disturbance forces. The vector α is an array of real values which represent quantities in the structure which can be varied by the engineer in the design process. For example, the elements of α could represent the diameters of members in a truss structure. The goal of control/structure optimization is to find a suitable combination of structural parameters and control force which minimizes the performance metric.

$$(\alpha^*, u^*(t)) = \arg \min_{u(t), \alpha \in \mathcal{D}} J(M(\alpha), D(\alpha), K(\alpha), F(\alpha), G(\alpha), N(\alpha), u(t)) \quad (2)$$

The set of allowable designs, \mathcal{D} , is usually constrained to contain only designs that are below some maximum value of size or mass either directly, or by including a component in the cost which penalizes these values. Furthermore, \mathcal{D} is usually restricted to include only those designs which have physical meaning. For example, one might constrain design variables representing member thicknesses to lie above zero.

Equation 1 can be transformed into a modal state space representation where the state vector is modal displacement, q , and frequency normalized modal velocity, q' :

$$\begin{aligned} \frac{d}{dt} \begin{bmatrix} q \\ q' \end{bmatrix} &= \begin{bmatrix} 0 & \omega \\ -\omega & -2\zeta\omega \end{bmatrix} \begin{bmatrix} q \\ q' \end{bmatrix} + \begin{bmatrix} 0 \\ \omega^{-1}\Phi^T F \end{bmatrix} u + \begin{bmatrix} 0 \\ \omega^{-1}\Phi^T G \end{bmatrix} v \\ y &= \begin{bmatrix} N\Phi & 0 \end{bmatrix} \begin{bmatrix} q \\ q' \end{bmatrix} \end{aligned} \quad (3)$$

The matrices ω and ζ are diagonal matrices containing the natural frequency and damping ratio of each mode and Φ is the modal transformation matrix:

$$r = \Phi q \quad q' = \omega^{-1}\dot{q} \quad \Phi^T M \Phi = I \quad \Phi^T K \Phi = \omega^2 \quad \Phi^T D \Phi \approx 2\zeta\omega \quad (4)$$

Altering certain matrices in Equation 3 corresponds exactly to altering the individual modal properties mentioned above. It is useful to make the following definitions.

$$\begin{aligned} \text{Frequency Matrix} & \quad \omega \\ \text{Damping Matrix} & \quad \zeta \\ \text{Controllability Matrix} & \quad \mathcal{F} = \omega^{-1}\Phi^T F \\ \text{Disturbability Matrix} & \quad \mathcal{G}_v = \omega^{-1}\Phi^T G \quad \text{or} \quad \mathcal{G}_d = \omega^{-2}\Phi^T G \\ \text{Observability Matrix} & \quad \mathcal{N} = N\Phi \end{aligned} \quad (5)$$

Note the appearance of inverse frequency in the expression for controllability. It reflects the inherent resistance of higher frequency modes to impulsive control forces. Similarly, there are frequency terms

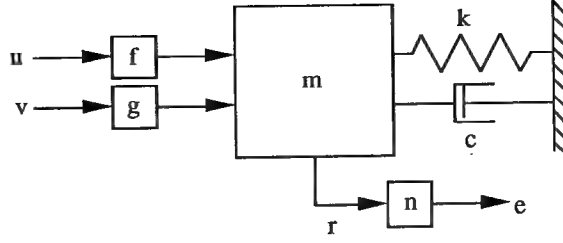


Figure 1: Typical section

in the disturbability expressions, except that there are two forms. The first corresponds to impulsive (velocity) disturbance forces, the second corresponds to static (displacement) disturbance forces. The choice of exponents in these expressions is clarified below.

Any alteration to the structure can be perceived as having two stages of effects. First, a change to the structure alters its modal properties. Second, the changes in these quantities alter the controlled performance of the system. This view of the problem is useful because it is relatively easy to understand how a change to the structure will influence its modal properties. If one could then understand the relative importance of these quantities in determining controlled performance, then one would have a good understanding of the entire problem. To develop this understanding, it is useful to study the system shown in Figure 1. This system is typical of a single mode of a flexible structure. For this reason this model and its associated controller are called a controlled structure typical section. The frequency, damping, controllability, disturbability, and observability matrices for the typical section are simply scalars:

$$\omega = \sqrt{\frac{k}{m}} \quad \zeta = \frac{c}{2m\omega} \quad \mathcal{F} = \frac{f}{m\omega} \quad \mathcal{G}_v = \frac{g}{m\omega} \quad \mathcal{G}_d = \frac{g}{m\omega^2} \quad \mathcal{N} = nm \quad (6)$$

and the equation of motion in state space form is:

$$\begin{aligned} \dot{x} &= Ax + Bu + Lv \\ y &= Cx \quad C = \begin{bmatrix} \mathcal{N} & 0 \end{bmatrix} \\ x &= \begin{bmatrix} q \\ q' \end{bmatrix} \quad A = \begin{bmatrix} 0 & \omega \\ -\omega & -2\zeta\omega \end{bmatrix} \quad B = \begin{bmatrix} 0 \\ \mathcal{F} \end{bmatrix} \quad L = \begin{bmatrix} 0 \\ \mathcal{G} \end{bmatrix} \end{aligned} \quad (7)$$

The next sections show how the above parameters influence the controlled performance for the optimally controlled system when two different performance metrics are used.

3 \mathcal{H}_2 Problem

One of the most common dynamic performance metrics is the infinite horizon, \mathcal{H}_2 performance metric:

$$J = E \left[\int_0^\infty (y^T(t)y(t) + u^T(t)Ru(t)) dt \right] \quad (8)$$

where $E[\cdot]$ is the expectation operator and R is a symmetric, positive-definite control weighting matrix. The disturbance is specified as an expected value of the outer product of the initial state. In this case, it is assumed that the initial state comes about due to either static or impulsive forces, v , applied to the disturbance inputs of the system:

$$\begin{aligned}
S = E[x(0)x^T(0)] &= \begin{bmatrix} E[q(0)q^T(0)] & 0 \\ 0 & 0 \end{bmatrix} && \text{displacement disturbance} \\
&= \begin{bmatrix} 0 & 0 \\ 0 & E[q'(0)q'^T(0)] \end{bmatrix} && \text{velocity disturbance} \\
E[q(0)q^T(0)] &= \mathcal{G}_d V \mathcal{G}_d^T \quad E[q'(0)q'^T(0)] = \mathcal{G}_v V \mathcal{G}_v^T \quad E[vv^T] = V
\end{aligned} \tag{9}$$

where V is the expected value of the outer product of the disturbance force v . The expectation operator appears in these expressions in order to allow for a statistical instead of a deterministic description of these forces. It should be noted that there is also a stochastic formulation of this performance metric. However, if V is taken to be the intensity of a Gaussian White Noise disturbance, then the resulting analysis would be identical to that for the velocity disturbance.

Notice that frequency does not appear in the above disturbance expressions. This was because any dependence of the disturbance properties of the system on frequency were absorbed into the definitions of the variables \mathcal{G}_v and \mathcal{G}_d . This was the chief reason for including frequency in these definitions for the disturbance matrices, as it reflects the differing resistance of stiffer modes to static and impulsive forces.

A well known result of optimal control theory, is that for an optimally controlled system described by Equations 7 and 9 the \mathcal{H}_2 cost is [2]:

$$J_{\text{opt}} = \text{tr} \{ PS \} \tag{10}$$

where P is the symmetric, positive-definite solution of:

$$PA + A^T P + C^T C - P B R^{-1} B^T P = 0 \tag{11}$$

For the typical section problem, these equations can be solved in closed form with the control penalty defined as $R = \rho^2$ [3]:

$$\begin{aligned}
J_{\text{opt}} &= \frac{V \mathcal{G}_d^2 \mathcal{N}^2}{\omega} \frac{1}{\beta^2} \left(\sqrt{\beta^2 + 1} \sqrt{4\zeta^2 + 2\sqrt{\beta^2 + 1} - 2} - 2\zeta \right) && \text{for a displacement disturbance} \\
J_{\text{opt}} &= \frac{V \mathcal{G}_v^2 \mathcal{N}^2}{\omega} \frac{1}{\beta^2} \left(\sqrt{4\zeta^2 + 2\sqrt{\beta^2 + 1} - 2} - 2\zeta \right) && \text{for a velocity disturbance} \\
\text{where } \beta &\equiv \left| \frac{\mathcal{N} \mathcal{F}}{\omega \rho} \right|
\end{aligned} \tag{12}$$

Notice that the optimal costs for both types of disturbances have two parts. The first part (containing V , \mathcal{G} , \mathcal{N} , and ω) represents the transmissibility of the disturbance to the performance outputs. The second part, containing only non-dimensional terms for damping, ζ , and control influence, β , represents the improvement in performance gained through the application of passive damping and control. These parts of Equation 12 are too complicated to make any easy inferences about the relationship between modal properties and performance. However, the two non-dimensional values, ζ (damping) and β (control influence) completely determine the character of the equations, and it is illustrative to consider the asymptotic behavior of the performance with respect to these values.

Table 1 shows how Equation 12 behaves for limiting values of control influence, β and damping ζ . The top row of this table shows the behavior of the cost as the control forces become ineffective compared to the internal forces of the damping. In that case, the control terms (\mathcal{F} and ρ) drop out,

Table 1: \mathcal{H}_2 Performance Costs

Control Type	Disturbance Type	
	Velocity	Displacement
Open Loop or Heavy Damping	$J_{\text{opt}} = \frac{V\mathcal{G}_v^2\mathcal{N}^2}{\omega} \frac{1}{4\zeta}$	$J_{\text{opt}} = \frac{V\mathcal{G}_d^2\mathcal{N}^2}{\omega} \left(\frac{1}{4\zeta} + \zeta \right)$
Expensive Control, Light Damping	$J_{\text{opt}} = \frac{V\mathcal{G}_v^2\mathcal{N}^2}{\omega} \beta^{-1} = \frac{V\mathcal{G}_v^2\rho \mathcal{N} }{ \mathcal{F} }$	$J_{\text{opt}} = \frac{V\mathcal{G}_d^2\mathcal{N}^2}{\omega} \beta^{-1} = \frac{V\mathcal{G}_d^2\rho \mathcal{N} }{ \mathcal{F} }$
Cheap Control, Light Damping	$J_{\text{opt}} = \frac{V\mathcal{G}_v^2\mathcal{N}^2}{\omega} \sqrt{2}\beta^{-3/2} = \frac{V\mathcal{G}_v^2\sqrt{2} \mathcal{N} \rho^3\omega}{\sqrt{ \mathcal{F} ^3}}$	$J_{\text{opt}} = \frac{V\mathcal{G}_d^2\mathcal{N}^2}{\omega} \sqrt{2}\beta^{-1/2} = \frac{V\mathcal{G}_d^2\sqrt{2} \mathcal{N} ^3\rho}{\sqrt{ \mathcal{F} \omega}}$

leaving an expression that represents the performance of the open loop system. The expressions for both disturbance cases are very similar with the exception of how damping influences performance. For damping levels less than 50%, increased damping improves performance for both disturbance types; however, for larger damping levels, increased damping actually inhibits performance for the displacement disturbance. This reflects the tendency of heavily damped systems to recover slowly from initial displacements.

The second and third rows of the table show the behavior of the performance when the damping becomes small relative to the control influence. In these cases, terms related to passive damping become insignificant and drop out of the cost. Physically, this means that the available control forces are greater than the internal damping forces and are therefore dominant in reducing cost. This will always be true in a system where it is necessary to use control to achieve a significant gain in performance. The implication is that damping should not be used to improve the performance of controlled modes directly. Instead, the damping design should concentrate on improving the performance of uncontrolled modes (modes which are either uncontrollable or outside the bandwidth of the controller) and adding robustness to the controlled modes.

The system shows two different types of behavior for low damping depending on the level of control effort. For low (or expensive) control effort, the costs for both disturbance cases are identical. This is because the low control is providing a small amount of active damping and the response of the system takes several cycles to attenuate (Figure 2). The cost is determined almost entirely by the response envelope and the phase difference in the responses imposed by the disturbance type has little effect. For higher control levels (expensive control), the response of the system attenuates in only one or two cycles and the phase difference becomes more important. Figure 3 depicts the response of a heavily controlled system for both types of disturbances. It is plain in the figure that the height of the peak response is a major factor in determining performance. However, the peak response for the system with the displacement disturbance is unaffected by control, while the peak response for the system with the velocity disturbance can be dramatically affected by control. This gives the costs fundamentally different behaviors at higher control levels for the different disturbance types. This effect appears in the last row of Table 1. In particular, the control influence parameter plays a large role in the cost for the velocity disturbance than it does in that of the displacement disturbance.

Using the information contained in this Table 1, and information about the sensitivity of frequency, damping, controllability, observability, and disturbability to the design parameters, α , one can infer which of these quantities should be adjusted and which should be ignored in designing a good controlled structure.

As an example, consider a case worked out by Milman *et.al.* [1] (Figure 4) This system consists of a three element, cantilevered, Bernoulli-Euler beam with a tip actuator and an impulsive disturbance also at the tip. The control in this case is optimal full state feedback and the design variables are the

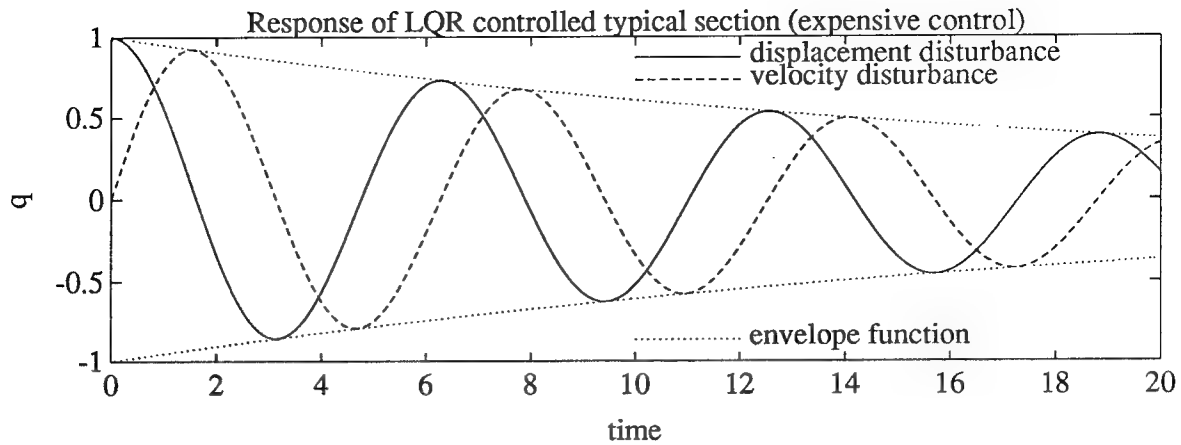


Figure 2: Response of single mass typical section for displacement and velocity disturbances: $\omega = 1, \zeta = 0, \mathcal{G}_d = \mathcal{G}_v = 1, \mathcal{N} = 1, \rho = 10$.

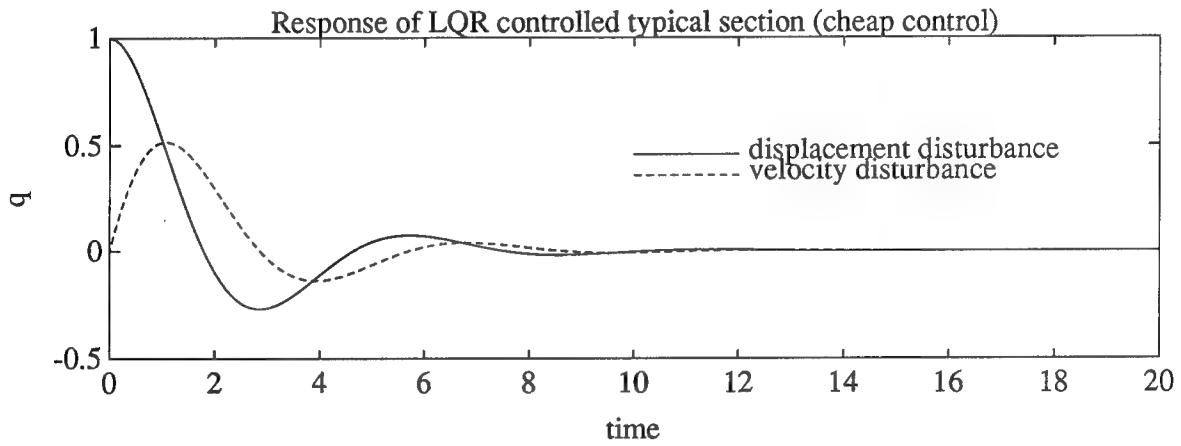


Figure 3: Response of single mass typical section for displacement and velocity disturbances: $\omega = 1, \zeta = 0, \mathcal{G}_d = \mathcal{G}_v = 1, \mathcal{N} = 1, \rho = 1$.

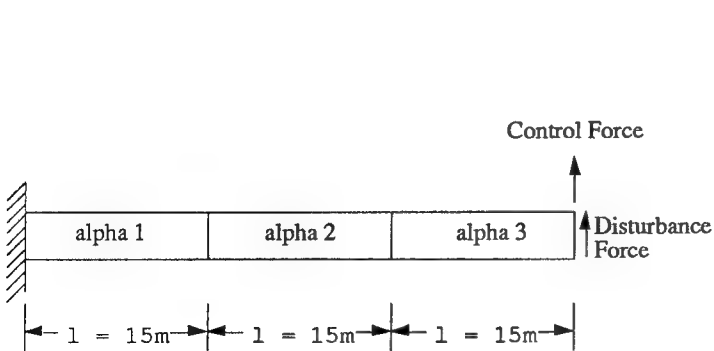


Figure 4: Beam example of Milman *et.al.*

Table 2: Results

λ	Optimal Design		
	α_1	α_2	α_3
0.0000	.10	.10	.10
0.0001	.10	.10	1.59
0.0010	.10	.31	5.00
0.0100	0.38	1.18	15.72
0.1000	2.50	5.48	53.04
0.2000	4.57	8.93	81.48
0.3000	6.58	12.02	108.66
0.4000	8.65	15.10	137.97
0.5000	10.95	18.56	171.79
0.6000	13.77	22.66	213.96
0.7000	17.59	28.22	271.95
0.8000	24.06	37.32	364.60
0.9000	40.21	60.07	565.21
0.9200	47.49	70.68	644.24
0.9400	58.71	87.88	756.79
0.9600	79.40	122.91	937.62
0.9800	136.80	233.95	1307.86
0.9900	230.35	402.91	1779.25

thicknesses of the three elements. The metric optimized was a combination of a dynamic performance metric penalizing strain and kinetic energy and a metric penalizing total mass.

$$J = \lambda W(\alpha) + (1 - \lambda) \int_0^\infty (r^T K r + \dot{r}^T M \dot{r} + \rho u^2) dt \quad (13)$$

The parameter, λ , is adjusted to obtain different levels of tradeoff between weight and performance. It can be shown that for any optimal design obtained for a given value of λ , the same design can be obtained by constraining $W(\alpha)$ and removing it from the performance metric. Hence Equation 13 is equivalent to Equation 2 with J set to the dynamic term and the set \mathcal{D} constrained to include only designs which satisfy a maximum mass constraint.

An important feature of this problem is that the actuator and the disturbance are collocated. Examining the first column of Table 1 reveals that reducing the disturbability and increasing the controllability will both have favorable effects on the performance. However, the table also shows that when the sensitivity of the disturbability, \mathcal{G} , and controllability, \mathcal{F} , to the design variables is equal (as in this case), then greater gains can be attained by reducing disturbability at the expense of controllability for all levels of control. Table 2 confirms this suspicion. For almost all values of λ , the design obtained through optimization placed the bulk of the mass at the tip of the beam, where its inertia could help resist any forces applied to the tip.

This multimode problem was fairly easy to analyze due to its structure (disturbance and control collocated). However, it is important to understand the implications of the interaction of several modes. The next section explores this problem.

4 \mathcal{H}_2 Problem for a multi-mode system

In a system consisting of a single mode, the expressions in Table 1 will be exact; however, it should be expected that the interaction of several modes with a controller will produce somewhat different results. To facilitate this discussion, it is useful to look at the form of the gradient for an optimally controlled system. This gradient can be computed by first combining the cost in Equation 10 and the constraint in Equation 11 into a Lagrangian.

$$L = \text{tr} \{ PS \} + \text{tr} \{ H (PA + A^T P + C^T C - P B R^{-1} B^T P) \} \quad (14)$$

Setting derivatives of this expression with respect to the matrices P and H to zero recovers the constraint equation and an additional equation:

$$\frac{\partial L}{\partial P} = H (A - B R^{-1} B^T P)^T + (A - B R^{-1} B^T P) H + S = 0 \quad (15)$$

It can be seen that the Lagrange Multiplier Matrix, H , is the covariance of the state of the closed loop system.

The derivative of the cost with respect to a particular parameter, α_i , is the derivative of the Lagrangian with respect to that parameter;

$$\frac{\partial J}{\partial \alpha_i} = \frac{\partial L}{\partial \alpha_i} = \text{tr} \left\{ P \frac{\partial S}{\partial \alpha_i} + H \left(P \frac{\partial A}{\partial \alpha_i} + \frac{\partial A^T}{\partial \alpha_i} P + \frac{\partial}{\partial \alpha_i} (C^T C) - P \frac{\partial}{\partial \alpha_i} (B R^{-1} B^T) P \right) \right\} \quad (16)$$

when P and H are given by Equations 11 and 15.

When A , B , C , and S are defined for a modal system description (Equation 3) then the different terms of the above equation describe changes in cost due to changes in individual modal properties. It is therefore useful to make the following definitions:

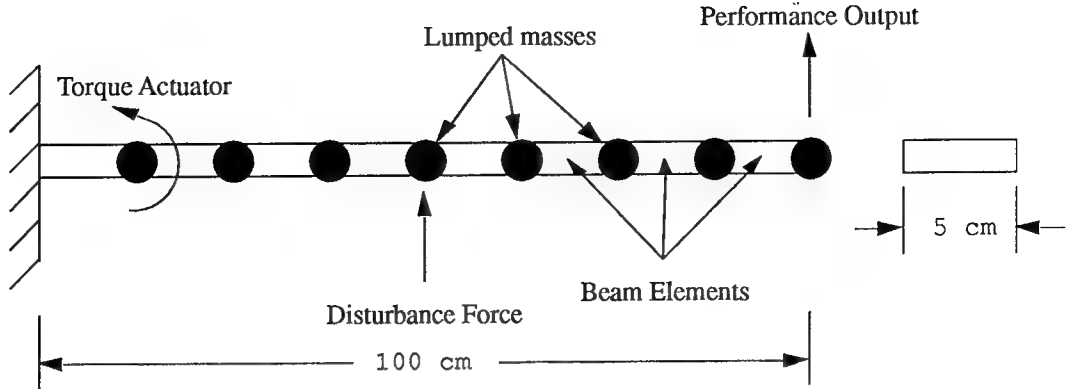


Figure 5: Cantilevered aluminum beam model. $E = 73\text{GPa}$, $\rho = 2700\text{kg/m}^3$

$$\begin{aligned}
 \delta J_{fre} &= \text{tr} \left\{ H \left(P \frac{\partial A}{\partial \alpha} + \frac{\partial A^T}{\partial \alpha} P \right) \right\} && \text{Frequency Subgradient} \\
 \delta J_{dis} &= \text{tr} \left\{ P \frac{\partial S}{\partial \alpha} \right\} && \text{Disturbability Subgradient} \\
 \delta J_{obs} &= \text{tr} \left\{ H \frac{\partial}{\partial \alpha} (C^T C) \right\} && \text{Observability Subgradient} \\
 \delta J_{con} &= -\text{tr} \left\{ H P \frac{\partial}{\partial \alpha} (B R^{-1} B^T) P \right\} && \text{Controllability Subgradient}
 \end{aligned} \tag{17}$$

It is illustrative to consider the application of these definitions to a simple problem. Figure 5 depicts a cantilevered beam model consisting of eight finite elements with lumped masses included at the nodes. The performance output is the tip displacement of the beam, the actuator is a torque applied near the root, and the disturbance is a transverse force applied at the midspan of the beam. The structural design variables in this problem are the thicknesses of the beam elements and the size of the lumped masses. These variables have been scaled so that an equal change in element thickness or lumped mass represents an equal change in mass.

$$\begin{aligned}
 \text{Beam element design variables } t_i^* &= \frac{t_i}{1\text{cm}} \\
 \text{Lumped mass design variables } m_i^* &= \frac{m_i}{(1\text{cm})w_b h \rho}
 \end{aligned} \tag{18}$$

where w_b and h are the element width and length and ρ is the material density. The total mass of the beam and lumped masses is constrained to be less than or equal to that of a 1 cm uniform beam with no lumped masses.

Figures 6-9 depict the magnitudes of the subgradients, normalized by the cost magnitude and projected onto the constant mass constraint, for a 1 cm uniform beam with no lumped mass. Figures 6 and 7 show these values for a displacement disturbance and model orders of one and four modes, respectively. Figures 8 and 9 show these same values for a velocity disturbance.

The horizontal axis in these figures represents the level of control penalty used in the LQR performance metric. The left side of each figure corresponds to cheap control or high control effort. The right side corresponds to expensive control or low control effort. The vertical lines are the different levels of control penalty at which the control influence parameter:

$$\beta = \left| \frac{\mathcal{N} \mathcal{F}}{\omega \rho} \right| = \left| \frac{N \phi_i \phi_i^T F}{\omega_i^2 \rho} \right| \tag{19}$$

is equal to unity for different modes. (Recall from Equation 4 that Φ is the modal transformation matrix and ω_i is the modal frequency.)

For the single mode models, these figures agree exactly with the results predicted in Table 1. The sensitivity of the cost to disturbability is unaffected by control effort, frequency rises from zero to

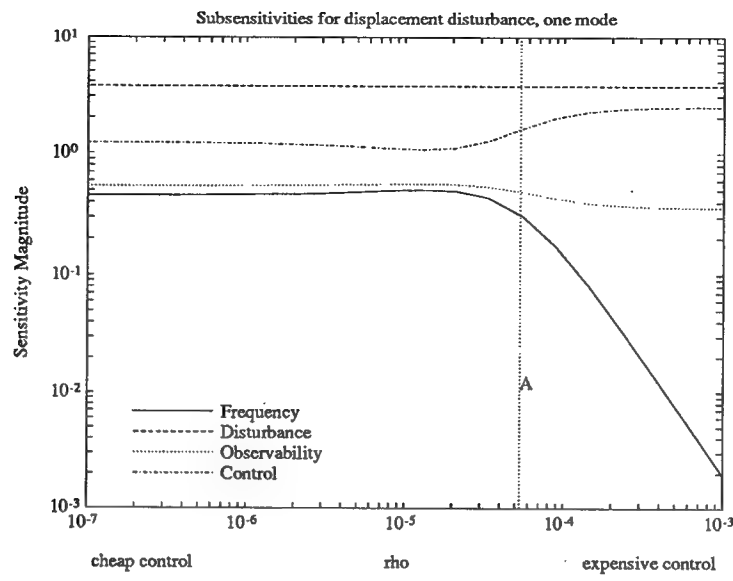


Figure 6: Magnitudes of subgradients normalized by cost for uniform beam with one mode and displacement disturbance versus control weighting; A: β for mode 1 = 1.

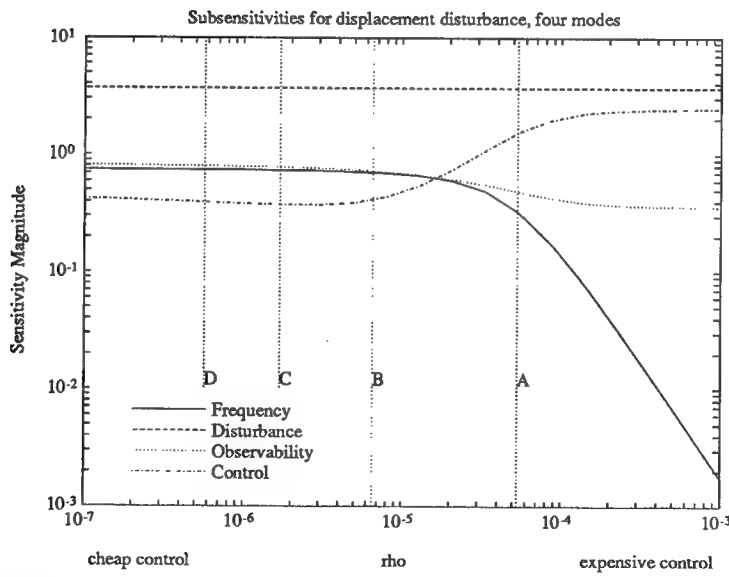


Figure 7: Magnitudes of subgradients normalized by cost for uniform beam with four modes and displacement disturbance versus control weighting; A: β for mode 1 = 1, B: β for mode 2 = 1, C: β for mode 3 = 1, D: β for mode 4 = 1.

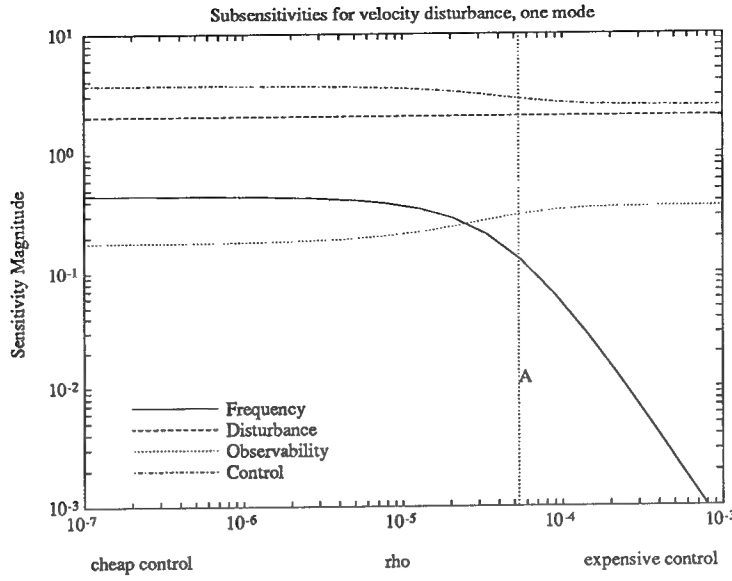


Figure 8: Magnitudes of subgradients normalized by cost for uniform beam with one mode and velocity disturbance versus control weighting; A: β for mode 1 = 1.

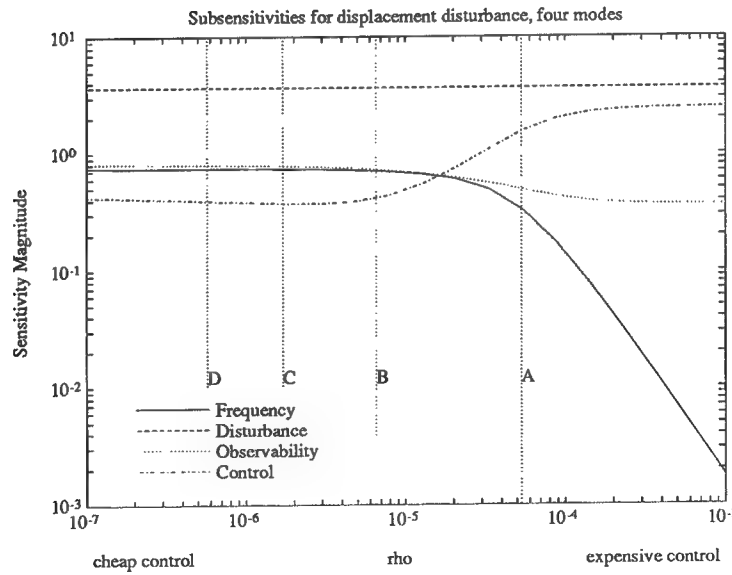


Figure 9: Magnitudes of subgradients normalized by cost for uniform beam with four modes and velocity disturbance versus control weighting; A: β for mode 1 = 1, B: β for mode 2 = 1, C: β for mode 3 = 1, D: β for mode 4 = 1.

finite importance with decreasing control cost, and for the displacement disturbance, increased control effort increases the importance of observability and decreases the significance of controllability while for the velocity disturbance, the opposite is true.

In the four mode model, there are several differences in the behavior of the cost. In the cheap control cases, there is a marked increase in the sensitivity of the cost to observability and a decrease in the sensitivity to controllability. Also, for the velocity disturbance, there is a slight increase in the sensitivity to disturbances. Yet, for expensive control, the sensitivities are almost identical to those for the single mode model. The reason for this discrepancy can be traced to the use of a single actuator to control several modes. At low levels of control, the actuator will need to provide only active damping for each mode. Velocity feedback will provide this active damping to all modes. At higher levels of control, however, each mode will require more shape control. Unfortunately the inputs required by each mode for shape control can be very different and the optimal control must represent a compromise. In other words, a shortage of actuators makes the control less effective at high levels. The effect this has on the cost is to reduce the role of the control influence term β in the expressions in the third row of Table 1. Terms which can reduce transmissibility of the disturbance to the performance output directly (*i.e.* disturbability and observability) will be enhanced in significance while controllability will be diminished. This is exactly the behavior in the results noted above.

5 \mathcal{H}_∞ Problem

Another performance metric in common use is the \mathcal{H}_∞ metric:

$$J = \sup_{\omega} (y(\omega)^T y(-\omega) + u(\omega)^T R u(-\omega)) \quad (20)$$

where the disturbance in Equation 7, v , is Gaussian White Noise of unit intensity. It can be shown that when there is a minimum positive value, γ , such that there exists a symmetric, positive-definite solution to the equation

$$PA + A^T P + C^T C - P \left(BR^{-1} B^T - \frac{1}{\gamma^2} LL^T \right) = 0 \quad (21)$$

then for optimal full state feedback control, the value of the performance metric is the square of this limiting value of γ [4].

For the typical section, it is possible to solve for this γ in closed form:

$$J_{\text{opt}} = \gamma_{\min}^2 = \begin{cases} \mathcal{G}^2 \left(\frac{\mathcal{F}^2}{\rho^2} + \frac{\omega^2}{N^2} 4\zeta^2 (1 - \zeta^2) \right)^{-1} & \zeta \leq \frac{1}{\sqrt{2}} \\ \mathcal{G}^2 \left(\frac{\mathcal{F}^2}{\rho^2} + \frac{\omega^2}{N^2} \right)^{-1} & \zeta \geq \frac{1}{\sqrt{2}} \end{cases} \quad (22)$$

The same proportionality to \mathcal{G}^2 that was present in the \mathcal{H}_2 case is also present in the \mathcal{H}_∞ case. However, the dependence on the remaining terms has an interesting form. For very expensive control ($\rho \rightarrow \infty$), the term containing the controllability drops out and the cost reverts to the open loop cost. This solution implies that for problems in which the disturbability is relatively insensitive to parameter changes ($\frac{\partial \mathcal{G}}{\partial \alpha} = 0$), then a structure which was optimized for open loop response will also have optimal closed loop response. In other words, sequential design of the structure and control will achieve the same result as simultaneous design. The insensitivity of a system to disturbability can occur frequently in controlled structure design. This is most likely to happen when the disturbance is not well known, or widely distributed and uncorrelated. Hence, there is a possibility that it may actually be easier to design many \mathcal{H}_∞ controlled structures than their \mathcal{H}_2 counterparts. However, the complexity of the \mathcal{H}_∞ problem makes it infeasible to show here that it applies to higher order systems.

6 Conclusions

The typical section is a useful tool for understanding the implications of structural changes under different types of control. The ability to formulate closed form solutions makes it very easy to understand the functionality of the performance on modal properties. As long as the coupling between modes in a structure remains light, the typical section results, which exactly capture the behavior of a single controlled mode, should be reliable in higher order systems. However at high control levels, the modal coupling becomes more severe and the typical section insights become less reliable. In particular, the importance of controllability is reduced when fewer actuators than modes are available.

There exists the possibility that for systems in which the disturbability is insensitive to design parameters, sequential design (open loop structural optimization followed by control optimization) can actually yield an optimal design. However, it remains to be shown that this conclusion, which is valid for the typical section, generalizes to more complicated systems.

References

- [1] M. Milman, M. Salama, R. Scheid, R. Bruno, and J.S. Gibson, JPL Technical Report D-6767, October, 1989.
- [2] R. Kwakernaak and R. Sivan, *Linear Optimal Control Systems*. John Wiley and Sons, Inc., 1972.
- [3] R.N. Jacques and D.W. Miller. MIT SERC Report 1-91, February 1991.
- [4] J.C. Doyle, K. Glover, P.P. Khargonekar, and B.A. Francis. *IEEE Transactions on Automatic Control*, 34(8), August 1989.

Smart Patch Piezoceramic Actuator Issues

S. F. Griffin, K. K. Denoyer, B. J. Yost
Phillips Laboratory
Edwards AFB, CA

Abstract

The Phillips Laboratory is undertaking the challenge of finding new and innovative ways to integrate sensing, actuation, and the supporting control and power electronics into a compact self-contained unit to provide vibration suppression for a host structure. This self-contained unit is commonly referred to as a smart patch. The interfaces to the smart patch will be limited to standard spacecraft power and possibly a communications line. The effort to develop a smart patch involves both contractual and inhouse programs which are currently focused on miniaturization of the electronics associated with vibrational control using piezoceramic sensors and actuators. This paper is comprised of two distinct parts. The first part examines issues associated with bonding piezoceramic actuators to a host structure. Experimental data from several specimens with varying flexural stiffness are compared to predictions from two piezoelectric/substructure coupling models, the Blocked Force Model and the Uniform Strain Model with Perfect Bonding. The second part of the paper highlights a demonstration article smart patch created using the insights gained from inhouse efforts at the Phillips Laboratory. This demonstration article has self contained electronics on the same order of size as the actuator powered by a voltage differential of approximately 32 volts. This voltage is provided by four rechargeable 8 volt batteries.

Introduction

The Phillips Laboratory has had a great deal of success in actively controlling vibration of structures with piezoceramic sensors and actuators, primarily through contractual efforts with TRW in Redondo Beach, CA. The manufacturing of composite structures with embedded or attached piezoceramic sensors and actuators, or smart structures, has advanced to the degree of at least a 99% success rate in the Advanced Composites with Embedded Sensors and Actuators

program with TRW. TRW has built smart specimens ranging in size from less than one foot long by two inches to seventeen foot long by five inch diameter tubes for the ASTREX test bed located at the Phillips Laboratory. Critical damping and beyond has been introduced into lightly damped structures using this technology.

The part of this technology that still needs further advancement is in the area of the support electronics. Since our goal is to eventually make this technology a viable solution to vibration problems in spacecraft, it is important to optimize the size and weight of the support electronics and to consider space environmental effects. For this reason, approaches which use low voltage per force output are being considered to minimize step up requirements on spacecraft voltage and thereby reduce the size and number of components in the necessary power electronics. The end result of satisfying these miniaturization goals will be the development of a small, lightweight smart patch which will have the ability to sense and control unwanted vibrations in a host structure. The smart patch will be very useful in providing solutions to unanticipated vibration problems in spacecraft programs without the need for major redesign. Also, surface mounted vibration suppression technology may be necessary for structures whose manufacturing process is too harsh to allow embedment of sensors, actuators, or electronics. With a surface mounted smart patch, issues such as bonding and actuator-structure interaction become even more important than the case where embedded sensors and actuators are designed into the structure.

At the Phillips Laboratory, our inhouse smart structures program is addressing some of the questions concerning smart patch technology. This paper describes two parts of this effort. The first part is a description of recent experimental efforts to better understand piezoceramic actuator and structure interaction. The second part of the paper concentrates on integration of sensor, actuator, and electronics into a smart patch. It describes a demonstration article constructed using insights gained from earlier inhouse efforts. This article consists of a graphite/epoxy substructure with an attached smart patch. The patch meets the basic goals of inherent sensing, actuation, and control. It runs on a voltage differential of approximately 32 volts.

Surface-Bonded Piezoceramic Actuator Models

There are several models in the literature that predict how a structure behaves with a surface bonded piezoceramic actuator when a voltage is applied to the piezoceramic. In this research, we were primarily interested in the bending behavior of a structure with surface bonded piezoceramics. For this reason, we will only review models as they relate to bending (in the models reviewed,

there is a simple path to go from bending behavior to extension and compression). The actuator/structure interaction has been modeled both analytically and through the use of finite element codes. The analytical models we examined range in complexity from a simple blocked force model which neglects the effects of the substructure and bending of the actuator and treats the piezoceramic as being "blocked" in extension and compression all the way to Uniform Strain Models which include the effects of the actuator, bonding layer, and substructure [3]* and two-dimensional models based on laminated plate theory. The finite element approach models the piezoceramic as a thermoelastic element and treats the applied actuator voltage as a temperature differential.[†] The models considered in this work are the blocked force piezoelectric model and the Uniform Strain models consisting of one model which assumes there is a finite bonding layer between the piezoelectric and the substructure and a second which assumes that the piezoelectric actuator is perfectly bonded. Both of the Uniform Strain Models assume that there is uniform strain in the piezoelectric and a linear Euler-Bernoulli strain distribution in the substructure. It will be shown that all three of these models are related and, in fact, converge on each other depending on material properties and geometry of the structure, piezoelectric actuator, and the bonding layer.

Uniform Strain Model with Finite Thickness Bonding Layer

The Uniform Strain Model with Finite Thickness Bonding Layer assumes a finite thickness bonding layer between the piezoceramic actuator and the substructure. Force is transferred in shear from the piezoceramic to the substructure through the bonding layer, leading to the classic shear lag problem. The amount of shear lag depends on the shear lag parameter Γ where

$$\Gamma^2 = \frac{G}{t_s} \left(\frac{1}{E_c t_c} + \frac{\alpha}{E_b t_b} \right) \quad (1)$$

G is the shear modulus of the bonding layer, t_s is the thickness of the bonding layer, E_c is the modulus of the piezoceramic, t_c is the thickness of the piezoceramic, E_b is the modulus of the substructure, t_b is the thickness of the substructure, and α is 6 for bending. When the shear lag parameter Γ is greater than 30, the assumption that the piezoelectric is perfectly bonded to the substructure "will provide results sufficiently accurate for engineering models" [1]. In light of this, we decided to establish the necessity of using this model for our experimental specimens. Using equation (1), we calculated the values of Γ for each of our experimental specimens. Since the lowest value of Γ was over 200, we elected to make our experimental comparisons using the Uniform Strain Model with Perfect Bonding and the Blocked Force Model which are described below. It has been shown that in the limit as Γ approaches infinity, the finite bonding layer

*References 1-3 are cited in the text.

†Bronowicki, A. J., Betros, R. S., course notes from "Active Damping Workshop."

solution converges to that of perfect bonding [1].

Uniform Strain Model with Perfect Bonding

In the Uniform Strain Model with Perfect Bonding, it is assumed that the piezoceramic actuator is perfectly bonded to the substructure. Since the shear stress applied to the substructure by the piezoelectric is concentrated at the ends of the piezoelectric in this case, the piezoceramic can be thought of as delivering a line force at its ends to the substructure. Briefly, the derivation of the forcing term involves a strain at the outer surface of the substructure due to bending given by

$$\epsilon = -\frac{My}{E_b I} \quad (2)$$

where I is the moment of inertia, y is the distance from the neutral axis and M is the applied moment. This strain is assumed to be the same as the uniform strain in the piezoelectric actuator which is given by

$$\epsilon = \frac{\sigma}{E_c} + \frac{d_{31}V}{t_c} \quad (3)$$

where σ is the in-plane longitudinal stress in the piezoceramic, d_{31} is a piezoelectric charge constant of the piezoceramic, and V is the applied voltage. Combining these equations and using the fact that the applied moment M in (2) is due to the line force generated by the piezoelectric, the expression for force applied to the substructure is given by

$$F = -\frac{E_b t_b b \left(\frac{d_{31}V}{t_c} \right)}{\frac{E_b t_b}{E_c t_c} + 6} \quad (4)$$

where b is the width of the piezoceramic.

Blocked Force Model

The Blocked Force Model makes the assumption that the force applied to the piezoelectric is exactly the same as the force that would be produced if the voltage were applied to the piezoelectric with its ends fixed in place. This results in the following force expression

$$F = -E_c b d_{31} V \quad (5)$$

It is easy to see that this expression is the limit of (4) as the ratio of $\frac{E_b t_b}{E_c t_c}$, the effective stiffness ratio, approaches infinity. It is interesting to note that since this expression exhibits no dependence on piezoceramic thickness in a voltage limited, but not necessarily power limited application, it would make sense to operate many thin piezoceramics in parallel rather than one thick one to increase force output. For example, if there were .010" of space allocated for piezoceramics and one .010" thick piezoceramic provided one unit of force per volt, two .005" thick piezoceramics would provide two units of force per volt. If this same exercise is undertaken by substituting typical piezoceramic values into the Uniform Strain Model with Perfect Bonding, a value of even higher than twice the original value is obtained. This neglects losses in actuation due to the additional bonding surfaces and no allowance is made for the thickness of the bonding layer. Also, there is a saturation limit that defines a maximum amount of voltage per thickness of the piezoceramic that has to be considered. However, even with these factors which will tend to decrease the force values from a multi-piezoelectric approach, it still may be more efficient from a size and power efficiency standpoint when compared to stepping up the voltage on a single thicker piezoelectric. Obviously this will be an optimization problem that will have to be solved for a given application.

Model Verification Experiment

To compare different actuator models and vary parameters of interest on several different test specimens, it was important to come up with a simple, reproducible test configuration. The configuration decided on was a cantilevered beam with surface bonded actuators near the base as shown in Figure 1. The poling directions of each of the piezoelectric wafers face the top of the page. The predicted and measured parameter was the deflection of the tip of the beam given a voltage applied to the piezoelectric actuators. A voltage could then be applied in the poling direction of one piezoceramic and in the opposite direction of another with the substructure providing a common ground. This configuration makes the entire structure a bender element with voltage applied in parallel and a large moment arm.

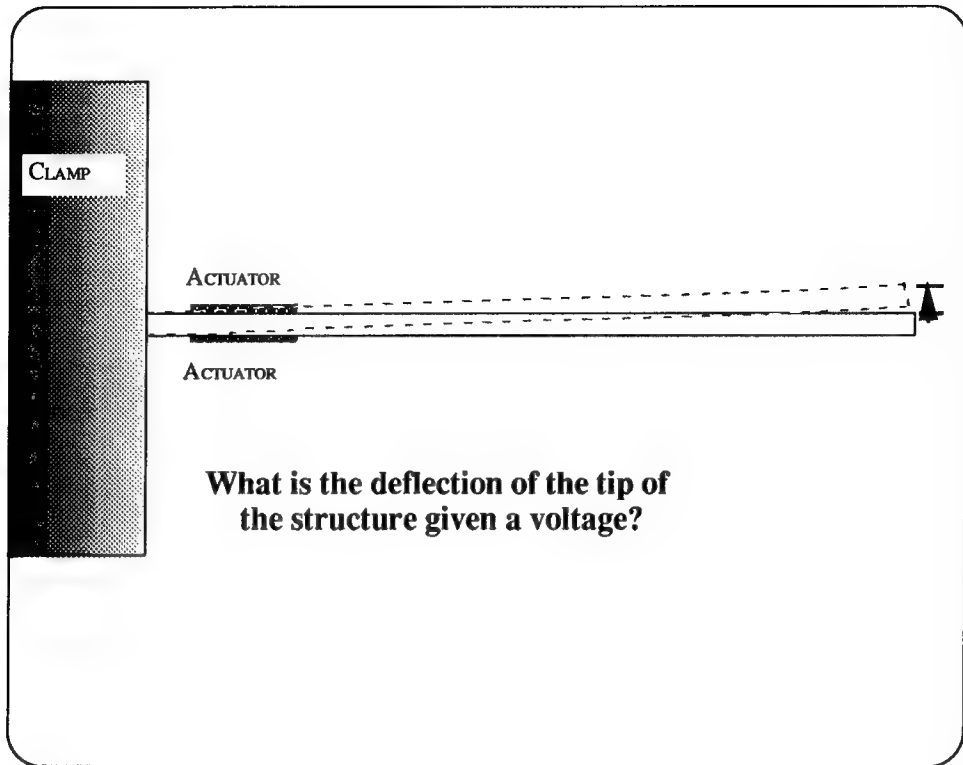
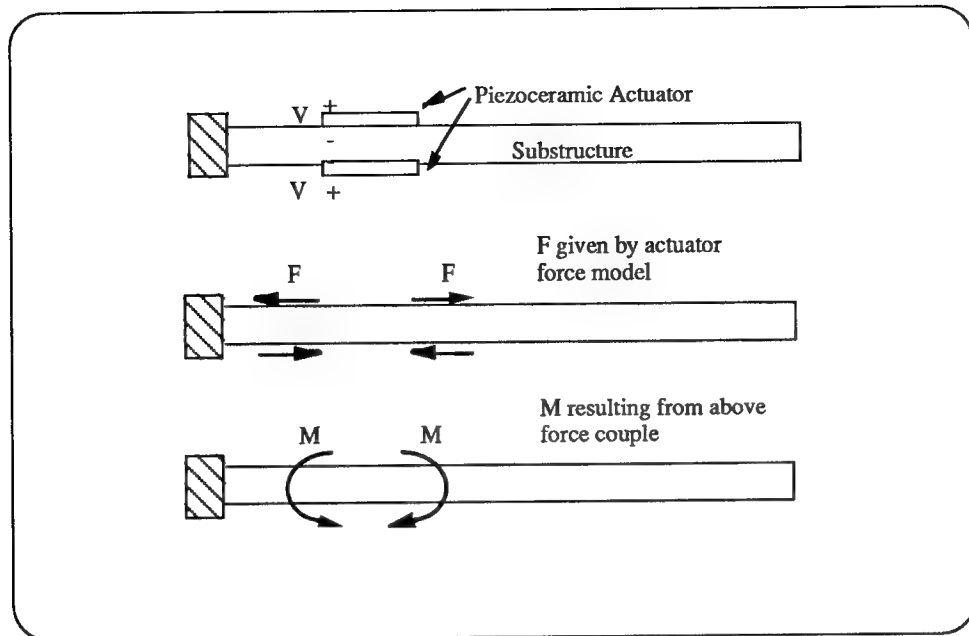


Figure 1

Voltage-Tip Deflection Relationships

To get the predicted voltage-tip deflection relationships, equations from elementary mechanics were used to calculate a tip deflection due to the force couples resulting from the actuator forces predicted by the piezoelectric/substructure coupling models. The evolution of these forces to applied moments is shown in Figure 2.



Development of Voltage - Tip Deflection Relationship

Figure 2

From elementary mechanics, the cantilever tip deflection is found to be

$$\Delta = \frac{M}{2E_b I} (2LX - 2La - L^2) \quad (6)$$

where I is the moment of inertia of the substructure, E_b is the flexural modulus of the substructure, M is the applied moment, L is the length of the piezoceramic and X is the length of the substructure. For each model, the appropriate M must be substituted into (6) to get the voltage-tip deflection relationship for that model.

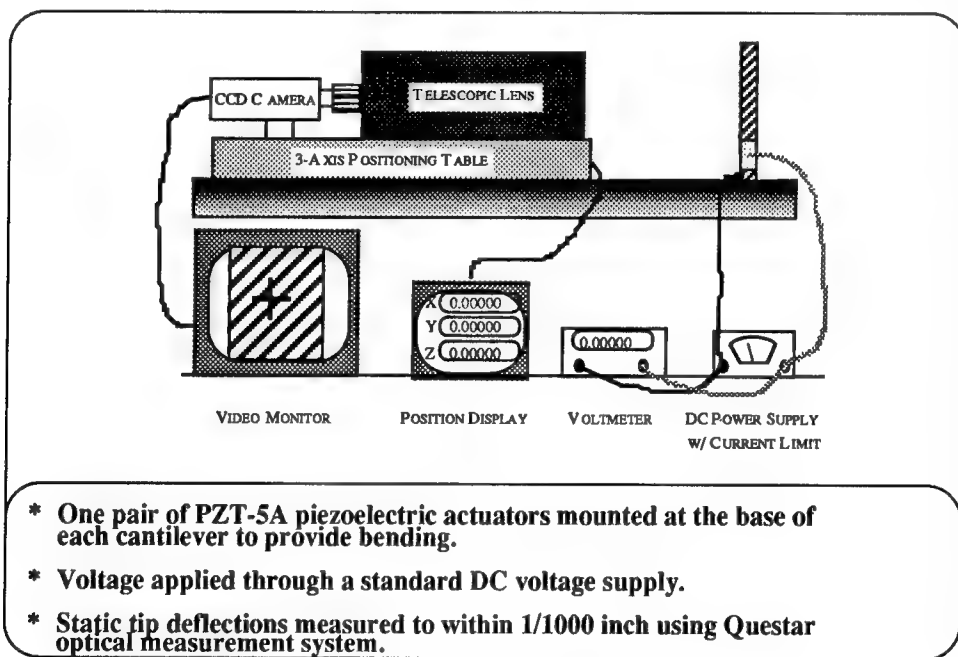
Experimental Specimens

Experimental specimens were fabricated as described with piezoceramic actuators located symmetrically near the base. The piezoelectric actuators used were PZT-5A, each wafer measuring 1.5" x 2.5" x .010". Specimens included aluminum and steel specimens and five composite specimens of varying flexural stiffness. The specimens had a clamped length of approximately 14 in., were 1.5 in. wide, and had thicknesses of about 0.05 in. The composite specimens were all fabricated from unidirectional graphite/epoxy prepreg. The fibers were relatively stiff (IM7) and the resin was a toughened resin suitable for spacecraft applications, 977-2. The composite specimens were 10 plies each with the most flexible lay-up to least flexible lay-up as follows:

[0,90,90,90,90]s, [0,0,90,90,90]s, [0,0,0,90,90]s, [0,0,0,0,90]s, [0,0,0,0,0]s, where s denotes a symmetric lay-up. Composite specimens were given the letter names A,B,C,D and E with A corresponding to the least flexible specimen and E corresponding to the most flexible specimen. Flexural modulus of the specimens was found by measuring the first resonant frequency of a cantilevered specimen and backing out the equivalent Euler beam flexural modulus from the Euler-Bernoulli frequency equation for a cantilever beam after measuring all other relevant beam parameters [2]. This method gave us a slightly lower, and we felt more realistic, flexural modulus than that predicted from manufacturer's properties and laminated plate theory which tend to give optimistic values for the modulus.

Experimental Setup

The experimental setup for measuring tip deflection given a voltage is shown in Figure 3.



Experimental Setup

Figure 3

Voltage was applied with a standard DC voltage current limited power supply. A precision voltmeter was placed in parallel with the voltmeter. Beam tip deflection was measured through a telescope with a magnification of approximately 100 to 1. The telescope was attached to a CCD camera which had an accompanying reference monitor with cross hairs. The camera and telescope were mounted on a high precision three axis positioning table. The position of a focused object

could be tracked to at least .001". Actual repeatable accuracy was closer to .0001", but only the one mil, or .001", digit was treated as accurate for the experimental data.

Figures 4 through 10 show measured tip deflection and predicted tip deflection versus applied voltage for each of the aluminum, steel, and composite specimens.

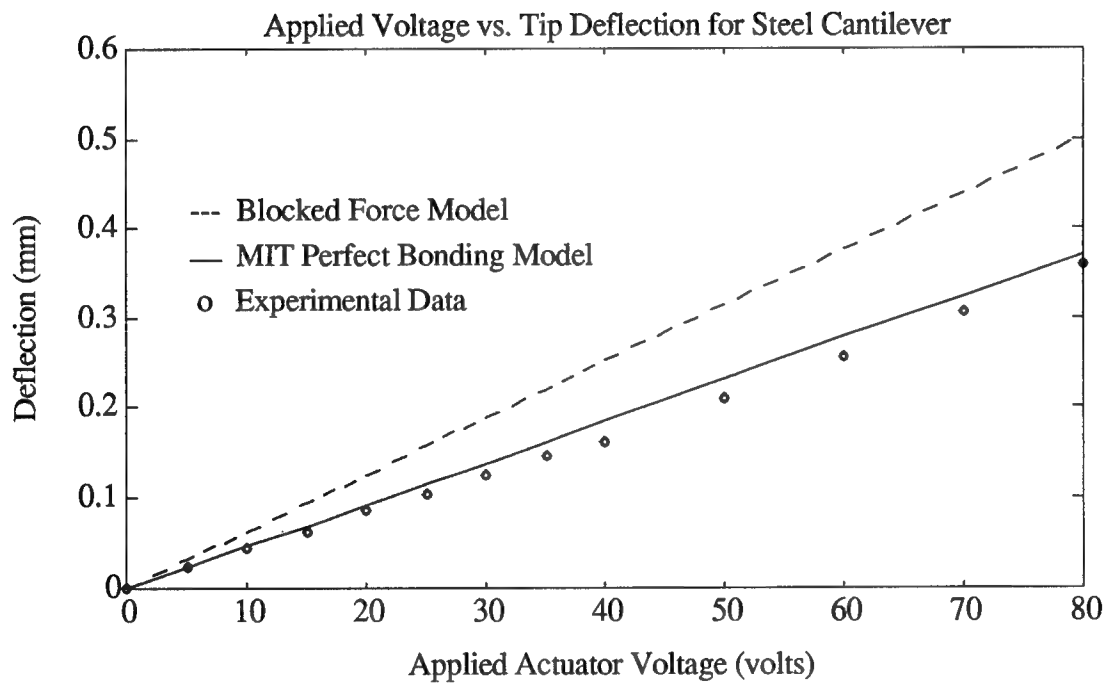


Figure 4

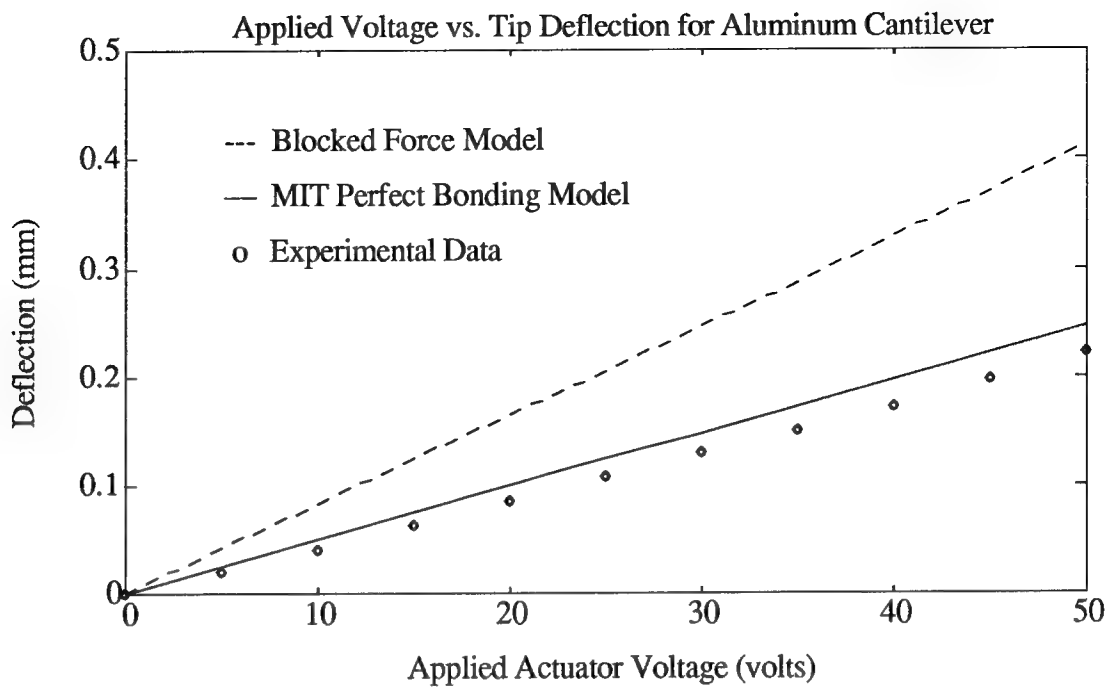


Figure 5

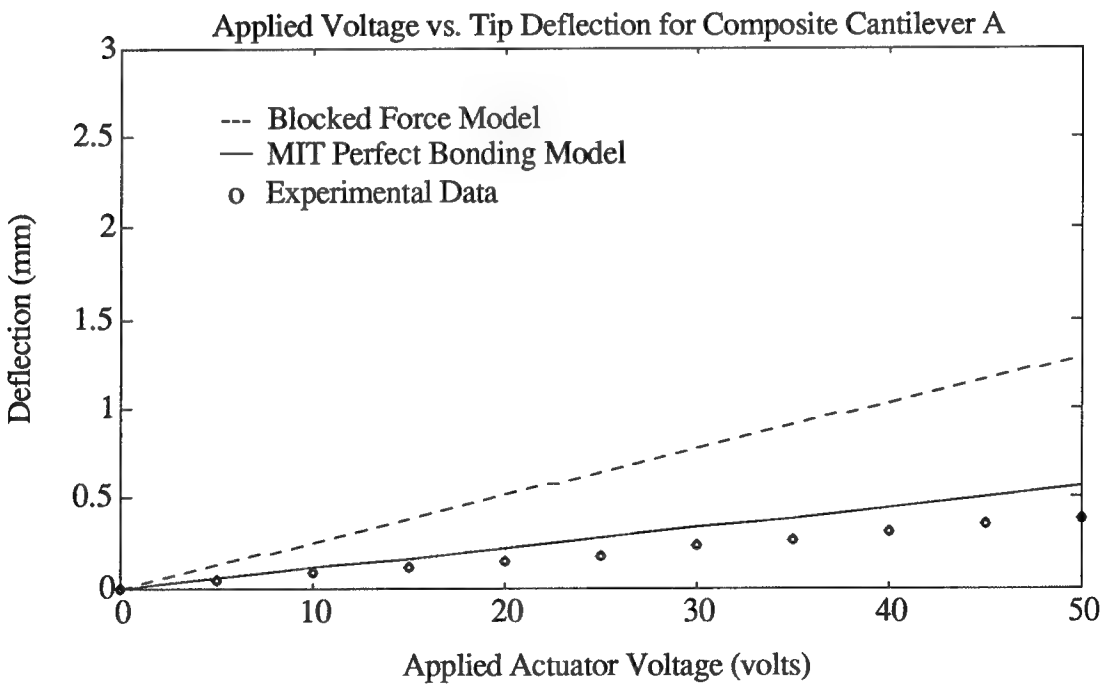


Figure 6

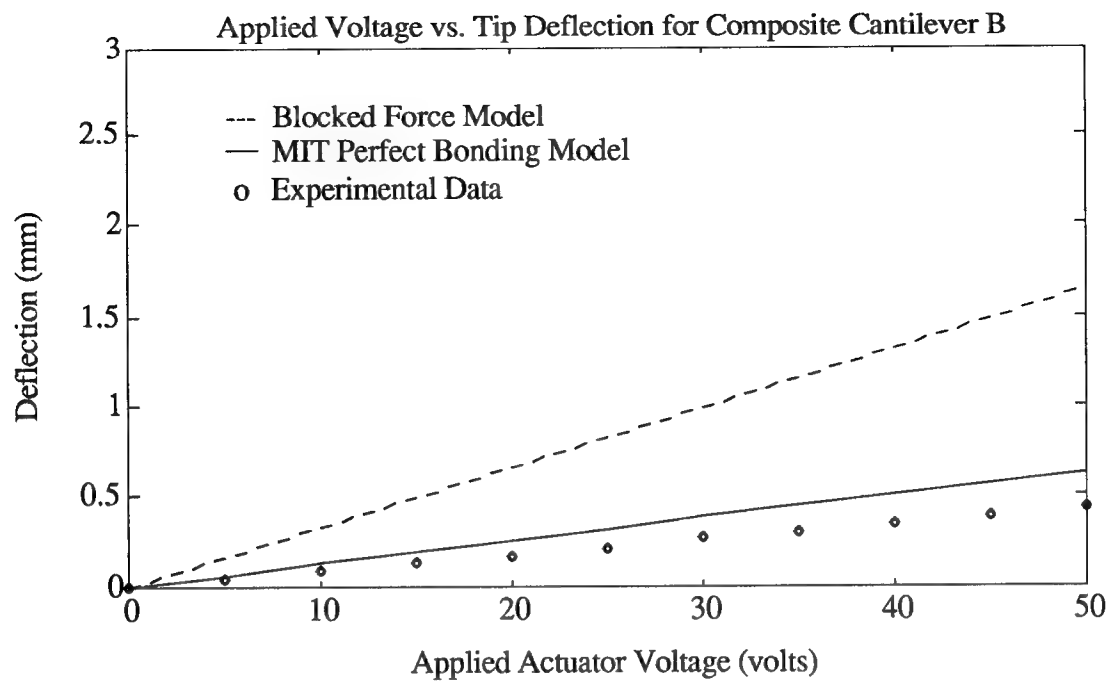


Figure 7

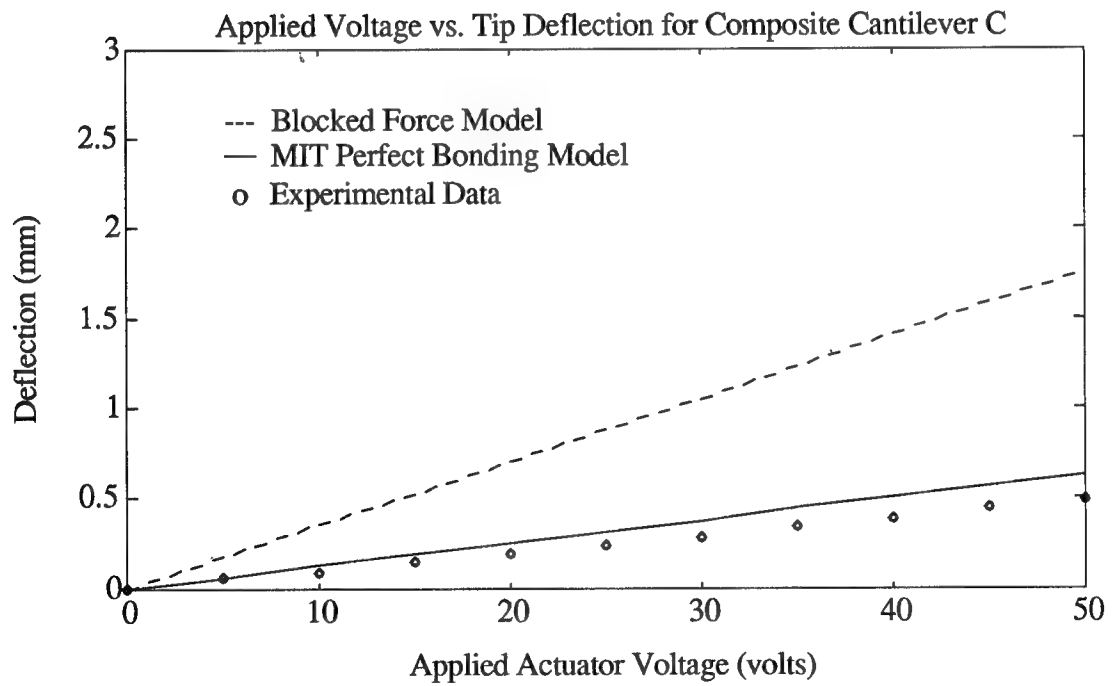


Figure 8

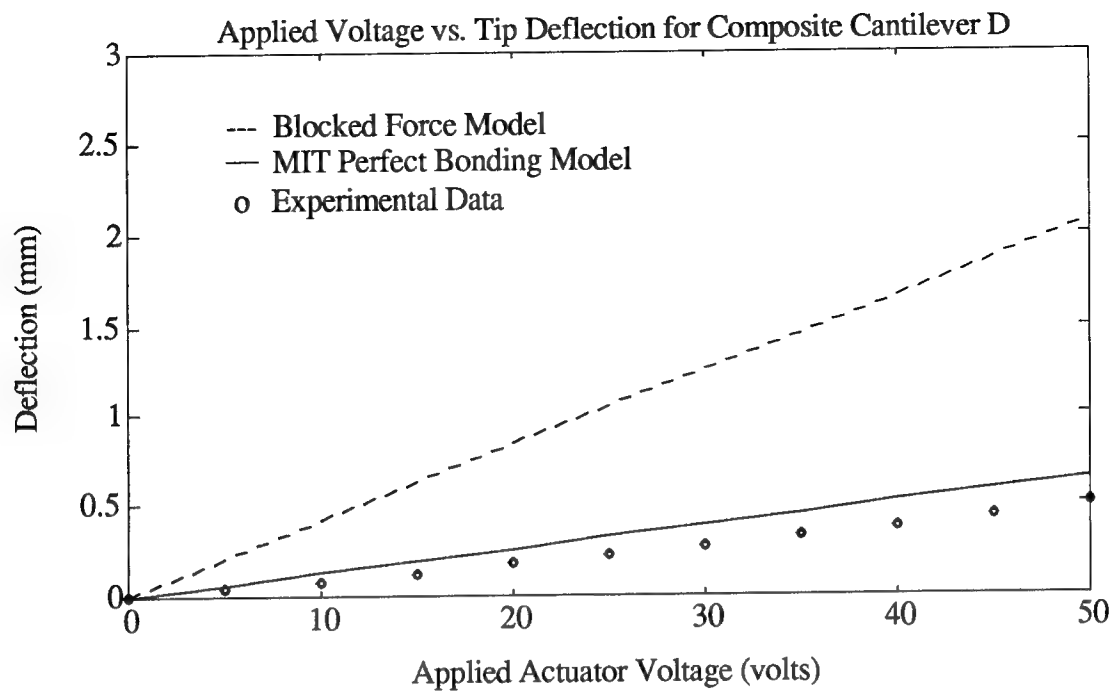


Figure 9

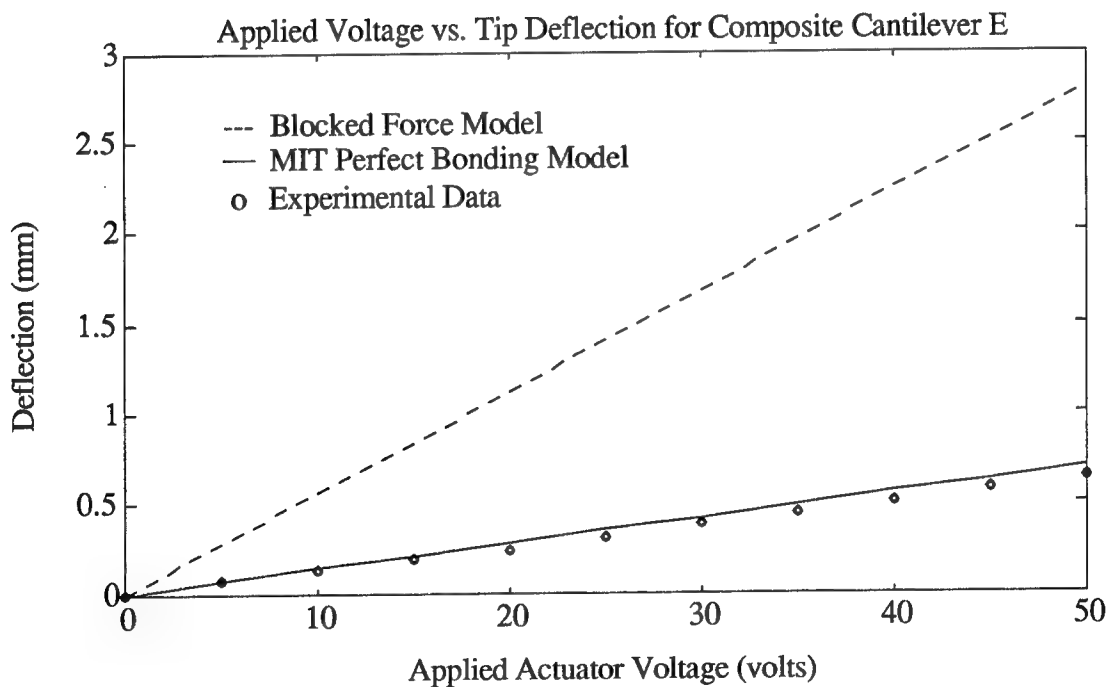


Figure 10

The first item to note from these plots is that the experimental data is consistent relative to the model predictions for all of the specimens showing the models give similar results for isotropic materials as well as the composite specimens. By examining the data for the composite specimens, several other trends become apparent.

- * The predictions of the Blocked Force Model become worse as the substructure becomes softer. This is to be expected since a soft, flexible substructure is less like the blocked end condition assumed by this model.
- * The predictions of the Uniform Strain Model with Perfect Bonding become better as the substructure becomes softer. This is also to be expected since the shear lag parameter (1) becomes larger for the softer structure and the bonding condition becomes more like that of a perfect bond.
- * The predictions of the Uniform Strain Model with Perfect Bonding correlate better with the experimental data than the predictions of the Blocked Force Model but the two predictions converge as the structure gets stiffer. This makes sense since the effective stiffness ratio (4) becomes higher and the Uniform Strain Model with Perfect Bonding begins to converge to the Blocked Force Model. Figure 11 shows how the two models would converge for a very stiff structure and diverge for a very soft structure.

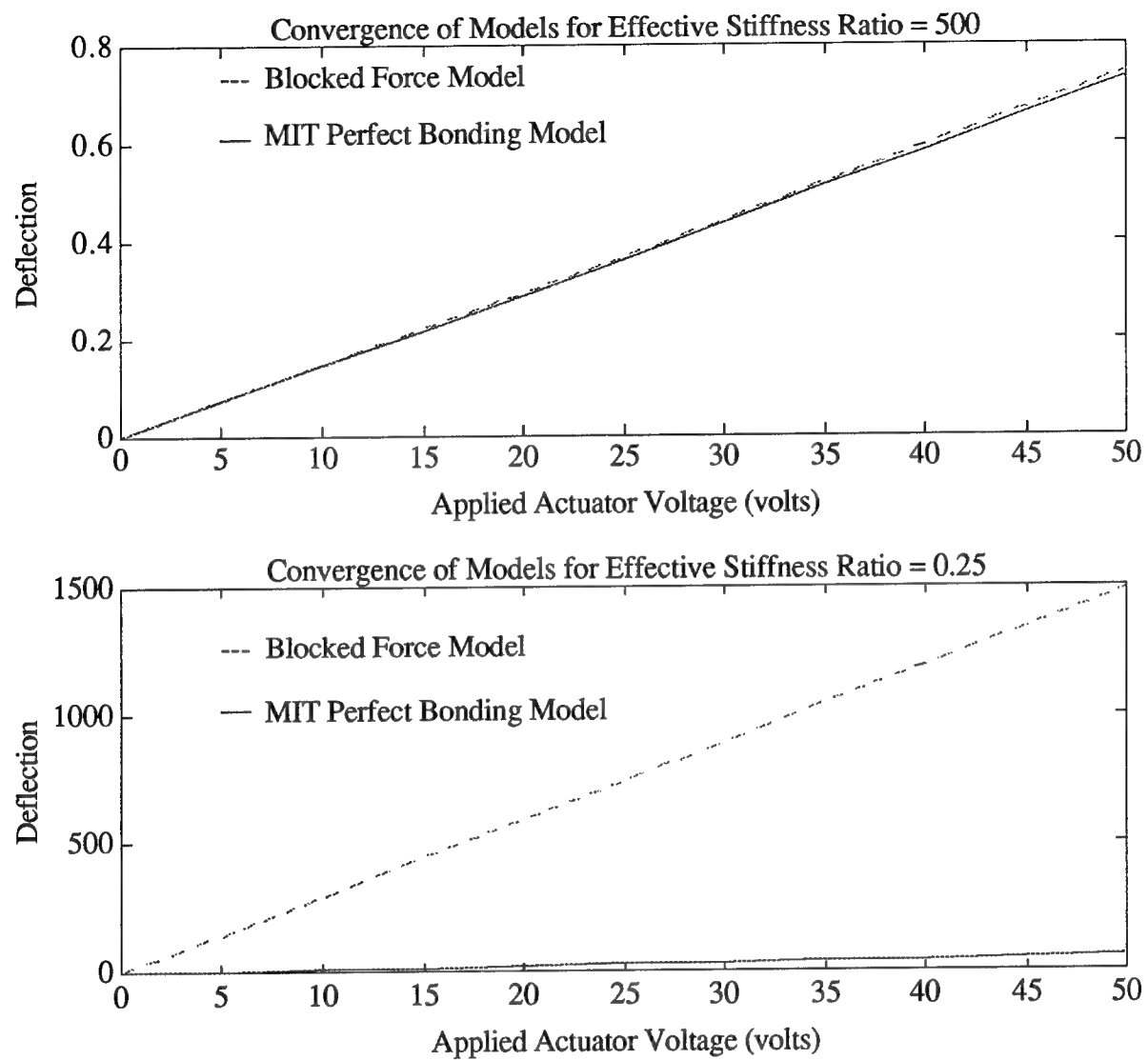


Figure 11

Construction of Smart Patch Demonstration Article

In this demonstration article, multilayer piezoelectric actuators are bonded to the base with a piezoelectric sensor and the necessary control and power electronics bonded to the substructure above the actuators. The size of the electronics is at least the same order of magnitude as the combined size of the sensor and actuators. The voltage differential provided to the electronics is approximately 32 volts. This is provided by four small rechargeable batteries housed in the base of the structure. The schematic of the demonstration article is shown in Figure 12.

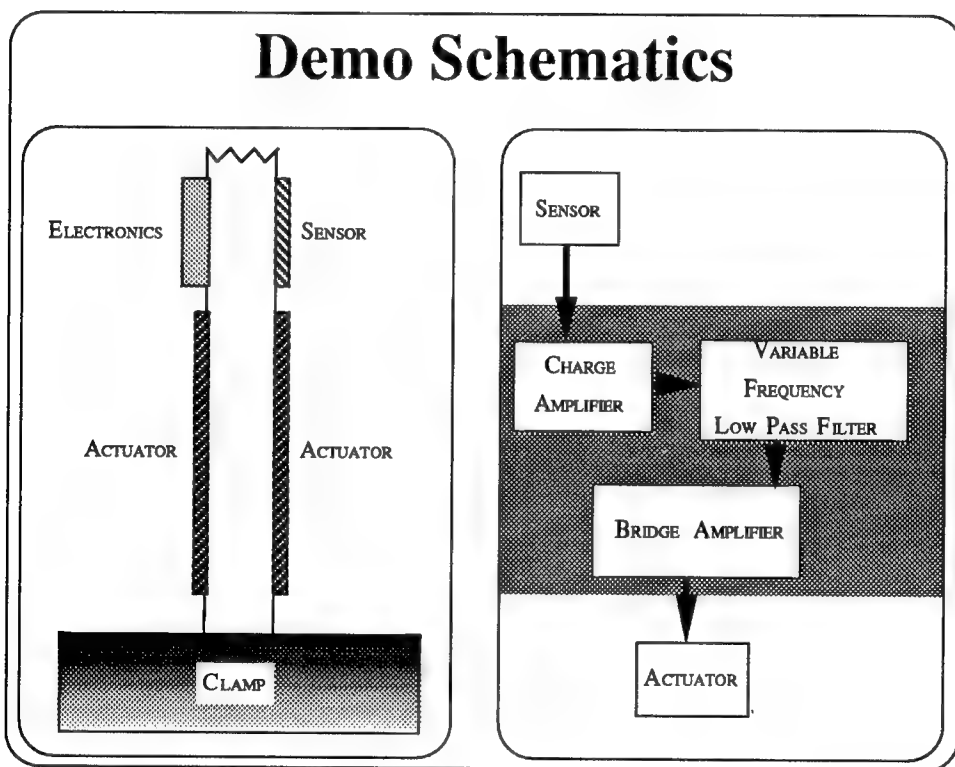
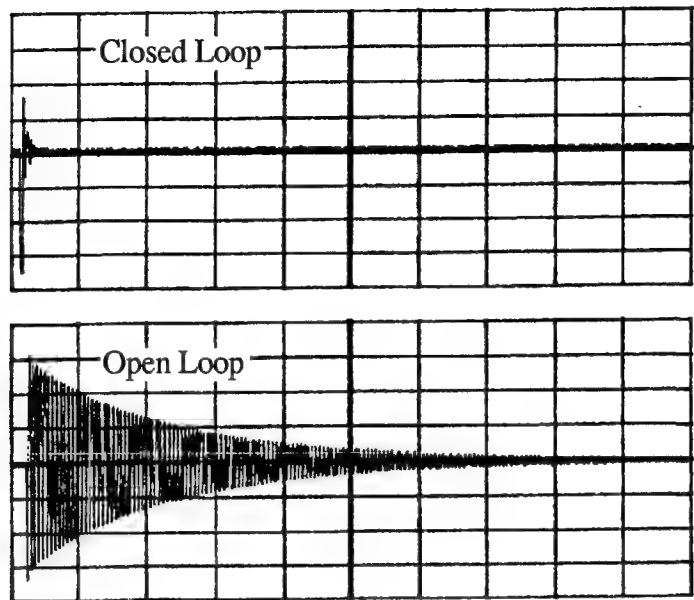


Figure 12

The control of the structure is provided by a two pole low pass filter which shifts the phase of the piezoelectric sensor output at the structures first resonance in relation to the output by 90 degrees of phase.* This provides active damping to the system which is illustrated by the open and closed

*Bronowicki, A. J., Betros, R. S., course notes from "Active Damping Workshop."

loop responses of the strain seen by the piezoelectric sensor which are shown in Figure 13.



Closed and Open Loop Response of Piezoelectric Sensor

Figure 13

Conclusions

We hope that the work presented in this paper will be useful to those interested in understanding some of the basic issues involved in the development of a piezoelectric based smart patch. The following are some of the important conclusions that can be made from this research.

- * Given a surface bonded piezoceramic actuator of fixed size and shape, even the simplest Blocked Force Model may be adequate for a relatively flexurally stiff substructure and a very good bond. It is not necessary to always use a more complex model to achieve good practical results.
- * The Uniform Strain Model with Perfect Bonding is necessary for relatively soft substructures. Given a fixed size and type of bonding layer, perfect bonding is a better approximation if the substructure is relatively flexurally soft. However, in

cases where bonding produces significant shear lag, it may be necessary to go to the more complex Uniform Strain Model with Finite Thickness Bond to adequately predict the actuator forces. Depending on the degree of accuracy needed, this may be necessary even for values of Γ greater than 30. Also, for substructure geometries other than an Euler-Bernoulli beam, it may be necessary to use other models such as those based on plate theory to get desirable results.

* Smart patch technology does not have to be costly and complex to be effective. This has been illustrated by the demonstration article which uses very simple strain rate feedback and a small compact smart patch design. The entire demonstration article material cost was less than \$100.00.

References

- [1] Crawley, E.F. and de Luis, J., "Use of Piezoelectric Actuators as Elements of Intelligent Structures", AIAA Journal, Vol.25, No.10, Oct. 1987, pp.1373-1385.
- [2] Thomson, W.T., Theory of Vibration with Applications, 2nd Edition. New Jersey, Prentice-Hall, 1981, Section 7.4.
- [3] Crawley, E.F. and Anderson, E.H., "Detailed Models of Piezoceramic Actuation of Beams", Journal of Intelligent Material Systems and Structures, Vol.1, No.1, Jan. 1990, pp.4-25.

A NUMERICAL APPROACH TO CONTROLLER DESIGN FOR THE ACES FACILITY

W. Garth Frazier¹ and R. Dennis Irwin²
Department of Electrical and Computer Engineering
Ohio University, Athens, Ohio

INTRODUCTION

In recent years the employment of active control techniques for improving the performance of systems involving highly flexible structures has become a topic of considerable research interest. Most of these systems are quite complicated, using multiple actuators and sensors, and possessing high order models. The majority of analytical controller synthesis procedures capable of handling multivariable systems in a systematic way require considerable insight into the underlying mathematical theory to achieve a successful design. This insight is needed in selecting the proper weighting matrices or weighting functions to cast what is naturally a multiple constraint satisfaction problem into an unconstrained optimization problem. Although designers possessing considerable experience with these techniques have a feel for the proper choice of weights, others may spend a significant amount of time attempting to find an acceptable solution. Another disadvantage of such procedures is that the resulting controller has an order greater than or equal to that of the model used for the design. Of course, the order of these controllers can often be reduced, but again this requires a good understanding of the theory involved.

As an alternative to these synthesis procedures, some numerical techniques have been proposed for achieving design constraints. One technique that appears to be effective is that of Boyd and Barratt (ref. 1). Their approach is to cast the constraints for the design problem into a form such that the optimization is convex over the set of controllers that stabilize a given model of the system. Therefore, the solution is the global optimum and is obtained by standard mathematical programming techniques. Unfortunately, some constraints cannot be cast into a form that is closed loop convex; important ones being open loop controller stability, controller order, and controller structure (e.g., diagonal). A mathematical model of the plant is also required.

A method close in spirit to the technique presented here is that proposed by Newsom and Mukhopadhyay (ref. 2). In their approach the singular value gradients of a return difference operator are used to iteratively change the parameters of a nominal controller in

¹Research Assistant

²Associate Professor

order to improve the stability robustness properties of a system. The parameter correction vector at each iteration is chosen to decrease a cumulative measure (sum of squares) of all constraint violations. The disadvantage of this correction vector is that while the cumulative measure may improve, the worst violation is not guaranteed to improve. Recently, Mukhopadhyay (ref. 3) has extended the approach to incorporate other constraints, although a cumulative measure is still employed to monitor each constraint's improvement.

The algorithm employed here for synthesizing a controller for the Active Control Technique Evaluation for Spacecraft (ACES) facility simultaneously includes performance constraints and stability robustness constraints. It also has the advantage that the worst constraint violations are improved at each iteration as long as the constraints are locally feasible in the parameter space. The algorithm can use data generated from a system model or, more importantly, data derived directly from the open loop plant.

SYMBOLS AND ABBREVIATIONS

I	= identity matrix
C	= set of complex numbers
R	= set of real numbers
$Re[\cdot]$	= real part of a complex quantity
$[\cdot]^H$	= complex-conjugate matrix transpose
$[\cdot]^T$	= matrix transpose
$C^{n \times m}$	= set of complex-valued $n \times m$ matrices
$R^{n \times m}$	= set of real-valued $n \times m$ matrices
$\sigma_k[\cdot]$	= k^{th} largest singular value of a matrix
$\partial f / \partial [\cdot]$	= a matrix with (i,j) entry equal to $\partial f / \partial [\cdot]_{ij}$
$\ \cdot\ $	= Euclidean norm of a vector

ALGORITHM DESCRIPTION

Let

$$\Omega = \{\omega_j; j=1,2,\dots,N_\omega\} \quad (1)$$

be a set of frequencies at which the frequency response data of the plant is available. Let

$$\mathbf{p} = [p_1 \ p_2 \ \dots \ p_{N_p}]^T \quad (2)$$

denote a vector of controller parameters upon which the frequency dependent functions

$$f_i(\mathbf{p}): \Omega \rightarrow \mathbf{R}, \quad i = 1, 2, \dots, N_c, \quad (3)$$

depend. Define the design constraints by

$$f_i(\omega_j; \mathbf{p}) \geq c_i(\omega_j), \quad \forall \omega_j \in \Omega, \quad i = 1, 2, \dots, N_c, \quad (4)$$

where each $c_i: \Omega \rightarrow \mathbf{R}$ is defined according to the desired shape of f_i . Now define the set of violations at the k^{th} iteration by

$$S_k = \{(i, j): f_i(\omega_j; \mathbf{p}_k) \leq c_i(\omega_j), i = 1, 2, \dots, N_c, j = 1, 2, \dots, N_\omega\}. \quad (5)$$

and let $h_{ij}(\mathbf{p}_k) = f_i(\omega_j; \mathbf{p}_k)$ if $(i, j) \in S_k$. Let N_t be the total number of elements in S_k . It follows that if the partial derivative of f_i with respect to \mathbf{p} exists that

$$\mathbf{g}_{ij}(\mathbf{p}_k) = \left[\frac{\partial h_{ij}}{\partial p_1}(\mathbf{p}_k) \quad \frac{\partial h_{ij}}{\partial p_2}(\mathbf{p}_k) \quad \dots \quad \frac{\partial h_{ij}}{\partial p_{N_p}}(\mathbf{p}_k) \right]^T. \quad (6)$$

A fundamental result from optimization theory states that to improve a single violation $h_{ij}(\mathbf{p}_k)$ a parameter correction vector \mathbf{d}_k must be chosen with the property $\mathbf{g}_{ij}^T(\mathbf{p}_k) \mathbf{d}_k > 0$. Since, in general, there are many violations to be improved at any one iteration, \mathbf{d}_k should be chosen to satisfy $\mathbf{g}_{ij}^T(\mathbf{p}_k) \mathbf{d}_k > 0, \quad \forall (i, j) \in S_k$. A sufficient condition for such a direction to exist is that the system

$$\mathbf{J}_k^T \mathbf{d}_k = \mathbf{w}_k \quad (7)$$

be consistent, where \mathbf{J}_k is a matrix whose columns are the vectors $\mathbf{g}_{ij}(\mathbf{p}_k)$ for all $(i, j) \in S_k$, and \mathbf{w}_k is a vector such that each entry $w_{kn} > 0, n = 1, 2, \dots, N_t$. This is an N_t by N_p system of linear equations. In practice equation 7 is almost always underdetermined because there are usually more free parameters than violations. Hence, there may be many solutions. To obtain the solution having a minimum 2-norm, suppose that \mathbf{J}_k has rank r . Then \mathbf{J}_k has the singular value expansion (ref. 4),

$$\mathbf{J}_k = \sum_{i=1}^r \sigma_{ki} \mathbf{u}_{ki} \mathbf{v}_{ki}^T, \quad (8)$$

where $\sigma_{ki} > 0, i = 1, 2, \dots, r$ are the nonzero singular values of \mathbf{J}_k , and $\mathbf{u}_{ki}, \mathbf{v}_{ki}, i = 1, 2, \dots, r$ are the associated left and right singular vectors. If \mathbf{w}_k is in the range of \mathbf{J}_k^T , then

$$\mathbf{d}_k = \sum_{i=1}^r \sigma_{ki}^{-1} (\mathbf{u}_{ki}^T \mathbf{w}_k) \mathbf{v}_{ki}. \quad (9)$$

Although the above development indicates a general procedure for choosing an acceptable correction vector, it does not indicate how to choose the precise entries of \mathbf{w}_k for good algorithm performance. Since it is desired to improve all the violations simultaneously,

it seems reasonable to choose w_k such that each of the violations is considered to be equally important. Following the development of Mitchell (ref. 5), if the elements of w_k are chosen such that

$$w_{kn} = \|J_{kn}\|, \quad (10)$$

where J_{kn} is the n^{th} column of J_k which is actually $g_{ij}(p_k)$ for some $(i,j) \in S_k$. Then from equation 7

$$g_{ij}^T(p_k) d_k = \|g_{ij}(p_k)\|, \quad j=1,2,\dots,N_i. \quad (11)$$

Using the fact that

$$g_{ij}^T(p_k) d_k = \|g_{ij}(p_k)\| \|d_k\| \cos \Theta_{ij} = \|g_{ij}(p_k)\|, \quad (12)$$

where Θ_{ij} is the angle between $g_{ij}(p_k)$ and d_k , it is clear that

$$\cos \Theta_{ij} = \|d_k\|^{-1} \quad \forall (i,j) \in S_k. \quad (13)$$

Therefore, this choice results in a correction vector that forms an equal angle between itself and each $g_{ij}(p_k)$. The choice of other values for w_k continues to be an area of research interest.

Due to the nonlinearity of the parameter space, it is necessary to determine a satisfactory step length for the correction vector at each iteration. In most iterative algorithms the determination of the step length at each iteration is treated as an optimization problem. Unfortunately, this optimization can require many constraint function evaluations and would be computationally prohibitive in this algorithm. Therefore, the choice of an appropriate step length parameter at each iteration is based upon several other criteria: (1) maintaining closed loop stability, (2) maintaining open loop controller stability properties, and (3) improvement of the violated constraints. In order to maintain closed loop stability using discrete frequency data (as opposed to a mathematical model) the multivariable Nyquist criterion (ref. 6) is employed. Although it is not a reliable indicator of relative stability margins, it has proven effective in this algorithm for maintaining closed loop stability. Controller stability is achieved by simply monitoring the controller's poles. Although controller stability is not an absolute requirement, it is desirable in most applications, e.g., when loop failure is possible. As for the third criterion, the violated constraints are simply checked for improvements at each iteration. If they have improved, the parameter vector is updated and the step length is increased by a user defined factor for use at the next iteration. If not, the step length is reduced and the constraints are checked again. This process is repeated until improvements are registered or until the minimum step length allowed is reached. If the minimum step length is reached, then either a violated constraint has reached a local minimum or two gradients are in local opposition. In the case of a local minimum, the design can either be accepted or the constraint relaxed. The action to be taken if two gradients are opposed is now discussed.

In the case of two gradients in local opposition, the matrix J_k will be nearly rank

deficient and the correction vector d_k , although defined, will almost be orthogonal to all the gradient vectors. Hence, improving the constraints with an acceptable step length is highly unlikely. If one of the opposing gradients is not associated with the worst violation for that particular constraint, the problem can be circumvented by dropping that gradient from J_k at the current iteration. If, however, both gradients are associated with the worst violations of different constraints, then the constraints are not locally feasible and this technique will fail to improve the constraints. Hence, the algorithm is not guaranteed to satisfy all the design constraints, but it will improve the violated constraints until no further local improvement is possible. It is also important to note that even if the constraints are satisfied, they are only satisfied at the frequencies for which the design was performed. A flowchart of the complete algorithm is given in figure 1.

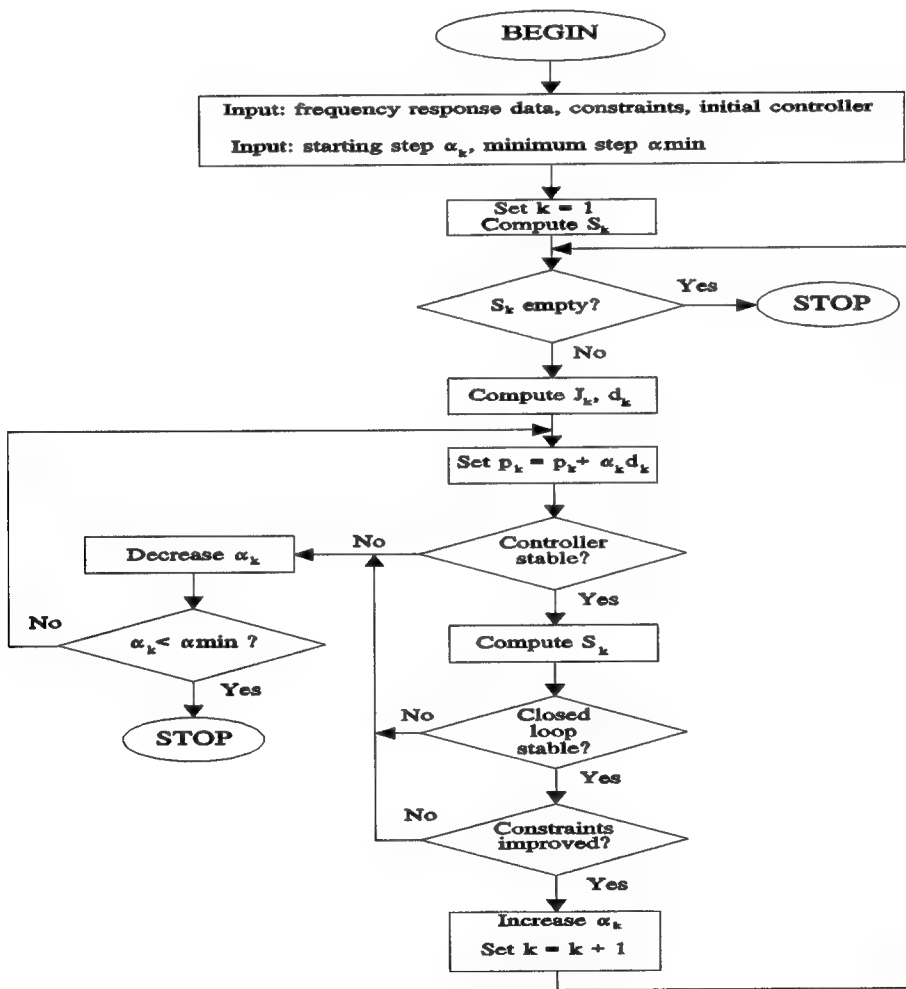


Figure 1: Algorithm Flowchart.

SELECTION OF A CONTROLLER REPRESENTATION

Two choices for a controller representation have been investigated. The most obvious choice is a state-space representation, i. e.,

$$K(e^{j\omega T}) = C(e^{j\omega T}I - A)^{-1}B + D, \quad (14)$$

where $K \in \mathbf{C}^{q \times p}$, $A \in \mathbf{R}^{n \times n}$, $B \in \mathbf{R}^{n \times p}$, $C \in \mathbf{R}^{q \times n}$, and $D \in \mathbf{R}^{q \times p}$ for an n^{th} -order discrete-time control law with p inputs and q outputs. It can be shown that if $f(Q) \in \mathbf{R}$, $Q = (A, B, C, D, \omega_i)$ (ω_i indicates a fixed frequency) is a function for which all the partials with respect to the entries of A , B , C , and D exist, then

$$\frac{\partial f}{\partial D}(Q) = \text{Re} \left[\left(\frac{\partial f}{\partial K}(Q) \right)^H \right]^T, \quad (15)$$

$$\frac{\partial f}{\partial C}(Q) = \text{Re} \left[\Phi B \left(\frac{\partial f}{\partial K}(Q) \right)^H \right]^T, \quad (16)$$

$$\frac{\partial f}{\partial B}(Q) = \text{Re} \left[\left(\frac{\partial f}{\partial K}(Q) \right)^H C \Phi \right]^T, \quad (17)$$

and

$$\frac{\partial f}{\partial A}(Q) = \text{Re} \left[\Phi B \left(\frac{\partial f}{\partial K}(Q) \right)^H C \Phi \right]^T, \quad (18)$$

where $\Phi = (e^{j\omega_i T}I - A)^{-1}$. An interesting property of this representation is that it is only unique up to a similarity transformation on (A, B, C, D) . Hence, the possibility exists that by judicious selection of state coordinates the characteristics of the parameter space may be chosen to impact algorithm performance. This issue is a subject of current research.

As an alternative to a state-space representation, the so-called Gilbert realization,

$$K(e^{j\omega T}) = \sum_{i=1}^n \frac{\mathbf{x}_i \mathbf{y}_i^T}{e^{j\omega T} - \lambda_i} + D \quad (19)$$

where $\lambda_i \in \mathbf{C}$, $\mathbf{x}_i \in \mathbf{C}^q$, and $\mathbf{y}_i \in \mathbf{C}^p$, has also been employed. An advantage of this representation is that for a given control law the number of parameters is considerably less than for a state-space representation. It has the disadvantage that the number of real poles and complex-conjugate pairs must remain the same throughout the iteration process.

ALGORITHM IMPLEMENTATION

At the present time the algorithm has been implemented in the FORTRAN programming language on a personal computer. Standard subroutine libraries in the public domain have been used extensively for singular value decompositions and eigen decompositions. The algorithm has also been implemented in the language of a popular matrix oriented software package.

CONTROLLER DESIGN FOR THE ACES STRUCTURE

A schematic of the NASA Marshall Space Flight Center ACES structure is shown in figure 2. The ACES structure is suitable for the study of line-of-sight (LOS) and vibration suppression control issues as pertaining to flexible aerospace structures. The primary element of the ACES structure, a spare Voyager magnetometer boom, is a lightly damped beam measuring approximately 45 feet in length and weighing about 5 pounds.

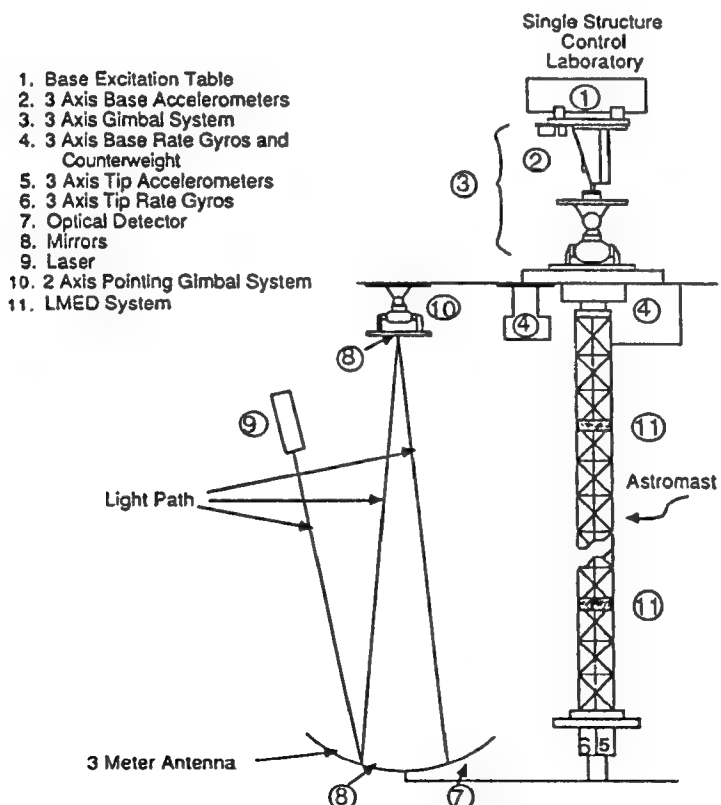


Figure 2: Schematic of the ACES Structure.

The goal of the control system design is to maintain the reflected laser beam in the center of the antenna (location of the detector) in the presence of disturbances at the base excitation table (BET). This is to be accomplished by use of the following actuators: Image Motion Compensation (IMC) gimbals (2-axes), Advanced Gimbal System (AGS) (3-axes), Linear Momentum Exchange Devices (LMED)'s (2 2-axes devices); and the sensors: base rate gyros (3-axes), tip accelerometers (3-axes), tip rate gyros (3-axes), LMED positions and accelerations (2-axes each) and the optical position detector (2-axes). As explained subsequently, our design only employed a subset of these sensors and actuators. The digital controller is to be implemented on the HP9000 computer located at the facility using the fixed sampling rate of 50 Hertz and a fixed, one sample period computational delay. The results of other controller designs for the ACES structure have been reported in the literature (ref. 7).

The experimental open loop frequency response from the y-axis IMC gimbal to the x-axis LOS error is shown in figure 3. The effect of the computational delay is quite apparent from analysis of the phase characteristic. The frequency responses of the other axes of the IMC-to-LOS are similar, although the cross-axis terms have less gain. The open loop frequency response from the y-axis AGS gimbal to the y-axis base gyro is shown in figure 4. This response reveals the numerous lightly damped modes of the structure. The frequency responses of other elements of the AGS-to-base gyros transfer matrix are similar. It is noted that the cross axis elements have considerable gains at some modal frequencies.

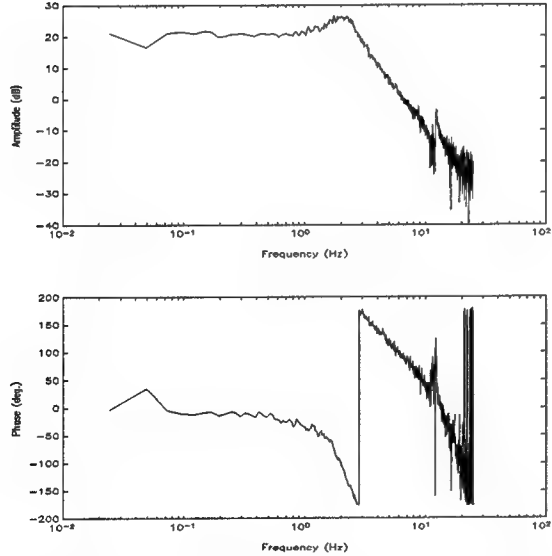


Figure 3: Experimental Frequency Response from y-axis IMC Gimbal to x-axis LOS Error.

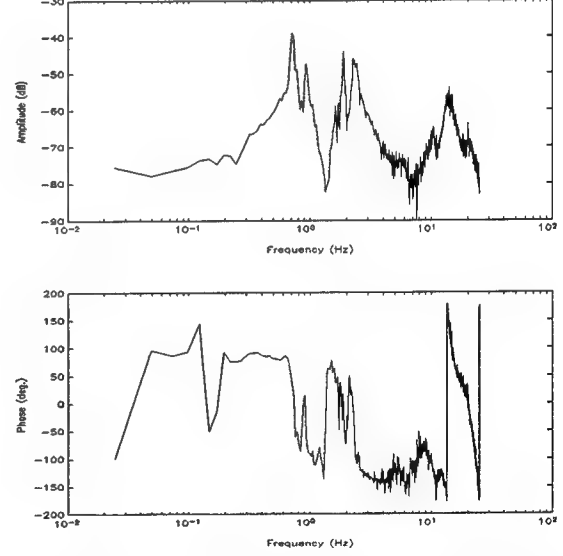


Figure 4: Experimental Frequency Response from y-axis AGS Gimbal to y-axis Base Gyro.

The basic design philosophy was to dampen the pendulum modes and the bending modes of the beam by using feedback from the base gyros to the AGS while using the IMC

gimbals with feedback from the detector to maintain the laser beam at the center of the detector. Due to sufficient decoupling, each two-input, two-output subsystem (AGS and IMC) was designed separately. One concern was the impact of disturbances that reach the IMC gimbals through the connecting arm that is attached to the base (as opposed to disturbances impacting the detector). Due to the inherently high optical gain from the IMC to the detector these disturbances can have a significant impact on the LOS error. To compensate for the effects of these disturbances it is not only necessary to maintain high loop gain over the frequency band of interest, but to also maintain high IMC controller gain as well. Analysis of figure 3 reveals that achieving high controller gain while also maintaining acceptable stability margins is difficult because of the combination of the high optical gain and the additional phase lag introduced by the computational delay. Fortunately, the impact of these disturbances can also be reduced by increasing the damping of the modes of the beam using the AGS; thereby reducing the motion of the base and the arm supporting the IMC gimbals.

The first step of the design procedure was the determination of a set of precise closed loop constraints such as those given in the first column of table 1. These constraints are primarily stability robustness constraints.

Table 1. Summary of Multivariable Design Constraint Values.

<u>Constraint</u>	<u>Initial</u>	<u>Final</u>
$\sigma_{\min} [I + GK(z)]_{IMC} > 0.5, f \in (0,25)$	0.2289	0.5090
$\sigma_{\min} [I + KG(z)]_{IMC} > 0.5, f \in (0,25)$	0.2276	0.5056
$\sigma_{\min} [I + (GK(z))^{-1}]_{IMC} > 0.6, f \in (0,25)$	0.2827	0.6072
$\sigma_{\min} [I + (KG(z))^{-1}]_{IMC} > 0.6, f \in (0,25)$	0.2805	0.6112
$\sigma_{\min} [I + GK(z)]_{AGS} > 18, f = 0.15$	10.002	14.100
$\sigma_{\min} [I + GK(z)]_{AGS} > 0.6, f \in (0,25)$	0.3649	0.5996
$\sigma_{\min} [I + KG(z)]_{AGS} > 0.6, f \in (0,25)$	0.3585	0.5988
$\sigma_{\min} [I + (GK(z))^{-1}]_{AGS} > 0.7, f \in (0,25)$	0.3600	0.6719
$\sigma_{\min} [I + (KG(z))^{-1}]_{AGS} > 0.7, f \in (0,25)$	0.3589	0.6712

IMC represents IMC subsystem

AGS represents AGS subsystem

G represents plant

K represents controller

$z = e^{j2\pi fT}, T = 0.02$ sec

The fifth constraint, a performance constraint, is included in particular to suppress the effect of a very lightly damped pendulum mode. Performance constraints were not included in the algorithm for the AGS subsystem, because after the design of the initial controllers, the primary concern for this subsystem was to guard against uncertainty. Analytical expressions for the gradients of these constraint functions were calculated using results from ref. 8 and equations 15-18.

Next, initial controllers were designed for the IMC-to-LOS and AGS-to-base gyro subsystems using graphical one-loop-at-a-time techniques with experimental frequency response data. Although the attempt was made to satisfy the constraints in designing the initial controllers, they were not satisfied as can be observed by comparing the first and second columns in table 1. The controller for each subsystem was 10th order. It should be noted that recently developed high fidelity models are 60th order for the AGS-to-base gyro loops alone (ref. 9). Design techniques such as LQG and H[∞] would yield controllers of at least this order (not including weighting).

The multivariable design (i.e., taking cross-axis coupling within each subsystem into account) for each subsystem was then performed using only experimental data and the presented algorithm. The algorithm was started with the initial 10th order controllers (using state-space representations) described above, with no restrictions other than stability placed on the structure of the controllers. To illustrate typical results from the algorithm, figure 5 and figure 6 show the experimental singular value frequency responses of $[I + GK]_{IMC}$ for the initial and final controllers, respectively. The final values of all the constraint functions are provided in the third column of table 1. The constraints for the AGS subsystem were not satisfied because the algorithm reached a point such that these constraint functions were in the condition of local opposition described previously.

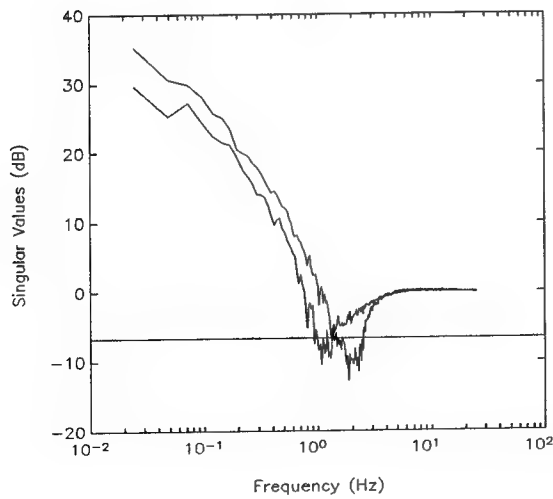


Figure 5: Initial Singular Value Frequency Response of $(I + GK)_{IMC}$.

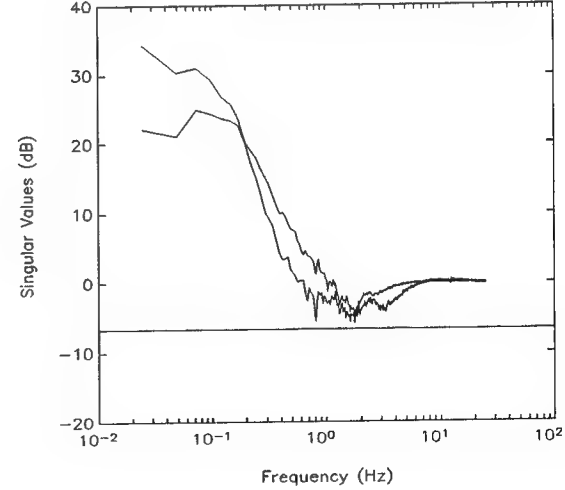


Figure 6: Final Singular Value Frequency Response of $(I + GK)_{IMC}$.

The resulting controller was implemented at the ACES facility. The open loop x-axis LOS error due to an x-axis BET disturbance (figure 7) intended to simulate the effect of spacecraft crew motion is shown in figure 8. The dominant behavior in the response is the lightly damped 0.15 Hz pendulum mode. After closing only the IMC-to-LOS loops the steady-state error and the impact of the pendulum mode were reduced as shown in figure 9. However, the first bending mode was still present. As shown in figure 10, closing the IMC-to-LOS *and* the AGS-to-base gyro loops further reduced the impact of the pendulum mode and almost eliminated the first bending mode. The y-axis LOS error was negligible.

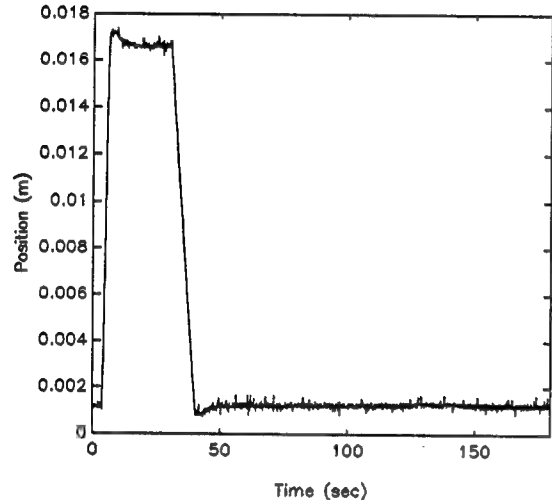


Figure 7: The x-axis BET Disturbance.

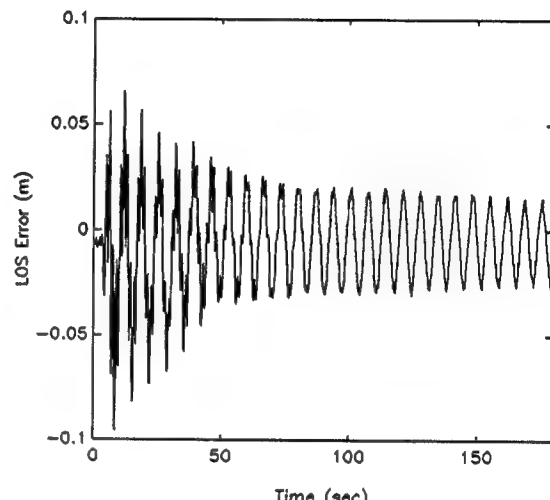


Figure 8: Experimental Open Loop x-axis LOS Error.

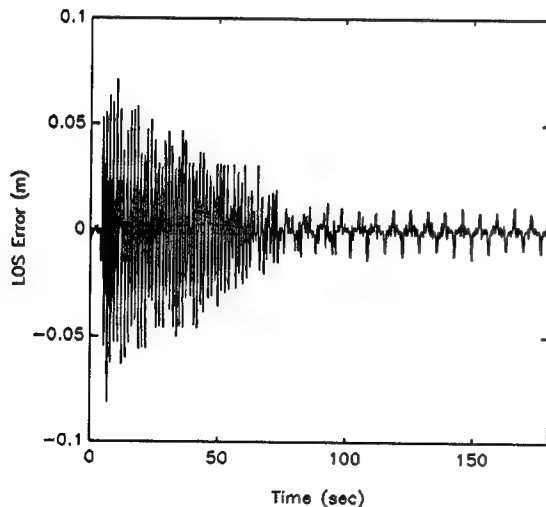


Figure 9: Experimental x-axis LOS Error with IMC Loops Closed.

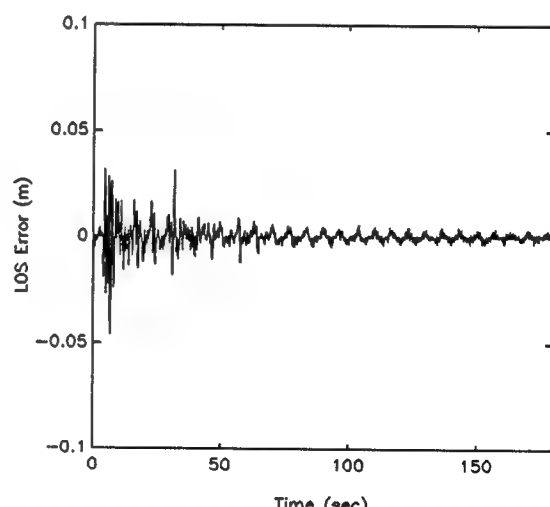


Figure 10: Experimental x-axis LOS Error with all Loops Closed.

To further indicate the effectiveness of the controller, x-y scatter plots of the LOS error are provided in figure 11 and figure 12, respectively.

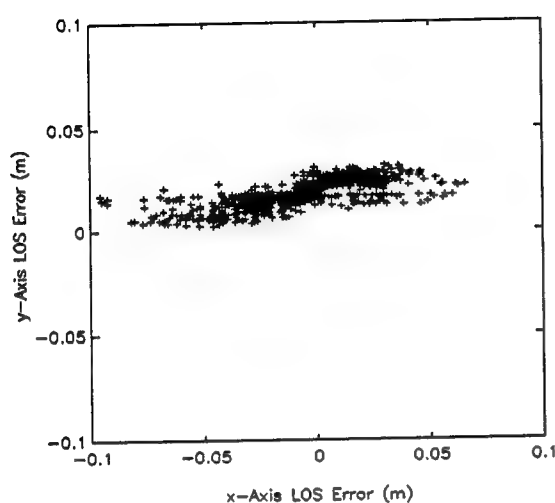


Figure 11: Experimental Open Loop x-y LOS Error.

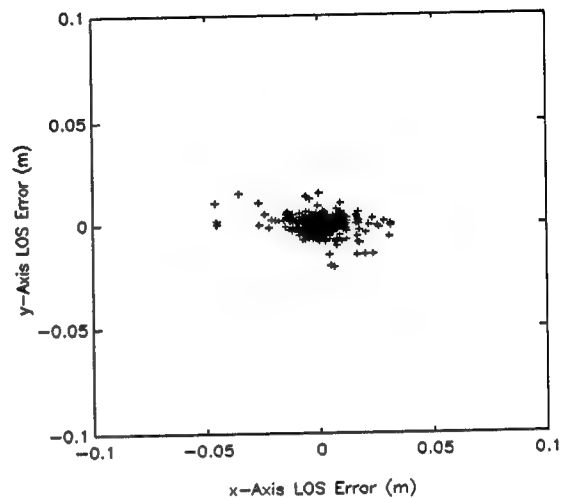


Figure 12: Experimental Closed Loop x-y LOS Error.

The same disturbance (figure 7) was applied to the y-axis of the BET. The open loop response of the x-y LOS error is shown in figure 13. The closed loop x-y LOS error is shown in figure 14.

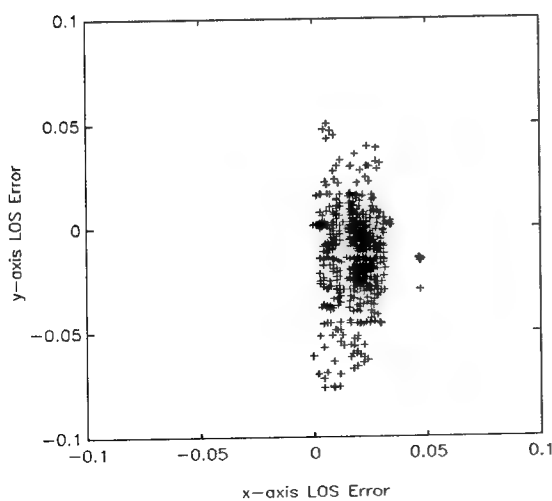


Figure 13: Experimental Open Loop x-y LOS Error.

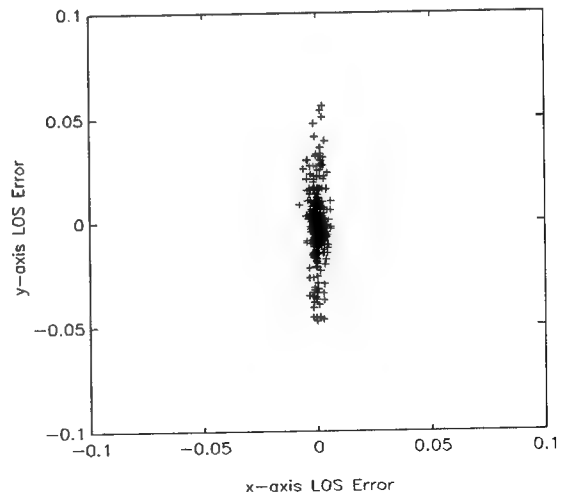


Figure 14: Experimental Closed Loop x-y LOS Error.

CONCLUSIONS

The application of an iterative numerical technique to controller design for a large space structure ground test facility has been presented, and the results appear to be very promising. The resulting controller was 20th order which was low compared to controllers resulting from procedures such as H[∞] or linear-quadratic-Gaussian. The presented technique has been shown to have the advantages that multiple closed loop design constraints can be simultaneously considered without the need for weighting schemes; the design engineer can have complete control over controller order and structure; the design can be performed with or without the use of a parametric plant model; and locally feasible, violated constraints can be improved at each iteration. Although the presented design example only involves constraints on matrix singular value frequency responses, there is no reason that the technique could not be applied to other constraints such as the shapes of individual elements of frequency response matrices and root-mean-square measures when such constraints are of interest.

ACKNOWLEDGMENTS

The authors would like to thank the NASA Marshall Space Flight Center and the Ohio Aerospace Institute for their support. Thanks is also due Dr. Jerrel Mitchell for his helpful comments.

REFERENCES

1. Boyd, Stephen P. and Barratt, Craig H., *Linear Controller Design: Limits of Performance*, Prentice-Hall, Englewood Cliffs, New Jersey, 1991.
2. Newsom, Jerry R. and Mukhopadhyay, V., "A Multiloop Robust Controller Design Study Using Singular Value Gradients," *Journal of Guidance, Control and Dynamics*, vol. 8, no. 4, pp. 514-519, July-August, 1985.
3. Mukhopadhyay, Vivek, "Digital Robust Control Law Synthesis Using Constrained Optimization," *Journal of Guidance, Control and Dynamics*, vol. 12, no. 2, pp. 175-181, March-April, 1989.
4. Golub, Gene H. and Van Loan, Charles F., *Matrix Computations*, 2 ed., The Johns Hopkins University Press, Baltimore, Maryland, 1989.
5. Mitchell, Jerrel R., *An Innovative Approach to Compensator Design*, Ph.D. dissertation, State College, Mississippi, May, 1972.

6. Postlewaite, I. and MacFarlane, A. G. J., *A Complex Variable Approach to the Analysis of Linear Multivariable Feedback Systems*, Springer-Verlag, New York, 1979.
7. Collins, E. G., Phillips, D. J., and Hyland, D. C., "Robust Decentralized Control Laws for the ACES Structure," *IEEE Control Systems Magazine*, vol. 11, no. 3, pp. 62-70, April, 1991.
8. Junkins, John L. and Kim, Youdan, "First and Second Order Sensitivity of the Singular Value Decomposition," *The Journal of the Astronautical Sciences*, vol. 38, no. 1, pp. 69-86, Jan.-March, 1990.
9. Medina, Enrique, *Multi-input, Multi-output System Identification from Frequency Response Samples with Applications to the Modeling of Large Space Structures*, M. S. Thesis, Ohio University, November, 1991.

MODEL REDUCTION RESULTS FOR FLEXIBLE SPACE STRUCTURES

Trevor Williams and Masoud Mostarshedi

Department of Aerospace Engineering
University of Cincinnati
Cincinnati, Ohio 45221

Abstract

This paper describes the novel subsystem balancing technique for obtaining reduced-order models of flexible structures, and investigates its properties fully. This method can be regarded as a combination of the best features of modal truncation (efficiency) and internal balancing (accuracy); it is particularly well suited to the typical practical case of structures which possess clusters of close modes. Numerical results are then presented demonstrating the results obtained by applying subsystem balancing to the Air Force Phillips Laboratory ASTREX testbed, the Jet Propulsion Laboratory antenna facility, and the NASA Marshall Space Flight Center ACES structure.

Introduction

Model reduction is a very important practical problem related to the control of flexible space structures (FSS), and a considerable amount of work has been carried out on this topic. Well-known methods include *modal truncation* [1], based either on the natural frequencies of the structure or its modal costs, and *balancing* [2] of the entire structure and then truncation to retain a dominant model for it. An advantage of the balancing approach is that it typically yields a more accurate reduced-order model than does simple modal truncation. This is particularly true when the structure possesses clustered natural frequencies, as is often the case for realistic flexible space structures. However, the disadvantages of balancing are its high computational cost, possible numerical sensitivity problems resulting from the large matrices being operated on, and the difficulty involved in providing a physical interpretation for the resulting balanced "modes".

The purpose of this paper is to investigate the practical performance of the alternative *subsystem balancing* technique when tested on realistic flexible space structures. This method, introduced in [3], retains the desirable properties of standard balancing while overcoming the three difficulties listed above. This is achieved by first decomposing the structural model into subsystems of highly correlated modes, based on

the *modal correlation coefficients* derived in [4] from the Grammians of the structure. Each subsystem is approximately uncorrelated from all others, so balancing each separately and concatenating the dominant reduced-order models obtained yields roughly the same result as balancing the entire structure directly. The computational cost reduction produced by this block-by-block technique is considerable: an operation count reduction by a factor of roughly \sqrt{r} , if the system decomposes into r equal subsystems. The numerical accuracy of the resulting reduced-order model is also improved considerably, as the matrices being operated on are of reduced dimension, and its modes do now permit a clear physical interpretation. This is a consequence of the fact that each correlated subsystem must necessarily only include modes with close natural frequencies. The balanced modes of each subsystem are, therefore, to first order linear combinations of repeated-frequency modes, and so can themselves be taken as an equally valid set of physical modes. Balancing the entire structure, on the other hand, combines modes of widely differing frequencies, making interpretation difficult.

The numerical results to be presented in this paper are for the Air Force Phillips Laboratory ASTREX structure, the Jet Propulsion Laboratory antenna testbed, and the NASA Marshall Space Flight Center ACES facility. The ACES data to be presented include results both for the *a priori* finite-element model and for a model identified from vibration tests of the structure. Details will also be given of the implementation of the algorithm, in particular, of the method used for determining the dimensions of each subsystem and the number of balanced modes that should be retained from each in the final reduced-order model. Confirmation will also be given of the efficiency advantages of the new method over standard balancing, in terms of floating-point operation counts, and comparisons given of the accuracy properties of the three model reduction procedures.

Problem Formulation

Consider an n -mode model for the structural dynamics of a modally damped, non-gyroscopic, non-circulatory FSS with m actuators and p sensors, not necessarily collocated. This model can be written in modal form [1] as

$$\begin{aligned} \ddot{\boldsymbol{\eta}} + \text{diag}(2\zeta_i\omega_i)\dot{\boldsymbol{\eta}} + \text{diag}(\omega_i^2)\boldsymbol{\eta} &= \hat{\mathbf{B}}\mathbf{u}, \\ \mathbf{y} &= \hat{\mathbf{C}}_r\dot{\boldsymbol{\eta}} + \hat{\mathbf{C}}_d\boldsymbol{\eta}, \end{aligned} \tag{1}$$

where $\boldsymbol{\eta}$ is the vector of modal coordinates, \mathbf{u} that of applied actuator inputs and \mathbf{y} that of sensor outputs, and ω_i and ζ_i are the natural frequency and damping ratio of the i^{th} mode, respectively. For the typical FSS [5], the $\{\zeta_i\}$ are quite low (e.g. 0.5 %), and the $\{\omega_i\}$ occur in clusters of repeated, or nearly repeated, frequencies as a result of structural symmetry. In order to ensure asymptotic stability, as needed in the next

section, we shall assume that all natural frequencies and damping ratios are non-zero. (This rigid-body mode restriction can actually be relaxed fairly easily if required.)

Defining the state vector $\mathbf{x} = (\dot{\eta}_1, \omega_1 \eta_1, \dots, \dot{\eta}_n, \omega_n \eta_n)^T$ for this structure yields the state space representation $\dot{\mathbf{x}} = A\mathbf{x} + B\mathbf{u}$, $\mathbf{y} = C\mathbf{x}$, where $A = blkdiag(A)_i$, $B = (B_1^T, \dots, B_n^T)^T$ and $C = (C_1, \dots, C_n)$, with

$$A_i = \begin{pmatrix} -2\zeta_i \omega_i & -\omega_i \\ \omega_i & 0 \end{pmatrix}, B_i = \begin{pmatrix} \mathbf{b}_i \\ 0 \end{pmatrix} \text{ and } C_i = (\mathbf{c}_r \quad \mathbf{c}_d / \omega_i); \quad (2)$$

\mathbf{b}_i is the i^{th} row of \widehat{B} , and \mathbf{c}_r and \mathbf{c}_d are the i^{th} columns of \widehat{C}_r and \widehat{C}_d , respectively.

The problem we shall study is that of obtaining a reduced-order model

$$\begin{aligned} \dot{\mathbf{x}}_r &= A_r \mathbf{x}_r + B_r \mathbf{u}, \\ \mathbf{y} &= C_r \mathbf{x}_r \end{aligned} \quad (3)$$

for this structure for which the normalized output error

$$\delta^2 = \frac{\int \|\mathbf{y}(t) - \mathbf{y}_r(t)\|_2^2 dt}{\int \|\mathbf{y}(t)\|_2^2 dt} \quad (4)$$

is acceptably small. Of course, the size of δ will depend on the order, n_r , chosen for the reduced model. A good model reduction procedure should ideally provide information allowing an intelligent choice for n_r to be made so as to achieve a specified upper bound on δ .

Two techniques for model reduction that have been extensively studied are those of *modal truncation* and *internal balancing* [2]. The purpose of the present paper is to compare the results they produce with those obtained by means of a new method, subsystem balancing, which can be regarded as an intermediate case between the two established techniques. In order to develop this algorithm, it is first necessary to study the *Grammian* matrices which form the basis of balancing. This is the subject of the next section.

Closed-Form Grammians

The controllability and observability Grammians, denoted by W_c and W_o , respectively, of the system described by (2) are the solutions of the algebraic Lyapunov equations

$$AW_c + W_c A^T + BB^T = 0 \quad (5)$$

and

$$A^T W_o + W_o A + C^T C = 0. \quad (6)$$

The block diagonal form of A can be exploited [6][7] to give closed-form solutions for these equations.

Taking W_c first and writing it in terms of its (2×2) blocks $\{W_{ij}\}$, we have

$$A_i W_{ij} + W_{ij} A_j^T + B_i B_j^T = 0. \quad (7)$$

Applying (2) then yields, after some algebra, the expression

$$W_{ij} = \frac{\beta_{ij}}{d_{ij}} \cdot \begin{pmatrix} 2\omega_i\omega_j(\zeta_j\omega_i + \zeta_i\omega_j) & \omega_j(\omega_j^2 - \omega_i^2) \\ -\omega_i(\omega_j^2 - \omega_i^2) & 2\omega_i\omega_j(\zeta_i\omega_i + \zeta_j\omega_j) \end{pmatrix}, \quad (8)$$

where $\beta_{ij} = \mathbf{b}_i^T \mathbf{b}_j$ and $d_{ij} = 4\omega_i\omega_j(\zeta_i\omega_i + \zeta_j\omega_j)(\zeta_j\omega_i + \zeta_i\omega_j) + (\omega_j^2 - \omega_i^2)^2$. The quantity d_{ij}^{-1} is essentially a measure of how closely correlated modes i and j are; it will be returned to below. Evaluating W_C by this method involves about $7n^2$ floating-point operations (exploiting the symmetry of W_C , i.e. $W_{ji} = W_{ij}^T$); by contrast, the Bartels-Stewart algorithm [8] for general matrices A and B requires order(n^3) operations.

The general expression (8) for W_{ij} simplifies considerably for exactly repeated frequencies, where we obtain

$$W_{ij} = \frac{\beta_{ij}}{2(\zeta_i + \zeta_j)\omega_i} \cdot I_2; \quad (9)$$

in particular, the diagonal blocks are just $W_{ii} = \frac{\beta_{ii}}{4\zeta_i\omega_i} \cdot I_2$. Simplifications also occur for widely separated, lightly-damped modes: in this case,

$$W_{ij} \rightarrow \frac{\beta_{ij}}{(\omega_j^2 - \omega_i^2)} \cdot \begin{pmatrix} 0 & \omega_j \\ -\omega_i & 0 \end{pmatrix} \text{ as } \zeta_i, \zeta_j \rightarrow 0. \quad (10)$$

It is important to note that (9) is inversely proportional to the damping ratios of the structure, while (10) is independent of damping. Thus, the only blocks of W_C which will be of significant magnitude for a structure with light damping are those on the diagonal, and those off-diagonal blocks that correspond to close frequencies. This reflects the well-known result [9]-[11] that the modal model of a flexible structure with widely separated natural frequencies is already approximately balanced. However, balancing a flexible structure with near-repeated frequencies is a much more challenging problem [6], as indeed is determining the controllability properties of its close modes [12].

The observability Grammian W_O for a system with rate measurements only ($\hat{C}_d = 0$) can be obtained in a similar fashion to the controllability Grammian, or more simply by noting that $A^T = PAP$ for flexible structures, where $P = \text{diag}\{1, -1, \dots, 1, -1\}$. Therefore, pre- and post-multiplying (6) by P gives

$$A[PW_O P] + [PW_O P]A^T + C^T C = 0. \quad (11)$$

Note that this equation makes use of the fact that $CP = P$ for such systems. Thus, W_O is essentially as given in (8), the only alterations being that the signs of the off-diagonal entries are changed and β_{ij} is replaced by

$$\gamma_{rij} = \mathbf{c}_{ri}^T \mathbf{c}_{rj}.$$

If displacement measurements are also allowed, the situation is much less simple; in fact, the analytical expressions that then result for W_o are really too complicated to be useful. The only exception to this is the expression for the i^{th} diagonal block of W_o for a lightly-damped structure ($\zeta_i \ll 1$), where we have the approximation

$$W_{oii} \approx \frac{(\omega_i^2 \gamma_{ri} + \gamma_{dii})}{4\zeta_i \omega_i^3} \cdot I_2 \quad (12)$$

with $\gamma_{dij} = \mathbf{c}_{di}^T \mathbf{c}_{dij}$. Although no general analytical expressions for W_o are now tractable, it is still possible to derive a semi-closed-form method to evaluate the observability Grammian that exploits the special form of the matrix A in (2). This method is nearly as efficient as the true closed-form controllability Grammian results derived previously, and is based on writing the (i,j) block of W_o as

$$W_{oij} = \begin{pmatrix} p & q \\ r & s \end{pmatrix}. \quad (13)$$

The equation which defines this block (from (6)) is $A_i^T W_{oij} + W_{oij} A_j + C_i^T C_j = 0$, which can be expanded and rewritten as the following system of four simultaneous linear equations.

$$\begin{pmatrix} -2(\zeta_i \omega_i + \zeta_j \omega_j) & \omega_j & \omega_i & 0 \\ -\omega_j & -2\zeta_i \omega_i & 0 & \omega_i \\ -\omega_i & 0 & -2\zeta_j \omega_j & \omega_j \\ 0 & -\omega_i & -\omega_j & 0 \end{pmatrix} \begin{pmatrix} p \\ q \\ r \\ s \end{pmatrix} = -\begin{pmatrix} \mathbf{c}_{ri}^T \mathbf{c}_{rj} \\ \mathbf{c}_{ri}^T \mathbf{c}_{dij} / \omega_j \\ \mathbf{c}_{dij}^T \mathbf{c}_{rj} / \omega_i \\ \mathbf{c}_{dij}^T \mathbf{c}_{dij} / \omega_i \omega_j \end{pmatrix}. \quad (14)$$

Solving this system by means of Gaussian elimination requires approximately 29 floating-point operations, where the special structure of the matrix on the left-hand side has been exploited. It therefore requires a total of about $15n^2$ flops to evaluate the entire symmetric W_o using this approach. It is interesting to note that the determinant of the matrix in (14) is just d_{ij} . This quantity therefore plays a similar rôle in the denominators of both the controllability and observability Grammians. It can also be shown that, just as for W_c , the only blocks of W_o which are large for a lightly-damped structure are those corresponding to two closely-spaced modes.

Finally, if $p \geq m$, as is typical of FSS applications, and there exists a matrix U with orthonormal columns which satisfies $C = UB^T P$, then (2) is said to be *orthogonally symmetric* [13]. A particular class of orthogonally symmetric systems is that of flexible structures with *compatible* (physically collocated and coaxial) actuators and rate sensors: we then have $C = B^T$, i.e. $U = I$. Associated with any orthogonally symmetric system is its *cross-Grammian* W_{co} , which is defined as the solution of the Lyapunov equation

$$AW_{co} + W_{co}A + BU^T C = 0. \quad (15)$$

The usefulness of W_{co} in balancing applications lies in the fact that it satisfies the relation $W_{co}^2 = W_c W_o$. In fact, as $C^T C = P B U^T U B^T P = B B^T$ and $B U^T C = B U^T U B^T P = B B^T$, (11) and (15) can be seen to reduce to the expressions [13]

$$W_{co} = W_c P = P W_o. \quad (16)$$

Thus, all three Grammians of an orthogonally symmetric system are given directly from (8) with suitable changes of sign, noting, of course, that $\beta_{ij} = \gamma_{rij}$ for such systems. This property will be shown to lead to significant simplifications when balancing models of collocated flexible structures.

Subsystem Balancing

It is always possible [2] to find a state transformation T that takes the model $\{A, B, C\}$ to an *internally balanced* state space representation $\{T^{-1}AT, T^{-1}B, CT\}$, i.e. one with equal and diagonal controllability and observability Grammians

$$\bar{W}_c = \bar{W}_o = \Sigma \equiv \text{diag}(\sigma_i), \quad (17)$$

where $\sigma_1 \geq \sigma_2 \geq \dots \geq 0$. These *Hankel singular values* lead to a simple procedure for obtaining a reduced-order approximation to the original system: delete those balanced states corresponding to all singular values below some specified threshold. The resulting dominant reduced-order model will match the full system with an accuracy related to the sizes of those Hankel singular values which were discarded, so giving a guideline for selecting an acceptable reduced model order n_r ; see [2] for further details. It should be noted that this model reduction procedure is very straightforward once the balancing transformation T has been found: it merely amounts to discarding trailing rows of the balanced A and B and trailing columns of A and C .

Computation of T can be shown to amount to the solution of a standard eigenproblem. This can be formulated in various different ways. The one which follows is not the best numerically (see [14] for a superior alternative), but it makes the significance of the transformation T clearest. Inspection of (5) and (6) reveals that the Grammians of the balanced system are related to those of the original system model as

$$\bar{W}_c = T^{-1}W_c T^{-T} \text{ and } \bar{W}_o = T^T W_o T; \quad (18)$$

multiplying these matrices then gives

$$\Sigma^2 = \bar{W}_c \bar{W}_o = [T^{-1}W_c T^{-T}][T^T W_o T] = T^{-1}[W_c W_o]T. \quad (19)$$

Thus, T is just the matrix of eigenvectors (suitably scaled) of $W_c W_o$, and the Hankel singular values of the system are the corresponding eigenvalues. The usefulness of the cross-Grammian for balancing orthogonally symmetric systems can now also be seen: as T is the eigenvector matrix of $W_c W_o = W_{co}^2$ it is also the eigenvector matrix of W_{co} , and we have $T^{-1}W_{co}T = \Lambda$ with $\Sigma^2 = \Lambda^2$, so $\Lambda = \text{diag}(\pm \sigma_i)$. It can be shown

[6] that the appropriate scaling for the eigenvectors making up T for a collocated flexible structure is such that the relation $T^T P T = P$ is satisfied, while the signs of the eigenvalues of W_{co} must alternate in the same way as the diagonal elements of P . This can certainly be seen to be true for the special case of light damping and widely spaced natural frequencies, as (17) and (9) then imply that the $\{\lambda_i\}$ occur in approximate pairs

$\{\pm \beta_i / 4\zeta_i \omega_i\}$; similarly, the Hankel singular values $\{\sigma_i\}$ of a lightly-damped flexible structure always occur in approximate pairs. The important point about evaluating T in terms of the cross-Grammian directly, rather than using the product $W_c W_o$, is that it is a *square root* method. It therefore possesses the improved accuracy properties typical of these techniques, as exhibited by such applications as least squares estimation by QR decomposition rather than the normal equations [15], Kalman filtering [16], and the FSS problems of on-orbit structural identification [17] and transmission zeros computation [18].

It has already been noted that the Grammians of a lightly-damped flexible structure with widely separated natural frequencies are diagonally dominant, i.e. a modal model of such a structure is already approximately balanced [10][11]. However, consider now the more realistic case of a lightly-damped structure with clusters of close modes, as is typical of flexible spacecraft. The Grammians of such a system will now be **block** diagonally dominant, with a diagonal block corresponding to each cluster of modes. The Grammian eigenvector matrix T obtained from $W_c W_o$ or W_{co} will consequently also be block diagonally dominant. It can therefore be replaced, to first order, by the block diagonal matrix whose (i,i) block is just the eigenvector matrix of the i^{th} dominant diagonal Grammian block. In other words, an approximation to the internally balanced representation of the given FSS can be obtained by balancing each subsystem of close modes independently and then concatenating the results.

This *subsystem balancing* approach, introduced in [3], has several significant advantages over standard balancing. The first is that it is clearly much more efficient to compute the eigenvectors of several small subsystems than it is to evaluate the eigenvector matrix of the entire system. In fact, as eigenstructure evaluation is an order(n^3) operation, this efficiency gain can be quite substantial. Consider for illustrative purposes the case where the structure being studied breaks down into r subsystems of equal dimension. It can then be shown that the standard balancing technique will require on the order of r^2 as many floating-point operations as will subsystem balancing. A second advantage is also a consequence of the fact that we are now operating on matrices of smaller dimension than if the entire system were balanced directly. This tends to reduce the *condition number* [15] of the state transformations being applied, and so limits the effects of rounding errors on the final computed state space model. This therefore helps overcome the numerical problems that have been noted [19][20] when applying classical balancing to systems of high dimension. The final advantage of subsystem balancing relates to the physical interpretation of the resulting balanced state variables $\bar{\mathbf{x}} = T^{-1} \mathbf{x}$. In the new method, the fact that T is taken to be block diagonal implies that each

balanced state will be made up of a linear combination of the states corresponding to a single cluster of close modes. This is, to first order, just the repeated eigenvalue case, where any linear combination of eigenvectors (mode shapes) is itself a valid eigenvector. The transformed states produced by subsystem balancing are therefore basically perturbed repeated modes, and so can be visualized quite easily. Standard balancing, by contrast, yields states which are made up of linear combinations of all the modes of the structure, making physical interpretation very difficult.

Model reduction by subsystem balancing therefore proceeds by first dividing the given structure into subsystems of close modes. Each subsystem is then balanced independently, and a reduced-order model for it generated by deleting all balanced states corresponding to Hankel singular values below some specified threshold. (Note that the modified truncation criterion of [21] could be used instead of the Hankel singular values, if desired, without changing the argument in any way.) The resulting reduced-order subsystem models so obtained are then combined to yield a dominant, approximately balanced, reduced-order model for the full system. This method can be applied to any flexible structure, collocated or non-collocated; however, it can be refined somewhat when analyzing collocated structures. In this case, it is possible to define a *modal correlation coefficient* [3][4] between modes i and j , so allowing the interaction between the two modes to be quantified more precisely than in the non-collocated case. This correlation coefficient, defined as

$$\rho_{ij}^2 = \frac{\|W_{co_{ij}}\|^2}{\|W_{co_i}\| \cdot \|W_{co_j}\|}, \quad (20)$$

can be shown to have magnitude lying between 0 and 1. It can also be shown to be small for modes with widely separated natural frequencies, and it may approach unity for close modes. However, it will also be small for modes which are close but have mode shapes which are nearly orthogonal. These correlation coefficients therefore provide a somewhat more precise means of defining the subsystems of structural modes which must be balanced together than does frequency separation by itself. Of course, it must be noted that the cross-Grammian is not defined for non-collocated systems, so (20) cannot be used for such systems. The question of whether a similar correlation coefficient can be defined for such systems is a topic of current research.

In summary, the two algorithms used to compute the state transformations needed for subsystem balancing of flexible structures can be summarized as follows. In both cases, approximate operation counts are given for each step for the illustrative case of a system of order n which breaks down into r equal subsystems.

Non-Collocated:

Define subsystems (by modal frequency separation)

For each subsystem:

Construct closed-form W_c and W_o :	$22(n/r)^2$ flops
Find Cholesky factorization $W_o = LL^T$:	$\frac{1}{6} \cdot (n/r)^3$ flops
Construct $X = L^T [W_c W_o] L^{-T} = L^T W_c L$:	$(n/r)^3$ flops
Find eigenstructure of symmetric X :	$5(n/r)^3$ flops
Transform by L to give eigenvectors of $W_c W_o$:	$\frac{1}{2} \cdot (n/r)^3$ flops
Total (all subsystems):	$\frac{20}{3} \cdot (n^3/r^2) + 22(n^2/r)$ flops

Collocated:

Define subsystems (by modal correlation coefficients)

For each subsystem:

Construct closed-form W_{co} :	$7(n/r)^2$ flops
Find eigenstructure of unsymmetric W_{co} :	$15(n/r)^3$ flops
Total (all subsystems):	$15(n^3/r^2) + 7(n^2/r)$ flops

These operation counts compare very favorably with the total of about $21n^3$ needed for standard balancing; they exhibit a reduction by a factor of approximately $\sqrt{r^2}$. It is also interesting to note that the collocated method has a higher count than the non-collocated algorithm, which uses the method described by Laub [14]. It may therefore be supposed that there is no advantage to treating collocated structures as a special case, as we have done. However, this ignores two factors. Firstly, use of the modal correlations (20) may permit smaller subsystems to be defined, without any loss of accuracy, than if frequency differences are used as the separation criterion. Secondly, the collocated method is a matrix square root method, and so should be expected to have superior numerical conditioning properties.

Results

Numerical results will now be provided which illustrate the behavior of the subsystem balancing technique when applied to realistic structures. The three structural models studied are the Air Force Phillips Laboratory ASTREX article, the Jet Propulsion Laboratory flexible antenna testbed, and the NASA Marshall Space Flight Center ACES facility. These three structures all possess light damping and a large number of

closely-spaced vibration modes. Furthermore, they allow the algorithm to be tested in both the collocated and non-collocated cases. Results will also be given for an identified model for ACES obtained from experimental vibration test data. (The interested reader is referred to [22] for further details.)

1. ASTREX

This graphite-epoxy truss structure [23] provides a good illustration of the application of subsystem balancing to a non-collocated flexible structure. The structural model considered has 22 modes with frequencies below 50 Hz: these are given in Table I. It can be noted that this system does indeed possess modes with close frequencies; for instance, modes 5 and 6 and 14 and 15 differ by only about 0.1 Hz. Each mode has an assumed damping ratio of 0.1 %.

Model reduction for this structure is actually quite challenging, as it is fitted with 8 actuators and 39 sensors. Any reduced-order model will therefore have to be able to approximately match the response of all 39 outputs of the true system to any of the 8 control inputs. Despite this difficulty, the subsystem balancing method was found to give good results when applied to ASTREX. The first step in the procedure is to break the complete model down into subsystems of close modes, based on their relative frequency separation. A separation threshold of 7 % was found to lead to a good balance between having excessively large subsystems (threshold too high) and obtaining inaccurate results as a result of separating modes which actually interact significantly (threshold too low). The subsystem modal groupings found for the chosen threshold are given in Table II. Note that modes 14 and 22, for instance, are included in the same subsystem even though they are separated by over 10 Hz and therefore do not interact directly. The reason for this is that they actually interact indirectly through the other modes in the subsystem: mode 14 is within 7% of modes 15 to 18; mode 18 interacts with mode 19, which in turn interacts with modes 20 and 21, which in turn interacts with 22. This is a common occurrence when defining subsystems of closely coupled modes.

The next step in the procedure is to balance each subsystem independently, making use of the closed-form expressions (8) and (14) to compute the relevant Grammians, and then truncate to give a dominant reduced-order subsystem model. These are then concatenated to obtain a dominant reduced-order model for the entire system. The last column of Table II shows the number of balanced "modes" that were retained from each subsystem when a Hankel singular value threshold of 0.2 was used. It can be seen that several groups of modes at both low and high frequencies do not contribute at all to the final reduced-order model, others are retained in their entirety, and still others are approximated to by a truncated balanced model. The composite reduced-order model so obtained has 11 modes, as opposed to 22 in the original model. Despite this substantial reduction in model order, the difference between the outputs of the full and reduced models, as measured by the normalized impulse response output error δ in (4), is a quite acceptable 6.65 %. As a

final point, note that the subsystem balancing technique does actually produce the claimed efficiency gains when applied to this practical system. In fact, the operation count required to balance the subsystems obtained above for ASTREX is only about 7.4 % as large as that required to balance the entire system directly.

2. JPL Antenna

This structure, designed to be representative of a flexible dish antenna, possesses 12 ribs symmetrically distributed about a central pivoted hub. The model provided by JPL for this structure has 84 modes, with the lowest natural frequency at 0.09 Hz; as a result of the symmetry of the system, many of these frequencies are essentially repeated. In the work presented here, a uniform damping ratio of 0.5 % has been assumed for all modes.

The extensive sensor/actuator distribution provided for this structure allows it to be studied in both a collocated and non-collocated configuration. Taking the non-collocated case first, 4 outer levitator sensors (LO1, LO4, LO7 and LO10, in the notation of the JPL model) and 4 actuators (rib root actuators RA1 and RA10; hub actuators HA1 and HA10) were considered to be in use, and all other sensors and actuators disabled. Applying the subsystem balancing technique to this system with a relative frequency separation threshold of 25 %, the 9 subsystems listed in Table III are obtained. (Note that the mode numbers of this system do not increase monotonically with frequency.) If each subsystem is then balanced independently and truncated with a Hankel singular value threshold of 0.0009, the number of balanced modes retained from each is given in the last row of Table III. It can be seen that subsystems 4 and 5 and the large, high-frequency subsystem 9 do not contribute at all to the final reduced model for the structure, whereas subsystems 1 and 3 are retained in their entirety. This 20-mode reduced model matches the output response of the 84-mode full system quite accurately, giving a normalized impulse response error of $\delta = 11.1 \%$. By contrast, a reduced model of the same order obtained by modal truncation gave a δ value of 18 %, considerably degraded as a result of ignoring significant interactions (*spillover*) between close modes. The results obtained by balancing the entire system and then truncating were also significantly worse than those obtained by subsystem balancing; in this case, a 20-mode model gave $\delta = 53.8 \%$. The reason for this is appears to be numerical conditioning problems that arise when balancing the large (168 states) full system model. Such difficulties are limited in the subsystem balancing approach, as no more than 40 states need ever be balanced at any one time. It should also be noted that the operations count required for subsystem balancing of this structure is only about 2.7 % of that used for standard balancing, a very considerable savings.

To illustrate the application of the collocated version of subsystem balancing, based on the modal correlation coefficients $\{\rho_{ij}\}$ defined by (20) from the cross-Grammian W_{co} , we shall now restrict the sensors and actuators used to the 6 collocated pairs which exist in the JPL model. These consist of the 4 rib root sensors and actuators RA1/RS1, RA4/RS4, RA7/RS7 and RA10/RS10, as well as the two hub pairs HA1/HS1 and HA10/HS10. Applying the subsystem definition procedure described previously, based on a correlation threshold of $\rho_{th} = 0.03$, yielded the 13 subsystems given in Table IV. It should be noted that there is a degree of correspondence between these subsystems of modes and those obtained by means of the frequency separation criterion (Table III). The main difference is that certain of the subsystems given in Table III have now been broken down into two non-interacting collections of modes. This agrees with the fact that all highly-interacting modes must have close natural frequencies, but all close modes do not necessarily interact strongly. Taking a Hankel singular value threshold of 0.039, a 32-mode reduced model was then obtained for the overall system; the number of balanced modes retained from each subsystem are given in the last row of Table IV. The resulting normalized impulse response error between the full and reduced-order models is $\delta = 4.5\%$; by contrast, a 32-mode model obtained by modal truncation gave an error of 11.2 %, and standard balancing led to $\delta = 15\%$. The new method can thus be seen to give very acceptable results, avoiding the spillover and/or numerical conditioning accuracy problems that affect the other two techniques.

3. ACES

The final system considered is the Astromast-based ACES structure. A 50-mode model for this system has natural frequencies as listed in Table V; as in the previous two examples, the presence of close modes can clearly be observed. ACES is outfitted with a total of 22 sensors and 9 actuators. However, the present model reduction work was carried out in conjunction with the positivity-based controller design discussed in [24], which requires the use of collocated actuators and rate sensors. The model considered here will therefore make use only of the 3 x-, y- and z-axis Advanced Gimbal System (AGS) torquers and their collocated Apollo Telescope Mount (ATM) rate gyros.

Applying the collocated version of subsystem balancing with a modal correlation coefficient threshold of 0.034 leads to the subsystem modal groupings given in Table VI. It is interesting to note that the modes in subsystems 11 and 12 are intermingled; for instance, modes 46 and 47 are extremely close in frequency, yet they are placed in different subsystems. This is another illustration of the fact that two modes can be close and yet nearly orthogonal, and so not highly interacting; the modal correlation coefficients reflect this. Each subsystem was now truncated, based on a singular value threshold of 0.0025, and a 15-mode reduced-order model obtained; the number of modes taken from each subsystem is given as the last column of Table VI. It can be seen that the high-frequency groups 9 through 12 do not contribute at all to the reduced model. For

this beam-like structure, it was found that the results obtained by standard balancing and modal truncation were not actually significantly different from those obtained by subsystem balancing, in contrast what was found for ASTREX and the JPL structure.

As a final point, subsystem balancing was also applied to a 15-mode model of the x-axis dynamics of ACES which was identified from vibrational test data. This model was reduced in this way to a 7-mode dominant approximation which matched the observed response well. The fact that the identified modes had quite considerable damping variations did not lead to any difficulties when computing the modal correlation coefficients. Subsystem balancing is therefore certainly not limited to structural models which possess uniform damping ratios.

Conclusions

This paper has described the novel subsystem balancing technique for obtaining reduced-order models of flexible structures, and investigated its properties fully. It was shown that this method can be regarded as a combination of the best features of modal truncation (efficiency) and internal balancing (accuracy); it is particularly well suited to the typical practical case of structures which possess clusters of close modes. Numerical results were then presented demonstrating the results obtained by applying subsystem balancing to the Air Force Phillips Laboratory ASTREX facility, the Jet Propulsion Laboratory antenna testbed, and the NASA Marshall Space Flight Center ACES structure.

References

1. R.R. Craig, *Structural Dynamics*, New York: Wiley, 1981.
2. B.C. Moore, 'Principal Component Analysis in Linear Systems: Controllability, Observability, and Model Reduction', *IEEE Transactions on Automatic Control*, Vol. 26, Feb. 1981, pp. 17-32.
3. T.W.C. Williams and W.K. Gawronski, 'Model Reduction for Flexible Spacecraft with Clustered Natural Frequencies', invited paper, 3rd NASA/NSF/DoD Workshop on Aerospace Computational Control, Oxnard, CA, Aug. 1989.
4. W.K. Gawronski and T.W.C. Williams, 'Model Reduction for Flexible Space Structures', *Journal of Guidance, Control, and Dynamics*, Vol. 14, Jan.-Feb. 1991, pp. 68-76.
5. M.J. Balas, 'Trends in Large Space Structure Control Theory: Fondest Hopes, Wildest Dreams', *IEEE Transactions on Automatic Control*, Vol. 27, 1982, pp. 522-535.
6. T.W.C. Williams, 'Closed-Form Grammians and Model Reduction for Flexible Space Structures', *IEEE Transactions on Automatic Control*, Vol. 35, Mar. 1990, pp. 379-382.
7. R.E. Skelton, R. Singh and J. Ramakrishnan, 'Component Model Reduction by Component Cost Analysis', *Proc. AIAA Guidance, Navigation and Control Conference*, Aug. 1988, pp. 264-274.
8. R.H. Bartels and G.W. Stewart, 'Solution of the Matrix Equation $AX + XB = C$ ', *Communications ACM*, 1972, pp. 820-826.
9. E.A. Jonckheere and L.M. Silverman, 'Singular Value Analysis of Deformable Systems', *Proc. 20th IEEE Conference on Decision and Control*, Dec. 1981, pp. 660-668.
10. C.Z. Gregory, 'Reduction of Large Flexible Spacecraft Models using Internal Balancing Theory', *Journal of Guidance, Control, and Dynamics*, Vol. 7, Nov.-Dec. 1984, pp. 725-732.
11. E.A. Jonckheere, 'Principal Component Analysis of Flexible Systems - Open-Loop Case', *IEEE Transactions on Automatic Control*, Vol. 29, Dec. 1984, pp. 1095-1097.
12. T.W.C. Williams, 'Degree of Controllability for Close Modes of Flexible Space Structures', *Proc. 30th IEEE Conference on Decision and Control*, Dec. 1991, pp. 1627-1628.
13. J.A. de Abreu-Garcia and F.W. Fairman, 'A Note on Cross-Grammians for Orthogonally Symmetric Realizations', *IEEE Transactions on Automatic Control*, Vol. 31, Sept. 1986, pp. 866-868.
14. A.J. Laub, 'Computation of "Balancing" Transformations', *Proc. Joint Automatic Control Conference*, Aug. 1980.
15. G.H. Golub and C.F. Van Loan, *Matrix Computations*, Baltimore: Johns Hopkins, 1983.
16. G.J. Bierman, *Factorization Methods for Discrete Sequential Estimation*, New York: Academic, 1977.
17. T.W.C. Williams, 'Identification of Large Space Structures: A Factorization Approach', *Journal of Guidance, Control, and Dynamics*, Vol. 10, July-Aug. 1987, pp. 466-473.
18. T.W.C. Williams, 'Computing the Transmission Zeros of Large Space Structures', *IEEE Transactions on Automatic Control*, Vol. 34, Jan. 1989, pp. 92-94.

19. M.S. Tombs and I. Postlethwaite, 'Truncated Balanced Realization of a Stable Non-Minimal State-Space System', *International Journal of Control*, Vol. 46, 1987, pp. 1319-1330.
20. M.G. Safanov and R.Y. Chiang, 'A Schur Method for Balanced Model Reduction', *Proc. American Control Conference*, 1988, pp. 1036-1040.
21. R.E. Skelton and P. Kabamba, 'Comments on "Balanced Gains and Their Significance for L^2 Model Reduction"', *IEEE Transactions on Automatic Control*, Vol. 31, Aug. 1986, pp. 796-797.
22. M. Mostarshedi, *Model Reduction of Flexible Structures using Subsystem Balancing and the Closed Form of the Grammians*, Master of Science Thesis, University of Cincinnati, Dec. 1991.
23. N.S. Abhyankar and J.L. Berg, 'ASTREX Model Information: Supplement to astabcd.mat File', Phillips Laboratory Internal Report, Aug. 15, 1991.
24. A.B. Bosse and G.L. Slater, 'Digital Implementation of Vibration Suppression Controllers for Large Space Structures', *Proc. 8th VPI & SU Symposium on Dynamics and Control of Large Structures*, May 1991.

Table I. Natural Frequencies (Hz) of the ASTREX Structure

Mode	Frequency
1	3.71
2	5.45
3	14.94
4	15.09
5	19.79
6	19.91
7	21.73
8	25.41
9	29.31
10	30.68
11	33.07
12	33.76
13	35.19
14	38.40
15	38.50
16	38.74
17	38.99
18	40.37
19	42.36
20	43.66
21	45.28
22	48.57

Table II. Subsystems Defined for the ASTREX Structure

Subsystem	Modes	Number in ROM
1	1	0
2	2	0
3	3, 4	2
4	5, 6	1
5	7	1
6	8	1
7	9, 10	0
8	11, 12, 13	0
9	14, ..., 22	6

Table III. Subsystems Defined for the Non-Collocated JPL Antenna

Subsystem	1	2	3	4	5	6	7	8	9
Modes included	8	1	9	2	11	3	4	5	6
	15	22	16	10	18	12	13	14	7
	29		17		19	20	21	27	
	36		23		24	25	26	28	
	43		30		31	32	33	34	
	50		37		38	39	40	35	
	57		44		45	46	47	41	
	64		51		52	53	54	42	
	71		58		59	60	61	48	
	78		65		66	67	68	49	
			72		73	74	75	55	
			79		80	81	82	56	
								62	
								63	
								69	
								70	
								76	
								77	
								83	
								84	
Number kept	2	7	2	0	0	4	3	2	0

Table IV. Subsystems Defined for the Collocated JPL Antenna

Subsystem	1	2	3	4	5	6	7	8	9	10	11	12	13
Modes included	1	2	3	4	5	6	8	9	11	15	16	18	22
	10	12	13	14	7								29
	17	19	20	21	27								36
	23	24	25	26	28								43
	30	31	32	33	34								50
	37	38	39	40	35								57
	44	45	46	47	41								64
	51	52	53	54	42								71
	58	59	60	61	48								78
	65	66	67	68	49								
	72	73	74	75	55								
	79	80	81	82	56								
					62								
					63								
					69								
					70								
					76								
					77								
					83								
					84								
Number kept	0	0	2	6	6	12	1	1	1	1	1	1	0

Table V. Natural Frequencies (Hz) of the ACES Structure

Mode	Frequency	Mode	Frequency	Mode	Frequency
1	0.0102	18	7.4870	35	28.5100
2	0.0268	19	7.5907	36	29.5787
3	0.1569	20	7.6027	37	29.5806
4	0.5051	21	7.8395	38	29.5806
5	0.9118	22	8.4980	39	33.6301
6	0.9292	23	9.6258	40	36.4142
7	3.4540	24	10.5690	41	43.3590
8	3.7229	25	11.4674	42	55.0998
9	3.7323	26	12.0870	43	55.3988
10	3.7855	27	12.0958	44	64.4592
11	4.4967	28	13.7005	45	68.0280
12	5.3601	29	13.9286	46	86.0042
13	5.5579	30	15.6527	47	86.8839
14	5.9523	31	16.8346	48	104.5961
15	5.9523	32	20.6836	49	109.1766
16	7.1019	33	20.7823	50	112.2931
17	7.3312	34	20.7917		

Table VI. Subsystems Defined for the ACES Structure

Subsystem	Modes	Number in ROM
1	1	0
2	2	1
3	3	0
4	4	1
5	5	1
6	6	0
7	7, ..., 15	4
8	16, ..., 34	8
9	35, ..., 38	0
10	39, 40, 41	0
11	42,43,44,46,49,50	0
12	45, 47, 48	0

An Application of the Observer/Kalman Filter Identification (OKID) Technique to Hubble Flight Data

Jer-Nan Juang, Lucas G. Horta, W. Keith Belvin
NASA Langley Research Center
Hampton, VA 23665

John Sharkey
Marshall Space Flight Center
Huntsville, AL 35812

Frank H. Bauer
Goddard Space Flight Center
Greenbelt, MD 20771

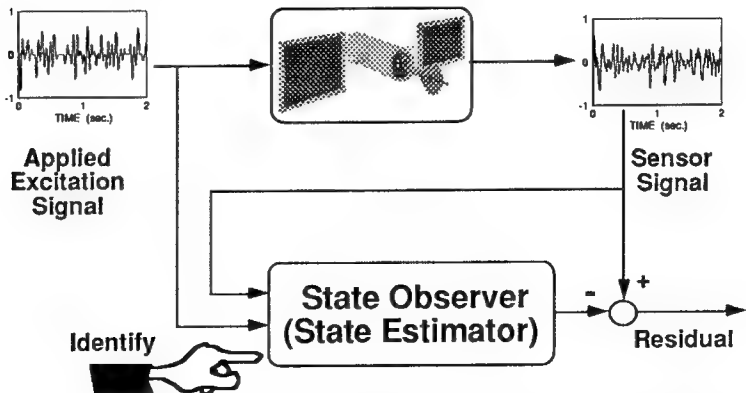
The objective of the current research is to identify vibration parameters, including frequencies, damping ratio and uncertainty characteristics, of the Hubble Space Telescope from flight data using an advanced system identification technique. The Observer/Kalman Filter Identification (OKID) technique is used to identify the vibration parameters. The OKID was recently developed by the researchers in the Spacecraft Dynamics Branch at NASA Langley Research Center.

OUTLINE

- Description of the Observer/Kalman Filter Identification (OKID)
- Brief Description of the Hubble Flight Data
- Identification Results

System identification is to develop or improve a mathematical model of a physical system using experimental data. The development of a model can be performed by processing the data in the frequency domain or time domain. The conventional identification methods in the structures field use the frequency-based transfer function matrix or the time-based free-decay responses for model representation. The knowledge of either the transfer function matrix or the free decay responses makes it possible to construct a data matrix as the basis for the identification of modal parameters including frequencies, damping ratio and mode shapes at the sensor points. The Eigensystem Realization Algorithm (ERA) or Eigensystem Realization Algorithm using Data Correlation (ERA/DC) developed in the Spacecraft Dynamics Branch was based on the data matrix from pulse response to compute a state space discrete-time model or the modal parameters. Recently, a time-based technique was developed for computation of pulse response samples directly from input and output data without using the frequency-based transfer function. Because it is a time domain technique, data periodicity is not needed as in most frequency-based procedures. The pulse responses thus computed include information of not only the system but also the characteristics of the system uncertainties, which lead to separate identification of the system model and its corresponding observer using ERA. This newly developed technique is now called the Observer/Kalman Filter Identification (OKID).

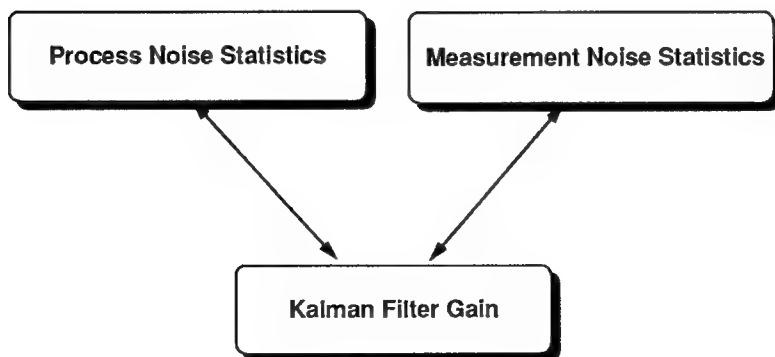
OBSERVER/KALMAN FILTER IDENTIFICATION (OKID)



- Identify a state space model and its corresponding observer/Kalman filter directly from input and output data for modal parameter identification or controller designs.

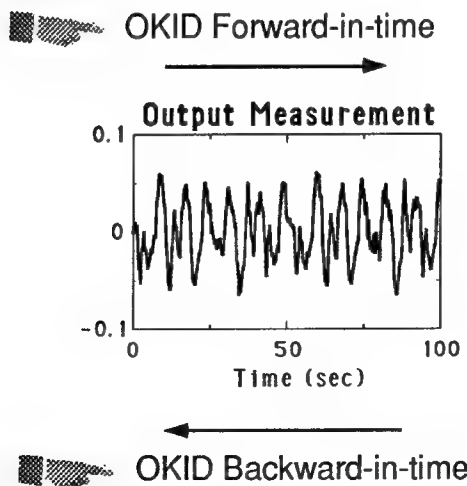
There are basically two ways to stochastically characterize system uncertainties including plant and measurement noises. One way is to describe the input and output uncertainties directly in terms of their covariances. Another way is to specify the Kalman filter equation with its steady state Kalman gain which is a function of the input and output uncertainty covariances. In the OKID, an observer is identified to characterize the input and output uncertainties. If the data length is sufficiently long, and the number of identified observer Markov parameters (pulse response time histories) is sufficiently large, then the identified observer of the system order approaches the Kalman filter.

CHARACTERIZATION OF UNCERTAINTIES



The OKID has two ways of processing the input and output data for system identification. One is the forward-in-time and the other is the backward-in-time. The forward-in-time means that the current output measurement can be fully estimated by the previous inputs and outputs, and is commonly used for the system identification. If one reverses time in the model to be identified, then what were damped true system modes become undamped true system modes, growing as the reversed time increases. Physically, it implies that the current output measurement can be fully estimated by the future inputs and outputs. On the other hand, the noise modes in the forward and backward identification still maintain the property that they are stable. This is intuitively reasonable. If the data set is sufficiently long, an unstable noise mode would predict noise contributions to the pulse response data that grow unbounded as the time step in the data set increases. This is inconsistent with the expected contribution of noise in data. Therefore, the backward identification has the advantage of shifting from positive damping to negative damping of the true system modes to distinguish these modes from noise modes. Real experiences have shown that the backward identification may fail to indicate certain system modes in experimental data, perhaps due to the unmatched uncertainty levels in forward and backward identification.

OBSERVER/KALMAN FILTER IDENTIFICATION (OKID)

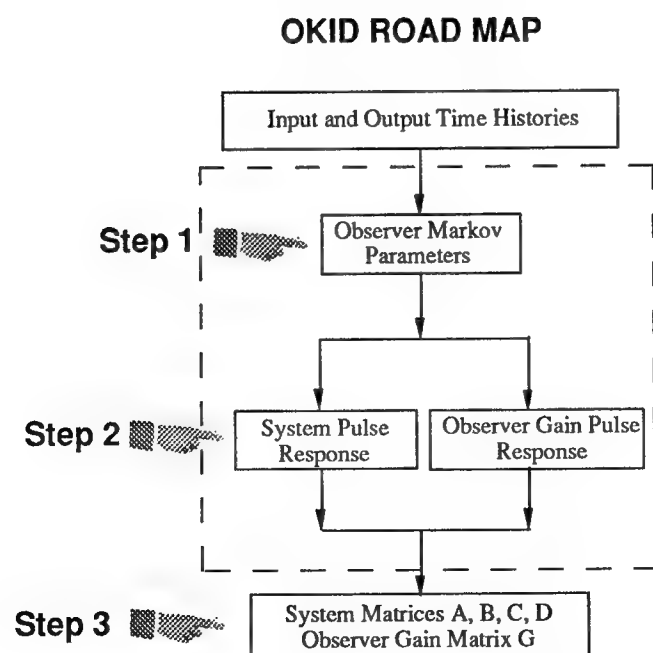


Given a set of experimental input and output data, the identification algorithm proceeds as follows.

Step 1: Choose a value of p which determines the number of observer Markov parameters to be identified from the given set of input and output data. The product of the number p and the number of sensors is required to be larger than the effective order of the system for identification of a state space model.

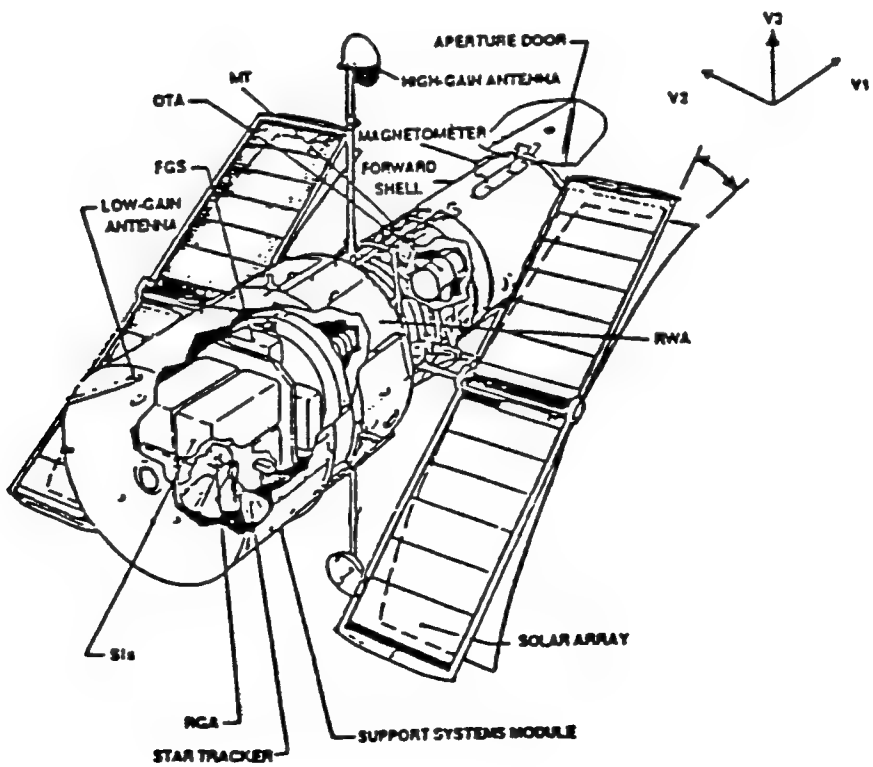
Step 2: Recover the combined system and observer gain pulse response samples from the identified observer Markov parameters.

Step 3: Realize a state space model of the system and the corresponding Kalman filter gain from the recovered pulse response samples using ERA or ERA/DC.



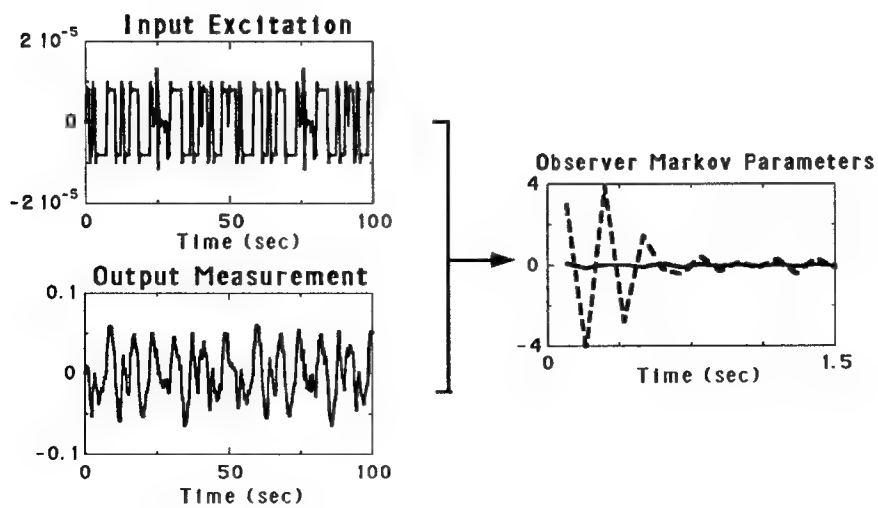
There are six gyros located on the Optical Telescope Assembly (OTA) and four torque wheels located on the Spacecraft Subsystem Module (SSM). The OTA is fixed inside the SSM. The gyros are used mainly to measure the motion of the primary mirror. Data from four out of the six gyros are recorded at a time. The measurement resolution is 0.005 arcsec/sec which implies that the gyro data are not adequate because the requirement is 0.007 arcsec pointing. The angular rates, which are measured along the four gyro directions, are combined and transformed using least-squares to recover the three rates in vehicle coordinates. Least-squares is used to smooth the poor resolution of the data. The input commands are given in terms of angular acceleration in the three rotational vehicle coordinates and then projected on the four torque wheel axes to excite the telescope mirror and the spacecraft. The data are sampled at 40 Hz. Pulses combined with sine-sweeping in the middle of an excitation period (50.975 sec) were used as input commands to the torque wheels. The excitation period was repeated six times for a total of approximately 12,000 samples taken for each experiment. The experiment was repeated three times for the other two vehicle coordinates. As a result, there were three inputs and four outputs for a total of three sets of 12,000 input samples and twelve sets of 12,000 output samples to be used for identification of vibration parameters.

HUBBLE SPACE TELESCOPE



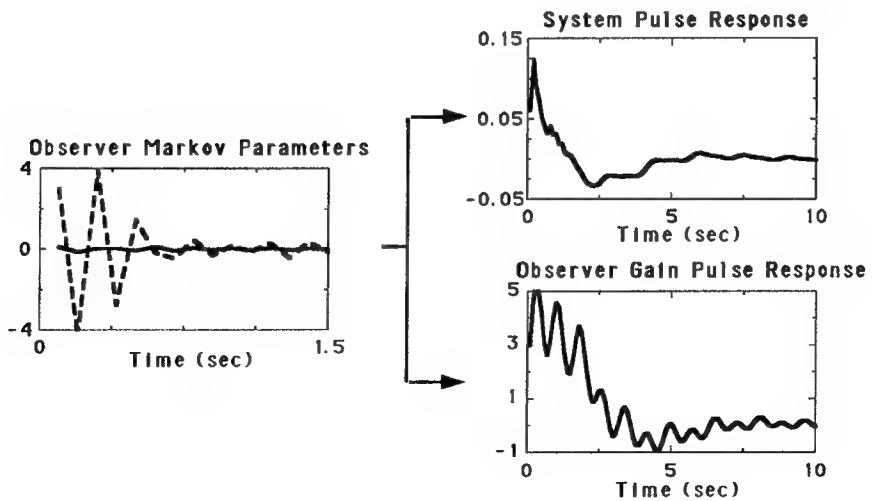
The usual practice of modal parameter identification uses the Fast Fourier Transforms (FFT) of the inputs and measured outputs to compute the sampled pulse response histories. A somewhat rich input is required to prevent numerical ill-conditioning in the computation. Another approach is to solve directly in the time domain for the pulse response histories from the input and output data. The drawbacks of this method include the need to invert an input matrix which necessarily becomes particularly large for lightly damped systems. Rather than identifying the pulse response histories directly which may exhibit very slow decay, the OKID uses an asymptotically stable observer to form a stable state space discrete model for the system to be identified. The primary purpose of introducing an observer is to compress the data and improve system identification results in practice. As shown in the figure, the input and output time histories are several order longer than the observer pulse response histories (observer Markov parameters). The modal parameters which are excitable by the inputs and measurable by the output sensors are embedded in the identified observer Markov parameters.

COMPUTATION OF OBSERVER MARKOV PARAMETERS (OKID - Step 1)



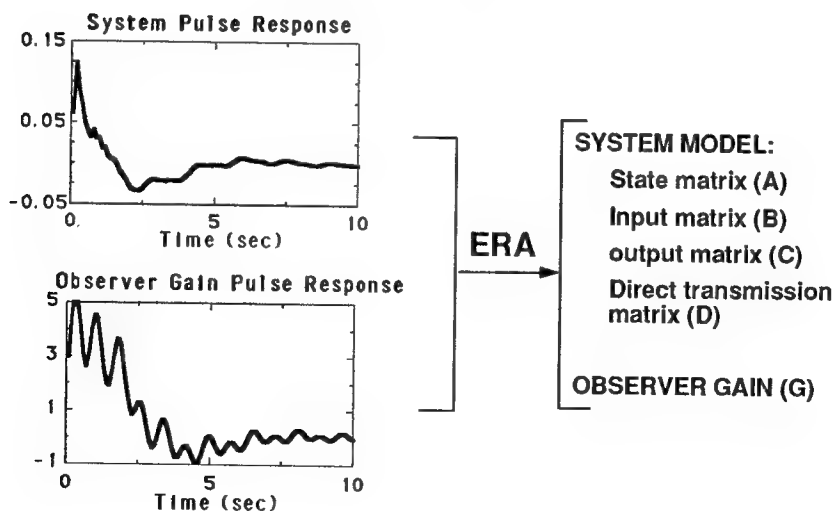
From the identified observer Markov parameters, the system pulse responses and the observer gain pulse responses can be easily computed using the formulations derived for the OKID. Although the number of identified observer Markov parameters is finite and generally very small, the number of system pulse response samples can be as large as desired. Note that the maximum number of independent system pulse response samples is equal to the number of identified observer Markov parameters. To solve for more system pulse response samples than the number of identified observer Markov parameters, simply set the extra observer Markov parameters to zero.

COMPUTATION OF PULSE RESPONSES (OKID - Step 2)



Knowledge of the actual system response samples allows one to use the ERA or ERA/DC to obtain a state-space realization of the system of interest. Modal parameters including natural frequencies, damping ratios, and mode shapes can then be found. In addition, the OKID can go further to identify an observer gain using the identified observer gain pulse response samples. The identified observer gain is related to the steady state Kalman filter gain which may be used to characterize the system uncertainties and measurement noises.

COMPUTATION OF SYSTEM MODEL BY ERA (OKID - Step 3)



A linear model and observer were identified for the Hubble Space Telescope. The system order was chosen to be 30 for realization of the system matrices, using the identified observer Markov parameters. Seven dominant modes were identified. The Mode SV in the table describes the singular value contribution of each individual mode to the pulse responses. It has been normalized relative to the maximum singular value. The 0.65 Hz mode is believed to be an in-plane bending mode of the solar array; the 1.29 Hz mode is a coupled solar and membrane mode; and the 2.45 Hz mode is the first mode of the primary deployment mechanism with the solar array housing attached. The identified dampings are higher than expected because there is an attitude control for maneuvering during testing and mechanical friction of the solar array mechanism.

FORWARD AND BACKWARD IDENTIFICATION

Forward Identification			Backward Identification		
Freq. (Hz)	Damping (%)	Mode SV	Freq. (Hz)	Damping (%)	Mode SV
0.147	55.6	0.76	0.161	46.3	0.84
0.155	58.4	0.98	0.151	47.6	0.88
0.169	67.4	1.00	0.166	29.6	1.00
0.633 ¹	5.73	0.68			
1.273 ²	4.06	0.37			
2.433 ³	5.23	0.02			
2.822	6.33	0.01			

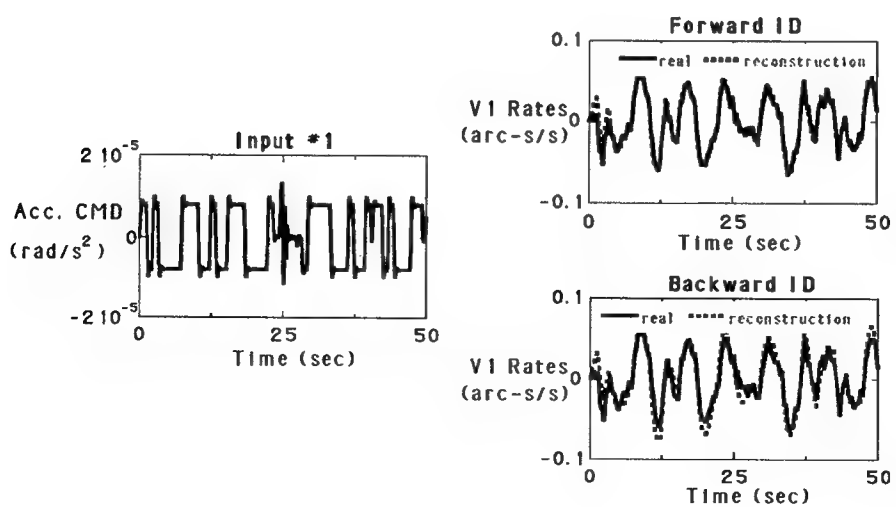
¹ In-plane bending mode of the solar panel

² Coupled solar and membrane mode

³ First mode of the primary deployment mechanism with the solar array housing attached

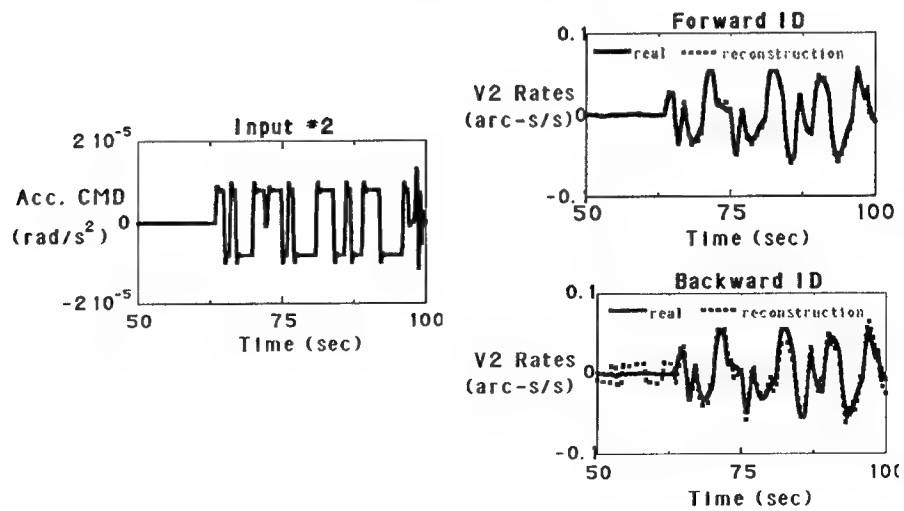
The left figure shows the excitation input signal including pulse combined with a sine-sweeping signal in the middle of an excitation period (50.975 sec). The figures on the right-hand side show a 50-second overlap of the reconstruction from the identified forward and backward system models, and the test data for the first vehicle axis. There are some visible differences in the backward identification between test and reconstruction, but overall the map from the input to the output is reasonably well. The forward identification is somewhat better than the backward identification in damping estimation. The damping ratio estimated from the backward approach appears to be a little low. It is important that the system model be accurate because it is this part that is used as a model for control design.

COMPARISON OF REAL AND RECONSTRUCTED DATA (Vehicle Axis #1)



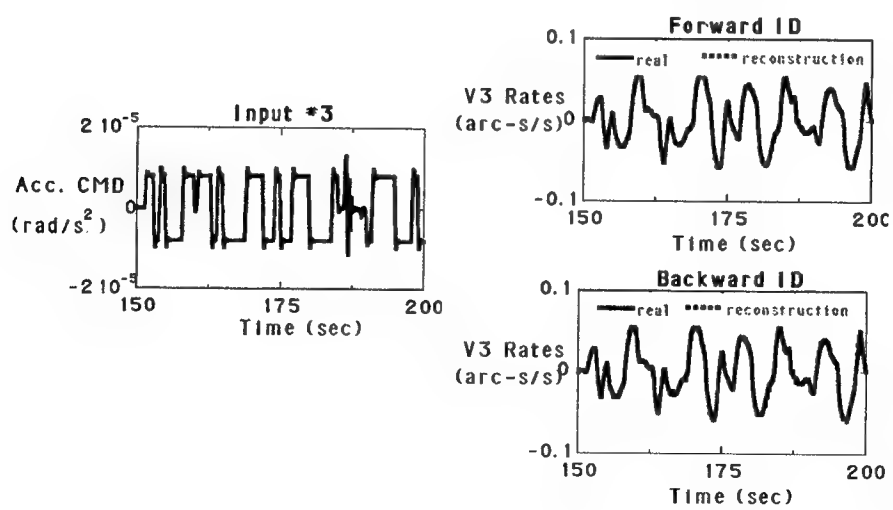
The left figure shows the excitation input signal including pulse combined with a sine-sweeping signal in the middle of an excitation period (50.975 sec). The excitation signal starting from approximately 60 seconds for the second vehicle axis is identical to that for the first vehicle axis. The figures on the right-hand side show a 50-second overlap of the reconstruction from the identified forward and backward system models, and the test data for the second vehicle axis. There are relatively more visible differences in the backward identification between test and reconstruction in comparison with the results shown in the last chart for the first vehicle axis. The forward identification is obviously better than the backward identification in this case.

COMPARISON OF REAL AND RECONSTRUCTED DATA (Vehicle Axis #2)



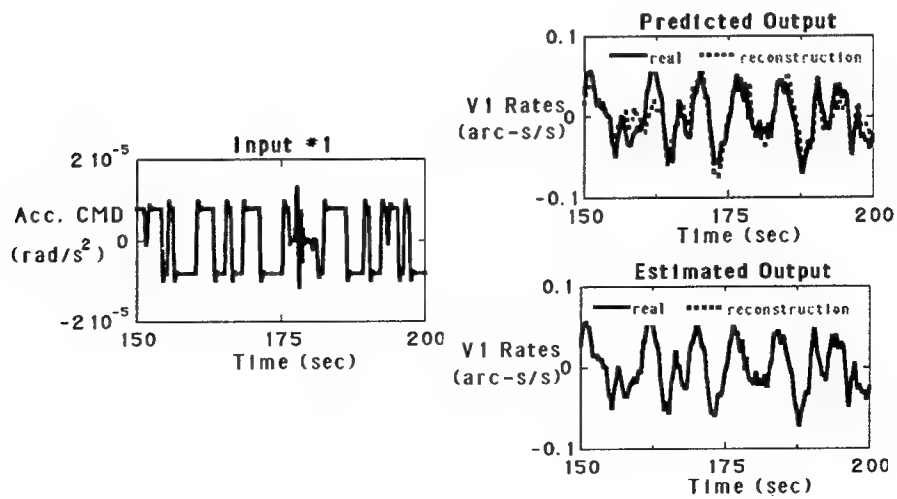
The left figure shows 50 seconds of an excitation input signal including pulse combined with a sine-sweeping signal in the middle of an excitation period (50.975 sec). The excitation signal starting from approximately 150 seconds for the third vehicle axis is identical to that for the first vehicle axis. The two figures on the right-hand side show a 50-second overlap of the reconstruction from the identified forward and backward system models, and the test data for the third vehicle axis. There are only very little visible differences between test and reconstruction, implying that the input/output map is excellent.

COMPARISON OF REAL AND RECONSTRUCTED DATA (Vehicle Axis #3)



The left figure shows the excitation input signal including pulse combined with a sine-sweeping signal in the middle of an excitation period. The figures on the right-hand side show a 50-second overlap of the reconstruction from the identified forward system models, and the test data for the first vehicle axis. The figure in the right-hand upper corner shows the predicted output in comparison with the real output data. The figure in the right-hand lower corner shows the estimated output in comparison with the real output data. The predicted output is the output reconstructed from the identified model only whereas the estimated output is the output reconstructed from the identified observer. There are visible differences in the predicted and estimated outputs. Comparison of the observer output with the measured response shows extremely good agreement, indicating that the observer is correcting for the system uncertainties including nonlinearities. The covariance of the estimated output residuals is about three order less than the predicted output residuals. Similar results of the predicted and estimated outputs were obtained for the second and third vehicle axes, and thus are not shown in this presentation.

COMPARISON OF PREDICTED AND ESTIMATED OUTPUT (Vehicle Axis #1)



The identified system model obtained by this method incorporates information about unmodeled dynamics and measurement noises into a system observer model. A system observer identified from measured response data is available for direct use in observer-based control law designs. Also the identified observer can be used to characterize system uncertainties and measurement noises which often require considerable engineering insight and judgement.

CONCLUDING REMARKS

- ★ The identified dampings are high due to an attitude control for maneuvering during testing and mechanical friction of the solar array mechanism.
- ★ The response of the identified model has good correlation with the measured response.
- ★ Comparison of the observer output with the measured response shows extremely good agreement, indicating that the observer is correcting for the system uncertainties.
- ★ The identified observer model is available for direct use in observer-based control law designs.
- ★ Further analysis of the existing Hubble flight data is undertaken to simultaneously identify the attitude controller and the open-loop system.

Bibliography:

- [1] Juang, J.-N., and Pappa, R. S., "An Eigensystem Realization Algorithm for Modal Parameter Identification and Model Reduction," *Journal of Guidance, Control, and Dynamics*, Vol. 8, No. 5, Sept.-Oct. 1985, pp. 620-627.
- [2] Juang, J.-N., Cooper, J. E., and Wright, J. R., "An Eigensystem Realization Algorithm Using Data Correlations (ERA/DC) for Modal Parameter Identification," *Control-Theory and Advanced Technology*, Vol. 4, No. 1, 1988, pp. 5-14.
- [3] Chen, C. W., Huang, J.-K., Phan, M., and Juang, J.-N., "Integrated System Identification and Modal State Estimation for Control of Large Flexible Space Structures," *Journal of Guidance, Control and Dynamics*, Vol. 15, No.1, Jan.-Feb. 1992, pp. 88-95.
- [4] Phan, M., Juang, J.-N., and Longman, R. W., "Identification of Linear Multivariable Systems from a Single Set of Data by Identification of Observers with Assigned Real Eigenvalues," *Proceedings of the AIAA 32nd Structures, Structural Dynamics & Materials Conference*, Baltimore, MD., April 8-10, 1991.
- [5] Phan, M., Horta, L. G., Juang, J.-N., and Longman, R. W., "Linear System Identification Via an Asymptotically Stable Observer," *Proceedings of the AIAA Guidance, Navigation and Control Conference*, New Orleans, Louisiana, Aug. 1991, NASA Technical Paper 3164, 1992.
- [6] Juang, J.-N., Phan, M., Horta, L. G., and Longman, L. G., "Identification of Observer and Kalman Filter Markov Parameters: Theory and Experiments," *Proceedings of the AIAA Guidance, Navigation and Control Conference*, New Orleans, Louisiana, Aug. 1991.
- [7] Horta, L. G., Phan, M., Juang, J.-N., Longman, R. W., and Sulla, J., "Frequency Weighted System Identification and Linear Quadratic Controller Design," *Proceedings of the AIAA Guidance, Navigation and Control Conference*, New Orleans, Louisiana, Aug. 1991.
- [8] Phan, M., Juang, J.-N., and Longman, R. W., "On Markov Parameters in System Identification," *NASA Technical Memorandum TM 104156*, Oct. 1991.
- [9] Juang, J.-N. and Phan, M., "Identification of Backward Observer Markov Parameters: Theory and Experiments," *NASA TP-3164*, June 1992.
- [10] Hollkamp, J.J. and Batill, S.M., "Automated Parameter Identification and Order Reduction for Discrete Series Models," *AIAA Journal*, Vol. 29, No. 1, 1991.
- [11] Juang, J.-N., Horta, L. G., and Juang, J.-N., "System/Observer/Controller Identification Tool Box," *NASA Technical Memorandum TM-107566*, Dec. 1991.

SESSION II

Chairman: Jerome Pearson
Wright Laboratory
WPAFB, Ohio

Co-Chairman: James Fanson
Jet Propulsion Laboratory
Pasadena, California

MICRO-PRECISION CONTROL/STRUCTURE INTERACTION TECHNOLOGY FOR LARGE OPTICAL SPACE SYSTEMS

Samuel W. Sirlin and Robert A. Laskin
Jet Propulsion Laboratory
California Institute of Technology
Pasadena, CA 91109

INTRODUCTION

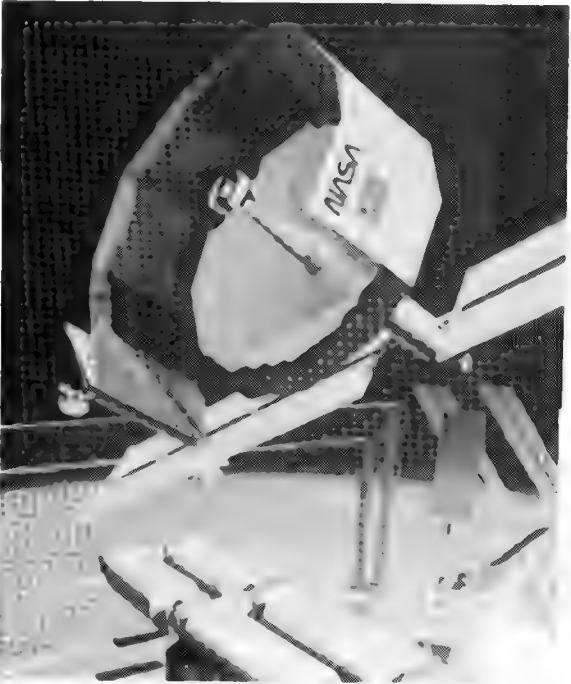
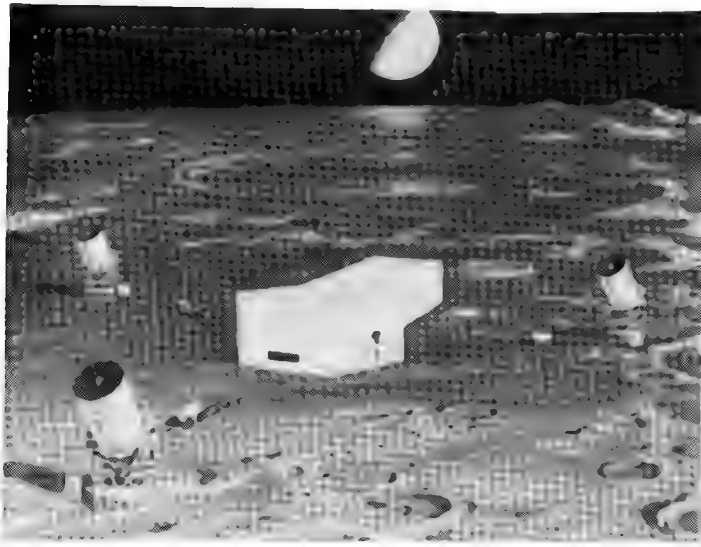
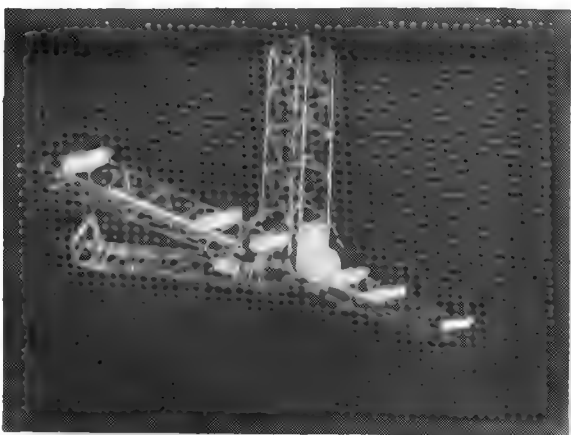
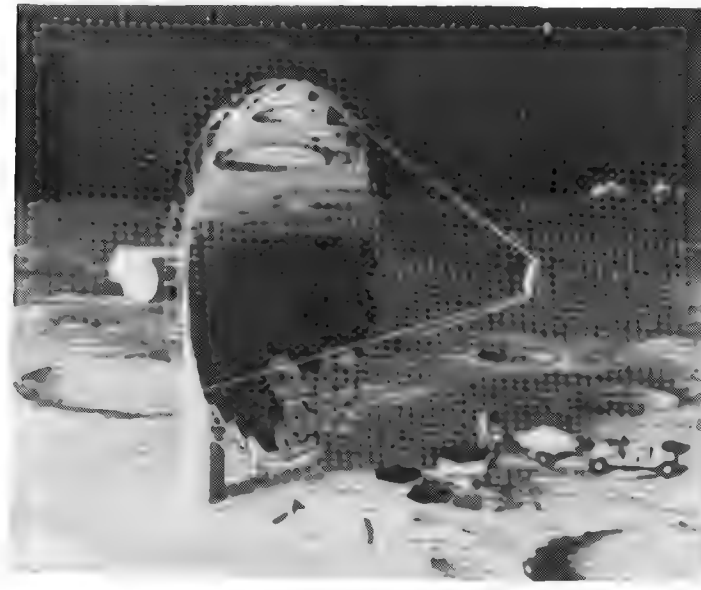
The CSI program at JPL is chartered to develop the structures and control technology needed for sub-micron level stabilization of future optical space systems. The extreme dimensional stability required for such systems derives from the need to maintain the alignment and figure of critical optical elements to a small fraction (typically $1/20^{th}$ to $1/50^{th}$) of the wavelength of detected radiation. The wavelength is about 0.5 micron for visible light and 0.1 micron for ultra-violet light. This $\lambda/50$ requirement is common to a broad class of optical systems including filled aperture telescopes (with monolithic or segmented primary mirrors), sparse aperture telescopes, and optical interferometers. The challenge for CSI arises when such systems become large, with spatially distributed optical elements mounted on a lightweight, flexible structure.

In order to better understand the requirements for micro-precision CSI technology, a representative future optical system was identified and developed as an analytical testbed for CSI concepts and approaches. An optical interferometer was selected as a stressing example of the relevant mission class. The system that emerged was termed the Focus Mission Interferometer (FMI).

This paper will describe the multi-layer control architecture used to address the FMI's nanometer level stabilization requirements. In addition the paper will discuss on-going and planned experimental work aimed at demonstrating that multi-layer CSI can work in practice in the relevant performance regime.

THE VIBRATIONAL STABILITY CHALLENGE

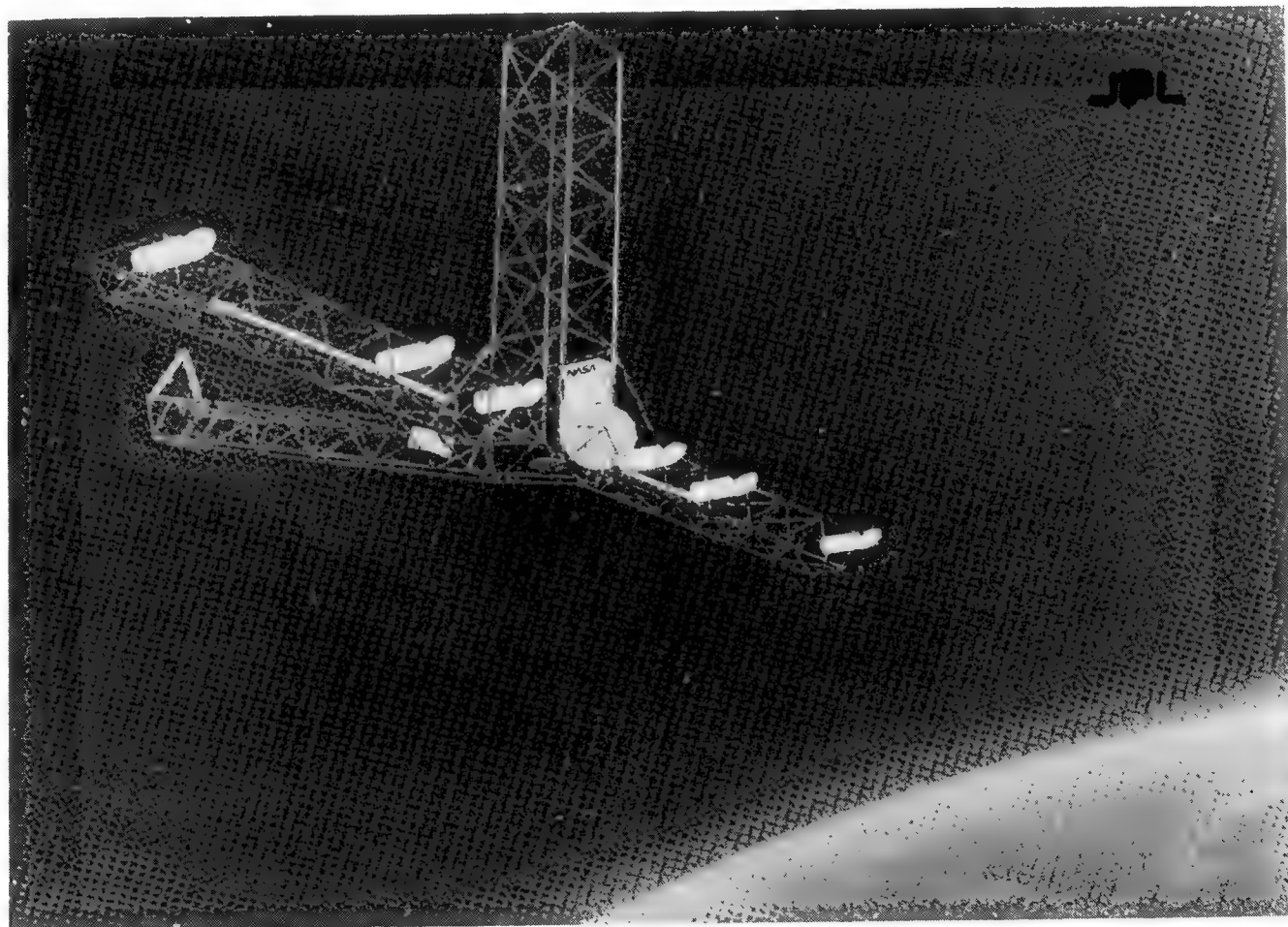
High performance space optical systems typically have total light pathlength stability goals on the order of $\lambda/50$ ($\approx 12\text{nm}$ visible, $\approx 2\text{nm}$ ultraviolet). Because the total pathlength stability budget must be allocated among several contributors, a reasonable stability goal for any one of the system's optical elements is in the neighborhood of $\lambda/200$ ($\approx 3\text{nm}$ visible, $\approx 0.5\text{nm}$ ultraviolet). Structural vibrations, even on very quiet spacecraft, are typically larger than the desired "nanometers" goal. (Consider that only four millionths of a "g" vibration level at 10Hz is ± 100 nanometers of motion.) Analysis of large optical structures indicates that between a few-hundred and a few-thousand nanometers of dynamic motion are caused by noise from even the extremely quiet Hubble Space Telescope reaction control wheels (RCW's) operated at less than 50% of their design spin rate (higher rate gives greater disturbance). Beyond RCW's, other disturbance sources, such as tape recorders, pointing drive mechanisms, control moment gyros, etc, have not yet been evaluated but they are likely to induce vibration levels at least as severe as the HST RCW's.



CSI FOCUS MISSION INTERFEROMETER

Future spacebased large optical systems can be divided into two broad categories: interferometers, where spatially distributed "small" collecting apertures are combined to synthesize the performance of a single large aperture; and filled aperture systems, which are essentially large conventional telescopes that typically incorporate segmented primary mirrors due to the difficulty (and inherent weight) of fabricating very large monolithic mirrors. JPL has selected a representative optical interferometer as the target application on which to focus its CSI technology development efforts - hence the name Focus Mission Interferometer (FMI). An optical interferometer can be used for high resolution imaging as well as extremely precise astrometry (astrometry is the mapping of stellar positions in the sky). When used for imaging, the FMI's effective baseline of 24 meters would give it roughly 10 times the resolving power of the Hubble Space Telescope. This translates into a resolution of 5 miliarcseconds.

The optical performance of the FMI relative to its 2.5 nanometer differential pathlength stabilization requirement has been analyzed in some detail and it has been determined that vibration attenuation factors of between 1,000 and 10,000 are necessary to meet the requirement with margin. In order to meet this challenge, CSI has adopted an approach that entails a multi-layer control architecture, with each layer responsible for providing between one and two orders of magnitude attenuation. The three layers are: structural control, disturbance isolation, and active optical control.



MULTI-LAYER CSI ARCHITECTURE

Rather than use only a single (centralized) control system, we have broken up the problem into autonomous subsystems, each of which has its own task. This autonomy makes the overall system more robust. In addition the first two systems help accomplish other objectives besides optical pathlength control, for example the siderostats need to be coaligned and the metrology tower should be kept quiet.

- THREE LAYERS OF CONTROL:

1. STRUCTURAL CONTROL - ADD DAMPING TO THE MODES. THIS REDUCES THE GENERAL VIBRATION LEVEL AND MAKES THE OPTICAL CONTROLS MORE ROBUST.
2. ISOLATION OF DISTURBANCE SOURCES - ATTACKS THE KNOWN SOURCES OF DISTURBANCES. IN OUR CASE WE SOFTMOUNT THE REACTION WHEELS.
3. OPTICAL CONTROL - CONTROL OF THE OPTICAL ELEMENTS DIRECTLY. THIS ACTUALLY ENCOMPASSES 3 SEPARATE CONTROL SYSTEMS FOR PATH-LENGTH CONTROL (TIMING BELT, VOICE COIL, AND PZT) ON EACH TROLLEY, AND A POINTING SYSTEM FOR EACH SIDEROSTAT.

STRUCTURAL MODEL

The FMI design [1]* incorporates 25 active struts of the truss to provide for structural vibration suppression. The struts are located symmetrically in the two "arms" of the interferometer as well as in the "tower." Strut locations were chosen via heuristic modal kinetic and strain energy arguments. Each active strut spanning two nodes of the interferometer truss is composed of a passive truss element and an active piezoelectric element in series. The specific stiffness of the active element was designed to be the same as that of the truss elements for complete interchangeability with other elements. Each active element incorporates its own force and precision displacement measurement system.

A NASTRAN finite element model of the FMI structure was built incorporating 527 modes. In former analyses [1,2], reduced order models were built, but in the present work the full model was used. Rather than combining the models for the plant and controllers in state space, which would produce state space models of order around 1300, (double the number of modes plus 25 active element controllers plus pathlength control and isolation) models were combined in the frequency domain. This requires inversions of the order of the number of loops, independent of the state order. Since each block of the model is brought into the frequency domain separately, special knowledge of each block can be used [3].

STRUCTURAL MODEL

- o NASTRAN FINITE ELEMENT MODEL
 - 297 GRIDS, 465 RODS, 17 BARS, 37 RBE2 ELEMENTS
 - 527 MODE DIAGONAL Pro-Matlab MODEL, DAMPING RATIO 0.1%.
 - 25 ACTIVE MEMBERS
 - REACTION WHEEL FORCE DISTURBANCE (FOUR WHEELS, SPIN UP FROM 0 TO 3000RPM)

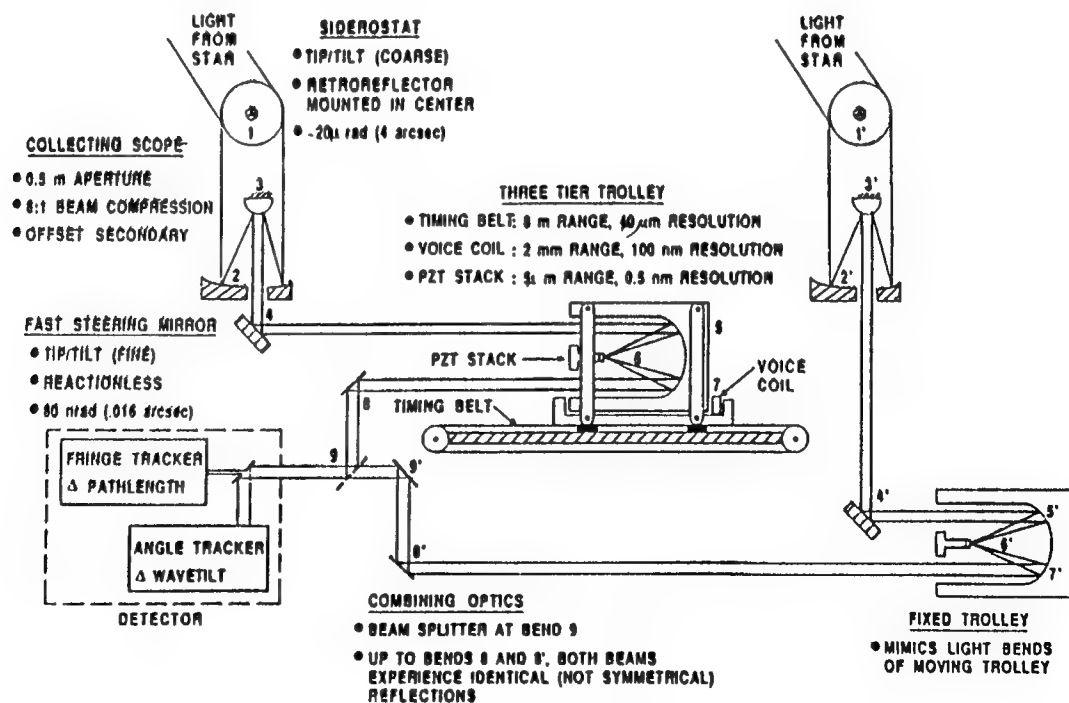
*References 1-8 are cited in text.

OPTICAL MODEL

Each interferometer (a pair of siderostats) takes light from the +Y and -Y arms, compressing the beam, adjusting the pathlength and tilt to compensate for structural vibration, and combines the beams at a focal plane. The optical train consisted of 19 elements, 9 on the +Y half, 9 on the -Y half, and the focal plane. One of the three interferometers of the FMI has been modeled using the Controlled Optics Modeling Package (COMP, based on [4]). One purpose of this tool is to determine the partial derivatives of the optical pathlength to the motion of the individual optical elements. This gives a matrix that transforms structural vibration (six degrees of freedom at each element) into optical pathlength, a component of the C matrix.

OPTICAL MODEL

- OPTICAL MODEL BUILT WITH THE CONTROLLED OPTICS MODELING PACKAGE (COMP)
- COMPLETE INTERFEROMETER, 19 OPTICAL ELEMENTS
- LINEAR CHIEF RAY MODEL OUTPUT TO Pro-Matlab



Optical Layout for Interferometer A

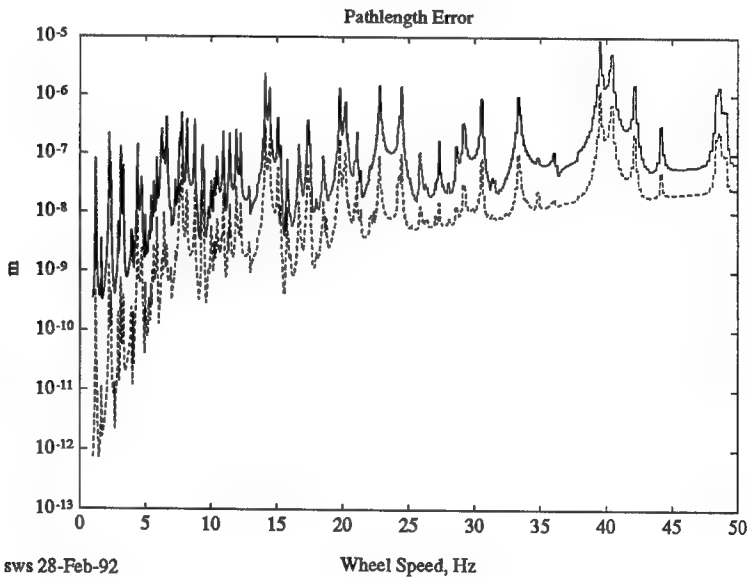
OPTICAL PATHLENGTH CONTROL

For the vibration analysis, the disturbance source used was the imbalance force from 4 Hubble Space Telescope reaction wheels spinning from 0 to 1200 RPM [1,2]. This spin up takes place slowly, for example at the orbital period to counter gravity gradient torques, and hence the disturbance may be applied quasi-statically in the frequency domain. At each wheel speed, the reaction wheel imbalance harmonics are multiplied by the appropriate values from the transfer function and combined using the rms.

To control the optical pathlength directly, a controller similar to that used in [1] is implemented. The primary difference is that while in [1] the bandwidth was limited to 10 Hz due to light levels, current studies [8] indicate that this is overly conservative, and hence a bandwidth of 250Hz was used.

OPTICAL PATHLENGTH CONTROL

- OPTICAL PATHLENGTH PERFORMANCE
- OPEN VERSUS CLOSED LOOP



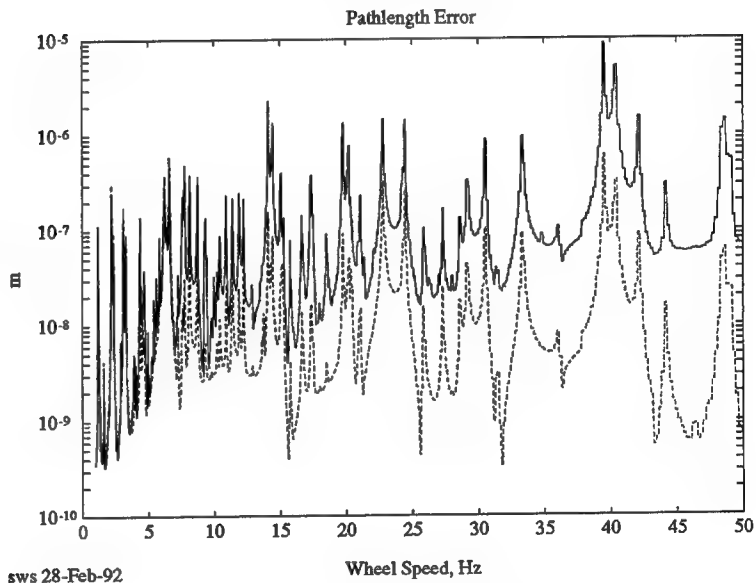
CONTROL	RMS PATHLENGTH ERROR
	(nm)
None	702
250Hz	94

VIBRATION ISOLATION

Vibration isolation can be carried out at the source of the disturbance - suspending the reaction wheels in the same manner as is done on the Hubble Space Telescope. This is implemented as a simple second order filter with 10Hz poles damped by $\zeta = 0.3$ on the disturbance source. Isolation has a large effect on high frequency disturbances, and is therefore very desirable. Of course in practice it is not possible to isolate all disturbances, leaving some (hopefully smaller) disturbances to be handled solely by the other layers.

VIBRATION ISOLATION

- OPTICAL PATHLENGTH PERFORMANCE
- NO ISOLATION
- 10 Hz ISOLATION



ISOLATION FREQUENCY (Hz)	RMS PATHLENGTH ERROR (nm)
∞	702
10	60

DIAL-A-STRUT CONTROLLER

A robust way of implementing a softening controller is with bridge feedback [5-7, 8] using both force and displacement measurements. At JPL a Dial-a-Strut controller has been developed that has a simple form, can easily be adjusted to work with a wide variety of structures, and is insensitive to plant and control parameter variations.

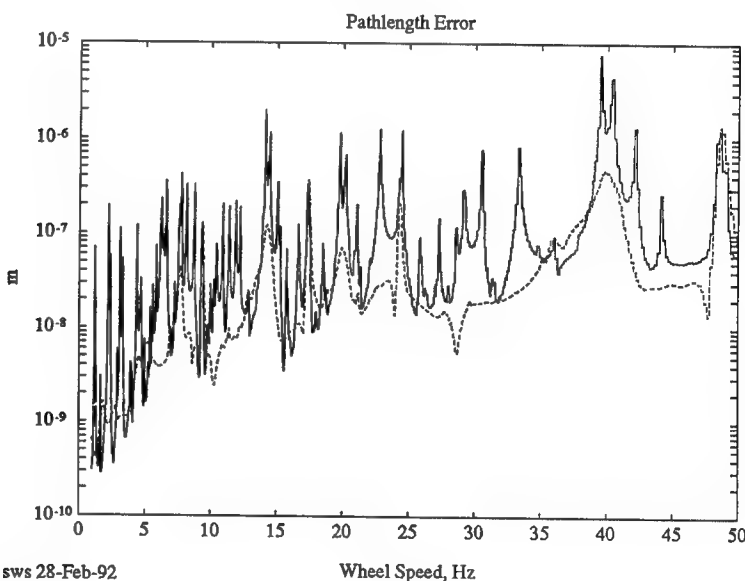
The Dial-a-Strut is designed to control the strut so its impedance (using the force-current analogy so we get $Z = \text{velocity/force}$) is determined by the impedance of selected electrical components:

$$Z \rightarrow \frac{1}{\gamma Z_d},$$

$$Z_d(s) = \left(C_1 s + \frac{C_2 s}{1 + R C_2 s} \right)^{-1}.$$

DIAL-A-STRUT CONTROLLER

- OPTICAL PATHLENGTH PERFORMANCE
- OPEN VERSUS CLOSED LOOP



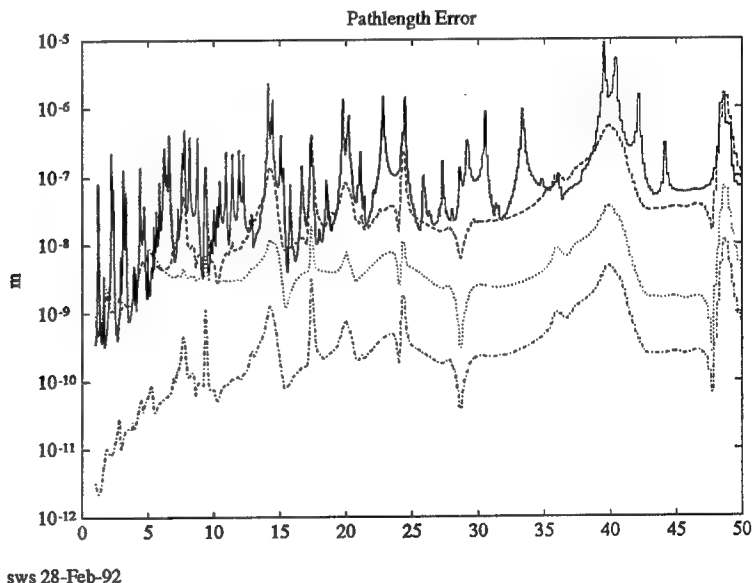
CONTROL	RMS PATHLENGTH ERROR (nm)
None	702
Dial-a-Strut	191

MULTI-LAYERED CONTROL SYSTEM

Combining the various control strategies yields the pathlength control results shown. The plot shows the results with (in order of descending pathlength error) no control, with Dial-a-Strut control (all 25 struts), with Dial-a-Strut and the disturbance isolator, and with all the controllers. The table shows that all the various layers are necessary to get down to the nanometer level. Implementing the high bandwidth pathlength control has not been examined carefully for the FMI, though similar bandwidths have been used on much simpler ground-based structures. The NASTRAN model is not accurate much above 100Hz. The highest bandwidth loop of the pathlength control moves only a small mirror, and is almost uncoupled from the structural modes. The voice coil loop that moves a trolley is coupled much more closely to the structure and it is likely that structural damping will be essential for that loop to be robust and high performance.

MULTI-LAYERED CONTROL SYSTEM

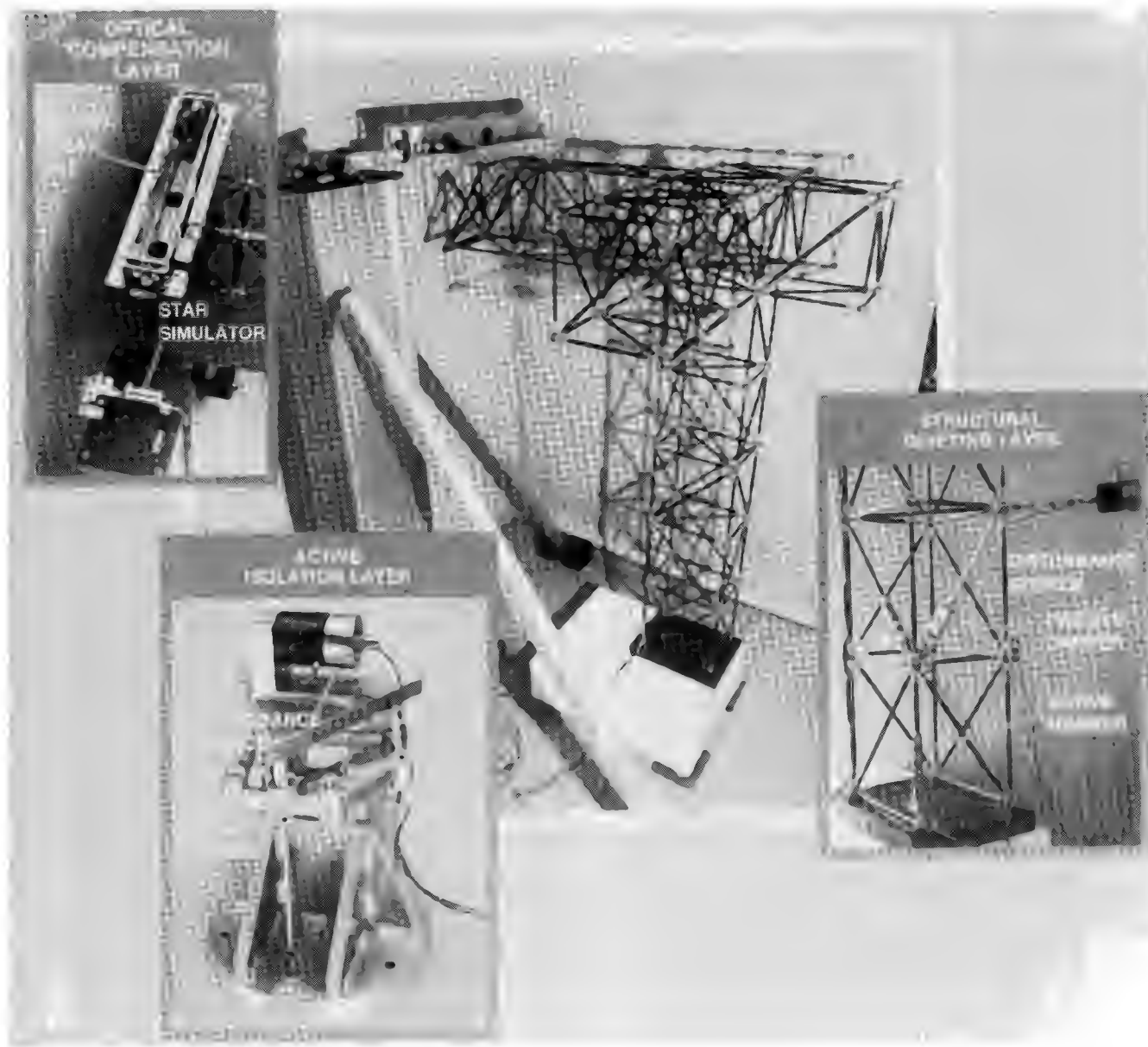
- OPTICAL PATHLENGTH PERFORMANCE
- ADDING SUCCESSIVE LAYERS



CONTROL	RMS PATHLENGTH ERROR (nm)
None	702
Dial-a-Strut	191
Dial-a-Strut + Isolator (10Hz)	10
Dial-a-Strut + Isolator (10Hz) + PL Control (250Hz)	1.5

CSI PHASE B MULTI-LAYER TESTBED

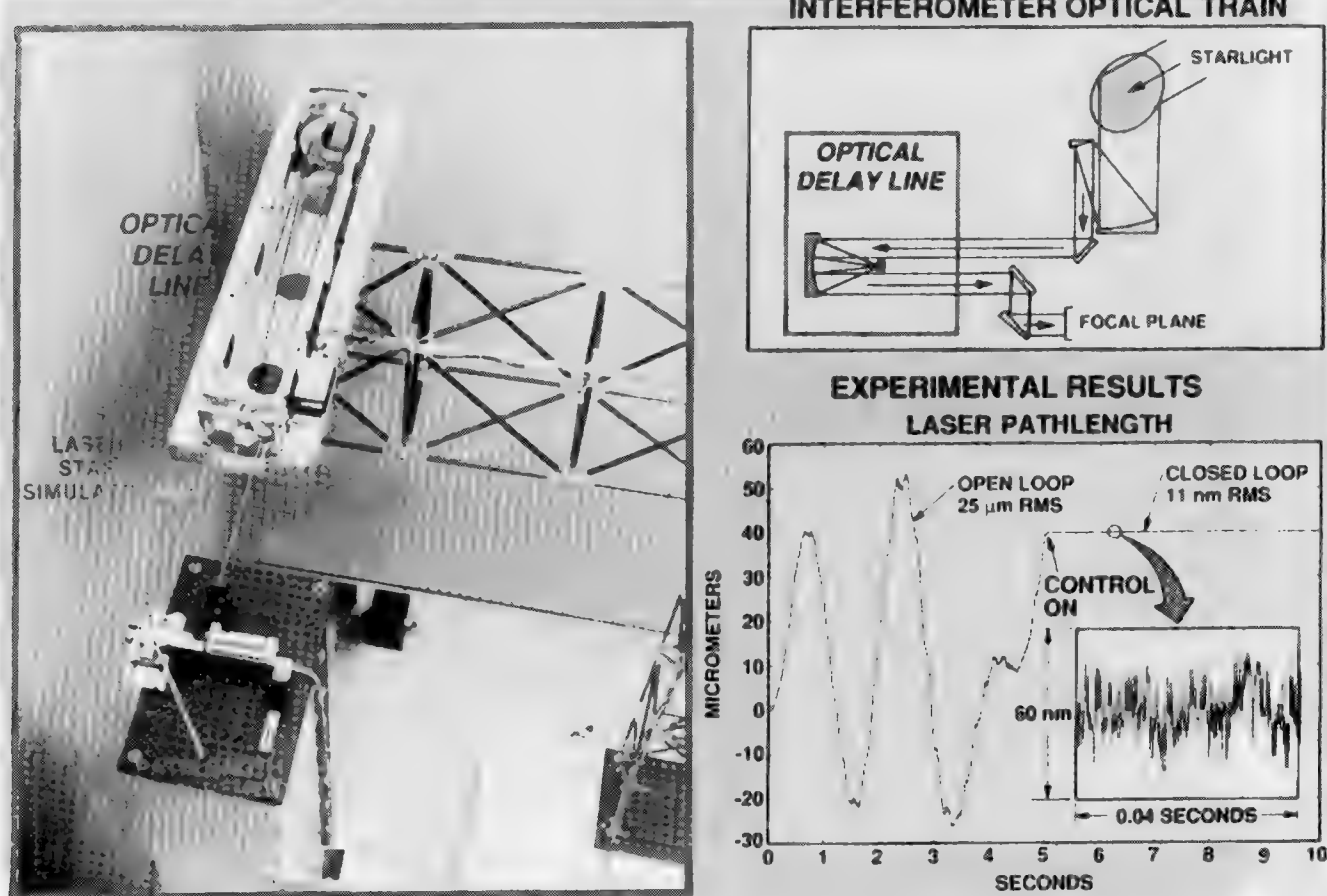
The Phase B Multi-Layer Testbed incorporates three layers of control which either attenuate or reject the effects of disturbances. They consist of the optical compensation layer, the structural quieting layer, and the disturbance isolation layer. The CSI Phase B Testbed Facility has been built to resemble a portion of an interferometer telescope, including a laser star simulator, a metering truss structure, an optical pathlength delay line, and the associated instrumentation and real time control computers. Preliminary experiments using the optical compensation layer have demonstrated the ability to reduce jitter in the optical pathlength by a factor of 4,000. Preliminary experiments using the structural quieting layer have demonstrated the ability to increase the amount of damping in the metering truss by a factor of 25, reducing the level of jitter in the optical pathlength by a similar factor. A prototype disturbance isolation layer has been tested separately from the Phase B Testbed, and preliminary experiments have demonstrated the potential to reduce the level of disturbance forces transmitted to the structure by at least a factor of 10. Future experiments will operate these three layers in combination, where the attenuation effects are expected to cascade, thereby multiplying together the benefits of each layer to achieve levels of disturbance rejection approaching 10,000.



CSI OPTICAL COMPENSATION EXPERIMENT

The optical delay line experiment was designed to capture the interaction between structural flexibility and optical pathlength as it would occur in a space-based optical interferometer such as the Orbiting Stellar Interferometer (OSI). Varying levels of control/structure interaction can be emulated by reconfiguring the testbed optical train. The approach is to conduct experiments with optical trains of increasing complexity, ultimately replicating the characteristics of an interferometer flight instrument system. The current optical delay line control is implemented by translating coarse and fine mirror stages based upon detected variations in the laser (star simulator) pathlength.

Experimental results obtained by closing control loops around the initial optical configuration pictured have demonstrated approximately 12 nanometers RMS laser pathlength stabilization, which represents a factor of 4,000 attenuation from open loop response to the laboratory environment. The challenge is to provide the same level of control when the optical train is reconfigured to couple more structural motion into the laser pathlength which is a situation more representative of a flight system. Meeting this challenge (planned for FY '92) will be a major step toward validating the CSI technology necessary to enable the next generation of precision space optical systems.



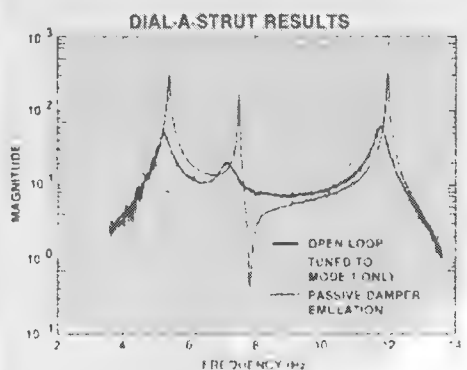
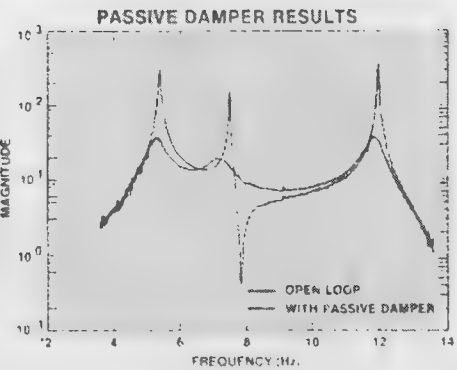
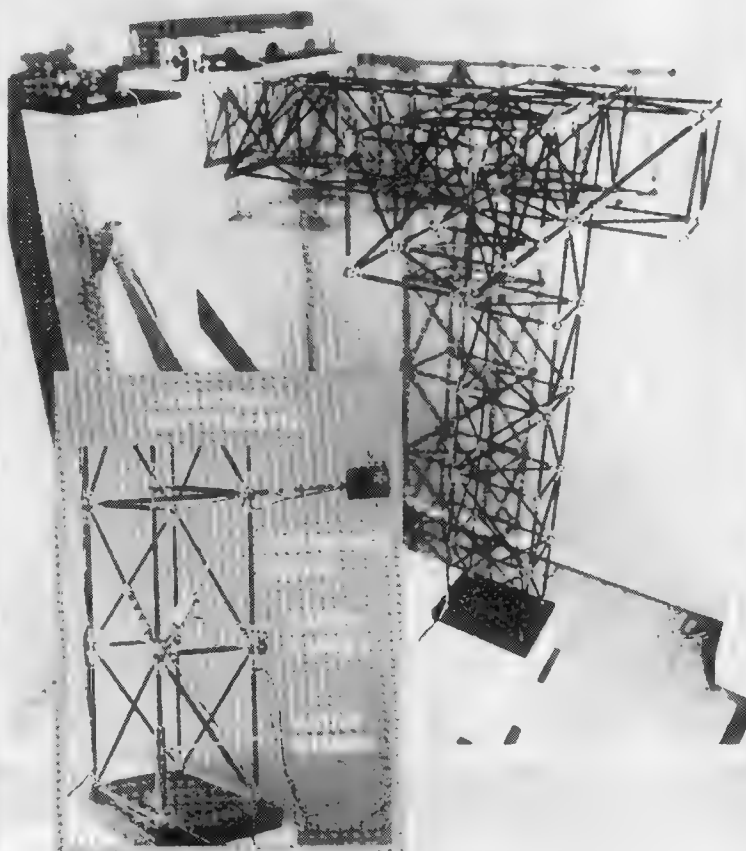
CSI STRUCTURAL QUIETING EXPERIMENTS

The CSI Structural Quieting Layer is specifically designed to reduce the level of vibration in the structure. This is accomplished through a combination of passive damping and active control using active structural members. Passive dampers have the advantages of simplicity of design and of requiring no power for operation. Preliminary experiments with passive dampers have demonstrated the ability to increase the level of damping in the structure by a factor of 25, reducing the degree of vibration in the structure by a similar amount.

Active structural members, which utilize an embedded piezoelectric actuator, have the advantage of being tunable for optimal performance even after the structure has been assembled and/or deployed. The active dial-a-strut control circuit cannot only be tuned to emulate passive dampers, but can also be designed to achieve a more exact impedance match to the structure, providing specific damping performance. For example, the active member can be tuned to specifically damp just the lowest structural mode, as is shown in the figure. Preliminary experiments using the dial-a-strut to emulate a passive damper have achieved results similar to a passive damper and have verified the control circuit design. Future experiments will explore the tunable nature of the active approach to provide the highest levels of performance.

CSI PHASE B STRUCTURAL QUIETING LAYER TEST RESULTS

CSI PHASE B MULTILAYER TESTBED

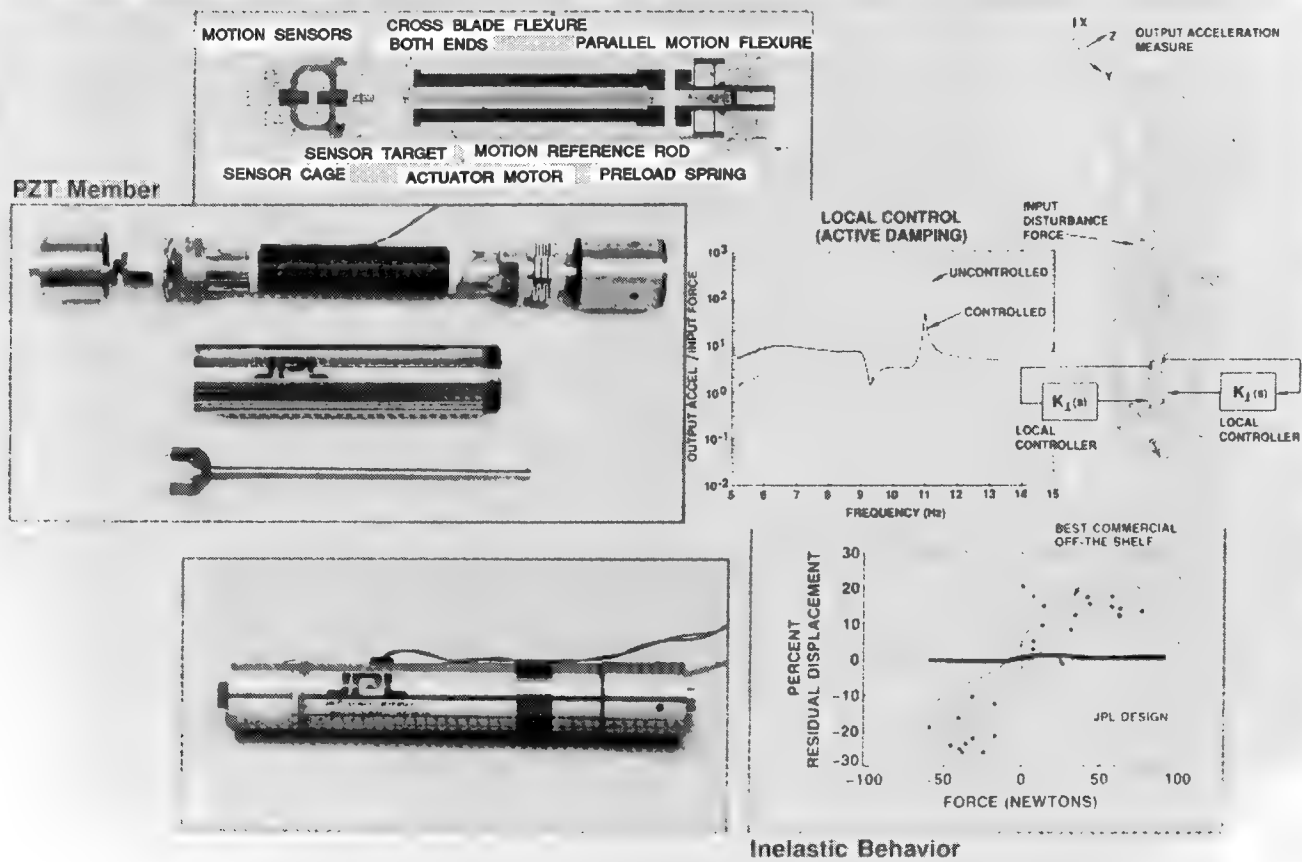


JPL ACTIVE MEMBER TECHNOLOGY

2nd Generation Active Members: JPL testing has established that even the best commercially available piezoelectric actuators exhibit hundreds of nanometers of stiction and nonlinear offset. The JPL 2nd generation Active Member actuator vastly reduces these nonlinear behaviors, and insures the feasibility of precision structural control at the nanometer level. The "Inelastic Behavior" scatter plot shows virtual elimination of nonlinear offsets with the JPL Active Member.

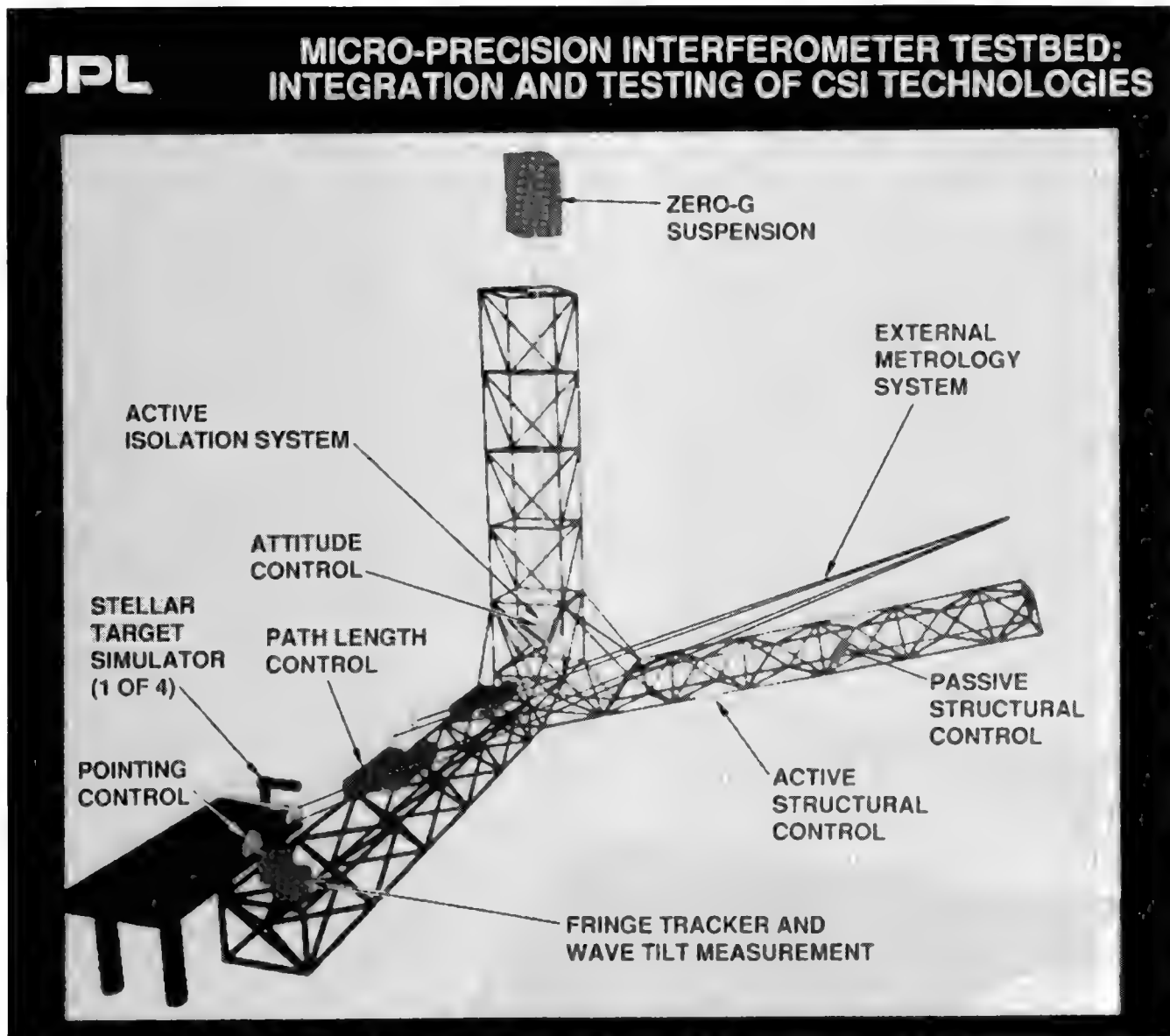
Impedance Based "Dial-A-Strut" Local Control: Structural control performance and robustness are both difficult to achieve on highly resonant structures. JPL has developed robust, impedance-based local controllers which "de-reverberate" the structure, greatly reducing resonant behavior. After the structure is de-reverberated, it becomes possible to design high performance robust global controllers to further stabilize the structure. The "Local Control (Active Damping)" frequency response plot shows successful de-reverberation of the JPL Phase 0 Precision Truss using impedance-based local controllers on two active members. These "Dial-A-Strut" controllers permit independent setting of active member stiffness and damping with the simple adjustment of a dial.

2ND GENERATION ACTIVE MEMBER



JPL MICRO-PRECISION INTERFEROMETER (MPI) TESTBED

As a follow-on to the Phase B Multi-Layer Testbed, JPL is in the process of constructing a more ambitious test facility with the goal of conducting system level ground validation tests of micro-precision CSI technology. The new facility, named the Micro-Precision Interferometer (MPI) Testbed, will incorporate the multi-layer architecture but will embody several additional features: attitude control (over small angles), a soft suspension system to simulate free-free boundary conditions, an external metrology system for precise sensing of structure geometry, and high precision pointing control of optical lines-of-sight. The physical scale of the structure will be approximately 7 meters by 7 meters by 7 meters resulting in roughly a one half scale "one-armed" version of the FMI. Perhaps most importantly, the MPI is expected to operate at a level of precision comparable to that of an ultimate interferometer flight system. From a scientific standpoint, the MPI will clearly demonstrate end-to-end operation of a multi-baseline optical interferometer. From an engineering standpoint the MPI represents the ultimate ground-based demonstration that micro-precision CSI technology is ready for application to a broad class of future precision optical space systems.



CONCLUSIONS

A large class of future astronomy and astrophysics space missions will entail the development of large optical systems that will be distributed over lightweight, flexible structures. Maintaining the required nanometer level alignment and stability of optical surfaces for such systems will be a challenge of the first order. JPL's CSI Program is developing structures and control technologies to address this challenge, and is conducting both analytic and experimental research toward this end.

This paper has presented an analytical study that demonstrates the feasibility of applying a multi-layer control architecture to a representative large optical space system. The three to four orders of magnitude vibration attenuation predicted in this analysis is currently being buttressed by the results of laboratory tests on the CSI Phase B Multi-Layer Testbed. Future CSI experiments on the Micro-Precision Interferometer Testbed (pictured below undergoing structural assembly) will demonstrate similar levels of vibration attenuation while performing at the relevant nanometer level in an end-to-end fashion on a large scale structure. The MPI Testbed should be completed by the summer of 1993 and ready to begin coarse testing shortly thereafter.



ACKNOWLEDGEMENT

This work was performed at the Jet Propulsion Laboratory, California Institute of Technology, under a contract with the National Aeronautics and Space Administration.

REFERENCES

1. R. A. Laskin, A. M. San Martin, "Control/Structure System Design of a Spaceborne Optical Interferometer," AAS/AIAA Astrodynamics Specialist Conference, August 1989.
2. S. W. Sirlin, R. A. Laskin, "Sizing of Active Piezoelectric Struts for Vibration Suppression on a Space-Based Interferometer," 1st Joint U.S./Japan Conference on Adaptive Structures, November 1990.
3. S.W. Sirlin, "Pro-Matlab Functions for Frequency Response," JPL EM 343-1163, December 1989 (internal document).
4. D.C. Redding, W.G. Breckenridge, "Optical Modeling for Dynamics and Control Analysis," AIAA Journal of Guidance, Control, and Dynamics, Volume 14, Number 5, 1991.
5. B. J. Lurie. Feedback Maximization, Artech House, Deadham, MA, 1986.
6. G.-S. Chen et al, "Active Member Control for Vibration Suppression in Truss Structures," Intern. Workshop on Intelligent Structures, Taipei, Taiwan, 1990.
7. B. J. Lurie, S. W. Sirlin, J. F. O'Brien, J. L. Fanson, "The Dial-a-Strut Controller for Structural Damping," ADPA Active Materials & Adaptive Structures Conference, November 1991.
8. S.W. Sirlin, "Active Structural Control for Damping Augmentation and Compensation of Thermal Distortion," 2nd Joint Japan-U.S.A. Conference on Adaptive Structures," Nagoya, Japan, November 1991.

STATIC AND DYNAMIC CHARACTERISTICS OF A PIEZOCERAMIC STRUT

Brett Pokines

State University of New York at Buffalo
Buffalo, NY

W. Keith Belvin

NASA Langley Research Center
Hampton, VA

Daniel J. Inman

State University of New York at Buffalo
Buffalo, NY

ABSTRACT

The experimental study of a piezoceramic active truss strut is presented. This active strut is unique in that the piezoceramic configurations allow the stroke length of the strut not to be dependent on the piezoceramic material's expansion range but on the deflection range of the piezoceramic bender segment. A finite element model of a piezoceramic strut segment was constructed. Piezoceramic actuation was simulated using thermally induced strains. This model yielded information on the stiffness and force range of a bender element. The static and dynamic properties of the strut were identified experimentally. Feedback control was used to vary the stiffness of the strut. The experimentally verified model was used to explore implementation possibilities of the strut.

INTRODUCTION

This paper presents the static and dynamic characteristics of a new active piezoceramic strut. The actuation mechanism is based on strain induced bending. A prototype strut has been constructed, modelled and tested. The results of this experimental

investigation will lead to the development of parameters for a strut to improve vibration suppression in the NASA Langley Research Center evolutionary model.

The primary motivation for the investigation of this actuator is that the strut's stroke length is independent of the expansion range of the piezoceramic and the strut performs the same whether a tensile or compressive load is applied to it.

STRUT DESCRIPTION

The device consists of a series of bender elements connected by a rigid shaft. These bender elements consist of a thin metal plate (Figure 1) with piezoceramics laminated to opposite sides. The poled direction of the piezoceramics is aligned so that a voltage applied across the bender element contracts one side and expands on the other. Straining the piezoceramics results in a bending motion of the element. A shaft joins the bender elements in a parallel configuration. This results in an additive effect of the individual bender elements. The total applicable force, stiffness and structural load bearing ability of the strut increases as the number of bender elements increases.

A prototype bender element strut was constructed. The limitation of material availability was the primary factor in the selection of the bender element size. The prototype used two bender elements for actuation. The piezoceramic disks were made of Piezo Electric Products Inc. lead zirconate titanate G-1195 material. A two part epoxy was used to laminate the .01" thick piezoceramic material to a .01 inch thick 6061-T6 aluminum disk. Figure 2 details the dimensions of the strut.

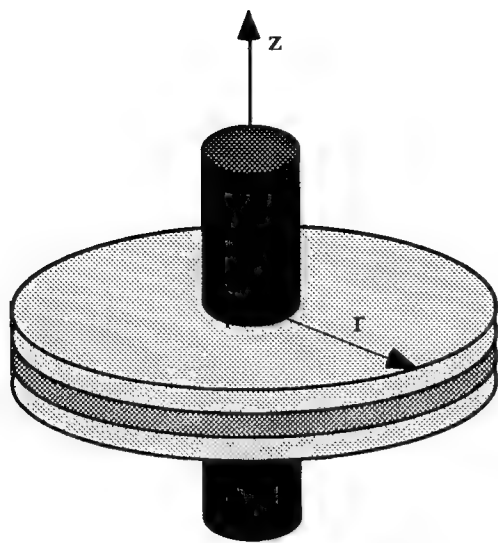
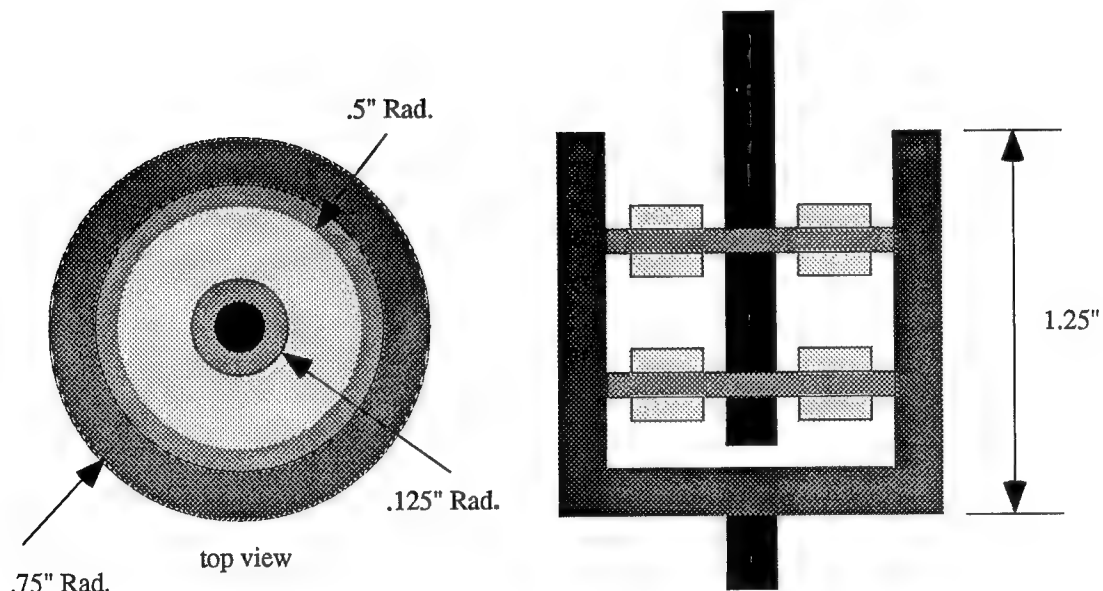


Figure 1. Single bender element



Cut Away Side View

6061-T6



piezoceramic material



stainless steel



Figure 2. Prototype strut

FINITE ELEMENT ANALYSIS

A finite element model of the prototype strut was constructed. A cross section of one bender element was modelled. Axisymmetric trapezoidal rings were used to model the bender element. The motion induced on the bender elements from the expansion and contraction of the piezoceramic disks was simulated by applying a temperature load to the nodes of the bender element modelled. The results of this model were extrapolated to model the prototype strut (Table I). The finite element modelling process is essential to the refinement of the strut's geometry. An increase in the force to stiffness ratio through a more efficient geometry is necessary and possible using the finite element modelling technique.

Table I. Finite element results

	Stiffness (lbf/in)	Max force range (lbf)
Finite element prototype model	10052	.604

EXPERIMENTAL RESULTS

The prototype bender element strut was evaluated experimentally. This evaluation investigated the static and dynamic properties of the strut. Two experiments were conducted. The first experiment involved placing the prototype strut between two rigid plates and a force transducer (Figure 3). A voltage signal was applied across the bender elements to strain the piezoceramic material. Time histories and transfer functions between the input voltage and force transducer output were recorded. The second experiment consisted of clamping the base of the strut to a rigid mass and forcing the active end of the strut with a regulated and measured force. A voltage proportional to the forcing signal was input into the strut. Displacement measurements during the experiment were acquired using optical displacement sensors.

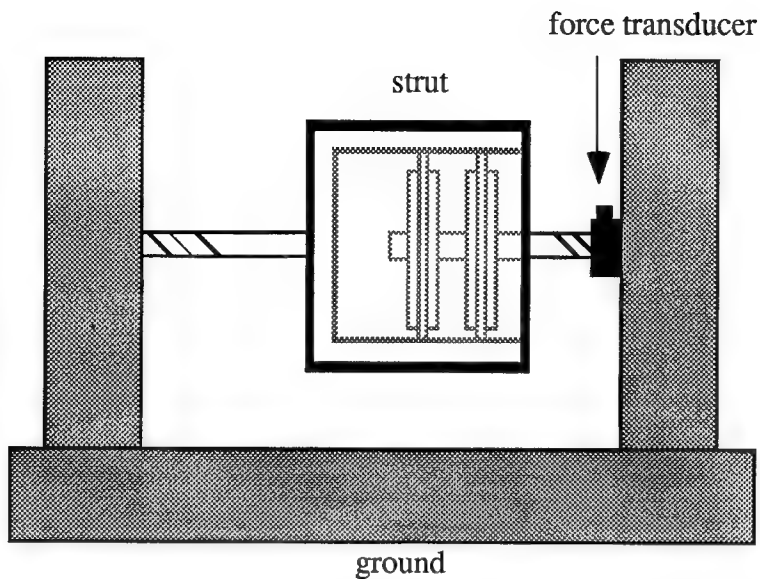


Figure 3. Experimental configuration

The result of forcing the strut at 5 Hertz between 2 rigid masses is shown in Figure 4. Figure 4 displays the force applied to the transducer versus the voltage applied to the bender elements of the prototype strut. Hysteresis appears due to the energy that is stored as elastic strain energy. The hysteresis is primarily due to the piezoceramics natural hysteresis and the bonding layer between the piezoceramic and the thin plate of the bender element. The maximum hysteresis value is 13.5%. This value falls near the expected range for G-1195 piezoceramic of .1% to 10%.¹ This indicates that the bender element configuration is an efficient means of force conveyance. The linearity of the strut can also be inferred from Figure 4.²

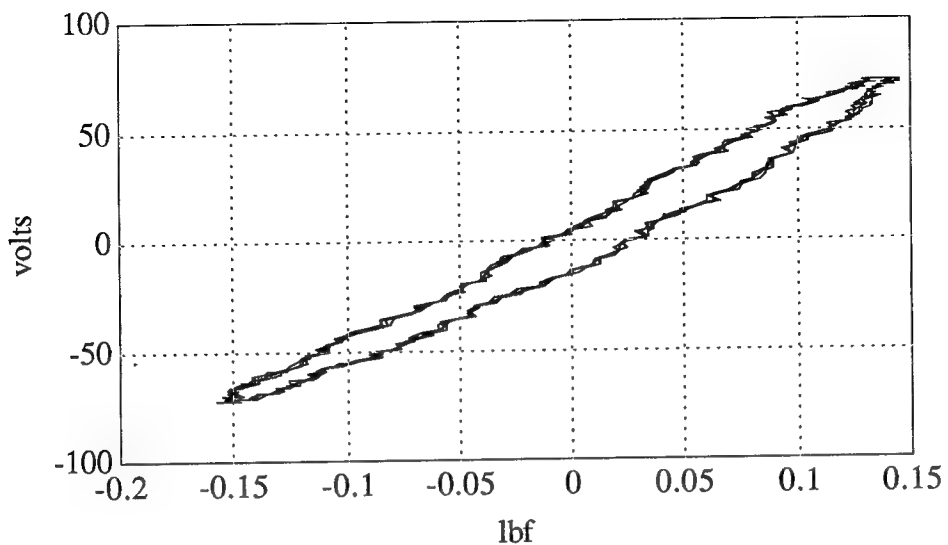


Figure 4. Force output and voltage input

A bode plot was constructed using a transfer function between the input voltage and the force output of the strut (Figure 5). The frequency of interest for the strut is approximately 0 to 100 Hertz; within this range the dynamic response of the strut is flat. The evolutionary model's first 85 modes are below 50 Hertz.³

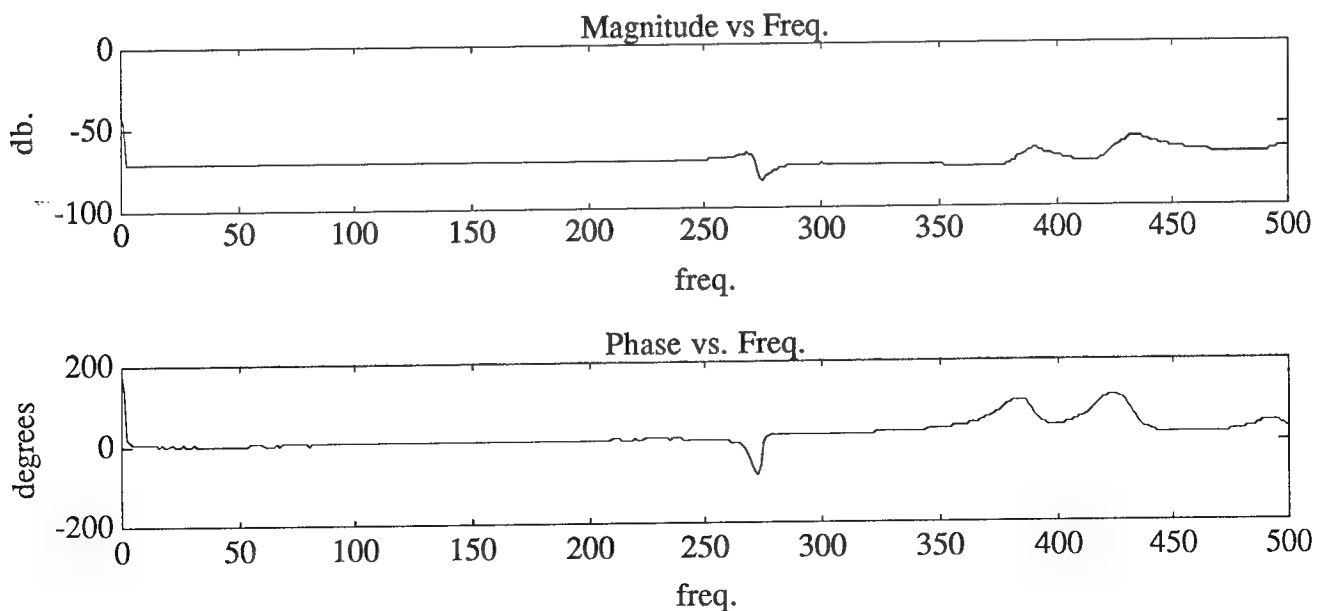


Figure 5. Dynamic response

In the second experiment a signal proportional to the regulated and measured force acting on the strut was input to the prototype strut. A 10 percent change in the stiffness was consistently recorded for forcing frequencies from 1 to 50 Hertz using the feedback scheme. The maximum displacement for this experiment was .0034". The results of a 5 Hertz signal is displayed in table II.

Table II. Experimental feedback results

Max total force (lbf)	Short circuit stiffness (lbf/in)	Feedback stiffness (lbf/in)
.55	6182	7011.18

FUTURE STRUT PARAMETERS

Using the strut in the evolutionary model would require a stiffness of approximately 100,000 lbf/in. By using this value, parameters can be established for a larger bender element strut. The results of this are listed in table III. The strut applies significantly less force than a more common piezoceramic stack type strut.⁴ The reduced force ability may be offset by the greater stroke length of the bender element strut in some applications. It should be noted that the prototype geometrical dimensions are not optimal. Restraint on material availability prevented the construction of the optimal strut. Improvements in performance and efficiency may be achieved in a full scale strut.

Table III. Extrapolated strut results

Number bender elements	Stiffness (lbf/in)	Max. total force (lbf)
32	98912	17.6

SUMMARY

The static and dynamic characteristics of a new active replacement strut have been examined. The new strut type uses the bender elements in a series configuration to affect vibration suppression. This strut can be modelled using finite element methods. This strut has acceptable levels of hysteresis and linear characteristics. The dynamic response of the strut is flat for low frequencies, which is the range of operation and offers a viable alternative to the piezo stack struts commercially available.

REFERENCES

1. Advanced Technology Group: Piezoelectric Motor/Actuator Kit Manual. Piezo Electric Products, Inc. Cambridge, MA, 1990.
2. Nashif, A.; Jones, J.; and Henderson, J.: *Vibration Damping*. John Wiley and Sons, Inc. 1985.
3. Belvin, W. K.; Kenny E. B.; Lucas, H.G; Bailey, J.; Bruner A.; Sulla, J. Won, J.; Ugoletti, R.: NASA Technical Memorandum 104165, NASA Langley, Hampton, VA 1992.
4. Anderson, E.; Moore, D.; Fanson, J.; and Ealey, M.: Development of an Active Member Using Piezoelectric and Electrostrictive Actuation for Control of Precision Structures, AIAA 90-1085, 1990.

System Identification and Structural Control on the JPL Phase B Testbed

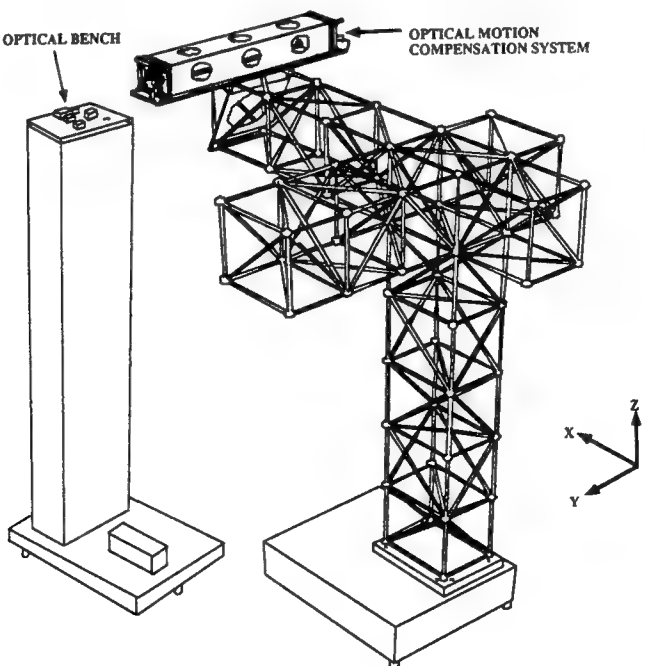
Jet Propulsion Laboratory
California Institute of Technology
Pasadena, CA

Cheng-Chih Chu
John F. O'Brien
Boris J. Lurie

Introduction

The primary objective of NASA's CSI program at JPL is to develop and demonstrate the CSI technology required to achieve high precision structural stability on large complex optical class spacecraft. The focus mission for this work is an orbiting interferometer telescope [1]. Toward the realization of such a mission, a series of evolutionary testbed structures are being constructed. The JPL's CSI Phase B testbed is the second structure constructed in this series which is designed to study the pathlength control problem of the optical train of a stellar interferometer telescope mounted on a large flexible structure. A detailed description of this testbed can be found in [2].

This paper describes our efforts in the first phase of active structural control experiments of Phase B testbed using the active control approach where a single piezoelectric active member is used as an actuation device and the measurements include both colocated and noncolocated sensors. Our goal for this experiment is to demonstrate the feasibility of active structural control using both colocated and noncolocated measurements by means of successive control design and loop closing. More specifically, the colocated control loop was designed and closed first to provide good damping improvement over the frequency range of interest. The noncolocated controller was then designed with respect to a partially controlled structure to further improve the performance. Based on our approach, experimental closed-loop results have demonstrated significant performance improvement with excellent stability margins.



JPL's CSI Phase B Testbed

Motivation

Structural vibration control is necessary to satisfy the stringent pointing and shape requirements for future large precision flexible structures where the vibrations are introduced into the structure by both internal and external disturbances. There are various ways for structural control; for example, by isolation, by a passive damping method, or by active control. In a physical structure, it may be necessary to use a combination of isolators, passive dampers, actuators, and sensors to accomplish the desirable performance requirements. The effectiveness of all these methods will be decided by

1. the number of passive/active devices required or available,
2. the locations of these devices placed, and
3. the “optimal” strategy (control law) of these devices to be utilized.

In this study, only the approach of active control will be considered. The active control method typically involves designing a robust closed-loop feedback control law using a number of colocated and noncolocated sensors/actuators such that the resulting closed-loop system satisfies performance requirements while preserving stability.

Robust structural quieting control is critical to the success of future high precision large flexible structures.

Ways for structural quieting include:

- **Passive Damping** (viscous dampers, viscoelastic dampers, etc.),
- **Active Damping** (sensor/actuator colocation),
- **Active Control** (feedback control with colocated and/or noncolocated sensors and actuators),
- Isolation,
- Combination of the above.

Effectiveness of these methods will depend on:

- location(s) to be applied (placement problem), and
- the optimal strategy to be utilized (control problem).

Optimal Active Member Placement

For this experiment, only the piezoelectric active members will be considered as the actuation device. Since only one active member will be involved, an exhaustive search was conducted for the placement of the active member. This is feasible since there are only 186 candidate locations on the truss structure. Therefore, an \mathcal{H}_2 optimization problem was performed for each of the candidate locations. It is found that the element location # 133 (between grid 111 and 211) is the optimal location.

Note that the weighting function W_p is used to emphasize the frequency range where the performance will be optimized. W_u is the weighting function for the actuator signals which not only penalizes the control energy but also indicates the desired spectral content in actuator signals. This is due to the fact that any physical actuation device can only provide finite control energy, which is usually described in terms of saturation level (magnitude) and finite bandwidth.

The general optimal active member placement problem can be posed as an \mathcal{H}_2 optimization problem:

$$\min_{B_a \in \mathcal{B}_A} \min_{K \in \mathcal{K}} \|\mathcal{F}_l(P(s; B_a), K)\|_2$$

where

$$P(s; B_a) = \left[\begin{array}{c|c} P_{11} & P_{12} \\ \hline P_{21} & P_{22} \end{array} \right] = \left[\begin{array}{cc|c} W_p G_{pd} W_d & 0 & W_p G_{pu}(s; B_a) \\ 0 & 0 & W_u \\ \hline G_{md} W_d & W_n & G_{mu}(s; B_a) \end{array} \right]$$

$$\mathcal{F}_l(P(s; B_a), K) = P_{11} + P_{12}K(I - P_{22}K)^{-1}P_{21}$$

W_p (W_u): weighting function for performance (actuator signals),

W_d (W_n): coloring filter for disturbances (sensor noises),

G_{pd} (G_{md}): transfer matrix from disturbances to performance (measurements),

G_{pu} (G_{mu}): transfer matrix from actuators to performance (measurements),

$\mathcal{K} \triangleq \{ K : \text{any stabilizing feedback controller} \}$

$\mathcal{B}_A \triangleq \{(b_{i_1}, b_{i_2}, \dots, b_{i_{n_a}}) : i_1, i_2, \dots, i_{n_a} \in \mathcal{N}_A, i_j \neq i_k, \forall j, k = 1, 2, \dots, n_a (j \neq k)\}$

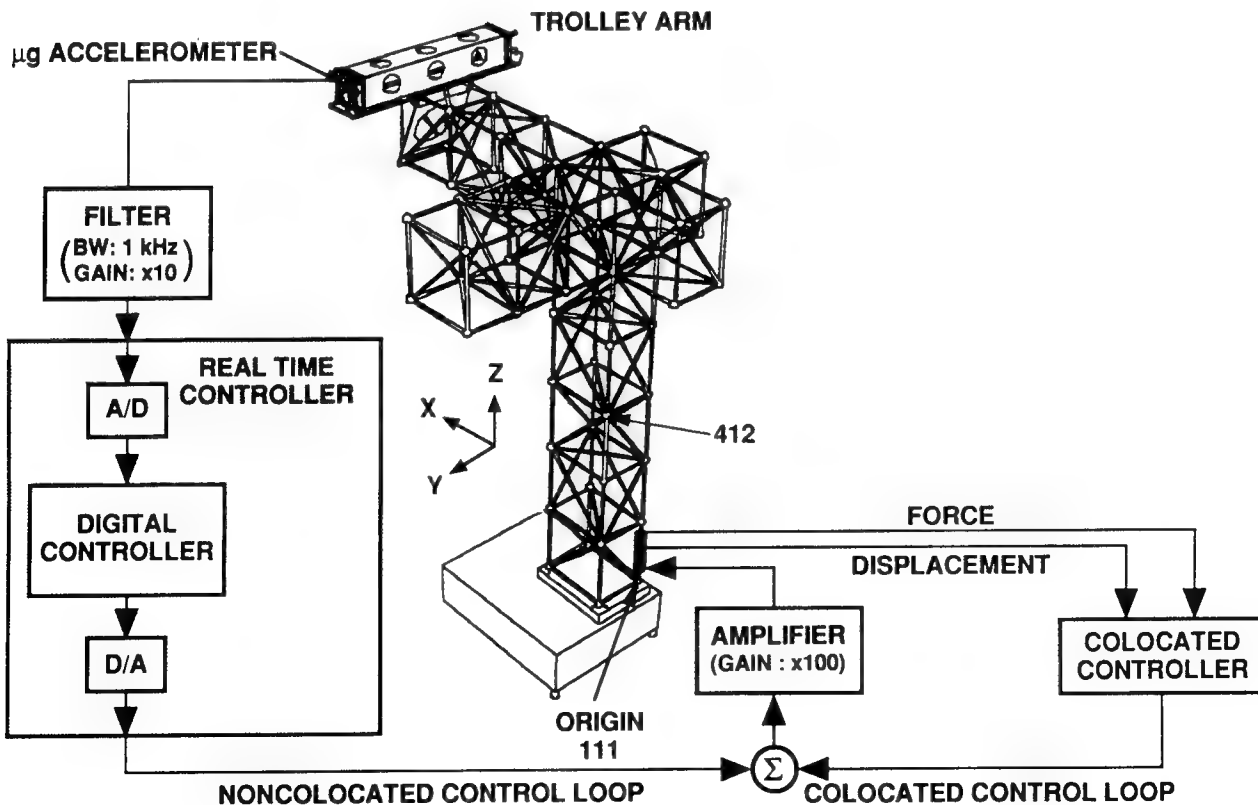
$\mathcal{N}_A \triangleq \{1, 2, \dots, N_a\}$ (N_a is the total number of candidate locations).

Colocated and Noncolocated Structural Control Loops

The single active member placement study resulted in one active member placed at location 133 (between grid 111 and 211) to serve as the actuation device. There are two colocated measurements on the active member (internal displacement and force measurement) which are available for the design of colocated control. To simplify the design while preserving the interest of optical compensation control, the noncolocated measurement is chosen to be the μg accelerometers. A μg accelerometer mounted at the tip of trolley in the Y direction was used to derive the model to facilitate the noncolocated feedback control system design. In addition, a suspended proof-mass shaker is used as an external disturbance input. The shaker injects an excitation force into grid point 412 via a stinger along the diagonal direction on the X-Y plane.

Our specific approach for the successive loop closing is to design the colocated control first. The noncolocated controller is then designed with respect to a partially controlled structure to further improve performance. Note that our colocated controller is implemented using the analog circuits. However, the noncolocated controller will be implemented digitally in a HUGH 9000 real-time controller [3].

It is our objective to demonstrate that using this approach, significant performance improvement can be achieved while providing excellent stability margins. Specifically for this experiment, the noncolocated measurement will also be used as the performance variable and the level of disturbance rejection from 3 to 13 Hertz will be used as the performance measure.



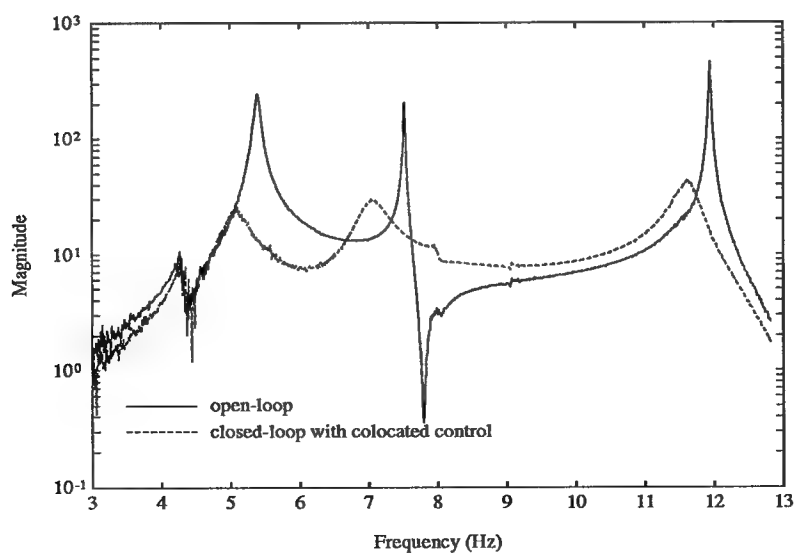
Colocated Control Design Using Impedance Matching

The impedance, defined as the ratio of velocity over force, of an active member is essentially reactive (like a spring). To introduce damping into a host structure in which the active member is embedded, two criteria must be met. First, the phase angle of the active member's impedance should be decreased from 90° (spring) to approximately 0° (viscous damper). Secondly, the magnitude of the active member's impedance should be increased (softening the strut) as to approximately match that of the rest of the host structure [4]. However, the static stiffness of the active member should be preserved so that it may still function as a stiff supporting strut.

For this experiment, only the colocated force measurement was used in designing the colocated controller. It is known that introducing constant colocated force feedback around an active member reduces its effective stiffness [5]. It does not, however, affect the phase angle of the active member's impedance. To reduce the phase angle, a Foster-form filter with a -4 db/octave roll-off was introduced in the force feedback loop which results in a phase lag of 60° . This phase lag dropped the phase angle of the active member's impedance. As a result, the two criteria for impedance matching are both met. Note that the force sensor used in this experiment is a piezo-type load cell which can measure dynamic loads only. Thus, the force feedback did not diminish the high static stiffness of the active member.

Experimental results show that approximately a factor of 10 in performance improvement (disturbance rejection) was achieved, and significant damping was introduced in the first 3 structural modes.

**Comparison of Open-Loop and Closed-Loop Frequency Response
(from disturbance shaker load cell to μg accelerometer at 752Y)**



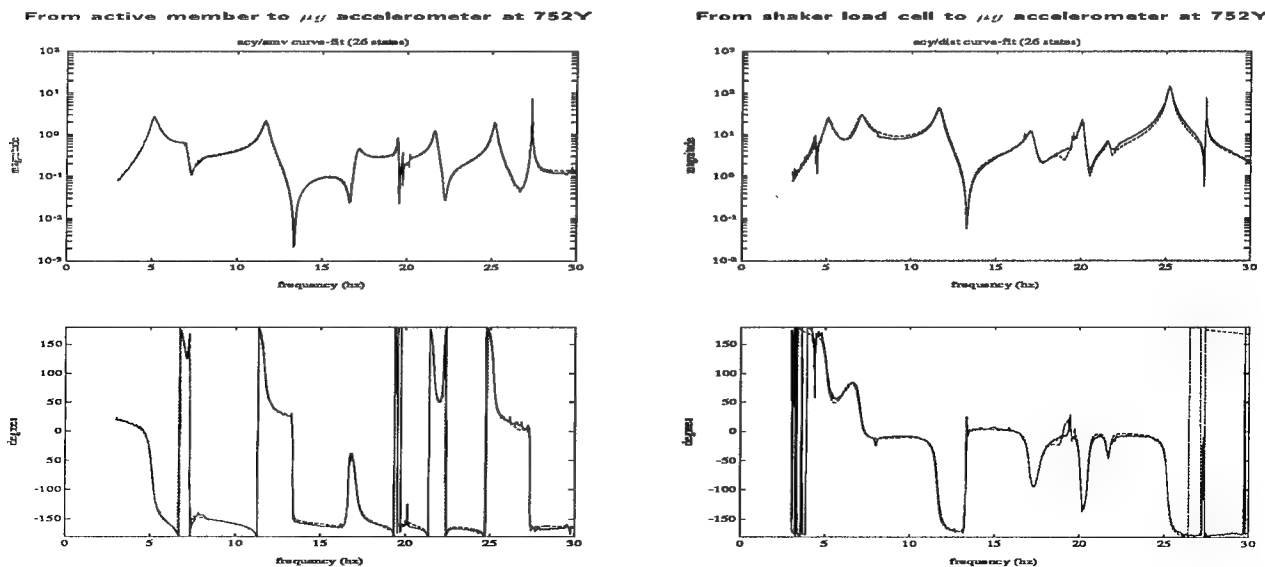
System Identification

With the colocated force feedback loop closed, system identification experiments were conducted where the high resolution, input-output frequency response data corresponding to the 2 inputs (active member voltage input and disturbance shaker load cell) and 1 output (μg accelerometer at grid 752Y) were measured.

To identify a linear state-space model corresponding to the measured data, two key steps are involved in our approach. The technique of Chebyshev polynomial curve fitting [6] is used first to derive a stable state-space model which qualitatively fits well to the measured frequency response data. This model is then refined using a linear least-squares curve fitting technique [7] to update the state-space matrices iteratively. As a result, a 2-input, 1-output, 26-state state-space model was identified for the measured data below 30 Hertz. This model includes 12 complex modes (see table below) and 2 real poles (14.3225 & 71.9783 radian/second). Comparison between the measured data (solid line) and frequency responses of the identified model (dashed line) shows an excellent match in both magnitude and phase. This model will serve as the nominal model in designing the noncolocated control system using the \mathcal{H}_∞ synthesis technique.

Identified Modal Frequency and Damping

Mode No.	Frequency (Hz)	Damping (%)	Mode No.	Frequency (Hz)	Damping (%)
1	4.3490	0.4311	7	19.4532	0.1429
2	5.0974	3.7001	8	20.0208	0.4657
3	7.0189	3.8321	9	21.6467	0.5338
4	11.6512	1.4961	10	25.1737	0.4463
5	17.0516	1.1378	11	27.3367	0.0355
6	19.0184	1.8772	12	27.3569	0.0271

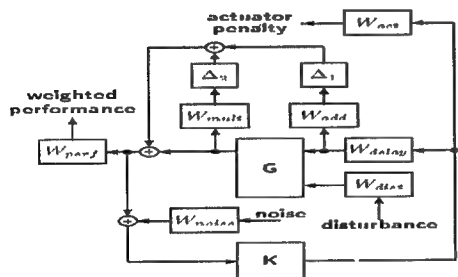


Robust Control System Design – \mathcal{H}_∞ Synthesis

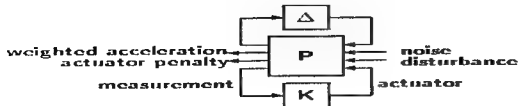
The noncolocated controller has been designed using the \mathcal{H}_∞ -synthesis approach [8,9]. Two types of uncertainty are used, multiplicative and additive. W_{mult} and W_{add} are frequency dependent uncertainty weights. The larger additive weighting, W_{add} , at frequencies greater than 15 Hz reflects the fact that the system is more uncertain at higher frequencies. A constant W_{mult} is used to capture the effects of mode shape errors [10]. W_{delay} is a Pade approximation of one sample delay — in this case $\frac{1}{1000}$ seconds. W_{perf} weights the acceleration output which has larger magnitude from 3 to 13 Hertz to emphasize the frequency range of primary control interest. W_{act} is used to penalize the active member voltage input signal at both higher and lower frequencies to avoid the amplification of high frequency noise and to prevent the controller from responding to accelerometer drift which may cause the saturation problem. W_{noise} reflected the sensor noise problem which also penalizes the lower frequencies more to account for the the same accelerometer drift problem. The disturbance weight, W_{dist} , rolls off sharply after 15 Hz as the disturbance is expected to be band limited to this range.

The associated control design problem can easily be rearranged to form the standard \mathcal{H}_∞ synthesis block diagram as shown below. All of the weighting functions, and the nominal model G derived from system identification, have been absorbed into the interconnection structure P . The \mathcal{H}_∞ synthesis problem now becomes to find K such that the closed-loop transfer function from the inputs (shaker disturbance & sensor noise) to the outputs (acceleration & actuator) is internally stable and has a minimum \mathcal{H}_∞ norm for all possible Δ , $\|\Delta\| \leq 1$.

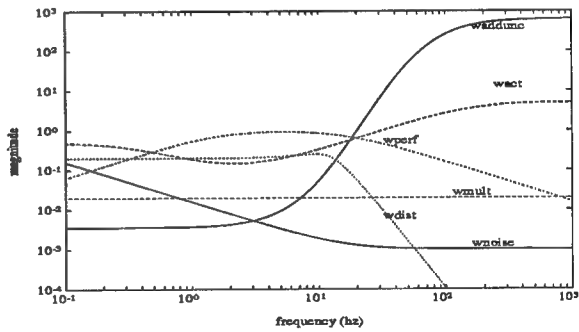
Block Diagram for Control System Design



Generic Interconnection Structure for Robust Control System Design



Weighting Functions



\mathcal{H}_∞ Synthesis

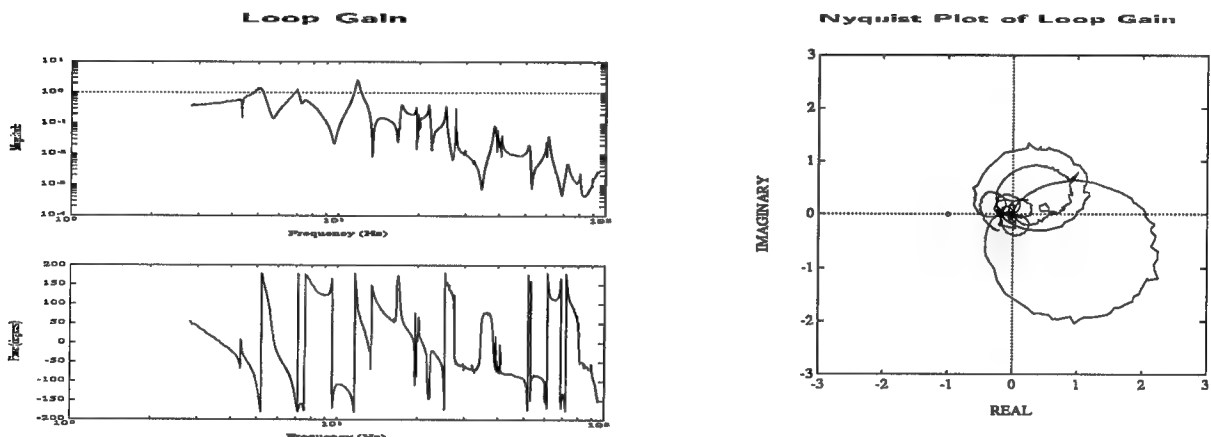
$$\text{Min}_{K \in \mathcal{H}_\infty} \|T_{yu}(K, \Delta)\|_\infty$$

Subject to $\|\Delta\| \leq 1$

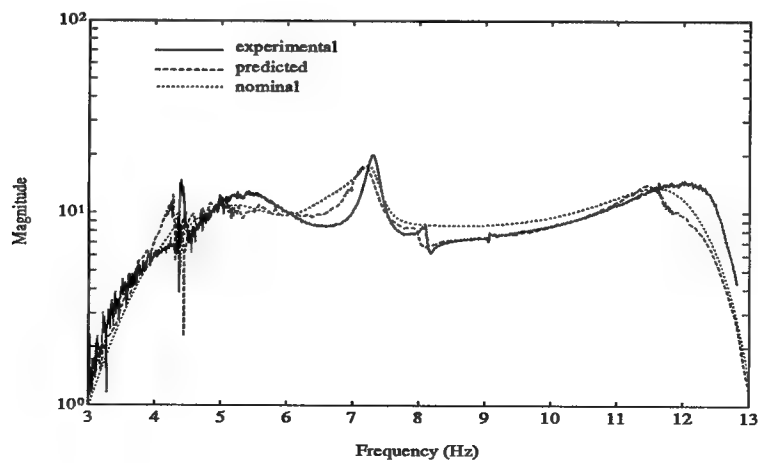
\mathcal{H}_∞ Design – Results

A stabilizing controller using the noncolocated measurement was obtained using the \mathcal{H}_∞ synthesis methodology. The bode plots of the loop gain show that the higher frequencies (> 15 Hertz) are gain-stabilized and the lower frequencies (< 15 Hertz) are phase-stabilized. A further examination of the corresponding Nyquist plot indicates that approximately 6.5 db of gain margin and 72° of phase margin were achieved by the closed-loop system. Therefore, this closed-loop system with both colocated and noncolocated control is robustly stable.

A comparison of the actual, predicted, and nominal disturbance rejection frequency response is also plotted which shows the predicted and the nominal performance are reasonably close to the experimental performance. This observation reassures us that the system identification and the digital implementation in our design process were carried out properly.



Experimental, Predicted, and Nominal Performance

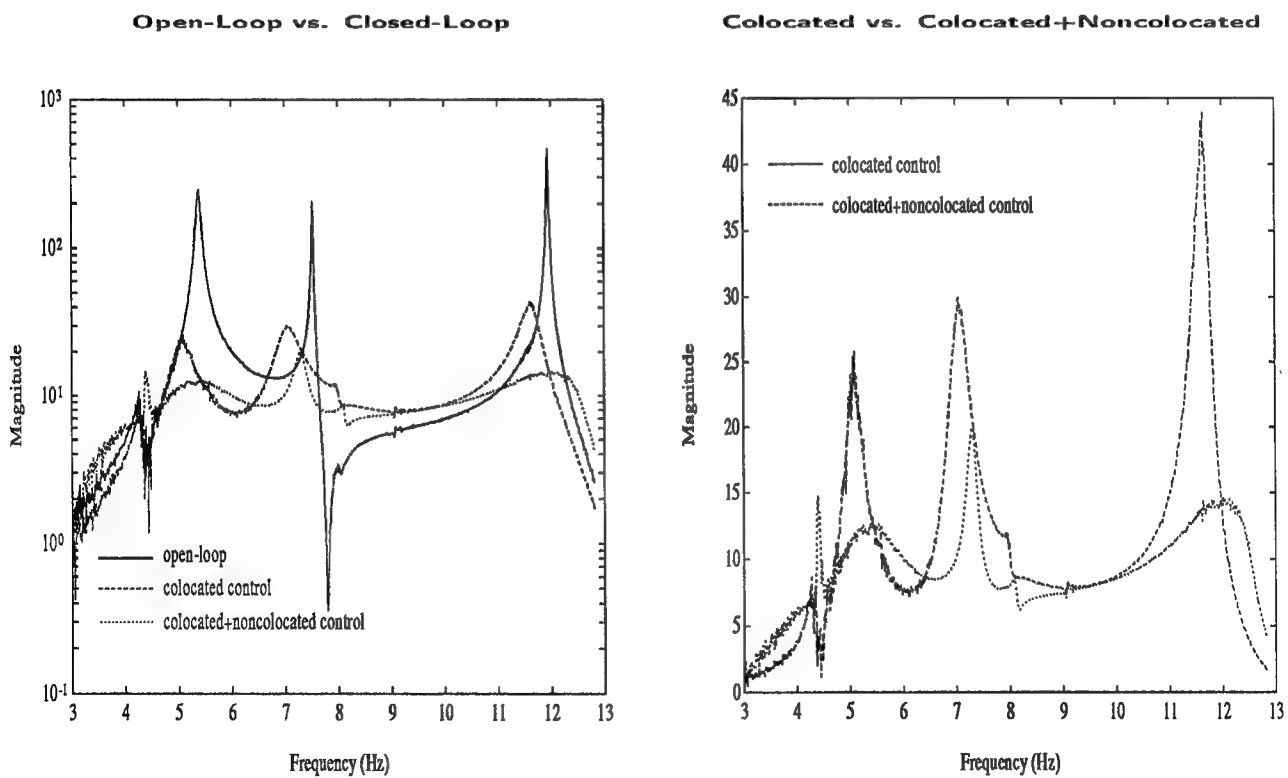


Performance (Disturbance Rejection) Comparison

The effect of feedback control on performance is shown below. Frequency responses from disturbance shaker load cell to μg accelerometer at 752Y are plotted for

1. the open-loop,
2. closed-loop with colocated control only, and
3. closed-loop with both colocated and noncolocated control.

Experimental results show that on the average, the colocated control alone achieves a factor of 10 improvement in performance (disturbance rejection) over the uncontrolled structure (open-loop). However, by means of closing the colocated and noncolocated control loop successively, a factor of 20 improvement has been achieved.



Conclusions and Future Work

In this study, the feasibility of the successive colocated and noncolocated control design and loop closing has been successfully demonstrated. It is shown that more than an order of magnitude performance improvement can be achieved easily with only one properly placed active member. It is our immediate plan to extend the noncolocated control bandwidth to the higher frequency region. This certainly will pose a much greater challenge to system identification and control design since more structural dynamics will be involved.

A parallel study is currently underway on the simultaneous design and closing of both colocated and noncolocated feedback control loops. It will be very interesting to compare the stability and performance aspect of these two (successive and simultaneous) approaches.

Our study of the passive damper placement and tuning problem [11] has shown that the dampers can be used very effectively to damp out modes in the frequency region which might be troublesome for the active control design. It is our goal that all these studies will eventually lead to a feasible solution to the multilayer structural control problem where multiple active and passive devices will be involved.

Acknowledgments

The research described in this paper was carried out by the Jet Propulsion Laboratory, California Institute of Technology, under contract with the National Aeronautics and Space Administration.

References

1. Laskin, R.A., and San Martin, M., "Control/Structure System Design of a Spaceborne Optical Interferometer," Proceedings of the AAS/AIAA Astrodynamics Specialist Conference, Stowe VT, 1989.
2. O'Neal, M., Eldred, D., Liu, D., and Redding, D., "Experimental Verification of Nanometer Level Optical Pathlength Control on a Flexible Structure," 14th Annual AAS Guidance and Control Conference, Keystone, CO, February, 1991.
3. Fanson, J.L., Briggs, H.C., Chu, C.C., Lurie, B.J., Smith, R.S., Eldred, D.B., and Liu, D. "JPL CSI Phase-0 Experiment Results and Real Time Control Computer," 4th NASA/DoD Control/Structures Interaction Technology Conference, Orlando, FL, Nov. 5-7, 1990.
4. Lurie, B.J., Sirlin, S.W., O'Brien, J.F., and Fanson, J.L., "The Dial-a-Strut Controller for Structural Damping," ADPA/AIAA/ASME/SPIE Conference on Active Materials and Adaptive Structures, Alexandria, VA, November 5-8, 1991.
5. Fanson, J.L., Lurie, B.J., O'Brien, J.F., Chu, C.C., and Smith, R.S., "System Identification and Control of the JPL Active Structure," 32nd AIAA/ASME/ASCE/AHS Structures, Structural Dynamics, and Material Conference, Baltimore, MD, April 8-10, 1991.
6. Dailey, R.L. and Lukich, M.S., "MIMO Transfer Function Curve Fitting Using Chebyshev Polynomials," SIAM 35th Anniv. Meeting, Denver, CO, 1987.
7. Smith, R.S., *Procedures for the Identification of Precision Truss*, JPL D-7791, 1990.
8. Doyle, J.C. and Chu, C.C., *Robust Control of Multivariable and Large Scale Systems*, Final Technical Report for AFOSR, Contract No. F49620-84-C-0088, March, 1986.
9. Doyle, J.C., Glover, K., Kharagonekar, P., and Francis, B.A., "State-Space Solutions to Standard \mathcal{H}_2 and \mathcal{H}_∞ Control Problems," IEEE Transactions on Automatic Control, Vol. 34, No. 8, 1989.
10. Balas, G.J., *Robust Control of Flexible Structures Theory and Experiments*, Ph.D. Thesis, California Institute of Technology, 1989.
11. Chu, C.C., Milman, M.H., and Kissil, A., "Optimal Passive Damper Placement and Tuning Using Ritz Model Reduction Method," ADPA/AIAA/ASME/SPIE Conference on Active Materials and Adaptive Structures, Alexandria, VA, November 5-8, 1991.

**THE DEVELOPMENT AND TESTING OF THE
LENS ANTENNA DEPLOYMENT DEMONSTRATION (LADD)
TEST ARTICLE**

Mark L. Pugh and Robert J. Denton Jr.
Rome Laboratory/OCDS
Griffiss AFB, NY 13441-5700

Timothy J. Strange
OL-AC Phillips Laboratory/VTSS
Edwards AFB, CA 93523-5000

ABSTRACT

The USAF Rome Laboratory and NASA Marshall Space Flight Center, through contract to Grumman Corporation, have developed a space-qualifiable test article for the Strategic Defense Initiative Organization to demonstrate the critical structural and mechanical elements of single-axis roll-out membrane deployment for Space Based Radar (SBR) application. The Lens Antenna Deployment Demonstration (LADD) test article, originally designed as a shuttle-attached flight experiment, is a large precision space structure which is representative of operational designs for space-fed lens antennas. Although the flight experiment was cancelled due to funding constraints and major revisions in the Strategic Defense System (SDS) architecture, development of this test article was completed in June 1989. To take full advantage of the existence of this unique structure, a series of ground tests are proposed which include static, dynamic, and thermal measurements in a simulated space environment. An equally important objective of these tests is the verification of the analytical tools used to design and develop large precision space structures.

INTRODUCTION

The development of affordable multi-mission Space-Based Radar (SBR) concepts is strongly dependent upon large space-deployable antenna technologies. For this application two types of antenna concepts are being considered, the corporate-fed array and the space-fed array. Due to satellite prime power limitations and the significant ranges that are involved, large antennas are needed to provide detection and tracking of small targets in the presence of clutter and jamming. These large antennas, however, must satisfy strict mass and stowed-volume constraints imposed by the launch vehicle. The vacuum of space and the zero gravity environment in which these systems will operate enables the deployment of very large, low-mass antennas. The ability of these large low-mass space structures to properly deploy and maintain antenna shape on-orbit is critical to radar performance. Even small deformations in the shape of the antenna can cause path length errors which can result in the loss of antenna gain, increased sidelobe levels, and beam pointing error.

According to J. Ruze ¹, distortion by an amount Δ in the surface of a corporate-fed array scanned to an angle θ creates a path length error ϵ defined by the equation

$$\epsilon = \Delta \cos \theta$$

In contrast, a similar distortion in the surface of a space-fed array creates a path length error

$$\epsilon = \Delta \left[\cos \theta - \frac{1}{\sqrt{1 + \left(\frac{r}{2f} \right)^2}} \right]$$

where f is the focal-length-to-diameter ratio (F/D); and r is the radial coordinate from the center of the aperture normalized to unity at the rim. It can be seen in this equation that the second term reduces the path length error. This error compensation significantly decreases the effect of out-of-plane distortions on radar performance for space-fed arrays. The result is that for small scan angles the space-fed array is about one order of magnitude less sensitive to out-of-plane distortion than the corporate-fed array. This result is significant for large antennas, especially considering that performance specifications for typical corporate-fed planar arrays require that flatness be maintained to within 1/10 wavelength (30 mm at L-band, 3 mm at X-band) across the entire array. Figure 1 provides a graphical interpretation of these equations with varying scan angle.

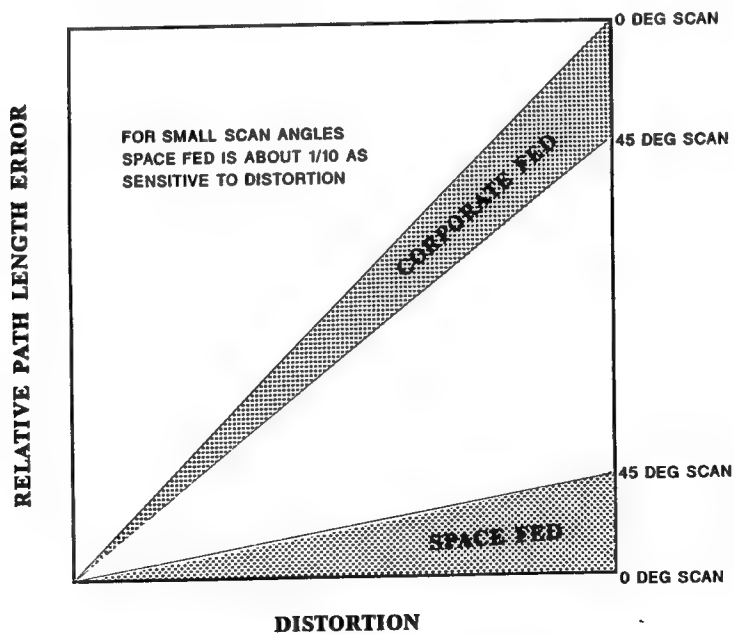


Figure 1. Path length error sensitivity to aperture distortion

The tolerance of the space-fed array to out-of-plane distortion may allow the design of SBR concepts that do not require electrical or mechanical compensation for path length errors to meet performance specifications. Reduced sensitivity to out-of-plane distortion also suggests that less rigid and correspondingly less massive support structures can be utilized. Additionally, the elimination of a constrained feed structure enables concepts to be developed which require fewer connections, allow for simpler deployment schemes, and are more manufacturable.

Figure 2 illustrates a space-fed phased array lens SBR concept deployed on-orbit. The concept depicted employs a single-axis roll-out, or "window shade", deployment scheme developed by Grumman Space Systems Division, Bethpage, NY. Primary components of the system are the RF feed at the end of a continuous-longeron deployable mast and the aperture which is deployed in a plane from the storage drum. Pretension forces in the long direction provide out-of-plane stiffness to the membrane as it is suspended within its space frame. The lightweight membrane supports transceiver modules that are powered by regulated dc through a power distribution system which is an integral part of the membrane structure. Antenna elements are attached to these modules. They receive both beam steering commands and radar signals from the remote feed. The module introduces the necessary phase shifting to steer the beam to the commanded direction and amplifies the radar signal. These in turn are passed to the target side antenna elements for radiation toward the target. The reflected signal is transmitted to the feed in an analogous manner.

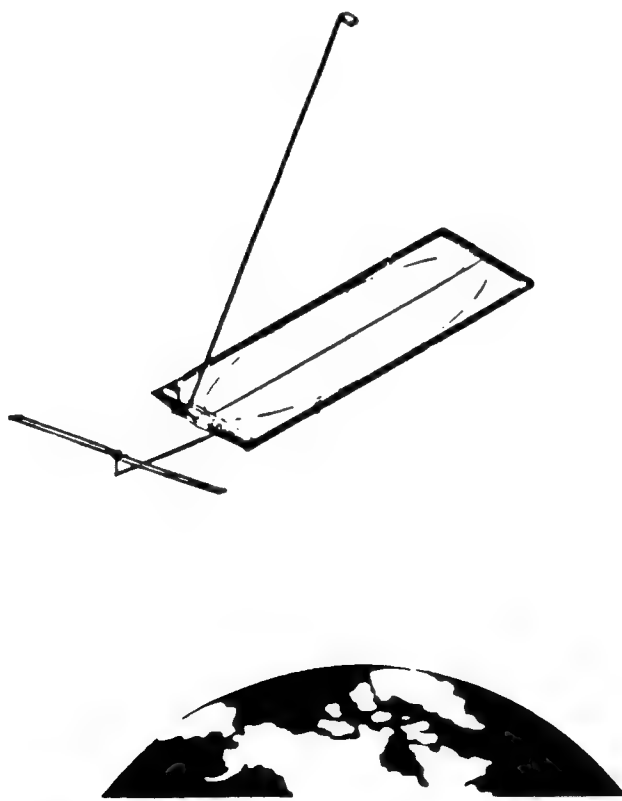


Figure 2. Space-fed phased array lens SBR concept

BACKGROUND

The potential benefits of space-fed arrays for SBR application prompted DOD development and testing of phased array membrane segments to validate concepts and support configuration development. Membrane test articles have been developed and tested in a fixed deployed condition for structural and RF evaluations. Since structures/mechanism validation of membrane deployment and retraction is critical to future system designs, recent efforts have focused on design and analysis of a deployment test article for ground and flight test demonstrations.

In Oct 1985 Rome Laboratory and NASA Marshall Space Flight Center, through contract to Grumman Corporation, initiated the design and fabrication of the LADD test article to perform structural/mechanical tests on-orbit as a shuttle-attached experiment for the Strategic Defense Initiative Organization (SDIO). Planned tests included functional, static flatness, dynamic, and thermodynamic measurements. Following the successful completion of these tests, an active X-band array could be installed in the article for a second flight to demonstrate imaging/discrimination for SDIO mission needs. Although major revisions to the Strategic Defense System (SDS) architecture eliminated space-based radar from the near-term system and therein caused the LADD experiment's shuttle manifest to be canceled, the test article was completed in Jun 89, essentially with a full flight pedigree.

The objective of this effort was to produce a space-fed lens antenna test article that could be used for ground, and shuttle testing in a subsequent phase, in order to demonstrate the structural feasibility and reliability of the single-axis roll-out deployable SBR approach. Now that the construction of the LADD test article is completed, analytical tools for predicting behavior can be verified and an initial indication of structural damping can be determined. Thus, it is now possible to obtain information on various aspects of the mechanical distortion of the membrane. From this measured data the RF performance of the single-axis roll-out deployable SBR can be predicted.

LADD DESCRIPTION

The LADD test article, shown in its stowed configuration in Figure 3 and its deployed configuration in Figure 4, consists of a 2.44 m x 6.10 m (8 ft x 20 ft) X-band phased array membrane, populated with approximately 5000 thermal representations of transceiver modules, that is automatically deployed utilizing a lightweight frame. This configuration is similar to that envisioned for large space-fed phased array SBR concepts which employ the single-axis roll-out aperture deployment technique. The frame is comprised of an end beam, two continuous-longeron canister-deployed side masts, and a storage drum which is supported on trunnions extending from the drum support beam that would also serve as the main spacecraft of a free-flying satellite. In this particular X-band antenna, the transceiver module is a four element subarrayed design: thus an active radar of this size would have about 20,000 radiating patch elements.

The membrane is fabricated as four .61 m (2 ft) wide panels that extend from the storage drum to the end beam. The two central panels are connected during deployment by an automatic seaming device that would be required in a large satellite which is folded to fit within the shroud of a launch vehicle. The outer strips are connected to the adjacent membrane through permanent, but very compliant interpanel splices. These connections provide RF isolation from one side of the membrane to the other.

It should be noted that as a shuttle-attached payload, the LADD test article was designed with considerably high margins of safety than would be required in a free-flying satellite. Therefore, as a structural frame the LADD test article is somewhat stiffer than a typical satellite.

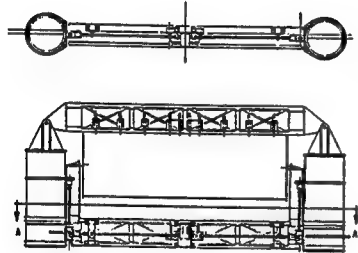


Figure 3. Stowed LADD test article

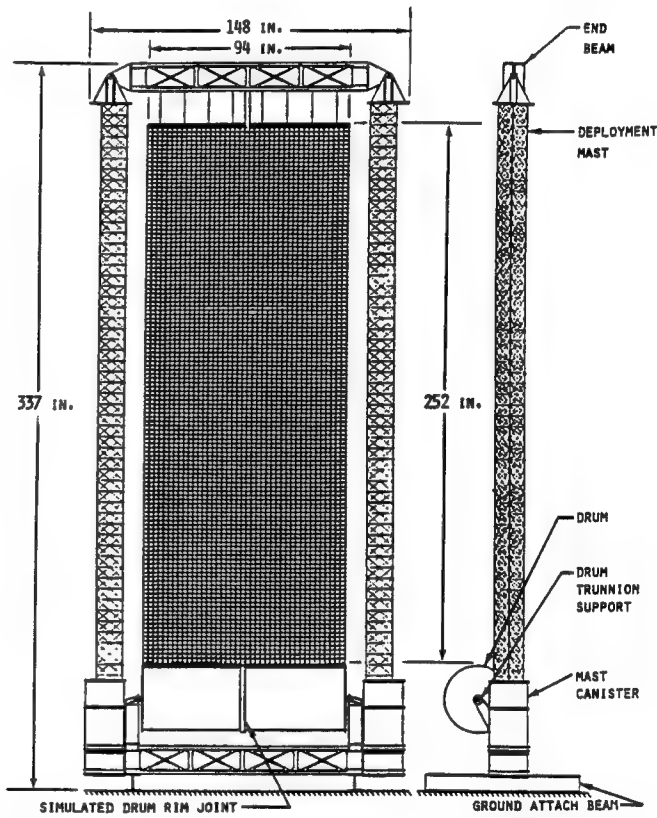


Figure 4. Deployed LADD test article

TEST PROGRAM

The LADD test article belongs to a class commonly referred to as large precision space structures. These structures typically have low spatial density, modes of vibration well under 1 Hz, many closely spaced modes, and interaction between the structure's dynamic behavior and the performance of the operational system. Since the LADD test article was originally designed as a shuttle-attached space experiment and is representative of operational designs for SBR, it provides a unique test opportunity to address issues of concern relating to

this class of structure. Specific areas of interest include testing of large flexible space structures in a gravity environment, modeling and analysis of low-mass pretensioned membranes, and system identification. To address these issues, a series of ground tests are proposed which includes static, dynamic, and thermal measurements in a simulated space environment.

Static tests will include multiple deployments of the LADD test article with corresponding membrane flatness and tension measurements taken after each deployment. These tests will establish the repeatability of the membrane static shape. To date, the LADD test article has been cycled through more than 100 deployments and retractions.

Thermal tests will include differential heating and deployment/retraction at temperature extremes. Membrane flatness, membrane tension, and membrane structure temperature measurements will be taken in each test case. The differential heating tests will establish the ability of the LADD test article to maintain required membrane flatness in and out of periods of solar illumination and eclipse while on-orbit. The thermal tests at the expected temperature extremes will establish the performance of the deployment mechanisms as a whole at those operating points.

Dynamic testing will be performed to determine the structural modal properties. Test results will be used to validate the analytical model, which will in turn be used to perform transient response analyses to predict the behavior of the structure in the presence of on-orbit disturbances.

All tests will be performed in a vacuum chamber with radiative heating and cooling capability. A non-contact displacement measurement system will be used to quantify the flatness of the LADD test article membrane during static tests. Photogrammetry techniques are being considered for this purpose. Both photogrammetry and multiplexed laser vibrometer system techniques are being considered for measuring vibration at numerous points on the membrane during modal tests. Conventional accelerometers will be used to measure vibration at points on the structure other than the membrane. The tension in the membrane will be measured using load cells. Thermocouples and calorimeters will be used to measure the temperature and heat flux during thermal tests.

An equally important objective of this test program is the verification of the analytical tools used to design and develop large precision space structures, such as the LADD test article. Testing of the LADD test article provides an opportunity to compare predicted behavior with actual test data to verify those analytical tools. A successful test program coupled with a detailed, comprehensive modeling effort will evaluate the ability of existing analytical methods to predict behavior of new designs.

A modeling effort was carried out by Grumman Space Systems Division under terms of the original LADD contract. This analysis considered the LADD test article attached to the shuttle in a microgravity environment. Although details of that modeling effort are considered proprietary, it can be said that the procedures and tools used are considered standard by the industry. Good correlation was obtained between the finite element

formulation and numerical solution of the characteristic equation derived from thin plate vibration theory for the membrane. The first five natural frequencies predicted by the finite element model are listed in Table 1. Figure 5a illustrates the finite element model and the corresponding mode shapes for the first five natural frequencies are illustrated in Figures 5b-f.

Table 1. Predicted natural frequencies of shuttle-attached LADD test article

Mode	Frequency (Hz)
1	0.205
2	0.270
3	0.307
4	0.312
5	0.325

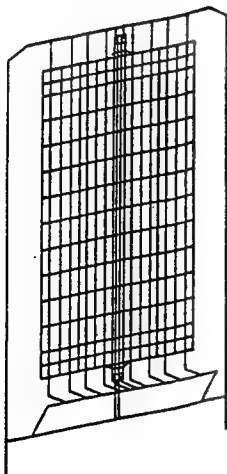


Figure 5a. LADD finite element model
(772 elements)

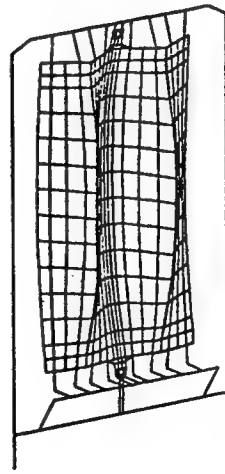


Figure 5b. Mode 1

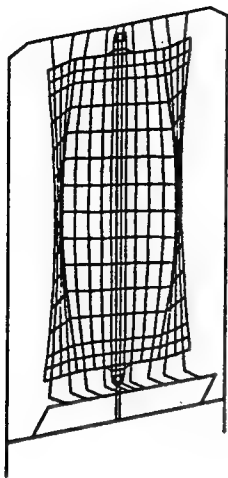


Figure 5c. Mode 2

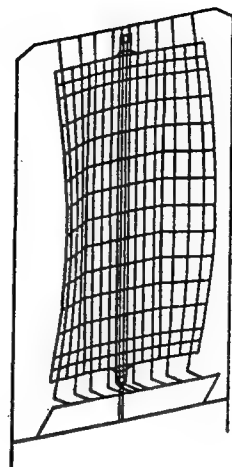


Figure 5d. Mode 3

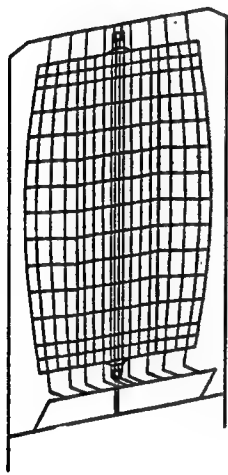


Figure 5e. Mode 4

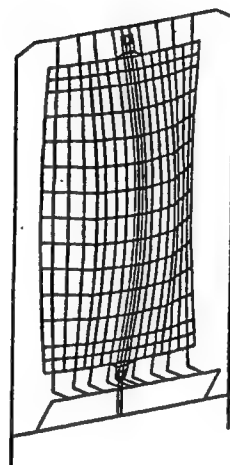


Figure 5f. Mode 5

REFERENCES

1. J. Ruze, "Pattern Degradation of Space Fed Phased Arrays", Lincoln Laboratory, ESD-TR-79-278, Dec 79, DTIC ADA-083264.
2. Grumman Space Systems Division, "Membrane Deployment/Retraction Test Article Design Study", Final Report, Jun 1986, Contract No. NAS 8-36113.
3. Grumman Space Systems Division, "Lens Antenna Deployment Demonstration Critical Design Review", Report No. 31.18, Nov 1987, Contract No. NAS 8-36621.

INTEGRATED DESIGN OF THE CSI EVOLUTIONARY STRUCTURE: A VERIFICATION OF THE DESIGN METHODOLOGY

P. G. Maghami, S. M. Joshi, K. B. Elliot, and J. E. Walz
Spacecraft Controls Branch
NASA Langley Research Center
Hampton, VA 23665

OBJECTIVE

- To develop and validate integrated controls-structures design methodology for a class of flexible spacecraft which require fine pointing and vibration suppression with no payload articulation
 - Integrated design methodologies using various optimization approaches have been developed (CSI-DESIGN CODE)
 - Validation through fabrication and testing of an integrated design structure is warranted

One of the main objectives of the Controls-Structures Interaction (CSI) program is to develop and evaluate integrated controls-structures design methodology for flexible space structures. Thus far, integrated design methodologies for a class of flexible spacecraft, which require fine attitude pointing and vibration suppression with no payload articulation, have been extensively investigated. Various integrated design optimization approaches, such as single-objective optimization, and multi-objective optimization, have been implemented with an array of different objectives and constraints involving performance and cost measures such as total mass, actuator mass, steady-state pointing performance, transient performance, control power, and many more [1–3].* These studies have been performed using an integrated design software tool (CSI-DESIGN CODE) which is under development by the CSI-ADM team at the NASA Langley Research Center. To date, all of these studies, irrespective of the type of integrated optimization posed or objectives and constraints used, have indicated that integrated controls-structures design results in an overall spacecraft design which is considerably superior to designs obtained through a conventional sequential approach [1–3]. Consequently, it is believed that validation of some of these results through fabrication and testing of a structure which is designed through an integrated design approach is warranted. The objective of this paper is to present and discuss the efforts that have been taken thus far for the validation of the integrated design methodology.

* References 1–6 are cited in text.

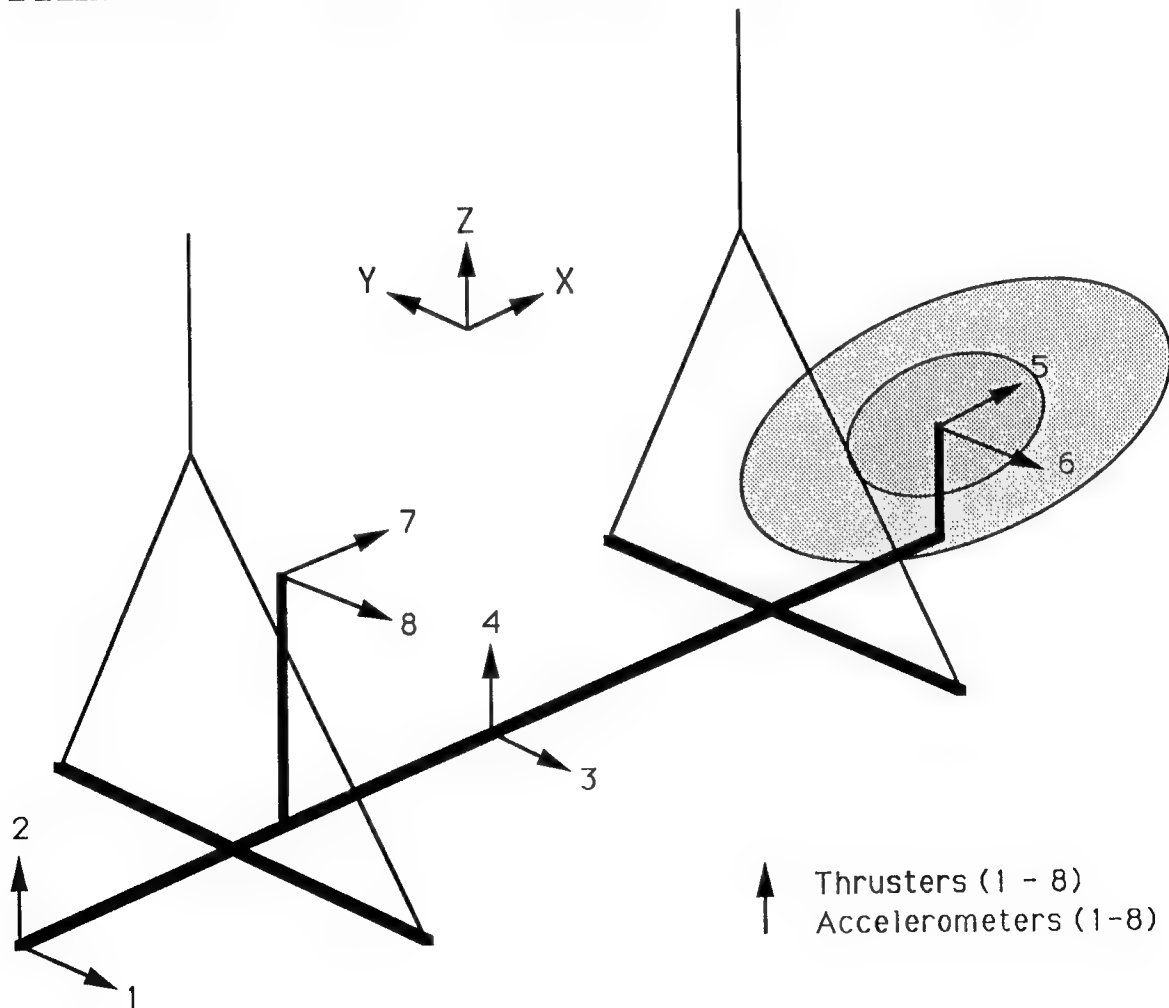
APPROACH

- Pose an integrated design optimization problem for the current CSI Evolutionary Structure (phase-0 structure)
- Design optimal controllers for the phase-0 structure
- Obtain an optimal integrated design structure (phase-1 structure)
- Fabricate the closest structure to the phase-1 design
- Validate the integrated design methodology by comparing phase-0 and phase-1 designs

The approach taken here is to use the CSI Evolutionary Structure for the validation of the integrated controls-structures design methodology. First, an integrated design optimization problem for the current CSI structure, referred to as the Phase-0 structure, is considered. Next, an optimal integrated design structure is obtained (which is optimal with respect to both the structure and control design variables). This structure is referred to as the CSI Phase-1 structure. Since it may not be practical or possible to build a structure to the exact specifications that come out of the integrated design process, the closest buildable structure to the Phase-1 design is fabricated. Meanwhile, optimal controllers for the Phase-0 structure are obtained in order to have a fair comparison with the Phase-1 design. Finally, the integrated controls-structures design methodology is validated through comparison of the overall performance of the Phase-0 and Phase-1 designs.

CSI Evolutionary Model is a laboratory testbed designed and constructed at the NASA Langley Research Center for experimental validation of the control design methods and the integrated design methodology [6]. The Phase-0 Evolutionary Model, shown in the figure, basically consists of a 62-bay central truss, with each bay 10 inches long; two vertical towers; and two horizontal booms. The structure is suspended using two cables as shown. A laser source is mounted at the top of one of the towers, and a reflector with a mirrored surface is mounted on the other tower. The laser beam is reflected by the mirrored surface onto a detector surface 660 inches above the reflector. Eight proportional, bi-directional, gas thrusters provide the input actuation, while collocated servo accelerometers provide output measurements.

THE CSI EVOLUTIONARY STRUCTURE



The basic problems in control systems design for flexible spacecraft arise because i) the order of a practically implementable controller is generally much lower than the number of elastic modes, and ii) the parameters, i.e., frequencies, mode-shapes and damping ratios, are not known accurately. The type of controller used in the integrated design should be robust (i.e., should maintain stability, and possibly performance) to unmodelled dynamics and parametric uncertainties mentioned above. In addition, it should be practically implementable, as well as be amenable for inclusion in an optimization process. One class of controllers which has these desired properties is the dissipative controllers [5], and includes “static” and “dynamic” dissipative controllers. The static (or constant-gain) dissipative controller employs collocated and compatible actuators and sensors, and consists of feedbacks of the measured attitude vector y_p and the attitude rate vector y_r using constant, positive-definite gain matrices G_p and G_r . This controller is robust in the presence of parametric uncertainties, unmodelled dynamics and certain types of actuator and sensor nonlinearities [4]. However, the performance of such controllers is inherently limited because of their structure.

CANDIDATE CONTROLLERS

Static Dissipative Controllers

$$u = -G_r y_r - G_p y_p$$

- Collocated sensors and actuators
- Positive definite gain matrices
- Robust in presence of model uncertainties
- Limited performance

In order to improve the performance of static dissipative controllers, an additional dynamic outer loop can be introduced as shown below, where z is the compensator state vector. The matrices A_c , B_c , and G denote the compensator system, input, and output matrices, respectively. These matrices satisfy certain additional conditions to establish dissipativity (A_c has to be strictly Hurwitz and Kalman-Yacubovich relations must hold) as described in [5]. The resulting controller is called a “dynamic dissipative controller”, and is guaranteed to be robustly stable in the presence of unmodelled dynamics as well as parametric uncertainties. It should be noted that standard high-performance model-based controllers (e.g., $H_2(LQG)$ or H_∞ designs) are generally not robust to real parametric uncertainties [5], which makes dynamic dissipative controllers distinctly advantageous.

CANDIDATE CONTROLLERS

Dynamic Dissipative Controllers

$$\dot{z} = A_c z + B_c y_r ; \quad u = -Gz$$

- Collocated sensors and actuators
- A_c is strictly Hurwitz, and the following Kalman-Yacubovich relations hold:

$$A_c^T P + P A_c = -Q ; \quad G = B_c^T P$$

- Robust in presence of model uncertainties
- Enhanced performance

Here, two of the eight available actuators were used to generate persistent white-noise disturbances, while the remaining six actuators were used for feedback control. The static dissipative controller uses a 6×6 diagonal rate-gain matrix with no position feedback (since this system has no zero-frequency eigenvalues, position feedback is not necessary for asymptotic stability). Thus, in the integrated design with the static dissipative controller, the total number of design variables was 27 (21 structural plus 6 control design variables). The dynamic dissipative controller used in the design was a 12th-order controller consisting of six 2nd-order compensators (one for each control channel). Each of the 2nd-order compensators were defined in a controllable canonical form as shown below. There are four control design variables associated with each control channel, resulting in a total of 24 control design variables and 45 combined (structural and control) design variables.

CONTROL DESIGN VARIABLES

- Static dissipative controller: elements of the Cholesky factor matrix of the rate gain matrix

$$G_r = L_r L_r^T$$

- Dynamic dissipative controller: elements of the compensator state and gain matrices (in a controllable canonical form)

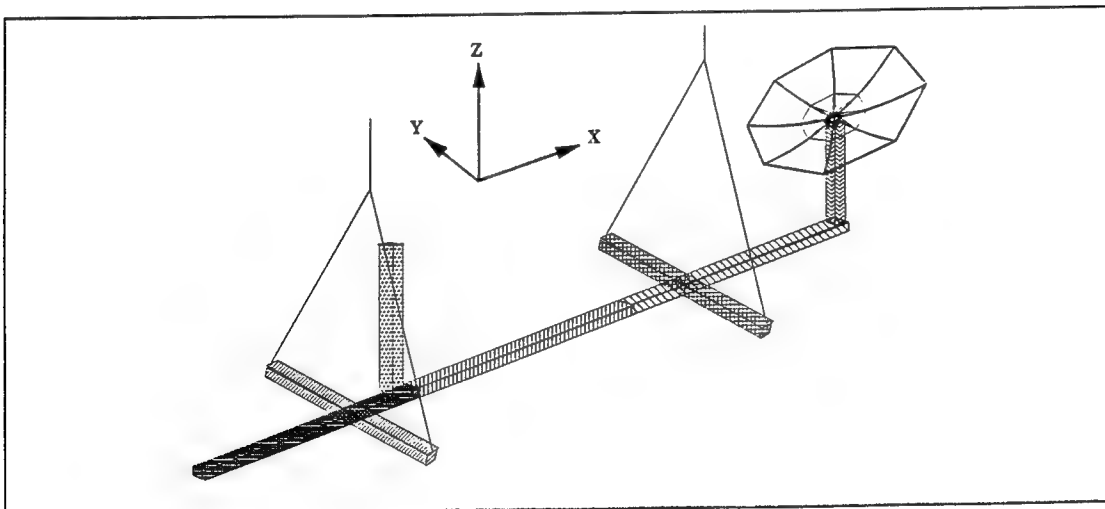
$$A_c = \begin{bmatrix} 0 & 1 & 0 & \dots & 0 \\ 0 & 0 & 1 & \dots & 0 \\ 0 & 0 & 0 & \dots & 0 \\ 0 & 0 & 0 & \dots & 1 \\ \vdots & \vdots & \vdots & & \vdots \\ -\alpha_n & -\alpha_{n-1} & -\alpha_{n-2} & \dots & -\alpha_1 \end{bmatrix} ; \quad B_c = \begin{bmatrix} 0 \\ 0 \\ 0 \\ \vdots \\ 0 \\ 1 \end{bmatrix}$$

$$A_c^T P + P A_c = -Q \quad ; \quad G = B_c^T P$$

To perform the integrated design, the structure was divided into seven sections, three sections in the main bus, and one section each for the two horizontal booms and two vertical towers. The main bus structure is divided into three sections. Three structural design variables were used in each section; namely, the effective cross-sectional area of the longerons, the battens, and the diagonals, making a total of 21 structural design variables.

STRUCTURAL DESIGN VARIABLES

- Structure is divided into seven sections
- The effective cross-sectional areas of longerons, battens and diagonals are chosen as design variables
- Total of 21 structural design variables



An integrated controls-structures design was obtained by minimizing the steady-state average control power in the presence of white noise input disturbances with unit intensity (i.e., standard deviation intensity = 1 lbf.) at actuators No. 1 and 2 (located at the end of the main bus nearest to the laser tower), with a constraint on the steady-state rms position error at the laser detector (above the structure) for reasonable steady-state pointing performance, and a constraint on the total mass to have a fair comparison with Phase-0 design. Both static and dynamic dissipative controllers were used in the integrated design of the CSI Evolutionary Model. The six remaining actuators were used in the control design, along with velocity signals (required for feedback by the dissipative controllers) obtained by processing the accelerometer outputs. Additional side constraints were also placed on the structural design variables for safety and practicality concerns. Lower bound values were placed on these variables to satisfy structural integrity requirements against buckling and stress failures. On the other hand, upper bound values were placed on these variables to accommodate design and fabrication limitations.

DESIGN PROBLEM

- Pose the integrated controls-structures design as a simultaneous optimization problem
- Minimize the average control power

$$J \equiv \text{Trace}\{E\{uu^T\}\}$$

subject to

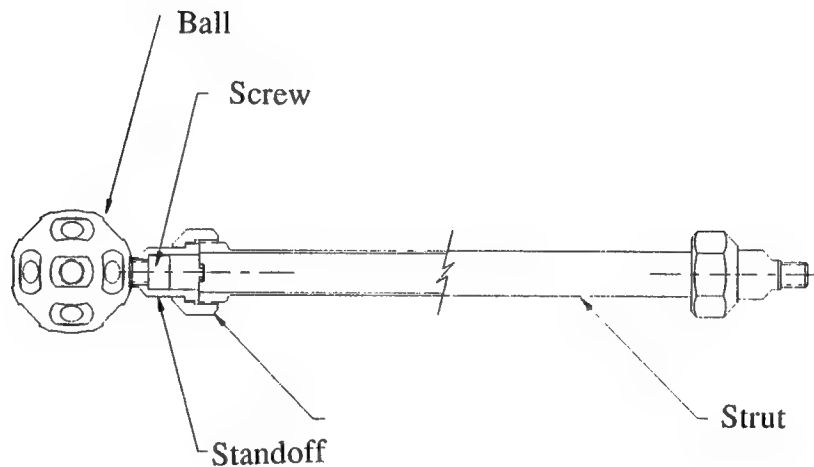
$$\text{Trace}\{E\{y_{los}y_{los}^T\}\} \leq \epsilon$$

$$M_{tot} \leq M_{budget}$$

- side constraints on the structural design variables to accommodate safety, reliability, and fabrication issues

A typical strut of the Phase-1 design is shown in the figure below. The strut is composed of three sections, namely, ball, joint and tube. In an ideal design, the effective density of the strut (which is the density for an equivalent uniform and homogeneous strut) remains roughly constant. Here, however, the effective density varies considerably with the effective cross-sectional area of the strut (which is the cross-sectional area for an equivalent uniform and homogeneous strut) . The main reason for this variation is that due to the short bay size and strut length, this strut design is rather joint-dominated with respect to mass, i.e., a large portion of the total strut mass is concentrated at the joints. As for the stiffness of the strut, its upper bound value is limited due to the ball and joint stiffnesses, whereas its lower bound value is governed by tube size limitations in fabrication.

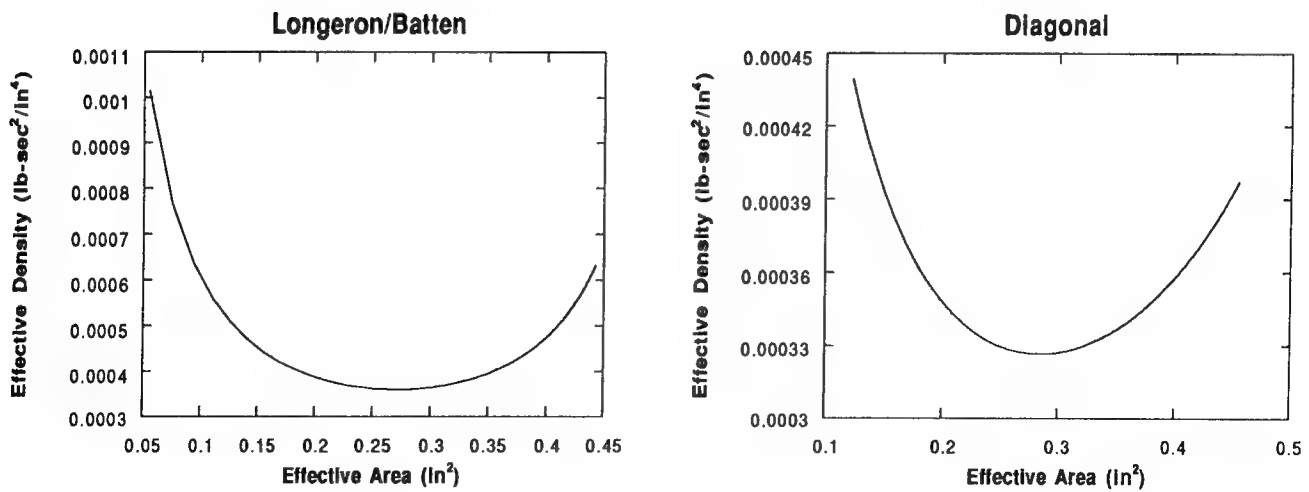
STRUT DESIGN



- Ideal Design: the effective density remains roughly constant
- Actual Design: the effective density varies considerably with the effective area
- The design is rather joint-dominated with respect to mass

In order to ensure that the design that comes out of the integrated design process is realizable, i.e., it is close to a structure that can be fabricated, strut design guides have been developed based on the strut shown in the preceding figure. The strut design guides for longerons, battens and diagonal are shown in the figures below. The curve on the design guide represents the lightest strut which can be manufactured for a given strut stiffness. These strut design curves have been developed assuming that the mass and stiffness properties of the ball and joint sections of the strut remain unchanged; and only the cross-sectional area of the tube portion of the strut changes. The beginning of the curve, corresponding to the lowest effective area, is governed by the load capacity of the tube portion, while the upper end of the curve is governed by the stiffness of the ball and joint sections.

STRUT DESIGN CURVES



Using a constraint on the maximum rms pointing error of 2.4 inches and a constraint on the total mass of 1.92 lb-s²/in (nominal mass of the CSI Phase-0 Evolutionary Structure), a conventional "control-optimized" design was performed first (with the structural design fixed at the initial values) using both the static and dynamic dissipative controllers, where the average control power was minimized with respect to the control design variables only. The static dissipative controller gave an average control power of 7.11 lb², while the dynamic dissipative controller gave a better average control power of 6.41 lb². The open-loop rms pointing error for the Phase-0 structure was 22.54 inches. Next, an integrated design with the static dissipative controller was performed, wherein the average control power was minimized with respect to both control and structural design variables. The integrated design reduced the average control power by about 40 percent to 4.21 lb². This integrated design (Phase-1 design) gave an open-loop rms pointing error of 18.34 inches, which, although better than the open-loop performance of the Phase-0 design, indicates that the task of achieving satisfactory pointing performance cannot be achieved through structural redesign alone. Using the same initial design, another integrated design using the dynamic dissipative controller was also performed. This design gave an almost 43-percent reduction in the average control power compared to its corresponding control-optimized design. These results clearly demonstrate the advantage of integrated design over the traditional sequential design.

CONVENTIONAL VS. INTEGRATED

	RMS Displacement	Control Power
Open Loop (Phase-0)	22.54	0.00
Open Loop (Phase-1)	18.34	0.00
Control-Optimized (S) Design	2.4	7.11
Control-Optimized (D) Design	2.4	6.41
Integrated Design (S)	2.4	4.21
Integrated Design (D)	2.4	3.64

The effective cross-sectional areas of the longerons, battens and diagonal are presented in the table for both the Phase-0 structure and the Phase-1 structure that was designed using the static dissipative controller. Keeping in mind that the tube cross-sectional areas of the nominal CSI Evolutionary structure are 0.134 in^2 for the longerons and battens and 0.124 in^2 inches for the diagonal, it is observed that the longerons of all three sections of the main bus, particularly the section closest to the disturbance sources, and the laser tower are considerably stiffened; while the horizontal booms and the reflector tower became more flexible, partly to satisfy the mass constraint. Generally, all the diagonals and the battens decreased in size, mainly because the design optimization has to satisfy a constraint on the total mass, i.e., the mass of Phase-1 design must be less than or equal to the mass of Phase-0 design. Consequently, mass was taken from the battens and diagonals and was redistributed to the longerons of some sections because they are quite more effective in increasing the stiffness of a section. This behavioral trend may be attributed to a trade-off between structural controllability, observability, and excitability. The areas near the disturbance sources (actuator locations) were stiffened in order to reduce the sensitivity of the structure to external disturbances at those locations, while ensuring that no appreciable loss of controllability and/or observability occurred.

STRUCTURAL DESIGN VARIABLES

(Static Dissipative Controller)

	Design	Phase-0	Phase-1
	Var.	Areas	Areas
Longerons	1	0.134	0.330
	4	0.134	0.085
	7	0.134	0.173
	10	0.134	0.260
	13	0.134	0.257
	16	0.134	0.095
	19	0.134	0.096
Battens	2	0.134	0.082
	5	0.134	0.083
	8	0.134	0.082
	11	0.134	0.082
	14	0.134	0.081
	17	0.134	0.081
	20	0.134	0.081
Diagonals	3	0.124	0.082
	6	0.124	0.085
	9	0.124	0.082
	12	0.124	0.081
	15	0.124	0.079
	18	0.124	0.079
	21	0.124	0.082

The optimal values of the structural design variables for the integrated design structure with the dynamic dissipative controllers are presented below. Generally, quite similar trends to those for the static dissipative controller design are observed. In fact, the effective cross-sectional areas of this integrated design are roughly within 20 percent of the design obtained using the static dissipative controller, thus indicating that the optimal structures for both the static and dynamic dissipative designs are essentially the same. Consequently, the integrated design with static dissipative controller was chosen for fabrication.

STRUCTURAL DESIGN VARIABLES (Dynamic Dissipative Controller)

	Design Var.	Phase-0 Areas	Phase-1 Areas
Longerons	1	0.134	0.330
	4	0.134	0.080
	7	0.134	0.142
	10	0.134	0.295
	13	0.134	0.258
	16	0.134	0.100
	19	0.134	0.117
Battens	2	0.134	0.077
	5	0.134	0.087
	8	0.134	0.086
	11	0.134	0.080
	14	0.134	0.078
	17	0.134	0.077
	20	0.134	0.083
Diagonals	3	0.124	0.098
	6	0.124	0.087
	9	0.124	0.082
	12	0.124	0.066
	15	0.124	0.066
	18	0.124	0.066
	21	0.124	0.083

It is not practical to expect that the optimal design that comes out of the integrated design process can be fabricated to exact specifications, mainly due to manufacturing and cost limitations. Consequently, any feasible design should allow for perturbations in the structural design variables (effective cross-sectional areas and effective mass densities of the struts). In order to evaluate the sensitivity of the optimal design with respect to perturbations in the structural design variables, the line-of-sight (Los) function and the control power function are approximated by a first-order Taylor's Series expansion. Then, upper bound values for Los pointing error and the control power are obtained for a maximum perturbation limit following a worst-case-scenario approach based on steepest ascent.

PERTURBATION ANALYSIS

- The integrated phase-1 design cannot be fabricated to exact specifications due to manufacturing and cost limitations
- Any viable integrated design should allow for possible perturbations in the structural design variables
- Carry out a post-design sensitivity analysis:

$$LOS(d + \delta) = LOS(d) + [\partial LOS / \partial \rho]^T \delta + \dots$$

$$POW(d + \delta) = POW(d) + [\partial POW / \partial \rho]^T \delta + \dots$$

- Upper bound values for the rms pointing error and control power

$$LOS_U = LOS(d) + |[\partial LOS / \partial \rho]^T| \delta_{max}$$

$$POW_U = POW(d) + |[\partial POW / \partial \rho]^T| \delta_{max}$$

The table below compares the rms pointing error and control power values of the nominal integrated design (with static dissipative controller) with a perturbed design and the final fabricated Phase-1 design. The perturbed design which allows for a 10-percent perturbation in the structural design variables gave a worst-case value of 4.42 for the control power (5-percent more than the nominal) and a worst-case value of 2.56 for the rms pointing error (7-percent more than the nominal), thus implying that the nominal integrated design is rather insensitive to structural parameters perturbations and, therefore, is a feasible design. The fabricated design which refers to the design that was chosen for fabrication gave a control power of 4.34 (3-percent off from the nominal) and an rms pointing error of 2.38 (1-percent off from the nominal) which are quite close to the nominal design values.

PERTUBATION ANALYSIS (CONT'D)

	Control Power	RMS Pointing Error
Nominal Design	4.21	2.40
Perturbed Design	4.42 (5%)	2.56 (7%)
Fabricated Design	4.34 (3%)	2.38 (1%)

The effective cross-sectional areas chosen for the fabrication of each of the 21 struts (corresponding to the 21 structural design variables) are presented in the table below. Out of the 21 possible struts, six unique struts were chosen for fabrication, with four for the longerons, one for the battens, and one for the diagonals. The reasons behind choosing only six unique struts are essentially cost limitations and/or closeness of the optimal design values. Most of the effective cross-sectional areas of the struts in the fabricated design are within 10-percent of the chosen integrated design (with static dissipative controller) and all are within 20-percent of the nominal values.

STRUCTURAL DESIGN VARIABLES (Fabricated Structure)

	Design Var.	Phase-0 Areas	Phase-1 Areas
Longerons	1	0.134	0.347
	4	0.134	0.106
	7	0.134	0.182
	10	0.134	0.274
	13	0.134	0.274
	16	0.134	0.106
	19	0.134	0.106
Battens	2	0.134	0.094
	5	0.134	0.094
	8	0.134	0.094
	11	0.134	0.094
	14	0.134	0.094
	17	0.134	0.094
	20	0.134	0.094
Diagonals	3	0.124	0.087
	6	0.124	0.087
	9	0.124	0.087
	12	0.124	0.087
	15	0.124	0.087
	18	0.124	0.087
	21	0.124	0.087

An integrated design of the CSI Evolutionary Structure (Phase-0 structure) has been performed as a step in the validation of the integrated controls-structures design methodology. The integrated design structure (Phase-1 structure) provides the same Los pointing performance as the Phase-0 structure with around 60 percent of the control power requirement. Because of the dissipative nature of the controllers used in the integrated design, it is expected to have good stability robustness characteristics. Moreover, linear perturbation analysis indicates that the Phase-1 structure should also have good performance robustness characteristics. The Phase-1 structure is currently being fabricated, and is scheduled for testing and comparison with the Phase-0 structure in mid FY 92, at which time the process of validating the integrated design methodology will commence.

CONCLUDING REMARKS

- Phase-1 integrated design provides the same LOS performance as the phase-0 design with 60 percent of the control power requirement
- The integrated phase-1 design demonstrates good performance and stability robustness characteristics
- Phase-1 design is scheduled for testing and comparison with phase-0 in mid FY 92

References:

1. Maghami, P. G., Joshi, S. M., Armstrong, E. S., and Walz, J. E., "Integrated Controls-Structures Design Methodology Development for a Class of Flexible Spacecraft," Proceedings of the Third Air Force/NASA Symposium on Recent Advances in Multidisciplinary Analysis and Optimization, San Fransisco, CA, Sept. 24–26, 1990.
2. Maghami, P. G., Joshi, S. M., and Gupta, S., "Integrated Controls-Structures Design for a Class of Flexible Spacecraft," Proceedings of the Fourth NASA/DOD Controls/Structures Interaction Technology Conf., Orlando, FL, Nov. 5–7, 1990.
3. Maghami, P. G., Joshi, S. M., and Lim, K. B., "Integrated Controls-Structures Design: A Practical Tool for Modern Spacecraft," Proceedings of the 1991 American Control Conf., Boston, MA, June 26–28, 1991.
4. Joshi, S. M., "Control of Large Flexible Space Structures," Berlin Springer-Verlag, Vol. 131, Lecture Notes in Control and Info. Sciences, 1989.
5. Joshi, S. M. and Maghami, P. G., "Dissipative Compensators for Flexible Spacecraft Control," Proceedings of the 1990 American Control Conf., San Diego, CA, May 23–25, 1990.
6. Belvin, W. K., Horta, L. G., and Elliot, K. E., "The LaRC CSI Phase-0 Evolutionary Model Testbed: Design and Experimental Results," Proceedings of the Fourth NASA/DOD Controls/Structures Interaction Technology Conf., Orlando, FL, Nov. 5–7, 1990.

CONTROL/STRUCTURE INTERACTION DURING SPACE STATION FREEDOM-ORBITER BERTHING

T. Hua and E. Kubiak

NASA Johnson Space Center, Mail Code EG2

Houston, Texas 77058

Yeongching Lin, M. Kilby and J. Mapar

Dynacs Engineering Co., Inc.

1110 NASA Road 1, Suite 650

Houston, Texas 77058

INTRODUCTION

The berthing maneuver is essential for the construction and assembly of Space Station Freedom (SSF) and has a direct effect on the SSF assembly build up and SSF/Orbiter operations. The effects of flexible body dynamics coupled with the available control system may impose new requirements on the maneuver. The problem is further complicated by the effect of the SSF control system on the Shuttle Remote Manipulator System (SRMS) (Figure A-1). These effects will play a major role in the development of operational requirements which need to be identified and validated in order to assure total safety and maneuver execution during SSF construction. This paper presents the results of ongoing studies to investigate the Control/Structure Interaction (CSI) during the berthing operations. The problem is formulated in terms of multi-flex body equations of motion for SSF and the SRMS and on-orbit flight control systems for the SRMS and the SSF, which includes the Control Moment Gyro (CMG) and Reaction Control System (RCS) Attitude Control Systems (ACS). The SSF control system designs are based on the Preliminary Design Review (PDR) version of the Honeywell design (Reference 1). The simulation tool used for the analysis is briefly described and the CSI results are presented for given berthing scenarios.

This paper also presents preliminary results of the verification of a new software analysis tool. This tool, referred to as the Station/Orbiter Multi-flex-body Berthing Analysis Tool (SOMBAT), is designed to analyze berthing operations for the Space Station Manned Base

(SSMB). Specifically, the results presented in this paper focus on the dynamic interaction of the Orbiter and the Shuttle Remote Manipulator System (SRMS) (Reference 2) with the control systems of the SSMB during the berthing process.

For this paper, operations consist of the berthing of the completed Stage-5 Space Station to the Orbiter at the beginning of the flight MB-6. The SRMS is used to perform the berthing operation. The SSMB assumes control of the combined system of the space station, Orbiter, and SRMS for this flight. The berthing operation is of interest because of the large change in mass properties of the combined system and the dynamic interaction with the station Attitude Control System.

ACRONYMS

ACS	- Attitude Control System
CDR	- Critical Design Review
CMG	- Control Moment Gyro
DRM	- Design Reference Mission
DRS	- Draper RMS Simulation
GG	- Gravity Gradient
LVLH	- Local Vertical, Local Horizontal
MB-6	- Mission Build 6
MM	- Momentum Management
PDR	- Preliminary Design Review
RCS	- Reaction Control System
SES	- System Engineering Simulator
SOMBAT	- Station/Orbiter Multi-body Berthing Analysis Tool
SRMS	- Shuttle Remote Manipulator System
SSEIC	- Space Station Engineering Integration Contractor
SSF	- Space Station Freedom
SSMB	- Space Station Manned Base
TEA	- Torque Equilibrium Attitude

CRITICAL ISSUES

The following issues are of concern during the berthing operations :

- Limitations on SRMS
 - a. Flexibility of arms -

The Space Station active attitude control may induce excessive loads on the SRMS flexure during berthing.
 - b. Payload capability -

The SRMS has been certified to handle payloads below 65,000 pounds. However, berthing the Orbiter to the Station assembly stages will involve payloads varying from 37,000 to over 250,000 pounds.
 - c. Joint velocity limit -

SRMS joint speeds are also affected by the weight of the payloads. The larger the payload, the slower the arms have to move.
- ACS attitude control authority
 - a. CMG and RCS -

CMG's capability to hold the desired attitude of the combined vehicles and RCS fuel consumption during the whole berthing operation needs to be investigated.
 - b. Jet firing constraints -

Jet pulsing frequency limit has to be imposed on RCS to avoid exciting the Station structures.
 - c. Mass property update -

The knowledge of Orbiter/SRMS position and orientation is required to update mass properties and controller gains.
- Power and thermal constraints -

Lack of power generation from the locked solar arrays may cause excessive discharge of the batteries. Without proper attitude control, the ammonia in the large articulating thermal radiator may freeze within 30 minutes.

SIMULATION TOOL - SOMBAT

The Space Station is envisioned as a complex, multi-flexible body configuration in an open-tree topology. The equations of motion for such systems are non-linear and become very complicated. The solution approach must be developed carefully to provide the required fidelity and accuracy and at the same time minimize computational cost associated with the time history simulation. Analysis for simulating the control and multi-flexible structure interaction

was performed using the SOMBAT software package because the traditional finite element method is not capable to analyze large translational and rotational motion. This tool is used for the studies of various berthing scenarios between the SSMB and the Orbiter.

Theoretical Developments

Because it is very difficult to derive a closed form solution for a given structure, finite element analysis is used to obtain the stiffness and mass matrices of the structure. Let \mathbf{q} be the total vector of independent coordinates or the degrees of freedom of the structure that includes three translational and three rotational rigid body motions. The motion of the flexible structure is governed by a set of second-order differential equations of motion that can be written in the following compact matrix form (References 3, 4):

$$\mathbf{M}\ddot{\mathbf{q}} + \mathbf{K}\mathbf{q} = \mathbf{u} + \mathbf{v} + \mathbf{w} \quad (1)$$

where \mathbf{M} is assumed to be a positive definite mass matrix associated with the independent coordinates which can be represented as

$$\mathbf{M} = \begin{bmatrix} \mathbf{m}_{rr} & \mathbf{m}_{r\theta} & \mathbf{m}_{rf} \\ \mathbf{m}_{\theta r} & \mathbf{m}_{\theta\theta} & \mathbf{m}_{\theta f} \\ \mathbf{m}_{fr} & \mathbf{m}_{f\theta} & \mathbf{m}_{ff} \end{bmatrix}$$

where

- \mathbf{m}_{rr} - the rigid mass matrix
- $\mathbf{m}_{\theta\theta}$ - the rigid body inertia matrix
- $\mathbf{m}_{r\theta}$ - the mass center
- \mathbf{m}_{rf} - the linear momentum
- $\mathbf{m}_{\theta f}$ - the angular momentum
- \mathbf{m}_{ff} - the modal mass matrix

and \mathbf{K} is the system stiffness matrix. Both \mathbf{M} and \mathbf{K} may be time varying. The input \mathbf{u} is the vector of generalized external forces associated with the independent coordinates, \mathbf{v} is the quadratic velocity vector that includes the gyroscopic and Coriolis force components, and \mathbf{w} is the closed loop control vector. The derivation is based on a nodal body formulation and

provides a convenient approach to use finite element output data. The derivation of equations of motion is discussed in detail in References 3 and 4.

The flexible body modelling techniques in SOMBAT are:

- A system made up of multiple components where relative motion of the components is modelled through joint kinematics and dynamics
- Components are modelled separately via NASTRAN
- An "order-N" algorithm is used to solve the equations of motion
- Integration of station control system with multi-body dynamics

SOMBAT Functional Overview

SOMBAT consists of several modules used in modelling the system under study, optimizing the software for the specific problem, simulating the problem and viewing the time history of the simulation. The organization of these modules is illustrated in Figure 1. These modules are:

- Model Definition (Setup) Module
- Symbolic Code Generator
- User Defined Code
- Simulation Shell
- Post Processing
- Optional Capabilities
- Flexible Body Data Preprocessor
- Inverse Kinematics Preprocessor (Appendix A)

SOMBAT Features

SOMBAT incorporates numerous features that make it ideal for rapid studies of berthing scenarios. Features currently provided by SOMBAT include:

- A complete orbital environment
- Automated, symbolic code generation for efficient, problem-specific simulation
- Rigid and flexible nonlinear multi-body dynamics (open and closed chain)
- A kinematic model of the SRMS
- A dynamics model of the SRMS (rigid and flexible)
- Honeywell PDR and CDR versions of the station ACS

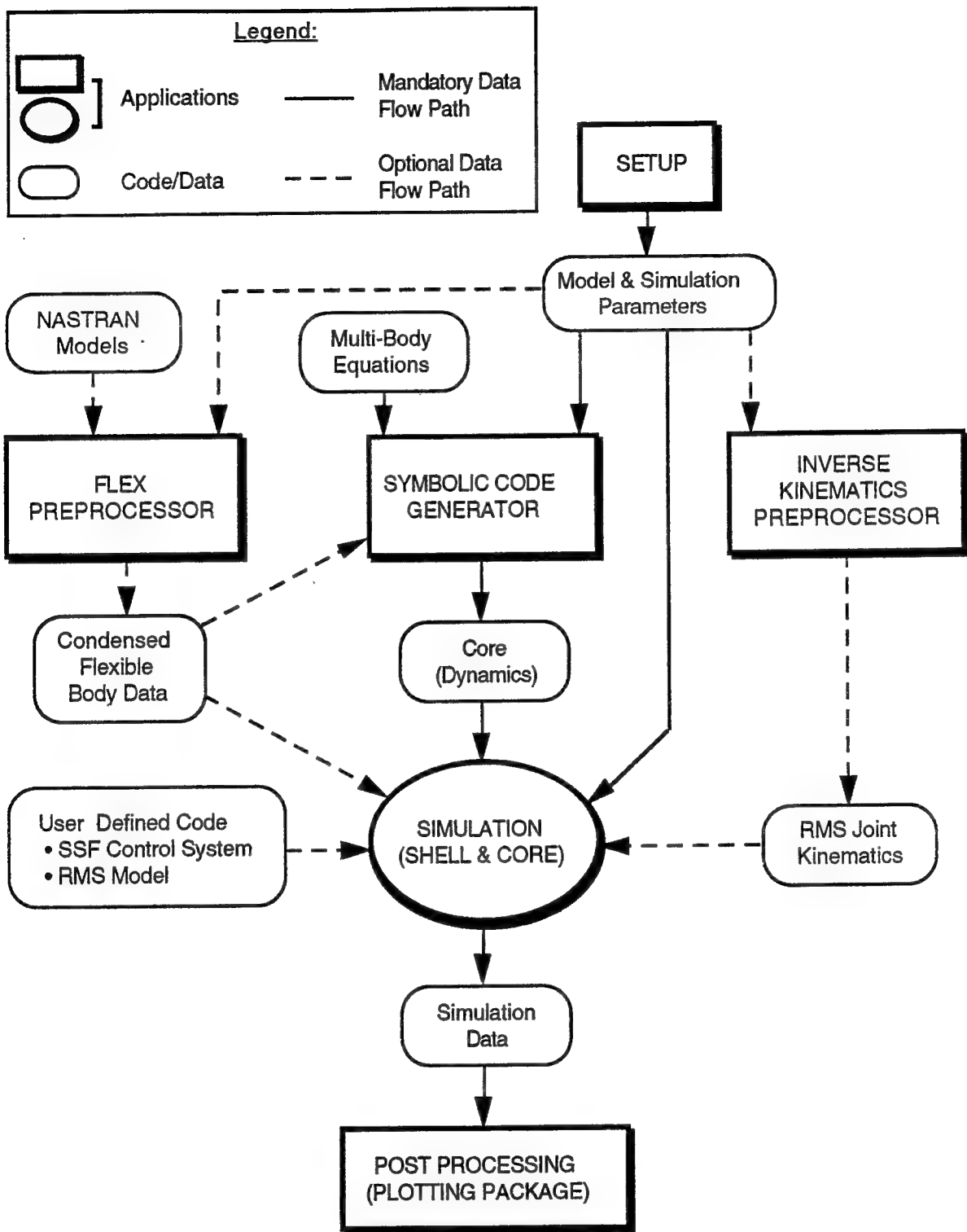


Figure 1: Organization of the SOMBAT Simulation Environment

- A high fidelity SRMS joint controller

ANALYSIS RESULTS

This section evaluates the SSMB PDR control systems during the berthing of the complete Stage-5 Space Station to the Orbiter, Figure 2. The scenarios examined for the berthing operations are modelled after the timeline (Appendix B) in the Design Reference Mission (**DRM**) (Reference 5). This study focuses only on the SSMB control system and no evaluations of the Orbiter and SRMS control systems were performed. Motion between the Orbiter and SSMB is via the prescribed motion of the SRMS joints.

The system under study consisted of the Orbiter, the SRMS, and the SSMB. The mass properties for flight MB-5 were obtained from SSEIC's Model Management System (Reference 6). These models are

- Orbiter - a single rigid body
- SRMS - seven rigid links
- SSMB - five rigid (scenarios 1 and 2) or flexible bodies (scenario 3)

Scenario 1

The scenario for case 1, illustrated in Figure B-1, considers the effects on the CMG/MM control system in maneuvering the combined structure to the TEA for the capture configuration from a gravity gradient attitude. The CMG retains control authority as the SRMS berths the SSMB to the Orbiter and then maintains the TEA for the berthed configuration. As shown by Figure 3, the scenario provides 10000 seconds for the CMG/MM system to maneuver to the capture TEA. After this period, the SRMS retracts the SSMB into the Orbiter payload bay for 3600 seconds followed by a period of 25000 seconds to achieve the berthed TEA.

Figure 3-a shows the composite vehicle attitude. From this figure, two sets of transients are observed. The first transient response is produced by the maneuver to the capture TEA. The second set is associated with the SRMS motion. The difference in the capture TEA and the berthed TEA can also be observed by comparing the attitude at 12000 seconds (capture) and at 30000 seconds (berthed). This change in TEA results from the change in mass properties.

Figure 3-b illustrates the CMG momentum. These figures show the CMG momentum capacity of 14000 ft-lb-seconds to be exceeded by the maneuver from gravity gradient to TEA

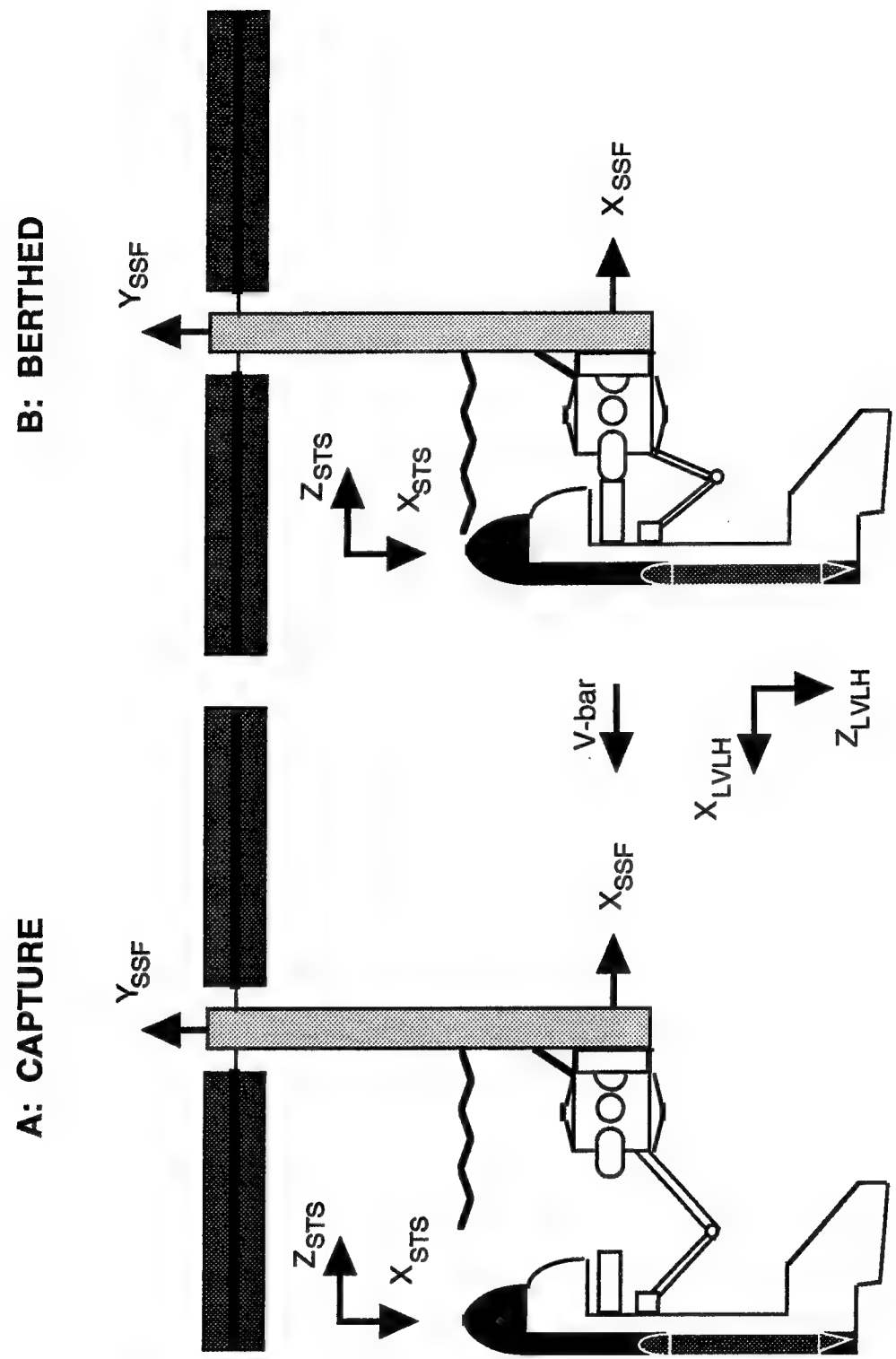


Figure 2: Initial and Final Configurations of the Orbiter/SRMS/SSMB Stack for Berthing Operations

and the SRMS retraction. As demonstrated by these results, the CMG/MM control system alone is unsuitable for the entire berthing operation.

Scenario 2

Based on the previous results, another scenario, Figure B-2, is developed to examine the operation of the RCS and CMG control systems for the entire berthing operation. The RCS control system is used to move the composite system near the estimated capture TEA in 2000 seconds. This is followed by a handover to the CMG/MM system to achieve TEA. At 12000 seconds, SRMS retraction proceeds until the SSMB is mated to the Orbiter 3600 seconds later. After berthing, the CMG/MM seeks the new TEA for the berthed configuration.

Figure 4-a illustrates the combined system attitude. From this figure, the capture TEA is achieved at 12000 seconds and the berthed TEA at 25000 seconds. Figure 4-b shows the CMG momentum. As in the previous case, two transients occur for the RCS/CMG handover and for SRMS operations. Figure 4-b indicates the CMG momentum is not exceeded at the RCS/CMG handover, but is exceeded for the SRMS operations. Saturation is produced by the variation in mass properties during retraction by the the SRMS without a corresponding update in the feedback gains.

Scenario 3

For this case, Figure B-3, a multi-flexible body station is examined. Usually, positioning a flexible structure, such as a space telescope or space station, will generally excite unwanted flexible modes in the structure. This case studies the oscillation in the elastic modes due to the jet firing. The scenario begins with the system in the capture configuration and is then commanded to the estimated TEA by the RCS control system. The estimated TEA for the capture configuration is 1.057 degrees (Roll), -22.889 degrees (pitch) and 14.137 (Yaw) with respect to LVLH.

Figure 5-a shows the attitude of the combined system. The commanded attitude is achieved after 1500 seconds. In Figure 5-b, the phase plane for the RCS indicates that the combined system is stable and controllable. Figure 5-c illustrates modal displacements of the first three modes of the core body. The natural frequencies of these modes are 0.483 Hz, 0.717 Hz, and 1.268 Hz. Figure 5-c indicates that the rigid body motion dominates the flexible body

Units:

TIME - seconds

THETA - degrees

Note: Euler 1-2-3 sequence

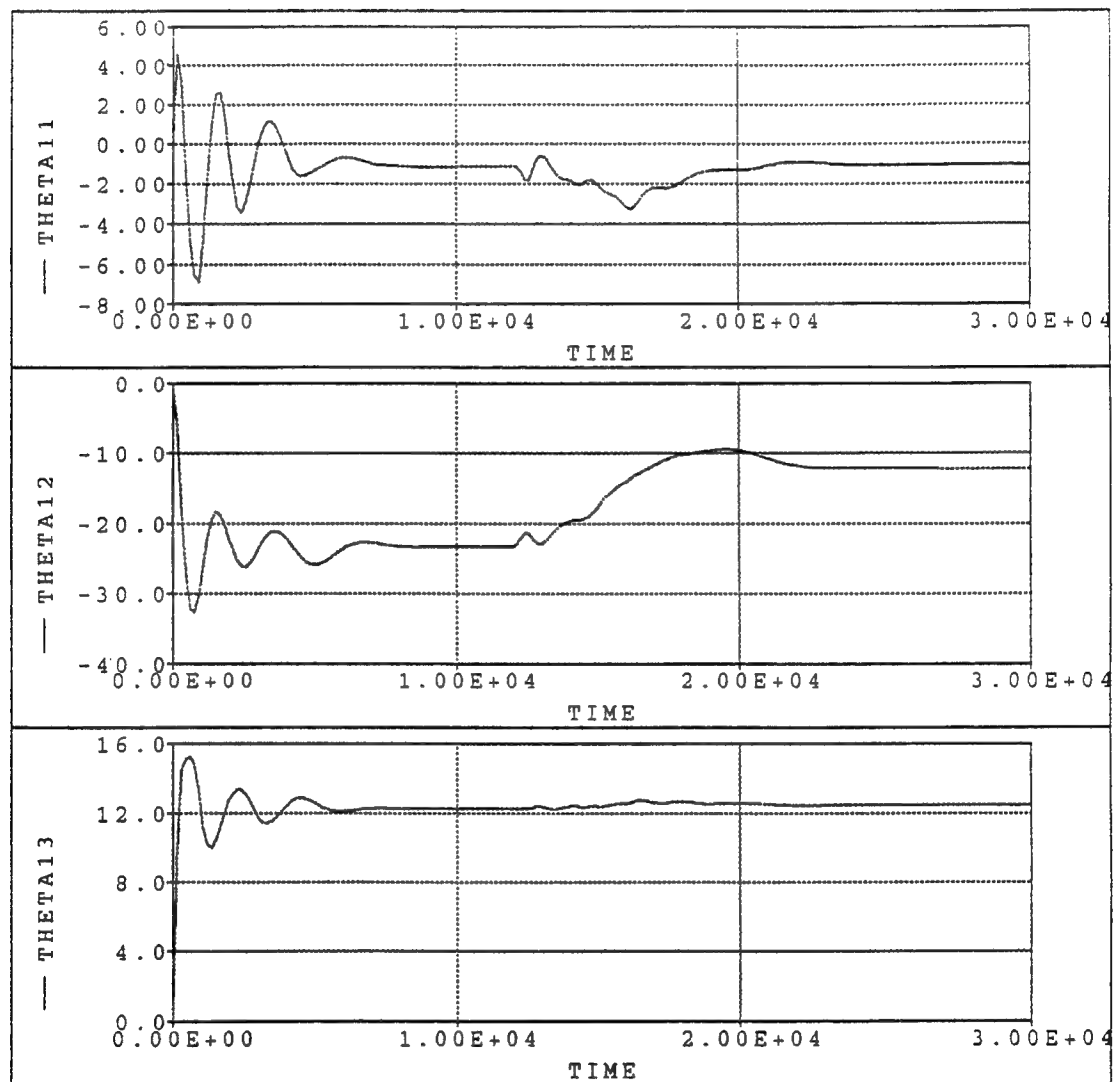


Figure 3-a: Vehicle Attitude w.r.t. LVLH, SSF CMG, Retraction via SRMS, Aerodynamics (Scenario 1)

Units:

TIME - seconds

HCMGV - ft-lb-sec

Note: Euler 1-2-3 sequence

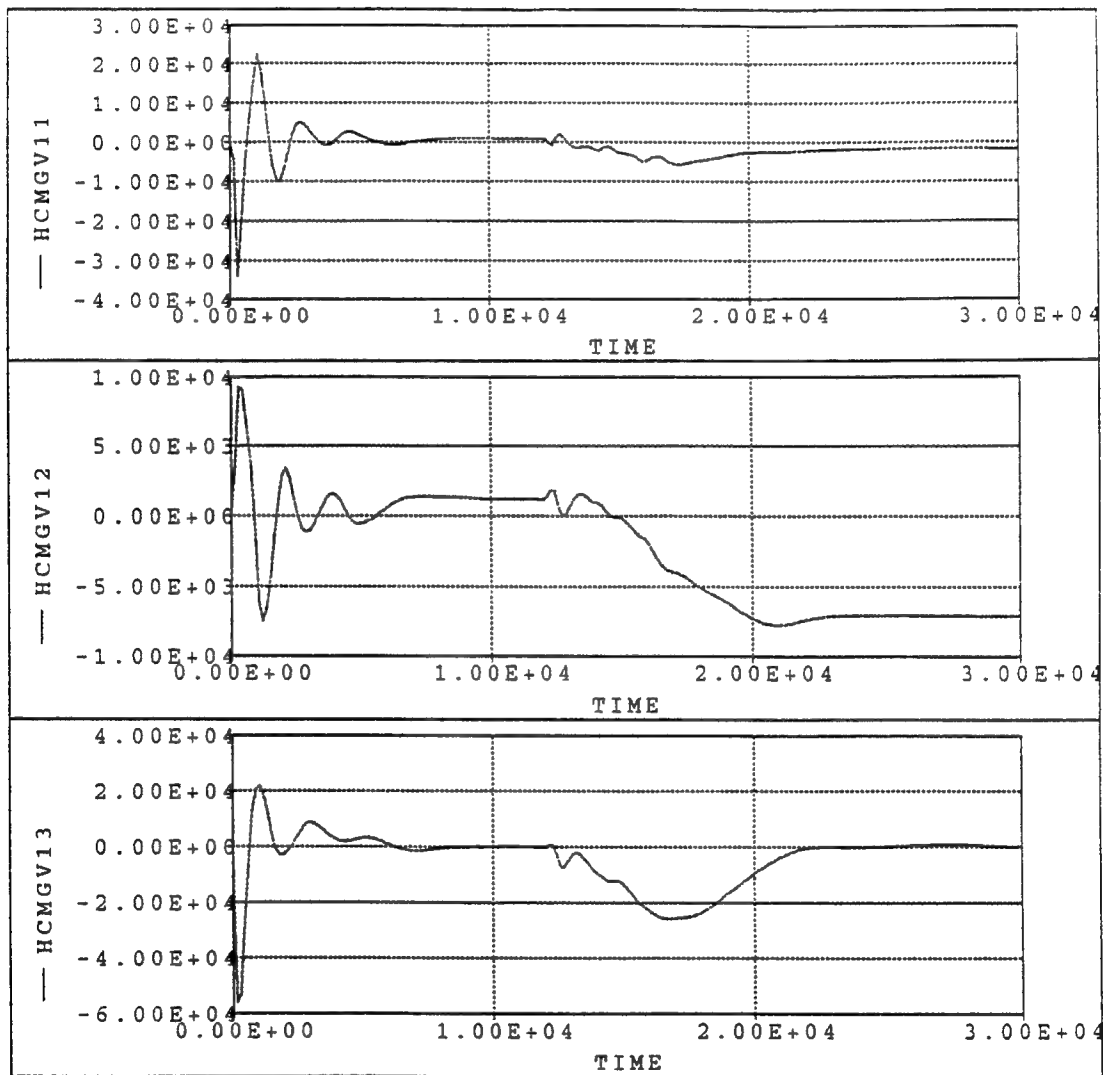


Figure 3-b: CMG Momentum in SSF Reference Frame, SSF CMG, Retraction via SRMS, Aerodynamics (Scenario 1)

Units:

TIME - seconds

THETA - degrees

Note: Euler 1-2-3 sequence

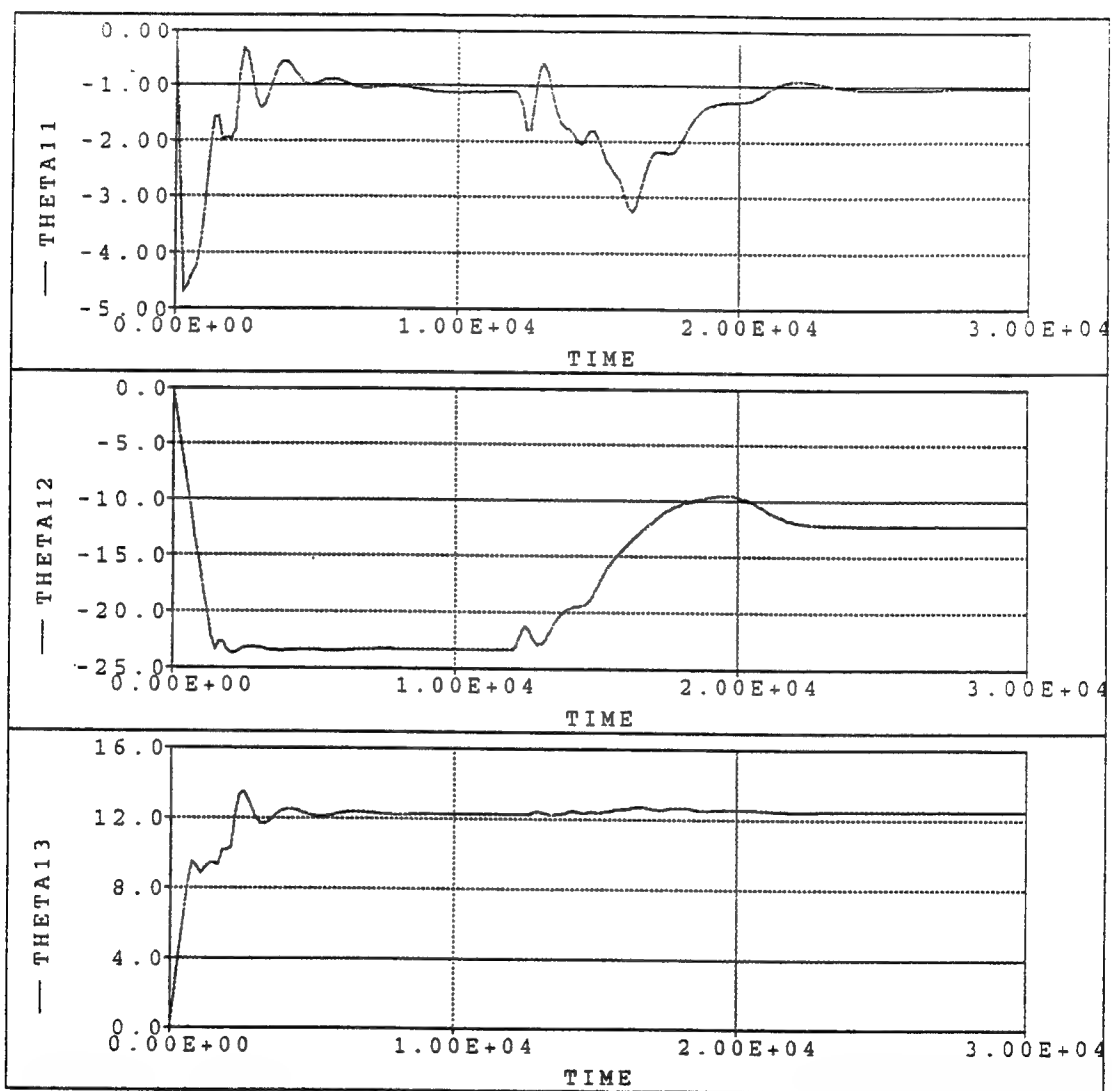


Figure 4-a: Vehicle Attitude w.r.t. LVLH, SSF RCS/CMG, Retraction via SRMS, Aerodynamics (Scenario 2)

Units:

TIME - seconds

HCMGV - ft-lb-sec

Note: Euler 1-2-3 sequence

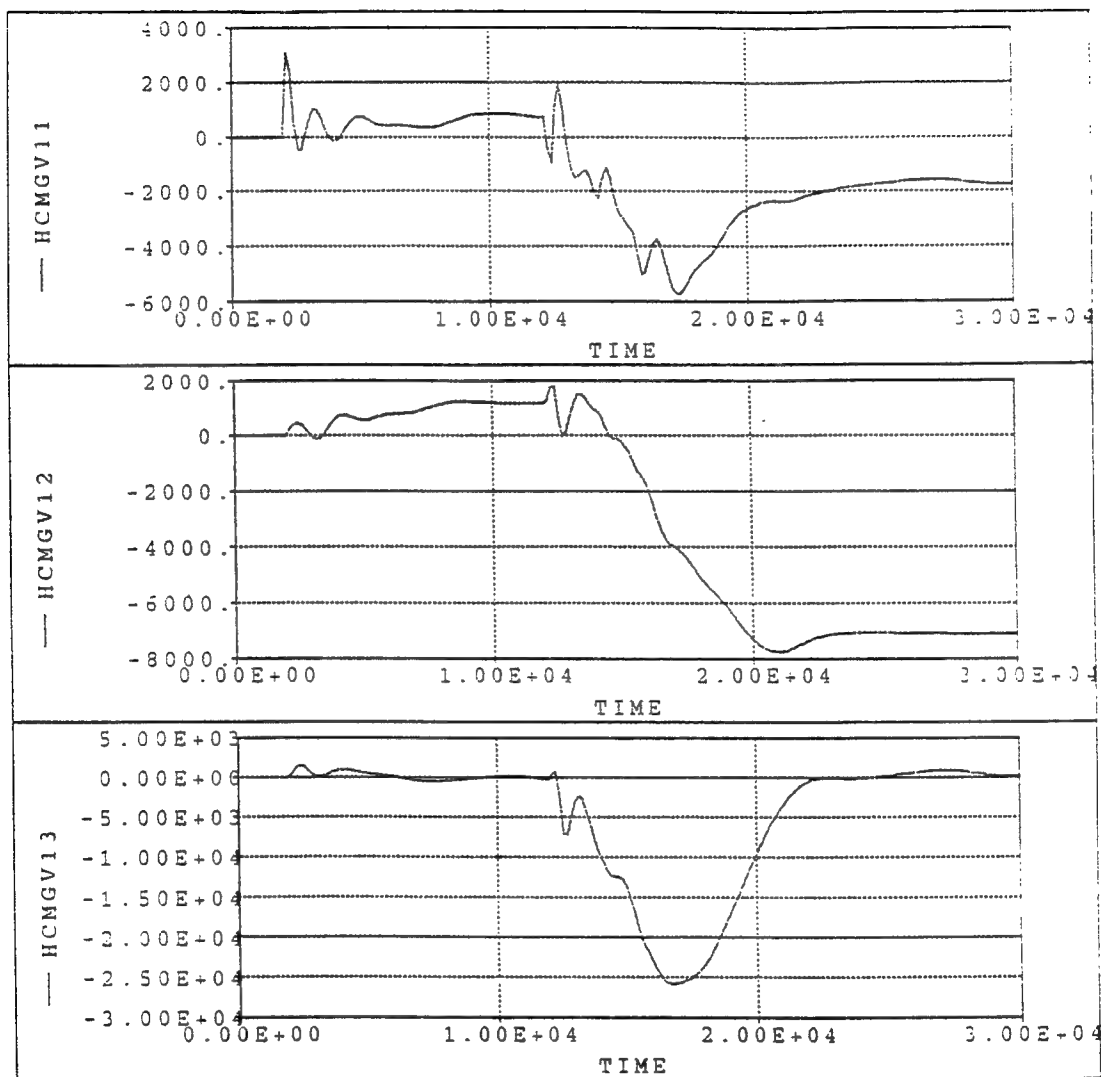


Figure 4-b: CMG Momentum in SSF Reference Frame, SSF RCS/CMG, Retraction via SRMS, Aerodynamics (Scenario 2)

Units:

TIME - seconds

THETA - degrees

Note: Euler 1-2-3 sequence

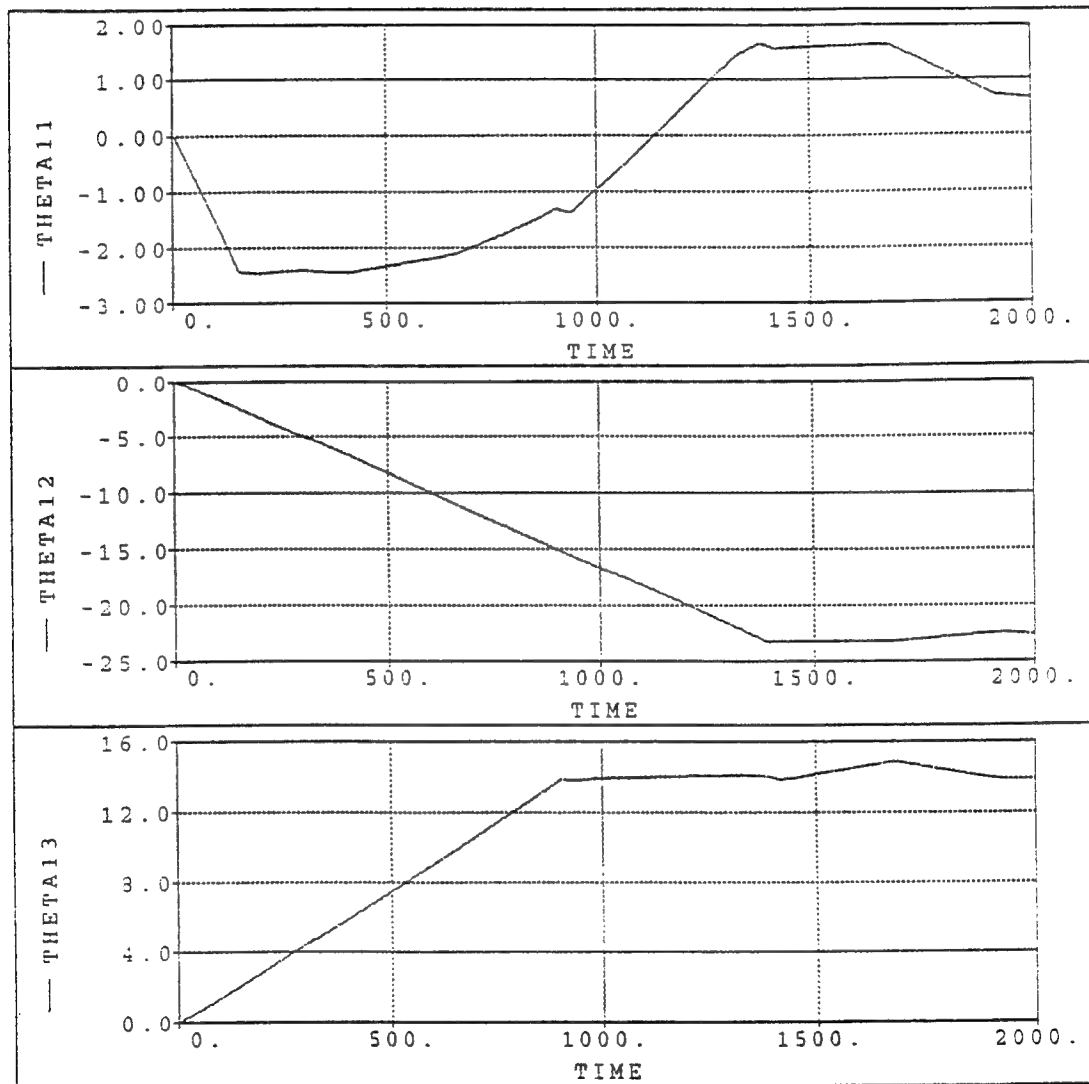
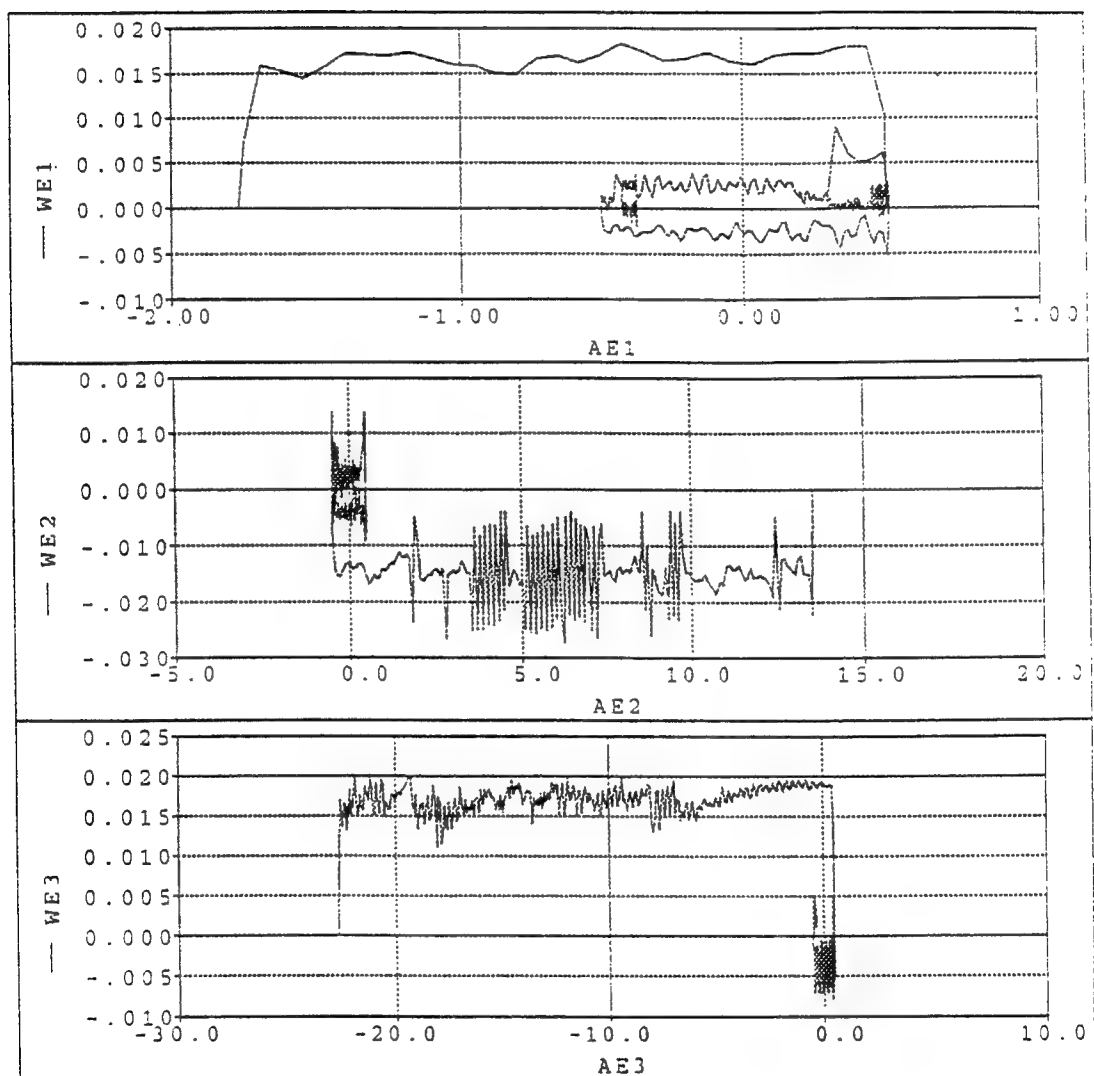


Figure 5-a: Vehicle Attitude w.r.t. LVLH, SSF RCS, SRMS Brakes on at Capture (Scenario 3)

Units:

AE - degrees

WE - degrees/sec



**Figure 5-b: Phase Plane for RCS Maneuver to GG-TEA, SSF RCS, SRMS
Brakes on at Capture (Scenario 3)**

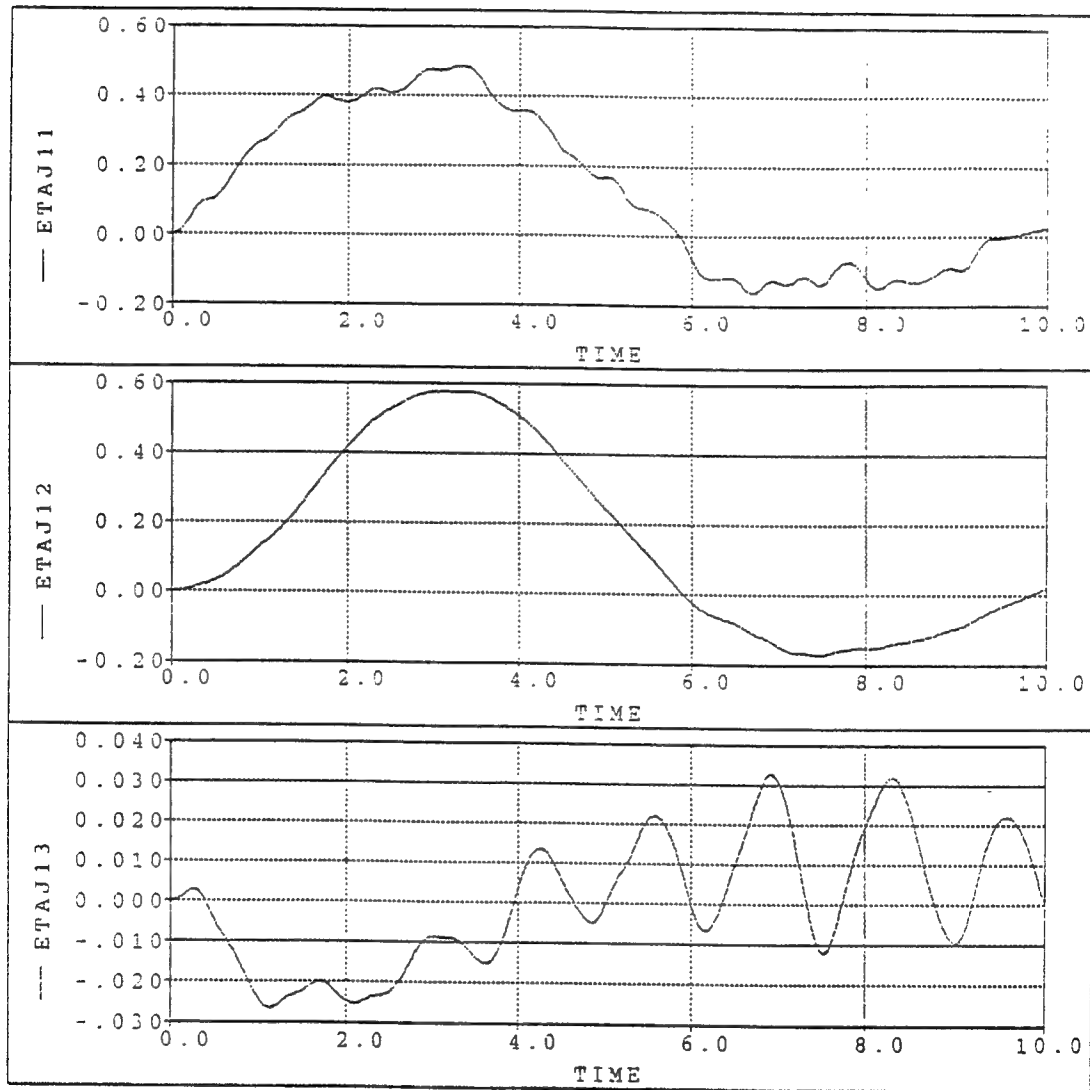


Figure 5-c: Modal Displacement for RCS Maneuver to GG-TEA, SSF RCS, SRMS Brakes on at Capture (Scenario 3)

response because the coupling terms between the rigid and deformable body are strong. This figure also shows that the energy in the elastic modes is not zero due to the berthing operation.

SUMMARY

The previous analysis studied 3 cases using multi-rigid/flexible bodies, a kinematic SRMS model, and the PDR ACS. From these scenarios the following observations were made:

- A CMG only mode may not be sufficient for controlling the combined system of the Orbiter, SRMS, and the SSMB during berthing operations. Results indicate that moving from a gravity gradient attitude to a TEA could result in saturation of the CMG controller.
- An RCS only mode may produce undesirable interaction with the SRMS and needs to be investigated in detail.
- The RCS/CMG mode proves to be the most promising in maintaining control of the combined system of the Orbiter, SRMS, and the SSMB during berthing operations. This control mode also prevents saturation of the CMG/MM system in maneuvering from the gravity gradient attitude to the TEA.
- The use of fixed gains computed at the capture position results in saturation of the CMG/MM control system during berthing operations. This arises from the large variation of the mass properties as the SRMS pulls the SSMB to the Orbiter for berthing.
- The interaction between the rigid and elastic body during the berthing operation needs to be evaluated.
- The CDR control system designed by Honeywell may be able to prevent the problems such as CMG saturation, structure vibration and fuel consumption.

REFERENCES

1. Space Station Simulation (SSSIM) User's Guide, Dynamic Simulation Revision 1.2, Controller Version C01A, January 15, 1991.
2. System Engineering Simulator On-Orbit Element Simulation Definition Document, LESC-Houston, LEMSCO-24111, January 1991.
3. Singh, R., Schubele, B., and Sunkel, J., "Computationally Efficient Algorithm for the Dynamics of Multi-Link Mechanisms," AIAA Guidance, Navigation and Control Conference, August 14-16, 1989, Boston, Massachusetts.

4. Shabana, A., *Dynamics of Multibody Systems*, John Wiley & Sons, New York (1989).
5. Space Station Freedom Design Reference Missions (DRM), Revision 1, Working Copy, SSP-TBD, July 1991.
6. "Transmittal of IDEAS Solid Models representing the MTC Phase Review Configuration, based on Level III DPDR data", SSEIC transmittal memo, PSH-312-M091-338, August 2, 1991.

APPENDIX A

Instantaneous Inverse Kinematics

The kinematics equations of a robotic manipulator relate the joint displacements to the end-effector position and orientation. For instance, a given set of joint displacements can be used to calculate the resultant end-effector position and orientation. This is referred to as the direct kinematics problem. In this report, the inverse kinematics problem is discussed. For this problem, we find the associated joint displacements when given the desired end-effector position and orientation. Once the joint displacements are calculated, the desired end-effector trajectory can be achieved by moving each joint to the determined value. Since the kinematic equations are nonlinear, numerical methods are used to calculate the desired joint displacements.

To formulate the instantaneous kinematic equations for a general n degree-of-freedom manipulator arm, we begin with the definition of the vector \mathbf{X}_e , $\mathbf{X}_e \in R^m$, representing the end-effector motion and \mathbf{p} , $\mathbf{p} \in R^n$, representing the joint displacements in global coordinates. The degrees of freedom of the manipulator are not necessarily six, but at least six. Letting $d\mathbf{X}_e = [dx, dy, dz, d\theta_x, d\theta_y, d\theta_z]$ be the $m \times 1$ vector, which represents the infinitesimal displacements of the end-effector, then the instantaneous kinematic equation for a general n degree-of-freedom manipulator arm is given by

$$\mathbf{J}\Delta\mathbf{p} = \Delta\mathbf{X}_e \quad (A1)$$

where the dimension of the manipulator Jacobian \mathbf{J} is $m \times n$, and the change in the joint coordinates, $\Delta\mathbf{p} = [\Delta p_1, \Delta p_2, \dots, \Delta p_n]^T$, is the $n \times 1$ vector required to achieve the final position for the end-effector.

The Jacobian represents the infinitesimal relationship between the joint displacements and the end-effector location at the present position and arm configuration. When \mathbf{J} is of full rank and n is larger than m , there are $(n-m)$ arbitrary variables in the general solution of (A1). The manipulator is said to have $(n-m)$ redundant degrees of freedom for the given task. Otherwise, there exists at least one direction where the end-effector cannot be moved.

An optimal solution to equation (A1) can be found if we fix the Jacobian at an appropriate arm configuration, and find the optimal solution assuming the Jacobian is of full row rank. We evaluate the solutions to equation (A1) by the quadratic cost function of the joint displacement vector given by

$$G = \frac{1}{2} \Delta \mathbf{p}^T \mathbf{W} \Delta \mathbf{p}, \quad (A2)$$

where \mathbf{W} is an $n \times n$ symmetric positive definite weighting matrix. The problem is to find the $\Delta \mathbf{p}$ that satisfies (A1) for a given $\Delta \mathbf{X}_e$ and \mathbf{J} while minimizing the cost function G . This problem can be solved by using Lagrange multipliers.

Consider the modified performance index

$$g = \frac{1}{2} \Delta \mathbf{p}^T \mathbf{W} \Delta \mathbf{p} + \lambda^T (\mathbf{J} \Delta \mathbf{p} - \Delta \mathbf{X}_e) \quad (A3)$$

where λ is an $(m \times 1)$ vector of Lagrange multipliers. The necessary conditions that the optimal solution must satisfy are

$$\frac{\partial g}{\partial \mathbf{p}} = \mathbf{W} \Delta \mathbf{p} + \mathbf{J}^T \lambda = \mathbf{0}$$

which gives us

$$\Delta \mathbf{p} = -\mathbf{W}^{-1} \mathbf{J}^T \lambda. \quad (A4)$$

Substituting (A4) in (A1) and solving for $\Delta \mathbf{p}$ by eliminating λ , we have

$$\Delta \mathbf{p} = \mathbf{W}^{-1} \mathbf{J}^T (\mathbf{J} \mathbf{W}^{-1} \mathbf{J}^T)^{-1} \Delta \mathbf{X}_e. \quad (A5)$$

This approach is referred to as a minimum norm solution. Since equation (A5) is nonlinear, iteration of (A5) is often necessary to solve it.

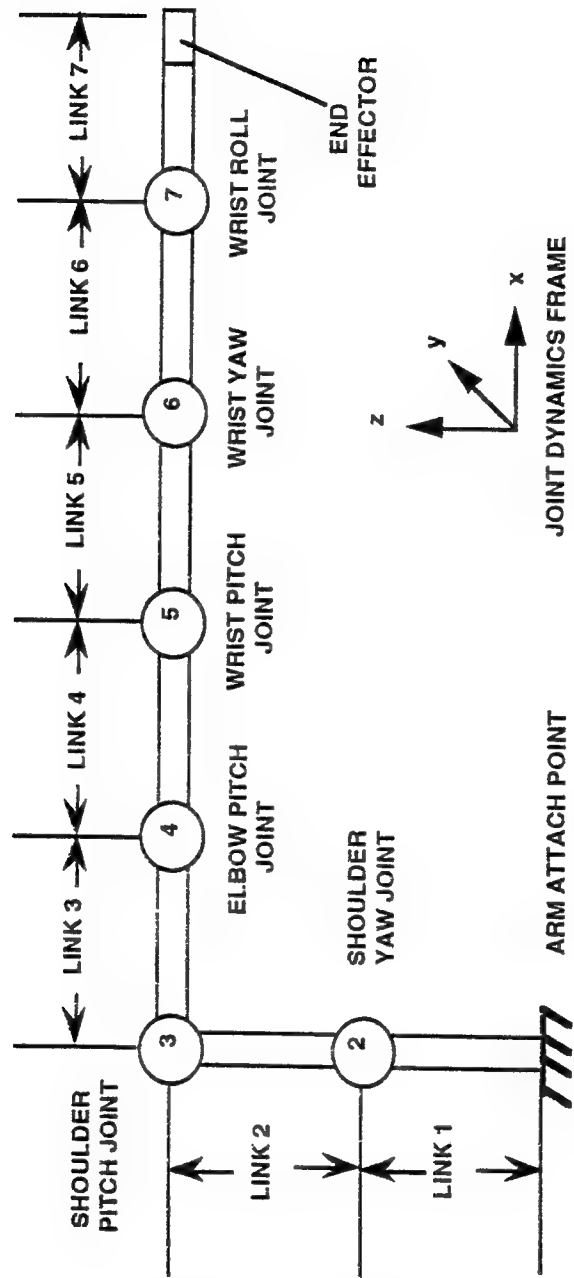


Figure A-1: SRMS Links

NOTE: Arm in reference configuration (not to scale).

Appendix B

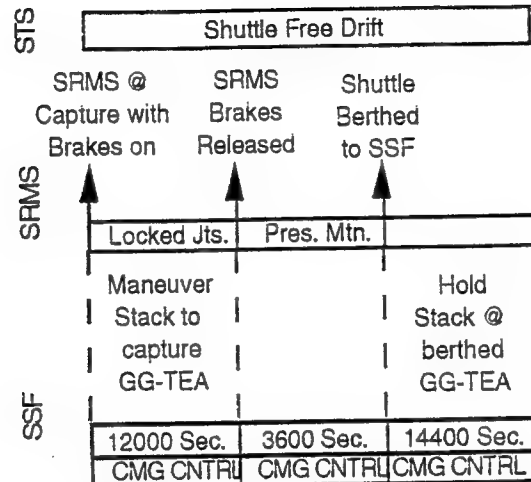


Figure B-1: Scenario 1

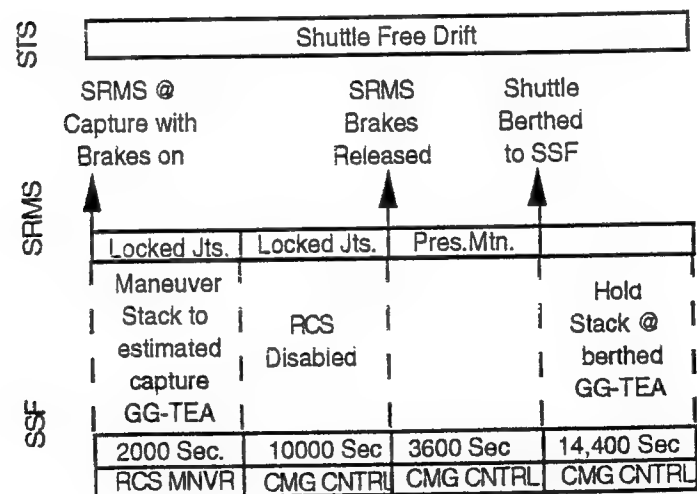


Figure B-2: Scenario 2

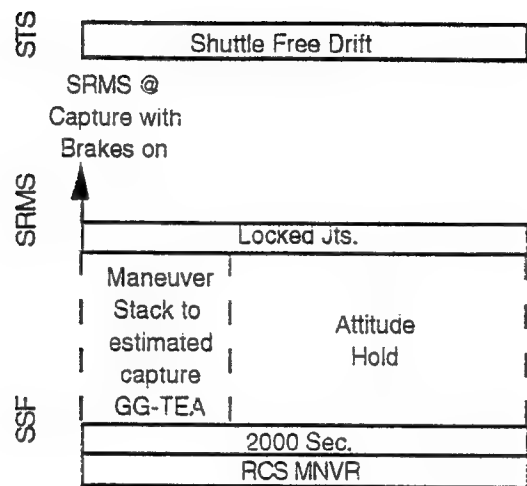


Figure B-3: Scenario 3

POSTER SESSION

**INTEGRATED MODELING OF
ADVANCED OPTICAL SYSTEMS**
Jet Propulsion Laboratory
California Institute of Technology
Pasadena, California
Hugh C. Briggs
Laura Needels
B. Martin Levine

This poster session paper describes an integrated modeling and analysis capability being developed at JPL under funding provided by the JPL Director's Discretionary Fund and the JPL Control/Structure Interaction Program (CSI). The posters briefly summarize the program capabilities and illustrate them with an example problem.

The computer programs developed under this effort will provide an unprecedented capability for integrated modeling and design of high performance optical spacecraft. The engineering disciplines supported include structural dynamics, controls, optics and thermodynamics. Such tools are needed in order to evaluate the end-to-end system performance of spacecraft such as OSI, POINTS, and SMMM.

This paper illustrates the proof-of-concept tools that have been developed to establish the technology requirements and demonstrate the new features of integrated modeling and design. The current program also includes implementation of a prototype tool based upon the CAESY environment being developed under the NASA Guidance and Control Research and Technology Computational Controls Program. This prototype will be available late in FY'92. The development plan proposes a major software production effort to fabricate, deliver, support and maintain a national-class tool from FY'93 through FY'95.

The proof-of-concept tools shown in the posters consist of the Controlled Optics Modeling Package (COMP) and the Integrated Modeling of Optical Systems (IMOS) Integration Workbench.

COMP is a stand-alone FORTRAN program for the analysis of optical systems. In COMP, a collection of optical elements are modeled as conical surfaces, fragments of conical surfaces, and surfaces tiled with hexagonal segments or refractive lenses. A mesh of rays, described by the user in the system input plane, is then propagated through the train of optical elements. Both geometric propagation and diffraction propagation are supported. Since COMP is intended to be used with structural dynamics modeling systems, methods are provided to compute the sensitivities of the optical system to perturbations in the element positions and orientations.

The IMOS Integration Workbench is a collection of Pro-Matlab functions to model structural dynamics by the finite element method and to integrate these models with COMP optical models. The discipline models are assembled in Pro-Matlab where the spacecraft end-to-end performance can be analyzed and trade studies conducted to design the system.

Application Examples

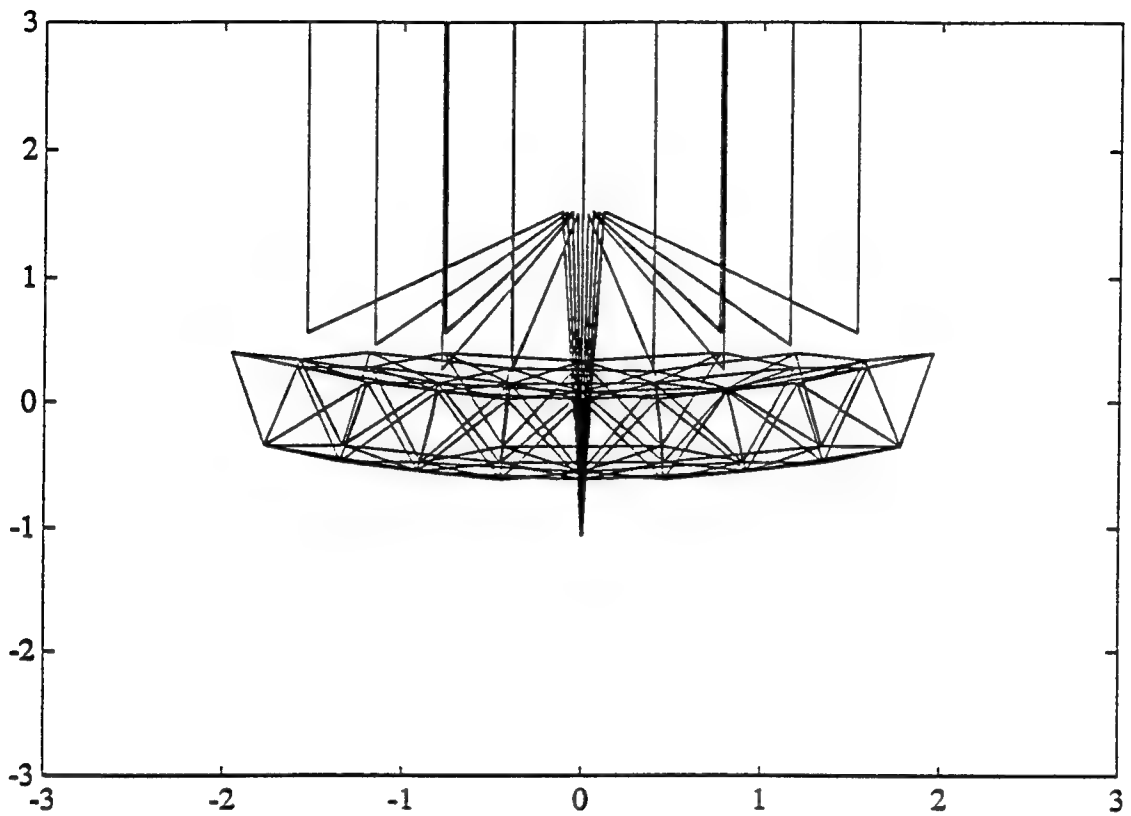
The capabilities of the proof-of-concept tools will be illustrated through two examples. A space telescope with a segmented primary reflector is the basis for the system model. The first case will show the impact of a typical vibration mode on the end-to-end performance of the telescope, and the second will consider a typical on-orbit temperature distribution. The point spread function and the spot diagram will, in both cases, be the measure of system performance. Other perturbations, not reported here, have included enforced base acceleration as might be expected in a laboratory test environment for the telescope.

The point spread function is considered the telescope optical impulse response function and is the image in the detector of a point source at infinity. The light from such a distant source enters the telescope as a plane wave and, in an unperturbed system, results in the delta-like function shown in the chart. Any perturbations to the telescope result in a reduction of the amplitude of the central spike and the introduction of significant off-axis or secondary lobes.

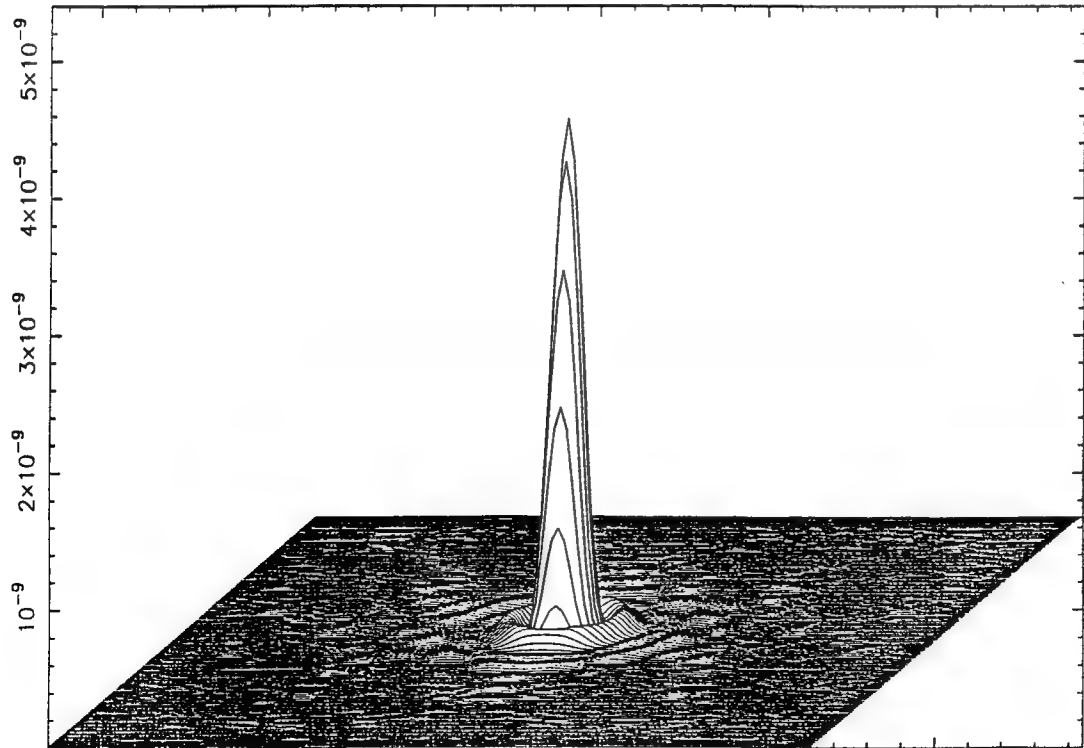
The spot diagrams represent the locations where rays pierce the plane of the detector. In an unperturbed focused system, all rays go through the focal point. When the system is perturbed, the rays no longer focus and hit the detector at other points. A system performance metric might be any function that measures the distance of these points from the focus.

The system model has structural dynamics elements to represent a primary-backup truss, a secondary with metering tower, and primary segments with three linear actuators for each panel. In the examples, the actuators are not commanded, as they might be to remove the distortion in the optical system, and maintain their nominal length. The optical system was modeled with COMP and included the primary segments and the secondary mirror. Surface-to-surface diffraction was utilized in computing the point spread functions while geometric optics was used to compute the spot diagrams.

Optical and Structural Model



The Unperturbed System Point Spread Function



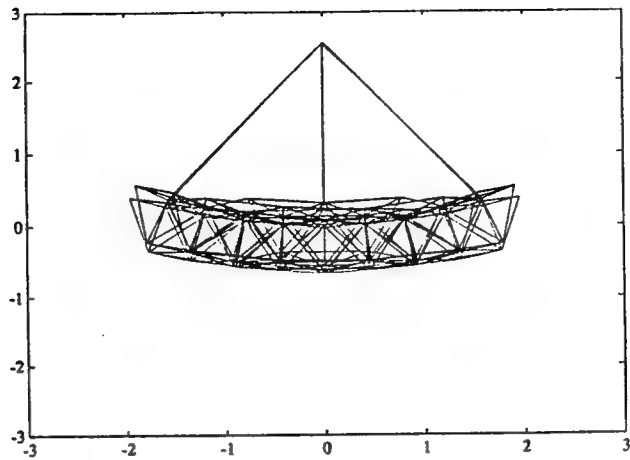
Impact of Modal Vibration

The integrated tools can be used to evaluate the performance impact of any system perturbation, where it is static or dynamic. This chart shows the 8th system mode of vibration, and the spot diagram and point spread function corresponding to this perturbation. The 8th mode is one of the lower frequency truss bending modes that, if uncorrected, alters the radius of curvature of the primary. The upper figure shows the deformed shape, greatly amplified for clarity, superimposed on the nominal structural model.

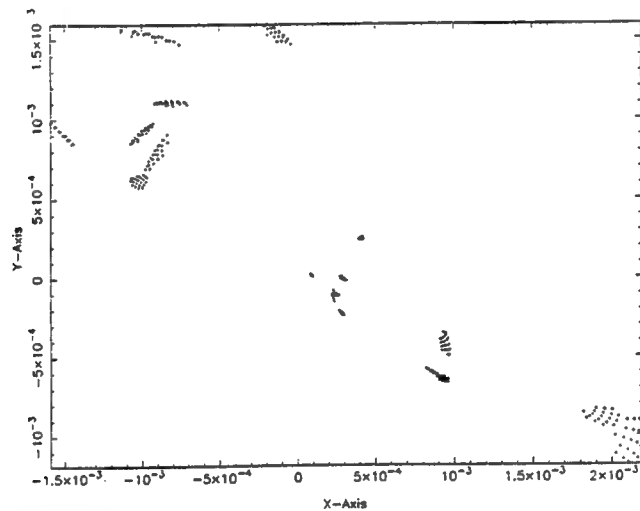
The middle figure shows the location of the rays in the plane of the detector and the lower figure shows the point spread function when the system is deformed into this shape. These figures were created in COMP by applying the 8th mode shape as a perturbation to the optical elements. Notice the reduction in the height of the central peak and the presence of side lobes.

Similar figures have been obtained to show the results of time domain simulations of response to base accelerations. Other measures of the performance might be time series of motions of the rays in the detector or animations of the point spread function. See, for example, "Integrated Control/ Structures/Optics Dynamic Performance Modeling of a Segmented Reflector Telescope" by H. C. Briggs, D. C. Redding, and C. C. Ih in the Proceedings of the Twenty-First Annual Pittsburgh Conference on Modeling and Simulation, 3-4 May, 1990.

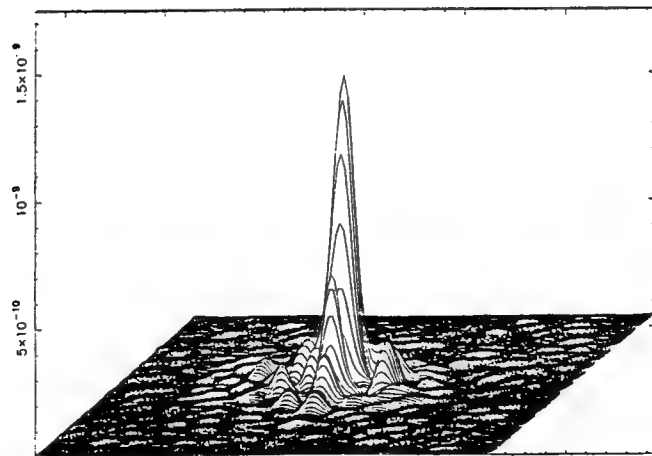
8th Structural Mode of Vibration



Spot Diagram for the 8th Mode



Point Spread Function for the 8th Mode



Impact of Temperature Variations

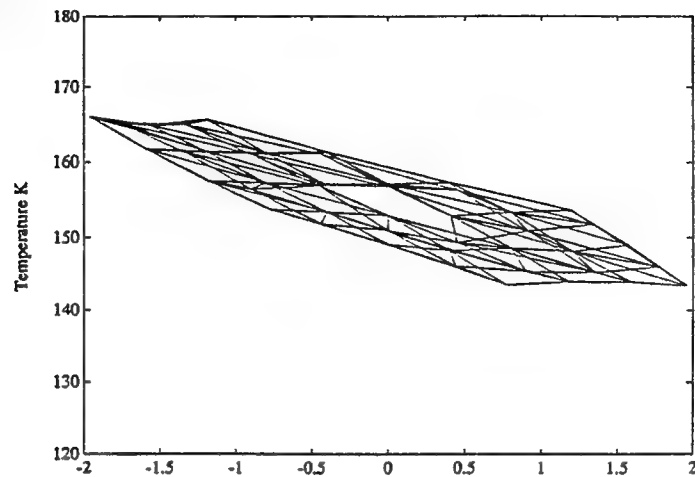
The second example illustrates the optical performance impact of a non-uniform temperature variation across the telescope. The upper figure shows the temperature distribution imposed upon the primary mirror support truss. The structural deformations resulting from thermal expansion were computed and applied to the optical model to compute the performance metrics below. The temperatures were taken from a study of an IR telescope in earth orbit and represent a single case that contained significant thermal variation. See "The Precision Segmented Reflector Program: On-Orbit Thermal Behavior of the Submillimeter Imager and Line Survey Telescope" by G. Tsuyuki and M. Mahoney, AIAA Paper 91-1304, for information concerning the independent thermal analysis.

Again, the middle figure shows the spot diagram and the lower figure shows the point spread function.

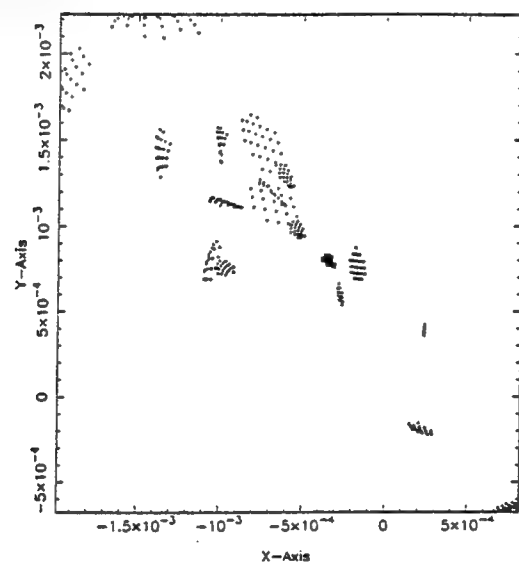
Acknowledgment

The research described in this paper was performed at the Jet Propulsion Laboratory, California Institute of Technology, under contract with the National Aeronautics and Space Administration.

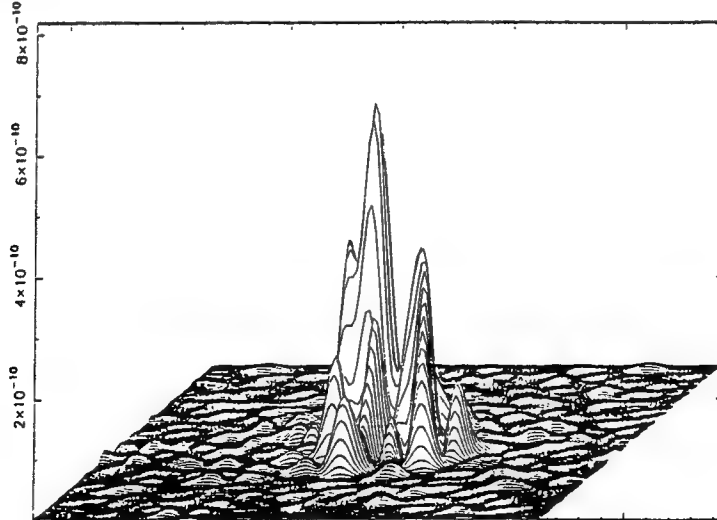
Temperature Variation Across the Truss

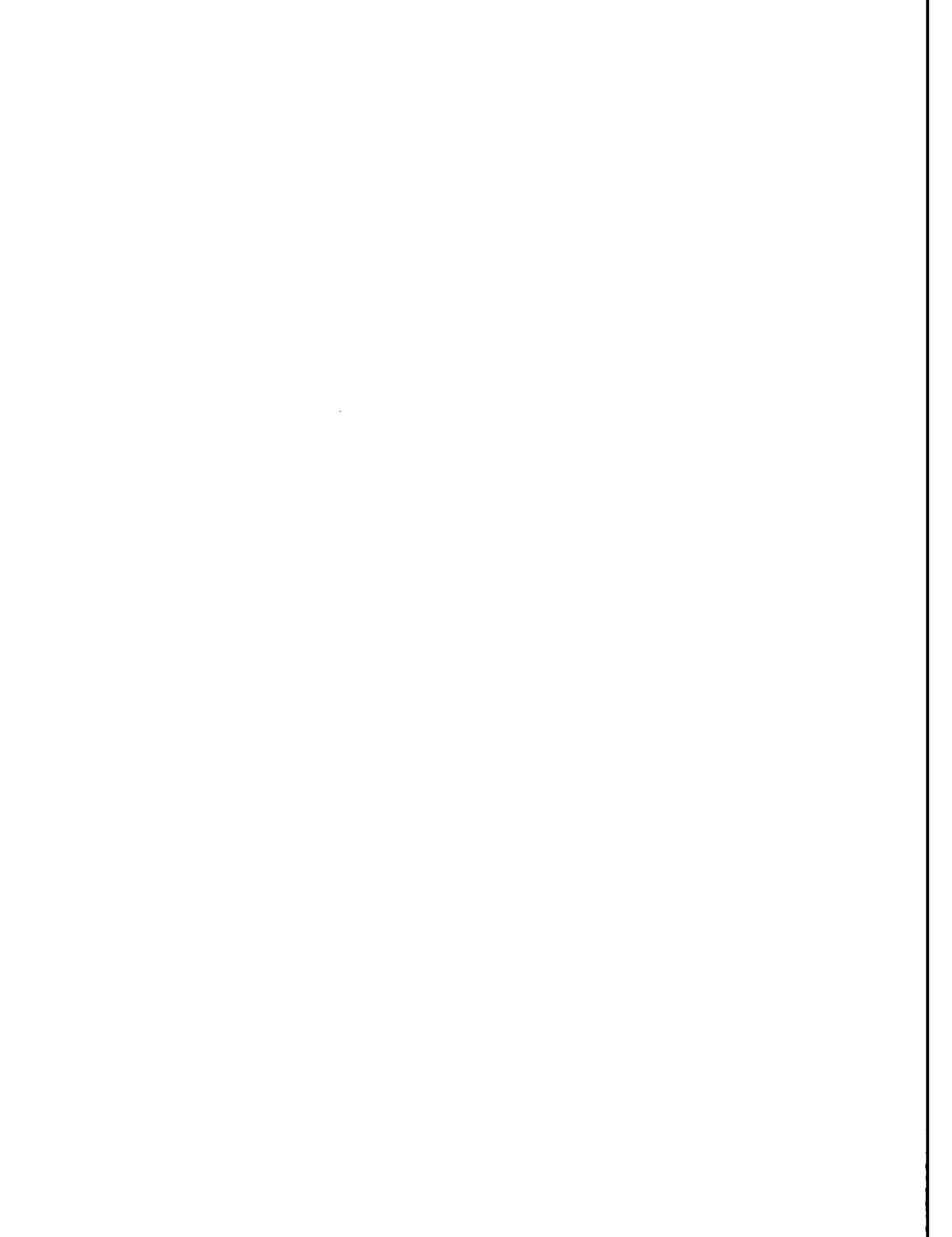


Spot Diagram for the Temperature Variation



Point Spread Function for the Temperature Variation



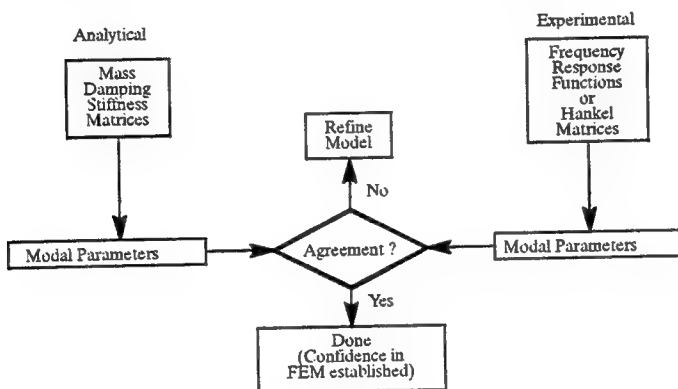


A Comparison of Refined Models for Flexible Subassemblies

Suzanne Weaver Smith
University of Kentucky

David C. Zimmerman
University of Florida

MODEL REFINEMENT – OVERVIEW



- Model Refinement Necessary to Validate Analytical Models
- Comparison of Analytical and Experimental Eigensolution Used to Assess Accuracy of Models
- Several Approaches Have Been Developed in Recent Years, but Performance Comparisons Have Not Been Available

Interactions between structure response and control of large flexible space systems have challenged current modeling techniques and have prompted development of new techniques for model improvement. Due to the geometric complexity of envisioned large flexible space structures, finite element models (FEMs) will be used to predict the dynamic characteristics of structural components. It is widely accepted that these models must be experimentally “validated” before their acceptance as the basis for final design analysis. However, predictions of modal properties (natural frequencies, mode shapes, and damping ratios) are often in error when compared to those obtained from Experimental Modal Analysis (EMA). Recent research efforts have resulted in the development of algorithmic approaches for model improvement [1], also referred to as system or structure identification.

MODEL REFINEMENT – METHODS

● Optimal Update Approach

- Methods are formulated as a constrained optimization problem
- FEM property matrices (K,D, or M) are updated

● Eigenstructure Assignment Approach

- Methods are formulated using pseudo–output feedback eigenstructure assignment
- FEM property matrices (K,D, or M) are updated

● Model Sensitivity Approach

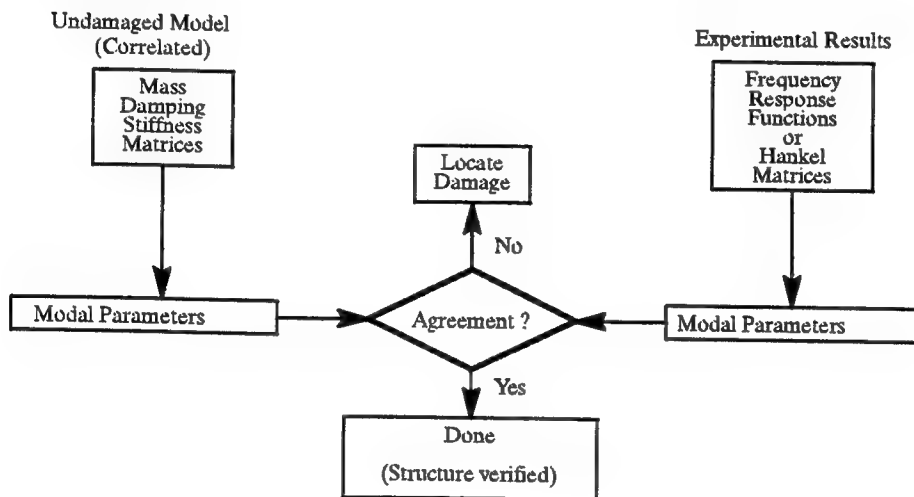
- Methods are formulated using design sensitivities
- Physical property parameters (areas, lengths, elastic moduli, etc.) are updated

● Other Approaches

Among others, three approaches for linear–system identification are; optimal–update [2–5], eigenstructure assignment [6–9] and design sensitivity [10,11]. Optimal–update identification techniques produce, through the solution of a constrained optimization problem, updated property matrices (i.e., stiffness, damping or mass matrices) to more closely match the experimental modal properties. Eigenstructure assignment techniques for structure identification use a pseudo–output feedback formulation to update the structure property matrices. Design sensitivity techniques use parameter sensitivities from the initial model and use modal properties from the test structure to determine parameter adjustments. The adjusted parameters may represent physical or material properties, like cross–section area or elastic modulus. Comparisons between techniques and between general approaches are not readily available. In this work, two promising system identification approaches are examined and compared through a study of flexible components that are subassemblies of more complex structures.

DAMAGE DETECTION

- Some Model Refinement Techniques May Prove Useful For Nondestructive Damage Detection
- Damage Location is Analogous to Model Refinement with a Localized Error
- An Initial Model Correlated to the Undamaged System is Required



With the approaches that have been developed for model refinement, a similar framework can be used to monitor structural integrity. For damage location, an initial model that has been accepted as an accurate representation of the undamaged structure is necessary. Predictions of dynamic characteristics from this model are compared to modal characteristics that are determined experimentally. Model refinement techniques employ differences between these characteristics to produce adjusted models that are then compared to the initial correlated model to indicate the location of possible damage. Structural damage is likely to occur at discrete locations, whereas modelling errors may be either discrete or "smeared" or both, due to uncertainties in the material properties, assumptions in the modeling process or errors in part fabrication, among others. Therefore, different mathematical formulations may be required for the different situations of model refinement and damage location.

OPTIMAL UPDATE APPROACH

- For the Update, the Refined Model Must Satisfy
A Constrained Optimization Problem

Formulation 1:

$$\begin{aligned} & \min \| A - A_a \|_F \\ & \text{subject to } AS = Y, A = A^t \text{ and other constraints} \end{aligned}$$

Formulation 2:

$$\begin{aligned} & \min \| AS - Y \|_F \\ & \text{subject to } A = A^t \text{ and other constraints} \end{aligned}$$

- Preservation of the Zero/Nonzero Pattern in the Update Reduces the Amount of Data Required
- Optimal-Update Techniques are Well-Suited for the Identification of Sparse Truss Models

A recent work [4] separated techniques encompassed by the “optimal-update” classification into two formulation viewpoints. These are based on the cost function and the constraints of the minimization problem that is established to produce the update. The first view was used by Baruch and Bar Itzhack [2] and by Smith and Beattie [3] in their methods for stiffness matrix adjustment. Generally in this view, the cost function is formulated to minimize the distance from the initial model. Additional constraints preserve symmetry and represent the imposition of the measured modal data, among others. Here, A is the $n \times n$ adjusted property matrix, A_a is the $n \times n$ initial-model property matrix, and S and Y are the $n \times p$ matrices that define the constraints with the measured data. The matrix Frobenius norm is used for the distance measure. The second view for framing the optimal-update problem follows a slightly different formulation allowing for the probability of inconsistent data, modal data which cannot be matched exactly, due to noise and errors. Generally in techniques from this viewpoint, the cost function minimizes the residual between the updated property matrix and the measured data. Then additional constraints are imposed as well. Techniques in both viewpoints have been developed to preserve the zero/nonzero pattern of the property matrix which reduces the number of measured modes that are needed. These methods are especially suited for truss structures, which have considerable sparsity in the FEM mass and stiffness matrices.

EIGENSTRUCTURE ASSIGNMENT APPROACH

- For Stiffness Update, the Refined Model Must Satisfy The Eigenproblem for Each Measured Mode

$$MV_d \Lambda_d + KV_d = \Delta K_d V_d$$

$$\Lambda_d = \text{diag}(\lambda_{d_1}^2, \lambda_{d_2}^2, \dots, \lambda_{d_p}^2) \quad (\text{Measured Eigenvalues})$$

$$V_d = [v_{d_1}, v_{d_2}, \dots, v_{d_p}] \quad (\text{Measured Eigenvectors})$$

- Translate Perturbation Matrix into Pseudo-Output Feedback

$$MV_d \Lambda_d + KV_d = \Delta K_d V_d = (B_o G) V_d \quad G = FC = HB_o^T$$

where $B_o = MV_d \Lambda_d + KV_d$, the Control Influence Matrix
Required for Perfect Eigenstructure Assignment (B_o also provides information concerning DOF damage)

- The Perturbation Matrix

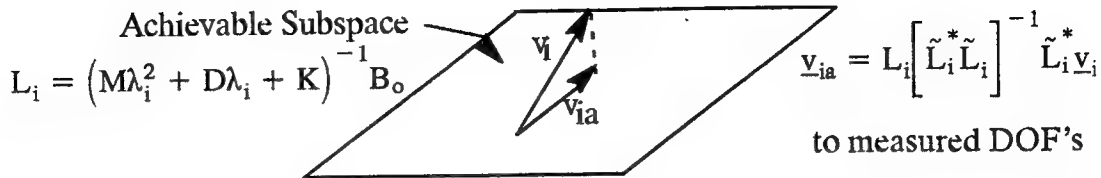
$$\Delta K_d = B_o (B_o^T V_d)^{-1} B_o^T$$

- Results in a Rank p Update of Model

Several Eigenstructure Assignment based approaches have recently been investigated. The simplest, in both equation and computational complexity; involves the problem of an undamped multi-degree-of-freedom (MDOF) system in which the mass matrix is assumed to be correct and it is desired to determine a symmetric stiffness adjustment such that the updated model matches the p measured eigenvalues/vectors [8]. The technique uses the mathematical framework of a pseudo-output feedback eigenstructure assignment where the pseudo-outputs are the structural positions. The control influence matrix B_o is chosen such that perfect eigenvector assignment is achieved [9]. In Ref. 8, it is proven that: (i) the update is symmetric if the assigned eigenvectors are mass orthogonal and (ii) that if the exact perturbation matrix (which is essentially what model refinement procedures are attempting to estimate) is a rank p matrix, the calculated perturbation is the exact matrix if p correct (i.e. no measurement errors) eigenvalues/vectors are measured. This makes this technique especially well-suited for discrete model errors/damage. Techniques to incorporate damping and mass changes have also been developed.

EIGENVECTOR EXPANSION

- Optimal Least Squares Technique Involves Both Expansion and Projection Into Achievable Subspace



- Orthogonal Procrustes Expansion

$$v = \begin{bmatrix} u_e \\ d_e \end{bmatrix} = \begin{bmatrix} u_a \\ d_a \end{bmatrix} P_{op}$$

u – measured DOF's eigenvectors
 d – unmeasured DOF's eigenvectors
 $(\cdot)_e$ – experimental
 $(\cdot)_a$ – analytical(FEM)

- Optimal Rotation of Analytical Into Experimental

$$\min_{\substack{\text{wrt} \\ P_{op}}} \|u_e - u_a P_{op}\|_F \quad \text{subject to } P_{op}^T P_{op} = I_p$$

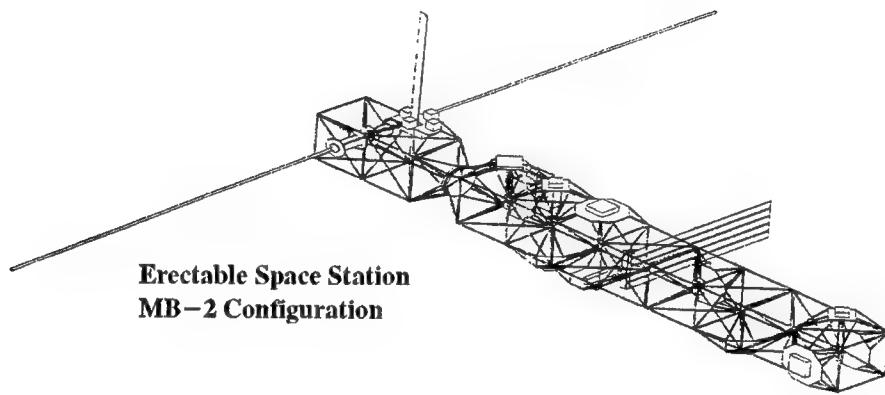
- Two Possible Expansions

$$v = \begin{bmatrix} u_a \\ d_a \end{bmatrix} P_{op} \quad v = \begin{bmatrix} u_e \\ d_a P_{op} \end{bmatrix}$$

Common to all model refinement algorithms, the dimension of the experimentally measured eigenvectors is usually much less than that of the FEM eigenvectors due to practical EMA testing limitations. One solution to this problem is to employ a model reduction technique so that the reduced dimension and DOF's of the analytical model match that of the experimentally measured eigenvector. An alternative approach, which is employed in this work, is to expand the measured eigenvector to the size of the analytical eigenvector [1]. An examination of the eigenvalue problem reveals that the expanded eigenvector must lie in the space spanned by the columns of L_i , which depends both on the original FEM, the measured eigenvalue, and an arbitrary matrix B_o . Two techniques have been investigated: one involves the expansion and projection of the eigenvectors into the achievable subspace. An alternate approach uses the mathematical framework of the classic Orthogonal Procrustes Problem to rotate a portion of the analytical modal matrix into the experimental modal matrix. It is then assumed that this rotation matrix can be used to rotate the unmeasured components to provide an estimate of the complete eigenvector [12].

CASE STUDIES

- **8-Bay Laboratory Truss Structure**
 - a subassembly of the Dynamic Scale Model Technology (DSMT) program at NASA Langley Research Center
 - 96 dof model; 6 measured frequencies, 96 measured dofs
- **CASE I**
 - Model refinement for the undamaged truss
- **CASE II**
 - Damage location of a missing member

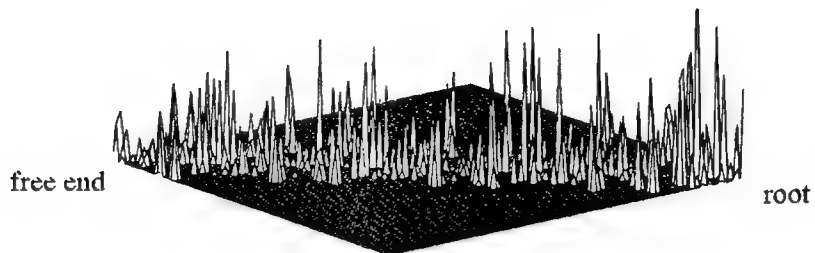


The 8-bay hybrid-scaled truss structure used for this investigation is part of a series of structures designed for research in dynamic scale model ground testing of large space structures. This truss, with the same number of bays as the primary structure in the erectable Space Station MB-2 configuration, is a focus structure in an ongoing effort to examine damage detection [13]. For testing, the truss was cantilevered and instrumented with 96 accelerometers to measure three translational DOF's at each node. The number of acceleration measurements (at all degrees of freedom of the model) is unusual, but provides an opportunity to select subsets of the measurements in future studies of instrumentation placement schemes. Three simultaneous excitation sources were used. Six frequencies and corresponding mode shapes were extracted using the Polyreference complex exponential technique. Each truss member was modeled as a rod element. Concentrated masses were added at the nodes to represent the nodes and instrumentation. Tests were conducted for an undamaged situation and a damaged situation, with truss element number 35 removed.

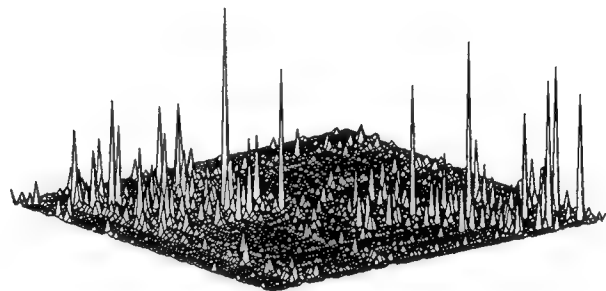
CASE I

Undamaged 8-Bay Truss Structure

- Optimal-Update Approach



- Eigenstructure Assignment Approach

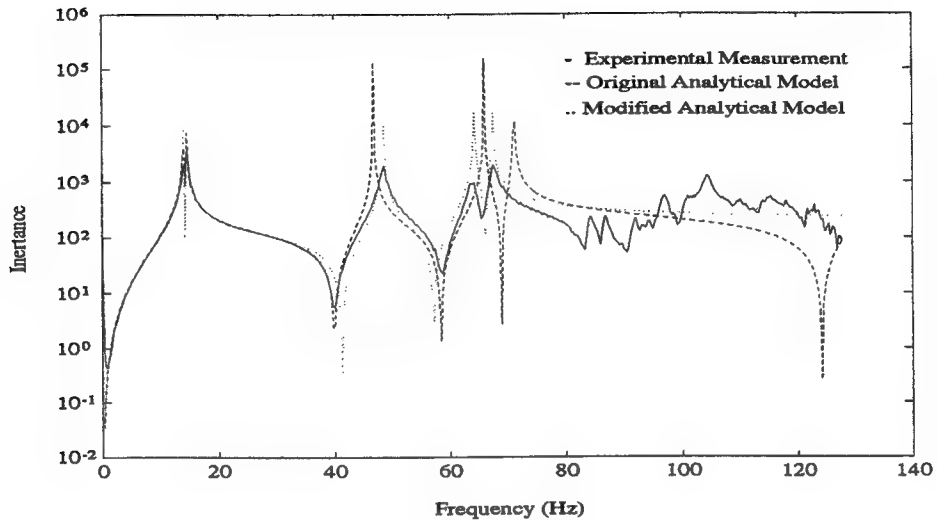


A mesh plot of the difference matrix ($\Delta K_d = K_{\text{final}} - K_{\text{initial}}$) provides a visual representation of the stiffness update. Here, the absolute values of the difference matrix are plotted for the two approaches. An iterative, first-viewpoint, optimal-update approach [5] produced an adjusted stiffness model which had the largest changes at the cantilevered end of the truss, but numerous changes at the free end. The sparsity preserving eigenstructure assignment approach used 10 iterations to achieve its refined stiffness model. As can be seen from the mesh plot of the perturbation matrix (ΔK_d), this algorithm clearly focuses the majority of the changes at the cantilever end and the free end. The model refinement is obviously correcting for the imperfect cantilever condition. In addition, it should be noted that test shakers, which were not included in the analytical model, were mounted near the free end.

CASE I

Undamaged 8-Bay Truss Structure

● Eigenstructure Assignment Approach

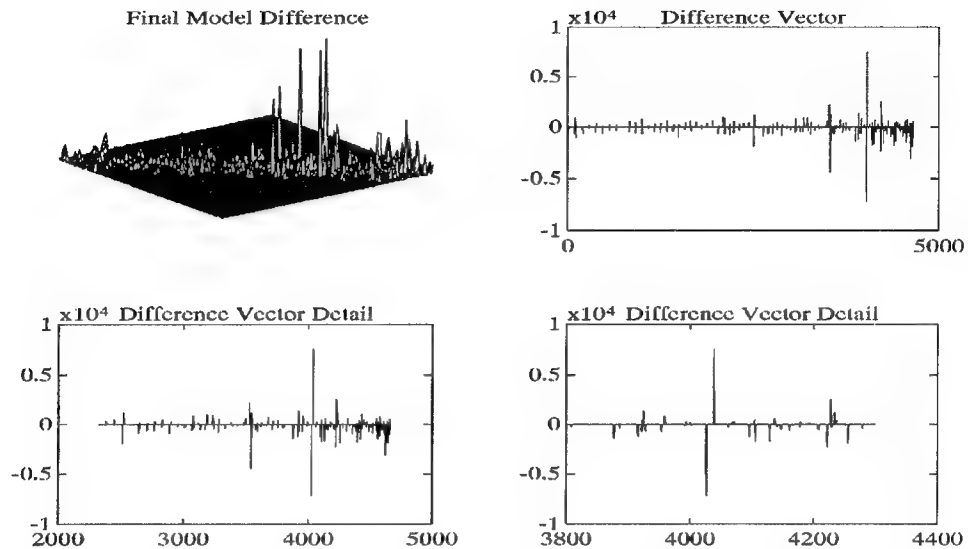


A frequency response function for one driving point of the truss is shown in the figure above. In the figure, the solid line corresponds to the experimental measurement, the dashed line corresponds to the initial FEM, and the dotted line corresponds to the refined FEM from the eigenstructure assignment approach. Note that both FEM's have a zero damping matrix. The importance of including a damping model is seen in Case Study III. This comparison of the results shows some discrepancy between the experimental ff and the updated model version. The measured frequencies used for the update do not correspond exactly to the peaks of this function. Even with that, the updated model is considerably improved.

CASE II

“Case H” Damage for the 8–Bay Truss

- Optimal–Update Approach



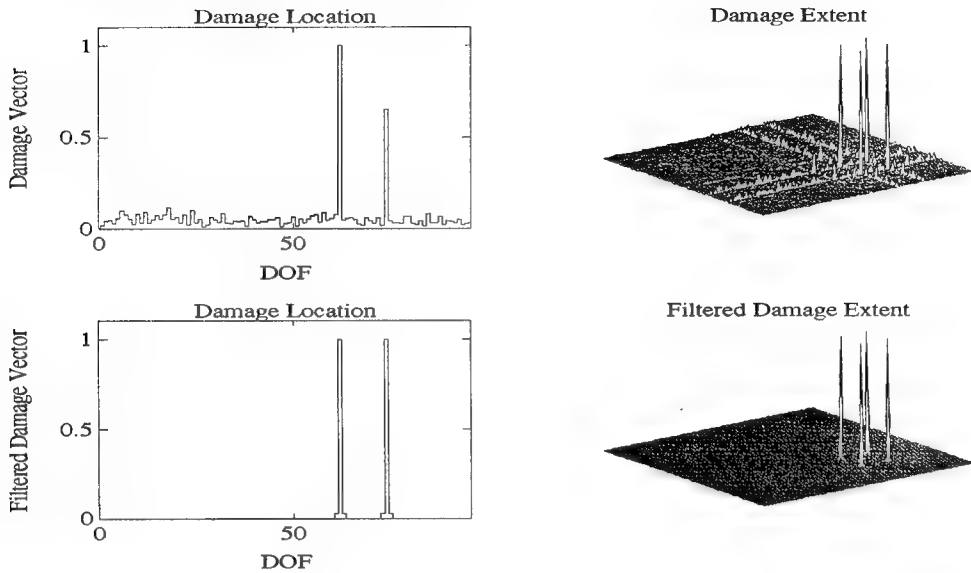
- Model Difference is ΔK_d ; Difference Vector is Upper Triangle of ΔK_d
- Typical Damage Pattern is Evident for Element from dof 62 to dof 74 – Member 35

“Case H” damage of the 8-bay truss is the removal of longeron member number 35. The iterative optimal update approach produced an adjusted stiffness model for the truss using the six measured frequencies and mode shapes. The mesh plot of the difference between the refined model and the model representing the undamaged truss indicates the location of the damaged member. The maximum difference occurs for the matrix off-diagonal elements (62,74) and (74,62), indicating the truss member that connects these two DOF’s – member number 35. A vector that stores the upper triangle of the difference matrix, row by row, is plotted to examine the magnitude of the damage. Here the maximum difference is of the same order as the stiffness of the removed member, indicating the considerable loss of stiffness in this case. Detail plots show a typical damage pattern for a damaged longeron or batten. At the root and free ends, the relatively small effects represent the update for the undamaged situation, which was not incorporated prior to this case study.

CASE II

“Case H” Damage for the 8–Bay Truss

- Eigenstructure Assignment Approach



- Upper Left is B_o the Damage Vector; Upper Right is ΔK_d
- Filtering of Experimental Measurements Making Use of the Damage Vector Enhances ΔK_d Estimate

In the eigenstructure assignment approach for damage detection, damage location and extent can be decoupled. Inspection of the B_o vector (or matrix if more than one eigenvector is measured) gives a direct indication of which degrees of freedom have been most affected by damage. In fact, when B_o is calculated using noise-free measurements (perfect eigenvalue/eigenvector information), degrees of freedom that are not directly influenced by damage will have a corresponding zero element in B_o . From the upper left plot, which has the elements of B_o plotted versus degree of freedom, it is clear that two degrees of freedom (62 and 74) have been most affected by damage. These are exactly the degrees of freedom that were coupled before the truss member was removed. The small numerical elements at all other degrees of freedom can be attributed to experimental measurement errors. Note that the damage location problem is performed independent of the damage extent problem. The upper right figure shows ΔK_d using the B_o of the upper left figure. To improve the damage extent estimate, a filtering algorithm for B_o has been developed which sets to zero those elements of B_o that are below a specified threshold (related to the maximum element of B_o). The results of applying the filtering algorithm are shown in the lower two plots. Details of this decoupled damage location and extent algorithm can be found in Zimmerman and Kaouk [9].

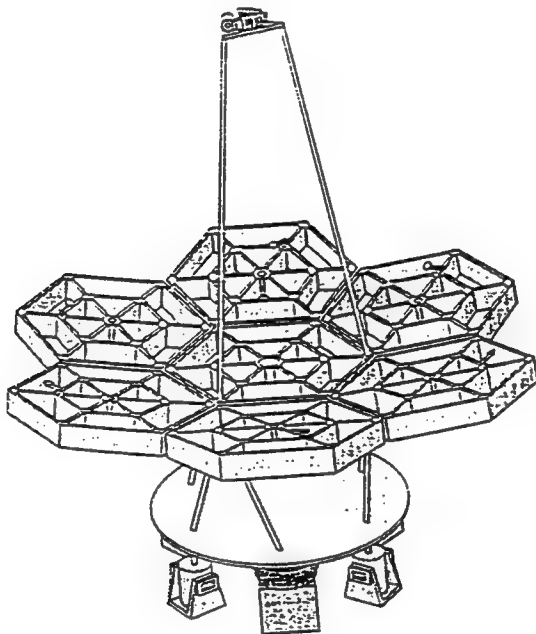
CASE STUDIES

- **Tower Substructure**

- a subassembly of the Multi-Hex Prototype Experiment at Harris Corporation
 - 57 dof model; 8 measured eigenvalues, analytical eigenvectors

- **CASE III**

- Model refinement for the tower structure

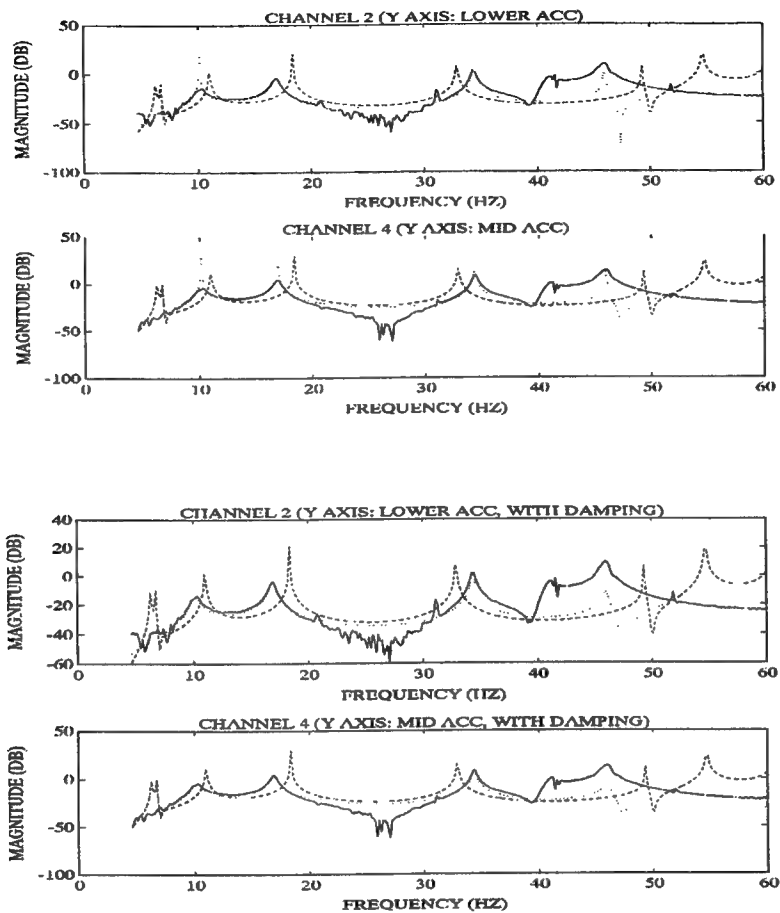


The Harris Multi-Hex Prototype Experiment (MHPE) test structure design incorporates many of the features and technology of the Harris Solar Dynamic Concentrator. The major structural subsystems include the reflector surface (the seven panel array), the secondary tower (tripod) and the base plate/support system. In this particular study, the secondary tower was removed from the reflector surface and hard mounted to ground. Three linear precision actuators (LPACTS) were used as excitation sources in performing the modal survey of the tower. One leg of the tower was instrumented with 6 translational accelerometers. Velocity estimates at the LPACT locations served as 3 additional outputs. The three tower struts were modeled as 12 beam elements (4 per strut). The tower top was modeled as 9 beam elements. Fittings connecting the tower struts to the tower top and to the center panel were included as point masses, as was the stationary part of the LPACT. The moving proof-mass of each tower LPACT was modeled as a point mass attached to the tower top by springs. The Eigensystem Realization Algorithm (ERA) was used to estimate the experimental eigenvalues and eigenvectors. Because of the limited sensor spatial resolution, only the experimental eigenvalues were used. It has been assumed that the original analytical eigenvectors match those that would have been measured.

CASE III

Model Refinement for the Tower Structure

Optimal-Update Approach

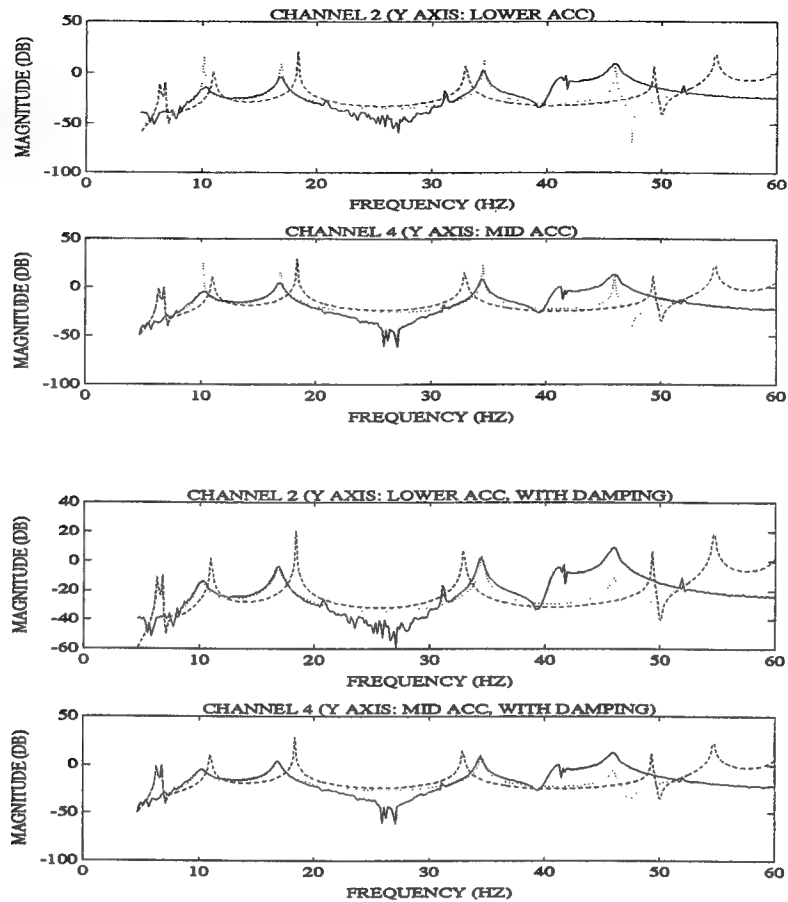


In each figure above (showing results of the optimal-update approach) and for the next slide (showing results of the eigenstructure assignment approach) the solid line corresponds to the experimental measurement, the dashed line corresponds to the initial FEM (provided by Harris), and the dotted line corresponds to the refined FEM. In the top pair of plots, both FEM's have a zero damping matrix; the finite peaks at the resonant frequencies are only due to the frequency spacing at which the frequency response functions have been calculated. It is obvious that there is improvement in frequency matching; however the amplitude mismatch between experiment and refined FEM is of some concern. There are two main causes of this mismatch (i) using the original mode shapes and (ii), not including the effects of damping. It should be noted that for both approaches, the magnitude of the elements of the perturbation stiffness matrix was quite small. In fact, the maximum element was of the order 10, whereas the original stiffness elements are several orders of magnitude higher. This result is not surprising in that it is known from control theory that moving eigenvalues requires less control effort than moving both eigenvalues *and* eigenvectors.

CASE III

Model Refinement for the Tower Structure

- Eigenstructure Assignment Approach



In the second test for both approaches, a “modal” damping matrix was calculated using the measured eigenvalue ($2\zeta_i\omega_n$) and the original eigenvectors. With the original eigenvectors mass orthogonalized, a physical damping matrix was approximated by the following:

$$C = MU \text{ diag}(2\zeta_i\omega_n) U^T M,$$

where M is the mass matrix, U is the orthonormal eigenvector matrix, and $\text{diag}(2\zeta_i\omega_n)$ is a diagonal “modal” damping matrix. The effect of introducing this damping matrix in the frequency response calculation is shown in the bottom pair of plots for each approach. Here, the solid line corresponds to the experimental measurement, the dashed line corresponds to the initial FEM, and the dotted line corresponds to the FEM in which both the stiffness matrix has been updated and the experimental damping matrix has been included. In comparing the two figures for both approaches, it is clear that introduction of the damping model greatly enhances the amplitude matching of the resonant peaks, as well as providing better matching throughout the frequency response.

SUMMARY

- **Two Promising Approaches for Model Refinement were Examined and Compared with Data from Real Structures**
- **Optimal-Update Methods are a Viable Approach for Model Improvement and Damage Location**
 - Refined analytical results agree with experiment
 - Techniques are well-suited for sparse models
- **Output Feedback Approach Produces Excellent Agreement Between Analytical and Experimental Results**
 - With p measured modes, produces a rank p update
 - Algorithm computationally feasible for large FEM's (inverse of a $p \times p$ matrix)
- **Continuing Studies Will Examine Other Structure Types, Sensor Placement, and Model Refinement for Assemblies**

To date, new techniques for model refinement have most often been presented with an application to a simulated example, without a basis for comparison of different methods and approaches. In this work, performance of techniques from two approaches were compared through studies with real data via the updated stiffness matrix results, frequency response of the improved models with respect to experimental measurements, and physical interpretation of the refinements. Optimal-update and eigenstructure assignment approaches both demonstrate their viability for model refinement and damage location. Differences in the approach formulations have been examined. With these results, strengths and weaknesses of approaches and specific techniques are more readily available for CSI applications of model improvement.

Acknowledgements

Suzanne Weaver Smith's work was supported by NASA grant NAG-1-1246. David C. Zimmerman's work was supported by a joint grant from Harris Corporation and the Florida Space Grant Consortium. The authors also wish to thank M. Kaouk and G.W. Felts for their assistance with the numerical illustrations.

References

1. Zimmerman, D.C. and S.W. Smith, "Model Refinement and Damage Location for Intelligent Structures," to appear in Intelligent Structural Systems, H.S. Tzou, and G. L. Anderson Editors, Kluwer Academic Publishers, 1992.
2. Baruch, M. and I.Y. Bar Itzhack, "Optimum Weighted Orthogonalization of Measured Modes," AIAA Journal, Vol. 16, No. 4, April 1978, pp. 346-351.
3. Smith, S.W. and C.A. Beattie, "Secant-Method Adjustment Using Mode Data," AIAA Journal, Vol. 29, No. 1, January 1991, pp. 119-126.
4. Smith, S.W. and C.A. Beattie, "Optimal Identification Using Inconsistent Modal Data," Proceedings of the AIAA/ASME/ASCE/AHS/ASC 32nd Structures, Structural Dynamics and Materials Conference, Baltimore, Maryland, April 8-10, 1991, pp. 2319-2324.
5. Smith, S.W., "Iterative Use of Direct Matrix Updates: Connectivity and Convergence," Proceedings of the 33rd AIAA SDM Conference, Dallas, Texas, April 13-15, 1992, pp. 1797-1806.
6. Minas, C. and D.J. Inman, "Matching Finite Element Models to Modal Data," ASME Journal of Vibration and Acoustics, Vol. 112, January 1990, pp. 84-92.
7. Zimmerman, D.C. and M. Widengren, "Correcting Finite Element Models Using a Symmetric Eigenstructure Assignment Technique," AIAA Journal, Vol. 28, No. 9, September 1990, pp. 1670-1676.
8. Zimmerman, D.C. and M. Kaouk, "Structural Damage Detection Using a Subspace Rotation Algorithm," Proceedings of the 33rd AIAA SDM Conference, Dallas, Texas, April 13-15, 1992, pp. 2341-2350.
9. Zimmerman, D.C. and M. Kaouk, "An Eigenstructure Assignment Approach For Structural Damage Detection," AIAA Journal, Vol. 30, No. 4, July 1992, pp. 1848-1857.
10. Flanigan, C.C., "Correlation of Finite Element Models Using Mode Shape Design Sensitivity," Proceedings of the 9th International Modal Analysis Conference (IMAC), Florence, Italy, 1991.
11. Martinez, D.R., et. al., "System Identification Methods for Dynamic Structural Models of Electronic Packages," Proceedings of the AIAA/ASME/ASCE/AHS/ASC 32nd Structures, Structural Dynamics and Materials Conference, Baltimore, Maryland, April 8-10, 1991, pp. 2336-2345.
12. Smith, S.W. and C.A. Beattie, "Simultaneous Expansion and Orthogonalization of Measured Modes for Structure Identification," Proceedings of the AIAA SDM Dynamics Specialist Conference, Long Beach, California, April 5-6, 1990, pp. 261-270.
13. Kashangaki, T.A.-L., "On-Orbit Damage Detection and Health Monitoring of Large Space Trusses - Status and Critical Issues," Proceedings of the AIAA/ASME/ASCE/AHS/ASC 32nd Structures, Structural Dynamics and Materials Conference, Baltimore, Maryland, April 8-10, 1991, pp. 2947-2958.

THE JPL PHASE B INTERFEROMETER TESTBED

Daniel Eldred and Mike O'Neal
Jet Propulsion Laboratory
Pasadena, CA 91109

INTRODUCTION

Future NASA missions with large optical systems will require alignment stability at the nanometer level. However, design studies indicate that vibration resulting from on-board disturbances can cause jitter at levels three to four orders of magnitude greater than this. Feasibility studies have shown that a combination of three distinct control layers will be required for these missions, including disturbance isolation, active and passive structural vibration suppression, and active optical pathlength compensation. The CSI technology challenge is to develop these design and control approaches that can reduce vibrations in the optical train by a factor of 1000 to 10,000.

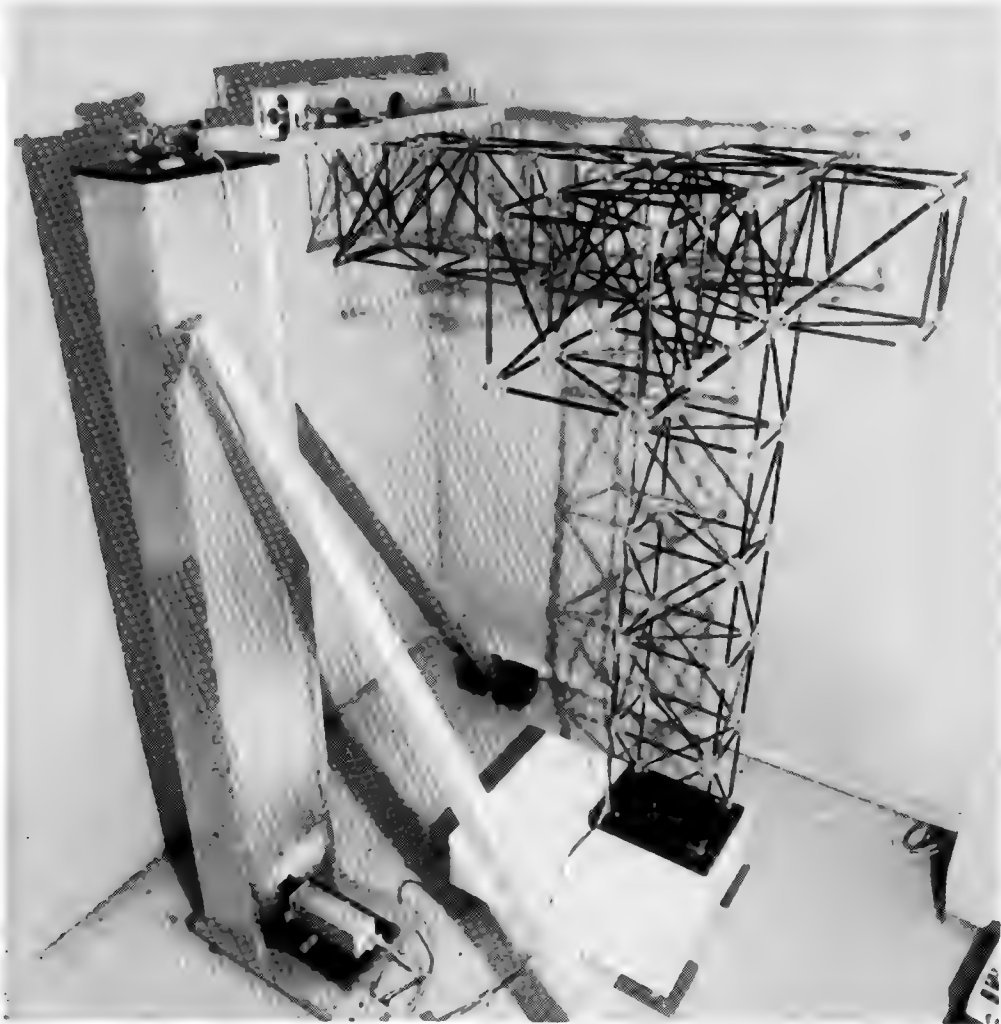
The JPL Phase B Testbed, part of an evolutionary chain of testbeds at JPL, has been developed to demonstrate and validate these control approaches. The Testbed structure was designed to resemble a portion of a concept design for an optical interferometer telescope, and is made with truss construction and includes multiple resonances within the control bandwidth. The Phase B Testbed also includes a full complement of sensors and actuators for isolating disturbances, suppressing structural vibrations, and compensating the optical pathlength, and fast real-time computers for implementation of the control algorithms and recording the results. In addition, the development environment has been designed to maximize turnaround time for new control designs. Thus far, the optical compensation and structural vibration suppression control layers have been demonstrated, and development of the disturbance isolation control layer is ongoing. Experimental work in the near future will focus on combining these three control layers in the expectation that the disturbance rejection of the combined system will achieve the required attenuation.

This paper was presented as a poster session at the Fifth NASA/DOD Controls-Structures Interaction Technology Conference, March 3-5, 1992 at Lake Tahoe, Nevada. The focus of the paper is on describing the Phase B Testbed structure and facility, as the experimental results are included in other papers presented at this same conference.

THE JPL PHASE B TESTBED STRUCTURE

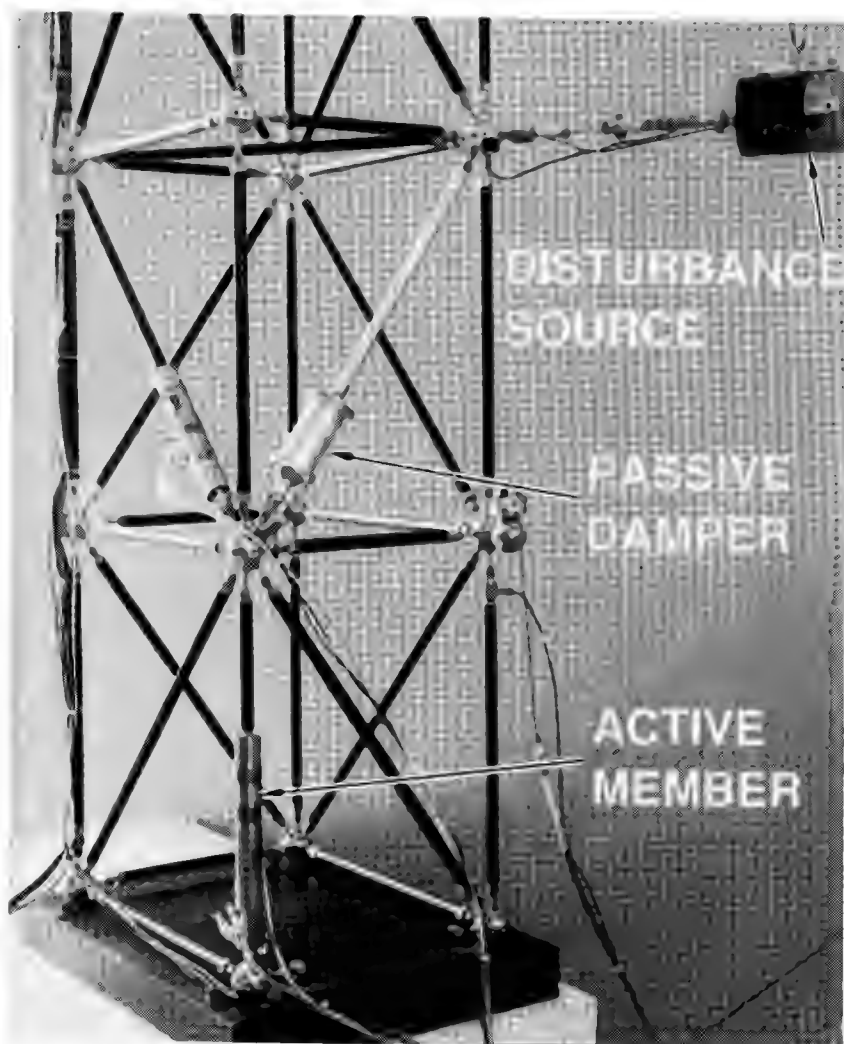
The Phase B Testbed structure consists of a truss structure 2.5 m high with two horizontal arms which support optical components similar to those that would be required on a functioning optical interferometer. The optical pathlength compensation system is attached to the end of one of these arms, and can be seen in the photograph below. The structure is constructed from aluminum tubes which can be removed easily, allowing for inserting active and passive damping truss elements or for changing the experiment configuration without major disassembly. The truss elements attach to aluminum nodes which have threaded holes drilled at the proper angles. If required for modal testing or structural control, accelerometers can also be attached to these nodes. Input disturbances can be injected into the structure at any of the nodes using modal shakers. A NASTRAN model of the structure predicted 16 vibratory modes below 100 Hz, and this was verified experimentally.

A second, rigid structure or "tower" was constructed for the purpose of supporting an optical bench on which the simulated star source is mounted. Due to its large surface area the tower design was potentially susceptible to acoustic noise, and accordingly it was constructed with damping material in all its joints. The Testbed structure, which is more affected by seismic disturbances, is mounted on a 1500 kg block of steel. Despite these precautions, the ambient disturbances in the laboratory cause motion in the optical pathlength of tens of microns--several orders of magnitude greater than the required stability--and thus increase the challenge of meeting the requirements. In fact, the ambient noise constitutes a convenient disturbance source for control experiments, and many of the initial experiments used no additional auxiliary disturbance source.



STRUCTURAL QUIETING LAYER

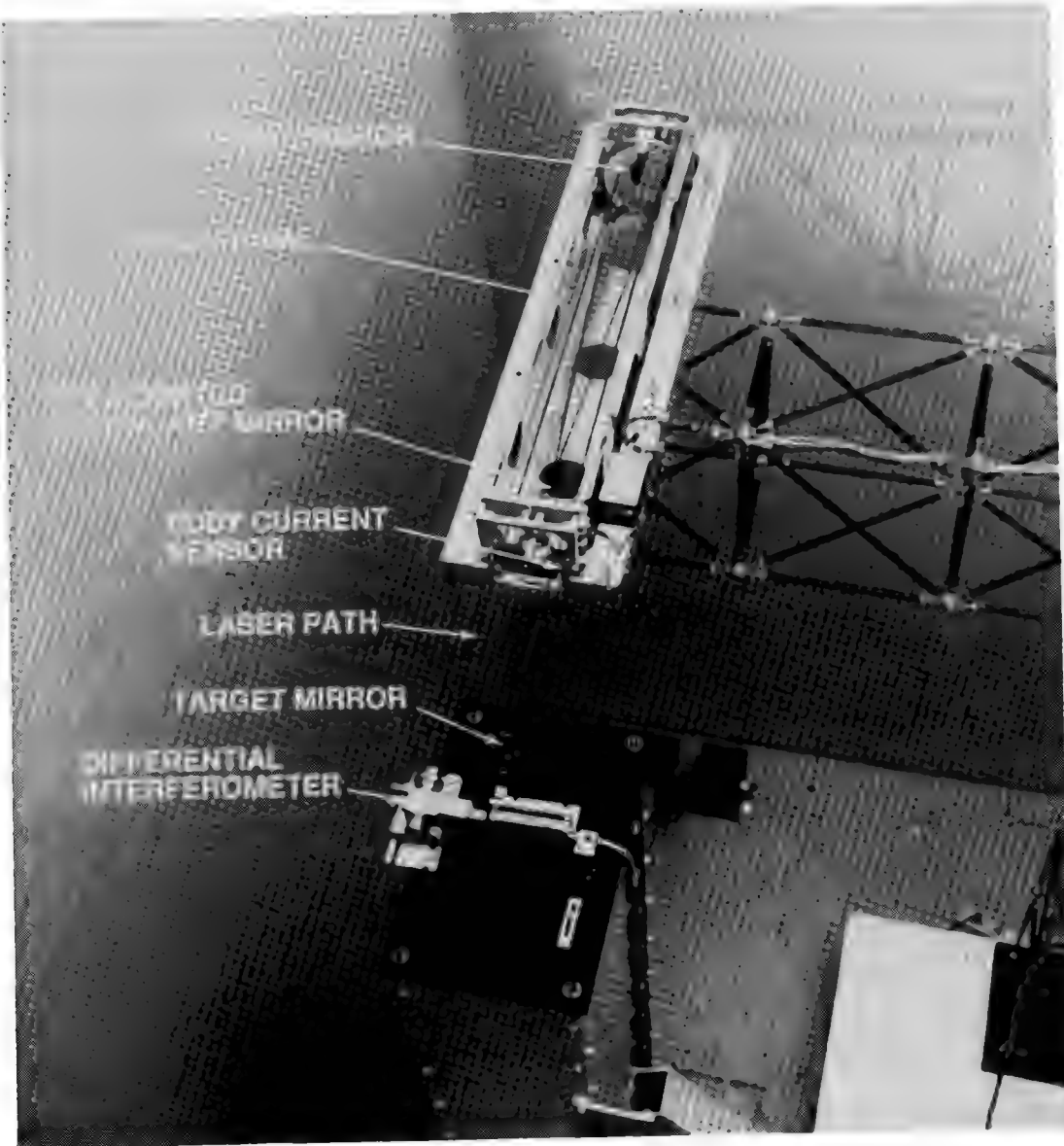
The structural quieting layer is designed to reduce the vibration level in the structure to provide disturbance attenuation before it acts directly on the optical elements. This is accomplished through a combination of passive damping and active control. Due to the design of the truss structure, passive or active members can be substituted easily for aluminum truss elements. Passive dampers, which employ a viscous fluid, have the advantages of being robust, simple in design, and requiring no power. Experiments using passive dampers have demonstrated the ability to attenuate disturbances in the structure by a factor of 40. Active members utilize a piezoelectric actuator embedded within the structure. Two schemes for controlling the active members have been demonstrated thus far: dial-a-strut, and state feedback structural control. The dial-a-strut controller can be made to emulate any passive member, though its greater value lies in its ability to electronically fine-tune the mechanical impedance of the active member to maximize energy dissipation. The other scheme consists of using full state feedback to generate control signals to the active members. This strategy is theoretically capable of achieving higher control performance, but is more sensitive to modeling errors in the system. In practice combined control and structure optimization will be used to determine the locations for and the optimal blend of passive and active members.



OPTICAL COMPENSATION LAYER

The object of the optical compensation control layer is to maintain a desired optical pathlength through the optical train by moving optical elements with actuators. This system consists of a cat's eye retroreflector, which employs a primary and a secondary mirror and which has the property of returning a reflected laser beam parallel to the incoming light path. A heterodyne laser interferometer is used to measure pathlength through the optical train, with a resolution of 2.5 nanometers. Two actuators are used in this system. The first consists of a piezoelectric stack to which the secondary mirror is mounted. An identical actuator is used to force a counterweight in the opposite direction to that of the secondary mirror, rendering this system essentially reactionless.

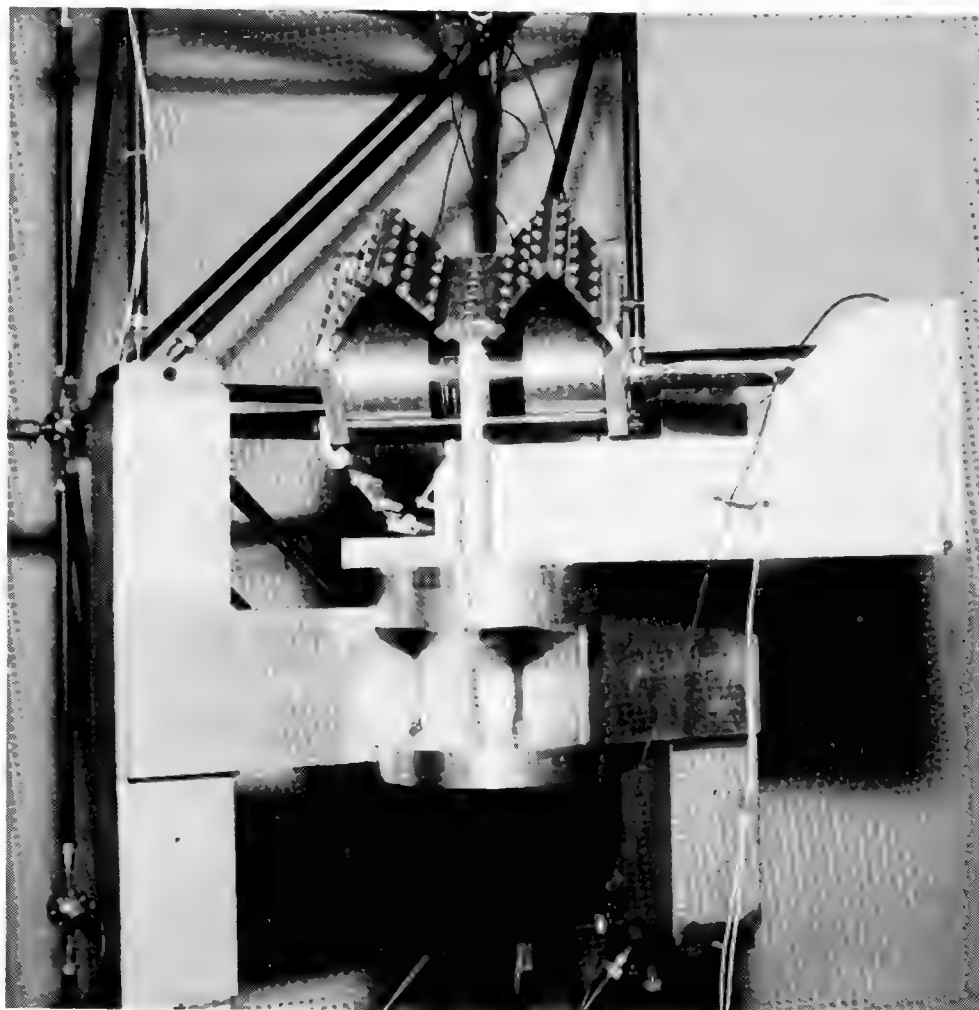
The second actuator consists of a voice coil actuator which reacts between the retroreflector assembly and the aluminum frame mounted to the truss structure. The retroreflector assembly uses Invar in its construction for thermal stability, and is suspended from the aluminum frame using flexures in a parallelogram geometry. An eddy current sensor is used to sense the relative position of the retroreflector and the frame. The combination of the voice-coil and piezoelectric actuators provides the control system engineer with the capability to perform high-bandwidth optical pathlength compensation.



ISOLATION FIXTURE

The function of the isolation fixture is to demonstrate disturbance isolation on the Phase B structure. Disturbances such as those resulting from reaction wheel dynamics are simulated using a modal shaker with 10 N maximum force output. The shaker, which is configured as a proof-mass actuator, is mounted in a flexure mechanism which supports its weight yet allows straight-line motion. The body of the shaker motor and hardware holding it constitute the reaction mass. Reaction forces from the shaker are coupled to the structure through the horizontal "L" shaped bracket seen in the photograph below. This bracket is mounted on a turntable so that the direction of action can be altered. The isolation fixture can be attached to the Phase B structure in more than a dozen different locations.

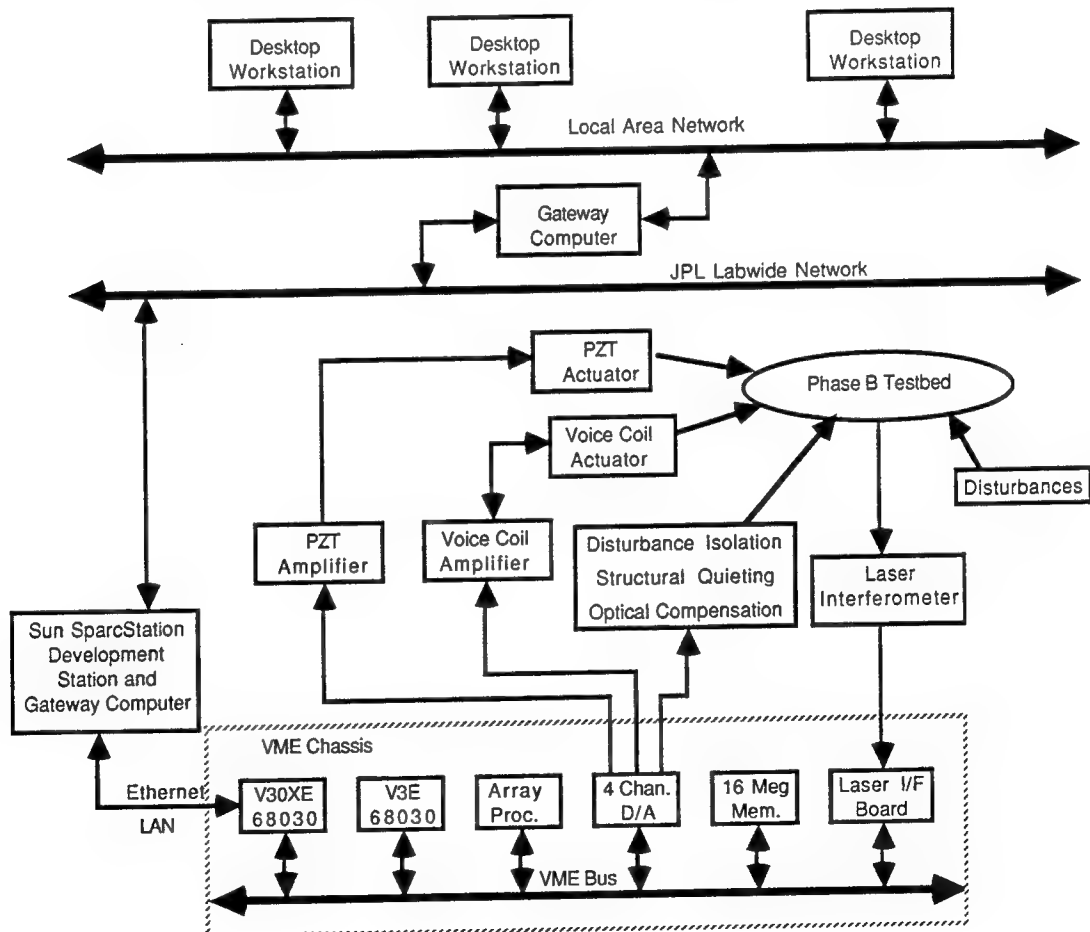
Disturbance isolation is achieved by mounting an isolator between the shaker and the "L" bracket. An active strut is shown in the photograph, though passive struts can also be substituted in the same location. By replacing the isolator with a rigid element, the isolation fixture becomes a controlled disturbance source. The isolation fixture is a recent addition to the Phase B Testbed, and experiments in disturbance isolation are in progress.



REAL-TIME COMPUTERS

Control of the Testbed structure and optical pathlength is achieved using single board computers (SBC's) mounted in a VME chassis. Heurikon 68030-based SBC's are used in conjunction with a CSPI Supercard II array processor, which is used for the computationally intensive control loops. In addition, 16 bit analog to digital and digital to analog conversion is performed by Data Translation converters, and a custom board made in-house is used for interfacing the laser interferometer to the VME bus. The real-time computers are connected through ethernet to a Sun Sparc workstation, which is used to compile, load, and execute programs on the SBC's and also to archive and display experimental results. Compilation is performed using GNU's cross-compiler. The VxWorks operating system is used to arbitrate and synchronize among multiple tasks within the SBC's and to load and run software.

JPL's CSI laboratory was designed to facilitate the rapid development, implementation, and analysis of experiments. The workstation and the real-time computers are interconnected via ethernet to form a local area network (LAN) within the laboratory, which is also connected to JPL's main network using the SparcStation as a gateway. This connectivity makes it possible for anyone connected to the nationwide Internet network to remotely log into the real-time computers, and in fact, most development work for the experiments is performed from the analysts' offices using their workstations for network access.



SUMMARY AND CONCLUSIONS

Experiments to date have included demonstration of optical compensation and structural quieting resulting in stability of the optical pathlength of tens of nanometers. Details of the experimental results can be found in references 1-6 and in other papers presented at this conference. Control designs for disturbance isolation using the isolation fixture are currently being developed, which will be followed by the simultaneous application of all three layers of control. Disturbance rejection of four orders of magnitude or greater is anticipated.

ACKNOWLEDGEMENTS

The research described in this paper was performed by the Jet Propulsion Laboratory, California Institute of Technology, under contract with the National Aeronautics and Space Administration.

REFERENCES

1. J. L. Fanson, E. H. Anderson, D. M. Moore, and M. A. Ealey, "Development of an Active Truss Element for Control of Precision Structures," *Optical Engineering*, Vol. 29, No. 11, Nov. 1990, pp. 1333-1341.
2. J. L. Fanson, H. C. Briggs, C. C. Chu, B. J. Lurie, R. S. Smith, D. B. Eldred, and D. Liu, "JPL CSI Phase 0 Experimental Results and Real Time Control Computer," 4th NASA/DoD Control/Structures Interaction Technology Conference, Orlando Florida, Nov. 5-7, 1990.
3. M. O'Neal, D. Eldred, D. Liu, and D. Redding, "Experimental Verification of Nanometer Level Optical Pathlength Control on a Flexible Structure," 14th Annual AAS Guidance and Control Conference, Keystone Colorado, Feb. 2-6, 1991.
4. R. A. Laskin and M. San Martin, "Control Structure System Design of a Spaceborne Optical Interferometer," AAS/AIAA Astrodynamics Specialist Conference, Stowe Vermont, Aug. 1989.
5. J. T. Spanos and M. O'Neal, "Nanometer Level Optical Control on the JPL Phase B Testbed," ADPA/AIAA/ASME/SPIE Conference on Active Materials and Adaptive Structures, Alexandria, Virginia, Nov. 1991.
6. B. Lurie, J. O'Brien, S. Sirlin, and J. Fanson, "The Dial-a-Strut Controller for Structural Damping," ADPA/AIAA/ASME/SPIE Conference on Active Materials and Adaptive Structures, Alexandria, Virginia, Nov. 1991.

Design, Analysis and Testing of High Frequency Passively Damped Struts

Y.C. Yiu	Lockheed Missiles & Space Co., Sunnyvale, CA
Porter Davis	Honeywell Incorporated, Phoenix, AZ
Kevin Napolitano	CSA Engineering, Palo Alto, CA
Rory Ninneman	Phillips Laboratory, Kirtland AFB, N.M.

The work presented here was performed under the SPICE Investigation of Critical Technology for the Active Control Subtask. It is a collaborative effort of a team of engineers from LMSC, Honeywell, CSA and the Phillips Lab.

Objectives

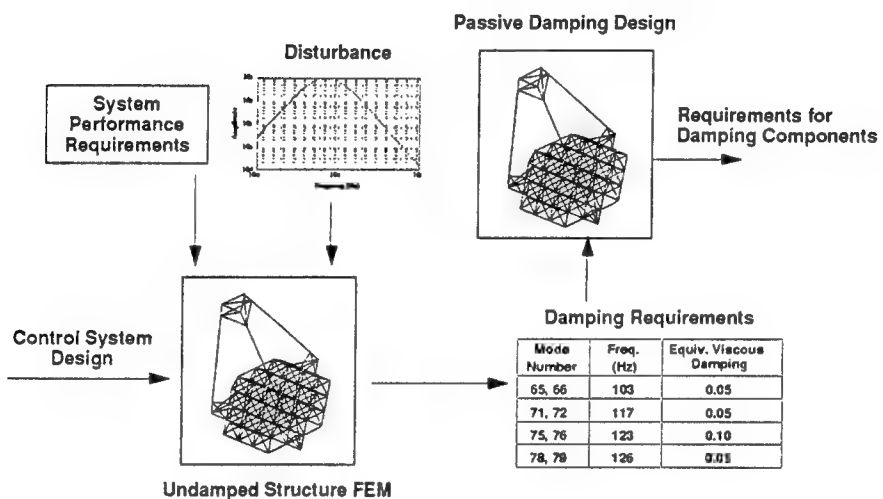
- **Develop design requirements for damped struts to stabilize control system in the high frequency cross-over and spill-over range**
- **Design, fabricate and test**
 - **viscously damped strut**
 - **viscoelastically damped strut**
- **Verify accuracy of design and analysis methodology of damped struts**
- **Design and build test apparatus, and develop data reduction algorithm to measure strut complex stiffness**

In order to meet the stringent performance requirements of the SPICE experiment, the active control system is used to suppress the dynamic responses of the low order structural modes. However, the control system also inadvertently drives some of the higher order modes unstable in the cross-over and spill-over frequency range. Passive damping is a reliable and effective way to provide damping to stabilize the control system. It also improves the robustness of the control system. Damping is designed into the SPICE testbed as an integral part of the control-structure technology.

Precision highly damped struts operating at high frequency are essential to the success of the SPICE experiment. The performance and precision of these struts have never been demonstrated. The objectives of this subtask are to design, fabricate, and test two damped struts based on two damping mechanisms: viscous fluid and viscoelastic material. The methodologies of design and analysis will be verified scientifically to ensure future design

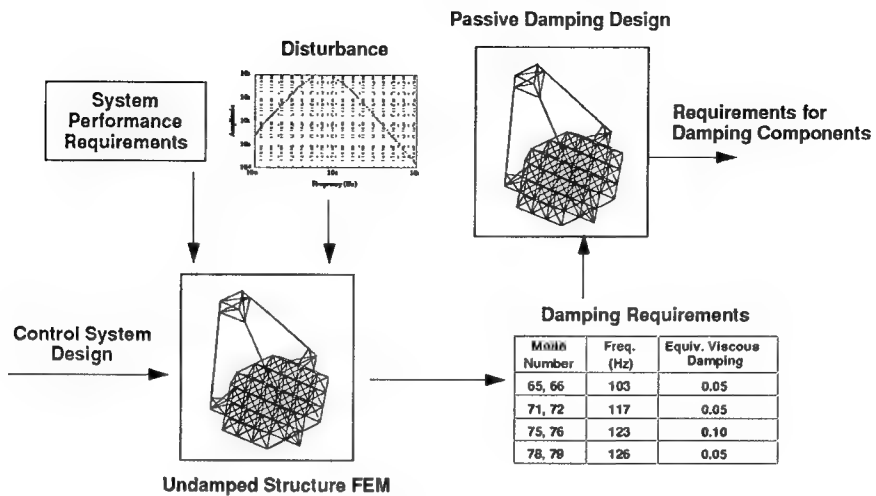
can be readily achieved. A test apparatus was also designed and built to accurately measure the complex stiffness of these struts.

System Level Damping Design



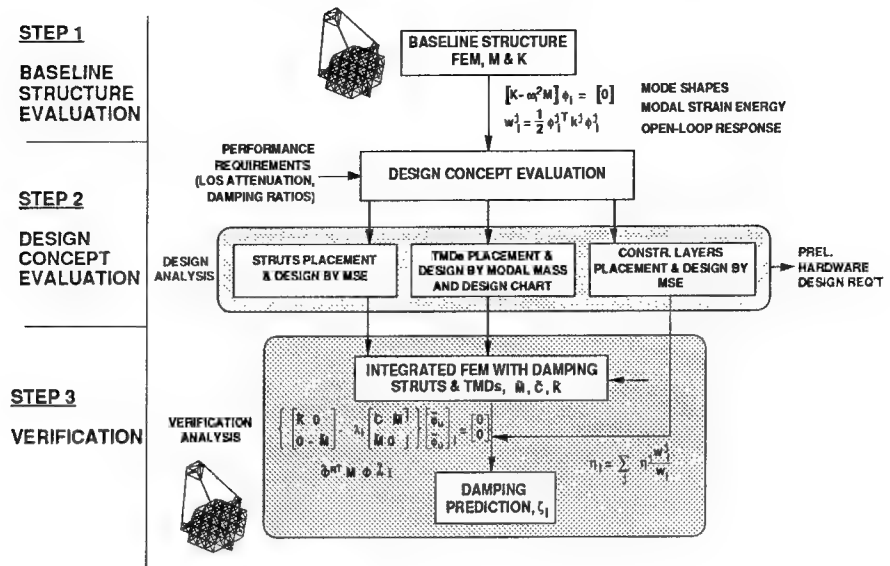
The preliminary control system design was based on a baseline finite element model with nominal structural damping. Equivalent viscous damping ratios for a set of high order modes were specified for a stable control system. High damping ratios, 0.05 to 0.10, are required for these target modes. It is technically challenging to design high damping in high order modes. Based on this damping schedule, a system level passive damping design was performed. As a result of this design, the requirements for passive damping components are established.

System Level Damping Design



The preliminary control system design was based on a baseline finite element model with nominal structural damping. Equivalent viscous damping ratios for a set of high order modes were specified for a stable control system. High damping ratios, 0.05 to 0.10, are required for these target modes. It is technically challenging to design high damping in high order modes. Based on this damping schedule, a system level passive damping design was performed. As a result of this design, the requirements for passive damping components are established.

Passive Damping Design Synthesis



The passive damping design synthesis is a three-step process: baseline structure evaluation, design concept evaluation and verification analysis.

The modal characteristics of the baseline finite element model were first analyzed for each target mode: mode shape, modal strain energy distribution and open-loop response.

Three types of damping devices were considered to provide passive damping: constrained layer treatments, damped struts and tuned mass dampers. For each target mode, the applicability of these devices was studied. The device which can most effectively provide the necessary damping was selected.

The finite element model was updated to incorporate these damping devices, and a system level analysis was then performed to ensure that the integrated damping design will meet the system level requirements.

Strut Design Requirements

- **SPICE experiment requires struts having**
 - **high damping at frequency of high order modes**
 - **high stiffness**
 - **high load capacity**

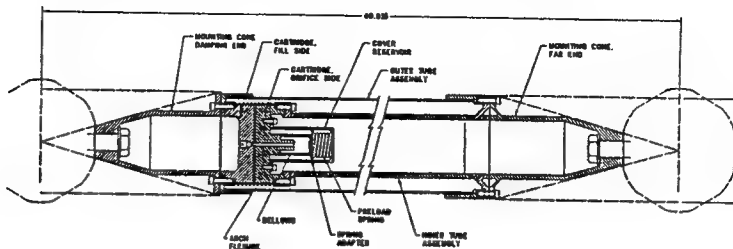
Description	Requirement
Physical Dimensions	Length 40.615" between centers of node balls
	Diameter Not interfere with other struts
Interface	Joint Compatible with existing node balls
Loads	Yield ± 3150 lb
	Ultimate ± 5250 lb
Stiffness	Static $K(f=0 \text{ Hz}) \geq 80,000 \text{ lb/in}$
	Dynamic $K(f=100 \text{ Hz}) = 160,000 (\pm 10\%) \text{ lb/in}$
Damping	loss factor ≥ 0.4 , $70 \text{ Hz} \leq \text{freq} \leq 130 \text{ Hz}$
Temperature	Operation $65^\circ\text{F} \leq T \leq 85^\circ\text{F}$
	Storage $20^\circ\text{F} \leq T \leq 120^\circ\text{F}$
Weight	Minimize
Materials	Space compatible
Life	10 years
Linearity	Maximize

The design requirements for the damped strut were then formulated. The damped struts will be used to replace existing struts. The damped strut must be compatible with the existing structural configuration and meet the strength requirements.

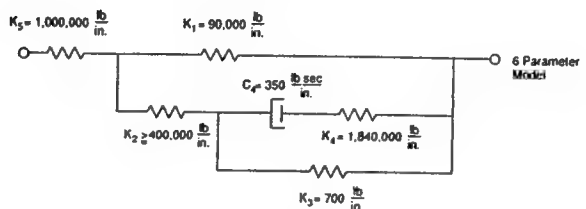
Since the control system and system level damping design is still being designed, the requirements for the damped struts were set conservatively but realistically for practically damped strut design purposes. The most important aspects of these requirements are that the required damping, frequency, stiffness and load for the damped struts are all quite high. These aspects significantly increase the challenge of the strut design.

D-strut Design

- Damping medium - viscous fluid



Sketch of D-strut



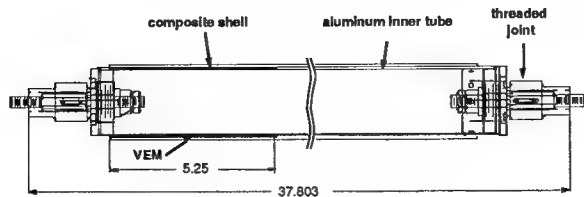
Lumped Parameter Model of D-strut

The viscous strut uses the viscous fluid flowing through an orifice as the energy dissipation mechanism. The strut comprises an outer aluminum tube and inner graphite/epoxy tube with an arched flexure/bellow assembly to contain the viscous fluid. When the strut is forced in the axial direction, the inner tube forces the fluid to flow through the orifice and dissipates mechanical energy into heat.

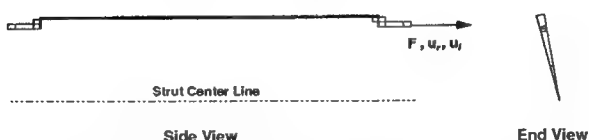
The device is modeled as a lumped parameter model with discrete springs and dashpot. The mechanical design entails the selection of proper spring and dashpot parameters to meet the strut requirements. These parameters are achieved physically by sizing of the sub-components and material selection.

V-strut Design

- Damping medium - viscoelastic material (VEM)



Sketch of V-strut



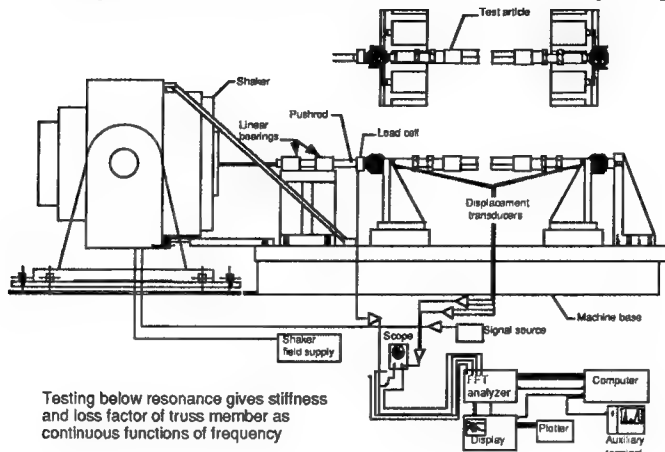
Axisymmetric Finite Element Model of V-strut

The viscoelastic strut uses the hysteretic behavior of the viscoelastic material as the energy dissipation mechanism. The strut comprises an inner aluminum tube and outer graphite/epoxy tube with viscoelastic material bonded in between. When the strut is forced in the axial direction, the viscoelastic material is subject to shear stress and dissipates mechanical energy into heat.

The device is modeled as an axisymmetric finite element model using plate and solid elements. A direct frequency response technique is used to compute the complex stiffness of the strut at selected frequency points. The mechanical design entails proper material selection and sizing of sub-components to ensure performance requirements are met.

Direct Complex Stiffness Test

- Low frequency test (1-55 Hz)
- Apparatus avoids resonance
- Random force input
- Complex stiffness as continuous function of frequency



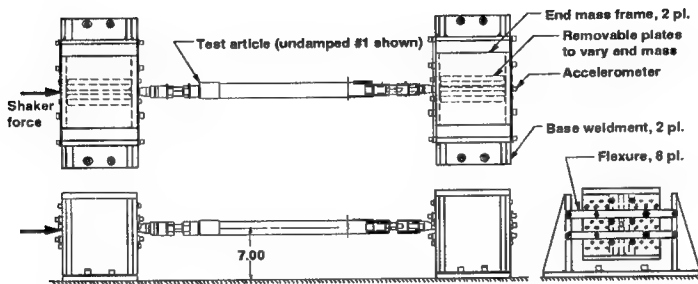
Fixture resonance is an important factor in measuring the strut stiffness and damping accurately. For measuring low frequency stiffness properties, the test fixtures were designed to be stiff and have resonance frequencies above the highest measurement frequency.

The strut will be pushed at one end and fixed at a support at the other end. A load cell measures the force level at the push rod and two transducers measure the strut end displacements. By using random force input, the damping mechanism will not be subject to excess heat due to energy dissipation.

A quick and accurate measurement over a wide frequency band (1 to 55 Hz) can be obtained. The complex stiffness of the strut can be computed from the measured data using the Fourier analyzer.

Resonant Complex Stiffness Test

- High frequency test (60-200 Hz)
- Apparatus induces resonance with simple known mode shape
- Random force input
- Complex stiffness measured in the neighborhood of resonance frequency

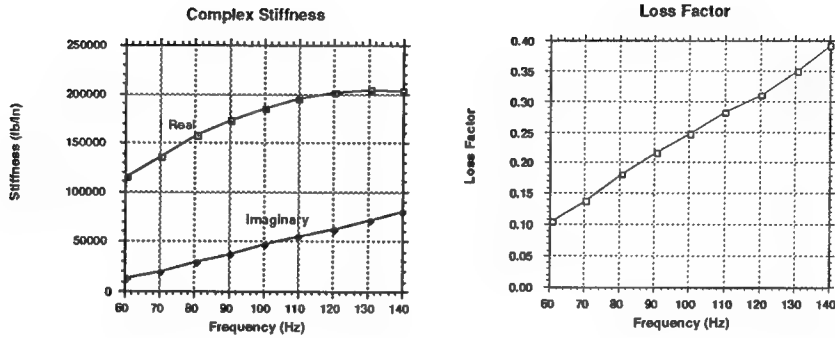


To measure the strut complex stiffness in the high frequency range, 60 to 200 Hz, a different test apparatus is required. This apparatus was designed to avoid fixture resonance in the frequency range of interest and also an accurate knowledge of the support stiffness was not required. The test apparatus simulates a free-free strut with two equal end masses. The end masses are supported by flexures. The flexures were designed to have a "free-free" resonance much lower than the resonant frequency of the strut/mass assembly.

The strut is pushed in the axial direction at one end and the accelerations of the end masses are measured. Since the apparatus is a simple two degrees-of-freedom system in the axial direction, the complex stiffness can be computed easily from the measured data. Also by varying the end masses, different resonance frequencies can be induced. This provides an accurate means of measuring the complex stiffness in the frequency band of interest.

Preliminary Test Results

- Preliminary results from a damped strut resonant test indicate complex stiffness and loss factor can be extracted from test data over a range of frequency



A preliminary test using the resonant test apparatus provided an opportunity to shake out the test apparatus and the design of the viscoelastic strut. The test results demonstrated that the data reduction method could provide accurate complex stiffness data in the neighborhood of the resonance frequency. It also indicated that the stiffness of the connection between two strut pieces must be increased to improve damping performance.

Work-in-progress

- **V-strut**
 - **finalize design and permanent assembly**
- **D-strut**
 - **complete testing and parameter correlation**
- **Direct Complex Stiffness Test Apparatus**
 - **upgrade apparatus to increase maximum frequency to 55 Hz**
- **Resonant Complex Stiffness Test Apparatus**
 - **upgrade data processing to extend measurement range downward to 50 Hz**
- **Perform stiffness and damping test on V-strut**
- **Correlate V-strut finite element model with test results**

Significant progress was made in understanding the important parameters to build highly damped struts in the high frequency range. More work is still in progress to complete this subtask.

The designs of the struts will be finalized. The direct complex stiffness test apparatus will be improved to increase its maximum frequency to 55 Hz. The data processing method for the resonant complex stiffness test will be upgraded to extend the measurement range down to 50 Hz. The struts will be assembled and tested for their dynamic performance. The data will be reduced and correlated to the analytical models and hence the design and analysis methods will be verified.

The findings of this subtask will be used to design the damped struts for the SPICE control-structure (active/passive) experiment.

A COMPARISON OF VISCOELASTIC DAMPING MODELS

Joseph C. Slater
116 Jarvis Hall
University at Buffalo
Buffalo, New York 14260

W. Keith Belvin
Mail Stop 230
NASA Langley Research Center
Hampton, VA. 23665

Daniel J. Inman
1012 Furnas Hall
University at Buffalo
Buffalo, New York 14260

Modern finite element methods (FEMs) enable the precise modeling of mass and stiffness properties in what were in the past overwhelmingly large and complex structures. These models allow the accurate determination of natural frequencies and mode shapes. However, adequate methods for modeling highly damped and highly frequency dependent structures did not exist until recently. The most commonly used method, Modal Strain Energy^{1,2}, does not correctly predict complex mode shapes since it is based on the assumption that the mode shapes of a structure are real. Recently, many techniques have been developed which allow the modeling of frequency dependent damping properties of materials in a finite element compatible form. Two of these methods, the Golla-Hughes-McTavish^{3,4} method and the Lesieutre-Mingori^{5,6} method, model the frequency dependent effects by adding coordinates to the existing system thus maintaining the linearity of the model. The third model, proposed by Bagley and Torvik⁷, is based on the Fractional Calculus method and requires fewer empirical parameters to model the frequency dependence at the expense of linearity of the governing equations. This work examines the Modal Strain Energy, Golla-Hughes-McTavish and Bagley and Torvik models and compares them to determine the plausibility of using them for modeling viscoelastic damping in large structures.

THE MODAL STRAIN ENERGY MODEL

The most common method used for the modeling of viscoelastic damping in structures presently is the Modal Strain Energy method suggested by Ungar and Kerwin². This method assumes that proportional damping (*Rayleigh Damping*) is an adequate model of the damping mechanisms of a structure. This implies that the modes of the damped structure are the same as that of the undamped structure.

Modal Strain Energy begins with the complex stiffness representation of material damping properties. In this representation, the complex stiffness $K^* = K' + K''j$ where j represents the square root of -1, and K' and K'' are the real and imaginary parts of the complex stiffness, respectively. The ratio K''/K' is the material loss factor. A more detailed description of the complex representation is given by Nashif, Jones and Henderson⁸.

The loss factor of any mode i is given by the summation of the strain energy in each element, multiplied by its material loss factor, and divided by the total strain energy of the mode, i.e.,

$$\eta^i = \sum_{j=1}^n \frac{V_j^i \eta_j^i}{V^i} \quad (1)$$

The variable η^i is the loss factor of the i^{th} mode, η_j^i is the loss factor of the j^{th} element at the i^{th} natural frequency, V^i is the strain energy of the i^{th} mode at a given amplitude, and V_j^i is the strain energy in the j^{th} element when the structure is deformed in the i^{th} mode shape at the same amplitude. The strain energy V^i in a structure or element with the stiffness matrix defined by K and the deformation defined by x is

$$V = x^T K x \quad (2)$$

Since the imaginary part of the global stiffness matrix is the assembly of the imaginary parts (K'') of the elemental stiffness matrices, equation (1) may be written

$$\eta^i = \frac{\mathbf{x}_i^T K'' \mathbf{x}_i}{\mathbf{x}_i^T K' \mathbf{x}_i} \quad (3)$$

where K' is the real part of the global stiffness matrix and is denoted as K for the undamped and viscously damped systems. Note that this is precisely true in the case of the single degree of freedom system. This is a useful representation of the modal strain energy equation and will be referred to repeatedly.

Although intuitively the concept of using energy ratios weighted by element loss factors is appealing, it has no theoretical basis. In the past there has not been an explanation of why modal strain energy is correct when the imaginary part of the stiffness matrix is proportional to the mass and stiffness matrices. It can be shown that modal strain energy is nothing more than the modal decoupling of a viscoelastic system where it is assumed that the imaginary part of the stiffness matrix must obey $K''/\omega = C$.

The equations of motion for an unforced viscously damped multiple degree of freedom (MDOF) system may be written as

$$M \ddot{\mathbf{y}} + C \dot{\mathbf{y}} + K \mathbf{y} = \mathbf{0} \quad (4)$$

Assuming a solution of the form

$$\mathbf{y} = \mathbf{u} e^{i\omega t} \quad (5)$$

then substituting (5) into (4) gives

$$-M \omega^2 \mathbf{u} + C i \omega \mathbf{u} + K \mathbf{u} = \mathbf{0} \quad (6)$$

The system equations written in terms of complex modulus corresponding to (4) are then

$$M \ddot{\mathbf{y}} + (K' + K''i) \mathbf{y} = \mathbf{0} \quad (7)$$

Substituting (5) into (7) similarly gives

$$-M \omega^2 \mathbf{u} + (K' + K''i) \mathbf{u} = \mathbf{0} \quad (8)$$

Comparing (6) and (8), it is seen that for any given frequency, ω_j ,

$$C \omega_j = K'' \quad (9)$$

which is the multiple degree of freedom representation of $c = k\eta/\omega$.

Likewise, substituting

$$\mathbf{y} = P \mathbf{v} \quad (10)$$

into (4), where P is the matrix of normalized eigenvectors of $M^T K$ and premultiplying by P^T , equation (4) becomes

$$\begin{aligned} & P^T M P \ddot{\mathbf{v}} + P^T C P \dot{\mathbf{v}} + P^T K P \mathbf{v} \\ & = \text{diag}(m_i) [\ddot{\mathbf{v}} + \text{diag}(2\zeta_i \omega_i) \dot{\mathbf{v}} + \text{diag}(\omega_i^2) \mathbf{v}] = 0 \end{aligned} \quad (11)$$

where m_i are the modal masses. This is true if and only if C is proportional to M and K . Likewise, for the complex system, substituting (9) and (10) into (7), and premultiplying by P^T gives

$$\begin{aligned} & P^T M P \ddot{\mathbf{v}} + P^T K^T P \mathbf{v} + P^T C \omega_j P i \dot{\mathbf{v}} \\ & = \text{diag}(m_i) [\ddot{\mathbf{v}} + (\text{diag}(\omega_i^2) + \text{diag}(2\zeta_i \omega_i) \omega_j i) \mathbf{v}] = 0 \end{aligned} \quad (12)$$

again if and only if C is proportional. This is identical to requiring that K'' be proportional (i.e., $K''/\omega = \alpha M + \beta K$). From (12) it can be seen that

$$(P^T K^T P)^{-1} (P^T C \omega_j P) = \text{diag}(2\zeta_i) = \text{diag}(\eta^i) = H \quad (13)$$

when $\omega_j = \omega_i$. However, using (9) gives

$$(P^T K^T P)^{-1} (P^T K'' P) = \text{diag}(2\zeta_i) = \text{diag}(\eta^i) = H \quad (14)$$

Denoting the i^{th} eigenvector as \mathbf{x}_i , equation (14) may be written as

$$\eta^i = \frac{\mathbf{x}_i^T K'' \mathbf{x}_i}{\mathbf{x}_i^T K \mathbf{x}_i} \quad (15)$$

which is identical to equation (3). Therefore, the same rules which apply to decoupling viscously damped systems apply to the proper use of modal strain energy. For non-proportionally damped systems, the matrix H defined by (14) will be non-diagonal and will give some indication of the non-proportionality of the system.

Thus, the modal strain energy technique is nothing more than the modal decoupling of a system with complex modulus damping. Also, the criteria used to define whether or not modal strain energy is a proper method for finding loss factors of a structure described by a complex modulus have been shown to be identical to those for decoupling a viscously damped system.

THE GOLLA-HUGHES-MCTAVISH MODEL

The Golla-Hughes-McTavish (GHM) model is based upon the generalized standard linear model; however, it has been developed for direct incorporation into the finite element method. In the GHM model, the material complex modulus is written in the Laplace domain in the form

$$E^*(s) = E_0(1 + h(s)) = E_0 \left(1 + \sum_{n=1}^k \hat{a}_n \frac{s^2 + 2\hat{\zeta}_n \hat{\omega}_n s}{s^2 + 2\hat{\zeta}_n \hat{\omega}_n s + \hat{\omega}_n^2} \right) \quad (16)$$

where the hatted terms are free variables for curve fitting to complex modulus data and s is the Laplace domain operator. From (16) it can be seen that $E^*(\omega) = E_0$ for $j\omega = 0$ which means that no creep is allowed in this model. Also, the number of expansion terms, k , may be modified to represent the high or low frequency dependence of the complex modulus. In general between two and four terms are adequate.

The finite element form of the GHM model for a single modulus and single expansion term is

$$\begin{bmatrix} M & 0 \\ 0 & \frac{\hat{\alpha}}{\hat{\omega}^2} E_0 \Lambda_e \end{bmatrix} \begin{bmatrix} \mathbf{x}(s) \\ \mathbf{z}(s) \end{bmatrix} s^2 + \begin{bmatrix} 0 & 0 \\ 0 & \frac{2\hat{\alpha}\hat{\zeta}}{\hat{\omega}} E_0 \Lambda_e \end{bmatrix} \begin{bmatrix} \mathbf{x}(s) \\ \mathbf{z}(s) \end{bmatrix} s \\ + \begin{bmatrix} (1 + \hat{\alpha}) E_0 \tilde{K} & -\hat{\alpha} E_0 R_e \Lambda_e \\ -\hat{\alpha} E_0 \Lambda_e R_e^T & \hat{\alpha} E_0 \Lambda_e \end{bmatrix} \begin{bmatrix} \mathbf{x}(s) \\ \mathbf{z}(s) \end{bmatrix} = \begin{bmatrix} \mathbf{F}(s) \\ \mathbf{0} \end{bmatrix} \quad (17)$$

where M is the original mass matrix, $E_0 \tilde{K}$ is the original element stiffness matrix, Λ_e is the diagonal matrix of the non zero eigenvalues of \tilde{K} , and R_e is the matrix of the eigenvector associated with the eigenvalues of Λ_e . Even for the most complex linear elements, the GHM finite element remains linear and second order. Although the GHM system state

equations are much larger than the original undamped equations, the GHM state matrix is only slightly larger than the state matrix for a viscously damped system. Where the size of the state matrix for a viscously damped system is $2n \times 2n$, the state matrix of the GHM model is $m \times m$ where

$$m = \sum_{i=1}^n k_i p_i \quad (18)$$

Here n represents the number of viscoelastic elements, and p_i and k_i represent the number of non-zero eigenvalues and number of expansion terms used in the i^{th} element. One drawback of this method which may be overcome simply is the addition of fictitious overdamped modes. These should be recognized as fictitious and discarded.

FRACTIONAL CALCULUS - THE BAGLEY AND TORVIK MODEL

The Bagley and Torvik fractional calculus viscoelastic model has been proposed based on the observations of Nutting⁹, Gemant^{10,11}, Caputo^{12,13}, Caputo and Minardi¹⁴, and Scott-Blair¹⁵ that the mechanical properties of viscoelastic materials seem to vary as a function of frequency raised to fractional powers. In the time domain, this represents fractional derivatives as defined by

$$\frac{d^{\alpha}}{dt^{\alpha}} x(t) = \frac{1}{\Gamma(1-\alpha)} \frac{d}{dt} \int_0^t \frac{x(\tau)}{(t-\tau)^{\alpha}} d\tau \quad 0 < \alpha < 1 \quad (19)$$

where α represents the power of the derivative, Γ is the gamma function, and τ is a dummy variable of integration. This in turn can be represented in the Laplace domain as

$$\mathcal{L} \left\{ \frac{d^{\alpha}}{dt^{\alpha}} x(t) \right\} = s^{\alpha} x(s) \quad (20)$$

where \mathcal{L} represents the Laplace transform operator. The general form of the fractional derivative model is then

$$\sigma + \sum_{n=1}^{\infty} b_n \frac{d^{\beta_n}}{dt^{\beta_n}} \sigma = E \varepsilon + \sum_{m=1}^{\infty} E_m \frac{d^{\beta_m}}{dt^{\beta_m}} \varepsilon \quad (21)$$

The experimental results of Bagley and Torvik demonstrated that, for many materials, the stress-strain relation can be modeled well using only the first expansion term in each series. In the Laplace domain, the Bagley and Torvik viscoelastic model is

$$\sigma(s) = \frac{E_0 + E_1 s^\alpha}{1 + b s^\beta} \epsilon(s) = \mu(s) \epsilon(s) \quad (22)$$

where $\mu(s)$ represents the complex modulus in the Laplace domain. In order to solve the final equations, α and β are restricted to fractional form. In the interest of brevity, no derivation is shown. One may be found in Bagley and Torvik⁷.

The final form of the equations of motion are

$$\{B_1 s^{1/m} + B_2\} \mathbf{y}(s) = \tilde{\mathbf{F}}(s) \quad (23)$$

where m is the smallest common denominator of α and β , B_1 and B_2 are matrices of order $nm(2 + b) \times nm(2 + b)$, and $\mathbf{y}(s)$ and $\tilde{\mathbf{F}}(s)$ are the appropriate state vector and forcing function vector respectively. Equation (23) may be posed as an eigenvalue/eigenvector problem (setting $\tilde{\mathbf{F}}(s) = \mathbf{0}$) in order to solve for $\mathbf{y}(s)$ and $s^{1/m}$. The system eigenvalues, s , and the system eigenvectors, $\mathbf{y}(s)$, may then be found using (23). However, notice that the order of the system is dramatically increased. For a second order viscously damped system, the size of the eigenvalue problem is $2n$. The size of the Bagley and Torvik eigenvalue problem is $[m(2+\beta)] n$. For the simplest possible Bagley and Torvik viscoelastic model, with $a = b = 1/2$, the order of the system is already $5n!$. This will take 6.25 times more memory and about four times as much time to calculate. Note that in the strictest sense this is not a finite element method, since no viscoelastic element has been developed which could be assembled into an existing finite element model in order to create a global FEM model. Another drawback of this method is the occurrence of unstable eigenvalues as described by Bagley and Torvik⁷. Although these may be disregarded when only interested in mode shapes and loss factors of modes, the forced response of this model would be unstable, which does not agree well with the real behavior of viscoelastic materials.

It should be noted that much work has been done by Morgenthaler¹⁶ of Martin Marietta using the Bagley and Torvik Model on the PACOSS program. The essence of his work is a numerical algorithm incorporating the accelerated subspace iteration technique to the complex modulus problem. Although the initial form of the stiffness matrix is assumed to be the fractional derivative, the algorithm's first step is to evaluate the complex stiffness

matrix at a frequency near the desired natural frequency. Then the desired natural frequency is found, the complex stiffness matrix is evaluated at the new frequency, and the desired natural frequency is found. The procedure iterates until the desired accuracy is reached, although it is mentioned that one iteration may be enough in many cases. The final state matrix is found by recoupling the eigenvalues and eigenvectors.

This method discards the benefit of the Bagley and Torvik model by evaluating the frequency dependent stiffness matrix instead of solving the complete set of frequency dependent equations derived by Bagley and Torvik⁷. This is not bad if all you are interested in are the correct mode shapes and eigenvalues. However, if that is the only goal, then there is no need to use the fractional derivative model. Any other Laplace domain representation which fits the modulus in the frequency domain would work equally as well. There is no reason not to simply use material data sheets directly to evaluate the complex stiffness matrix and avoid the curve fitting altogether. The end result of this method may model the system well, but it does not incorporate all of the frequency dependence of the materials in the final model. Any structural modification requires the complete recalculation of all of the desired eigenvalues and eigenvectors in order to find the new state space matrix, where the GHM method simply requires the assembly of a new element into the existing finite element model.

AN EXAMPLE - THE EVOLUTIONARY VISCO-STRUT

These three models have each been used to model a viscoelastic strut designed for use in the evolutionary model at NASA Langley. The Visco-Strut is a load bearing member capable of supporting tensile and compressive forces in excess of 2000 lbs. In its present configuration, it has a static stiffness on the order of 30,000 lb/in. The viscoelastic material used is G.E. SMRD, manufactured by the General Electric Astro Space Division. Both the GHM and the Bagley and Torvik models have proven to be capable of modeling the frequency dependent complex modulus of the Visco-Strut well, while the Modal Strain Energy method simply uses the raw damping data for any element and therefore is not constrained by the need to curve fit. The results of the curve fitting for the GHM and Bagley and Torvik models are shown below in figures 1 and 2.

For the GHM model, $K_0 = 3.11 \times 10^4$. The remaining parameters are shown in Table 1.

	i=1	i=2	i=3
α_i	2.29	.520	.319
ζ_i	9.83×10^{14}	2.58×10^{23}	7.97×10^{20}
ω_i	1.91×10^{18}	4.44×10^{25}	2.17×10^{22}

Table 1. GHM Parameters for the Visco-Strut.

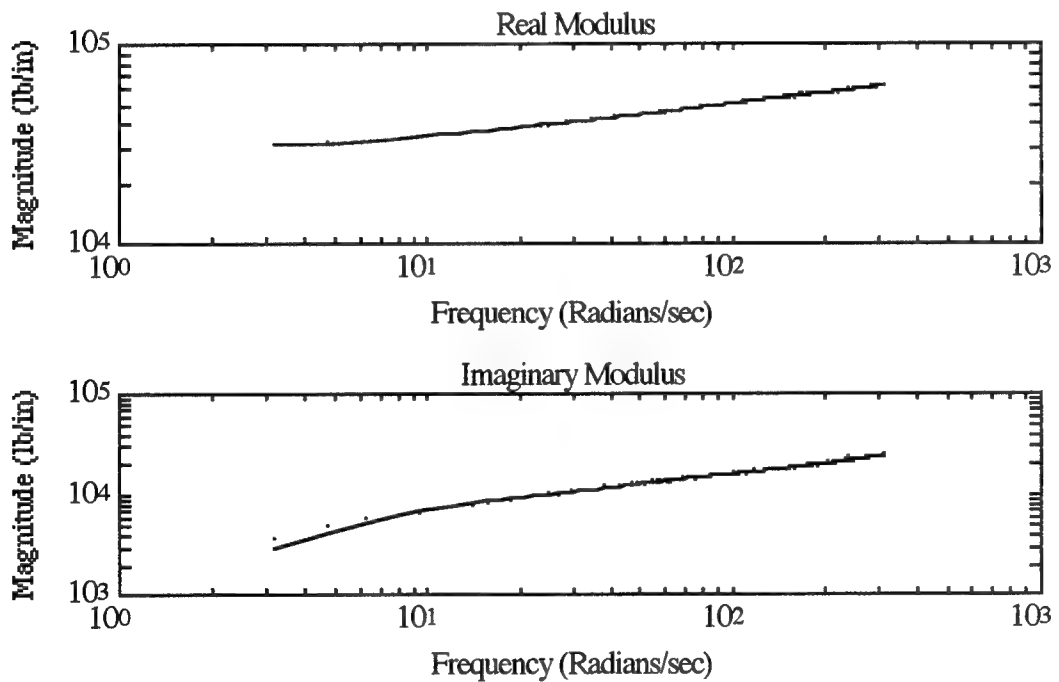


Figure 1. Comparison of the GHM model (solid line) of the complex modulus and test data (dots).

For the Bagley and Torvik model the parameters are $K_0=2.86\times 10^4$, $K_1=3.6163\times 10^3$, $b=1.9028\times 10^{-2}$, and $\alpha=\beta=1/2$.

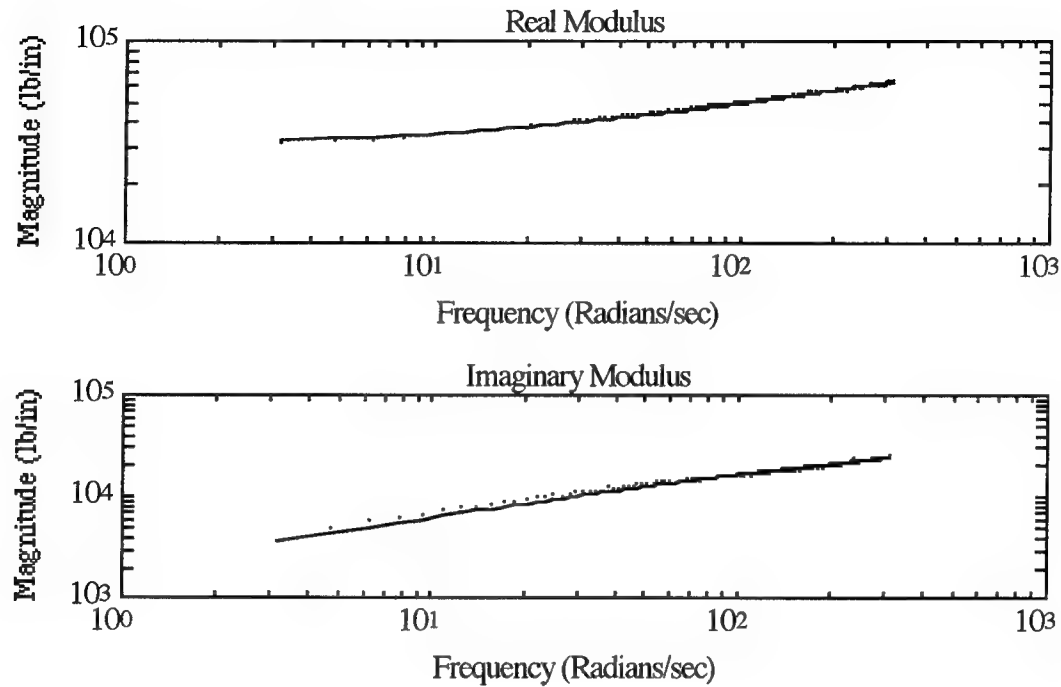


Figure 2. Comparison of the Bagley and Torvik model (solid line) of the complex modulus and test data (dots).

Some first attempts have been taken to model the effects of the Visco-Strut when placed in a small nine bay truss. To date, the only model which has been solvable is the MSE model. The Modal Strain Energy method is simple and quick because it uses the results from the dynamic model of the structure to find modal loss factors using equation (1) or (3). It has been shown by Johnson and Kienholz¹ to correctly find loss factors even when the damping is not proportional. Both the GHM and Bagley and Torvik model solutions have encountered numerical difficulty. The GHM global FEM is ill-conditioned, while the size of the Bagley and Torvik model (1185 x 1185) has caused significant numerical errors. Neither method has yielded useful results for this problem.

CONCLUSIONS

The most robust method for determining modal loss factors is clearly the Modal Strain Energy method. If the system is proportionally damped (as determined by the matrix H in equation (14) being diagonal) then there is no need to use either the GHM or Bagley and Torvik method. Even when the structure is non-proportionally damped, there is little benefit to using either of the higher powered models unless there is a need to predictively model the mode shapes of the damped structure, or model the response of the structure to different excitations. However, if precise modeling of the response is necessary, one must decide whether the GHM modal will become too ill-conditioned for solution, or whether the large increase in the model size using Bagley and Torvik is acceptable.

ACKNOWLEDGMENTS

This work was supported by NASA Langley Research Center, Grant No. NGT50541, under the direction of Dr. W. Keith Belvin. The viscoelastic material used was donated by Dennis Hill of the General Electric Corporation, Astro Space Division.

REFERENCES

- ¹Johnson, C. D. and Kienholz, D. A., "Finite Element Prediction of Damping in Structures with Constrained Viscoelastic Layers," *AIAA Journal*, Vol. 20, No. 9, 1982, pp. 1284-1292.
- ²Ungar, E. E. and Kerwin, E. M., "Loss Factors of Viscoelastic Systems in Terms of Energy Concepts," *The Journal of the Acoustical Society of America*, Vol 34, No. 7, 1962, pp. 954-957.
- ³Golla, D. F., and Hughes, P. C., "Dynamics of Viscoelastic Structures—A Time Domain, Finite Element Formulation," *Journal of Applied Mechanics*, Vol. 52, 1985, pp. 897-906.
- ⁴McTavish, D. J., "The Mini-Oscillator Technique: A Finite Element Method for the Modeling of Linear Viscoelastic Structures," University of Toronto Institute for Aerospace Studies, Toronto, Ontario, UTIAS Report Number 323, March 1988.

⁵Lesieur, George A. and Mingori, D. L., "Finite Element Modeling of Frequency-Dependent Material Damping Using Augmenting Thermodynamic Fields," *Journal of Guidance and Control*, Vol 13, No. 6, 1990.

⁶Lesieur, George A., "Finite Elements for Modeling Frequency-Dependent Material Damping Motivated by Internal State Variables," *International Symposium on M3D: Mechanics and Mechanisms of Material Damping*, 1990.

⁷Bagley, R. L. and Torvik, P. J., "Fractional Calculus—A Different Approach to the Analysis of Viscoelastically Damped Structures," *AIAA Journal*, Vol 21, No. 5, 1983.

⁸Nashif, A. D., Jones, D. I. G., and Henderson, J. P., *Vibration Damping*, John Wiley, New York, 1985.

⁹Nutting, P. G., "A New General Law of Deformations," *Journal of the Franklin Institute*, Vol. 191, 1921, pp. 679-685.

¹⁰Gemant, A., "A Method of Analyzing Experimental Results Obtained from Elasto-Viscous Bodies," *Physics*, Vol. 7, 1936, pp. 311-317.

¹¹Gemant, A., "On Fractional Differentials," *Philosophical Magazine*, Vol. 25, 1938, pp. 540-549.

¹²Caputo, M., *Elastica e Dissipazione*, Zanichelli, Bologna, Italy, 1969.

¹³Caputo, M., "Vibrations of an Infinite Plate with a Frequency Independent Q," *Journal of the Acoustical Society of America*, Vol. 60, 1976, pp. 637.

¹⁴Caputo, M. and Minardi, F., *Pure and Applied Geophysics*, Vol. 91, 1971, pp. 134-147.

¹⁵Scott-Blair, "The Phenomenological Method in Reology," *Research*, London, 1953, pp. 92-96.

¹⁶Morgenthaler, D. R., "Practical Design and Analysis of Systems With Fractional Derivative Materials and Active Controls," *Proceedings of Damping '91*, Vol. 1, 1991, pp. BCA.

Structural Control Sensors for the CASES GTF

H.W. Davis ¹ and A.P. Buckley ²

ABSTRACT: CASES (Controls, Astrophysics and Structures Experiment in Space) is a proposed space experiment to collect x-ray images of the galactic center and solar disk with unprecedented resolution. This requires precision pointing and suppression of vibrations in the long flexible structure that comprises the 32-m x-ray telescope optical bench. Two separate electro-optical sensor systems are provided for the ground test facility (GTF). The Boom Motion Tracker (BMT) measures eigenvector data for post-mission use in system identification. The Tip Displacement Sensor (TDS) measures boom tip position and is used as feedback for the closed-loop control system that stabilizes the boom. Both the BMT and the TDS have met acceptance specifications and were delivered to MSFC in February 1992. This paper describes the sensor concept, the sensor configuration as implemented in the GTF, and the results of characterization and performance testing.

1. CASES GTF DEVELOPMENT

The Controls-Structures Interaction (CSI) Advanced Development Facility (ADF) is under development at Marshall Space Flight Center (MSFC) for the purposes of supporting ground testing of future flight experiments, the investigation of advanced control and system identification methodologies, and structural dynamics studies. The baseline configuration of the facility is that of the Controls, Astrophysics, and Structures Experiment in Space (CASES), a proposed shuttle-based flight experiment that will initiate on-orbit demonstrations of CSI technology. The experiment will provide active control of a 32-m extendible boom structure, using gas thrusters at the tip for pointing and angular momentum exchange devices (AMED) for active damping to suppress vibrations. The boom mechanically links an occulter plate at the boom tip with proportional counters located at the base to comprise an x-ray telescope. The controller goal is to provide accurate alignment of these devices for the purpose of x-ray observation of the galactic center and the Sun. Variations on this proposed experiment include a CASES without the x-ray devices (Controls And Structures Experiment in Space) or a free-flying version launched either by the Shuttle or an expendable booster.

¹ Ball Electro-Optics/Cryogenics Division (BECD)

² NASA/Marshall Space Flight Center (MSFC)

The CASES ground test facility (GTF) will provide an environment in which advanced control laws, system identification techniques, failure detection and compensation schemes, real-time flight software, and experiment data handling techniques can be verified. Prototypes of sensors, actuators, and flight computers can be functionally verified in the laboratory, as can actual flight hardware. Boom deployment and retraction dynamics, which will require active control, can also be investigated. Rapid reconfiguration capability in the laboratory will allow various flight configurations to be tested and verified, thus reducing development cost, time, and risk.

2. FACILITY DESCRIPTION

The CASES GTF is located in the Load Test Annex high bay in Building 4619 at MSFC. The test article, the boom from the Solar Array Flight Experiment (SAFE) flown in 1984, is suspended vertically from a platform at the 40-m level. The disturbance system, comprised of two electromagnetic shakers, a tripod floated on air bearings, and an annular ring support surface, provides two translational degrees of freedom. A simulated Mission Peculiar Experiment Support Structure (MPESS), suspended from the center of the tripod through the annular ring support, interfaces the disturbance system with the test article to simulate a flight experiment interface with the Shuttle, MPESS, and the payload experiment. The boom supports a simulated occulting plate at the boom tip. The control objective of the flight experiment is to maintain alignment of the tip plate with the detector at the base of the boom on the Shuttle as the occulting plate is pointed towards a star to perform an x-ray experiment. Similarly, the ground experiment will strive to align the tip plate with the simulated detector at the MPESS. Control authority will be provided by the AMEDs for vibration suppression and the bi-directional linear thrusters at the tip. Gravitational effects on the experiment will be processed out. Reference 1 provides a detailed description of the CASES GTF. See Appendix A for the poster session presentation of this paper.

The key sensor systems to be used in the GTF are the Boom Motion Tracker (BMT) and the Tip Displacement Sensor (TDS) under development by BECD (Figure 1). The TDS will be used in closed-loop controller experiments as the feedback element, providing information on the precise alignment of the tip plate. The BMT will be used for the identification of boom mode shapes. Initially, the BMT data will be processed post-facto. Future upgrades to the facility will provide the capability to use BMT data real-time in closed-loop control.

3. ROLE OF THE RAMS SENSOR

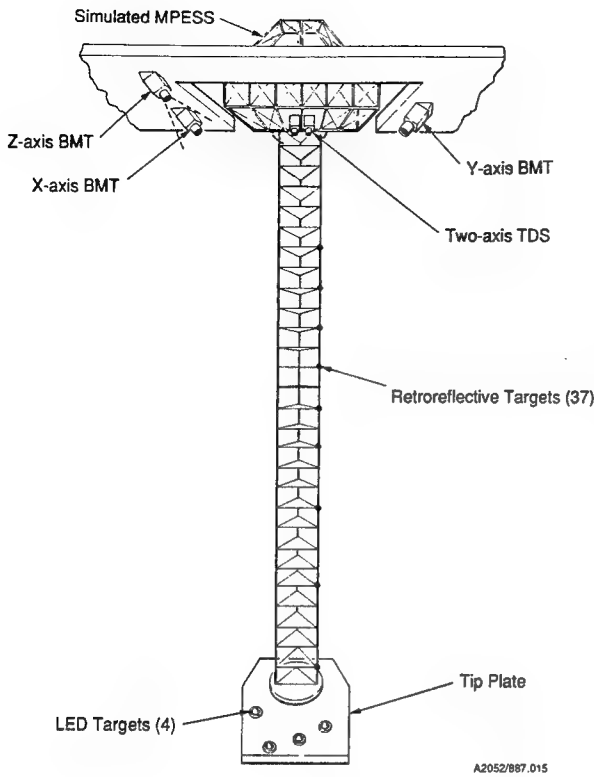


Fig. 1.

The Remote Attitude Measurement Sensor (RAMS) was designed by BECD under IR&D to measure dynamic behavior of large, flexible space structures. RAMS provides an unobtrusive sensor with update rates, accuracies, and target capacities which exceed present technology. This capability is needed for both system identification and control feedback applications in space.

In the CASES GTF, the BMT observes and records dynamic behavior of the flexible boom structure. Three single-axis sensors are mounted at the base of the cantilevered boom and each monitors the translational displacements (within its sensitive plane)

for 37 reflective targets distributed along the length of the boom. The X and Y sensors are offset equidistant from the base of the boom and oriented such that their sensitive planes are orthogonal to each other. The third (Z) sensor is offset further from the boom but along the same radial line as the X sensor. The increased offset distance improves sensitivity to z-axis motion, which is calculated by subtracting the effect observed by the X sensor. The BMT illuminates and monitors targets at ranges up to 32 m while measuring displacements to accuracies of 0.40 mm for the x and y axes. The Z sensor is less sensitive and measures displacements to an accuracy of 7 mm. Expected target motion for all three sensors is ± 25 cm. The BMT updates the position of each target at 100 Hz. Displacement data is output to the CASES control processor in the form of BMT pixel number, with data for all targets multiplexed in digital format.

The TDS provides position feedback for the closed-loop control system that maintains tip position. Two single-axis sensors are mounted near the base of the cantilevered boom and measure 2-axis translational displacements for the four (4) light-emitting diode (LED) active targets. The targets are arranged in a fashion that ensures no overlap of targets in either sensed direction. The TDS observes the four targets at a range of 32.3 m and measures displacements to an accuracy of 0.60 mm. Update rate is selectable between 25 and 500 Hz. Displacement data is output to the CASES control processor in the form of TDS pixel number, with data for each target assigned to a dedicated line and in analog form. A ± 10 V change in signal corresponds to a ± 25 cm displacement of a TDS target.

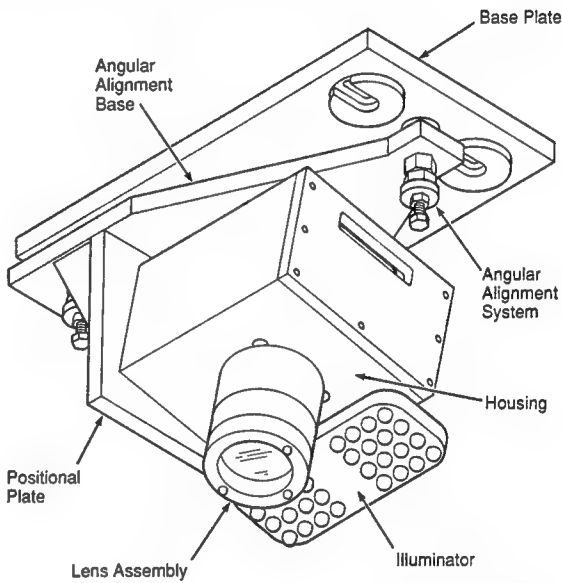
4. RAMS IN THE GTF

The RAMS design is derived from proven space sensor technology. The electronic design concepts and interpolation algorithms for RAMS have been demonstrated in space hardware, including the Retroreflector Field Tracker (RFT) that was flown on the Shuttle in 1984 and a variety of Ball-built star trackers. RAMS consists of a simple electro-optical design. It uses a cooperative light source (typically an LED) to illuminate reflective targets within its field of view (FOV). The reflected images are focused onto a linear charge-coupled device (CCD) detector by a cylinder lens to produce a line image. Displacement of a target causes the focused image to shift position on the CCD, giving an accurate indication of the angular displacement. Knowing the range of the target, translational displacement can be calculated.

RAMS (Figure 2) uses a CCD detector with 1 x 2,098 pixels and proprietary BECD interpolation algorithms that permit centroiding of target images to approximately 2% of a pixel. High update rates are achieved by pipeline processing of the CCD data in analog form. RAMS can provide resolution to better than 1:100,000 and update rates of 500 Hz for each of 50+ targets. It uses off-the-shelf, low-cost parts such as Nikon OEM lens, Newport alignment flexures, Kodak CCD detectors and AND brand light-emitting diodes. A detailed description of RAMS and CASES is provided in Reference 2.

4.1 BMT Design

The BMT X and Y sensors are oriented such that their detectors are in the same plane as the boom and tilted at a slope that provides proper focus for every target. (This is guaranteed by the "Scheimpflug" condition.) The required FOV of each sensor (approximately 20 deg) is determined by the viewing geometry (e.g., offset distance from boom, distance to nearest and farthest targets, expected range of motion). The actual FOV exceeds this amount and is based on the detector pixel size, number of pixels, and the focal length of the lens (85 mm). The achievable resolution is determined by the angular subtense of each pixel and the degree to which subpixel interpolation can be achieved. Target distance varies from 3.6 m to 31.3 m. The major design challenges for the BMT are achieving the desired image shape and sufficient optical return signal from the farthest target. These considerations are influenced by the



A2052/887.018

Fig. 2.

radiometric characteristics of the illuminator and by the size, shape, and retroreflective properties of the target material.

The BMT targets are made from 3M-brand Model 2000X retroreflective tape. This high-gain material contains microscopic corner cubes laminated beneath a protective film. The targets are diamond-shaped, as viewed by each sensor, and sized to subtend a specified angle within the FOV. Thus, target size will vary with range, but image width will remain constant. This condition is necessary in order to maintain precision in the interpolation algorithms. Incident light on this tape material is retroreflected with a luminance factor of 3000 and primarily within a 1.1 deg conical beam (full angle). The targets are illuminated by an array of 36 LEDs mounted on each sensor head. The illuminators must be positioned near the optical axis of the sensor because of the retroreflective nature of the targets. Most of the LEDs are aimed at the farthest target. The quasi-Gaussian illuminator beam pattern provides an appropriate amount of radiance on the mid-range targets. Some LEDs are also tilted towards the upper targets to illuminate them. Each LED is rated at 13 candelas and has a beam divergence of approximately 4 deg.

The sensor head is comprised of a thick-walled aluminum box on which a lens assembly is mounted (Figure 3). The lens assembly includes the off-the-shelf Nikon camera lens which is fitted with a cylinder lens to provide line images and a wide-band filter to reduce background illumination. The CCD detector, preamplifier circuitry, and detector mounting hardware are installed within the sensor head. Proper orientation and positioning of the detector with respect to the lens is crucial to accurate measurement of target position. The Kodak KLI-2103 CCD detector has 2,098 pixels, each $14 \times 14 \mu\text{m}$ in size. This detector was selected for its low noise characteristics, high responsivity, and uniformity of photo-response between adjacent pixels. Data is transferred at rates exceeding 1 MHz and handed off to a separate electronics box containing the analog and digital processing circuitry. The analog pipeline processor detects the presence of targets, interpolates the position of each to within 2% of a pixel, and tags the data with a target number. This analog data is converted to digital form and multiplexed prior to output. The BMT data interface is a 32-bit parallel data word which is read by the CASES control computer upon generation of a strobe by the BMT.

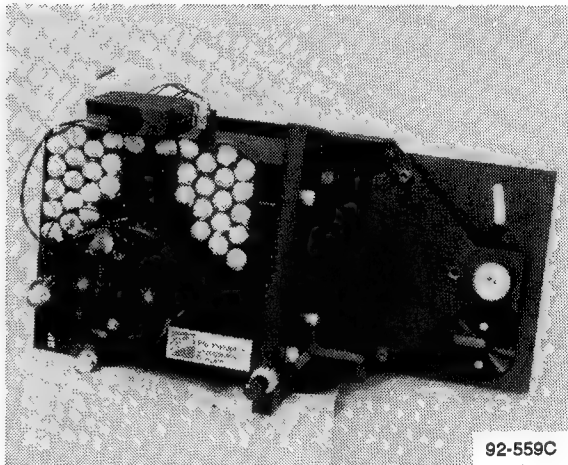


Fig. 3

4.2 TDS Design

The TDS sensors are mounted orthogonal to each other and observe the four (4) LED targets mounted on the upper surface of the tip plate. Using the known locations and unique pattern of the targets with respect to the tip plate, the motion of the tip plate reference point (i.e., target centroid) can be monitored. The required FOV of each TDS sensor (2.3 deg) is determined by the target range, target spacing, and the maximum expected motions of ± 25 cm. The actual FOV (5 deg) is larger than necessary because of the intentional use of common detectors for both the TDS and the BMT. The FOV would actually be larger (approximately 15 deg) except that 70% of the pixels have been electronically disabled to preclude the detection of extraneous images (false targets). The major design challenges for the TDS are high update rate, target range and high resolution. The use of active (LED) targets rather than passive (retroreflector) targets improves the radiometric performance significantly and allows the shorter integration times needed for higher update rates. The four TDS targets consist of individual LEDs fitted with an adjustable spherical lens that expands the illumination beam to 15 deg (Figure 4). Beam divergence is based on the angular offset with respect to the sensor head plus an expected tilt of the tip plate of ± 5 deg.

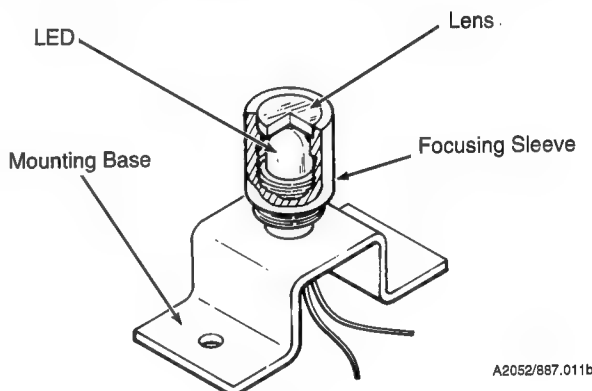


Fig. 4.

The TDS sensor head is identical to the BMT sensor, with two minor exceptions. There are no illuminators on the TDS sensor because active targets are used (Figure 5). The detector mounting block holds the detector normal to the optical axis (rather than tilted) because the targets are equidistant in range and require the same image distances. The TDS uses eight dedicated analog circuits to transmit analog position data for each of the four targets measured by each of the two sensor heads. Each target has a unique offset voltage at its stationary position, such that maximum resolution can be gained from the ± 10 V range of the analog output.

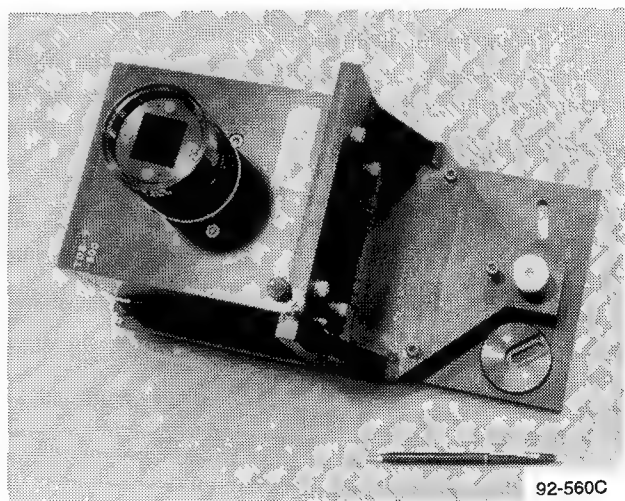


Fig. 5.

5. CURRENT STATUS

The BMT and TDS systems were delivered to MSFC in February 1992, following extensive testing and acceptance at BECD earlier that month. Both systems performed exceptionally well and satisfied MSFC's specifications for accuracy, update rate, translation range, number of targets, and system weight. Power consumption was the only area that exceeded specification limits, and this was due in part to the addition of LED illuminators and larger power supplies.

Characterization testing of the BMT and TDS illuminators demonstrated ample margins for both radiance and beam angle (Figure 6). Further improvements in the uniformity of the radiation patterns can be achieved by exploiting the characteristic double-hump shape of the LED beam and overlapping the peaks and valleys of adjacent beams.

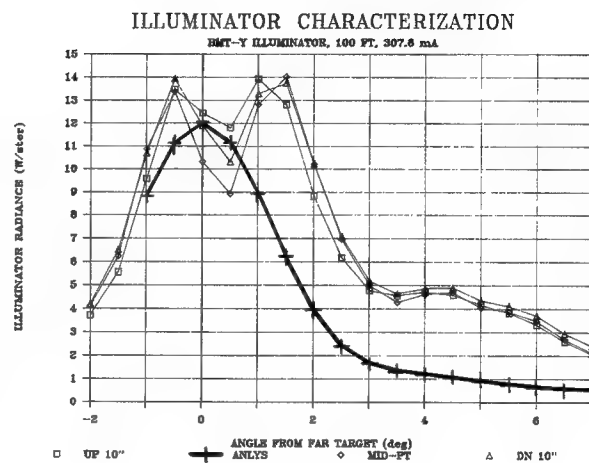


Fig. 6.

Characterization testing of the BMT sensors demonstrated concurrent focus for all 37 targets (as dictated by the "Scheimpflug" condition) and the required image quality for successful implementation of the interpolation algorithms. High signal-to-noise ratio was achieved (Figure 7), which is directly related to low noise-equivalent-displacement and the attainment of high accuracy. A high degree of sub-pixel linearity was achieved (approximately one percent), which is essential for high accuracy performance (Figure 8). Field of view margins were as high as 100%, signifying good coverage by both the optical elements and the illumination beams.

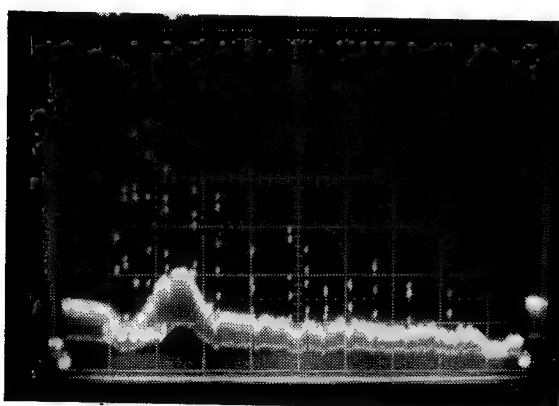


Fig. 7

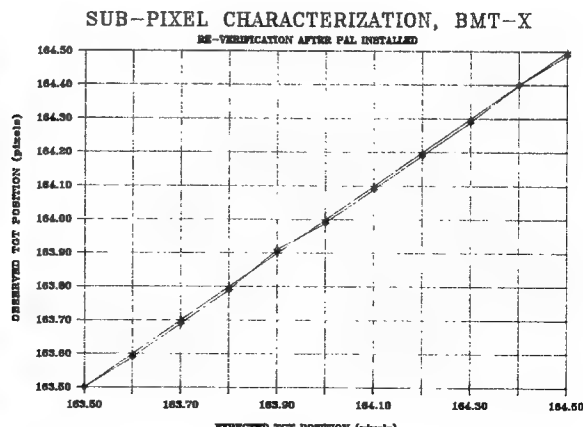


Fig. 8.

The results of the acceptance tests are shown in Table I for both the BMT and the TDS.

TABLE I
TEST RESULTS

PARAMETER	BMT	TDS
Accuracy: Translation	< 0.015 in. @ 102 ft (X,Y)	< 0.024 in. @ 105 ft
Angular Translation	< 2.5 arcsec (X,Y) < 0.27 in. @ 102 ft (Z)	< 3.9 arcsec
Field of View	20 deg by 4 deg	5 deg by 5 deg
Update Rate	100 Hz	25 Hz to 500 Hz (10 selectable steps)

At the time of publication of this paper, the BMT and TDS systems had not been integrated into the CASES facility at MSFC. The performance of both systems in a dynamic environment will be demonstrated and reported in a future technical paper.

References:

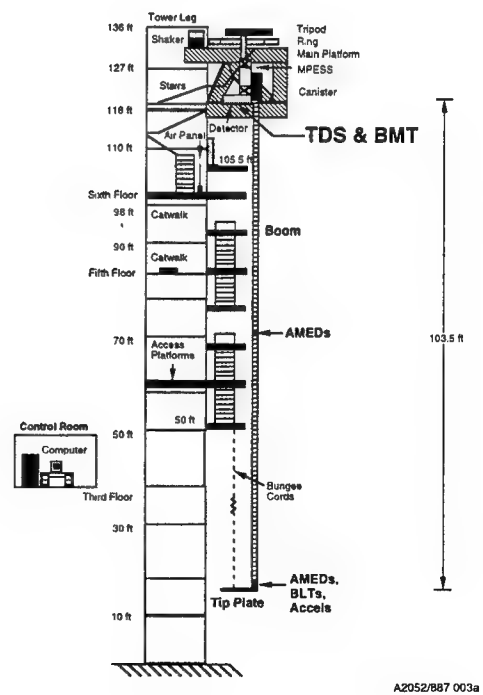
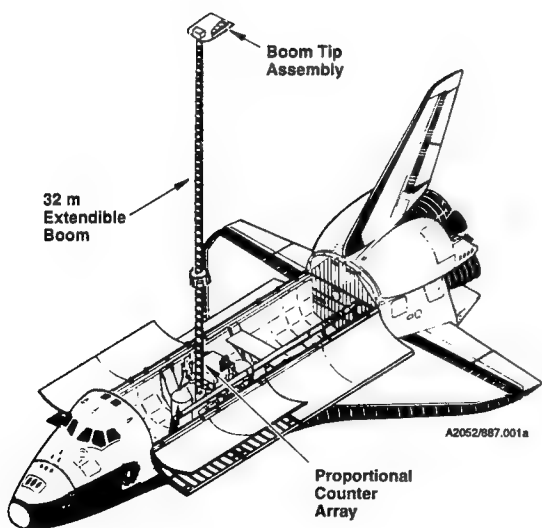
1. Jones, V.L., Buckley, A.P. and Patterson, A.F., "NASA/MSFC Large Space Structures Ground Test Facility," Proc. AIAA Guidance & Control Conf., New Orleans, LA, August 1991.
2. Davis, H.W., Sharkey, J.P., and Carrington, C.K., "Structural Control Sensors for Control, Astrophysics, and Structures Experiment in Space (CASES)," Advances in Optical Structure Systems, Volume 1303, Proc. SPIE, Orlando, FL, April 1990.

APPENDIX A:

Structural Control Sensors for the CASES GTF

H. W. Davis
Ball Electro-Optics/Cryogenics Division

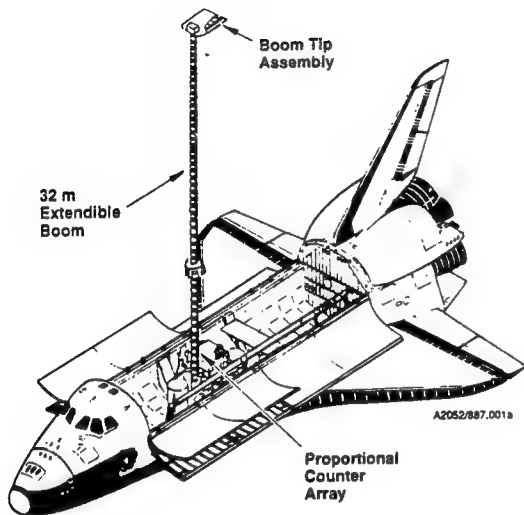
A. P. Buckley
Marshall Space Flight Center



CASES Flight Experiment

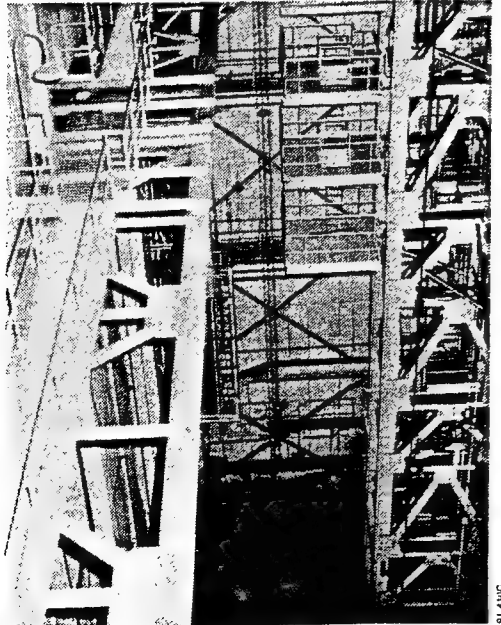
CASES Ground Test Facility (GTF)

CASES (Controls, Astrophysics, and Structures Experiment in Space)



CASES Flight Experiment

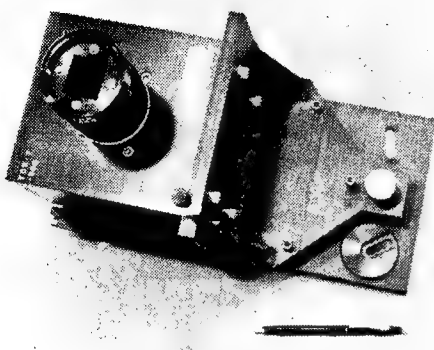
- CASES is a proposed space experiment to conduct x-ray science and CSI research
- The science portion provides x-ray imaging of the galactic center and the Sun with unprecedented resolution
- Requires precision pointing and suppression of vibrations in the x-ray telescope comprised of a 32-m flexible boom, an occulter plate at the tip, and proportional counters at the base
- The CSI mission provides stabilization for precise telescope pointing plus an on-orbit testbed for demonstrating alternative control methods
- Variations under consideration include a free-flyer version or a CASES without the x-ray devices



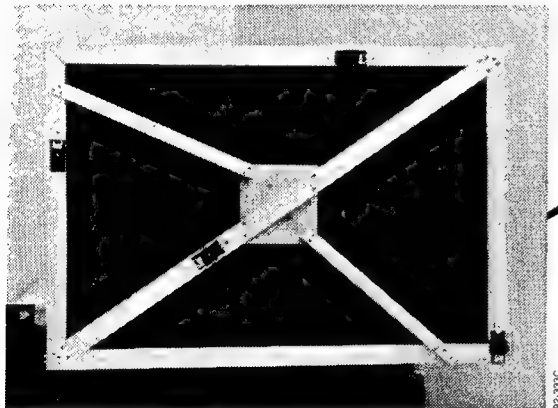
- GTF baseline configuration is modelled after the CASES flight experiment
- GTF development will support verification and validation of flight hardware and software:
 - Advanced control laws
 - System identification techniques
 - Failure detection/compensation
 - Real-time flight software
 - Experiment data handling methods
 - Prototype sensors and actuators
 - Prototype flight computers
 - Actual flight hardware
- Structural dynamics investigations planned:
 - Modal behavior of the boom
 - Boom deployment/retraction
 - Disturbance characteristics and effects

CASES Ground Test Facility (GTF)

Tip Displacement Sensor (TDS)



TDS Sensor Head

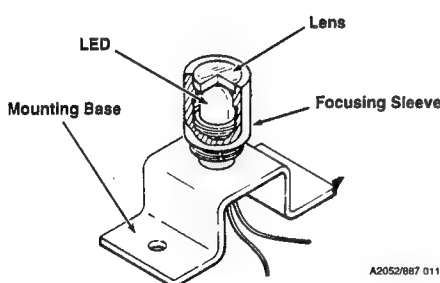


Test Fixture With TDS Illuminators (Targets)

92-5690C

92-5690C

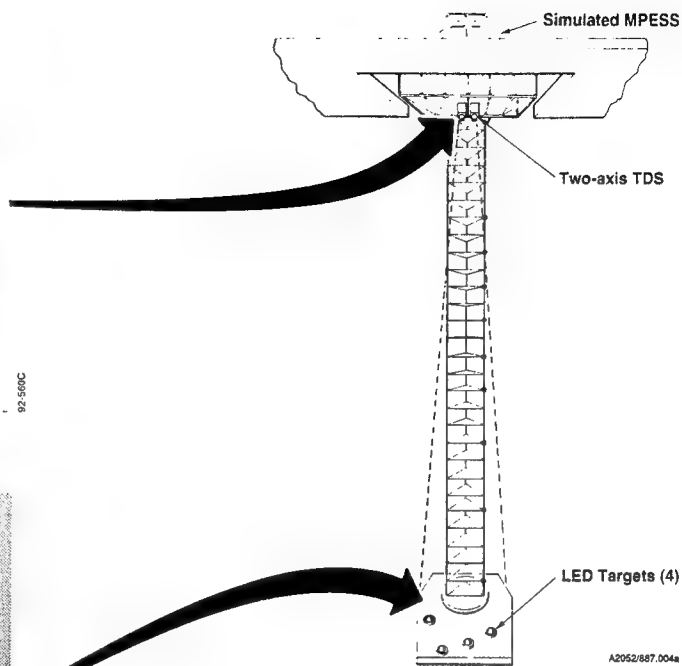
A2052/887 011b



TDS Illuminator/Target

A2052/887 011b

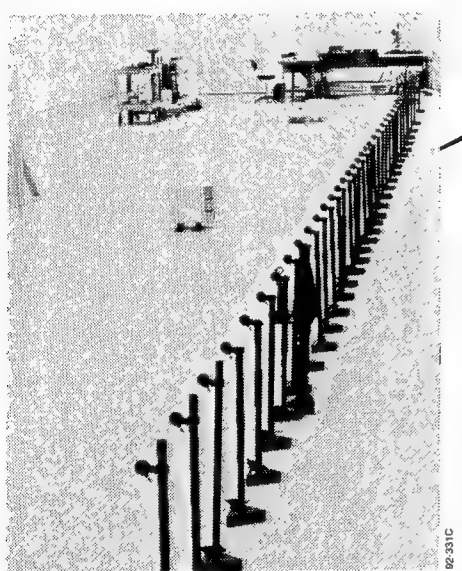
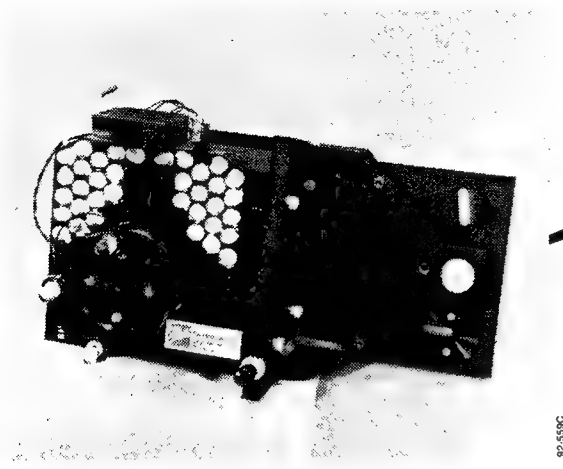
- Illuminator/Target:
 - Four (4) separate active targets
 - Each uses one HP 15-candela LED
 - Adjustable lens expands LED beam to 15 deg



A2052/887.004a

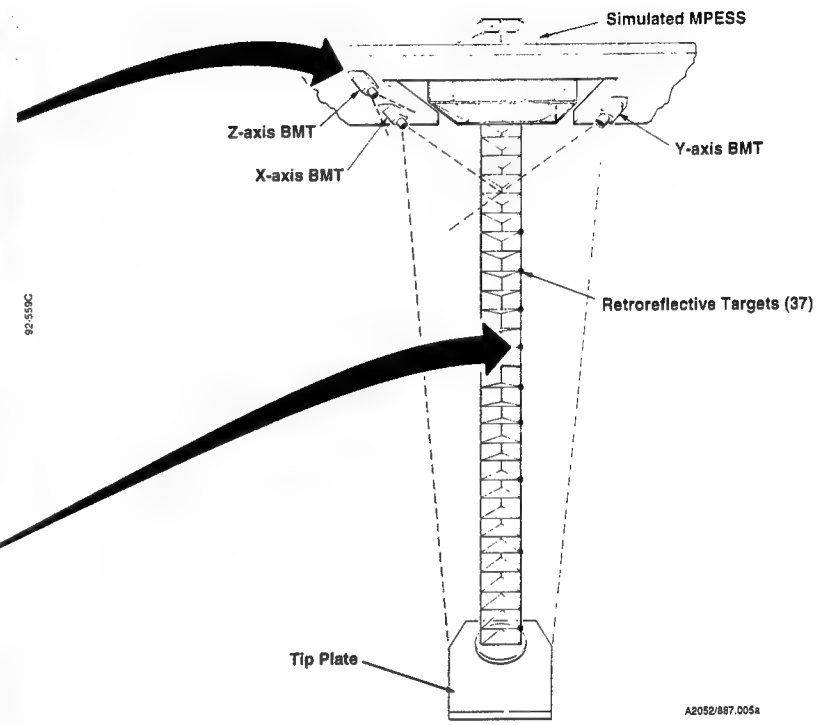
- Two single-axis electro-optical sensors mounted at the base of the boom
- TDS sensors view 4 active (LED) targets on the tip plate (32.3 m range)
- TDS sensors measure motions in two orthogonal directions (X, Y) to an accuracy of 0.60 mm
- Update rate for target position is selectable between 25 and 500 Hz
- Data output in analog form (± 10 V) on eight (8) dedicated circuits to the CASES control computer
- System Characteristics:
 - Field of view: 2.3 deg (required)
 - Target range: 32.3 m
 - Update rate: 25 to 500 Hz (selectable)
- Sensor Head Description:
 - Nikon 105 mm f/2.5 lens
 - Cylindrical lens: -425 mm
 - Same detector and filter as BMT design
 - Detector is mounted normal to optical axis

Boom Motion Tracker (BMT)



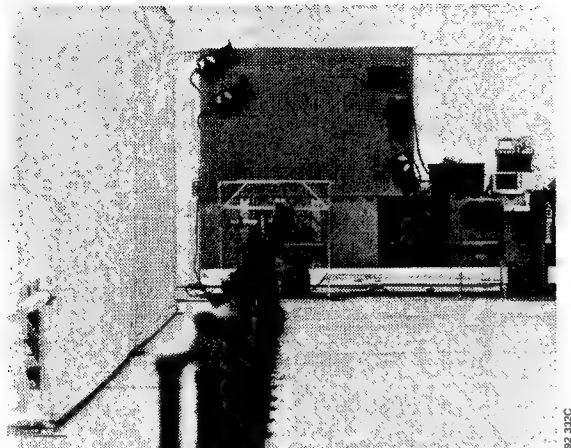
Test Array of Retroreflective Targets

- **System Characteristics:**
 - Field of view: 20 deg (Approx.)
 - Target range: 3.6 to 31.3 m
 - Update rate: 100 Hz
- **Sensor Head Description:**
 - Nikon 85 mm f/1.8 lens (X,Y sensor)
 - Nikon 70 mm f/1.8 lens (Z sensor)
 - Kodak KLI-2103 CCD detector (tilted)
 - Cylindrical lens: -425 mm (X/Y)
-300 mm (Z)
 - Long pass glass filter (0.59 to 3 μ m)

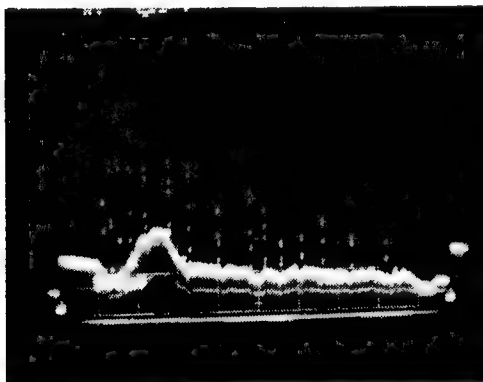


- Three single-axis electro-optical sensors mounted at the base of the boom and offset by approximately 1 meter
- BMT sensors view 37 retroreflective tape targets distributed along the length of the boom
- BMT measures 3-axis translational motions (X,Y,Z) to an accuracy of 0.40 mm (7 mm for Z axis)
- Update rate for each target is 100 Hz
- Output data is multiplexed for all 37 targets and all three sensors; output is in digital form

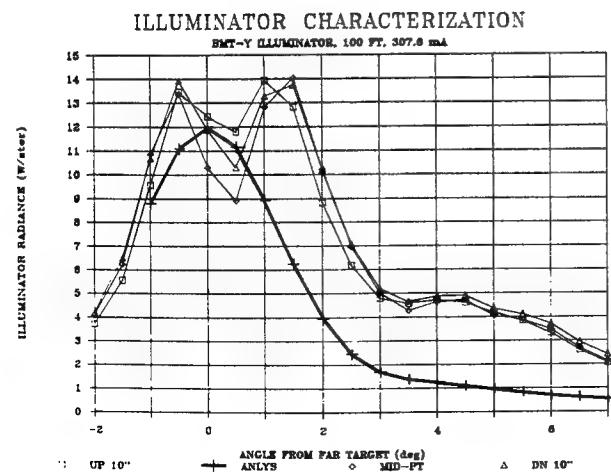
Verification Methods & Results



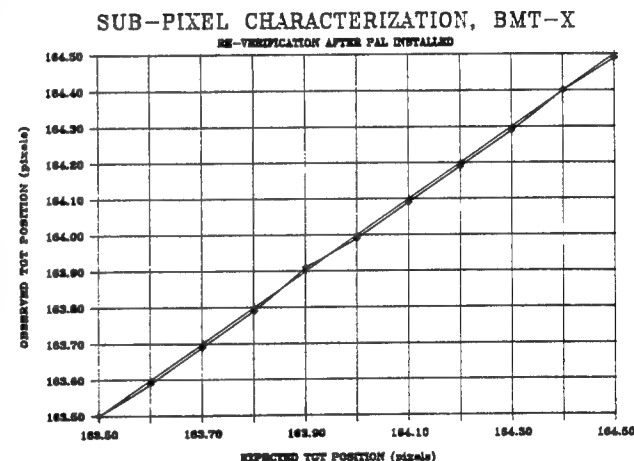
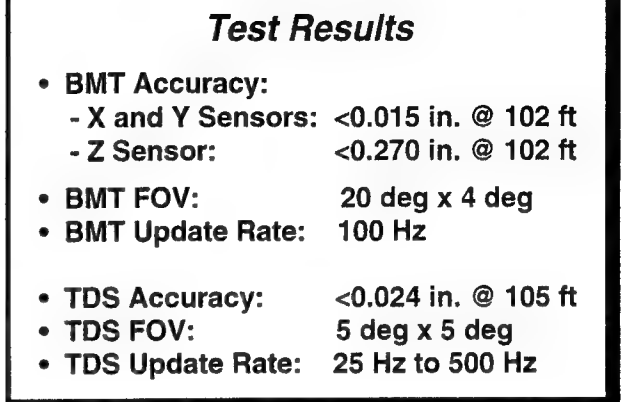
ADF RAMS Test Facility



Oscilloscope Picture of BMT X-sensor
Showing 15 Targets



Photometer measurements
of the BMT illuminator
showed *good agreement*
with predictions



*Demonstrated high degree
of linearity across a pixel*

SSF LOADS AND CONTROLLABILITY DURING ASSEMBLY

C.R. LARSON, S. GHOFRANIAN, E. FUJII

Rockwell International, Space System Division, Downey, California

The Orbiter Primary Reaction Control System (PRCS) pulse width and firing frequency is restricted to prevent excessive loads in the Space Station Freedom (SSF). The feasibility of using the SSF Control Moment Gyros (CMG) as a secondary controller for load relief is evaluated. The studies revealed the CMG not only reduced loads but were useful for other SSF functions: vibration suppression and modal excitation. Vibration suppression lowers the g level for the SSF micro-g experiments and damps the low frequency oscillations that cause crew sickness. Modal excitation could be used for the modal identification experiment and health monitoring. The CMG's reduced the peak loads and damped the vibrations. They were found to be an effective multi-purpose ancillary device for SSF operation.

INTRODUCTION

The Shuttle Digital Auto Pilot (DAP) software determines jet-firing commands for attitude hold or attitude maneuvers. The desired Orbiter attitude and/or rates are determined by the DAP for automatic control or requested by the crew (via hand controller) for manual control (see reference 1). The DAP then attempts to achieve and maintain these attitude and rate commands within the crew-specified: attitude error deadbands, and rate limits. The errors are the difference between the DAP commands and the estimates of the states, derived from the Inertial Measurement Unit (IMU) data. Jet firings are commanded whenever the errors exceed the margins.

For Space Station Freedom (SSF) assembly, the standard Orbiter DAP induces large loads on the SSF; thus an alternate mode of operation (ALT mode) in which the jet firing pulse width, time between firings, and number of jets fired are restricted. The PRCS ALT mode reduces induced loads on the SSF with a pulse width restriction of 80 ms, a maximum of two simultaneous jet firings, and long delay times. Controllability becomes a problem when the delay time exceeds 10 seconds. The potential loads/controllability problems led to consideration of two alternate concepts: active CMG's and a damping platform. In this paper, the CMG studies performed at Rockwell International with IR&D funds are presented.

RESULTS

CMG 's WITH PARALLEL PROCESSING :

The study results showed that the four SSF CMG's can:

1. provide vibration suppression which should reduce ALT DAP restrictions during mated PRCS maneuvers,
2. improve the environment for micro-gravity experiments,
3. reduce the trampoline vibrations which cause crew sickness,
4. provide load relief and vibration suppression during docking/berthing,
5. excite the SSF structural modes for modal identification and health monitoring.

The CMG's can perform these tasks in parallel with SSF attitude control or during mated Orbiter PRCS attitude control. The effectiveness of the CMG's for vibration suppression or modal excitation depends on their locations relative to the anti-nodes of the system structural modes. For micro-gravity vibration suppression, effectiveness also depends on the capability to measure the low levels of vibration. The measured rates are needed for the controller feedback.

In Figure 1, the CMG controller is shown in parallel with the SSF attitude control system. The CMG controller removes the rigid body component of the angular rate with a $s/(s+a)$ high pass filter and produces a torque proportional to the angular rate. The CMG's have a capability to produce a torque of 200 ft-lb for short periods of time and 100 ft-lb for longer periods. The CMG's can respond to 50 Hz inputs. This capability is not used for the low bandwidth (0.04Hz), low sample rate (10 samples/second) SSF attitude control system. The CMG parallel processor needs a sample rate of 60 samples/second to damp modes with frequencies below 15 Hz. The constant (a) in the CMG parallel processor was chosen as 0.1 rad/second (0.02 Hz). With a 60 Hz sampler the CMG's would respond to signals with frequencies between 0.02 and 15 Hz.

The generic SSF model (see figure 2) used in the IR&D study was a nine node beam model with SSF MB5 pre-PIT (Pre-Integrated Truss) mass properties and an equivalent truss structural stiffness. The beam model was coupled to a rigid Orbiter. The CMG's were attached to the seventh node 3000 inches from the Orbiter. The torque from the CMG's was filtered (with a limiter) to prevent torques above 400 ft-lb (4800 lb-in). The CMG's can produce 800 ft-lb of torque for short periods of time but a conservative evaluation was sought. An 80 ms pulse with an amplitude of 900 lb (simulates a PRCS single jet firing with a minimum pulse width) was applied to the Orbiter where the tail jets are located. The present SSF MB configurations extend forward of the Shuttle when mated. The nose jets are not fired because of plume impingement. The interface loads, CMG applied torque, Orbiter angular rate, and the angular rate at the location of the CMG's were recovered. The simulation was performed with the Dynamic Analysis and Design System (DADS) program. The Craig Bampton NASTRAN beam model component modes were generated and converted to DADS format. Two sets of modes were used in the study: a 21-mode set with four x-directional bending modes and a 38-mode set with eight x-directional bending modes. No structural damping was included, so the CMG's were the only source of damping.

The interface load for a single pulse with and without an active CMG controller is shown in figure 3. The peak moment of 60,000 lb-in is reduced to 50,000 lb-in with the active CMG's. The CMG's damp the low frequency amplitudes from 50,000 to 25,000 in one cycle (11% damping), but the higher frequency (1 Hz) amplitudes are lightly damped. The CMG's may be located near the 1 Hz anti-node of that mode. The CMG's produce a torque proportional to the angular rate (at the CMG location). The angular rate (see figure 4) is dominated by the low

frequency component. The angular rate and CMG torque in figure 4 show some small amplitude 1 Hz motion. The CMG torque peaks are clipped by the 4800 lb-in torque limiter. If this CMG parallel processor was invoked for each SSF mated configuration, the amount of peak load reduction and damping would be a function of that configuration. Without CMG's, SSF has one percent structural damping. A 50,000 lb-in quarter Hz oscillatory interface moment would take 11 cycles or 44 seconds to decrease to 25,000 lb in. The interface moments for the SSF mated MB2 configuration have significant quarter Hz frequency content.

In a loads problem, one always considers the possibility that more input modes are needed for convergence. Four cases were run with 2,4,6, and 8 modes. The response for the 2 mode case was different but the other three were similar. In figure 5, the responses for 2 and 8-mode inputs are displayed. Four modes were sufficient for convergence.

Using the CMG's for vibration suppression would require an SSF DAP redesign or adding an additional micro-processor. Both alternatives are expensive and would impact the SSF schedule. Justification for that change would only happen if the load margins proved to be insufficient. If that change was made, the CMG could be designed for other modes of operation with no impact. For example, the CMG's could have an operational mode for mode excitation (it would be used for modal testing).

A Modal Identification Experiment (MIE) is planned for SSF. A similar experiment was performed on the Shuttle. The Program Test Inputs (PTI) shown on the top in figure 6 were input to the elevons and the rudder at three different times of flight. The inputs contained 2 cycles of oscillation at four frequencies. The data was used to determine damping and frequency information for assessment of flutter margins. Similar inputs could be used to generate torques for SSF, eg., 2 cy of 1.07 Hz and 5 cy of 3.3 Hz (shown on the bottom in figure 7). The CMG torques are generated with open loop inputs. The two cycle 1.07 Hz torque excited both the 1.07 Hz mode and the 0.2 Hz modes as seen in figure 7. The interface moment magnitude in figure 7 is dominated by the 1.07 Hz frequency but the low frequency component is seen in Orbiter angular rate. The five cycle 3.3 Hz torque excites two modes (see figure 8) but the 3.3 Hz response dominates. A better way of exciting the vehicle and controlling the amplitude would be to input an oscillatory signal that increased slowly in amplitude and was terminated when the response reached some predetermined value. The vehicle would have less energy in secondary modes with this approach. This could be used for health monitoring.

SSF structure may be damaged by space debris or meteorites. The damage could impair the operation of the SSF. The SSF structural health could be monitored by inputting PTI's and periodically checking the signature of accelerometers and/or rate gyros. The signatures must be updated when the configuration changes. Health monitoring is important from a safety standpoint.

The CMG's vibration suppression capability could be used to damp low frequency modes (these low frequency vibrations can cause astronaut sickness) and may be able to damp modes exceeding required micro-g experiment levels. In both cases, measurement of the vibration levels for the feedback controller would be difficult. For example, in the phase B SSF studies, a 25 lb crew member push off caused vibration levels 300 times the acceptable g level of 1E-05

g's. The push off also caused an attitude angle at the base of a payload pointing experiment of 24 arc-sec with an oscillatory component of about 2 arc-sec /sec. Laser type rate gyros can sense changes of 1-2 arc-sec. In this case, it would be difficult to damp the vibrations below 1 arc-sec/sec. In reference 2, the authors claim that they can reduce the quantization by several orders of magnitude. Their zero-lock laser gyro has a resolution of 1.5 arcseconds without enhancement and 0.001 arcseconds with resolution enhancement. The problem of measuring the vibration levels with resolution enhancement or relocating the sensor may solve this problem.

The oscillatory acceleration levels for micro-g experiments could be removed with electro-magnetic isolation systems, but there are problems associated with them. The isolators are designed for light objects and would need increased power to accommodate the heavy material processing experiments, and there also is a problem at the interface between SSF and the experiment. The isolator levitates the payload but the experiment needs power and cooling fluids to flow across the interface. These secondary paths can eliminate the isolation provided by the electro-magnetic system. It may be easier to suppress the vibration on the entire SSF. More studies are needed to determine if the CMG's could improve the environment for micro-g experiments.

CONCLUSIONS

The interface loads caused by a single pulse PRCS firing for a pre-PIT MB5 SSF mated configuration were reduced with an active CMG parallel processing controller by 20% and the controller added 11% damping to the system. The amount of load reduction and damping for actual mated SSF configurations will be configuration dependent. Without CMG's, the existing one percent structural damping will take 11 cycles (44 seconds for a 0.25Hz oscillation) to reach half amplitude. The changes necessary to implement CMG vibration suppression are expensive and would impact the SSF schedule. If the ALT DAP does not provide enough margin for loads while maintaining control during assembly, alternate concepts would be considered. The CMG's provide an ancillary control system which serves multi-purpose functions. The CMG's can provide damping and load relief for every phase of SSF operations. It can also be used for mode identification and health monitoring. With sensitive sensors, the CMG's can remove low frequency vibrations which cause astronaut sickness and remove the crew-induced oscillatory g-levels for a better environment for the micro-g experiments.

REFERENCES

1. *"Space Shuttle Orbiter, Operational, Level C, Functional Subsystem Software Requirements, Guidance/Navigation/Control, Part C flight Control, Orbiter DAP"*, STS83- 009C-01-20 November 29, 1990.
2. M. Fernandez, B. Ebner, & N. Dahlen, "Zero-Lock Laser Gyro", 12th Annual AAS Guidance and Control Conference Feb 4-8, 1989, Keystone, Colorado.

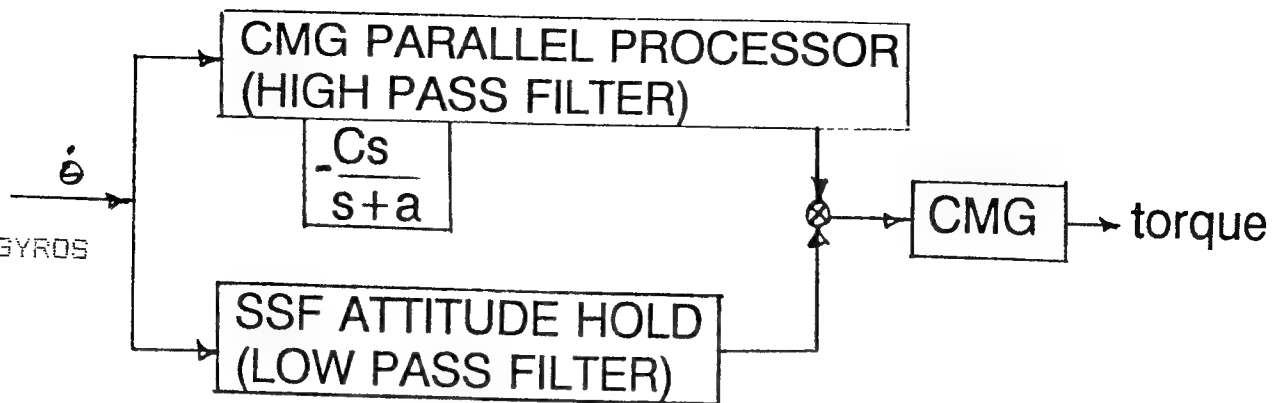


FIGURE 1. CMG PARALLEL PROCESSOR

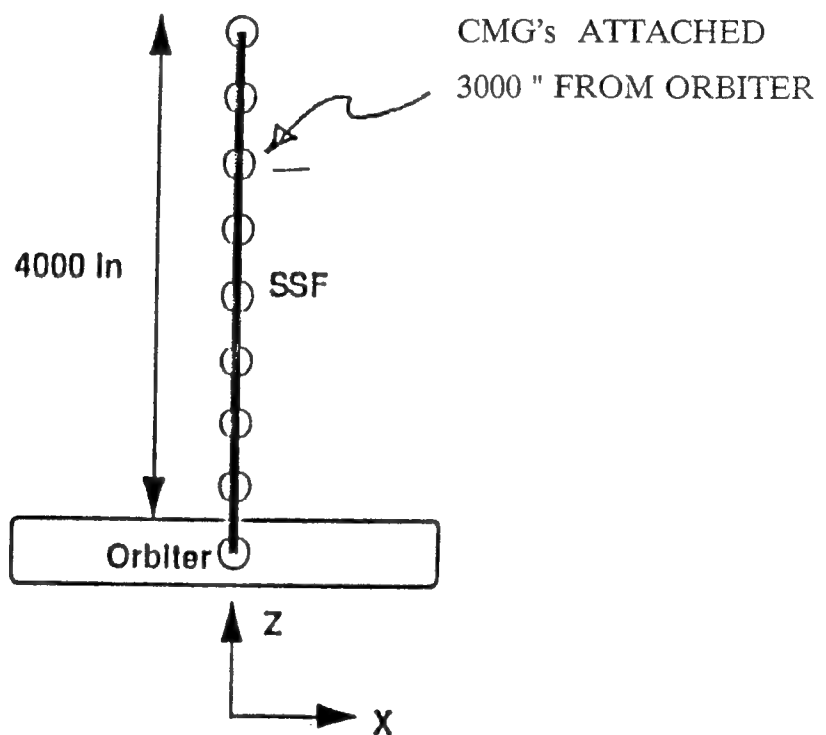


FIGURE 2. GENERIC SSF / ORBITER SIMULATION MODEL

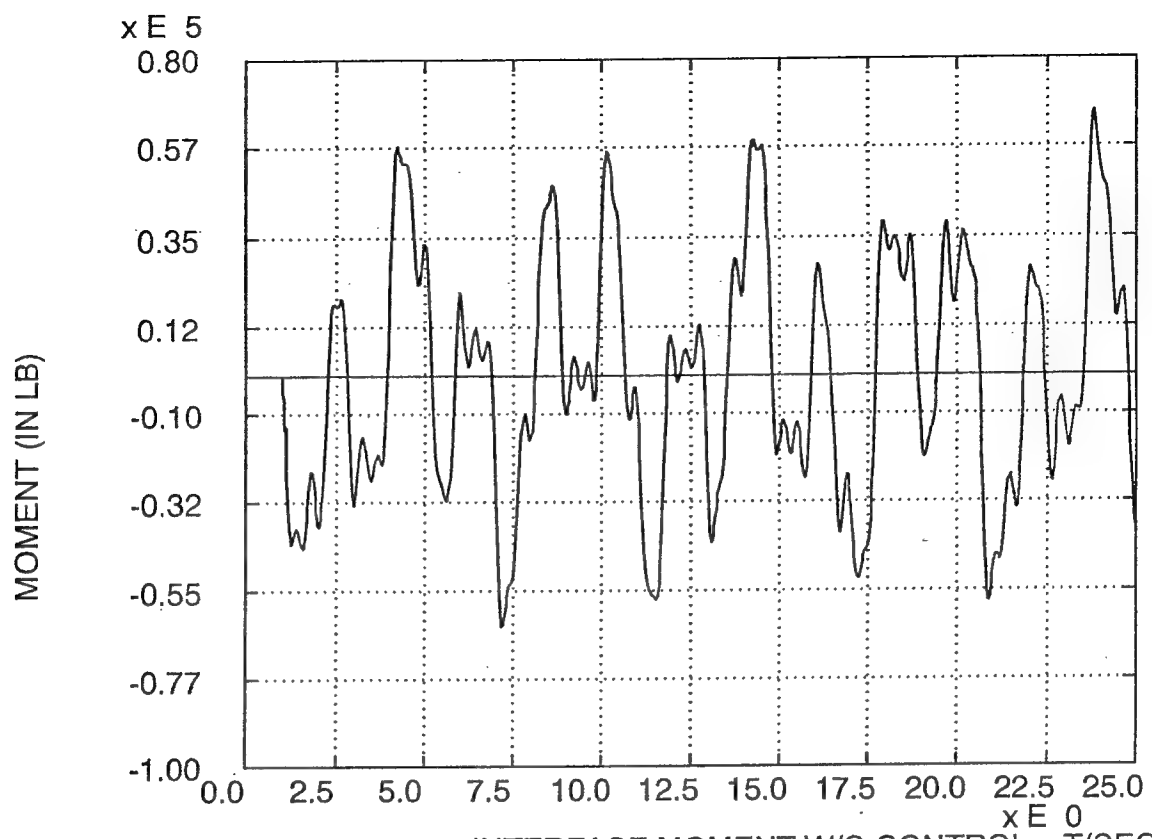


FIGURE 3A. INTERFACE MOMENT W/O CONTROL T(SEC)

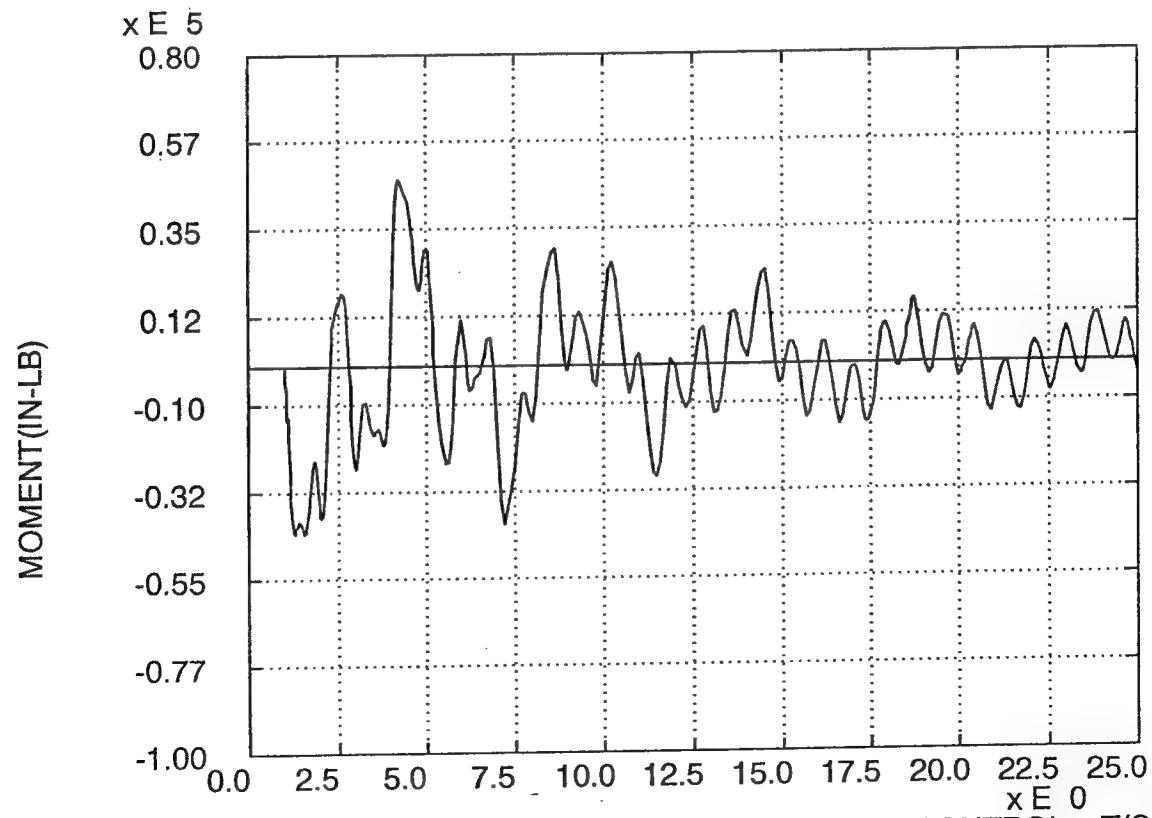


FIGURE 3B. INTERFACE MOMENT W CMG CONTROL T(SEC)

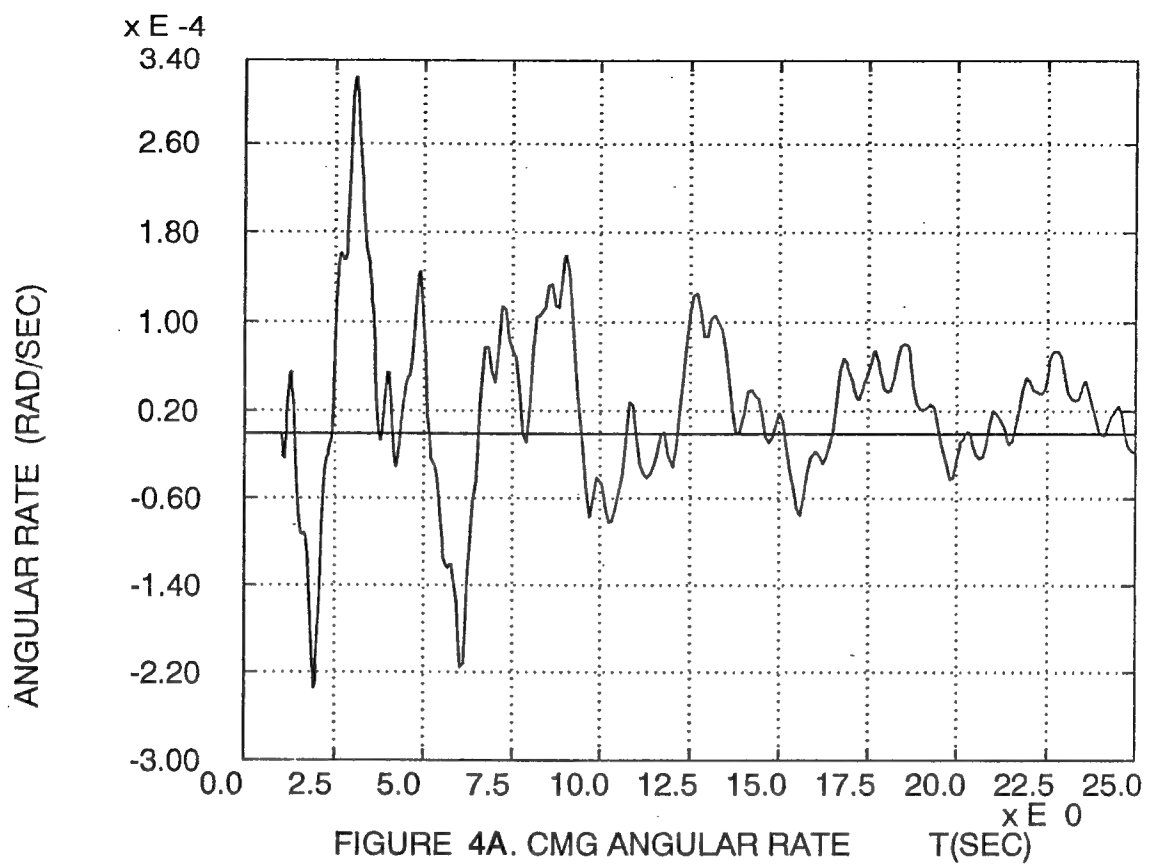


FIGURE 4A. CMG ANGULAR RATE

T(SEC)

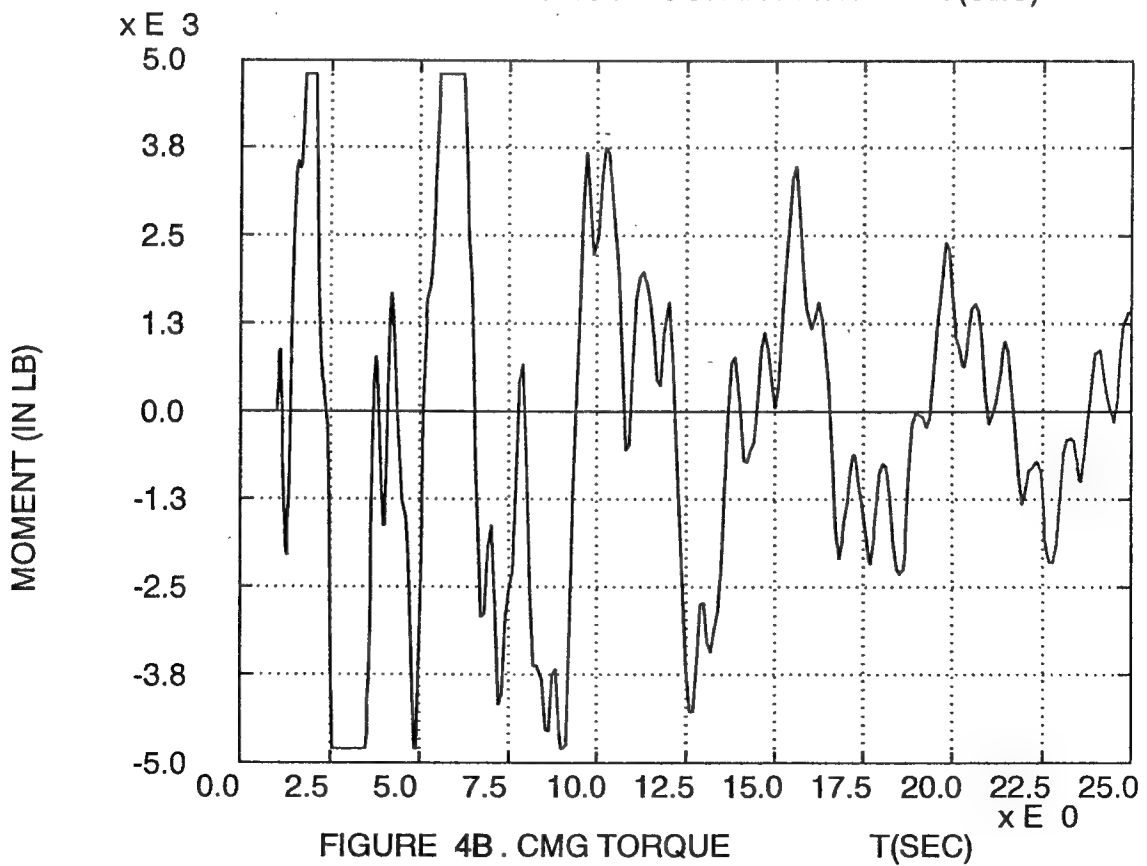


FIGURE 4B . CMG TORQUE

T(SEC)

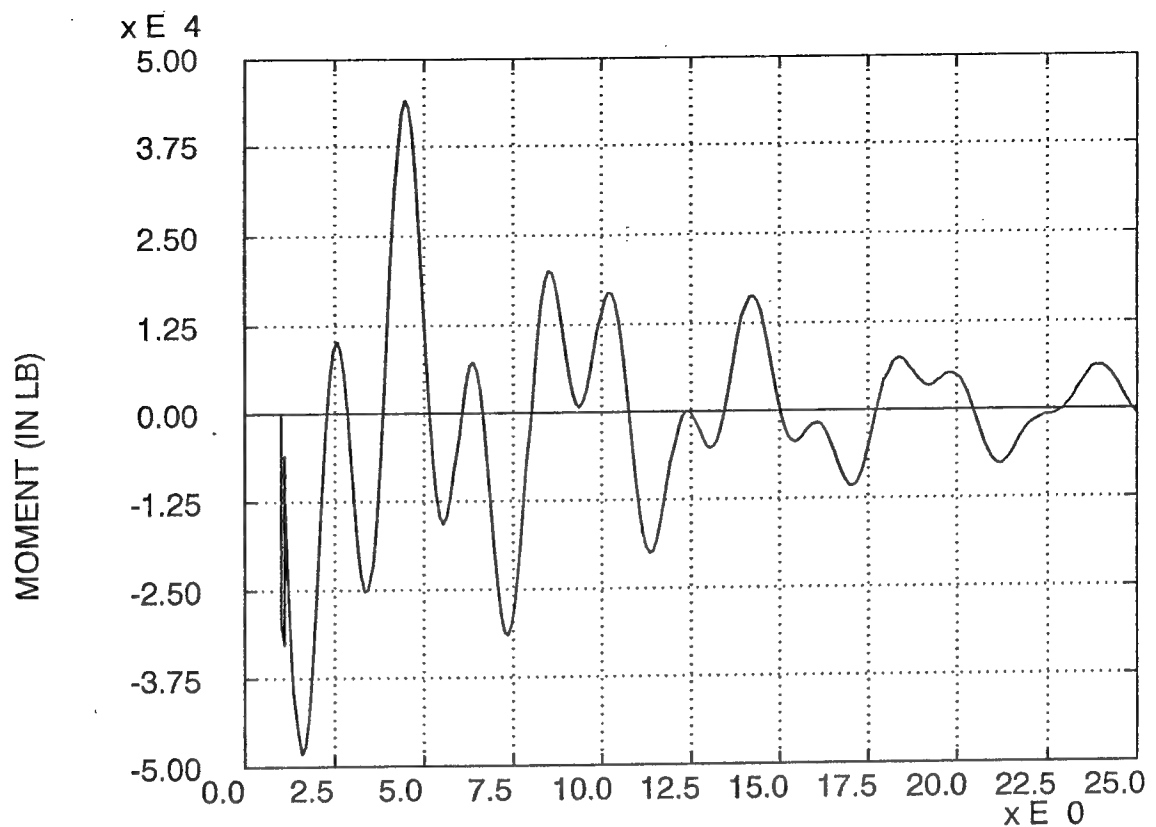


FIGURE 5A. INTERFACE MOMENT - 2 MODE INPUT T(SEC)

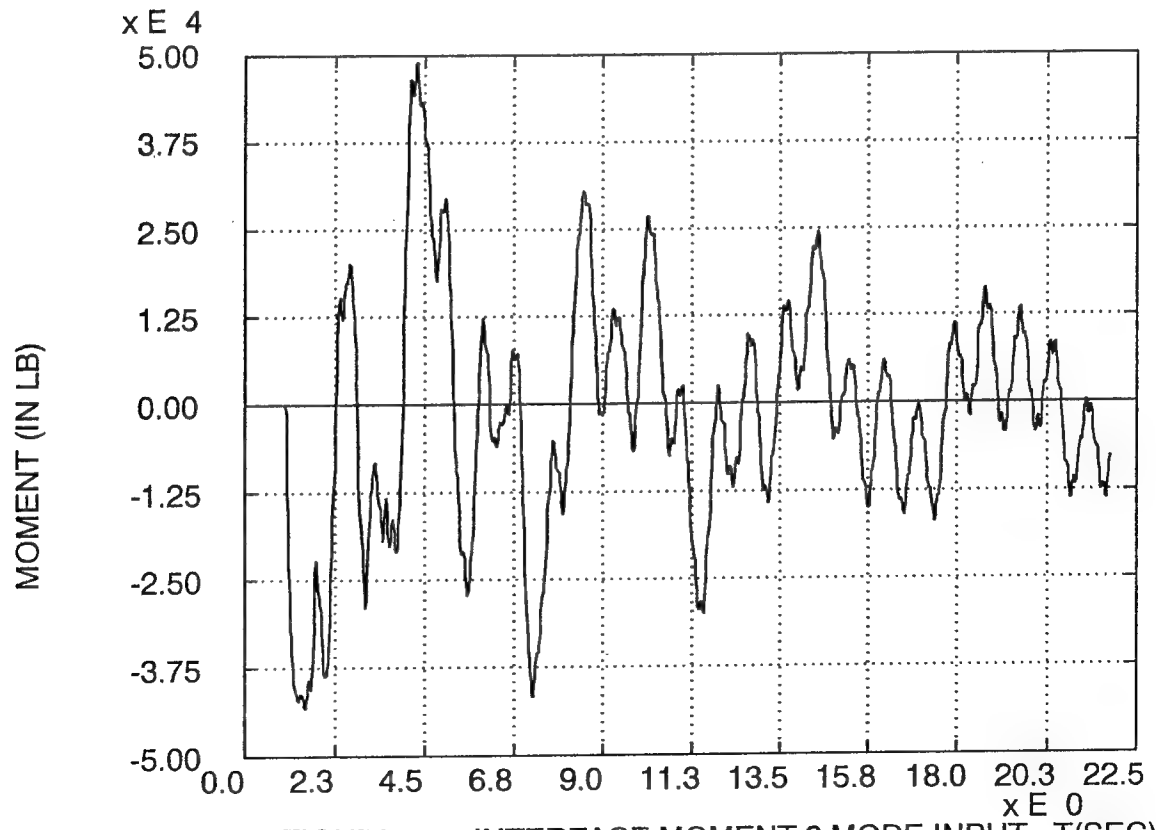
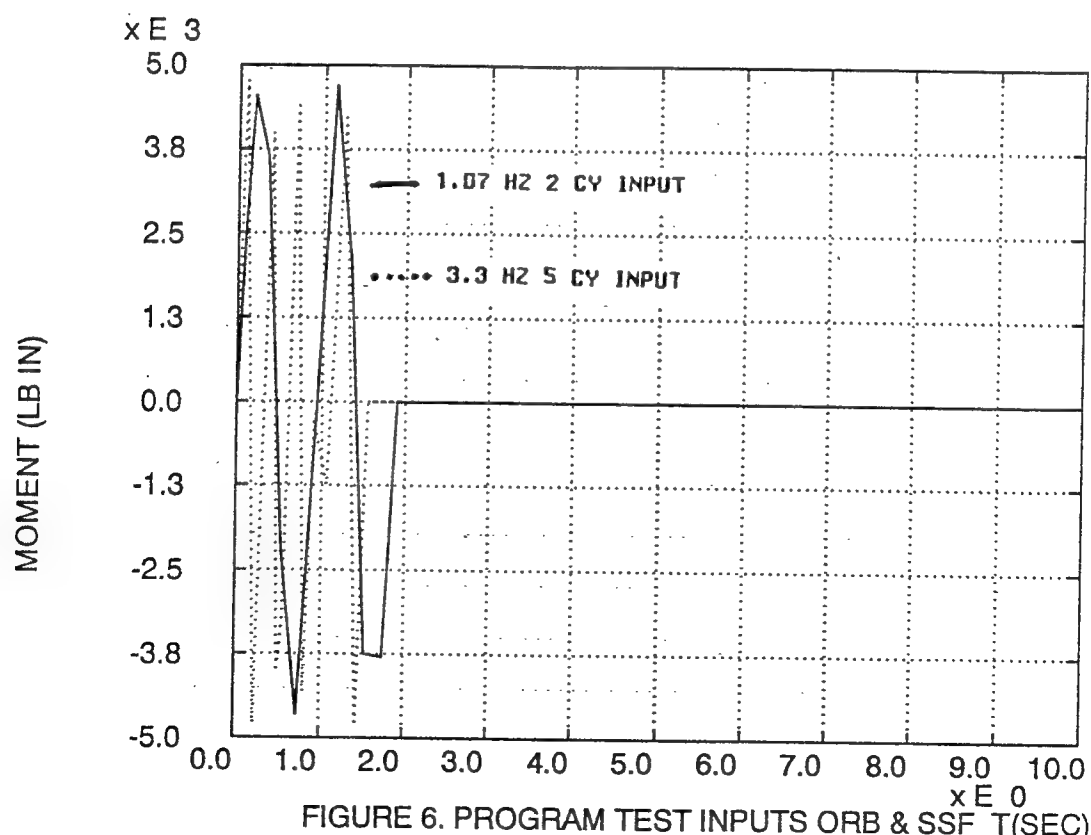
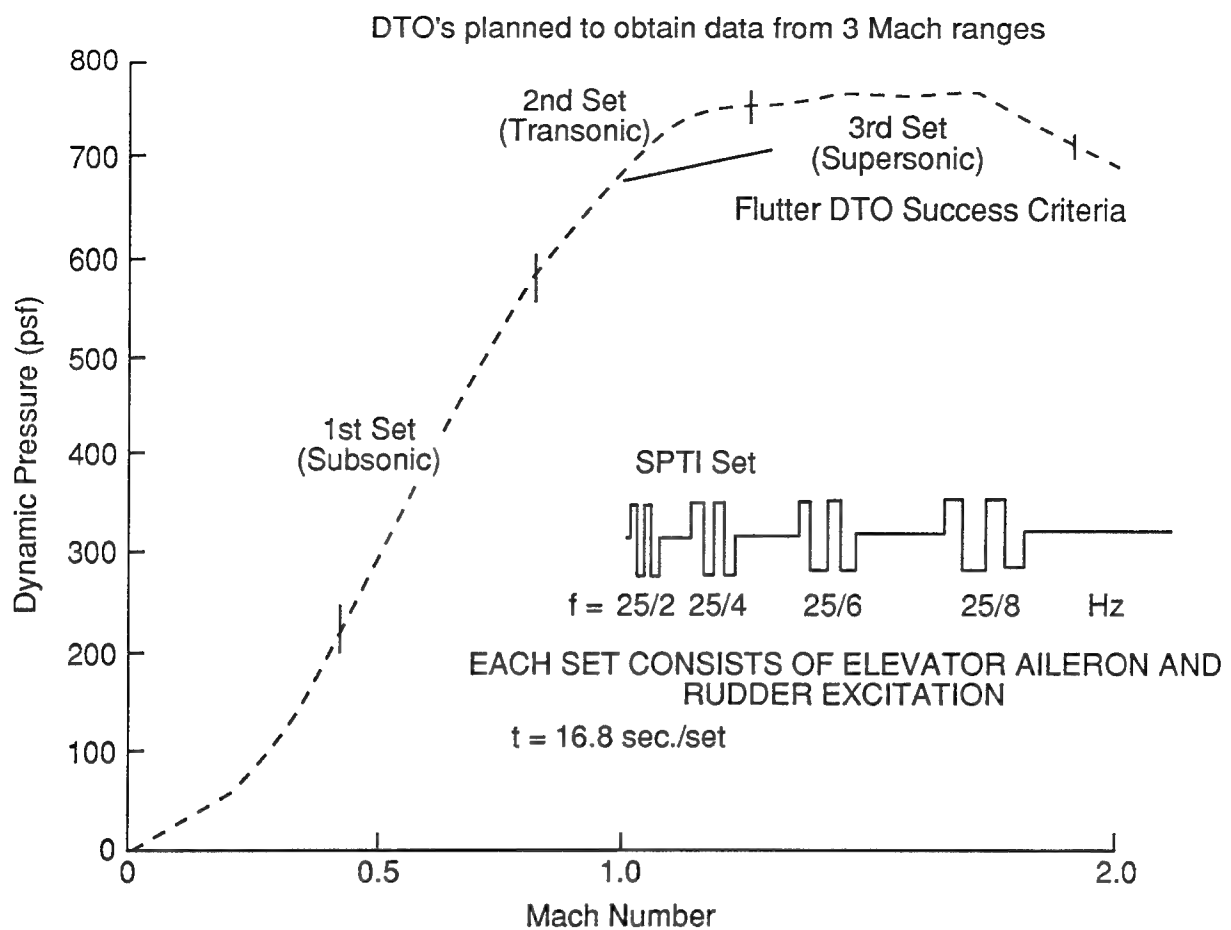


FIGURE 5B. INTERFACE MOMENT-8 MODE INPUT T(SEC)



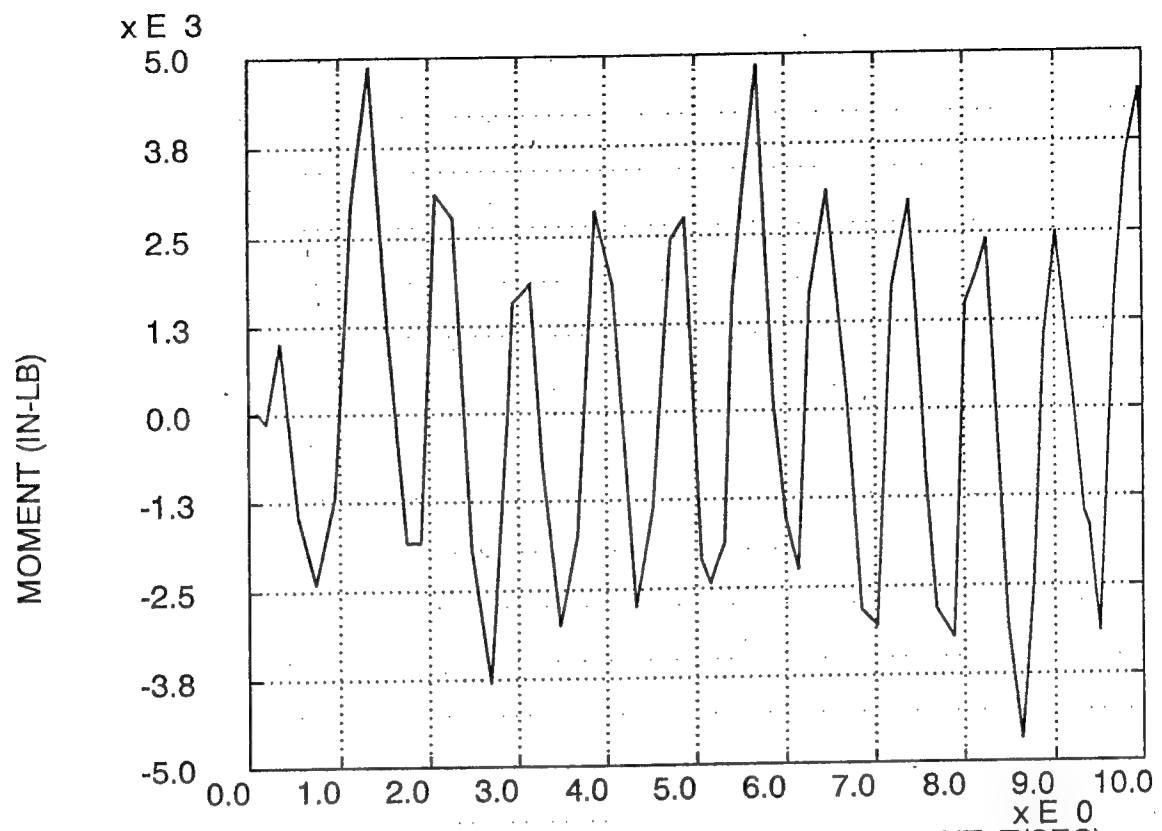


FIGURE 7A. RESPONSE TO 1.07/2 CY INPUT T(SEC)

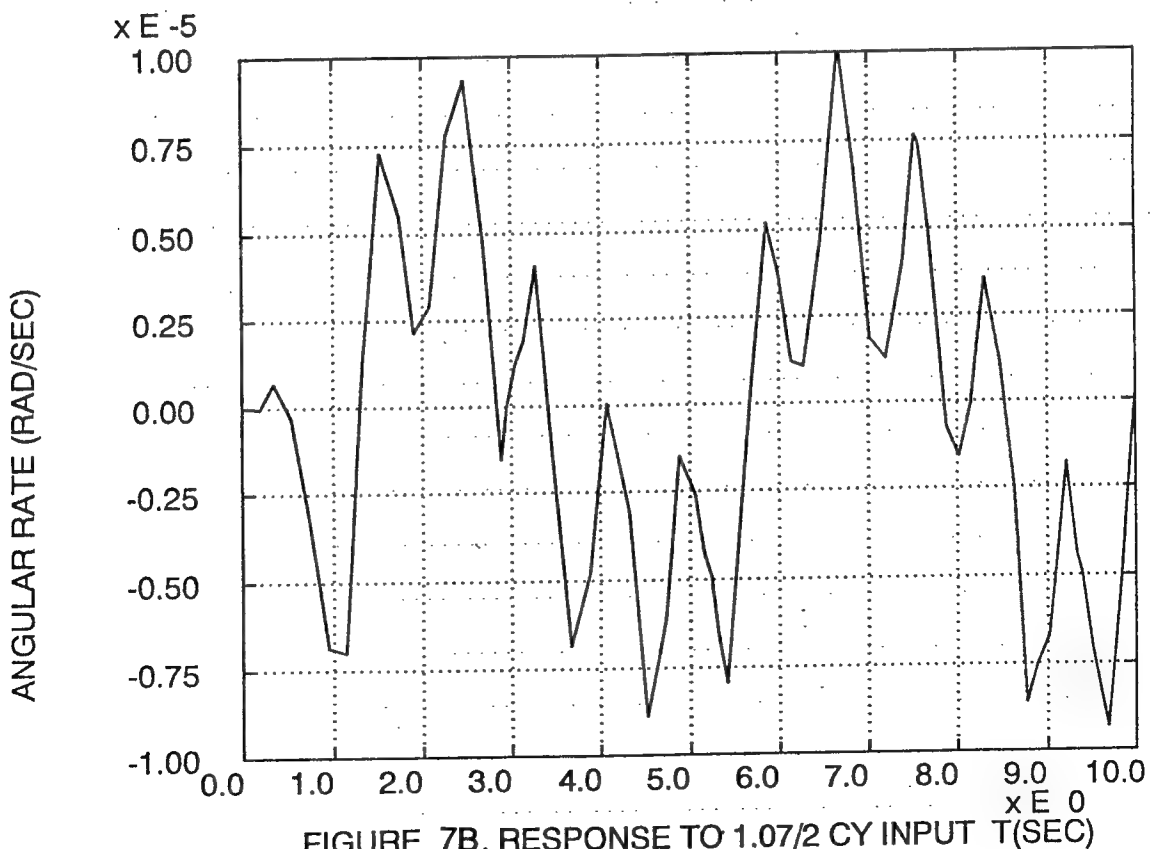
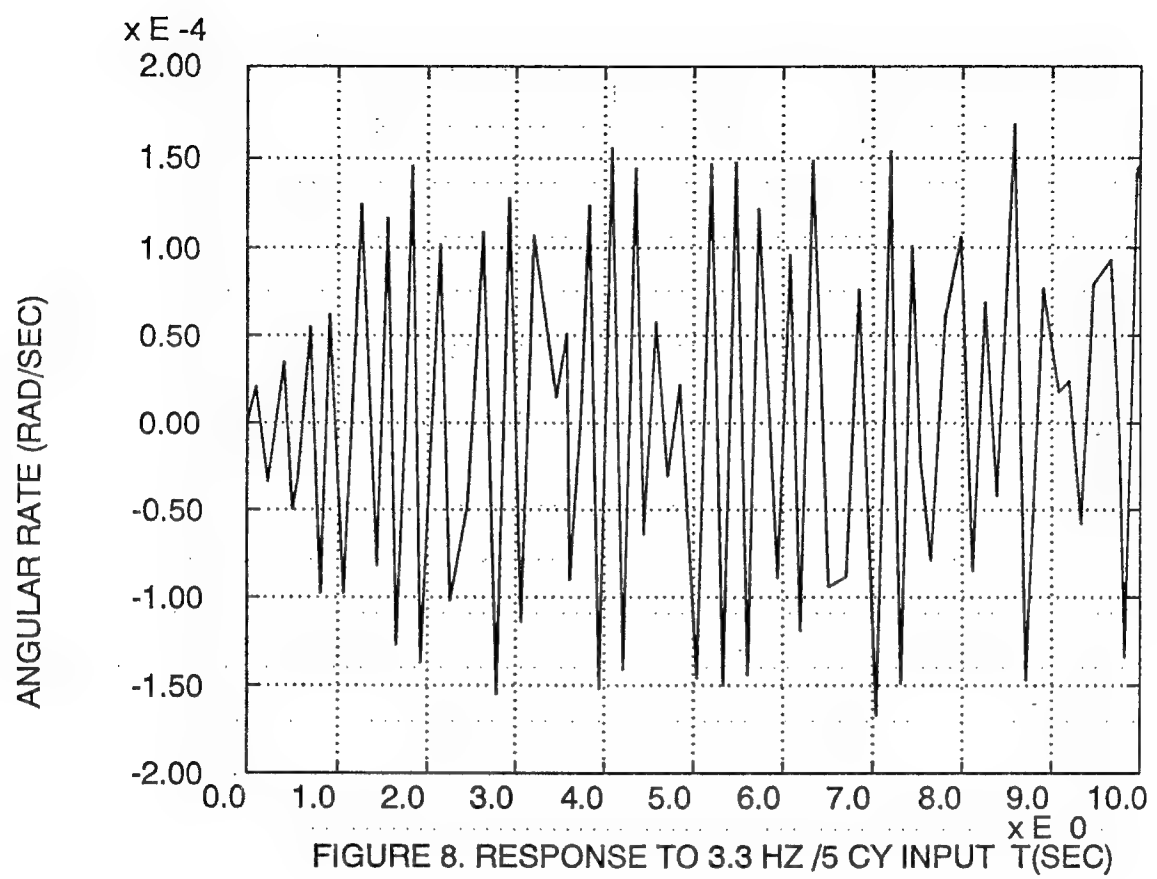


FIGURE 7B. RESPONSE TO 1.07/2 CY INPUT T(SEC)



EVALUATION OF INERTIAL DEVICES FOR THE CONTROL OF LARGE, FLEXIBLE, SPACE-BASED TELEROBOTIC ARMS

Raymond C. Montgomery¹, Sean Kenny¹,
Dave Ghosh², and Joram Shenhav³
NASA Langley Research Center
Hampton, VA

ABSTRACT

Inertial devices, including sensors and actuators, offer the potential of improving the tracking of telerobotic commands for space-based robots by smoothing payload motions and suppressing vibrations. In this paper, inertial actuators (specifically, torque-wheels and reaction-masses) are studied for that potential application. Batch simulation studies are presented which show that torque-wheels can reduce the overshoot in abrupt stop commands by 82 percent for a two-link arm. For man-in-the-loop evaluation, a real-time simulator has been developed which samples a hand-controller, solves the nonlinear equations of motion, and graphically displays the resulting motion on a computer workstation. Currently, two manipulator models, a two-link, rigid arm and a single-link, flexible arm, have been studied. Results are presented which show that, for a single-link arm, a reaction-mass/torque-wheel combination at the payload end can yield a settling time of 3 s for disturbances in the first flexible mode as opposed to 10 s using only a hub motor. A hardware apparatus, which consists of a single-link, highly flexible arm with a hub motor and a torque-wheel, has been assembled to evaluate the concept and is described herein.

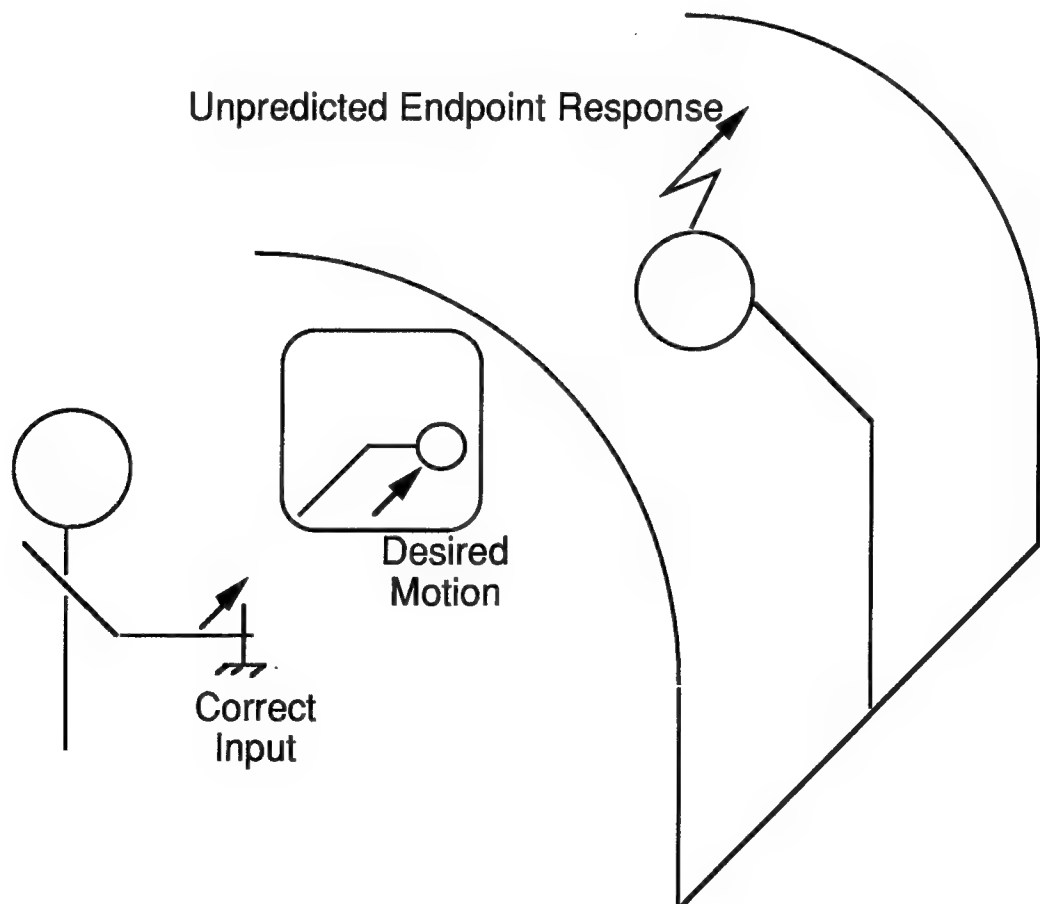
¹ Aero-Space Technologist, NASA Langley Research Center.

² Principal Engineer, Lockheed Engineering and Sciences Co., Hampton, VA.

³ Staff Engineer, Lockheed Engineering and Sciences Co., Hampton, VA.

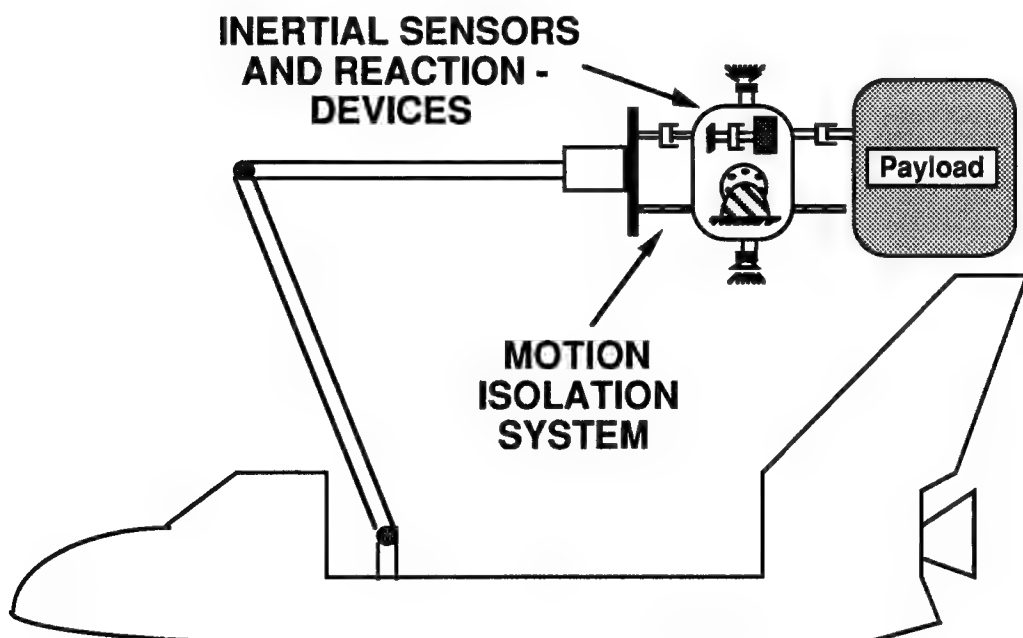
THE PROBLEM

The problem addressed in this research is illustrated in this chart. A human operator moves a hand-controller according to what is perceived as the correct input to maneuver a payload. This is based on observation of the payload via an out-the-window view and closed-circuit television monitors. Based on the hand-controller input and joint sensors, the control system moves the payload via a kinematic linkage. The motion, instead of being what the operator expects, is characterized by unwanted motions which result from the inability to predict the motion of the system based solely on sensors at the joints (typically angle encoders) and from complex structural vibrations. The prediction errors and the structural vibrations are related to the size of the linkage. For the space shuttle remote manipulator (approximately 50 ft. in length) the vibrations can be in the order of 6 in. peak-to-peak with a frequency as low as 0.2 Hz. This behavior, therefore, limits precision payload operations and results in loss-of-time in planning actions and waiting for vibrations to settle after excitation.



SOLUTION CONCEPT

The idea is to place an inertial control unit at the interface between the payload and the kinematic linkage. This unit would possibly use torque-wheels, reaction-mass actuators, reaction-jets, and motion isolation subsystems to isolate the payload from vibrations of the kinematic linkage and still allow transmission of the payload maneuvering loads eliminating the problems with non-collocation in the design frequency range. The purpose of the unit is to isolate the payload from structural vibrations of the kinematic linkage and to reduce or eliminate lags in the response of the linkage which are caused by structural vibrations and nonlinearities in joint motor response. The sizing of the inertial components is, thus, a function primarily of the characteristics of the linkage and, is believed, independent of the payload.



CONTROL WITH CONVENTIONAL JOINT MOTORS

One approach to the problem is to employ additional inertial sensors to determine the track of the payload, and to develop a control law that overcomes the difficulties in non-collocation of the control actuators (at the joints) and the desired response variables (at the payload-end of the arm). Over approximately the last fifteen years, this approach has been researched with no adequate resolution of the problem for precision operations with large, flexible robot arms. This chart lists some of the difficulties. The major one is non-collocation of the actuators with the point of interest. The phase of all vibrations in the control system bandwidth must be predicted accurately in order to get high gains in the control loop, or the control system must be gain stabilized resulting in a low loop-gain with associated poor performance. This difficulty has led us to another hardware-based approach of using inertial actuators (torque-wheels, reaction-mass actuators, etc.) to solve the problem.

FEEDFORWARD CONTROL -

- NO DISTURBANCE REJECTION**

FEEDBACK CONTROL -

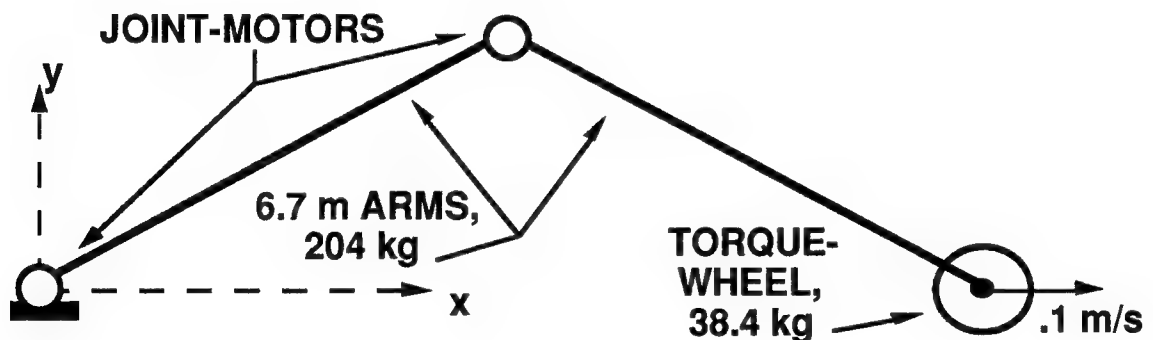
- NON-COLLOCATION CURRENTLY LIMITS GAIN**

ALTERNATIVE -- USE COLLOCATED DEVICES

BATCH SIMULATION

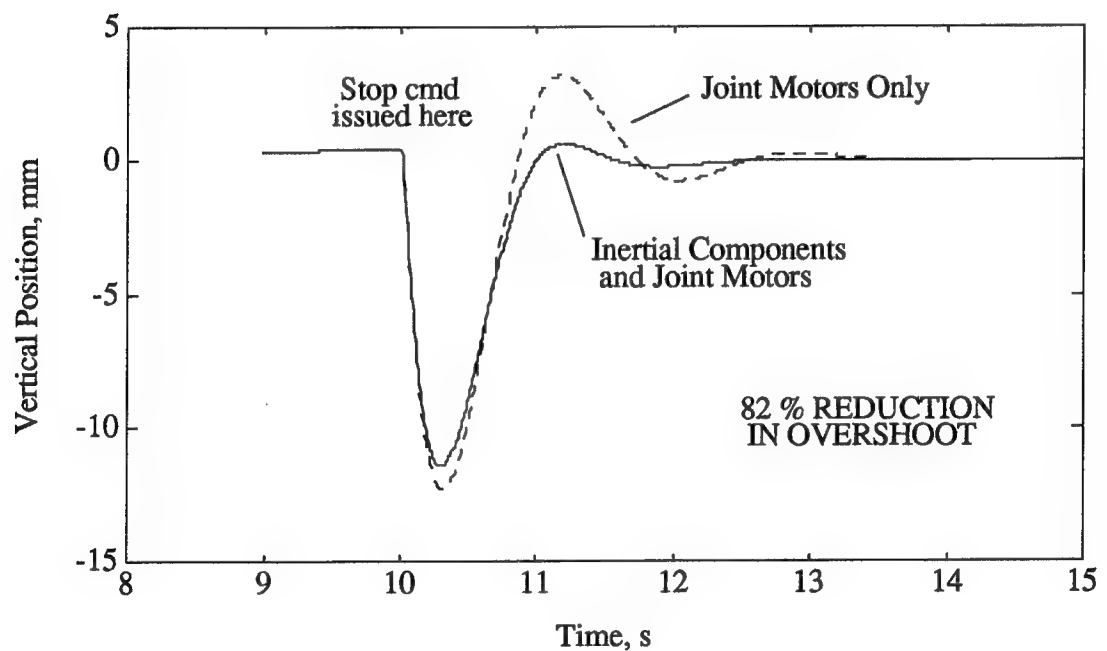
MODEL

A batch simulator has been used to study space-based arms of the Space Shuttle Remote Manipulator System (RMS) class. The simulator includes the dynamics of a planar model of a two-link arm and a torque wheel attached to the free end. The diagram illustrates the arm model used. Dynamic elements included in the simulator are two links, the joint motors, and the torque-wheel. Parameters of the arm were selected to be representative of a large, space-based, RMS-class robotic arm. Specifically, the links are of equal length, 6.7 m, and each has a mass of 204 kg. Parameters of the torque wheel are similar to those of the Langley torque-wheels. The torque-wheel total mass was 38.6 kg and its maximum output was 60 N-m at .5 Hz. The simulator implements a digital joint motor controller as well as the torque-wheel controller. The joint motor control scheme uses inverse kinematics to generate joint angle commands from telerobotic translational command inputs and a proportional-integral-derivative (PID) controller that generates joint motor angular velocity command signals given the joint angle commands. The torque-wheel controller uses collocated rate feedback.



BATCH SIMULATION RESULTS

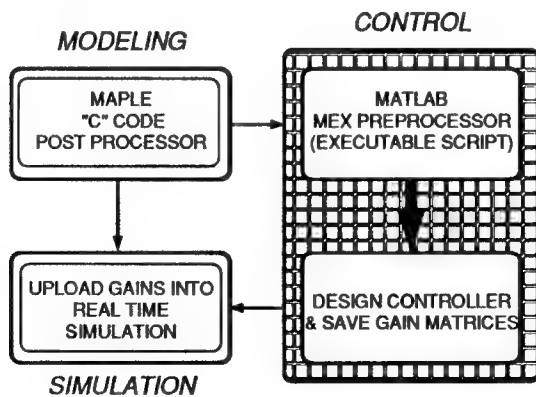
A simulation study was undertaken to suppress vibrations following an abrupt stop input. The arm was given command inputs for horizontal translation of the end-point at a constant velocity for 10 seconds followed by an abrupt stop. The time history compares the vertical motion responses, which are ideally zero, both with and without the torque-wheel. The torque-wheel, while operating within its design capability, substantially affects the second overshoot of the vertical motion response. The conclusion is that, subject to the limitations of a batch simulation, a torque-wheel of the size developed at the NASA Langley Research Center can be of value in the control of the arm.



REAL-TIME SIMULATOR

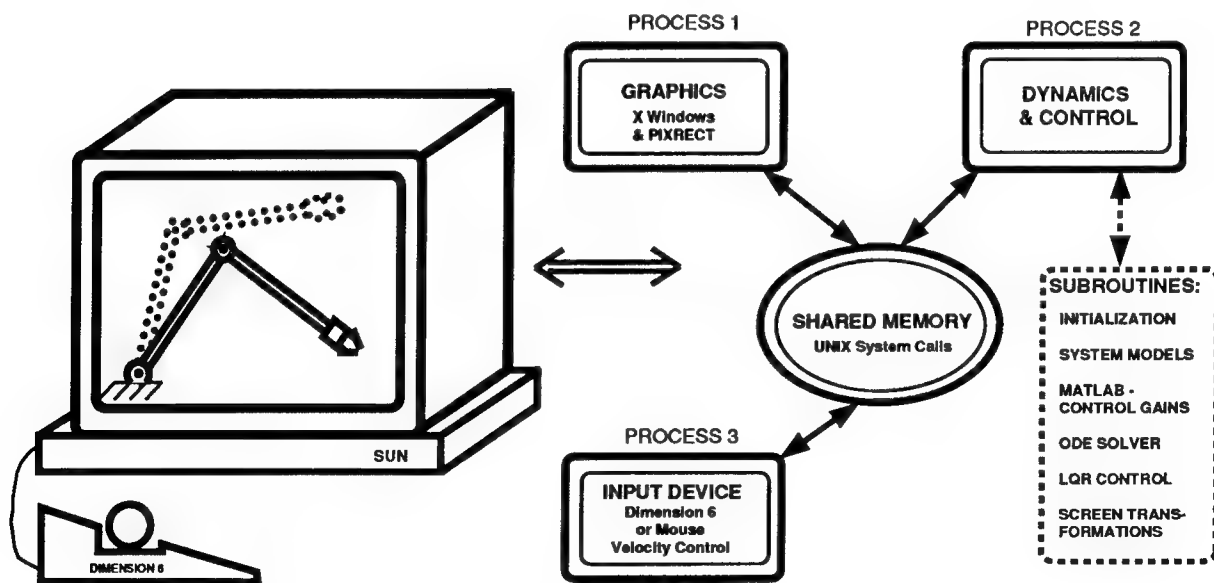
INTEGRATED SOFTWARE ENVIRONMENT

Modelling, control, and simulation of flexible link manipulators requires a set of reliable and efficient software tools. Symbolic manipulation programs represent one of the most versatile software environments currently available for modelling complex dynamical systems. This versatility provides the researcher a high degree of flexibility in terms of the ability to implement theoretically different modelling methods. In addition to their versatility, most of the symbolic manipulation programs have the ability to be integrated with commercially available control design packages. The integration of different software packages is primarily related to the sophisticated pre- and post-processing capabilities available within the respective packages. The figure below presents an integrated software environment which utilizes two commercially available packages for modelling and control, and an in-house developed real-time simulator. The symbolic manipulation program is used to generate executable "C" code for the flexible link manipulators system models. This code is then the input to the control package's preprocessor which converts the "C" code into executable script. Control design may then be accomplished by uploading the preprocessed script. The output of the control design, i.e., the gain matrices, may then be directly uploaded into the real-time simulator.



REAL-TIME SIMULATION ENVIRONMENT

To evaluate the usefulness of inertial actuators for maneuvering and vibration control of single and multi-link flexible manipulators, a real-time man-in-the-loop simulator has been developed. This simulator utilizes a SUN workstation to graphically display the dynamic response of the manipulator system as well as permit man-in-the-loop control through the use of an external input device. The workstation serves as a computational platform which is used to sample the input device, solve the nonlinear equations of motion, and graphically display the resulting motion. Currently, several manipulator models have been developed and successfully implemented in this simulator. These include both a two-link rigid arm and a single link flexible arm. In addition to simulating elastic and rigid body motions, task scenarios are also simulated. A typical task involves maneuvering the manipulator to a payload, capturing the payload, and then maneuvering the payload/manipulator system to a specified target. This payload capture task will facilitate the further evaluation of inertial actuators for man-in-the-loop control of flexible manipulators. The simulator, as shown below, consists of three processes which pass data back and fourth via the shared memory UNIX interprocess communication facilities resident on a SUN workstation.



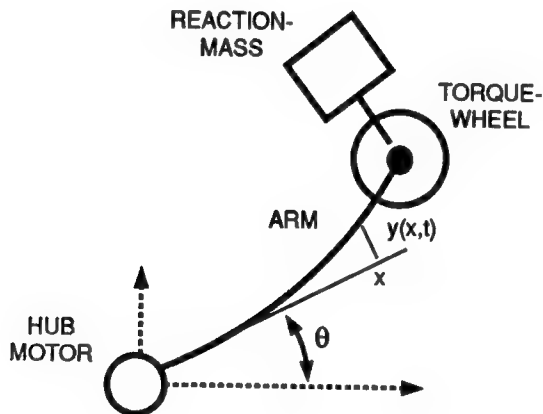
REAL-TIME SIMULATIONS

MODEL

The model used in the real-time simulator is a long single link flexible manipulator that is similar in physical dimensions to the Space Shuttle's Remote Manipulator System (RMS). The flexible arm, as shown below, is equipped with three actuators, one hub actuator and two inertial tip actuators. The inertial actuators used for this model are a torque-wheel, which is used to provide a torque input about the arm's bending axis, and a reaction-mass actuator to provide an input force in the arm's plane of motion.

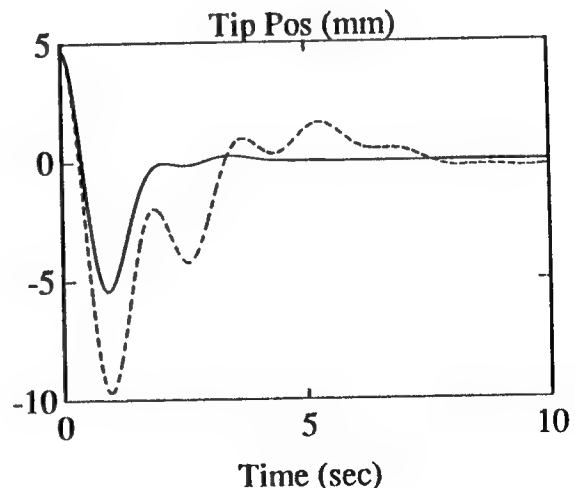
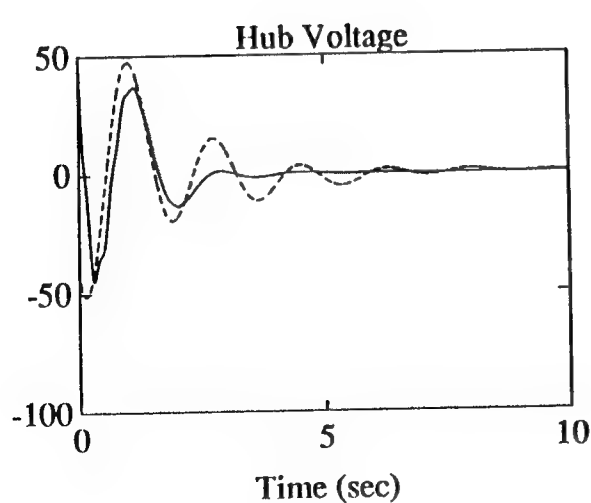
Model Parameters

HUB MOTOR	
$T_{max}=2.8 \text{ N-M}$, $\omega_{max}=213 \text{ rad/s}$, $E_{max}=50 \text{ Volts}$	
TORQUE-WHEEL MOTOR	
$T_{max}=67.8 \text{ N-M}$, $\omega_{max}=6.5 \text{ rad/s}$, $E_{max}=50 \text{ Volts}$	
REACTION-MASS MOTOR	
$F_{max}=128 \text{ N}$, $\dot{y}_{pmax}=1 \text{ M/s}$, $E_{max}=50 \text{ Volts}$	
ARM	
$\rho=55.16 \text{ Kg/m}$, $E=1.38e11 \text{ N/M}^2$, $L=13.42 \text{ M}$, $I=2.08e-5 \text{ M}^4$	



REAL-TIME SIMULATION RESULTS

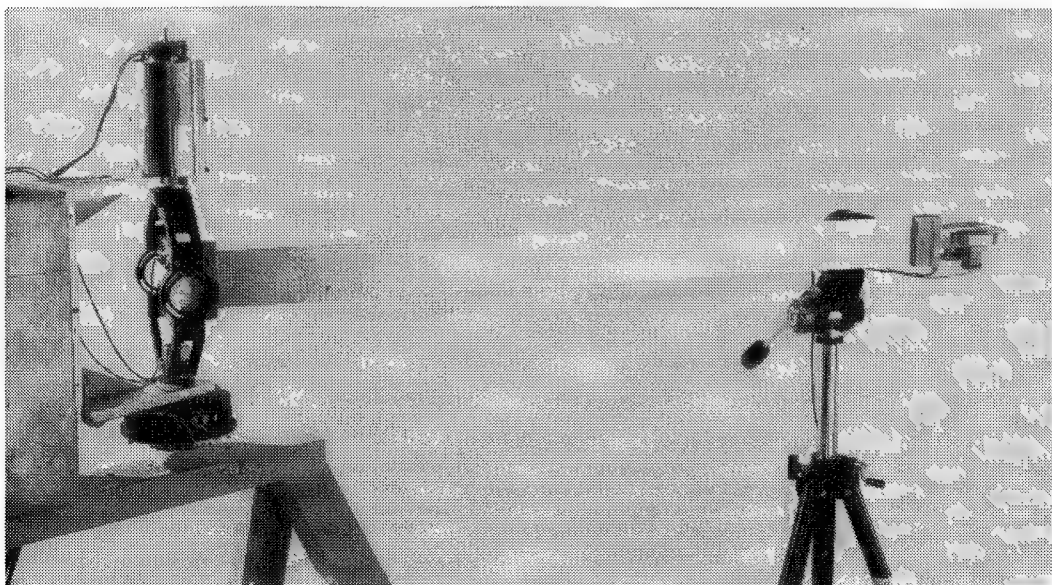
The time history results, as shown below, present the disturbance rejection capabilities for both models, i.e., models with and without inertial actuators. The disturbance considered herein was a perfect first mode displacement initial condition. The analysis and control models both considered three flexible modes, corresponding to the first three "cantilever type" modes with the appropriate boundary conditions to account for the inertial devices. For control system design, a full-state feedback law was obtained using Linear Quadratic Regulator (LQR) design theory. The selection of the Q and R weighting matrices required several iterations to satisfy state constraints on the inertial actuators, e.g., maximum torque-wheel velocity, reaction-mass stroke, and reaction-mass velocity. The objective for the controller design was to achieve operation of the inertial devices near their maximum specifications. The simulation results show that the model using the inertial actuators (solid line), for this type of disturbance, reduced the tip position settling time by more than sixty percent over conventional hub motor only control (dotted line).



HARDWARE TESTBED

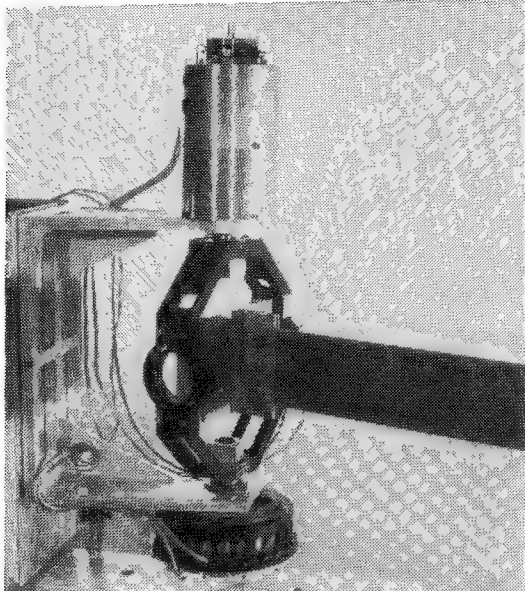
FLEXIBLE ARM EXPERIMENTAL SETUP

The flexible arm test article consists of three major elements: a base-mounted hub assembly (on the left), a flexible beam (at the center), and a beam-tip sensor-actuator assembly (on the right). The hub assembly is comprised of a gimbaled bracket (to provide a rotational, one degree-of-freedom motion to the root of the beam about the vertical axis), a torque motor (to drive the gimbaled bracket), a low rate capability tachometer, and an angular position resolver (to provide rate and position measurements, respectively). The design of the beam was accomplished using constrained optimization. The constraints consisted of maintaining 2-deg/ft-lbf in static torsional stiffness and a 0.8-Hz for the frequency of the lowest bending mode. The optimization criteria was to minimize the end deflection of the beam as subject to gravity loading. This produced an 891-mm long beam with a 75x2.38-mm rectangular cross-section made of Al 6061-T6. The tip sensor-actuator assembly is comprised of a torque wheel with an optical sensor for flywheel rate detection. Both manual and automatic control tests can be conducted using a control computer that has A/D and D/A converters and a timer for precise timing of data sampling processes. An analog-output, hand-controller will be used to provide manual inputs. A linear accelerometer will be mounted on the tip bracket to sense the tip acceleration. A proximity sensor, mounted on an independent pedestal near the tip of the beam, generates a signal for feedback control, for driving an oscilloscope display, and for performance monitoring of manual and automatic control tasks.



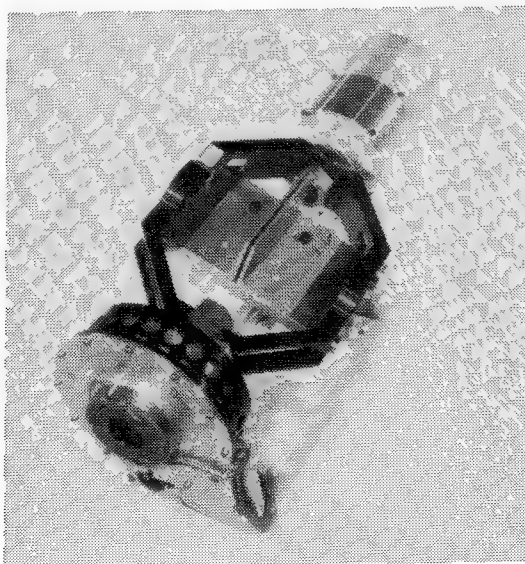
BASE-MOUNTED HUB ASSEMBLY

The photograph depicts the gimbaled bracket with the mounted beam. The hub torque motor appears in the lower part and also provides the support for the hub tachometer, mounted underneath the torque motor housing. The angular position resolver (sine-cosine wire-wound potentiometer) is mounted on the top end of the gimbal axle.



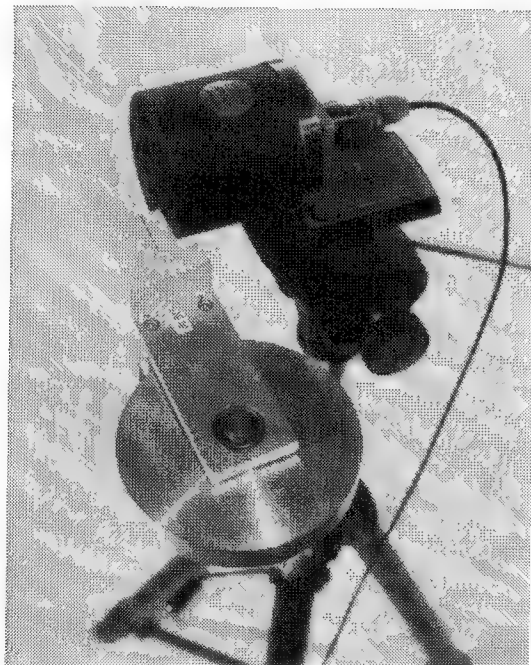
HUB TORQUE MOTOR AND TACHOMETER ASSEMBLY

The photograph depicts a bottom view of the hub torque motor showing a view of the low rate capability tachometer.



BEAM-TIP SENSOR-ACTUATOR ASSEMBLY

The photograph depicts the tip sensor-actuator assembly. The torque wheel fork-bracket provides support for the flywheel axle as well as the optical sensor for flywheel rate detection. The linear accelerometer will be mounted on the tip bracket to sense tip acceleration. Near the tip an independent pedestal holds a beam proximity sensor. This sensor generates a signal for feedback control, for driving an oscilloscope display, and for performance monitoring of manual and automatic control tasks.



A DARWINIAN APPROACH TO CONTROL – STRUCTURE DESIGN*

David C. Zimmerman
University of Florida
231 Aerospace Building
Gainesville, Florida 32611

GENETIC ALGORITHMS

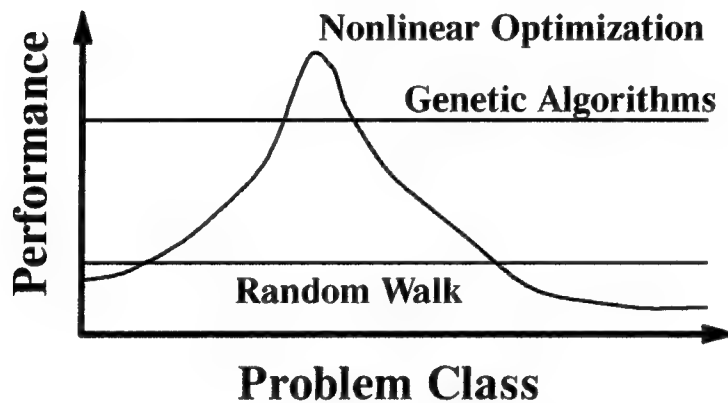
- **Based on Darwin's "Survival of the Fittest" Theories**
- **Shows Great Potential for**
 - **Multi-Modal Objective Functions**
 - **Discrete and/or Continuous Design Variables**
 - **Discontinuous Design Space**
- **Works With a Coding of the Design Variables,
*Not the Design Variables Themselves***
- **Searches From a Population of Designs,
*Not a Single Design Point***
- **Uses Payoff (Objective Function) Information,
*Not Gradient Information***
- **Uses Probabilistic Transition Rules,
*Not Deterministic Rules***

Genetic algorithms (GA's), as introduced by Holland (1975), are one form of directed random search. The form of direction is based on Darwin's "survival of the fittest" theories. GA's are radically different from the more traditional design optimization techniques. GA's work with a coding of the design variables, as opposed to working with the design variables directly. The search is conducted from a population of designs (i.e., from a large number of points in the design space), unlike the traditional algorithms which search from a single design point. The GA requires only objective function information, as opposed to gradient or other auxiliary information. Finally, the GA is based on probabilistic transition rules, as opposed to deterministic rules. These features allow the GA to attack problems with local-global minima, discontinuous design spaces and mixed variable problems, all in a single, consistent framework.

* Research Sponsored in part by the NASA CSI Program Office,
NASA Grant Number NAG-1-1017.

GA's – ALGORITHM OVERVIEW

- Initial Population of Designs Created – Random or Heuristic
- Initial Population Allowed to “*Evolve*” Over Generations
- Conjecture – Evolution is the Best Compromise Between Determinism and Chance
- Motivation – GA's are Robust Over a Wide Range of Problems



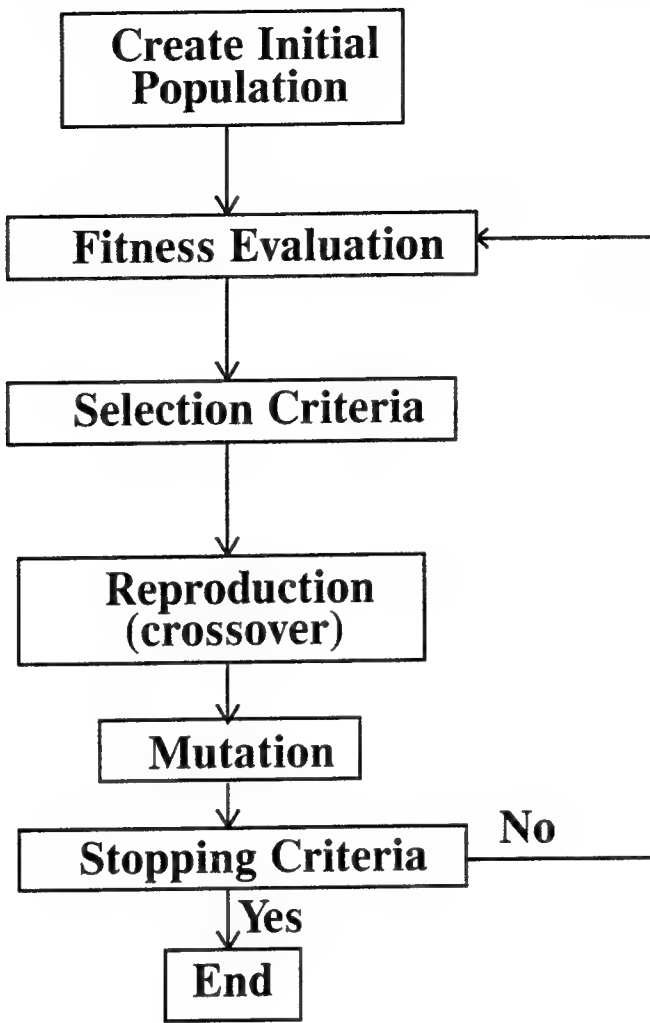
In GA's, a finite number of candidate solutions or designs are randomly or heuristically generated to create an initial population of designs. This initial population is then allowed to evolve over generations to produce new, and hopefully better, designs. The basic conjecture behind GA's is that evolution is the best compromise between determinism and chance. The basic motivation behind the development of GA's is that they are robust problem solvers for a wide class of problems. However, it should be noted that they are not as efficient as nonlinear optimization techniques over the class of problems which are ideally suited for nonlinear optimization; namely continuous design variables with a continuous differentiable unimodal design space.

GENETIC ALGORITHM MODULES

- Design Variables *Coded* as a q-Bit Binary Number
 - Continuous Variables Like A/D Converter
 - Discrete Variables Have Unique Binary Strings
 - A Population Member is Just a String of Design Variables
- GA *Evaluation*- Level of *Fitness* Assigned to Each Member
 - Fitness Chosen to be Related to Objective Function
 - GA's Maximize Fitness
- GA *Selection* – Determination of Which Individuals in Current Population Chosen to be Parents
 - Biased Towards More Fit Members
 - Proportional Bias – $p_i^{\text{member}} = \frac{\text{fitness}_i}{\sum_{j=1}^{\text{pop}} \text{fitness}_j}$
- GA *Crossover* – Transfer of Design Information From Parents to Prodigy
- GA *Mutation* – Low Probability Random Switch of Bits
 - Retain Design Information Over Entire Design Space
 - Aides Search For Global Optimal Solution

Each design variable is *coded* as a q-bit binary number. A continuous design variable is approximated by 2^q discrete numbers between lower and upper bounds set for the design variable. Discrete variables would each be assigned an unique binary string. A population member is obtained by concatenating all design variables to obtain a single string of ones and zeros. *Evaluation* is the process of assigning a fitness measure to each member of the current population. Because GA's attempt to maximize the fitness of each member, an objective function which is to be minimized must be converted into an equivalent maximization problem. *Selection* is biased towards the most fit members of the population. Therefore, designs which are better as viewed from the fitness function, and therefore the objective function, are more likely to be chosen as parents. *Crossover* is the process in which design information is transferred to the prodigy from the parents. Many crossover operators (1-point, 2-point, uniform) have been investigated. *Mutation* is a low probability random operation which may perturb the design represented by the prodigy. The operator works on a bit-by-bit basis and is governed by the probability of mutation, p_m . At each bit, a biased coin toss is used to determine whether the bit should be logically "NOTed". The mutation operator is used to retain design information over the entire domain of the design space during the evolutionary process.

GENETIC ALGORITHMS – SUMMARY



In the implementation of the GA shown above, the prodigies are produced until the number of prodigies created is equal to n_{pop} , the population size. At that point, the current population of parents are discarded and the prodigies are in turn made parents which are capable of producing the next generation of prodigies. Thus, the production of n_{pop} prodigies can be viewed as the completion of one generation cycle in the evolutionary process. During this procedure, it is possible that both the fitness of the most fit member and the average population fitness can be temporarily reduced during the evolutionary process. To overcome this, the concept of a steady-state GA was implemented. In a steady-state GA (SSGA), the fitness of the children after they have been mutated is evaluated. These fitness values are then compared to the fitness of the two least fit parents in the current population. If the mutated child's fitness is higher than the least fit member in the population, the child will replace that member and will instantly become a candidate parent. To keep intact the concept of a generation, a generation is defined to be complete when the number of children produced, but not necessarily accepted into the population, is equal to n_{pop} .

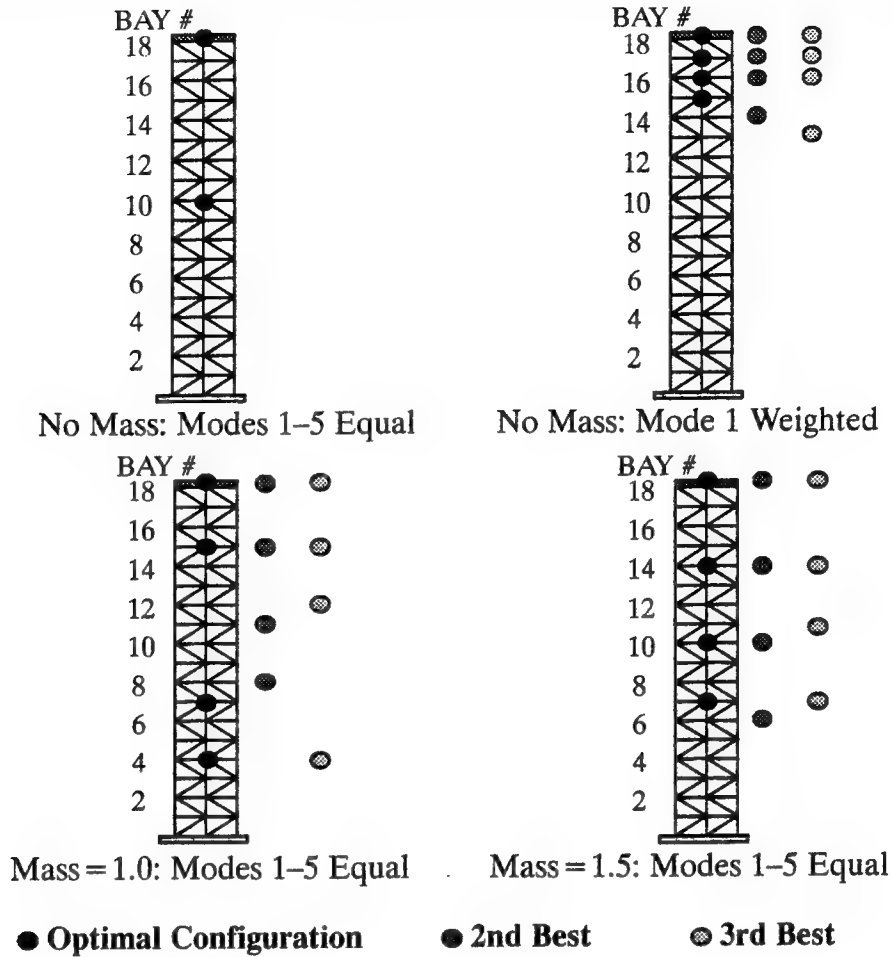
GA EXAMPLE - ACTUATOR PLACEMENT FOR MINI-MAST (discrete design problem)

- **PROBLEM – Given “N” Candidate Actuator Locations and a Maximum of “K” Actuators, Each of Mass M, Determine the Optimal Configuration**
- **Actuator Placement**
 - Criterion Representing Desirability of Configuration
 - Simple Method of Evaluation
 - Algorithm for Cycling Through Configurations – GA’s
- **Criterion: Energy Optimal Degree of Controllability**
(Longman) – maximize the “size” of the state space that can be returned to origin in prescribed time and energy
- **FITNESS = EDOC – (soft penalty function)**
 - Soft Penalty Function Penalizes Configurations Which Have More Than Allowable Number of Actuators
- **In Addition to Identifying Optimal Configuration, “Nearly” Optimal Configurations Also Found**

Fundamental to the problem of actuator placement are: (i) the definition of an appropriate criterion representing the desirability of actuator configurations, (ii) the development of a computationally efficient method for the evaluation of this criterion, and (iii) the development of algorithms to cycle through possible candidate actuator configurations. To date, the greatest amount of work has focussed on problems (i) and (ii). The approach taken for problem (iii) by most researchers has been an exhaustive search. That is, given n candidate locations to place m actuators, $m < n$, evaluate the effectiveness criteria for all configurations. The numbers aspect (i.e. place m or less actuators) has rarely been investigated. In this demonstration of the GA, the energy degree of controllability (EDOC) developed by Longman (1989) is used as an actuator configuration effectiveness measure. The effects of actuator mass are incorporated into the EDOC. The energy degree of controllability (EDOC) is related to the size of the region in the state space that can be returned to the origin in a prescribed amount of time T using less than a prescribed amount of energy e . The larger a given actuator configuration’s EDOC is, the greater its control authority. The optimal actuator configuration is that which maximizes the EDOC. Therefore, the objective function used for evaluation is taken as $J = EDOC - W(n_{act} - n_{actmax})\mu(n_{act} - n_{actmax})$ where W is an arbitrary weight function, n_{act} is the number of actuators, n_{actmax} is the maximum allowable number of actuators, and μ is the unit step function. The second term is essentially a soft penalty function which reduces the objective function for a given actuator configuration only if the configuration has more actuators than the maximum allowable. Actuator configurations which have less than the maximum allowable are not penalized by this term. Therefore, the optimal number of actuators is also determined. It is possible in this problem that the optimal number of actuators is less than the maximum allowable because of actuator mass effects. Details of this work are presented in Zimmerman (1991).*

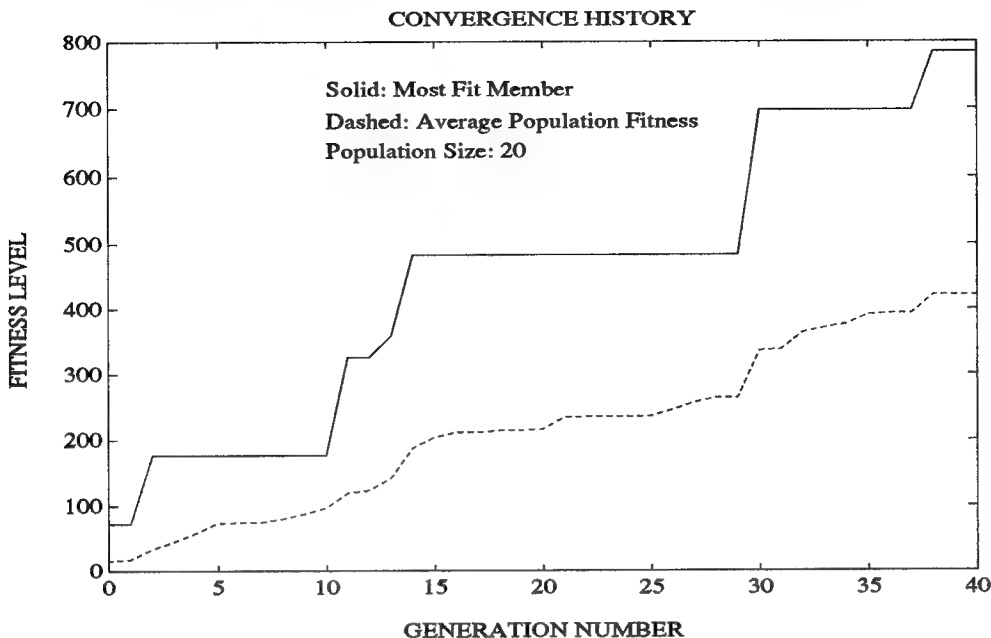
*Zimmerman, D.C. (1991). “A Darwinian Approach to the Actuator Number and Placement Problem with Nonnegligible Actuator Mass.” to appear, Journal of Mechanical Systems and Signals.

ACTUATOR PLACEMENT – RESULTS



Four test cases were run. In each figure, the optimal actuator configuration is shown pictorially with the solid ovals. In addition to identifying the optimal configuration, the final generation of designs also provides valuable information concerning other “nearly optimal” solutions. This is of significance in that (i) insight into the optimization process can be gained and (ii) it allows for human judgement to factor in other criteria not embodied in the objective function in comparing the “nearly optimal” designs to the “true optimal” design as dictated by the fitness function. These “nearly optimal” designs are indicated to the right of each figure. In the top-left case, the optimal configuration for placing two massless actuators was determined with equal mode 1-5 weighting (171 possible combinations). It should be noted that the results correspond to the actual Mini-Mast configuration. To increase the possible number of combinations, the remaining problems looked at placing four or less actuators (4047 possible combinations). The top-right case was for no actuator mass and control of only mode one deemed important. The GA results are consistent with physical intuition. The bottom two cases demonstrate the effects of actuator mass on the placement problem. For actuator mass normalized to unity (mass = 1), the optimal configurations are shown in the bottom-left figure. For an increase in actuator mass of 50%, the optimal actuator configurations are shown in the bottom-right figure. Comparing these two figures demonstrates the obvious importance of including actuator mass in any placement algorithm. All GA results presented above were validated by exhaustive search. This was possible due to the size of the factorial problem investigated. The results showed that the final GA population included a minimum of five of the top seven actuator configurations (including the optimal) for each case.

CONVERGENCE HISTORY

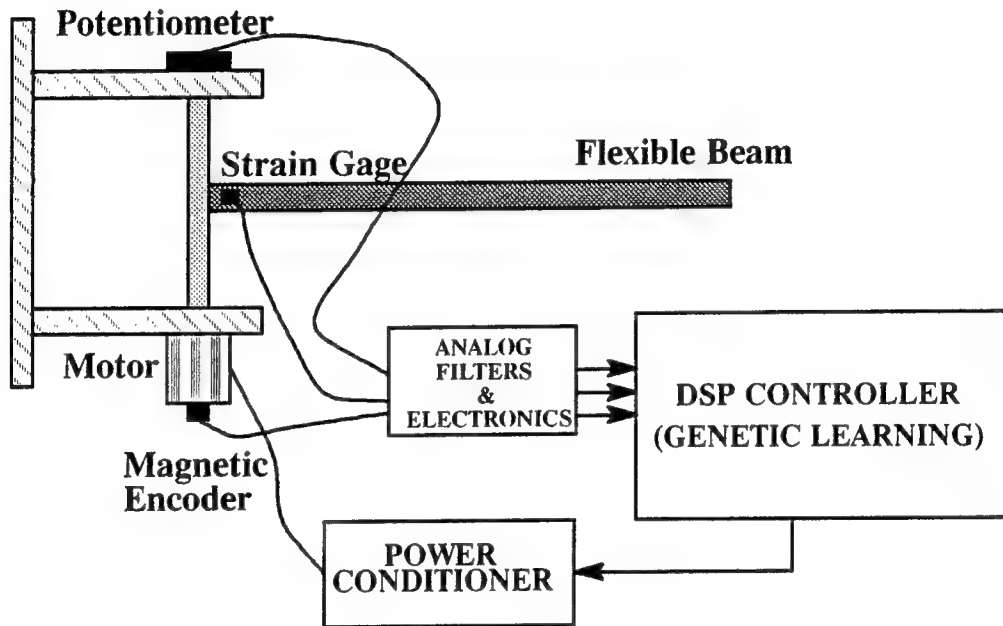


- **Average Population Increase With Each Generation – Characteristic of Steady-State GA**
- **Population Size = 20, Generations = 40, Therefore 800 Function Evaluations (4047 possible combinations)**

The above figure shows the convergence history of the GA for the case of placing 4 actuators with no actuator mass. The GA identified the optimal solution after 38 generations, although the algorithm was run for a total of 40 generations. With a population size of 20 members, the GA required 800 function evaluations to arrive at the optimal solution (exhaustive search would require 4047). At a given generation number, the maximum fitness value represents the most fit member in the population, whereas the average fitness is the mean fitness of the entire population. It can be seen that the average fitness increases with each new generation, which is a property of the SSGA used. In a study of a large combinatorial problem not shown (906,192 possible solutions, optimal solution known), the GA was able to determine the optimal solution in less than 2500 function evaluations. Although no optimization algorithm can guarantee convergence to the global optimal solution, experience with the GA has shown that GA's are a powerful tool to improve CSI designs.

GENETIC ALGORITHM LEARNING CONTROL

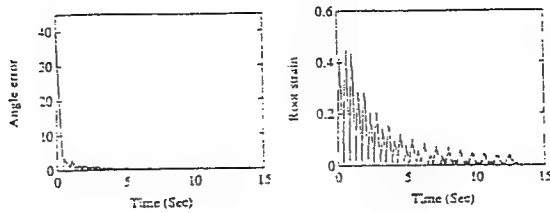
- Utilize Genetic Principles to Evolve Controller Making
Use of On-Line Experimental Measures of Fitness
- Focus Application – Single Link Large Angle Slewing
- Weighted Fitness Function – Strain and Angle Error



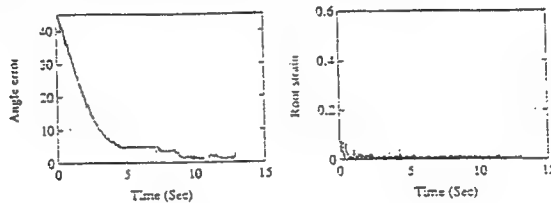
In this application of GA's, a Genetic Algorithm Learning Control (GALC) formulation is investigated (Layton and Zimmerman, 1992). In learning control, the control law is adapted from information gained by repeating the desired operation. In the GALC, various controller forms (i.e., parameterized control laws) are formulated. The evolutionary principles of Genetics are then utilized to not only select the optimal control law parameters, but also to select the optimal control law form. For this particular test case, the desired maneuver is a rest-to-rest 45 degree slew. Available sensor information included angle, angle rate, and beam root strain. In simulation studies, the optimal control law form was determined (as well as the optimal control parameters). Experimentally, the control law form was fixed with the GALC varying the control parameters. Fitness information was obtained experimentally by integrating the angle error (square difference of the desired and actual angle) and the square of the root strain signal. The objective of the GALC was to minimize a weighted integral of angle error and root strain. All processing was done digitally using a DSP controller with an approximate update rate of 33kHz.

GENETIC LEARNING

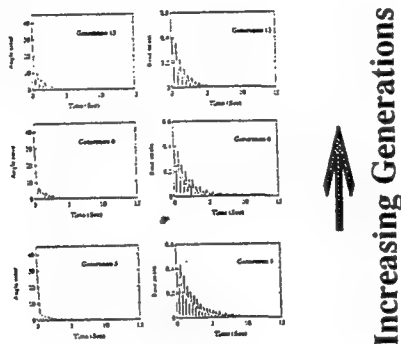
● Heavy Weighting on Angle Error



● Heavy Weighting on Strain Error



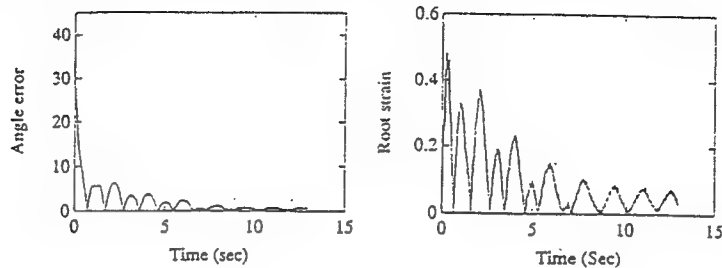
● Relative Weighting Learning



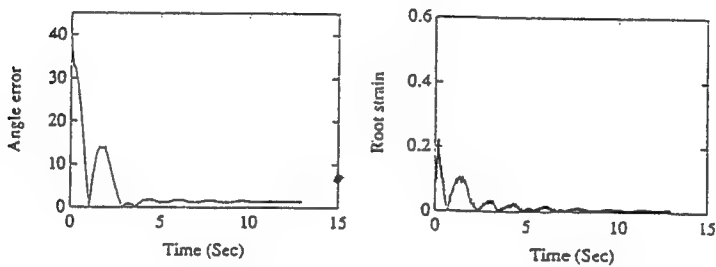
Three experimental case studies were investigated. In all cases, the initial population was selected randomly and was not biased with any knowledge of the beam, actuator, or sensor dynamics. In other words, there was no need to develop a system model as far as the experiment was concerned. Fitness functions were developed using experimental sensor signals. The repeatability of these calculations was nominally 8% error. Thus, issues of noisy function evaluation were addressed. In the first experiment, the fitness function was weighted such that there was no penalty on the strain signal. The results are in agreement with physical reasoning: the motor slews as quickly as possible to reduce the angle error regardless of the strain signal. The second experiment is just the opposite of the first; no penalty associated with the angle error. Again, the result of learning control agrees with physical reasoning: slew the beam slowly to minimize the strain signal. Finally, the third experiment provided for approximate equal weighting (in a voltage sense) of the angle and strain signal. The waterfall plot shows the progressive learning of the controller. It should be noted that the cost function also included a time cubed weighting factor within each integral. This effect clearly is demonstrated in the above figures.

GENETIC LEARNING FOR CHANGED SYSTEM

- Mass Added to End of Flexible Beam (76g)
(Mass of Flexible Beam - 112g)
- Previous Optimal Control on Perturbed System



- Maxfit Member After Five Generations



In this experiment, a 76g mass was added at the tip of the beam. The mass of just the flexible beam was 112g. Obviously, the tip mass greatly influenced the system dynamics. The top graph shows the angle error and root strain time histories when the control optimized for the previous system (i.e. no tip mass) is used to maneuver the beam with tip mass. In comparing this figure with the bottom figure of the previous slide, it is obvious that performance has been seriously degraded. The second figure of this slide shows the angle error and root strain time histories after five generations of learning. It is obvious that the GALC has adapted the control law to better match the "new" system dynamics. It would be expected in this case that the strain signal would have a larger RMS level than the angle error signal, and thus "equal" weighting between angle error and strain is no longer achieved with the same weighting values. In the time history shown above, the weighting values were kept the same as in the previous case. This causes the angle error to remain at a non-zero value as time increases. If the weight on angle error is increased, the angle error would go to zero in the steady-state.

SUMMARY

- **Genetic Algorithms Represent a New Class of Optimization Tools Which Are Applicable To Many CSI Design Problems**
- **Genetic Can Handle Discontinuous Design Spaces and Both Discrete and Continuous Design Variables**
- **Demonstrate Quick Convergence to Near Optimal Solution, Then Slows Down (hybrid solution techniques possible)**
- **Because GA's Require Function Evaluations, Instead of Gradient Information, Well-Suited For Noisy Experimental Function Evaluations**
- **Demonstrated For Both Actuator Placement and Learning Control, But Other Applications Tested Include**
 - **Truss Configuration and Sizing**
 - **Constrained Layer Damping Treatment Placement**
 - **Actuator Placement with Simultaneous Control Design**

In this work, the use of Genetic Algorithms (GA's) in solving various CSI design problems was presented. The basic principles of GA's were addressed as well as the motivation of applying GA's to CSI design problems. Two case studies were presented. The first problem involved actuator number and placement, a discrete design problem. The focus structure was the NASA Mini-Mast. The results indicate the promise of GA's in solving large order combinatorial problems. The second problem addressed the development of a Genetic Algorithm Learning Control technique. Experimental results for the slewing of a flexible beam demonstrated the learning ability of the controller. Most importantly, the control law was able to adapt even in the worst case of no prior knowledge of system dynamics. The adaption was driven making use of experimental measures of performance. Of course, prior knowledge of system dynamics can be used to bias the initial GA population to enhance GA learning. In this case, GA learning would compensate for analytical modelling errors (including unmodelled effects).

REFERENCES

Holland, J.H., (1975), *Adaption in Natural and Artificial Systems*, The University of Michigan Press, Ann Arbor, Michigan.

Longman, R.W., and Horta, L.G., (1989), "Actuator Placement by Degree of Controllability Including the Effect of Actuator Mass," Proceedings of the 7th VPI&SU/AIAA Symposium on the Dynamics and Control of Large Structures, Blacksburg, Virginia.

Layton, D.S. and Zimmerman, D.C. (1992), "Genetic Algorithm Learning Control of Large Angle Slewing Maneuvers," AeMES TR-92-03-01, Department of Aerospace Engineering, Mechanics & Engineering Science, University of Florida.

SESSION III

Chairman: Robert A. Laskin
Jet Propulsion Laboratory
Pasadena, California

Co-Chairman: Richard Martin
Phillips Laboratory
Edwards AFB, California

CSI Flight Computer System and Experimental Test Results

**D.W. Sparks, Jr. (804) 864-4349
Mail Stop 230**

**F. Peri, Jr. (804) 864-7102
Mail Stop 433**

**P. Schuler (804) 864-6732
Mail Stop 125A**

**NASA Langley Research Center
Hampton, VA 23665**

INTRODUCTION

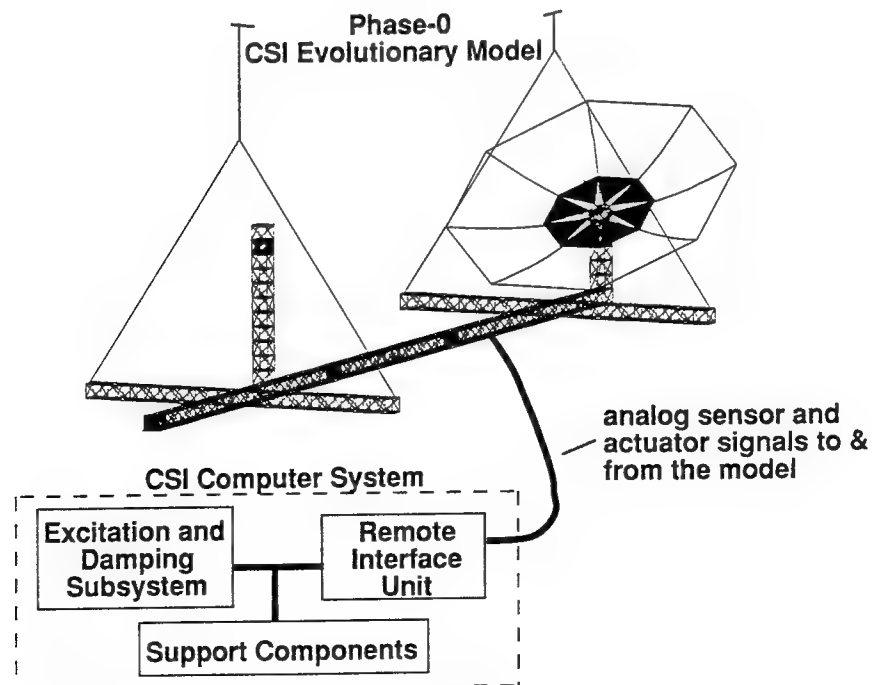
This paper describes the CSI Computer System (CCS) and the experimental tests performed to validate its functionality. This system is comprised of two major components: the space flight qualified Excitation and Damping Subsystem (EDS) which performs controls calculations; and the Remote Interface Unit (RIU) which is used for data acquisition, transmission, and filtering. The flight-like RIU is the interface between the EDS and the sensors and actuators positioned on the particular structure under control. The EDS and RIU communicate over the MIL-STD-1553B, a space flight qualified bus. To test the CCS under realistic conditions, it was connected to the Phase-0 CSI Evolutionary Model (CEM) (Ref. 1) at NASA Langley Research Center. The following schematic shows how the CCS is connected to the CEM. Various tests were performed which validated the ability of the system to perform control/structures experiments.

The EDS is capable of acquiring, from the RIU, up to 16 digital sensor values and calculating up to 8 actuator outputs for the RIU. The EDS software resides on a space flight qualified computer which was designed to be configurable to various applications requirements. The current card complement for this specific application consists of: a MIL-STD-1750A computer, serving as the master processor; a MIL-STD-1553B card, used to communicate with the RIU; and a high-speed array processor, used to perform matrix multiplications for control law computations. The software for the MIL-STD-1750A was written in the Ada programming language and the array processor was programmed in microcode. The EDS can be configured to: perform output and state feedback controls calculations; calculate excitation commands; and perform sensor safety limit checks. In addition, the rate at which sensor data is acquired from the RIU is user configurable. The CSI Computer System has three support components. The Console Debugger/PROM Programmer (CDPP) is used to download code to, or burn PROM's for, the EDS. The Ground Support Equipment (GSE) is used to supply power to the EDS. The last component, the Ground Support Equipment Terminal (GSET), is the user's interface to the system. It communicates with the EDS and the RIU via the MIL-STD-1553B. The functions of the GSET include: configuring the RIU and EDS for a particular experiment; recording in real-time the sensor and actuator data transmissions between the RIU and EDS; and reporting any errors encountered during experiment executions.

The RIU is the interface between the structure under control and the EDS. It is capable of acquiring up to 16 analog sensor signals and providing up to eight analog actuator outputs. It transmits sensor data from the structure to the EDS, and then receives actuator data from the EDS and sends it to the structure. The RIU is a modular instrument comprised of several flight-like components. It was designed so that minimal repackaging would be necessary to harden the RIU for space flight. The instrument is comprised of the following: a MIL-STD-1750A computer; a Digital Signal Processor (DSP); a MIL-STD-1553B card; and various in-house designed and fabricated boards to handle data processing. The software for the MIL-STD-1750A computer was written in Ada and programmed to initialize upon power-up. The DSP is used to filter the sensor signals. The RIU can be configured to filter multiple channels simultaneously with a variety of predefined and user defined digital filters implemented in the DSP. Sensor inputs are arranged in groups of eight and each group has a configurable sampling rate of either 60, 600, or 6000 Hz. In addition, the RIU has the capability of performing control law computations without the EDS. In this standalone mode, the RIU is connected to the sensors and actuators of the structure but not to the EDS or support components. The sensor data is sent to the DSP, where it is processed in the programmed control law to compute the required actuator commands. Any remote computer can download the control law to the RIU via a standard RS-232 serial port. By operating the RIU autonomously, higher system sampling rates can be achieved.

The CSI Computer System (CCS) tests, conducted on the CSI Evolutionary Model (CEM), included the following: open-loop excitation, safing, closed-loop control, and RIU digital filtering. The intent of these tests was to thoroughly check the functionality of the CCS under actual laboratory operations. For example, typical excitation inputs were used to excite the CEM in the open-loop tests. In addition, existing control laws, previously verified on other real-time computer systems (i.e., a CYBER 175 and a VAX workstation 3200), were executed on the CCS to verify closed-loop control. By using existing open and closed-loop test parameters, the results obtained from the CCS could be verified with previously known results. As a further form of validation, computer simulations of these tests were developed and executed off-line. In all cases, the results obtained from the CCS agreed with those from other CEM real-time computer systems and from the simulations.

TEST FACILITY



CSI COMPUTER SYSTEM (CCS) TIMING AND CONTROL FLOW DIAGRAM

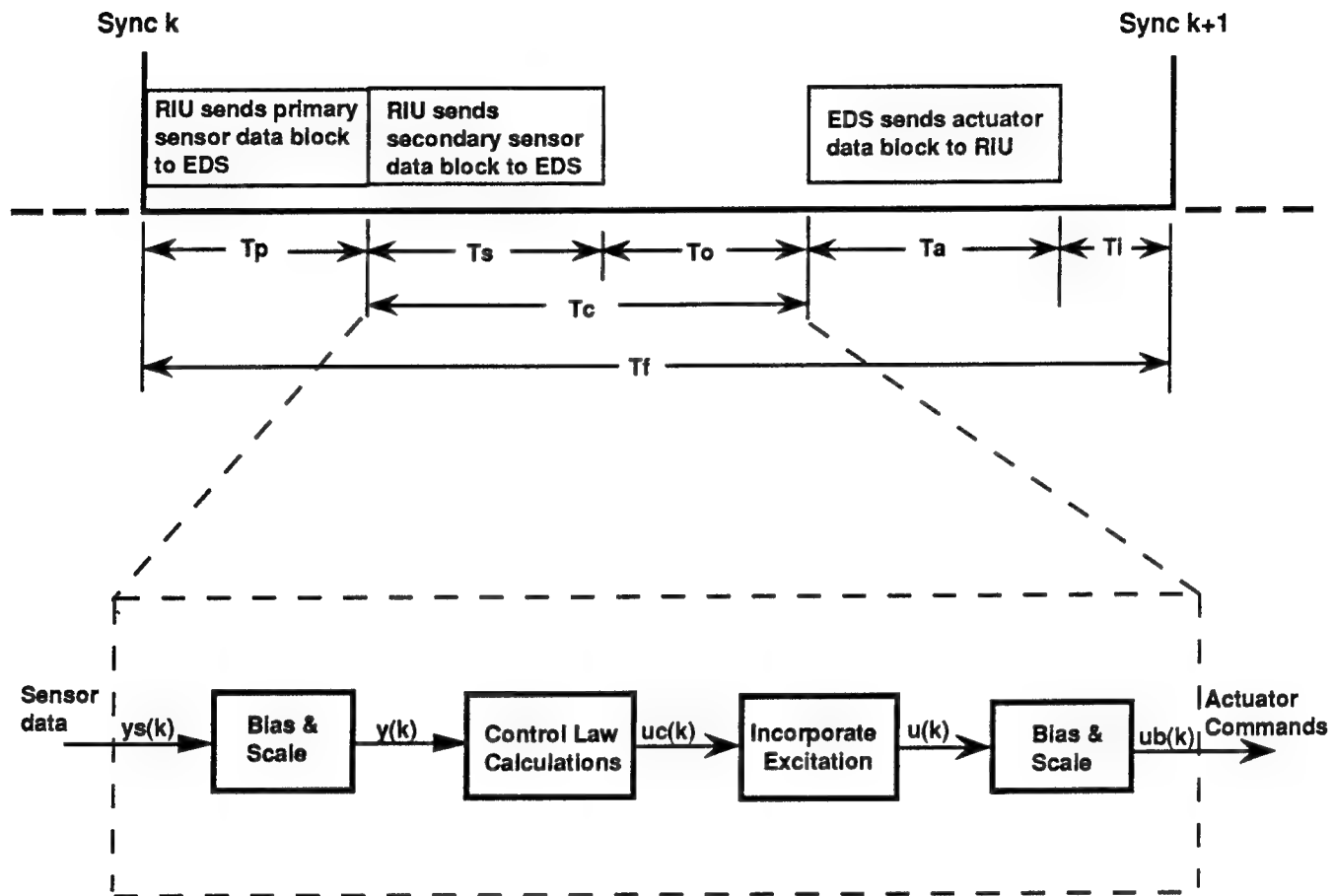
The following diagram shows the data transfers across the MIL-STD-1553B bus during a typical timeframe k . It also shows a subset of the calculations performed on that data by the Excitation and Damping Subsystem (EDS). The length of a timeframe is defined by the user specified sampling rate. A timeframe starts when the EDS sends a MIL-STD-1553B sync command to the Remote Interface Unit (RIU) and the RIU responds by recording the current values of the sensor data. A timeframe ends when, according to the user specified sampling rate, it is time to record sensor data again. However, during the entire timeframe the RIU continues to sample the sensor signals. It is only when the RIU receives the MIL-STD-1553B sync command that the sensor values are recorded on the local memory of the RIU for subsequent transmission to the EDS.

Once the MIL-STD-1553B sync command is transmitted, the EDS checks to determine if the experiment time has expired or if the user has issued the stop-test command. If neither of these have occurred, the EDS requests from the RIU a primary sensor data block. The primary data block contains the vector $ys(k)$. The vector $ys(k)$ is biased and scaled to make the sensor units compatible with those of the control law. The resulting vector $y(k)$ is then used in the control law calculations. Depending on the option chosen by the user, prior to system configuration, either output feedback or state feedback control will be used to calculate the appropriate actuator commands, $uc(k)$. User specified excitation values are then incorporated into the vector $uc(k)$ to produce the vector $u(k)$. The elements of $u(k)$ are then biased and scaled, to make the units compatible with those of the actuators, and transmitted via the actuator data block to the RIU.

The RIU transmits to the EDS one primary sensor data block each timeframe. The EDS starts performing calculations on the primary block of data as soon as it arrives. The EDS may request the optional secondary sensor data block from the RIU immediately after the primary block has been received. Each sensor value from the primary and secondary data block is checked to determine if it is within the prescribed safety limits. These checks are performed by the MIL-STD-1750A computer while the array processor is performing the control law computations. If any of the sensors have exceeded their safety limits, the elements of the vector $u(k)$ are set to zero. The vector is then biased and scaled to create $ub(k)$, which is transmitted to the RIU via the actuator data block, and the test is terminated. The sensor data from the primary data block is used in the control law computations and the safety checks. The data from the secondary data block is only used for additional safety checks. The EDS safety and control law computations must be completed and the actuator data block transmitted to the RIU before sync $(k+1)$.

Test configurations that specify large primary data blocks and actuator data blocks will cause a degradation in system throughput. Therefore, a compromise must be made between the amount of data that is to be transmitted over the MIL-STD-1553B bus and the desired sampling rate. By limiting the amount of bus traffic, times T_p and T_a can be decreased, thereby increasing the computation interval, T_c , for a given timeframe, T_f .

CCS TIMING AND CONTROL FLOW DIAGRAM



Where:

- T_p = Primary RIU to EDS sensor data transfer time
- T_s = Secondary RIU to EDS sensor data transfer time
- T_c = EDS safety and control law computations
- T_o = Unused bus time during EDS computations ($T_c - T_s > 0$)
- T_a = EDS to RIU actuator data transfer time
- T_i = Idle time prior to start of next timeframe ($T_i = 0$ when the CCS is running at full capacity)
- T_f = Timeframe

EXCITATION AND DAMPING SUBSYSTEM (EDS) REQUIREMENTS

Each sample period, the EDS is required to obtain a primary data block containing up to 16 sensor values from the Remote Interface Unit (RIU). The values must be biased and scaled to make the units compatible with those of the control law. The EDS is also required to perform user defined state and output feedback control law calculations to compute up to eight actuator commands. Sine wave, uniform random, and single pulse excitations are then incorporated into the actuator commands specified by the user. The actuator commands are then biased and scaled and transmitted to the RIU before the end of the sample period. All data transmissions between the EDS and the RIU are performed via the MIL-STD-1553B bus.

The EDS is responsible for controlling the length of the experiment and the sampling rate. The EDS is also responsible for verifying that the sensor data has not exceeded the prescribed safety limits. If this occurs, or if an emergency arises and the user issues the stop-test command, the EDS is required to transmit a zero command to the RIU for each of the actuators. Finally, the EDS is required to obtain a secondary data block containing up to 16 additional sensor values from the RIU. These values are not used in the control law calculations but are checked against the prescribed safety limits as an additional safety precaution.

The EDS software is designed to obtain and transmit data to more than one RIU, although this capability was never verified under actual lab operations. In addition, by increasing the value of the constants specified in the software, the EDS can operate with primary, secondary, and actuator data blocks of up to 32 words each. All data blocks are limited to 32 words since the message size for a MIL-STD-1553B bus transmission is limited to a maximum of 32 words.

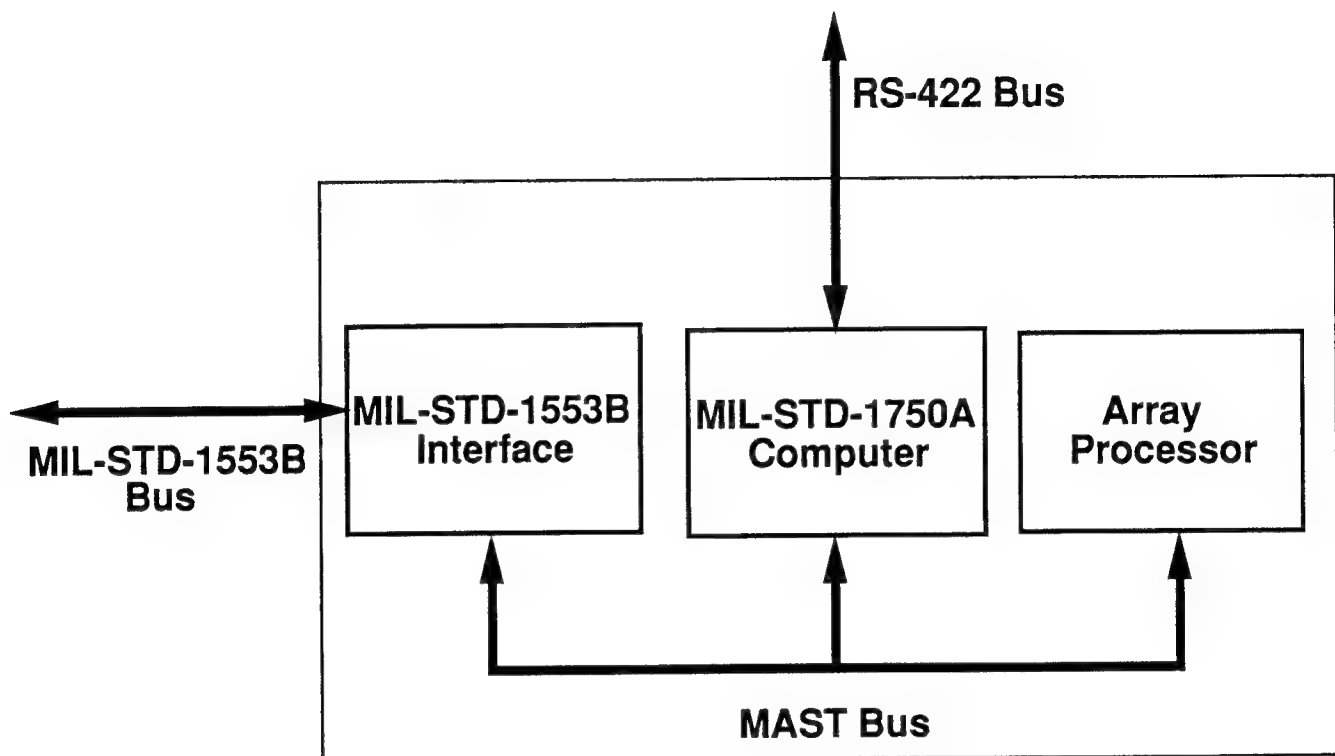
- **Perform user defined state and output feedback control calculations**
- **Scale and bias sensor and actuator data**
- **Provide sine wave, uniform random, and single pulse excitation**
- **Control experiment timing according to user specified parameters**
- **Perform experiment safety and emergency shutdown procedures**

EXCITATION AND DAMPING SUBSYSTEM (EDS) BLOCK DIAGRAM

The EDS software was developed in-house, and resides on the commercially available, space flight qualified, Multi-processor Architecture Space Technology (MAST) computer, manufactured by SCI Systems, Inc. (Ref. 2). The MAST Computer was designed to be modular so that it could be configured with different combinations of processor, memory and I/O interface boards to support various applications requirements. The block diagram shows the configuration used with the CSI Computer System (CCS). The MIL-STD-1750A computer controls the EDS and was programmed primarily in the Ada language. However, assembly language was used for the math library, interrupt routines and utilities to perform activities such as block memory moves. The entire Ada program fit in the 64k RAM provided by the MIL-STD-1750A board. Memory words use 16 bit resolution with an additional 6 bit code for Error Detection and Correction (EDAC). The MIL-STD-1750A uses a floating point representation composed of two 16 bit words. The board also provides an RS-422 serial port which was used by the CCS system operator to issue a stop-test command directly to the MIL-STD-1750A if an emergency arose during test execution. A single array processor, programmed in microcode, was used to perform all control law matrix multiplications. Under the current configuration, the maximum size matrix that the single array processor can hold is 128x128 and the cumulative sum of the number of elements contained within the actuator, sensor and state vectors must not exceed 128. Lab experiments have been performed to demonstrate that the addition of a second array processor could be used for matrices larger than 128x128, but this substantially reduced throughput due to the increased overhead of moving large data blocks in and out of the array processor memory. The array processor was designed specifically to efficiently process large matrices such as those used in structural dynamics applications. The processor is built around the Analog Devices 3200 series chip set which adheres to the IEEE standard 754 for floating point arithmetic. The clock speed is 6.7 MHz, and the maximum theoretical throughput is 13.4 MFLOPS. The MIL-STD-1553B card handles all the communications with the Remote Interface Unit and the Ground Support Equipment Terminal. The card provides the three standard operational modes of Bus Controller, Remote Terminal, and Bus Analyzer. For this CSI application, code was written for both Bus Controller and Remote Terminal modes. The three boards described are mounted in three of the 16 slots provided by the motherboard and communicate through the MAST Bus located on the motherboard.

Tests that were run at Marshall Space Flight Center qualified the design of the MAST computer, with its full card complement, for levels called out for Shuttle and Titan IV general computer use. The MAST computer was designed to provide: data collection and storage; high-speed data processing; output control and communication with other computers of its own type, and with standard space shuttle and experiment interfaces. Although they were not used for this CSI application, the MAST computer is capable of supporting several other different types of cards: a Serial Input-Output board; a Buffered Input-Output board for discrete inputs and outputs; a High Rate Multiplexer board; an analog multiplexer/analog-to-digital converter board; and a Mass Memory board configured to provide 256k words of additional memory.

EXCITATION AND DAMPING SUBSYSTEM BLOCK DIAGRAM



REMOTE INTERFACE UNIT (RIU) REQUIREMENTS

The primary requirement of the RIU is to support data acquisition and filtering for flexible combinations of sensors and actuators. To speed the control law computations in the Excitation and Damping Subsystem (EDS), the sensor data is ordered in the RIU to create the proper sensor vector required by the control law. The sensors and actuators are hardwired to the RIU channels but a flexible test configuration is maintained since the sensor signals can be ordered within the RIU.

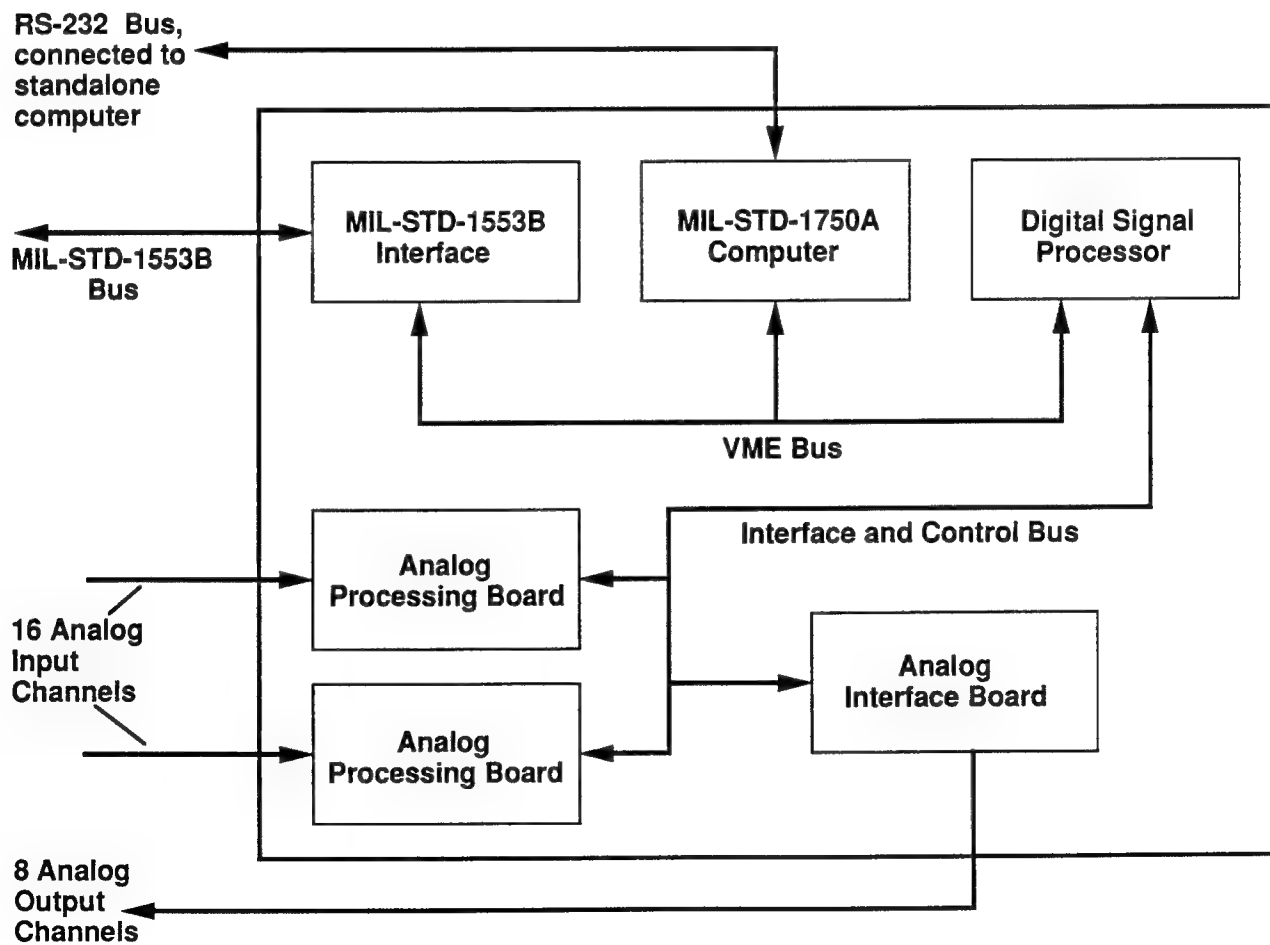
To accommodate various types of sensors, the RIU provides the capability to process input data with different analog and digital filters. Digital filters provide enhanced filtering capabilities compared to analog filters. However, the analog filters are necessary to avoid aliasing when using digital filters. The RIU uses variable gain amplifiers for each sensor channel to support different sensor gains.

Another requirement of the RIU is to perform control law computations without the EDS. In this standalone interface configuration the sensor data is fed through local RIU filters implementing the control law and sent to the actuator channels. The limiting factor for the system sampling rate is the speed at which data can be transferred to the MIL-STD-1553B interface. By eliminating the use of this interface, higher system sampling rates can be achieved. However, the control laws must be limited to those that can be implemented with the RIU digital filters.

- **Order sensor data to conform to control law state variables**
- **Provide variable gain amplifiers, and variable bandwidth analog filters to support a variety of sensors**
- **Provide digital filters for greater filtering flexibility**
- **Support multiple interfaces for different host configurations**

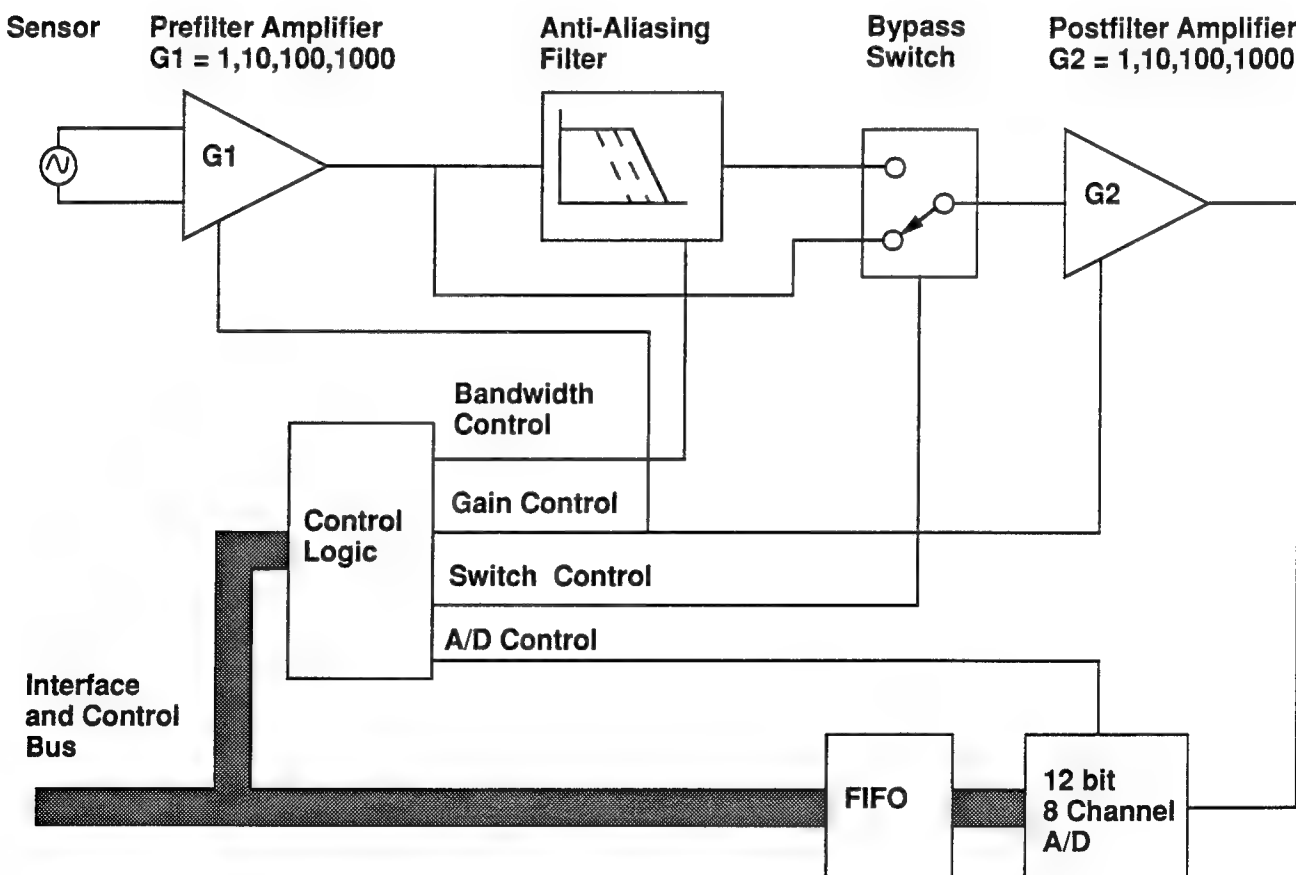
REMOTE INTERFACE UNIT (RIU) BLOCK DIAGRAM

The RIU is comprised of several components interfaced via two buses, a VME bus, and a custom designed Interface and Control Bus. Each of the components is a circuit board that is contained within a card cage. A MIL-STD-1553B bus is used to provide communications between the RIU, the Excitation and Damping Subsystem, and the Ground Support Equipment Terminal. A MIL-STD-1750A computer controls the operation of the RIU, maintains a dual ported RAM for local storage, and also has an RS-232 port for the RIU to use as the standalone interface. A Digital Signal Processor (DSP) provides digital filters for the RIU. Sensor signals can be filtered using Finite Impulse Response, or Infinite Impulse Response digital filters. The Analog Interface Board responds to commands from the DSP to record a data sample. This board is also responsible for providing the analog actuator outputs for the RIU. The components in the RIU exchange data via the VME and Interface and Control buses. The final component of the RIU is the Analog Processing Board. This board contains the analog to digital converter, multiplexer, analog amplifiers, and analog anti-aliasing filters. Two of these boards are used within the RIU and each of these boards supports eight sensor inputs. These boards are interfaced to the remaining components of the RIU via the Interface and Control Bus.



REMOTE INTERFACE UNIT (RIU) ANALOG PROCESSING BOARD

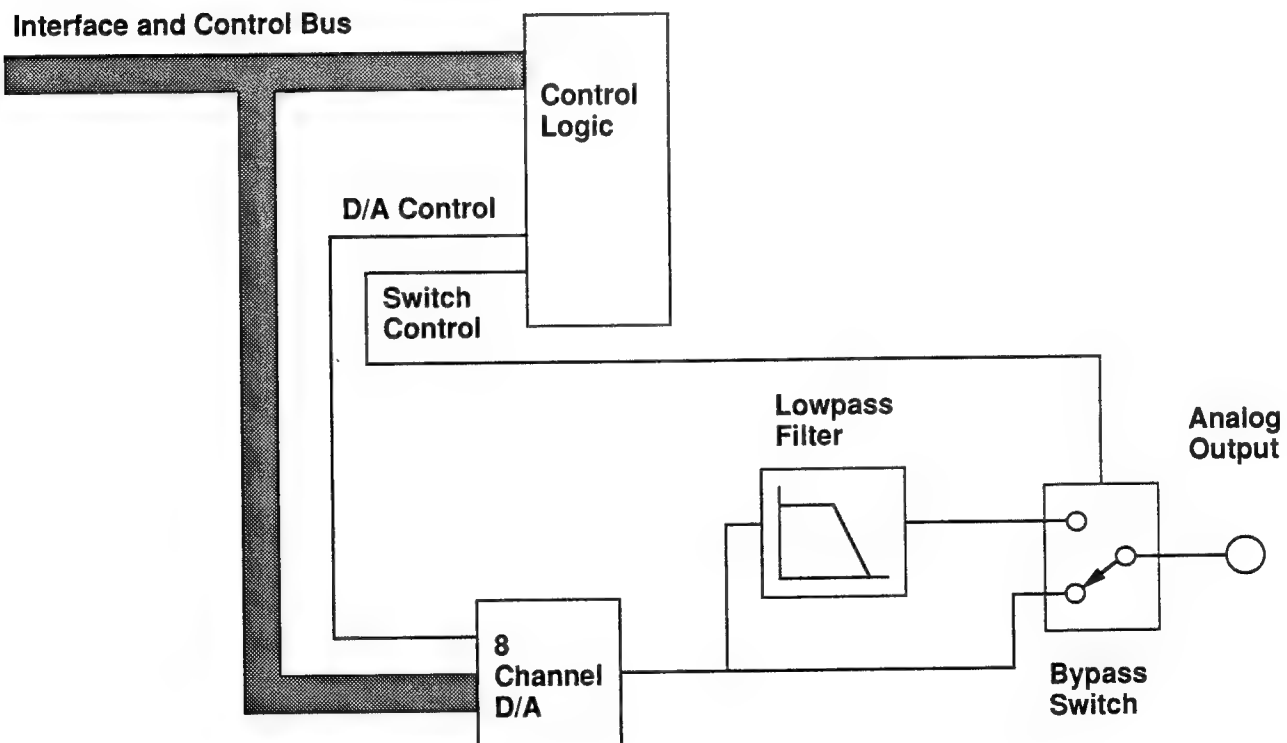
The Analog Processing Board was designed in-house to provide the RIU with an interface to the sensors on the structure. This board supports eight analog inputs, however, for simplicity the diagram only shows one analog signal path. The signal path consists of a prefiltering amplifier, an anti-aliasing analog lowpass filter, a postfiltering amplifier, and a 12 bit, eight channel analog to digital converter (A/D). The board is designed so that most of the functions can be either adjusted or bypassed. The amplifiers have programmable gains of 1, 10, 100, or 1000. This allows a variety of sensors to be connected to the RIU. The lowpass anti-aliasing filter has a variable bandwidth of 1666 Hz, 166 Hz, or 16 Hz. This filter can be bypassed if there is no concern for aliasing. A first-in-first-out (FIFO) buffer is used to store each of the eight samples from the A/D during an acquisition cycle to maintain phase coherency between channels. This board receives control signals from the Analog Interface Board and transmits data to the Digital Signal Processor via the Interface and Control Bus.



REMOTE INTERFACE UNIT (RIU) ANALOG INTERFACE BOARD

The RIU Analog Interface Board was designed in-house to provide the analog outputs that control the actuators on the structure. This board supports eight analog outputs, however, for simplicity the diagram only shows one analog signal path. This board converts the digital data received from the Excitation and Damping Subsystem over the MIL-STD-1553B bus into analog signals that can be applied to the actuators. A digital to analog converter (D/A) with an eight channel multiplexer is used to construct the analog signals. After the data is converted, the signals can be smoothed with an analog lowpass reconstruction filter. There is one analog filter for each actuator output. These filters can be bypassed if the signals do not contain frequency components above the sampling rate of the RIU.

This board also controls the operations of up to four Analog Processing Boards by providing the control signals to select the various gains and filter bandwidths.



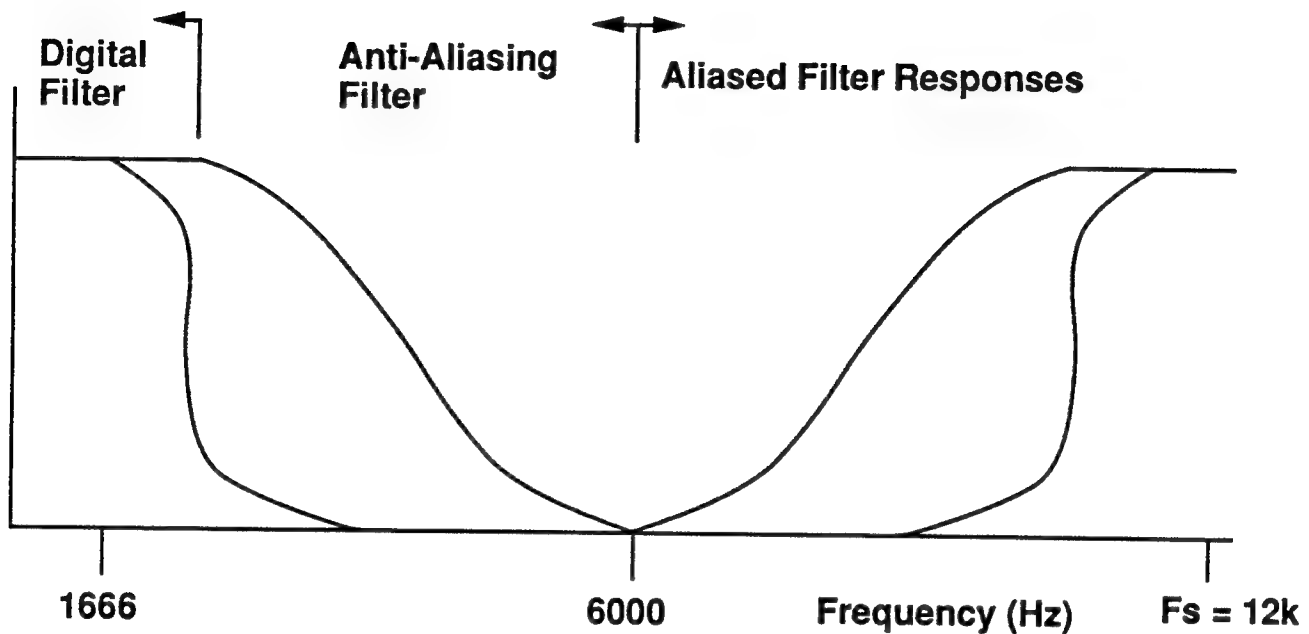
REMOTE INTERFACE UNIT (RIU) FILTER DESCRIPTION

The RIU contains both analog and digital filters. The analog filter is an eighth order lowpass Butterworth design. Three cutoff frequencies are available: 1666 Hz, 166 Hz, and 16 Hz. The corresponding RIU sampling rates for these three cases are: 6000 Hz, 600 Hz, 60 Hz. To avoid compromising the phase response of the digital filter by using sharp roll-off analog anti-aliasing filters, the transition region of the analog filter is extended. At the largest cutoff choice of 1666 Hz, the transition region of the analog filter starts at 1666 Hz and continues to approximately 6000 Hz. As shown in the first figure, the bandwidth of the digital filter is contained entirely within the passband region of the analog filter. In this region the phase shift from the analog filter is near zero. With the transition region of the analog filter extended beyond the digital filter cutoff frequency, the required sampling rate to eliminate all aliased components of the analog filter would be approximately 12 kHz. This sampling rate places a strenuous load on the data processing requirements for the MIL-STD-1750A computer; therefore, it is necessary to reduce the rate as much as possible. The sampling rate can be decreased at the risk of allowing some of the aliased components of the analog filter to enter the transition region of the digital filter. Since the resolution of the analog to digital converter (A/D) in the RIU is 1 bit in 12, which is a relative magnitude of -72 dB, the sampling rate can be lowered until the aliased portion of the analog filter response just reaches -72 dB. This will not allow any of the aliased frequency components to interfere with the signal of interest since the magnitude will be below the range of the A/D. The resulting sampling frequency is 6000 Hz. The second figure shows the resulting frequency responses of the digital and analog filters. Similar results apply to the analog bandwidths of 166 Hz and 16 Hz.

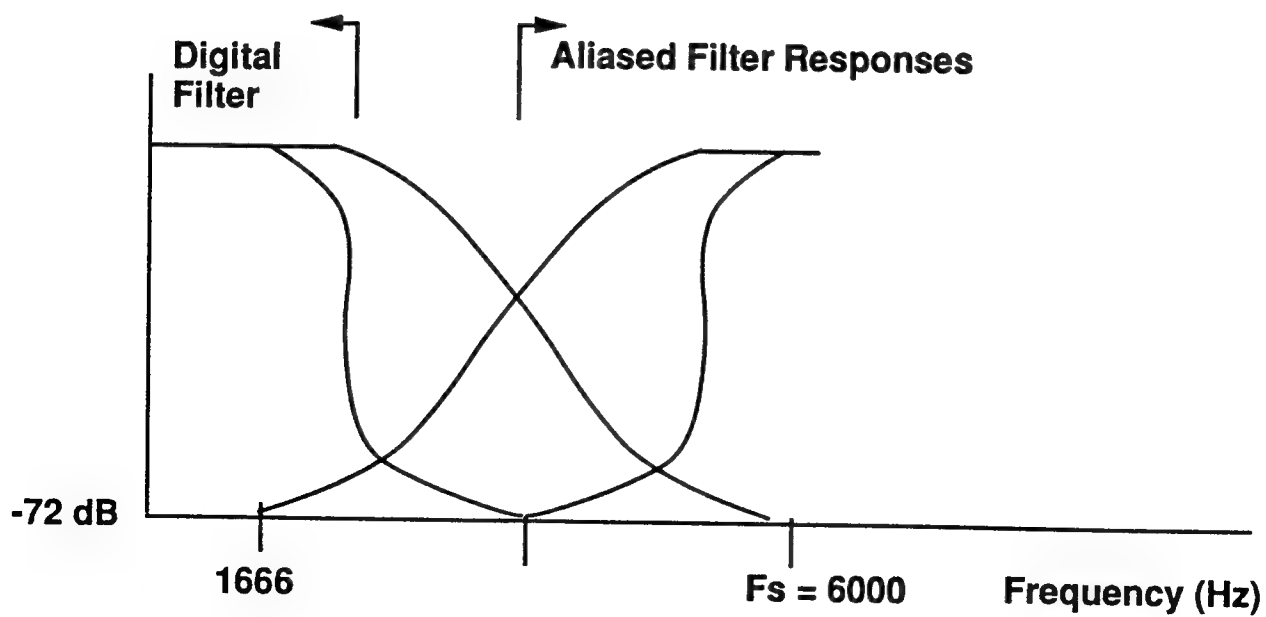
The RIU implements both Finite Impulse Response (FIR) and Infinite Impulse Response (IIR) digital filters in the Digital Signal Processor (DSP). The RIU has two predefined lowpass FIR filters and can support additional user defined filters. The first predefined filter has a length of 110 and was designed to have a sharp roll-off with little consideration given to phase shift. The second predefined filter has a length of 54 and was designed to have less roll-off and to introduce smaller phase shift. FIR filtering is accomplished by performing convolutions with the digital filter coefficients and blocks of sampled data (Ref. 3). The RIU can support two user defined IIR filters. The DSP processes sensor data with this filter by rearranging the IIR coefficients into a difference equation and computing the output from delayed values of the input and output data (Ref. 3).

REMOTE INTERFACE UNIT FILTER RESPONSES

Full sampling rate



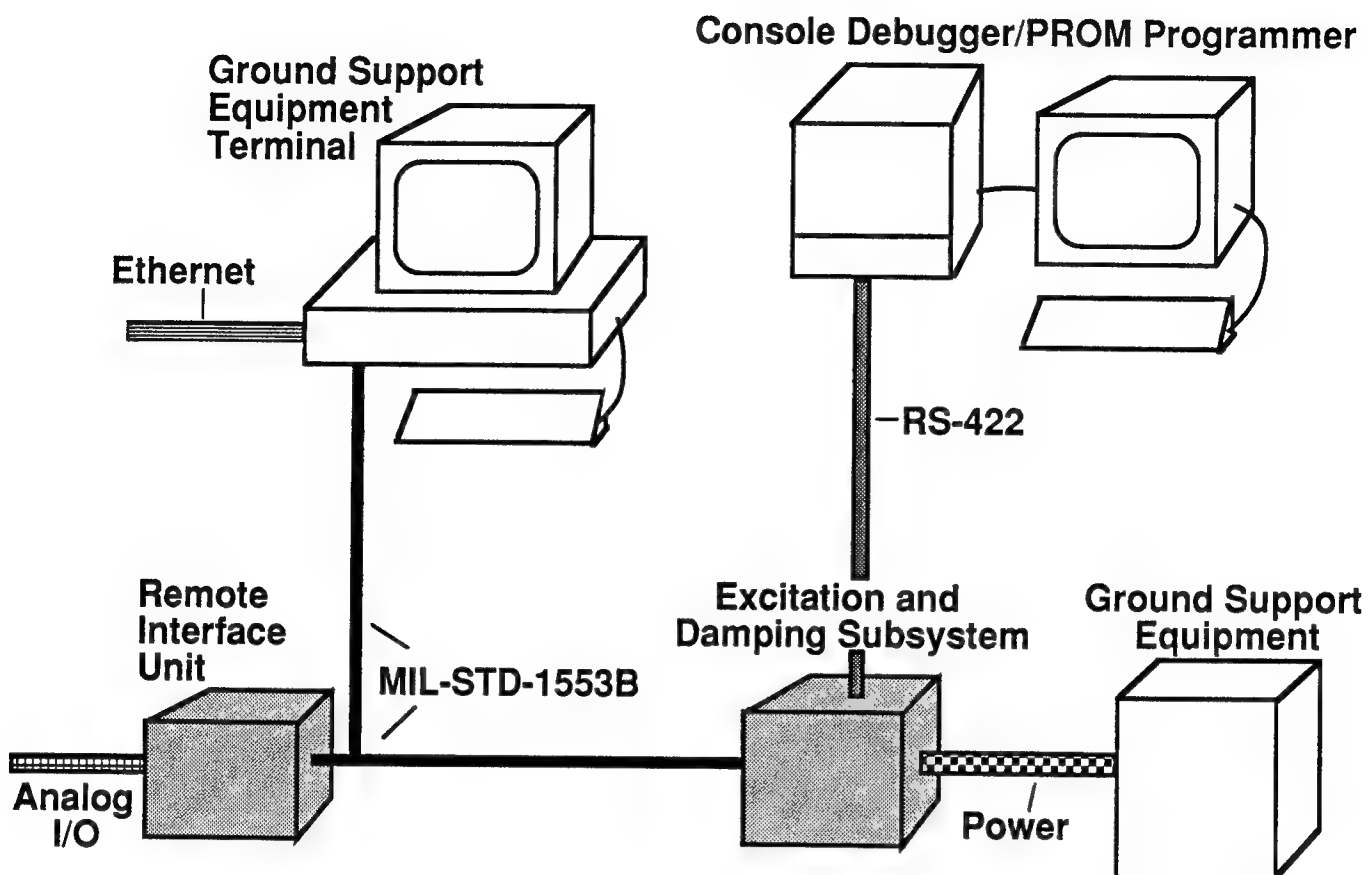
Undersampling



CSI COMPUTER SYSTEM (CCS) SUPPORT COMPONENTS

The CCS contains three support components. A diagram showing the components and their connections to the Excitation and Damping Subsystem (EDS) and the Remote Interface Unit (RIU) can be seen in the figure. The Console Debugger/PROM Programmer (CDPP) is a PC XT with an attached PROM burning expansion chassis. The CDPP has the capability to: download code, via a standard RS-422 interface, to the EDS; burn PROM's on boards designed for the MAST computer; and provide the user with a direct interface to the EDS, via the RS-422, in order to manually halt test execution in case of an emergency. In addition, the CDPP has debugging capabilities which were used extensively during development of the software for the EDS. The Ground Support Equipment (GSE) has only one function in the CSI Computer System and that is to supply power to the EDS. However, the GSE has data recording and numerous I/O capabilities to support communications with various MAST I/O boards which were not used by this CSI application. The third component, the Ground Support Equipment Terminal (GSET), is a PC AT which provides the user interface to the CSI Computer System. It is connected to the EDS and RIU via the MIL-STD-1553B bus. The GSET is responsible for configuring the RIU and EDS prior to test execution with parameters obtained from user provided files, a system file, and pretest calculations. Information such as RIU sensor channel gains and filter cutoff frequencies and EDS sensor critical limits and control matrix coefficients are contained within the parameters. It is those specified values that will define how a particular experiment will be executed. The GSET is also responsible for: recording, in real-time, the sensor and actuator data transmissions between the RIU and the EDS during the execution of an experiment; reporting any errors encountered during test executions; and post processing the experimental data once a test run is complete. After post processing is complete, the experimental data can be transferred to other systems, via Ethernet, where the actual test results can be compared with simulation results such as those obtained from PRO-MATLAB.

CSI COMPUTER SYSTEM SUPPORT COMPONENTS



CSI COMPUTER SYSTEM (CCS) VERIFICATION TESTS

After delivery and installation in the Space Structures Research Laboratory (SSRL), the following series of tests were conducted on the CCS to verify the functionality of the system in real laboratory operations. The first set of tests followed the SCI System Inc., procedures for verifying that the Excitation and Damping Subsystem (EDS) hardware and ground support components were functioning. These tests included checking the EDS power supply, the EDS memory and the capability of the EDS to properly communicate over the MIL-STD-1553B bus. After completing these tests, a series of additional tests were performed to verify that the CCS software requirements were met. These tests verified that the CCS could be configured for an experiment, compute the user defined excitations, perform the control law calculations and record test data.

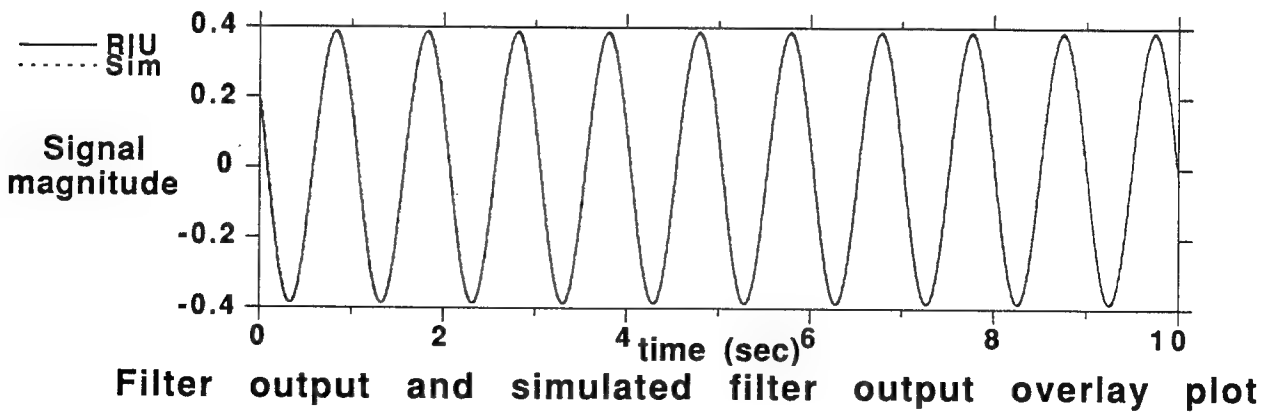
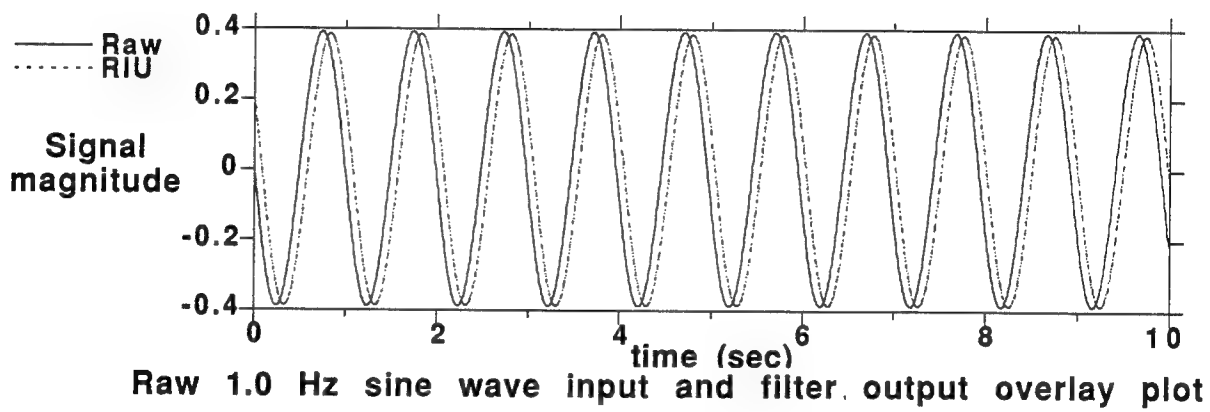
After completing the hardware and software requirements tests, the following operational tests were performed: Remote Interface Unit digital filtering tests; open-loop excitation tests; closed-loop control tests; software safety tests; and computational speed tests.

- **Excitation and Damping Subsystem hardware and ground support components**
- **Software computational requirements**
- **Remote Interface Unit digital filtering**
- **Open-loop excitation**
- **Closed-loop control**
- **Software safety requirements**
- **Computational speed**

REMOTE INTERFACE UNIT (RIU) DIGITAL FILTERING TESTS

To test the RIU predefined digital filters, the RIU input channels were connected to a signal generator. Fixed-frequency sine waves were then sent to the RIU to simulate the sensor signals. The same sine wave was sent to eight RIU sensor channels. However, different RIU digital filters were selected for various channels. All the sensor data was recorded on the Ground Support Equipment Terminal for later analysis. Post test analysis involved the comparison of the RIU digital filter outputs with PRO-MATLAB simulated filter outputs for the same sine wave input. Several tests were made, involving different frequency sine wave inputs; the results of one test are presented here. For these tests, the RIU sampling rate was 600 Hz.

The top figure shows a time history plot of the raw 1.0 Hz test sine wave produced by a signal generator superimposed over the plot of test output from the RIU filter with the sharp roll-off. The group delay effects of the initialization of the digital filter were not recorded because the RIU begins to process the sensor signals in the Digital Signal Processor as soon as the RIU is fully configured, not when the data recording begins (time = 0 on the plot). The bottom figure shows a comparison between the time history plots of the sharp roll-off filter output and a PRO-MATLAB simulation output of the same filter for the 1.0 Hz test sine wave input. The 1.0 Hz tests show excellent agreement between the test and simulation. Similar results were obtained in the filtering tests with lower and higher frequency sine waves. In addition, similar tests were successfully conducted with the second predefined filter.



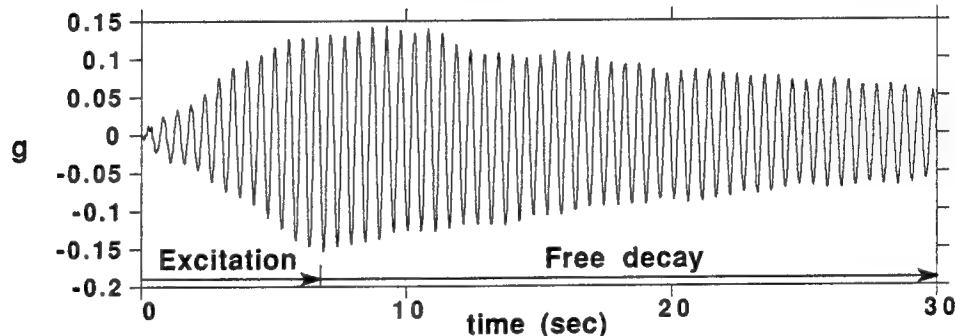
OPEN-LOOP TEST RESULTS WITH THE CSI EVOLUTIONARY MODEL (CEM)

For these tests, open-loop commands were sent from the CSI Computer System (CCS) to the thrusters on the CEM test article, and the responses of eight servo accelerometers were recorded. There were 16 separate thruster units on the CEM, commanded in pairs (Ref. 1). A single computer command signal sent to a thruster pair was split into two, one for each thruster making up the pair. The current CCS software is capable of commanding three different types of excitation for use as disturbances: sine waves, single pulses (of one sample period duration), and uniform random excitation. In the software, any thruster pair can be commanded to output any of the above three excitations during a test, although each thruster pair can only be commanded to perform one type of excitation per test.

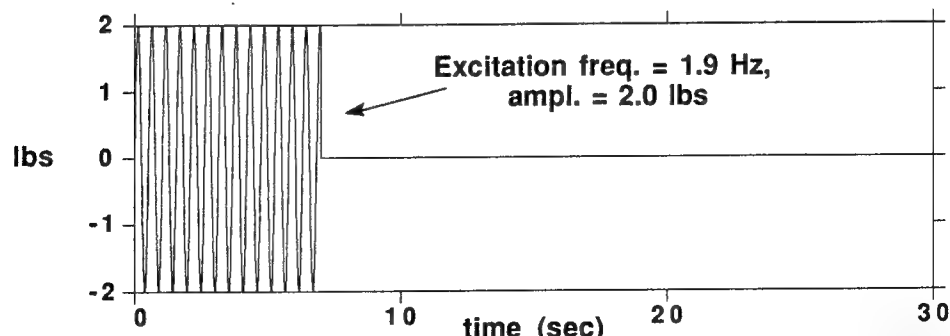
All three types of excitation were tested on the CEM. Results from a sine wave excitation test are presented. This test was 30 seconds long and involved exciting the CEM with four thruster pairs for 7 seconds, then turning off the excitations and allowing the motions to freely decay for the remaining 23 seconds of the test. The top figure shows a recorded sample accelerometer response. The bottom figure shows sample thruster commands. The sample thruster pair was commanded with a 1.9 Hz frequency, 2 lb amplitude sine wave. Note the open-loop response growing from 0 to 7 seconds, and the free decay response after the thrusters were turned off. For this sine wave test, all eight accelerometer responses matched those obtained on the existing VAX workstation 3200 real-time computer using the same open-loop excitation.

Similar to the sine wave excitation tests, the CCS also successfully passed the pulse and uniform random open-loop excitation tests.

OPEN-LOOP EXCITATION TESTS



Sample accelerometer response to an open-loop sine wave excitation



Sample thruster commands for open-loop sine wave excitation

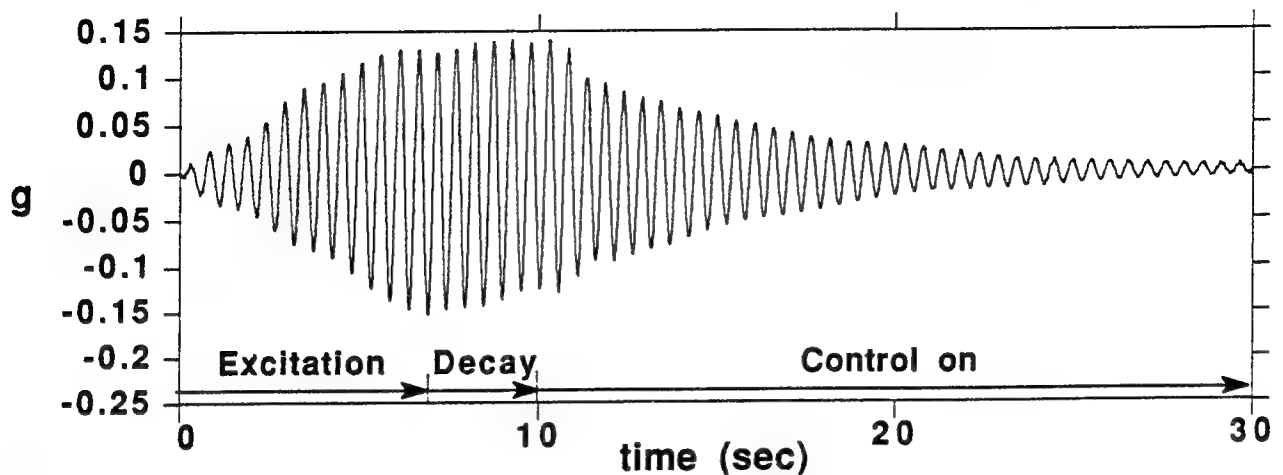
CLOSED-LOOP CONTROL TESTS WITH THE CSI EVOLUTIONARY MODEL (CEM)

Three different closed-loop state feedback control laws were executed on the CSI Computer System (CCS). The number of states were 16, 42 and 60, respectively. Each used 8 servo accelerometers and all 8 thruster pairs. The performance goal of damping the vibrational motions of the CEM was the same for all three control laws. Each control law test was 30 seconds long, and the same sine wave excitations which were described in the open-loop testing section were used to excite the CEM for the first 7 seconds of each test run. After a period of 3 seconds of free decay, the control law was then turned on for the remainder of each test run.

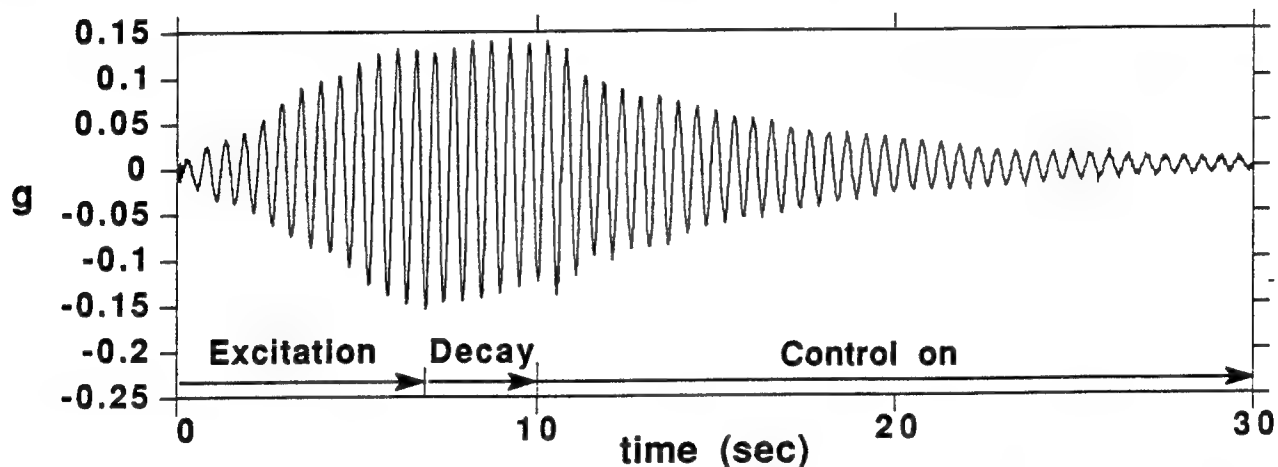
The first closed-loop control law tested was a 16 state control law (Ref. 4), digitally simulating second-order mass-spring-damper systems at accelerometer/thruster pair locations which actively absorb vibrational energy from the CEM. This control law was executed at 150 Hz and at 200 Hz; the results of the latter test are presented here. For verification purposes, the same control law was executed on the existing VAX workstation 3200 at 200 Hz. This VAX is used as the primary real-time control computer in the Space Structures Research Laboratory, and is tied into a Computer Automated Measurement and Control (CAMAC) rack which performs the data acquisition and conversion duties. The first two figures show a sample accelerometer response from the control law tests conducted on the VAX and CCS, respectively. The responses matched, although the accelerometer data from the CCS was noticeably noisier. This was attributed to the fact that the CAMAC A/D converters had 16 bit resolution, as opposed to only 12 bit resolution for the A/D converter in the RIU. This in turn led to the slight differences in thruster commands issued from the two computers. This can be seen in the last two figures, which show commands from the two respective computers for the same thruster. Another factor to be considered, when comparing the CCS to the VAX, is computational precision. The control law on the VAX was executed in double precision (i.e., 64 bits), while the CCS was limited to 32 bit precision in its computations on the array processor. As a final check, the accelerometer responses, from both computers, were fed into a PRO-MATLAB simulation of the 16 state control law. The resulting simulated thruster command time histories matched their respective CCS and VAX computed thruster commands.

The two other closed-loop control laws, H-infinity based designs of 42 and 60 states, respectively, were successfully executed on the CCS in real-time at 200 Hz.

CLOSED-LOOP CONTROL TESTS

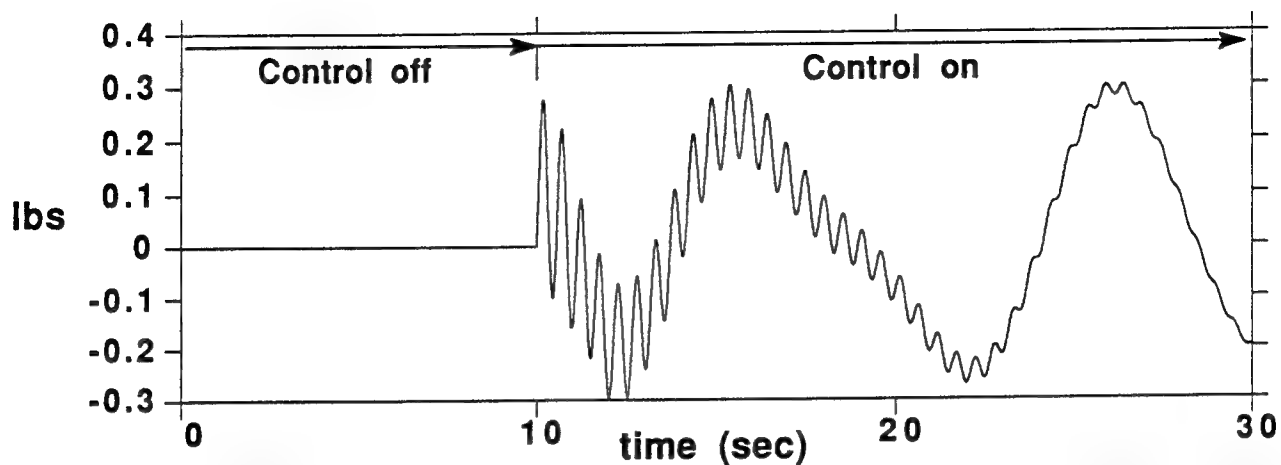


Sample accelerometer response from control test executed on VAX 3200

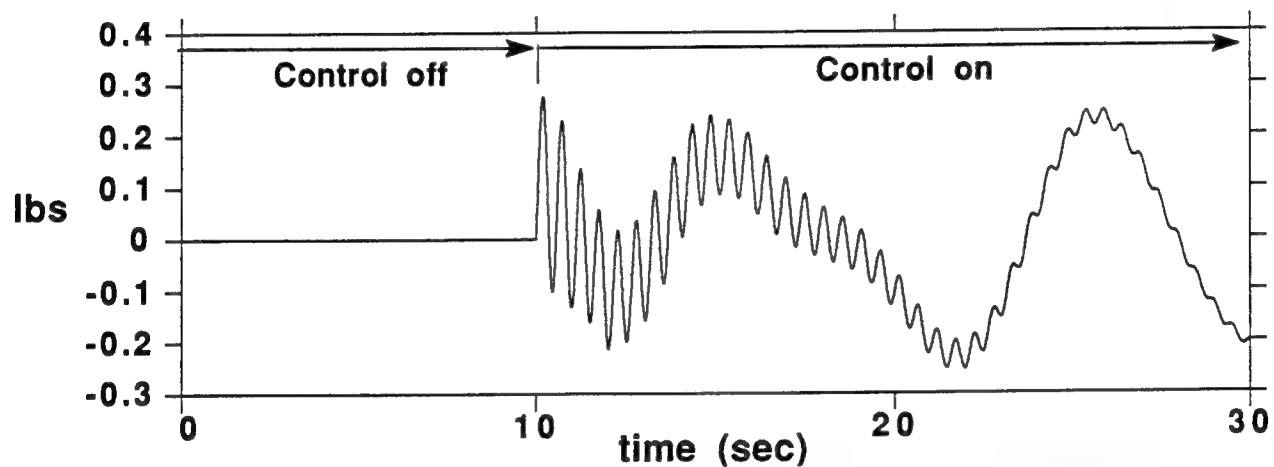


Accelerometer response from control test executed on CSI Computer System

CLOSED-LOOP CONTROL TESTS (CON'T)



Sample thruster commands from control test executed on VAX 3200



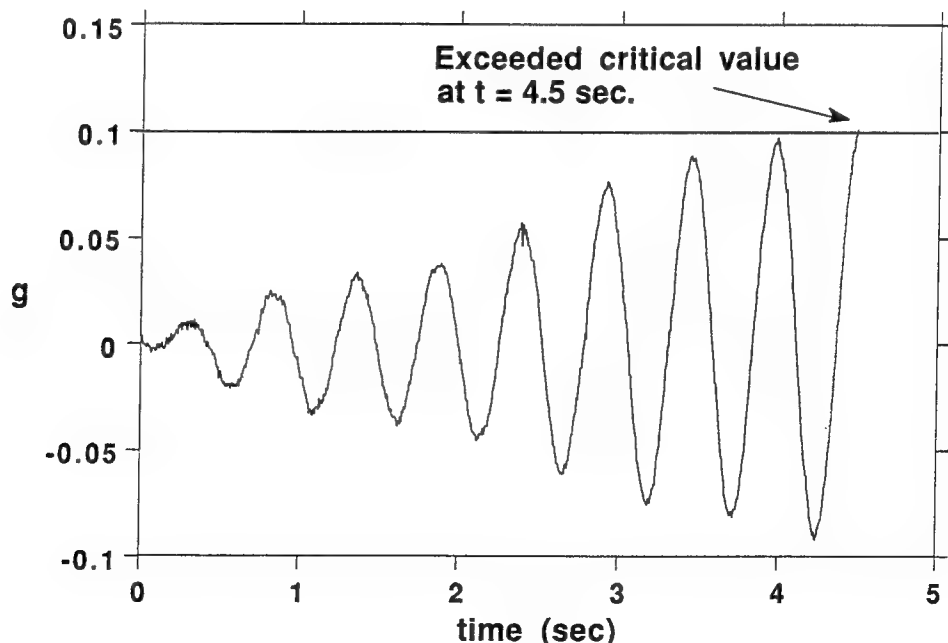
Commands to thruster from control test executed on CSI Computer System

SAFING TESTS WITH THE CSI EVOLUTIONARY MODEL (CEM)

One necessary feature of any computer system which is used to conduct dynamic experiments with large test articles, such as the CEM, is safing. During the open-loop command testing phase, both the manual shutdown command and the automatic safety shutdown features of the CSI Computer System (CCS) software were tested. Manual shutdown commands, issued by typing in "halt" on the Console Debugger/PROM Programmer (CDPP), were successful in zeroing all the thruster commands and stopping the experiment in all instances. During the closed-loop tests with the 16 state control law, the manual shutdown command from the CDPP was tested again, to ensure that it can function during an actual closed-loop control experiment. The manual shutdown command was tried on several closed-loop tests, always being issued after the control law was turned on. In each case, the halt command successfully zeroed out all of the thruster commands and terminated the control execution.

The automatic safety shutdown software keyed on the magnitude levels of the accelerometer signals. Each accelerometer was assigned a maximum allowable signal level, called the critical value. If any accelerometer signal magnitude exceeded its critical value during the test, all the thruster commands were automatically set to zero and the experiment was terminated. In order to test this automatic shutdown feature without exciting the CEM to a high (and potentially damaging) degree, artificially small critical values were assigned to the accelerometers. The sine wave excitation commands, described in the open-loop testing section, were used to disturb the CEM. The figure shows the response of an accelerometer which was assigned a critical value of 0.1g. In addition, the figure shows that the 0.1g level was exceeded at 4.5 seconds, at which time the experiment automatically stopped and the thrusters were issued a zero command. The messages indicating that a "sensor limit was exceeded" and the "experiment terminated" were correctly displayed on the Ground Support Equipment Terminal.

SOFTWARE SAFETY REQUIREMENTS TESTS

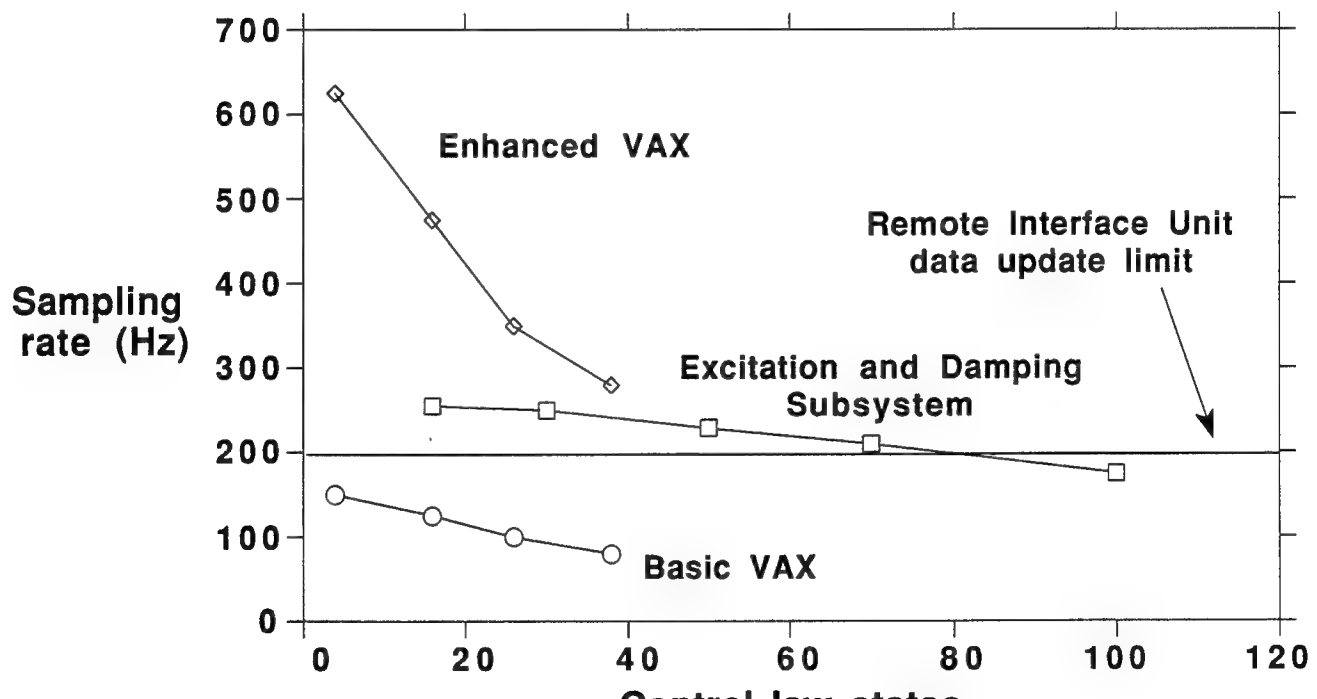


Sample accelerometer response from an automatic software shutdown test - critical value = 0.1g

CSI COMPUTER SYSTEM (CCS) COMPUTATIONAL SPEED TESTS

A set of five "dummy" control experiments were executed on the CCS to determine the achievable sampling rates for state feedback control laws of varying sizes. For these tests, the CCS was connected to the CSI Evolutionary Model (CEM), however, the computed thruster commands were not transmitted to the test article since the "dummy" control law matrices were not taken from real control laws, but were arbitrarily defined. Each one of these test runs was the same, with the exceptions being the control law size and the sampling rate. Each of the control laws used 8 servo accelerometer signals to compute commands for all 8 thruster pairs.

The figure shows a comparison of computational speeds, as a function of control law size, between the Excitation and Damping Subsystem (EDS) and the VAX workstation 3200. The "Basic VAX" plot represents the initial performance of the VAX workstation 3200 as delivered from the vendor. The "Enhanced VAX" plot represents the current performance after in-house optimization was completed on the workstation real-time software. The "EDS" plot represents the fastest speed that the EDS can process and compute a control law of a given size. These sampling rates are the rates at which the EDS requests data updates from the RIU; the current RIU, however, can only transmit updated sensor data to the EDS at a rate of 200 Hz. Thus, the control laws which were executed above 200 Hz were not using refreshed sensor data in every EDS sample period. For this reason, the maximum practical CCS sampling rate, for control laws with 80 states or less, is 200 Hz with the present system.



VAX workstation 3200 and Excitation and Damping Subsystem achievable sampling rates versus control law size

SUMMARY

The CSI Computer System (CCS) is composed of the Excitation and Damping Subsystem (EDS) software, resident on the space flight qualified Multi-processor Architecture Space Technology (MAST) computer, and the Remote Interface Unit (RIU), an in-house built, flight-like data acquisition/filtering system. Both the EDS and the RIU use MIL-STD-1750A computers which were successfully programmed in Ada. The CCS has been installed in the Space Structures Research Laboratory (SSRL) for testing. Both open and closed-loop tests have been successfully conducted with the CSI Evolutionary Model (CEM), and have demonstrated that the CCS system is capable of performing meaningful real-time control experiments on actual laboratory test articles. Also, these initial tests results have indicated that the CCS shows promise as a viable space flight computer, and further study in this direction is warranted.

- **The CSI Computer System is comprised of a flight qualified computer and a flight-like data acquisition and filtering subsystem**
- **The capability of the system to conduct control/structures experiments has been successfully verified on the CSI Evolutionary Model**
- **The system shows promise as a viable space flight computer and further study in this direction is warranted**
- **Demonstrated Ada programming expertise on a real-time embedded system**

REFERENCES

1. Belvin, W.K.; Elliott, K.B.; et. al.: *Langley's CSI Evolutionary Model: Phase-0*, NASA TM-104165, Nov. 1991.
2. SCI Systems, Inc., Huntsville, AL: *MAST Final Report*, SCI Report No. P007-001A, Jun. 1990.
3. Oppenheim, A.V.; and Schafer, R.W.: *Discrete-Time Signal Processing*. Prentice-Hall Publ. Co., Inc., 1989.
4. Bruner, A.M.; Belvin, W.K.; et. al.: Active Vibration Absorber For the CSI Evolutionary Model: Design and Experimental Results. AIAA 91-1123, Apr. 1991.

Optical Pathlength Control on the JPL Phase B Interferometer Testbed

John Spanos and Zahidul Rahman

Jet Propulsion Laboratory, California Institute of Technology
Pasadena, California 91109

Abstract

Design and implementation of a controller for optical pathlength compensation on a flexible structure is presented. Nanometer level pathlength control is demonstrated in the laboratory. The experimental results are in close agreement with performance predictions.

Introduction

Many future space missions will require major advances in the areas of controlling, aligning, and pointing optical instruments mounted on large flexible structures. One of the most challenging applications is optical pathlength control for stellar interferometry [1]. Figure 1 shows one possible configuration of a long baseline interferometer with six collecting telescopes mounted on a free flying truss structure. The optics are designed such that any two collectors can be used as a stand-alone interferometer. For the interferometer to perform its mission successfully, the variations in the length of the path traveled by light through a pair of collectors to the detector (see Fig. 2) must be no more than a few nanometers [1].

Achieving nanometer level pathlength control becomes more difficult as optical elements are mounted on larger, more flexible structures. Loosely stated, the larger the distance separating the collecting apertures the better the astrometric accuracy of the interferometer. However, a longer baseline translates into a more flexible structure which in turn implies a more severe interaction between the structure and the feedback control system.

To meet the control structure interaction challenge, the Jet Propulsion Laboratory, in conjunction with a NASA-wide Control Structure Interaction (CSI) program, has developed the Phase B Testbed [2] in order to explore, develop, and validate emerging

technologies and design methodologies. In particular, JPL has initiated efforts toward a multilayer control approach involving (1) piezoelectric active member structural control, (2) active isolation control of on-board disturbances, and (3) direct control of optical elements. This paper addresses the optical control layer, presents the control system design methodology, and discusses the experimental results achieved.

The JPL Phase B Testbed

In order to address the control structure interaction problem associated with optical pathlength control, the Jet Propulsion Laboratory has developed a ground testbed facility known as the Phase B testbed (Fig. 3). This is an eight foot tall truss structure cantilevered at the base and equipped with an optical motion compensation system.* The optical compensation system is framed in a rectangular shaped trolley and attached firmly to the truss structure. A voice coil actuator and a piezoelectric (PZT) actuator provide high bandwidth pathlength control. Earlier control experiments conducted by O'Neal and Spanos [3] using an optical configuration that isolated most structural motion from the optical path demonstrated closed loop performance to the level of 11 nanometers rms. This paper describes the control system design and implementation for a new optical configuration that introduces a larger degree of coupling between structural motion and optical pathlength.

Figure 4 represents the current optical configuration and shows how laser interferometry was implemented in our experiment. Retroreflector and plane mirror interferometry were combined in such a way that the optical alignment is maintained under X and Z lateral motions and X, Y and Z rotational motions. This optical configuration is considerably less sensitive to alignment errors induced by structural vibration than either plane interferometry or retroreflector interferometry alone. In this setup the two laser beams are placed very close to each other and the returning beam is directed to the receiver by an additional plane mirror. Note that the laser beam passes eight times through the trolley as compared to two times with retroreflector interferometry or to four times with plane mirror interferometry.

Control Law Design

The frequency response functions (FRF) for the two input one output system were measured with a Tektronix 2630 Fourier analyzer and are shown in Figure 5. Sine sweep

* A detailed description of the Phase B testbed is given by Eldred and O'Neal [2].

and band limited white noise inputs were used to generate the FRF's with high coherence levels. The PZT actuator to laser pathlength FRF is not affected by the dynamics of the flexible structure due to the fact that the mass of the PZT mirror is small and the balanced PZT stack provides momentum compensation. Note that while the magnitude is relatively constant across the measured frequency band, the phase drops linearly with a constant slope corresponding to 70 microseconds of pure time delay. This delay is associated with the time it takes to measure the optical pathlength and output the measurement from the computer to the spectrum analyzer.

The voice coil to pathlength FRF is significantly affected by structural flexibility. The dominant peak at 0.7 Hz is due to the flexure that attaches the trolley to the truss. All other peaks in the frequency response function correspond to structural modes of the truss. Observe that the peaks and valleys (i.e., poles and zeroes) in the FRF are alternating up to 80 Hz which guarantees that all the modes below this frequency will interact stably with a controller of the phase lead type. Beyond 80 Hz the phase drops rapidly while modal density and plant uncertainty increase considerably. As a result, we have chosen to limit the bandwidth of the voice coil controller to a frequency lower than 80 Hz.

The architecture of the two-input one-output optical pathlength control system is shown in Figure 6. Bode's classical control design methods [4] were used to shape the open loop response in the frequency domain. We point out that, unlike most modern control design methods, this design methodology does not require an explicit parametric model of the plant using instead the FRF measurement directly to synthesize robust controllers.

The control system architecture is similar to that of Colavita [5] in the sense that the output of the PZT controller drives both the PZT actuator and the voice coil controller. The objective of this configuration is to desaturate the limited stroke PZT actuator in the low frequency range where disturbances tend to have large amplitudes. Note that in Fig. 6 we have modeled the PZT-to-pathlength transfer function as unity while the measurement in Fig. 5 shows it to be approximately 4.5 dB or 1.7. We shall compensate for this simplification later by dividing the PZT controller $K_1(s)$, and multiplying the voice coil controller $K_2(s)$ by a factor of 1.7 after the two control laws are designed.

The open loop transfer function for the system of Fig. 6 is

$$L = K_1(1 + K_2 G_2) \quad (1)$$

The objective is to design the two compensators $K_1(s)$ and $K_2(s)$ such that the closed loop system is stable and the total loop gain $|L|$ is as large as possible over the largest achievable bandwidth. The design requirements are placed on $|L|$ since the disturbance rejection is inversely proportional to $|L|$ when $|L|$ is much larger than unity. The following three properties are observed from (1):

1. When $|K_2G_2| \gg 1$, $|L| \approx |K_1K_2G_2|$
2. When $|K_2G_2| \ll 1$, $|L| \approx |K_1|$
3. When $|K_2G_2| = 1$, $|L| \approx \phi |K_1|$

where $\phi = \text{angle}(K_2G_2) + \pi$ and $\text{angle}(K_2G_2)$ is the phase angle (in radians) of K_2G_2 at the frequency where $|K_2G_2| = 1$. Clearly, when the voice coil loop gain is large, the total loop gain is the product of the voice coil loop gain and the PZT loop gain. The total loop gain also approaches the PZT loop gain as the voice coil loop gain approaches zero. Also at the voice coil loop gain crossover frequency the total loop gain is the product of the PZT loop gain and the phase margin ϕ associated with the voice coil loop.

The control laws were designed one loop at a time. First, the voice coil controller was designed to stabilize the system assuming that it is driven directly by the laser pathlength measurement (i.e., $K_1(s)=1$) and the PZT actuator is disconnected. Using frequency domain loop shaping techniques, a voice coil controller with the following transfer function was obtained:

$$K_2(s) = (0.117) \underbrace{\left(\frac{s^2 + 245s + 204^2}{s^2 + 371s + 309^2} \right)}_{\text{LEAD}} \underbrace{\left(\frac{1,005^2}{s^2 + 402s + 1,005^2} \right)}_{\text{LOW PASS}} \underbrace{\left(\frac{s^2 + 50s + 503^2}{s^2 + 100s + 503^2} \right)}_{\text{NOTCH}}$$

The controller consists of (1) a second order lead filter that provides more than 30 degrees of phase at the gain cross over frequency, (2) a second order low pass filter that attenuates the high frequency lightly damped structural modes, and (3) a second order notch filter that attenuates the peak at 80 Hz so that the gain margin of the corresponding mode is approximately 6 dB. The low pass and notch filters are essential in ensuring a stable control structure iteration. The compensated voice coil to laser pathlength frequency response function is shown in figure 7.

Similarly, the transfer function of the PZT controller was designed:

$$K_1(s) = (3,137) \underbrace{\left(\frac{s + 378}{s} \right)}_{\text{LAG}} \underbrace{\left(\frac{s + 4,000}{s^2 + 440s + 394,784} \right)}_{\text{LOW PASS}}$$

The first order lag keeps the total loop gain high at low frequencies for good disturbance rejection. On the other hand, the second order low pass filter enforces a steep gain roll-off while maintaining adequate phase margin for stability robustness. Although the PZT actuator has very high bandwidth, the PZT loop bandwidth is limited by high frequency noise, digital implementation time delay, and phase lag from the power amplifier.

Figure 8 shows the loop transfer function L as well as the PZT controller K_1 . The effects of time delays due to the computer implementation have been taken into account. The frequency responses are clearly in agreement with the three properties described earlier.

Both control laws were discretized using the bilinear transformation and prewarping was used to match them to their analog counterparts at the respective gain crossover frequencies. The low bandwidth voice coil controller and the high bandwidth PZT controller were implemented at 2,000 Hz and 12,000 Hz respectively. The phase lags associated with the zero order hold and the computational delay were modelled as pure time delays since the sampling frequencies of both controllers are much higher than their respective bandwidths.

Experimental Results

Two closed loop experiments were carried out. The objective of the first was to reject the ambient laboratory disturbance environment and to establish the noise floor of the closed loop system. The objective of the second was to reject a sinusoidal disturbance tuned to the frequency of the fundamental truss mode (i.e., 5.3 Hz). The sinusoidal disturbance was induced by a proof-mass type shaker attached to the midspan of the truss via a stinger.

In both experiments, the open loop optical pathlength histories were recorded for the first 5 seconds at which time the control loop was closed and the closed loop pathlength histories were recorded for an additional 5 seconds. The results from the experiments are shown in Figures 9 and 10.

Figure 9 shows the optical pathlength variation reduced to 24 nanometers rms from an open loop ambient disturbance of 15 micrometers rms. This corresponds to 56 dB rejection of the ambient disturbance. It is emphasized that in these experiments the laser beam makes 8 passes through the trolley optics which implies that the equivalent path-

length error for a space interferometer (i.e., Figures 1 and 2) would be 3 nanometer rms. Spectral analysis of the open and closed loop signals indicates that the achieved controller bandwidth is approximately 500 Hz and that a large part of the closed loop error is due to noise at frequencies beyond the controller bandwidth.

Figure 10 illustrates the forced response experiment. The impact of the 5.3 Hz sinusoidal disturbance on the pathlength is clearly shown during the first 5 seconds of the time history. The closed loop response indicates that the disturbance is attenuated by more than 70 dB which is in close agreement with the total loop gain of Figure 8.

Conclusions and Future Work

We have successfully designed and implemented a two input one output optical pathlength control system on an experimental flexible structure. The control design was carried out in the frequency domain by directly shaping the measured actuator-to-sensor frequency response function and did not require a parametric model of the system. Experiments were conducted to reject the laboratory ambient disturbance environment and also shaker induced disturbances tuned to the fundamental structural frequency. The results we have obtained so far indicate that nanometer level control of optical pathlength is feasible in space.

Presently we are reconfiguring the optical path in order to introduce a stronger coupling between the optical pathlength and the structure. The laser beam will be reflected back from an additional point on the structure where large structural motion has been observed. We are also in the process of introducing additional layers of control (i.e., passive/active damping, and disturbance isolation) to improve the overall performance of the pathlength compensation system.

Acknowledgements

This research was performed at the Jet Propulsion Laboratory of the California Institute of Technology under a contract with the National Aeronautics and Space Administration sponsored by the Office of Aeronautics and Space Technology, Code RM.

References

- [1] Laskin R. A., and San Martin A., "Control/Structure System Design of a Spaceborne Optical Interferometer", AAS/AIAA Astrodynamics Specialist Conference, 1989.

- [2] Eldred D. B., and O' Neal M. C., "The JPL Phase B Testbed Facility", ADPA Active Materials & Adaptive Structures Symposium & Exhibition, 1991.
- [3] O'Neal M. C., and Spanos J. T., "Optical Pathlength Control in the Nanometer Regime on the JPL Phase B Interferometer Testbed" SPIE Intl Symposium on Optical Applied Science and Engineering, 1991.
- [4] Bode, H. W., *Network Analysis and Feedback Amplifier Design*, Van Nostrand, NY, 1945.
- [5] Colavita, M. M., et al, "Prototype High Speed Optical Delay Line for Stellar Interferometry", SPIE Intl Symposium on Optical Applied Science and Engineering, 1991.

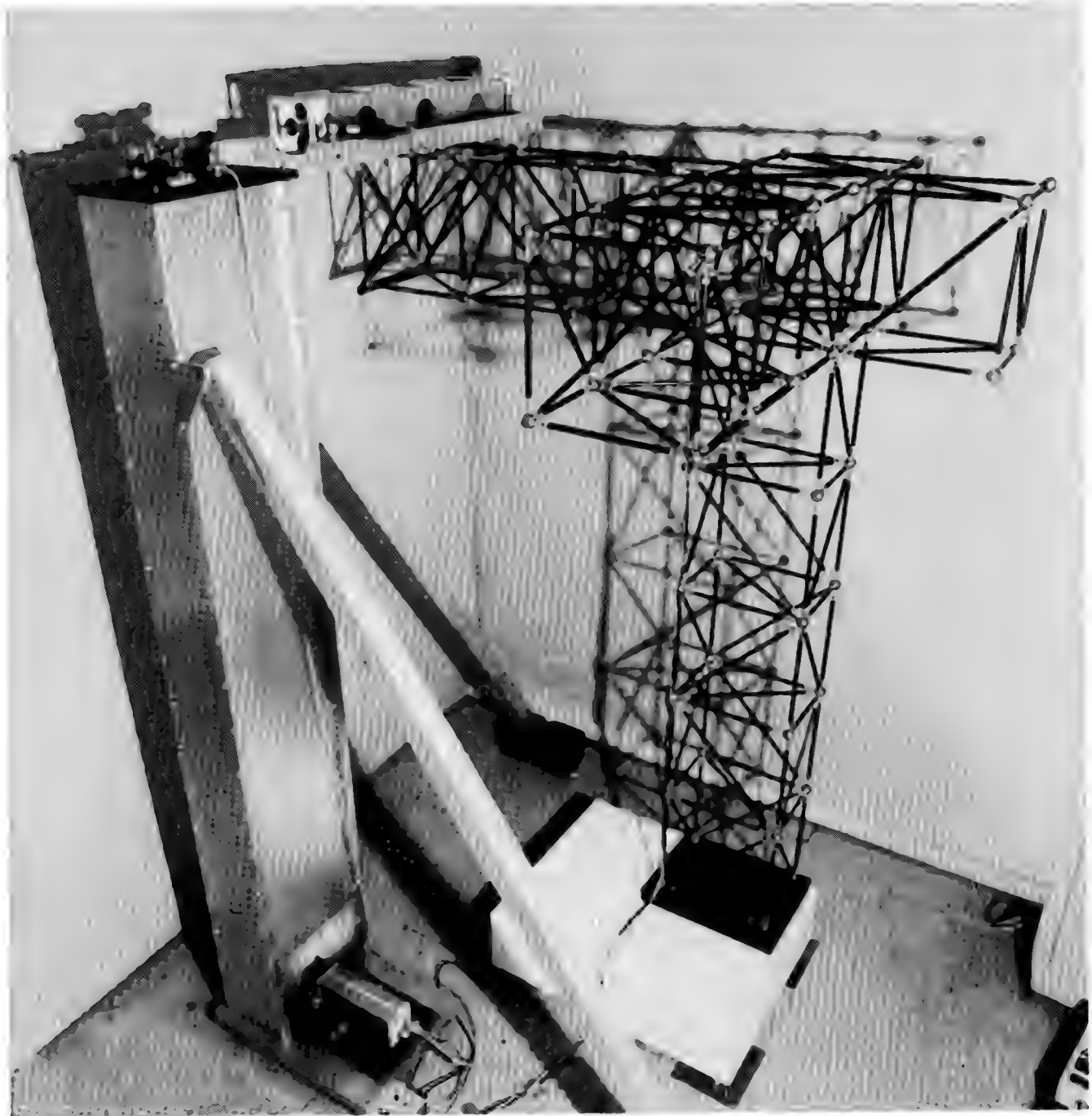


Figure 1. CSI Focus Mission Interferometer

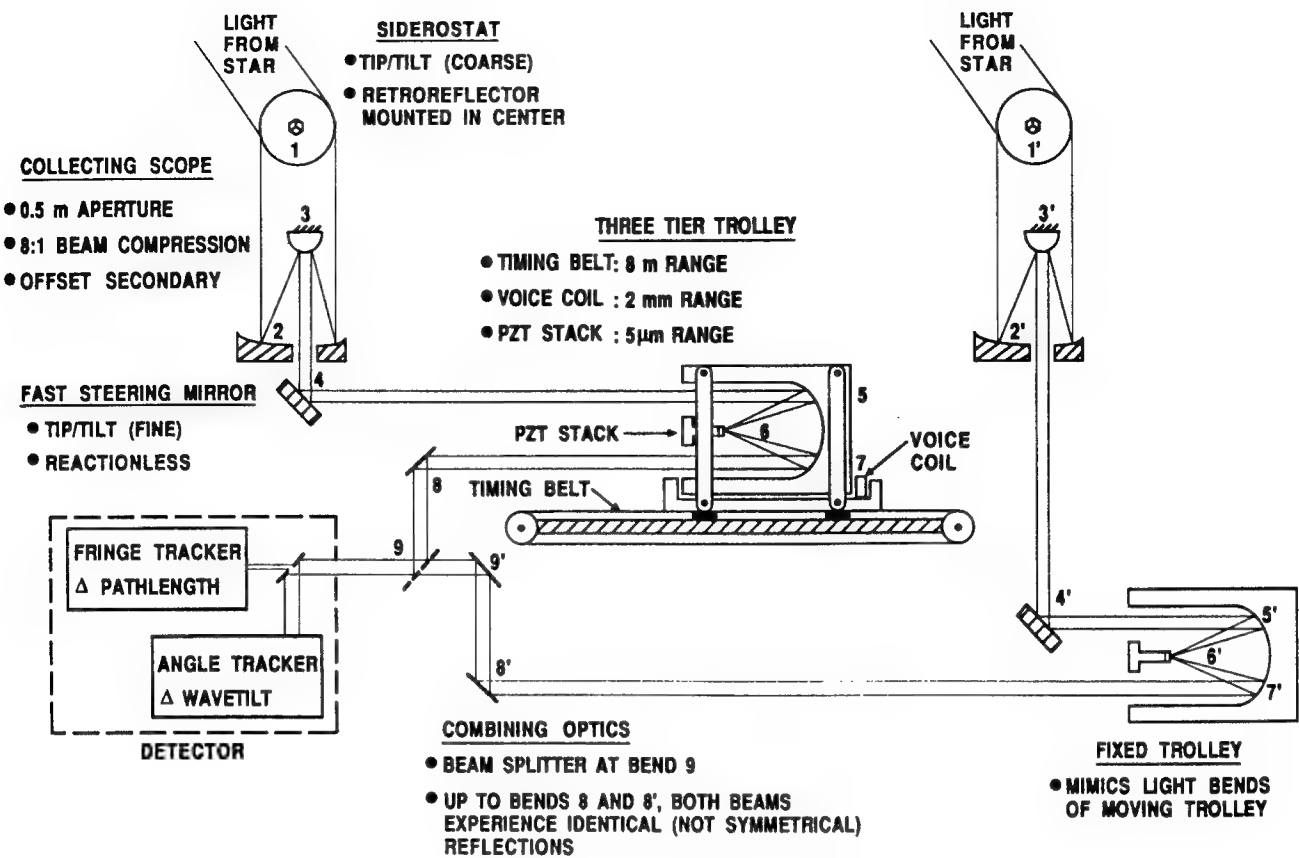
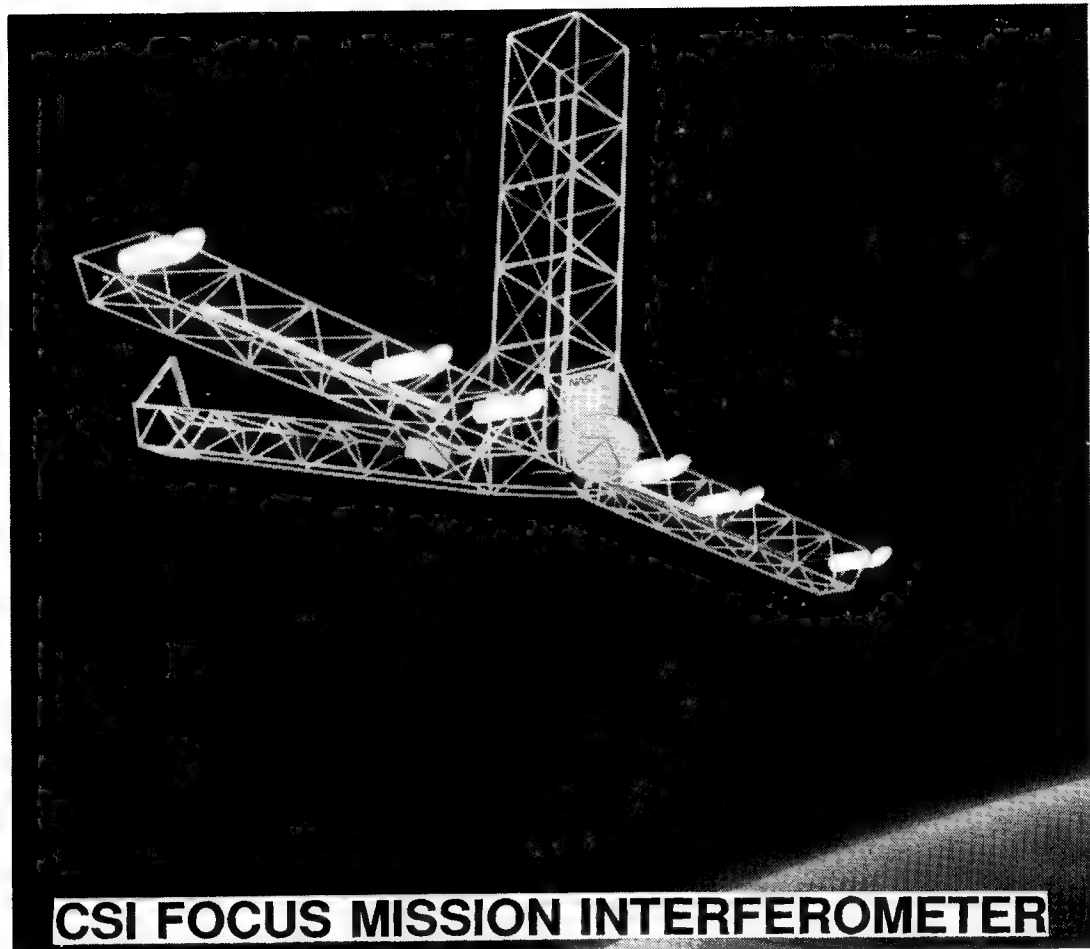


Figure 2. Optical Layout of an Interferometer



CSI FOCUS MISSION INTERFEROMETER

Figure 3. JPL CSI Phase B Testbed

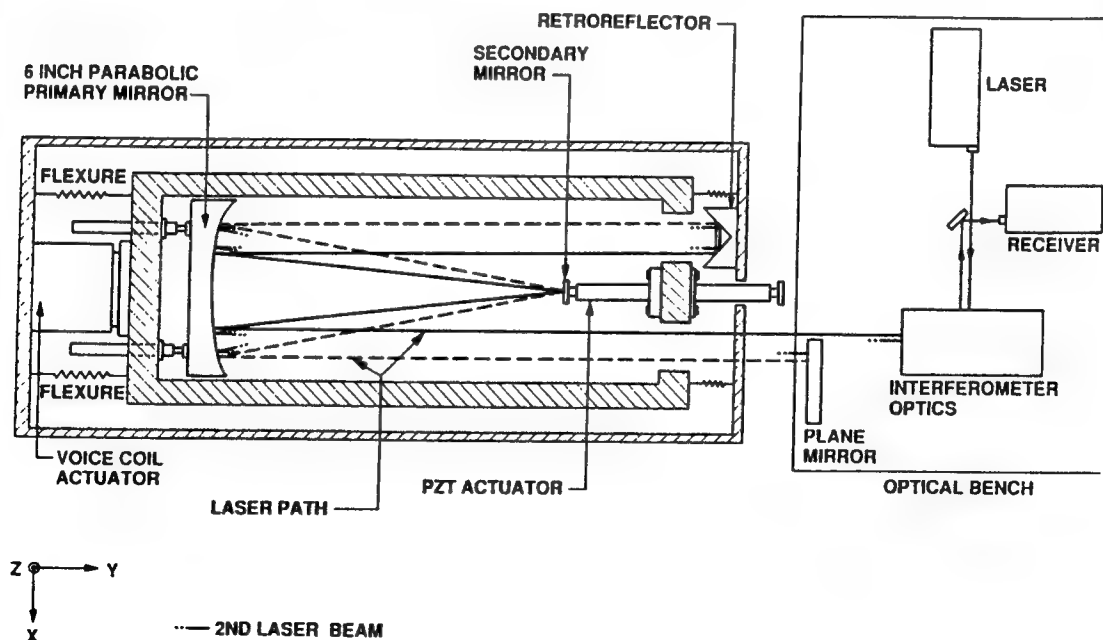
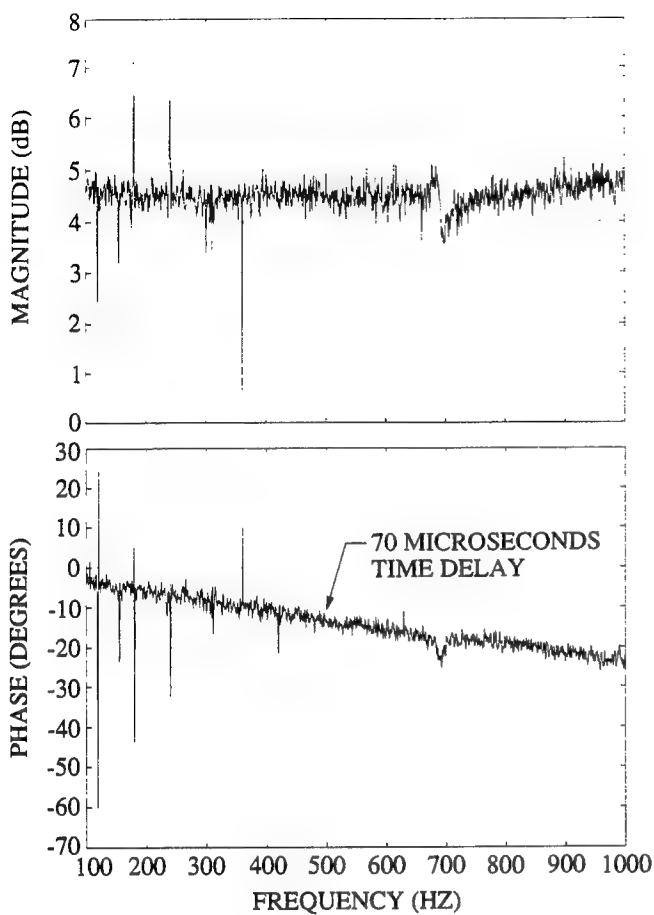


Figure 4. Optical Pathlength Compensation System

PZT TO PATHLENGTH TF



VOICE COIL TO PATHLENGTH TF

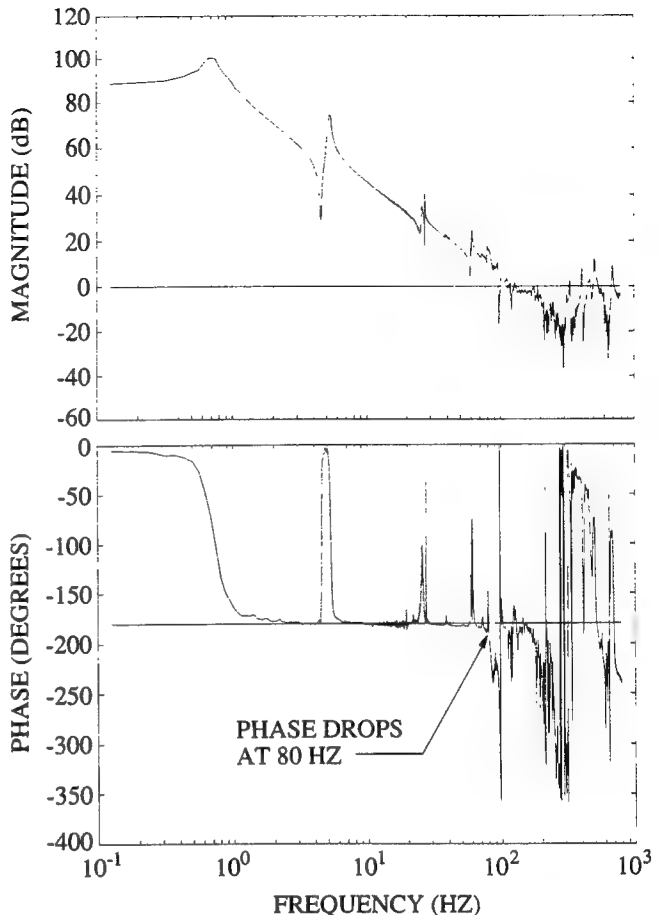


Figure 5. Identified Frequency Response Functions

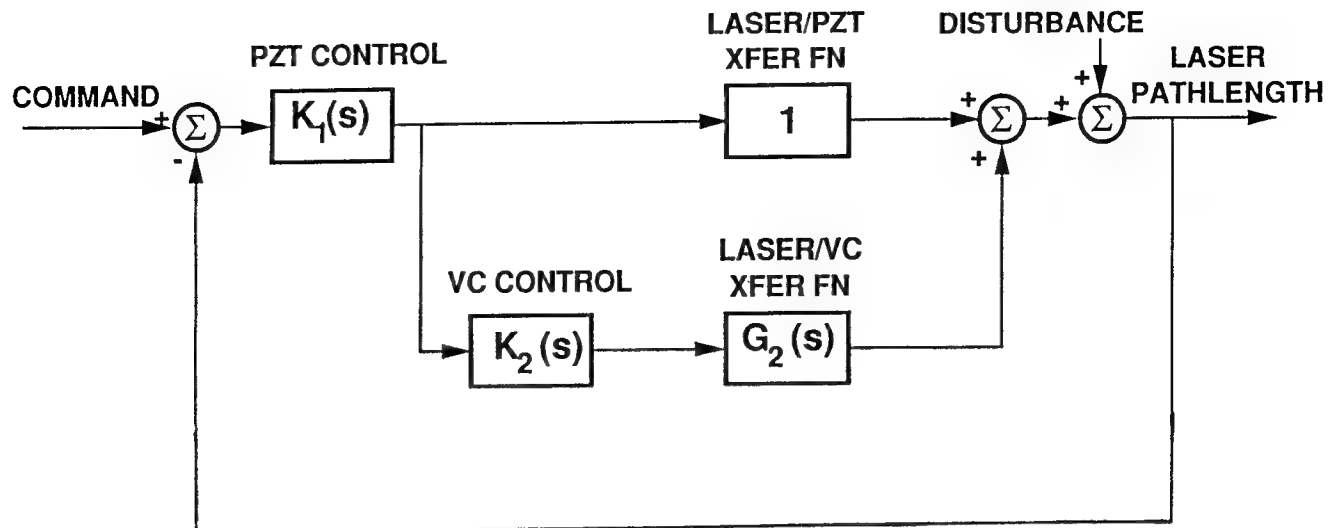
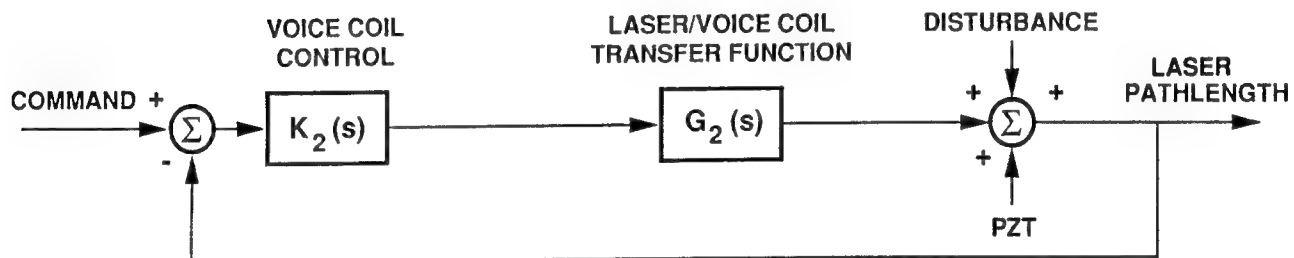


Figure 6. Control System Architecture



$$K_2(s) = (0.117) \underbrace{\left(\frac{s^2 + 245s + 204^2}{s^2 + 371s + 309^2} \right)}_{\text{LEAD}} \underbrace{\left(\frac{1,005^2}{s^2 + 402s + 1,005^2} \right)}_{\text{LOW PASS}} \underbrace{\left(\frac{s^2 + 50s + 503^2}{s^2 + 100s + 503^2} \right)}_{\text{NOTCH}}$$

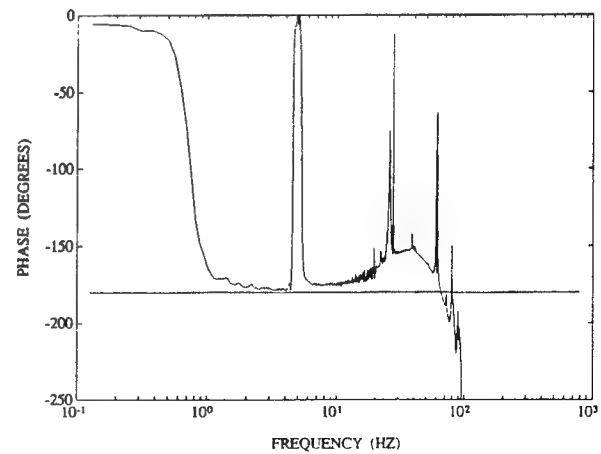
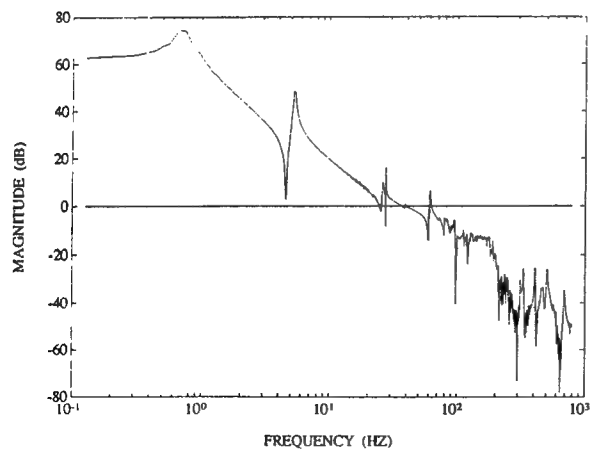


Figure 7. Voice Coil Loop Gain and Phase

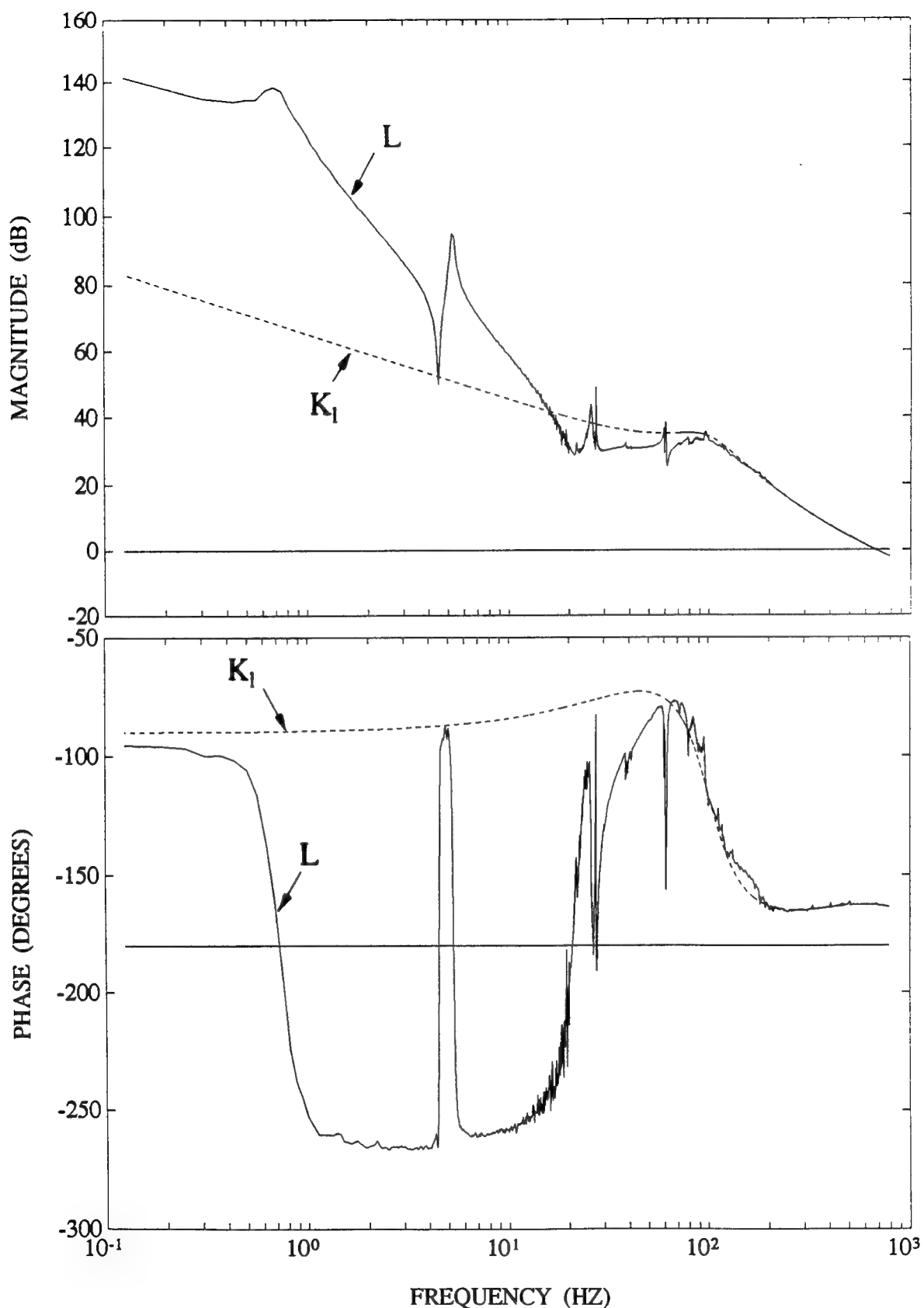


Figure 8. PZT and Total Loop Gain and Phase

DISTURBANCE: LABORATORY ENVIRONMENT

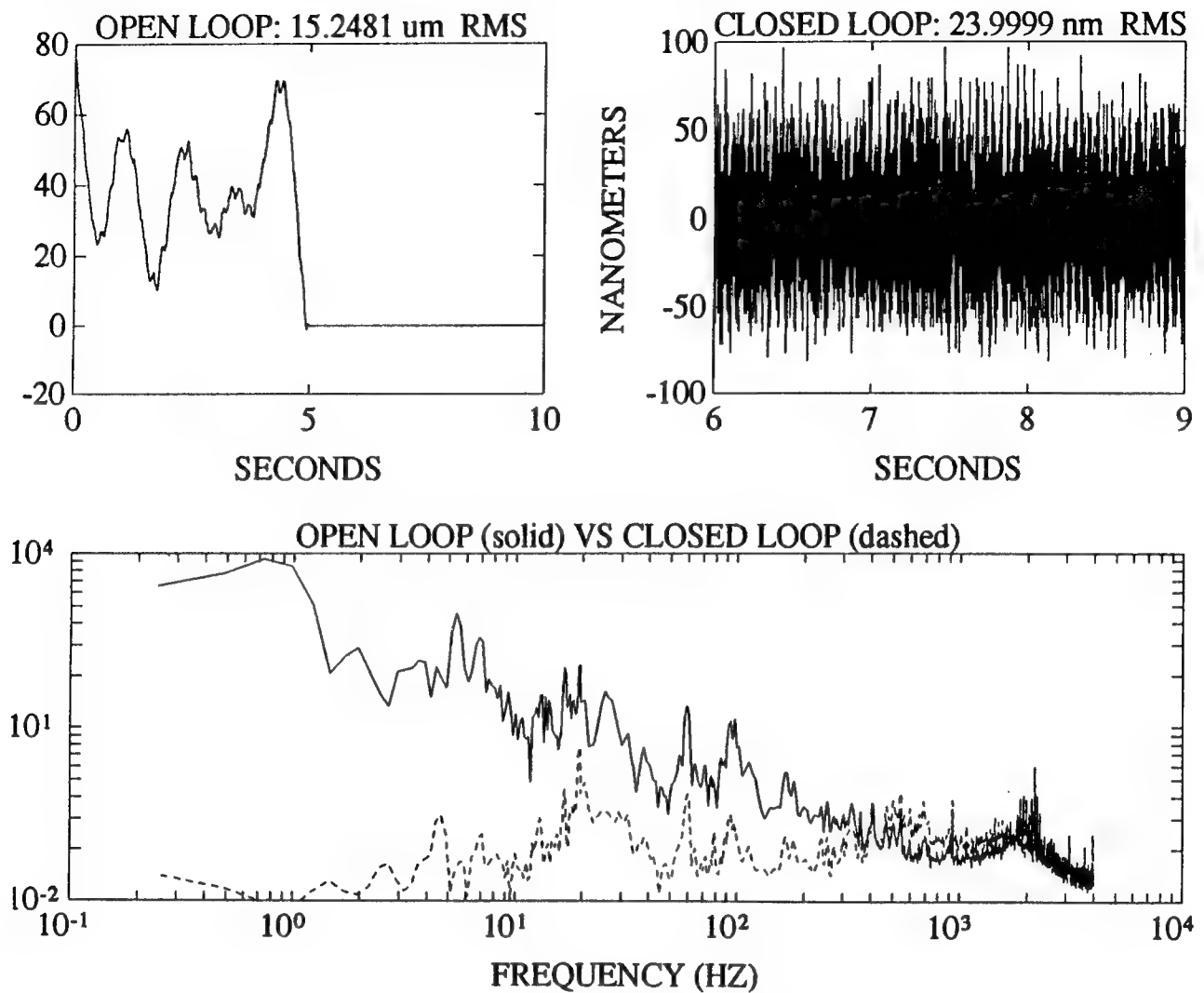


Figure 9. Closed Loop Optical Performance with Ambient Laboratory Disturbance

**DISTURBANCE:
SINUSOID TUNED TO FREQUENCY OF FIRST STRUCTURAL MODE**

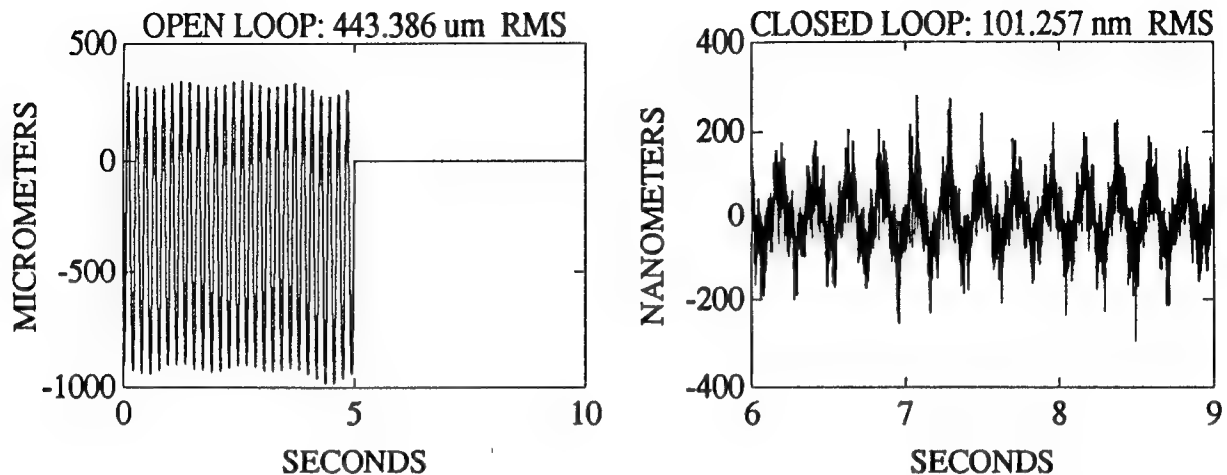


Figure 10. Closed Loop Optical Performance with Shaker Induced Sinusoidal Disturbance

DYNAMIC TEST RESULTS FOR THE CASES GROUND EXPERIMENT

Angelia P. Buckley and Alan F. Patterson
NASA Marshall Space Flight Center
Huntsville, Alabama

Victoria L. Jones
Logicon Control Dynamics
Huntsville, Alabama

INTRODUCTION

The Controls, Astrophysics, and Structures Experiment in Space (CASES) Ground Test Facility (GTF) has been developed at Marshall Space Flight Center (MSFC) to provide a facility for the investigation of Controls/Structures Interaction (CSI) phenomena, to support ground testing of a potential shuttle-based CASES flight experiment, and to perform limited boom deployment and retraction dynamics studies. The primary objectives of the ground experiment are to investigate CSI on a test article representative of a Large Space Structure (LSS); provide a platform for Guest Investigators (GI's) to conduct CSI studies; to test and evaluate LSS control methodologies, system identification (ID) techniques, failure mode analysis; and to compare ground test predictions and flight results.

The proposed CASES flight experiment consists of a 32 meter deployable/retractable boom at the end of which is an occulting plate. The control objective of the experiment is to maintain alignment of the tip plate (occultor) with a detector located at the base of the boom in the orbiter bay. The tip plate is pointed towards a star, the sun, or the galactic center to collect high-energy X-rays emitted by these sources. The tip plate, boom, and detector comprise a Fourier telescope. The occulting holes in the tip plate are approximately one millimeter in diameter making the alignment requirements quite stringent. Control authority is provided by bidirectional linear thrusters located at the boom tip and Angular Momentum Exchange Devices (AMED's) located at mid-boom and at the tip. The experiment embodies a number of CSI control problems including vibration suppression, pointing a long flexible structure, and disturbance rejection. The CASES GTF is representative of the proposed flight experiment with identical control objectives.

CASES GTF OVERVIEW

The CASES GTF provides a mechanism for testing many aspects of a flight experiment, such as vibration suppression, boom deployment and retraction, sensor and actuator performance, real-time computer software and hardware evaluation, electronics, power, optical measurement systems, and interfaces. Some aspects of the testing are affected by the earth's gravity and air damping. The dynamics of the boom and tip plate are modified by gravity, and sensor biases due to gravity and the earth's rotation must be eliminated through software. In addition, gravity precludes pointing experiments on the ground, and deployment and retraction is not possible with the tip plate attached. However, there are a number of ideas under investigation to overcome these problems and devise a scheme to perform pointing experiments and to perform limited deployment and retraction experiments. Such deployment and retraction experiments have been conducted on the boom without the tip plate in place.

The CASES GTF is located at MSFC in Building 4619 in the Load Test Annex (LTA) high bay area. A schematic of the facility is shown in Figure 1. The test article is suspended vertically from a platform at the 132 foot level. The disturbance system provides two translational Degrees Of Freedom (DOF). Disturbances representative of those which would be experienced on orbit may be imparted on the structure. A simulated Mission Peculiar Experiment Support Structure (MPESS) is the interface between the disturbance system and the test article to simulate a flight experiment interface between the Shuttle, MPESS, and the payload. The CASES test article consists of a 32 meter boom which supports a simulated occulting plate at the boom tip, and a simulated detector plate attached to the MPESS. As in the proposed flight experiment, control authority is provided by AMED's and two bidirectional linear thrusters.

The primary test article is the 32 meter Solar Array Flight Experiment-I (SAFE-I) boom which was modified for the CASES facility. The boom has 135 bays, weighs about 25 pounds, and retracts into a canister of length 1.83 meters. The boom has a triangular cross section with 25.4 centimeter sides. The longitudinal members (longerons) are continuous elements composed of a fiberglass composite. The boom canister is mounted to a simulated MPESS, which emulates interface between the Shuttle and the experiment. It has four horizontal bays, each measuring 0.7x0.7x0.6 meters, is 2.44 meters high, 2.13 meters wide, and is composed of aluminum elements. The mass of the structure is approximately 488 kilograms. The MPESS is connected to the tripod via a pipe which is 1.52 meters long and 40.6 centimeters in diameter, a 2.5 centimeters thick aluminum interface plate, and several additional interface plates which act as bending and torsional stiffeners. The tip plate, which simulates an occulting plate, is connected to the boom tip. The tip plate has four simulated masks, is about 2x2 meters excluding the boom/plate interface device, and has a mass of about 32 kilograms.

Two Unholtz-Dickie Model 6 shakers provide translational disturbances to a tripod supported on air bearings to which the simulated MPESS is attached. Each shaker provides 4448 newtons peak force with a ± 7.6 centimeter stroke and a 1000 Hz bandwidth. A Linear Motion System (LMS) interfaces each shaker with the tripod to allow for low-friction motion in two directions simultaneously. The tripod floats on an air bearing system which consists of an annular air bearing surface and three air pads. The ring, which has an outside diameter of 4.6 meters and an inside diameter of 2.7 meters, provides a large, flat surface on which the air bearings float. The three pressurized air pads provide for "frictionless" translation. At a given operating pressure and load, each air pad operates like a spring. The load and pressure can be adjusted to achieve a desired air pad stiffness. The air gap is monitored via an optical and capacitance system.

The control actuation system consists of two single-axis AMEDs at a mid-length position on the boom, three single-axis AMEDs at the boom tip, and two single-axis bidirectional linear thrusters at the boom tip. The AMEDs are used for vibration suppression at a mid-point and at the tip of the boom. Each AMED package consists of two motors attached to reaction wheels, two 2-axis gyros and the associated gyro electronics. The tip AMED package is augmented with a third motor and reaction wheel. The two orthogonal thrusters will be used primarily for pointing the boom in the flight experiment, but will be used for vibration suppression in the ground experiment. The linear thrusters have a force capability of ± 9 newtons at up to 10 Hz. Each thruster weighs approximately four pounds.

The measurement system consists of angular velocity and acceleration sensors at the base, boom angular velocity sensors in the mid-length and tip AMED packages, tip acceleration sensors, and an optical Tip Displacement Sensor (TDS). Each PCB accelerometer weighs one pound, has a resolution of 0.0001g with a range of ± 2 g, and has a bandwidth of 800 Hz. Each gyro weighs 150 grams, has a bandwidth of approximately 100 Hz, and a threshold rate of 0.01 degrees/hour. Auxiliary measurements include reaction wheel speed, AMED motor current, and fault indicators. The auxiliary measurements are available for health and safety monitoring. A Boom Motion Tracker records boom mode shapes for post processing.

The CASES computer system provides real-time control with 64 sensor inputs, 64 actuator outputs, and a 100th order controller at rates up to 250 Hz. Lower order controllers may be executed at higher rates. The computer system, developed by AP Labs, consists of a host computer and a separate real-time system. The host provides the user interface, performs the run-time plotting and storage, and provides applications for pre-processing (program development, debugging, and control design) and post-processing. The host is a Sun workstation on the VME bus running UNIX. Included in the host is a Sun SPARC 1e processor, 600 MB of hard disk space, 20 MB of memory, and a color graphics display. The real-time system performs input, scaling, control processing, and output functions. The real-time system is a VME bus based computer running AP Labs real-time IOS (Input/Output Subsystem) and includes a 68020 supervisory processor, 3 Sky Warrior II array processors, four 16-channel 12-bit A/D cards, eight 8-channel 12-bit D/A cards, and 8 MB global memory. Analog signal processing is performed via filtering, multiplexing, and demultiplexing systems located on the boom and in the control room.

MODAL TESTING OF THE CASES GTF

A modal survey of the CASES GTF was completed on January 24, 1992.[1] PCB Structcel 330A Accelerometers were mounted triaxially at 148 points on the facility for a total of 444 accelerometers. Accelerometer triads were located at 98 points along the boom, 7 points on the suspension tripod, 24 points on the simulated MPESS, and 19 points on the tip plate. The primary frequency range used in recording the response of the 148 triads was 0 to 64 Hz with data recorded for a reduced set of points over the ranges of 0 to 128 Hz and 0 to 256 Hz.

Three different excitation methods were used to excite the structure during the tests. The primary excitation source was the pair of Unholtz-Dickie Model 6 shakers driven with an HP 3565 front end that provided a random signal filtered from 0.5 to 55.0 Hz. Use of the shakers provided an *in situ* test scenario. Force levels of 138 newtons RMS and 156 newtons RMS were applied to the test structure via the shakers. Because the shakers failed to excite some of the lower frequency bending and torsional modes, particularly those below 2 Hz, additional excitation methods were used. To excite the torsional modes, a random input was applied at the tip plate using an APS Model 113 shaker driven by the HP3565. The frequency range used in recording the responses resulting from the forces applied at the tip was 0 to 64 Hz. Responses from all 148 locations were recorded. All force inputs applied by the shaker systems were measured using PCB Model 208A03 force transducers. The third excitation source used in the modal testing was the manual application of an impulse load. The impulse was required to excite the lowest frequency bending modes. Because this force could not be accurately measured, decaying acceleration sinusoids were observed on an oscilloscope for frequency identification. Mode shapes for the first bending modes and first torsion mode were visually observed. The frequencies of the first bending modes are on the order of 0.1 Hz.

Data acquisition and signal processing were accomplished using an HP9000/370SRX work station with an HP 3565 multiple channel front end system. Leuven Measurement System (LMS) F-monitor software was used to acquire transducer outputs, calculate frequency response functions (FRF's), and to store the FRF's on tape. Software developed by the University of Cincinnati was used to calculate the modal parameters, mode shapes, modal frequency, and modal damping, by means of a curve fitting algorithm applied to the FRF's. A Multiple Degree of Freedom (MDOF) curve fitting technique was used on the data because of the high modal density within a narrow frequency range and the lightly damped modes. Verification of the measured modes was accomplished using the Complex Mode Indicator Function (CMIF) and the Modal Assurance Criteria (MAC). The power spectrum from each load cell was monitored in real time and recorded using an HP 3562A Dynamic Signal Analyzer.

MODAL TEST RESULTS

Table I summarizes the results of the modal testing on the CASES GTF. The modal frequency and damping for the first 37 modes are listed in the table. Note that values of damping for the first 5 modes are not given because these low frequency modes were obtained via manual impulse and observation as described in the previous section. All 35 modes listed in the chart are below 32 Hz in frequency. The highest damping value is approximately 6.3 percent. Five modes are observed to be below 1.0 Hz in frequency. Characteristic LSS behavior is notable in the closely spaced clusters of modes, particularly in those frequencies below 10 Hz, making for a challenging controller design problem. Mode shapes for the modes listed in Table I have been plotted and are available in reference 1. The majority of the mode shapes, corresponding frequencies and damping values were identified by the FRF's obtained from the inputs to the base of the mast. The modes above 32 Hz (not shown in chart) were found using the CMIF, as were the five torsional modes between 3.12 Hz and 17.5 Hz. FRF's have been generated for all the sensor locations used in the test procedure. Shown in Figures 2 through 5 are typical FRF's taken from sensors located on the base, at mid-boom, and at the tip, respectively. The modal data collected will be further analyzed and used to tune the CASES finite element model which will then be incorporated into the facility simulation.

REFERENCE

1. Anderson, J. B., T. C. Driskill, P. Jefferson, and J. O. Lassiter, Controls, Astrophysics, and Structures Experiment in Space (CASES) Mast Modal Survey Test Report, NASA MSFC Technical Report number LSS(CASES)-DEV-ED92-001, Dynamics Test Branch, Structural Test Division, Structures and Dynamics Laboratory, NASA Marshall Space Flight Center, February 21, 1992.

Mode Number	Frequency	Damping (%)	Mode Type
1	0.112	-	Bending
2	0.120	-	Bending
3	0.210	-	Torsion
4	0.520	-	Bending
5	0.530	-	Bending
6	1.391	4.811	Bending
7	1.868	3.075	Bending
8	2.802	4.339	Bending
9	2.995	3.463	Bending
10	3.133	4.562	Torsion
11	4.215	6.323	Bending
12	4.598	3.787	Bending
13	4.974	2.241	Bending
14	6.027	1.438	Bending
15	6.565	3.730	Bending
16	6.703	1.881	Torsion
17	8.182	1.333	Bending
18	9.864	2.288	Bending
19	10.864	1.931	Torsion
20	12.312	3.125	Bending
21	14.537	1.381	Bending
22	15.243	1.396	Bending
23	15.855	0.609	Bending
24	16.816	3.671	Torsion
25	18.035	0.927	Bending
26	19.856	3.643	Bending
27	20.878	3.375	Bending
28	22.044	1.198	Bending
29	23.085	1.760	Bending
30	24.211	0.823	Bending
31	25.827	0.804	Bending
32	26.029	1.252	Bending
33	28.365	0.733	Torsion
34	29.764	1.988	Bending
35	31.650	1.325	Bending

Table I. Modal Frequencies, Damping, and Type for CASES GTF.

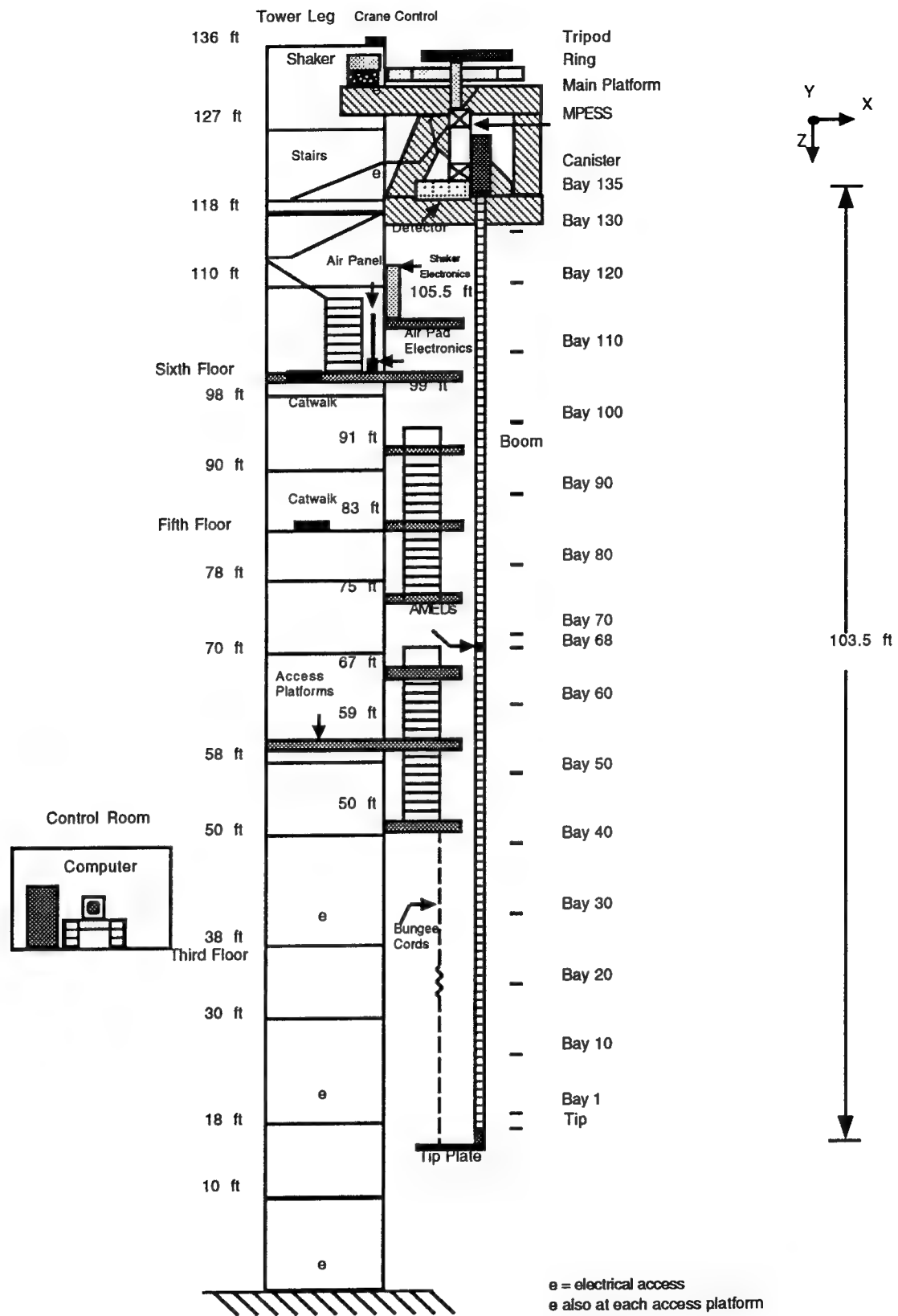


Figure 1. CASES GTF Schematic

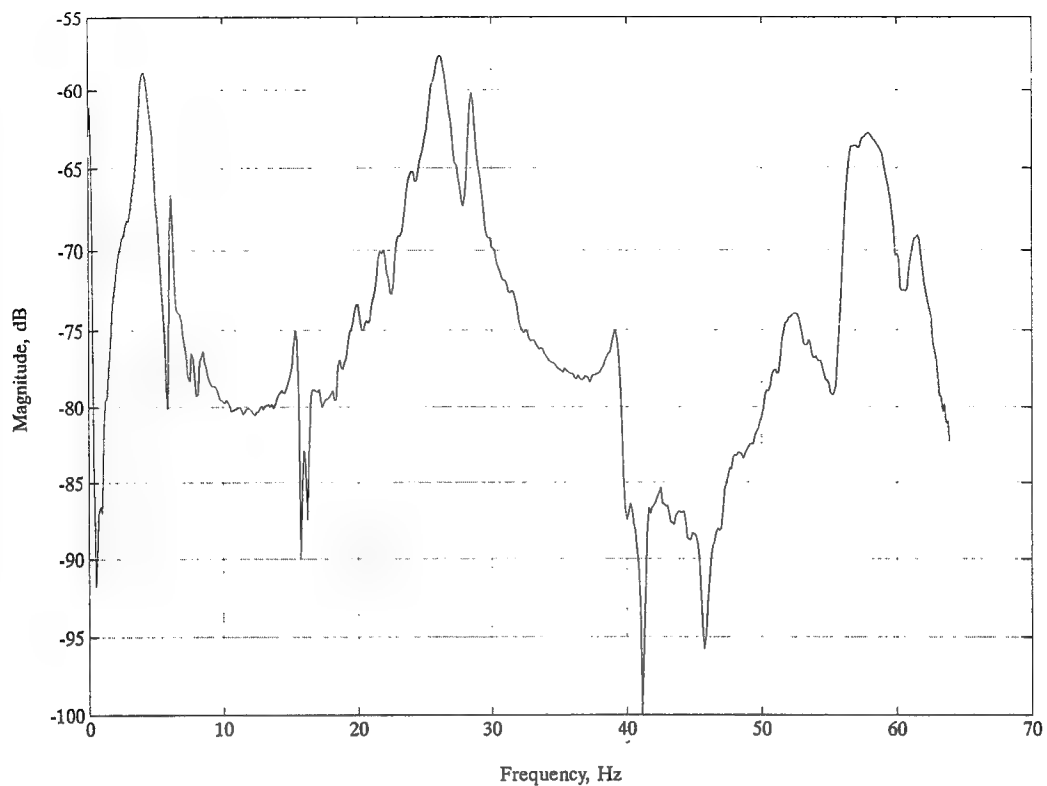


Figure 2. Base FRF, (X - Axis)

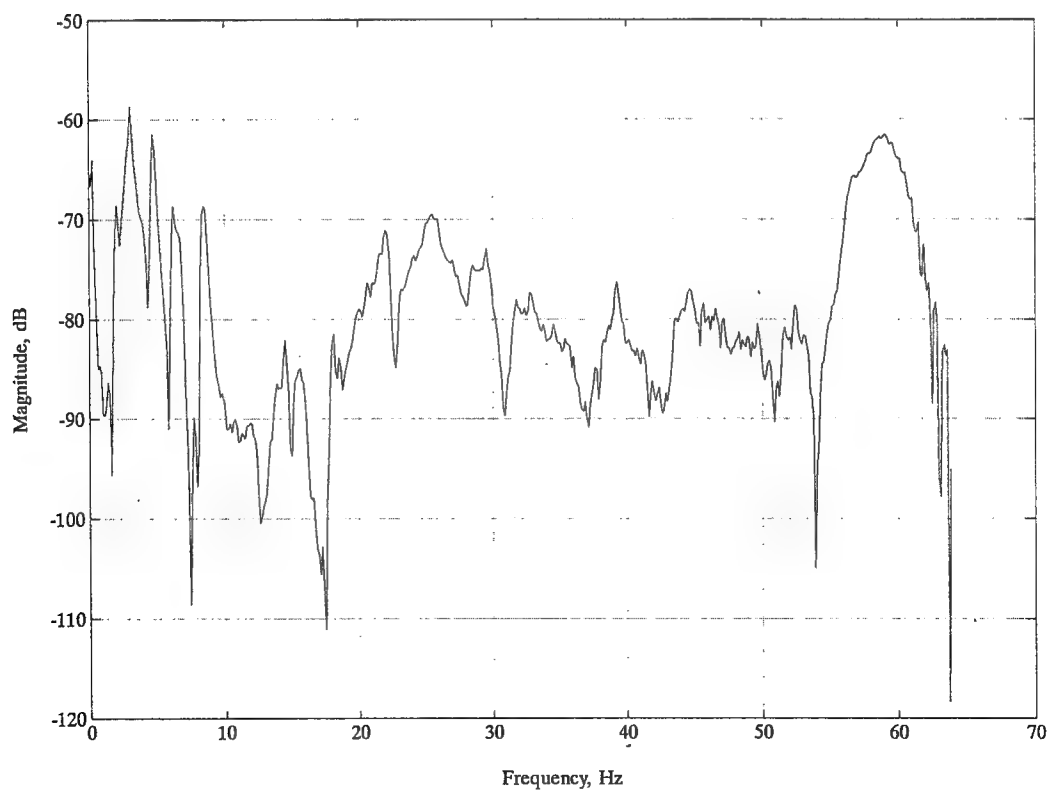


Figure 3. Mid-Boom FRF, (X - Axis)

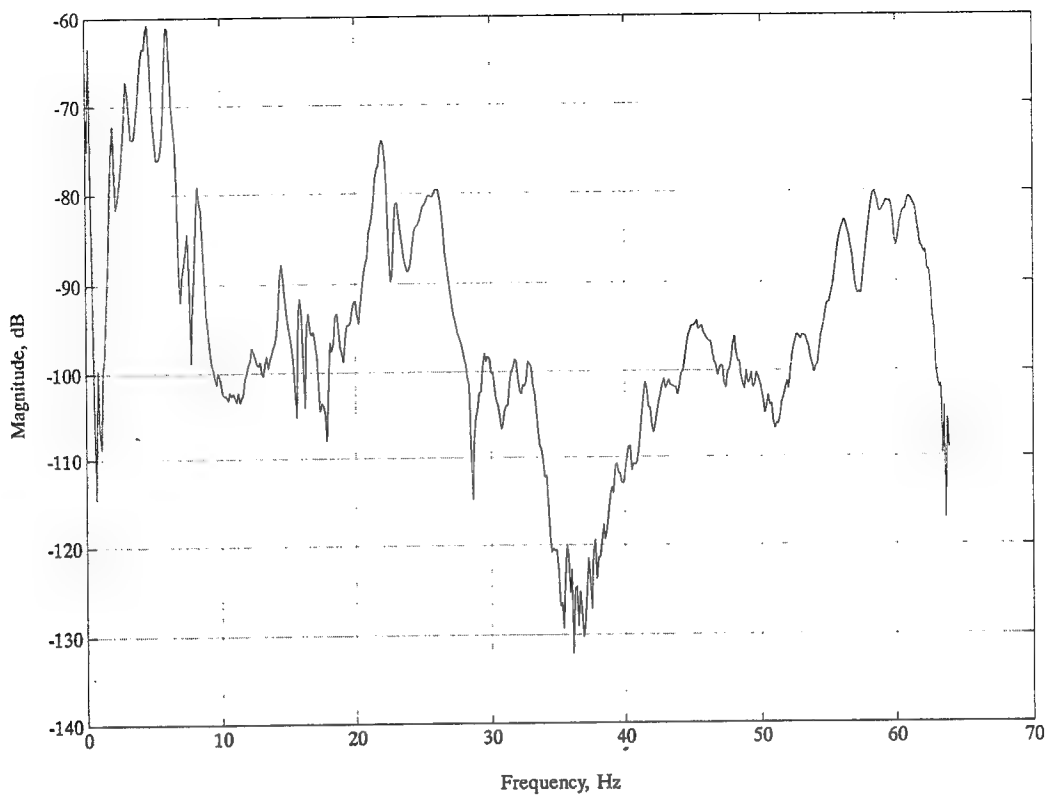


Figure 4. Boom Tip FRF, (X - Axis)

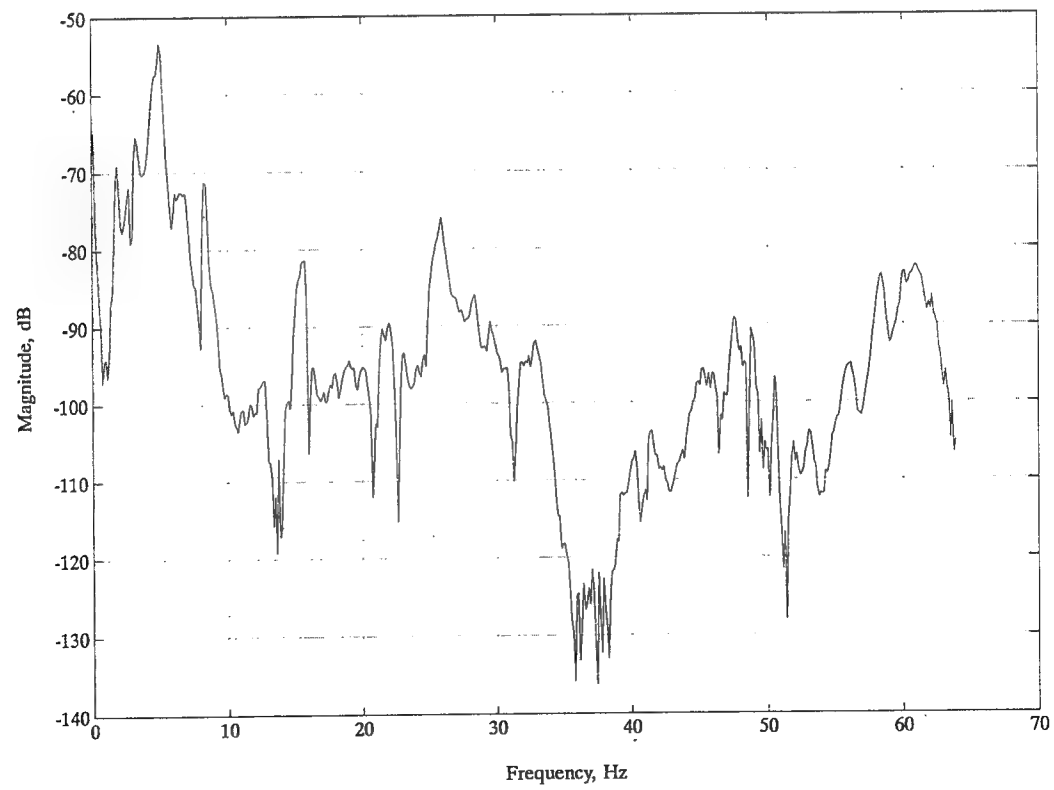


Figure 5. Boom Tip FRF, (Y - Axis)

RESULTS OF THE
ADVANCED SPACE STRUCTURES TECHNOLOGY RESEARCH EXPERIMENTS
(ASTREX)
HARDWARE AND CONTROL DEVELOPMENT

1Lt Derek F. Cossey
Phillips Laboratory
Edwards AFB, CA

INTRODUCTION

Future DOD, NASA, and SDI space systems will be larger than any spacecraft flown before. The economics of placing these Precision Space Systems (PSS) into orbit dictates that they be as low in mass as possible. This stringent weight reduction creates structural flexibility causing severe technical problems when combined with the precise shape and pointing requirements associated with many future PSS missions. Development of new Control Structure Interaction (CSI) technologies which can solve these problems and enable future space missions is being conducted at the Phillips Laboratory, On-Location Site, CA.

RESULTS OF ASTREX HARDWARE AND CONTROL DEVELOPMENT

The Phillips Laboratory, On-Location Site, Edwards AFB, CA, has developed the Advanced Space Structures Technology Research Facility (ASTREX) to serve as a test bed, shown in Figure 1, for demonstrating and integrating technological solutions to the challenges of spacecraft structural control. Unique features of the facility include a large-angle slew capability, a realistic, 11,000 lb dynamically scaled structural model of a 3-mirror Space-Based Laser (SBL) beam expander (see Figure 2), and a powerful, adaptable computer for real-time control and system identification. Currently there are a total of eleven on-going and scheduled projects which will demonstrate various technologies and techniques for CSI. The planned efforts involve representatives from industry, academia, NASA, and DOD.

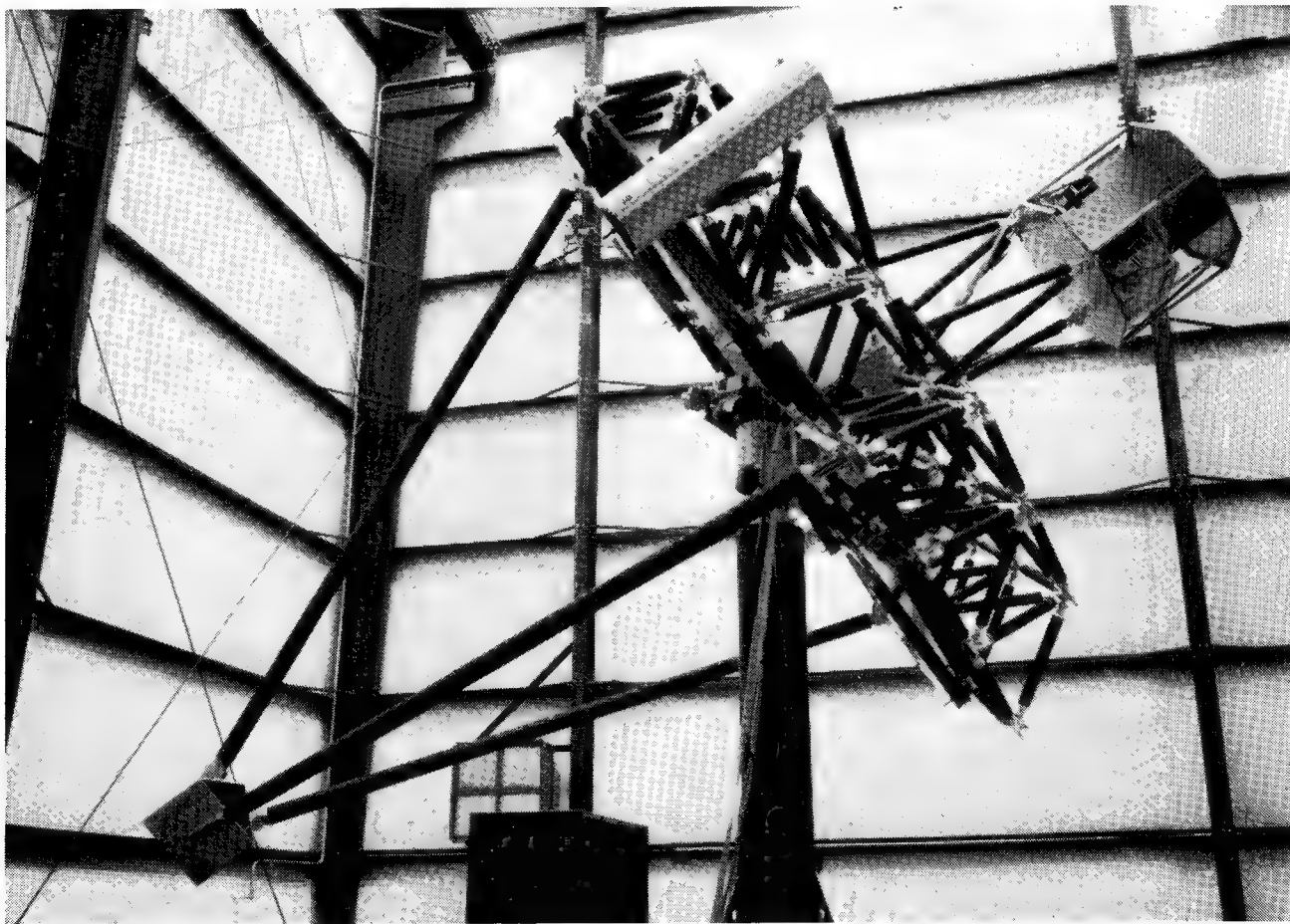


Figure 1. ASTREX Facility.

**ASTREX
TEST ARTICLE**

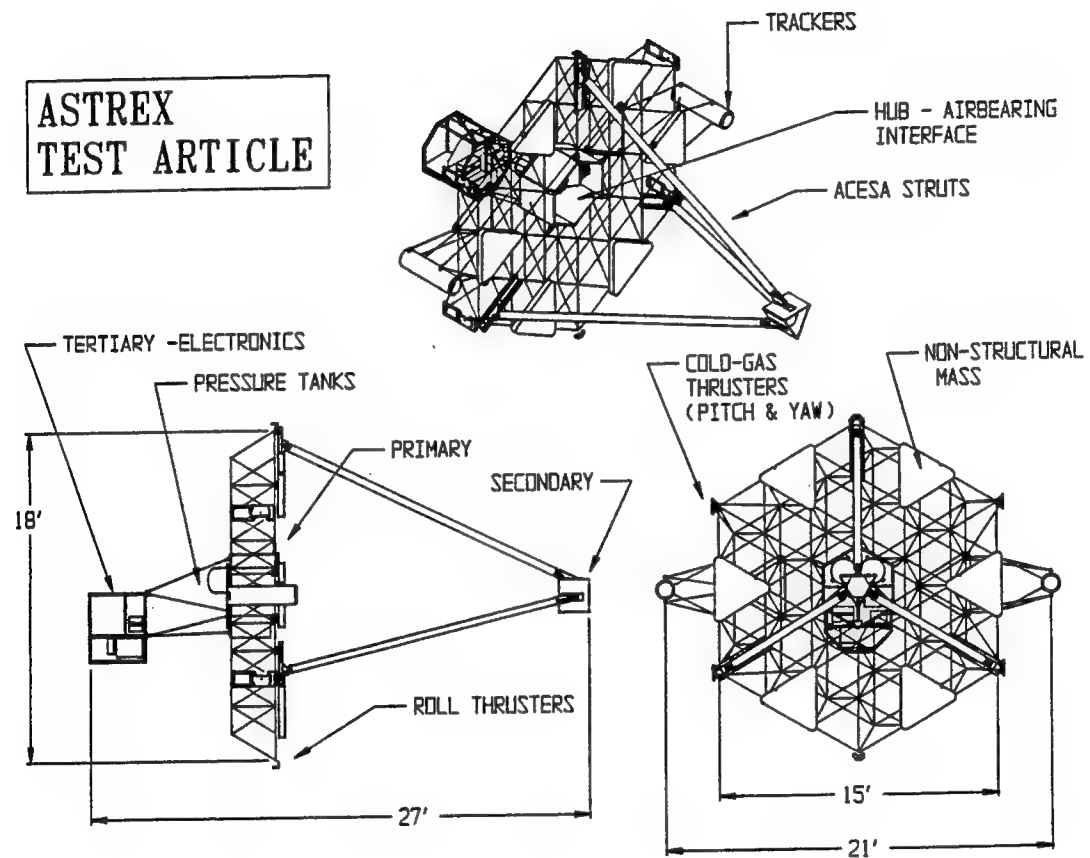


Figure 2. ASTREX Test Article.

In June 1991, engineers from Boeing Aerospace & Electronics installed and tested the 8 lb vernier thrusters on the ASTREX test article. Initial testing was limited to the compressor capability of only 200 psi. With the installation of a compressor with 500 psi ability and the eight 200 lbf thrusters in Dec 91, the reaction control system was finally assembled on the test article. Verification of thruster operation was completed in the second week of Feb 92 after hydrostatic testing of the flexible hoses and additional safety precautions were performed. The thrusters are available for use in research conducted by guest investigators. Currently, plans are being formalized to utilize the thrusters for in-house experiments in the Spring of 92. Additional testing of the thrusters was delayed to accommodate the installation of the Advanced Composite Embedded Sensors and Actuator (ACESA) struts developed by TRW.

The ACESA effort developed and produced three 17 ft struts which replaced the three non-active struts supporting the secondary mirror. These struts will be used to suppress vibrations caused by the tower modes, where most of the modal energy exists, of the Test Article. Installation of the struts was completed on 3 Feb 92. The electronics supporting the ACESA struts are being installed at the writing of this paper. Dr Allen Bronowicki of TRW managed the effort through the five phases of the program. An innovative manufacturing technique proved to be successful in embedding the sensors and actuators into a large graphite-epoxy tube. Dr Bronowicki is scheduled to test the struts for four months beginning in Mar 92. After the initial testing, the ACESA struts will be available for use by other guest investigators.

Additionally, a 2.5 ft-lbf reaction wheel built by Dr Thomas Pollock was installed on the secondary mirror to once again address the tower modes. The reaction wheel orientation is adjustable to accommodate one or two axes of authority. A second function of the reaction wheel allows it to operate as a disturbance source to be controlled by the actuators currently available and the actuators being developed. Dr Pollock is also building a larger reaction wheel with 12.5 ft-lbf torque ability. Plans to install the larger reaction wheel into the primary are being made.

Linear Precision Actuators (LPACT's) are being designed and built to be installed on the secondary mirror. The LPACT's are based on the proof mass actuator concept. However, they have been designed to avoid the non-linear effects associated with most proof mass actuators which use bearings.

The first active member to be delivered was the active strut developed and assembled by SatCon Inc. The strut was developed under the management of Dr Bruce Johnson using the magneto-restrictive material Terfonol-D. Testing has not been performed with this strut due to desires to test with other actuators first. In addition, an active strut using a cylinder piezoelectric

stack is being developed by the Jet Propulsion Laboratory of Pasadena. Dr Moktar Salama manages the development and the strut is scheduled to be completed in April 92.

Currently, in-house efforts are addressing several issues involving a line-of-sight (LOS) sensor, modal surveys, model update, slewing control, and vibration suppression. Two line-of-sight sensors are being developed. One uses a non-optical solution to determine LOS error by comparing angular rate sensor readings at the secondary mirror to sensor readings at the hub located in center of the primary mirror. This solution was chosen as the best candidate to measure LOS jitter of less than 1 micro-radian. The second solution uses a laser with a quad-cell detector. At this time the parts for this system are being acquired and measurement performance has not been determined.

The model update and modal survey effort is currently being worked by Dr Nandu Abhyankar. The possibility of bringing a third party to update the model is being heavily considered. All the work in this area is scheduled for completion by Jun 92. In-house goals also include the demonstration of slewing profiles and vibration suppression of the test article. This work accomplished by the in-house efforts will improve the work done by guest investigators at the facility.

Currently, three guest investigators, who will perform work at the ASTREX Facility, are participating in the NASA/DOD CSI Guest Investigator Program. Boeing Aerospace and Electronics is providing four control moment gyroscopes, CMG's, for one year. The CMG's will be installed on the primary mirror where slewing profiles with the CMG's will be demonstrated. The CMG's weigh 280 lbs and deliver from 200-800 ft-lbs of torque usable in slewing control. The project is being managed by Mr Dean Jacot. Texas A&M work will demonstrate control laws for near-minimum time slew maneuvers and vibration suppression. Using the thrusters and other available actuators, slewing profiles will be developed to minimize the disturbances caused during a slewing maneuver. Dr. Rao Vadali is managing this effort. MIT will be developing optimum passive damping using piezoelectric material. The basic idea is the dissipation of electrical energy created by the piezoelectric material through an RCL circuit. Dr. Andreas von Flotow is managing this effort. All of these efforts were started in Fall 91 and the efforts are scheduled for eighteen to twenty-four months.

The overall effort has been in the facility and hardware development stages for the past three years. With the scheduled research involving guest investigators and in-house personnel, the ASTREX Facility will demonstrate over eleven key technologies and ideas for spacecraft

structural control. Future ideas for testing at the ASTREX Facility are only limited by the creativity of researchers involved in addressing the CSI issue.

Bibliography

1. Das, Alok; Berg, Joel L.; et al: *ASTREX- A Unique Test Bed for CSI Research*, 29th IEEE Conference on Decision and Control, Dec 5-7, 1990.

DESIGN OPTIMIZATION OF THE JPL PHASE B TESTBED

M. Milman, M. Salama, M. Wette, C. Chu

INTRODUCTION

Increasingly complex spacecraft will benefit from integrated design and optimization of structural, optical, and control subsystems. Integrated design optimization will allow designers to make tradeoffs in objectives and constraints across these subsystems. The location, number, and types of passive and active devices distributed along the structure can have a dramatic impact on overall system performance. In addition, the manner in which structural mass is distributed can also serve as an effective mechanism for attenuating disturbance transmission between source and sensitive system components. This paper presents recent experience using optimization tools that have been developed for addressing some of these issues on a challenging testbed design problem. This particular testbed is one of a series of testbeds at the Jet Propulsion Laboratory under the sponsorship of the NASA Control Structure Interaction (CSI) Program to demonstrate nanometer level optical pathlength control on a flexible truss structure that emulates a spaceborne interferometer.

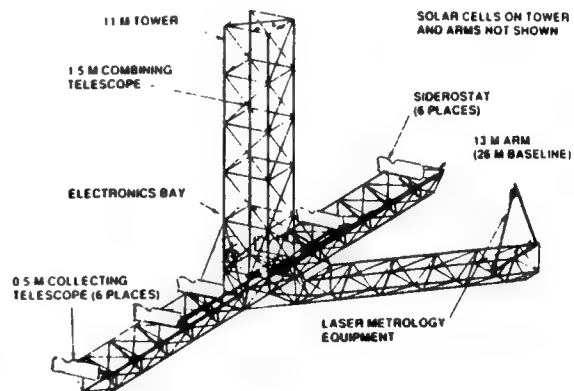
- o GOALS

- Minimize wavefront/LOS error
- Minimize total system mass
- Minimize power consumption
- Others

- o DESIGN VARIABLES

- Structure parameters
- Control gains
- Optical design variables
- Placement of active/passive devices

Proposed Space Interferometer



METHODOLOGY VALIDATION TESTBED

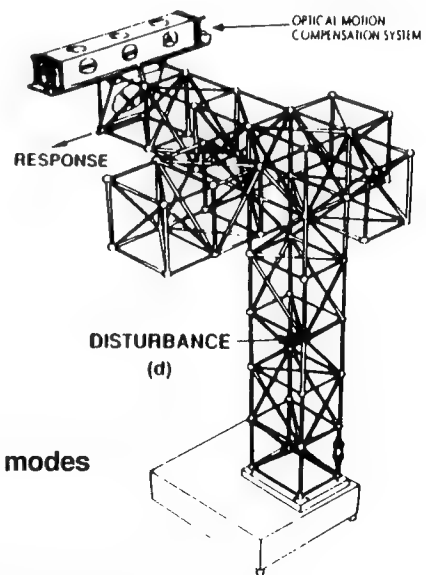
To demonstrate nanometer level optical pathlength control for the proposed interferometer, the Phase B CSI testbed structure was designed and built to emulate the dynamic characteristics of the interferometer. It consists of a vertical tower of length 2.5m with two horizontal arms at right angles to each other attached at the top of the tower. The tower and arms are trusses built from a total of 14 rectangular bays each with dimension 40.6 x 40.6 x 28.7 cm. Attached to one of the horizontal arms is the optical motion compensation system which is encased in a flexure mounted frame. The system was modeled using NASTRAN with beam elements for the individual struts. The resulting 666 degrees--of--freedom (dof) system was reduced by Guyan reduction to 252 dof.

The objective of the current study is to modify the structure using two methods: by resizing truss element diameters and by strategically placing and selecting parameters for passive dampers in the structure to attenuate motion at the optical compensation subsystem attachment points to the trolley due to a colored noise input disturbance at the location shown in the figure. An optimization approach is adopted to achieve this objective. The resizing optimization problem employs a multiobjective cost functional consisting of total structural mass and the H_2 norm of the transfer function between the input disturbance and the trolley attachment points. The multiobjective formulation generates a family of optimal designs that allows trades to be made between the competing components of the cost functional. In the damper placement and tuning optimization problems several performance metrics were considered. These include the H_2 metric described above and various metrics for damping specific structural modes.

This paper addresses two main questions regarding the optimization approach. First, can these methods be applied to the large scale applications that they are ultimately targeted for? And secondly, is there substantial payoff to implementing them? A combination of experimental and numerical simulation studies indicate affirmative answers to each of these questions.

- **Objective:** Demonstrate nanometer level optical pathlength control on a flexible structure that emulates the proposed interferometer.

- 660 D.O.F. (252 mass D.O.F.)
- 22 modes < 100 Hz
7 modes < 30 Hz
- 186 possible locations for dampers
- Disturbance: shaker force at 412 along diagonal (xy)
- Outputs: disp. at 8-attach pts. (trolley/truss)
- Perf. measure: H_2 norm of TF_{io} /damping of selected modes



- **Approach:**

- Opt. placement of passive dampers, followed by tuning and resizing of truss members

PLACEMENT/TUNING PHILOSOPHY

Passive damping is a highly effective means for improving performance of both passively and actively controlled systems, and is especially critical for the problematic class of lightly damped systems. Reducing peak responses in the vicinity of resonant frequencies not only enhances the stability of the open loop system, but it also allows for the implementation of more aggressive control strategies. Furthermore, since many current approaches to robust control design require a bound on the uncertainty in the model on which the design is based, when models are obtained from an identification process the resulting uncertainty (as measured by the H_{∞} norm) can be reduced by first damping the resonant peaks.

The effectiveness of viscous elements in introducing damping is a function of several variables including their number, their location in the structure and their physical parameters. The optimization studies to follow will treat the location and tuning problems in an independent manner. Future work will address hybrid approaches for developing strategies that combine these problems into a single framework.

- o Introduce passive damping into structure to
 - Passively and optimally attenuate disturbances
 - Enhance plant identification process/robustness
 - Improve closed loop system performance

- o Determine
 - Element locations
 - Element stiffness/damping
 - Number/combination of elements

APPROACH OPTIMAL PLACEMENT/TUNING

The viscous dampers are modeled as collocated position and velocity feedback elements in the nominal structure. In the case of a single damper, the feedback gains are scalar quantities corresponding to the damper spring and dashpot coefficients. In the multiple damper case the same system model results, with the exception that the feedback gains are now diagonal matrices with nonzero terms corresponding to the spring and dashpot terms of the individual dampers.

The placement problem is to optimize the control influence matrix B over the set of admissible locations for the dampers. The tuning problem is to optimize the matrices K_p and K_v over the parameter range of feasible designs for the dampers.

o System Model: $M\ddot{x} + Kx = Bu + f$

Single Element:

$$u = -b^T[k_p x + k_v \dot{x}]$$

$$M\ddot{x} + k_v b b^T \dot{x} + (K + k_p b b^T)x = f$$

Multiple Elements:

$$x = \Phi q; \quad \Phi^T M \Phi = I; \quad \Phi^T K \Phi = D = \text{diag}(\omega_1, \dots, \omega_n)$$

$$\ddot{q} + B K_v B^T \dot{q} + (D + B K_p B^T)q = \Phi^T f,$$

M = Mass; K = Stiffness; B = Damping selection matrix;

u = Damper force; f = Disturbance force

k_p = Damper spring coef.; k_v = Dashpot coef.; K_v, K_p = Diagonal damping/stiffness matrices.

TECHNICAL APPROACH OPTIMIZATION PROBLEM FORMULATION

The choice of performance metric in these optimization problems plays a central role in the character of the solution. Criteria should simultaneously reflect the physical objectives and be numerically tractable. For large scale problems this latter property is especially important. Thus cost functional evaluation must involve both numerically stable and efficient computations. In addition, the availability of analytical gradients is another very desirable feature. Two general sets of criteria meeting these requirements were implemented--an H_2 metric and a damping metric. The H_2 functional evaluation requires solving large scale Lyapunov equations, while computing the damping requires solving large nonsymmetric eigenvalue problems. Methods for accelerating these computations were developed, and will be discussed later.

Two distinct optimization strategies were used to solve the placement and tuning problems. The placement problem involves discrete optimization over a finite (but large) set, while the tuning problem can be treated in a continuous framework. A simulated annealing program was developed for optimizing the control influence matrix B for the placement problem, and a sequential quadratic programming (SQP) using the Stanford Computer Science Laboratory's NPSOL software was used to tune the damper gain matrices K_p and K_v .

- o Determine placements and damper parameters by optimizing physically meaningful performance criteria

Performance Functionals:

- Damping of selected modes
- Minimizing total system energy
- Optimizing H_2 norm of transfer function from disturbance inputs to outputs

Design Variables:

- Damper stiffness (K_p), damping coefficient (K_v), location (B)

Optimization Strategies:

- Sequential Quadratic Programming (SQP) for K_p , K_v
- Simulated annealing for B

- o Challenges

- Solving problems on big models

OPTIMAL PLACEMENT WITH RESPECT TO DAMPING OF SELECTED MODES

The ability to damp selected modes is very useful in control design applications where to ensure robustness and closed loop stability it is necessary to damp modes in the loop gain crossover region. Once these modes are targeted, a number of functionals can be introduced for this purpose. Two typical functionals are shown below. The first functional is simply the sum of the damping of the targeted modes, while the second is a weighted sum of the exponentials of the individual damping values. Although these functionals involve the same set of modes, they can lead to quite different results. For example if a particular mode can be heavily damped, the first of these metrics would have the propensity to find a solution that introduces large damping into this mode but ignores the others. The second metric is an approximation to a minimax functional and is better suited to more evenly distributing the damping in the individual modes. A possible problem that can arise here is that there may be a mode that is not easily damped, and additional damping in other modes may be sacrificed to introduce a modest amount of damping in the problem mode.

Let ξ_i = damping in i^{th} mode of system

$$\ddot{\mathbf{q}} + \mathbf{B}\mathbf{K}_v\mathbf{B}^T\dot{\mathbf{q}} + (\mathbf{D} + \mathbf{B}\mathbf{K}_p\mathbf{B}^T)\mathbf{q} = \Phi^T\mathbf{f}$$

Optimization Problem

$$\min_{\mathbf{K}_p, \mathbf{K}_v, \mathbf{B}} \mathbf{g}(\xi_1, \dots, \xi_m)$$

where \mathbf{g} is a smooth function

Examples:

$$(i) \quad \mathbf{g}(\xi_1, \dots, \xi_m) = \sum_{i \in I} \xi_i$$

$$(ii) \quad \mathbf{g}(\xi_1, \dots, \xi_m) = \frac{1}{\gamma} \sum_{i \in I} \mu_i \exp\{\gamma \xi_i\}$$

where I = set of targeted modes

*Solving large eigenvalue problem is difficult in optimization loop

OPTIMAL PLACEMENT WITH RESPECT TO H_2 METRIC

The H_2 norm of a transfer function is a general performance metric that can capture a variety of physical objectives. Penalties on the velocities and displacements of various nodal points can be accommodated by this formulation, as well as the total system energy. More generally any quadratic functional of the system state can be expressed in these terms. The stochastic physical interpretation of the H_2 norm is as the steady state rms error of the output due to a white noise input.

Computing the H_2 norm of a transfer function requires putting the system into first order form, and then solving a Lyapunov equation involving the state matrix, the control input matrix and the intensity matrix of the input disturbance. The solution of this equation is the covariance of the state. Obtaining the steady state value of a linear combination of state variables then requires only matrix multiply and trace operations.

o System:
$$\begin{aligned}\dot{x} &= Ax + Bv \\ z &= Cx,\end{aligned}$$

where

$$A = \begin{bmatrix} 0 & I \\ -D - BK_p B^T & -BK_v B^T \end{bmatrix}, \quad B = \begin{bmatrix} 0 \\ \tilde{B} \end{bmatrix}$$

v = zero mean white noise, $E(vv^T) = V$

o H_2 Cost:
$$\min_{K_p, K_v, B} J = \lim_{t \rightarrow \infty} E\{|z(t)|^2\};$$

$$J = \text{tr}(CC^TQ),$$

$$AQ + QA^T + BVB^T = 0.$$

o Examples:

- (i) C = selects displacement/velocity components at certain nodes
- (ii) C = determines system energy

$$C = \begin{bmatrix} D^{1/2} & 0 \\ 0 & I \end{bmatrix}$$

*Direct evaluation of J not tractable in optimization loop

COMPARISON OF METHODS FOR COST FUNCTIONAL EVACUATION

Solving large unsymmetric eigenvalue problems or Lyapunov equations within an optimization loop is extremely cumbersome, and can render the optimization routine ineffective. Two methods were developed to circumvent these difficulties.

A Newton method for updating specific eigenvalues as a function of the damper stiffness and dashpot coefficient matrices, K_p and K_v was developed. The method is based on finding the roots of an associated rational function whose zeros coincide with the system eigenvalues. Within the optimization loop the scheme is initialized by the current eigenvalues corresponding to the values of K_p and K_v . As K_p and K_v are updated in the optimization, the eigenvalues are also updated. The method is highly accurate and very efficient. To facilitate the solution of the large scale Lyapunov equation associated with computing the transfer function H_2 norm, a model reduction method based on augmenting a modally reduced model with Ritz vectors to statically correct the reduced model transfer function was implemented. This method also produces high fidelity approximations to the damped system eigenvalues.

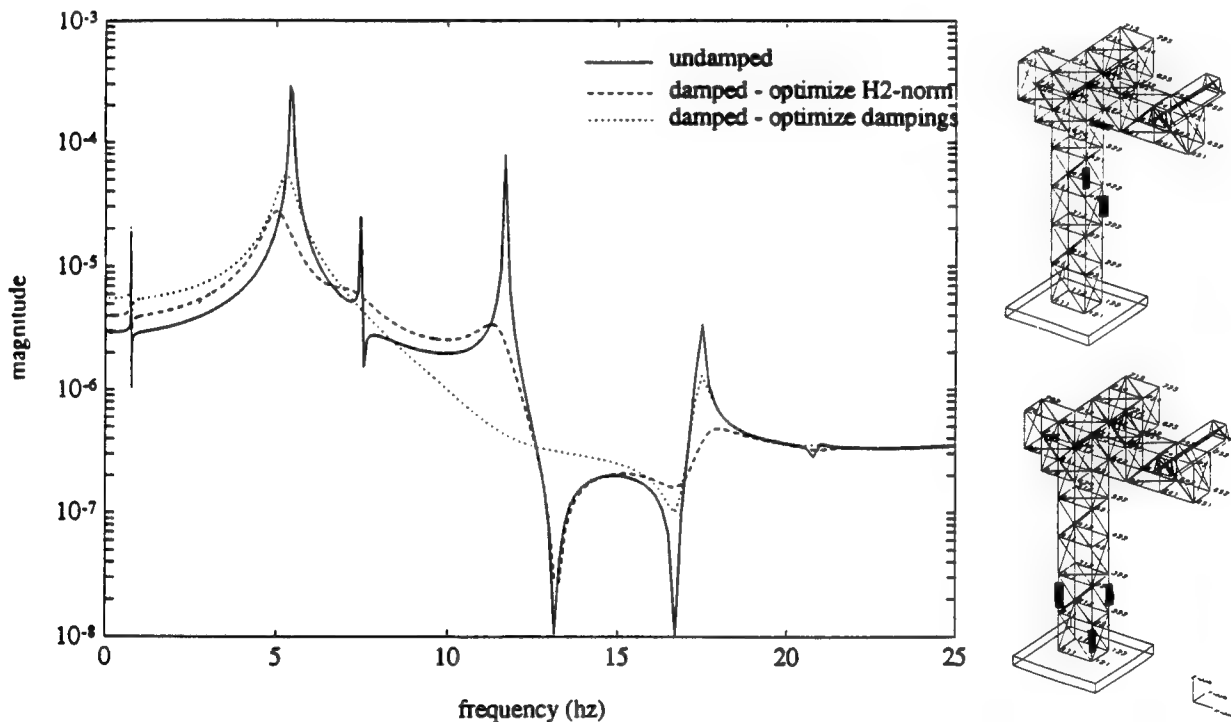
The tables below demonstrate the effectiveness of these two methods in approximating the eigenvalues of the structure with three dampers placed. The full testbed model in this study contains 249 modes and three dampers were inserted. The first column in the table contains the frequencies of the undamped system. The other values correspond respectively to the full order model, the Ritz reduction model containing the first twelve undamped modes plus three Ritz vectors corresponding to the damper inputs, the Newton method, and finally a modally reduced model obtained by retaining the first 15 undamped modes. The conclusion here is that the Ritz reduction technique and the Newton method yield high precision estimates with enormous reduction in operation count, while the modally reduced model produces inaccurate results.

Mode No.	Undamped System Frequency (Hz)	Damped System			
		Frequency (Hz)			
		249 Modes (full order)	12 Modes Plus 3 Ritz Vectors	Newton Method	15 Modes (truncation)
1	0.7427	0.7420	0.7420	0.7420	0.7425
2	5.4263	5.2940	5.2940	5.2940	5.3262
3	7.4564	7.0376	7.0376	7.0376	6.9540
4	11.6777	10.4862	10.4862	10.4862	10.4493
5	17.4248	17.4386	17.4386	17.4386	17.3444
6	20.8423	20.8236	20.8236	20.8236	20.7055
7	31.1387	31.2231	31.2231	31.2231	31.0481

Mode No.	Damped System			
	Damping (%)			
	249 Modes (full order)	12 Modes Plus 3 Ritz Vectors	Newton Method	15 Modes (truncation)
1	0.0179	0.0179	0.0179	0.0012
2	4.5744	4.5744	4.5744	0.6125
3	25.5358	25.5357	25.5358	2.3228
4	32.6380	32.6379	32.6380	5.5664
5	0.9033	0.9034	0.9033	0.4066
6	1.3197	1.3197	1.3197	0.5709
7	0.5013	0.5016	0.5013	0.5031

SIMULATED ANNEALING SOLUTION COMPARISON OF H_2 AND DAMPING OPTIMIZATION

A simulated annealing algorithm was used to optimally place three dampers in the Phase B Testbed structure. The algorithm was implemented twice. First, it was implemented with an H_2 metric with disturbance input generated by a sixth order low-pass filter with a bandwidth of 25Hz. The second time it was implemented with a metric to maximally damp the sum of the first seven modes. A comparison of the respective Bode plots of the resulting transfer functions is given in the figure below. As observed, large damping is introduced into the third and fourth modes as a result of optimizing the damping. However, this is at a sacrifice to the damping attained in the other modes. The H_2 norm optimization metric distributes the damping across the modes in a more even fashion. Values for the sum of the damping and H_2 norms for both performance metrics are given at the bottom of the page. This example indicates the disparity in performance that can result from choosing various cost functionals.



H_2 Optimization: H_2 error = 1.514×10^{-4} ; $\sum_i \xi_i = .261$

Damping Optimization: H_2 error = 2.143×10^{-4} ; $\sum_i \xi_i = .655$

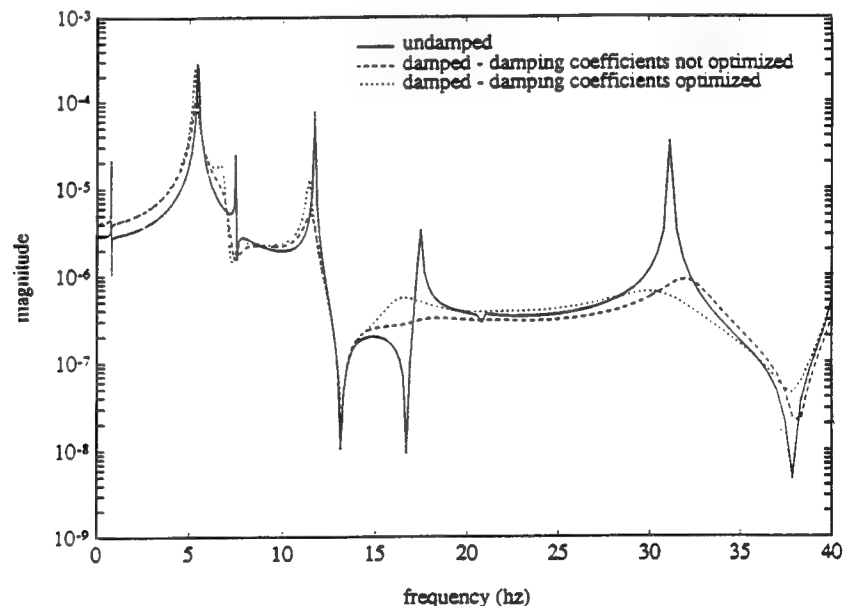
TUNING 3 DAMPERS

The optimal damping solution shown on the previous chart added very little damping to the fifth, sixth, and seventh modes. To remedy this situation the simulated annealing algorithm was implemented again, but with the performance metric $g = \exp(10\xi_5) + \exp(10\xi_6) + \exp(10\xi_7)$, where ξ_i = damping in the i^{th} mode. A new damper configuration emerges, and the resulting damping in these modes improves considerably. Furthermore, because g represents a "minimax" approximation, the damping in these modes are all within a factor of two of one another.

Once these damper locations were selected, we next optimized the damping coefficient matrices K_p and K_v using the SQP algorithm. The figure below contains the Bode plots for the resulting two closed loop systems, and the table at the bottom of the page contains the damping values for modes 5, 6, and 7 for the two solutions. As can be seen from these values, significant improvement in damping is obtained by optimizing the coefficients. In this case the solution called for *reducing* the spring constant of the damper to the minimum allowed and simultaneously *reducing* the dashpot coefficient by a factor of 2/3.

The damping obtained in these modes by a combination of placement and tuning optimization techniques demonstrates that very specific tailoring of the system response is possible by these methods.

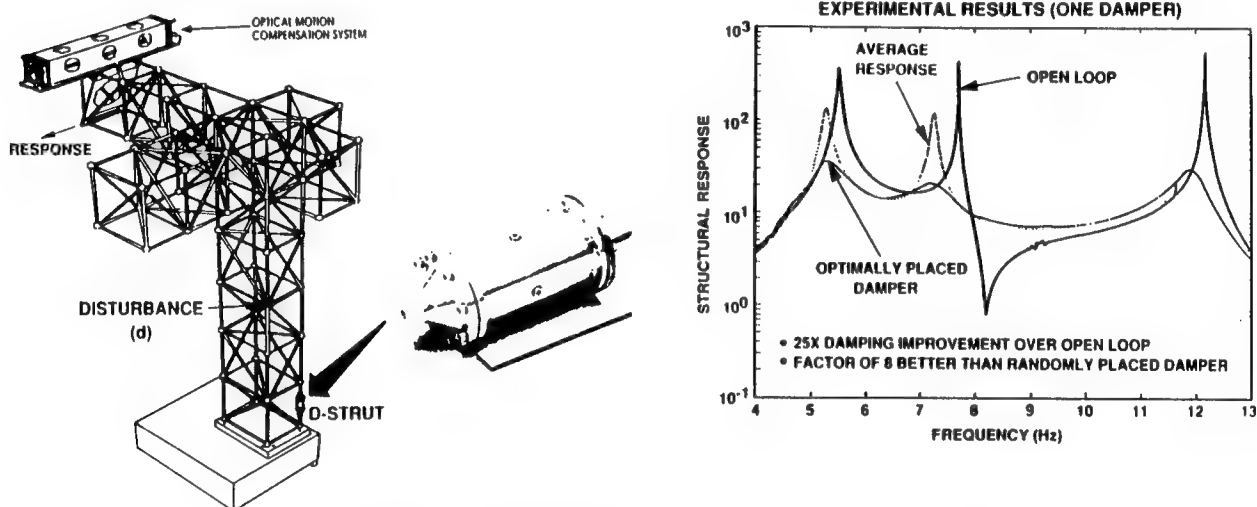
o Optimizing K_p , K_v with respect to $\sum_{i=5}^7 \exp \{10\xi_i\}$



Mode	Undamped		Damped ($K_v = 320$ lb/in)		Damped ($K_v = 105$ lb/in)	
	freq		freq	damping	freq	damping
5	17.4248		17.2668	8.1733	16.1907	6.5787
6	20.8423		21.3353	3.9098	20.1644	8.0746
7	31.1387		32.1426	3.7256	30.5854	7.4840

OPTIMAL PLACEMENT AND TUNING OF PASSIVE ELEMENTS

The foregoing discussions centered around simulated data. The figure below presents experimental data taken from the Phase B Testbed. The optimal placement of the damper here was determined via the H_2 performance metric with disturbance input and response locations as shown. An exhaustive search over the 186 locations was performed using the Ritz reduction technique to compute the solution to the associated Lyapunov equation. The figure contains the open loop response, the response obtained by the optimally placed damper, and finally an "averaged" response computed by averaging the transfer functions over all possible locations of the damper. The experimental results indicate a 25 times improvement in damping in the first three modes over open loop, and 8 times improvement in damping over the "averaged" locations.



- OBJECTIVE: OPTIMALLY PLACE/TUNE DAMPERS FOR STRUCTURE QUIETING
- DEMONSTRATED ANALYTICAL TECHNIQUES ON PRELIMINARY DESIGN PROBLEM
- WILL EXTEND TO MULTIPLE PASSIVE AND ACTIVE ELEMENTS

OPTIMAL RESIZING APPROACH

Given the optimum placement and characteristics of a number of passive dampers, the objective here is to find the optimal sizes (α_i^*) of the truss members. In this regard, one may choose any one or combination of the listed criteria J_1, \dots, J_6 as the objective function for the resizing problem. The optimization can be achieved by varying design parameters such as member sizes, control gains, and mirror geometry and relative position. The challenge one faces in this type of multi-criteria problem is the potential conflict among criteria, so that there is no single design that optimizes all criteria simultaneously. Here, one must look for Pareto optimal solutions. A solution is said to be "Pareto optimal" if there is no other solution that improves any criteria without making at least one other criterion worse.

Statement: For given damper placement, optimize the structure.

Possible Criteria: J_1 : LOS error of chief ray at some D.O.F.

J_2 : RMS wavefront error of multiple rays at focal plane

J_3 : Strains/stresses in selected members

J_4 : Displacements at selected D.O.F.

J_5 : Total mass

J_6 : Control cost

Design Variables: Structural - Member sizes

Control - Gains

Optical - Mirror sizes, rel. position

Criteria: Non-Commensurate and conflicting

Must look for Pareto optimal solutions

OPTIMAL RESIZING APPROACH (CONT'D)

In the results that follow, two criteria were selected for optimization; the total mass, J_1 , and the steady state mean square displacement, J_2 , (at the truss-to-trolley attachment points) in response to a white noise disturbance. Designating the matrix that maps the state variables x into the attachment points by H , we have $J_2 = \text{tr}(H Q H^T)$, where Q is the solution of the matrix Lyapunov equation shown, and $A = A(\alpha)$, $B_2 = B_2(\alpha)$, respectively, are the plant matrix and the disturbance coefficient matrix. Pareto optimal solutions can be found by determining the stationary values of the functional $J(J_1, J_2, \lambda)$ for various values of the weighting parameter $\lambda \in [0,1]$. By allowing λ to take on discrete values at small intervals from zero to one, one can propagate the solution along the λ path to provide a subset of Pareto optimal designs.

- o **Problem Statement:** For a given damper placement, optimize cross sectional areas of truss members to attenuate disturbance transmission from source to output D.O.F.
- o For testbed, let $J_1 = \text{total mass}$
 $J_2 = \text{steady state mean square displacements at trolley attach.}$
 $= \text{tr}(H_1 Q H_1^T)$
 $H_1: \text{Maps } x \text{ into observed displacements at trolley attachment D.O.F.}$
 $Q: \text{Solution of } (AQ + QA^T + B_2 B_2^T = 0)$
- o **Construct weighted criterion:** $J = (1-\lambda)J_1 + \lambda J_2; \lambda \in [0,1]$
 $\lambda: \text{TBD from system study of mission (not known in advance)}$
Starting with $\lambda=0$; $\rightarrow \text{Find } J^*(\lambda) \rightarrow$, till $\lambda=1$
$$\boxed{\lambda \leftarrow \lambda + \Delta\lambda}$$
- o Will provide a set of feasible Pareto optimal designs to optimally trade mass vs. performance

CSI PHASE B TRUSS - MODEL REDUCTION

Optimization of large order models makes model reduction a required step due to the need to solve one or more Lyapunov or Riccati equations. Model reduction consists of applying a model reduction transformation, T_r , to a full-order model. The transformation T_r is typically not recomputed for each parameterization of the model and hence the transformation T_r computed for one set of parameter values may be a poor transformation to use for another parameterization. The addition of a linear correction term to T_r , constructed from eigenvector gradients (EGs), may extend the range of parameter variations over which T_r is valid.

Our optimization program uses a "Parameter Variance Tolerance" (PVTol) to allow the user to specify how much the parameters may vary before T_r is recomputed. The program also allows the user to specify whether EGs are used in the construction of T_r . The computation of T_r is a CPU time intensive task. Therefore, there exists a tradeoff between added computation time and accuracy of the models used in optimization. Questions which naturally arise are "*What impact do these options have on run time?*" and "*What impact do these options have on the results of the optimization?*"

The left figure shows a plot of CPU time versus PVTol for a certain problem. The "x"-marks show the timings for runs without EGs and the "+"-marks show timings for runs with EGs. As one can see, the change in PVTol 0.10 to 0.50 causes roughly a factor of two in CPU time. The use of EGs increased the CPU time by roughly a factor of four over not using EGs.

The right figure illustrates how the optimal cost from several runs changed with varying PVTol and whether or not EGs were used. For each PVTol (0.10, 0.25, and 0.50) three optimization points were obtained both with and without use of EGs. All costs are shown relative to the best (i.e. smallest) optimal cost for each of the optimization runs. As one can see, the runs which used the EGs always produced the smallest optimal cost and the results were consistent for all values of PVTol. The results for no EGs show that the resulting optimal costs were not really optimal and varied somewhat with PVTol.

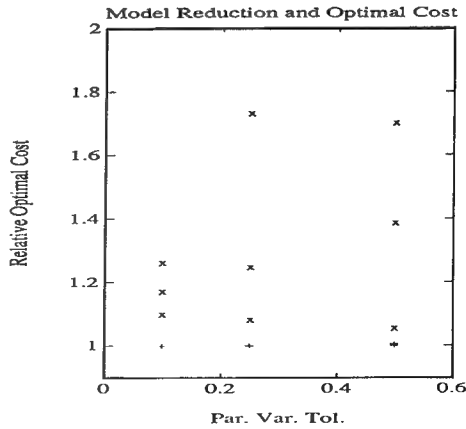
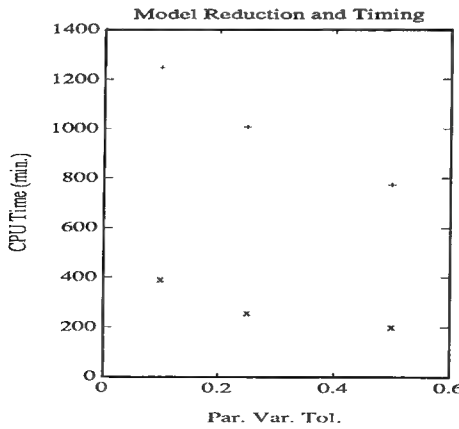
The conclusion drawn from this analysis was that using EGs is preferred. The timing was brought down to a manageable size by setting the PVTol to a value of 0.50. The computation time is about twice what would be obtained by using no EGs with a PVTol of 0.10.

What effect does

- parameter variation tolerance
- use/non-use of eigenvector gradients

have on ...

- CPU Time
- Optimal control (i.e., performance) cost



OPTIMAL RESIZING APPROACH

An important step in the optimization process is the parameterization of the structure. The parameters chosen for optimization of the truss were the rod member cross-sectional areas. Independent parameterization of each member would have led to 186 parameters, probably making the optimization run time quite long: we needed to reduce the number of parameters. Choosing too few parameters, and thus a low order design space, would have lead to poorer results. A natural way to compromise is to take advantage of symmetry in the structure. We did this in the following way:

1. Each bay in the tower was budgeted three parameters: one for the longerons, one for the battens, and one for the diagonal elements. However, the bottom bay required only two parameters because its longerons were attached to the base. Thus the tower gave us 14 parameters.
2. The first, second and third pairs of bays of the two three-bay arms were budgeted three parameters each as above. This gave us another 9 parameters.
3. The two single-bay arms were parameterized with one parameter.
4. The bay at the intersection of the tower and the arms was parameterized with one parameter, giving a total of 25 parameters.

- o Issues

- Number of parameters
- Distribution of parameters - symmetry
- Solving large scale eigenvalue and Lyapunov equations

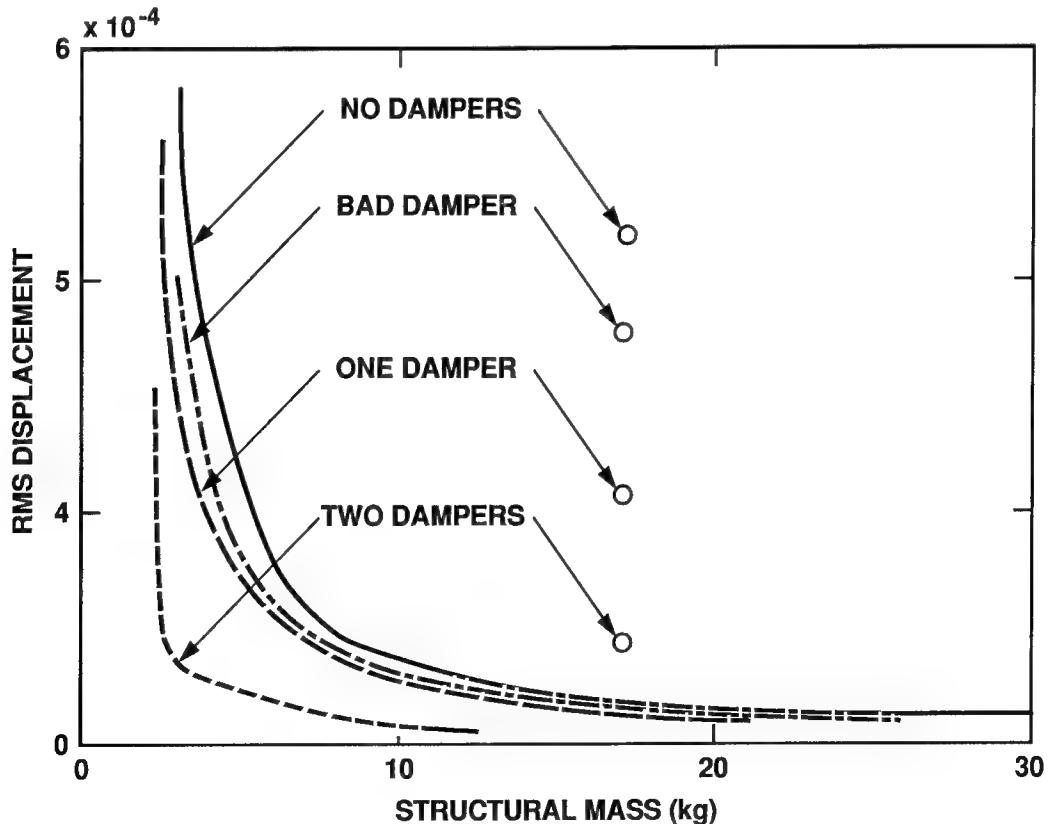
- o Solution

- Three parameters per bay for tower and three-bay arms
- One parameter per bay for one-bay arms and intersection
- Total of 25 design variables
- Ritz model reduction using eigenvectors/eigenvector derivatives

CSI PHASE B TRUSS OPTIMIZATION RESULTS

In this figure the results for four cases are depicted in the criteria space (J_1, J_2) . The four cases represent (1) no dampers are present, (2) one arbitrarily placed damper is used, (3) one damper is optimally placed, and (4) two optimally placed dampers. For each case, the performance of the nominal (initial) design is represented by a single point in the (J_1, J_2) space, and the performance of the Pareto optimal design is represented by a curve joining multiple points, each point corresponds to a λ -value $\lambda \in [0,1]$. A number of observations can be made

- (1) Considering the damper optimization alone, for a fixed mass an arbitrarily placed damper shows only 25% improvement in transfer function over the no damper case, while an optimally placed damper shows a factor of two improvement. When two dampers are optimally placed, the improvement is increased from a factor of two to five.
- (2) For the same mass (~17.00lb), optimal resizing of the truss members results in impressive improvement in the transfer function, where a reduction by a factor of 7 to 12 is achieved, depending on the number and location of the dampers.
- (3) A definite corner point near the origin of the Pareto optimal curve is typical of non-competitive criteria that admit a single optimal solution. Optimally placed dampers tend to sharpen the (J_1, J_2) curve, and thereby make minimization of the mass and rms response more achievable.

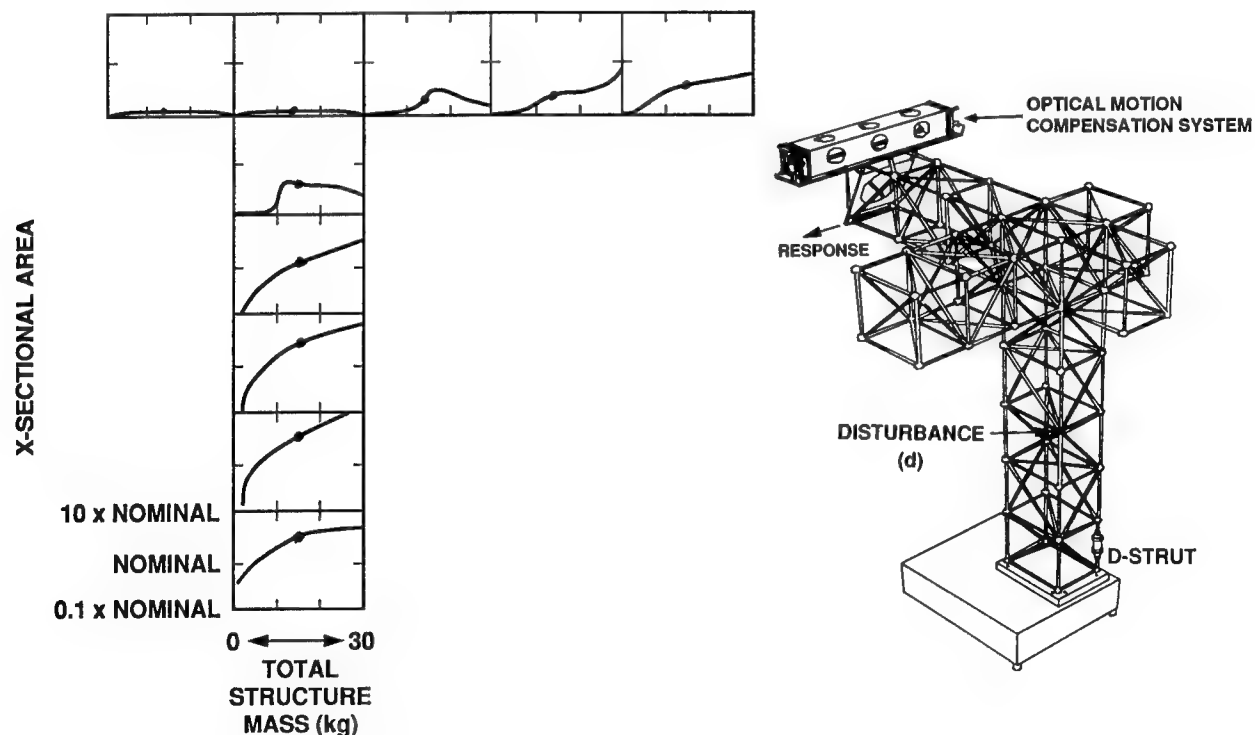


CSI PHASE B TRUSS OPTIMIZATION RESULTS DISTRIBUTION OF MASS IN PARETO OPTIMAL SET

The chart illustrates the distribution of mass in the set of optimized structures for the single optimally placed damper on the previous page. In the figure on the left each plot shows variation of the structural mass of individual bays versus the total structural mass of the optimized structure. The ordinate is a logarithmic scale covering the range of the allowed bay mass (corresponding to the allowed variation of parameters). For this case the parameters were allowed to vary in a range of plus-or-minus an order of magnitude from nominal. For the two single-bay and two three-bay arms, the plots show the combined structural mass of the corresponding bays on each arm.

As one can see, the majority of the mass for the optimized structures lies in the tower near the base. A suitable explanation is that the mass is being added to stiffen the structure between the disturbance input and the grounded base. There is also some mass added to the three-bay arms, to make the structure near the trolley heavier, and hence more resistant to vibration.

The general trend in the way mass was added within each bay was that the majority of mass was added to the longerons and diagonals, implying that the battens play a small role in the system performance.

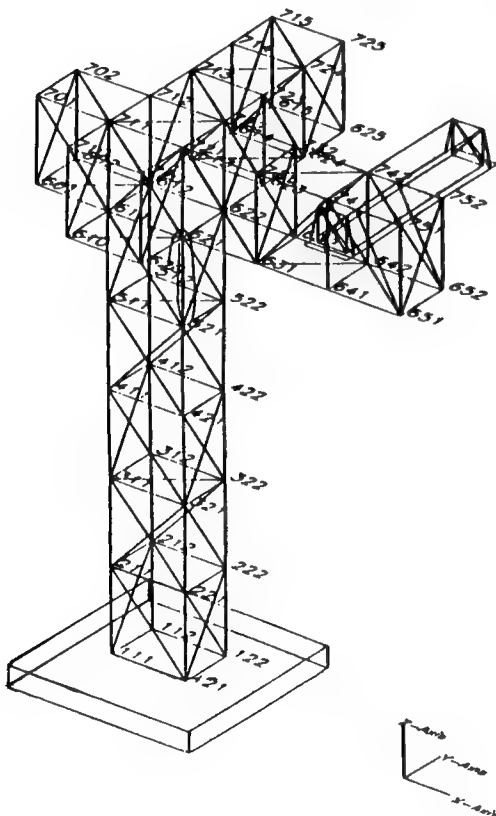


BUCKLING OF OPTIMAL DESIGN UNDER ONE - "G"

During optimization, lower and upper bounds on the design vector α , with components α_j , were imposed so that $(5. \times 10^{-6}) \leq \alpha_j \leq (5. \times 10^{-4})$. As a result of the optimization, some members were driven toward the lower bound where buckling instability may be of concern. To check whether or not the resulting design is viable, a worst case buckling analysis under one-g loading was conducted for the case of one optimally placed damper. To simplify this analysis, instead of using 25 different cross sectional areas, the member sizes were grouped in three intervals: $(5. \text{ to } 9.9) \times 10^{-6}$, $(1.0 \text{ to } 9.9) \times 10^{-5}$, and $(1.0 \text{ to } 5.0) \times 10^{-4}$. After computing the forces in all members under one-g, the maximum compressive load (labeled P_{\max}) on any of the members belonging to a given group was checked against the fundamental critical buckling load (labeled P_{cr}) for the member with the smallest cross section and greatest length in that group. The smaller the ratio $(P_{\max}/P_{cr}) < 1.0$, the greater the degree of conservatism of the design against buckling.

One damper optimal design at mass = 15.54 Kg

Considered 3-Intervals for x-sec. areas: $(5. \text{--} 9.) \times 10^{-6}$; $(1. \text{--} 9.) \times 10^{-5}$; $(1. \text{--} 5.) \times 10^{-4}$



$$P_{1\max} = 312 \text{ N}; \quad P_{1cr.} = 544 \text{ N};$$

$$\text{Ratio} = 0.57$$

$$A = 5.3 \times 10^{-6}; \quad = 0.41; \quad R = 5 \times 10^{-3}; \quad t = 0.17 \times 10^{-3}$$

$$P_{2\max} = 509 \text{ N}; \quad P_{2cr.} = 1,954 \text{ N}$$

$$\text{Ratio} = 0.26$$

$$A = 1.79 \times 10^{-5}; \quad = 0.41; \quad R = 5 \times 10^{-3}; \quad t = 0.6 \times 10^{-3}$$

$$P_{3\max} = 563 \text{ N}; \quad P_{3cr.} = 150,000 \text{ N}$$

$$\text{Ratio} = 0.004$$

$$A = 4.67 \times 10^{-4}; \quad = .575; \quad R = 12.5 \times 10^{-3}; \quad t = 6.0 \times 10^{-3}$$

SUMMARY/CONCLUSIONS

This paper has addressed several design optimization problems for the JPL testbed structure. The two classes of problems considered were the optimal resizing of truss element areas, and the placement and tuning of viscous dampers. Various measures of performance were defined for these problems including minimizing RMS error due to input disturbances and maximizing damping in selected structural modes.

The testbed structure is of sufficient complexity to expose the numerical challenges and issues related to practically solving these optimization problems. A number of different economizing techniques were introduced and validated to meet these challenges. Each of these methods proved to be very well suited for their particular target optimization application.

The resulting optimized design in each instance led to significant improvement in performance. Although each optimization problem was attacked individually, future work will focus on integrating the approaches.

- o Developed and applied analysis/design tools for optimal placement/tuning of passive dampers and optimal resizing of structural mass
- o Developed efficient solution techniques for optimization problems
- o Demonstrated significant improvement in performance both analytically and experimentally on CSI testbed structure using optimization approach
- o Established real benefits to the methods, and their applicability to large systems

PIEZOELECTRIC DEVICES FOR VIBRATION SUPPRESSION: MODELING AND APPLICATION TO A TRUSS STRUCTURE

C.C. Won*, D.W. Sparks, Jr.†, W.K. Belvin†, and J.L. Sulla*

* Lockheed Engineering & Sciences Company
Hampton, VA 23666

† NASA Langley Research Center
Hampton, VA 23665

ABSTRACT

For a space structure assembled from truss members, an effective way to control the structure may be to replace the regular truss elements by active members. The active members play the role of load carrying elements as well as actuators. A piezo strut, made of a stack of piezoceramics, may be an ideal active member to be integrated into a truss space structure. An electrically driven piezo strut generates a pair of forces, and is considered as a two-point actuator in contrast to a one-point actuator such as a thruster or a shaker. To achieve good structural vibration control, sensing signals compatible to the control actuators are desirable. A strain gage or a piezo film with proper signal conditioning to measure member strain or strain rate, respectively, are ideal control sensors for use with a piezo actuator. The Phase 0 CSI Evolutionary Model (CEM) at NASA Langley Research Center used cold air thrusters as actuators to control both rigid body motions and flexible body vibrations. For the Phase 1 and 2 CEM, it is proposed to use piezo struts to control the flexible modes and thrusters to control the rigid body modes. A tenbay truss structure with active piezo struts is built to study the modeling, controller designs, and experimental issues. In this paper, the tenbay structure with piezo active members is modelled using an energy method approach. Decentralized and centralized control schemes are designed and implemented, and preliminary analytical and experimental results are presented.

OUTLINE

The use of piezoelectric devices for vibration suppression has received much interest recently [1-5].* The application of the piezoelectric effect to actuation and sensing devices has allowed the investigation of the use of these components in experimental testbeds. The outline of this presentation includes the objectives, a description of the piezo strut and piezo film devices used, and discussion of modeling and implementation issues. A comparison of the analytical model and experimentally measured model for vibration suppression studies is presented.

- **Objectives**
- **Experimental setup description**
- **Modeling and model reduction**
- **Controller designs and experiment**
- **Summary/Future work**

*References 1-16 are cited in text.

OBJECTIVES

The NASA Langley Phase 0 CSI evolutionary model (CEM) used cold gas thrusters as actuation devices for line of sight pointing and vibration suppression testing [6]. Since the use of thrusters for flexible body vibration control may be impractical, alternative actuation devices are considered for the Phase 1 and 2 models of the CEM. Piezoelectric strut actuators show promise in this application. The objective of this work is to obtain experience in the application of these devices to vibration suppression of a truss structure. This includes modeling and control law design and implementation.

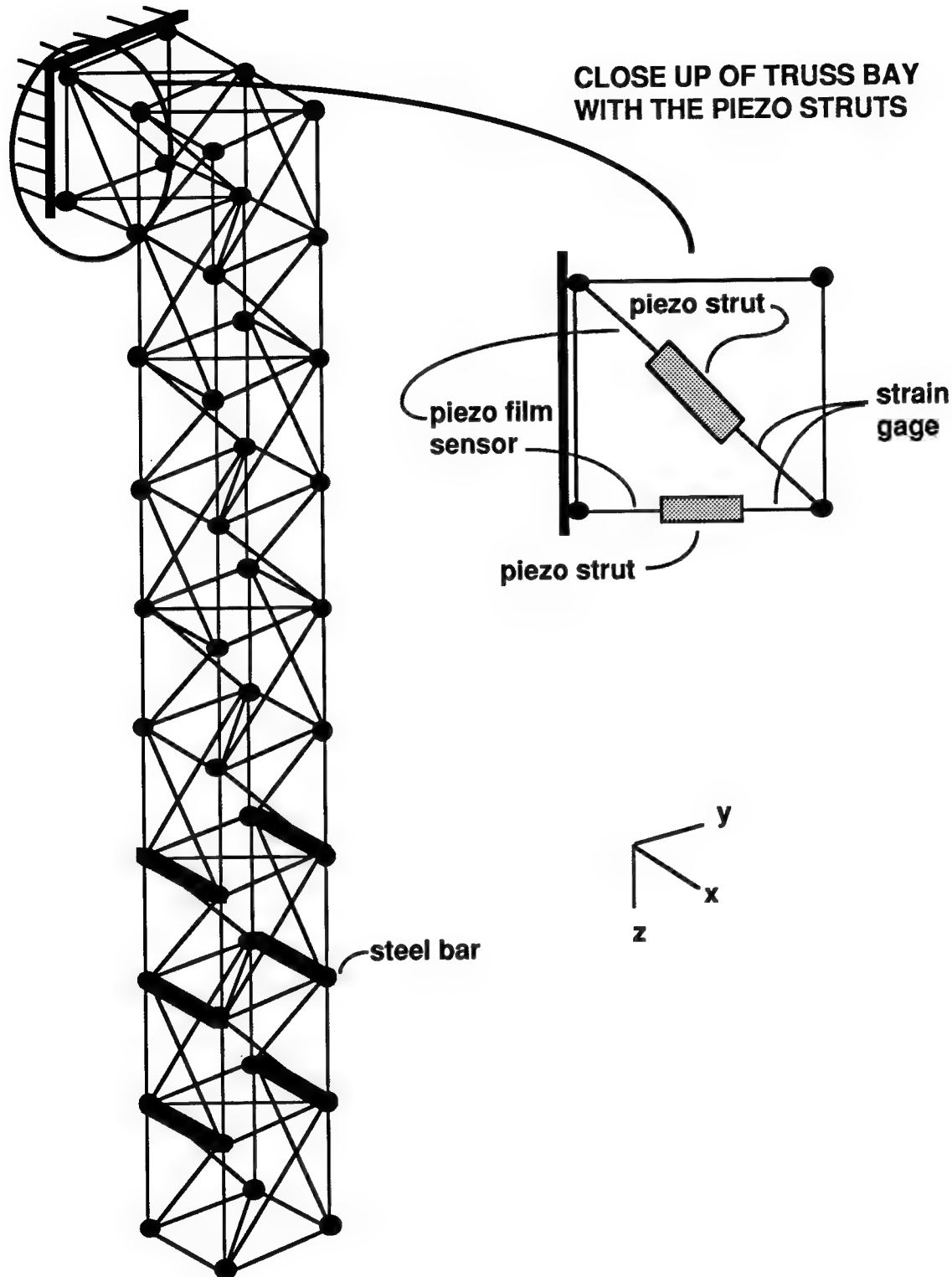
- **Demonstrate use of piezoelectric actuators and sensors for vibration suppression of a truss structure**
- **Derive model of structure system with active devices**
- **Obtain practical "hands on" experience using available piezoelectric actuators and sensors**

TEST SET-UP DESCRIPTION

The following figure is a drawing of the tenbay truss test article, showing the sensor and piezoelectric strut actuator locations. The truss is in an inverted L shape, with a 20 inch section cantilevered horizontally from a base plate and a 90 inch section extending vertically downward. There are a total of ten bays, each bay of the truss is 10 in. x 10 in. x 10 in. in size. The individual struts are made of aluminum, as are the corner ball joints connecting each bay; threaded steel rods are used to secure the struts to the ball joints. In addition, six steel bars of 7 pounds each are mounted on the lower truss battens, 3 each on either side, to reduce the bending frequencies of the structural modes (the first two modes were lowered to below 10 Hz).

Two commercial piezoelectric struts, obtained from Physik Instrumente of Germany, are mounted in the truss bay closest to the support - one as the lower horizontal member (longeron) and one as the adjacent diagonal member. These actuators take the places of the nominal struts, with steel support studs used to connect the piezoelectric struts to the ball joints. The chosen locations correspond to those determined by a finite element model (FEM) of the truss that had the highest strain energy.

Instrumentation consists of a strain gage and a piezo film mounted on opposite ends of each actuator, a tri-axial servo accelerometer set mounted on the free end of the truss and a single axis servo accelerometer mounted midway up the truss. The piezo film is a pre-cut strip of piezoelectric material which senses the relative velocity between its two ends. An additional piezo film sensor and strain gage are placed on the diagonal strut in the truss bay face directly opposite to the face containing the piezoelectric struts. The two piezoelectric strut actuators are driven by a two channel Model 50/750 high voltage power amplifier, from Trek, Inc. of Medina, N.Y., capable of producing DC voltages of up to 1500 V at an average current level of 50 mA. Separate current amplifiers convert the current collected by the piezo films to voltage outputs. This instrumentation is interfaced to a Control and Measurement and Control (CAMAC) rack, which performs the analog to digital (A/D) and the digital to analog (D/A) conversions and the analog filtering of the sensor signals, and a Vax workstation 3200 for real-time control tests. A GenRad 2515 is also used for frequency response measurements.



Schematic of a tenbay active structure

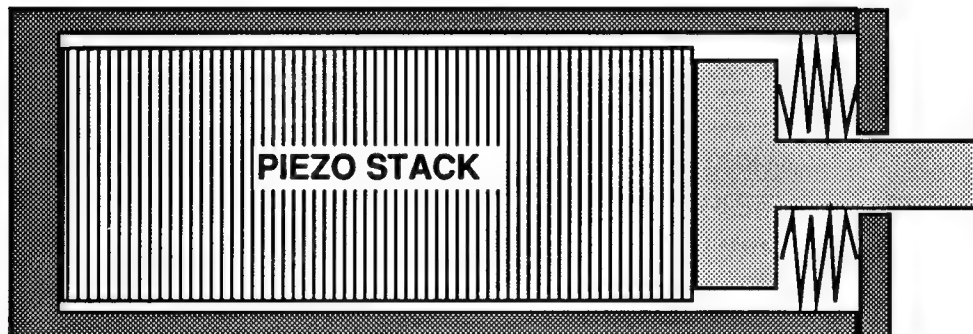
PIEZOELECTRIC SENSOR AND ACTUATOR

The constitutive equations of a piezoelectric material describe the relationships of the six strains, six stresses, three electric displacements, and three electric fields at any time and any point in the piezoelectric material [7-8]. A piezoelectric material is anisotropic, and its constitutive conditions depend on the polarization direction. Due to the piezoelectric effect, a piezoelectric device can transfer mechanical energy to electric energy, or vice versa. In the generator mode, charge and electric field are produced when external forces are applied, and a piezoelectric transducer can be used as a sensor. In the motor mode, dimensional changes occur when electric sources are applied, and it can be used as an actuator.

- **Constitutive equations: electro-mechanical coupled equations**
- **Properties of a piezoelectric material**
 - **Direct piezoelectric effect: charge produced when forces are applied**
 - **Indirect piezoelectric effect: dimension changed when electric sources are applied**

PIEZOELECTRIC ACTUATOR

The piezo strut is made of a stack of piezoceramic disks. It has a preload mechanism to prevent the piezoceramics from experiencing tensile forces. To prevent depolarization of the piezoceramic, an electric field is applied in the same direction as the DC electric field that polarized the piezoceramic. Normally, the housing of a piezo strut is grounded, and a negative voltage is applied to the piezoceramics inside the housing. For a dynamic application, a piezo strut is biased by a negative DC voltage with an AC dynamic signal superimposed.

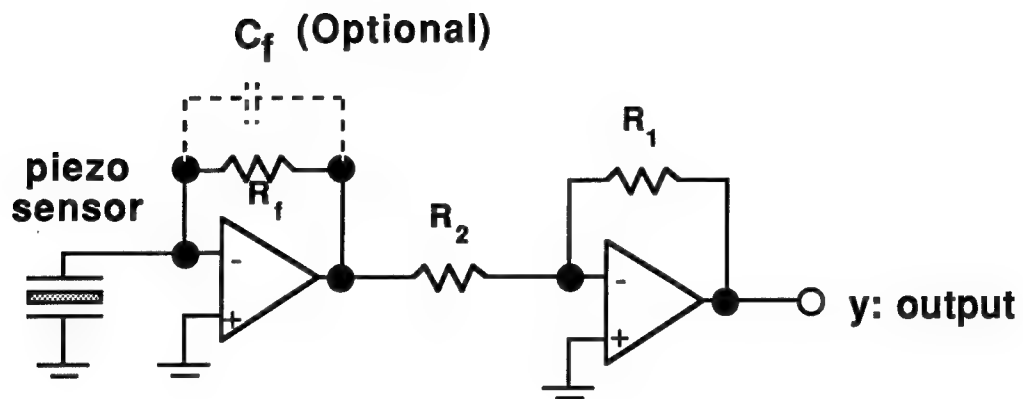


Commercial Piezoelectric Strut Data [14]

Strut Parameter	Longeron Strut	Diagonal Strut
Model No.	P243.30	P243.40
Expansion at -1000 volts	40 microns	60 microns
Expansion at -1500 volts	60 microns	90 microns
Stiffness (lb/in)	1.1992×10^6	0.7995×10^6
Total length (in)	4.58	5.67
Weight (lb)	2.75	3.25
Resonant frequency (Hz)	4500	2200

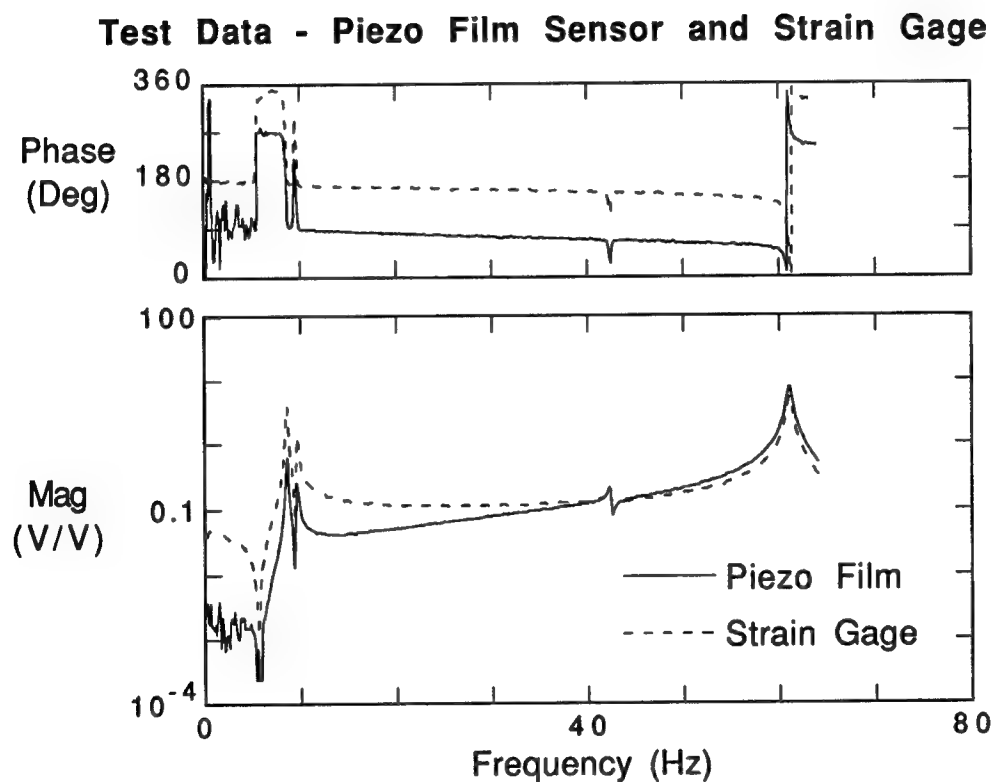
PIEZOELECTRIC SENSOR AND CURRENT AMPLIFIER

A piezo film sensor is a self-generating transducer, and does not require an external power supply. However, a signal conditioner is needed to convert the charges collected on the electrodes of the piezo film. A current amplifier converts the current drawn from the piezo film to a voltage output. The circuit diagram of a current amplifier is illustrated below.



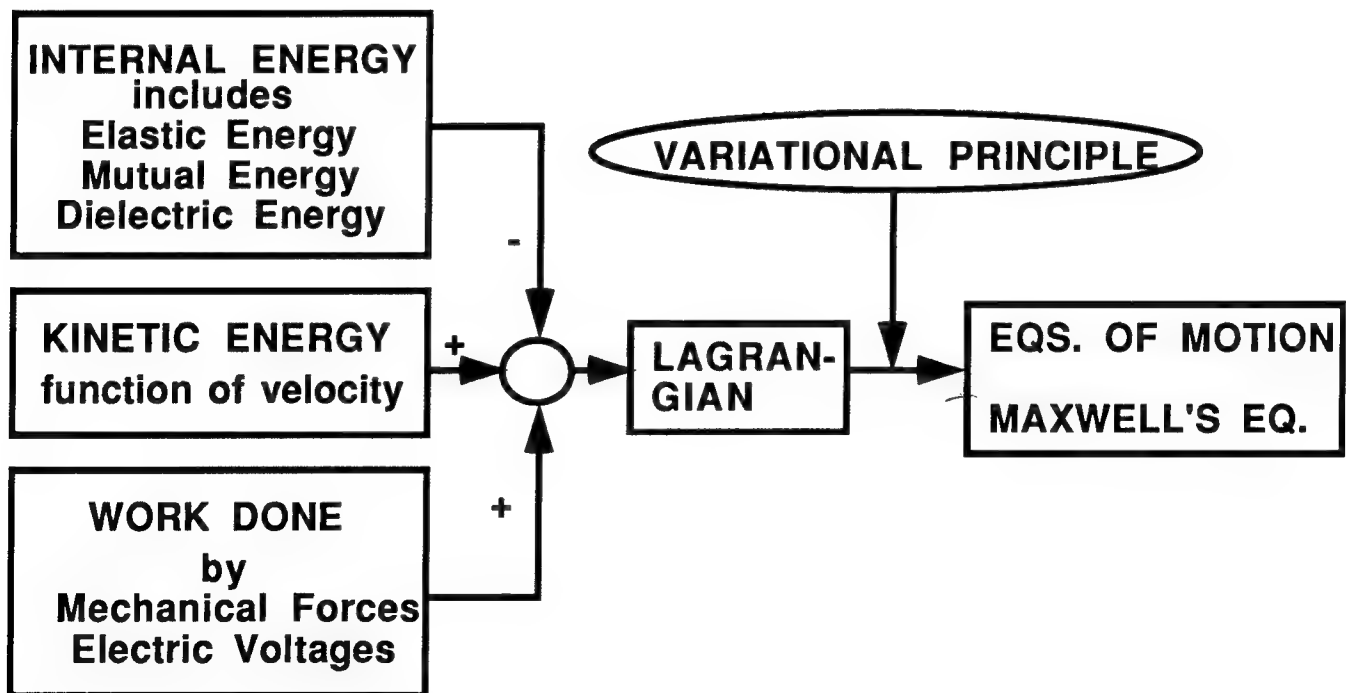
STRAIN AND RELATIVE VELOCITY MEASUREMENTS

The use of the piezo film as a relative velocity sensor can be seen in the following figures. The top figure shows the respective phase plots for a strain gage and a piezo film strip collocated on the tenbay truss; the bottom figure shows the magnitude plots of the two sensors. The two measurements are not independent, but differ only by a scalar factor of $j\omega$, implying a phase lag of $\pi/2$ and a magnitude ratio of ω .



SYSTEM MODELING

System governing equations are derived here based on an energy method developed in Ref. [13]. Lagrangian is defined as a function of internal energy, kinetic energy, and work done by the external forces and voltages. The internal energy consists of elastic energy, mutual energy, and dielectric energy, and is a function of mechanical and electric displacements. The kinetic energy is a function of velocity. The work is done by the surface tractions applied on the surface of the piezoelectric medium less the flux of electric energy flowing outward across the surface [9]. The variational principle yields the displacement equations of motion and Maxwell's second equation, and they are coupled through the piezoelectric effect. The equations of motion describe the force equilibrium conditions, and Maxwell's second equation states that the curl of electric fields is zero in the electrostatic case. The applied mechanical forces appeared in the equations of motion as driving forces, and the external electric voltages in Maxwell's second equation.



MODEL REDUCTION OF A STRUCTURE WITH PIEZO STRUTS

Since only a quasi-static electric field is considered, Maxwell's second equation is algebraic in the electric displacement. One can solve Maxwell's second equation for electric displacement in terms of mechanical displacements, and back substitute into the equations of motion to decouple the mechanical and electric displacements in the equations of motion. By doing this, the external electric voltage is converted to a pair of piezoelectric axial forces asserted on the nodal point of the piezo strut. The piezoelectric axial forces have the same magnitude but opposite sign.

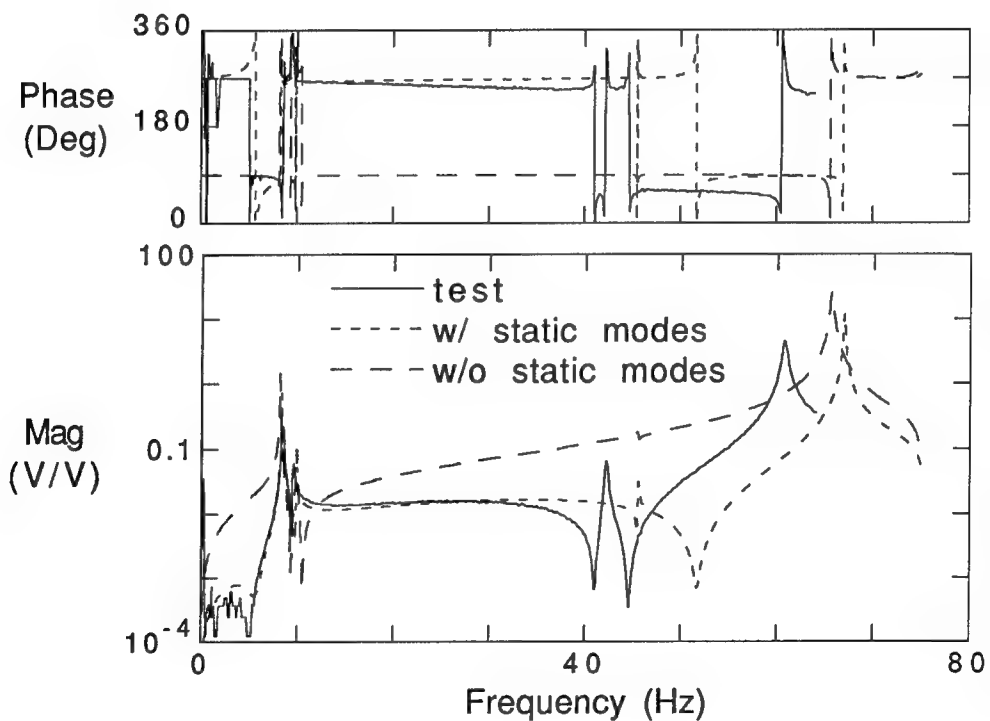
A polyvinylidene fluoride film (PVDF) can be used as a piezo sensor. A current amplifier is used to convert the current generated from the piezo film to electric voltage. The input terminals of the current amplifier are virtually grounded, therefore the system governing equations described above are good for a piezo medium used as either a sensor or actuator. The piezo film incorporated with a current amplifier generates a signal proportional to the relative velocity of the ends of the piezo film [3,10-11].

A reduced model was derived from a finite element model by considering the piezo strut and the supporting studs as a single element. Transfer functions calculated from the model were compared with the test data. Although the model predicted the global responses accurately, large errors were observed for the sensors situated in the same and the adjacent truss elements of piezo struts. It indicated strong local stress concentration is introduced from the forces asserted by the piezo strut. Static mode shapes were used together with vibrational mode shapes in the model reduction to alleviate the modeling error due to the local effect [12-13].

- **Internal forces are produced from the piezoelectric strut due to the piezoelectric effect**
- **Local strain concentration is introduced from the forces applied by the piezoelectric strut**
- **Static mode shapes are used together with vibrational mode shapes in the model reduction to alleviate modeling error due to the local effect**

MODELING ISSUES

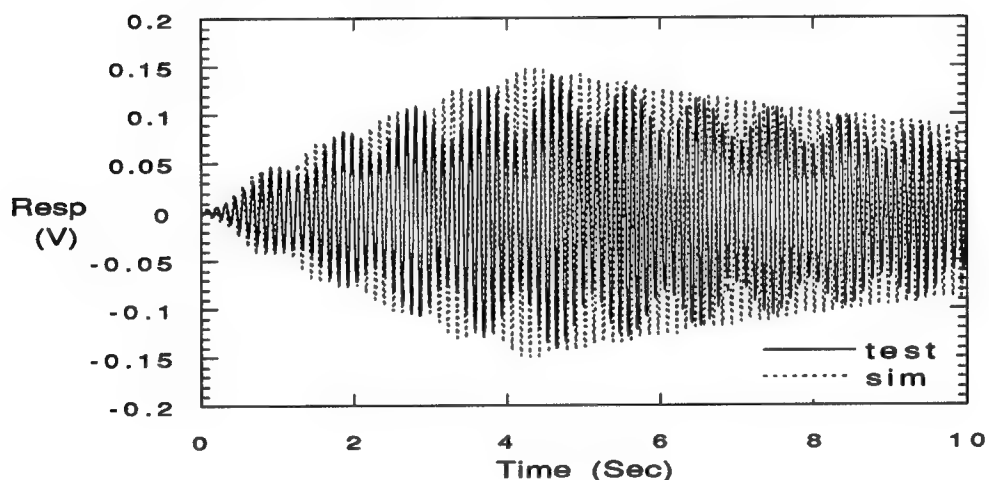
The improvement to the analytical model of the tenbay truss brought on by including the static modes can be seen in the following figures. The bottom figure shows the magnitude plots for the respective transfer functions between a piezo strut and a sensor located in an adjacent strut, as directly measured on the GenRad, as computed from a finite element model (FEM) with vibrational modes only, and as computed from a model which included both vibrational and static modes. The top figure shows the phase plots for the three respective transfer functions. As both figures show, the model with the static modes better represents the dynamics of the tenbay truss, particularly in the region around the first two modes.



EXPERIMENTAL PROCEDURE

Each controller was tested on the truss structure by commanding the two piezo struts at 8.4 Hz and 9.5 Hz respectively for 4.5 seconds to excite the first two bending modes of the structure. For the open loop case, the structure was allowed to free decay for the remainder of the 5.5 second test duration. For the closed loop tests, the controller was switched on at 4.5 seconds to actively damp the truss. The open loop response is shown below overlaid with simulated results from the finite element model. The "beating" effect was not observed in the simulated results due to modal frequencies being slightly different from the actual system.

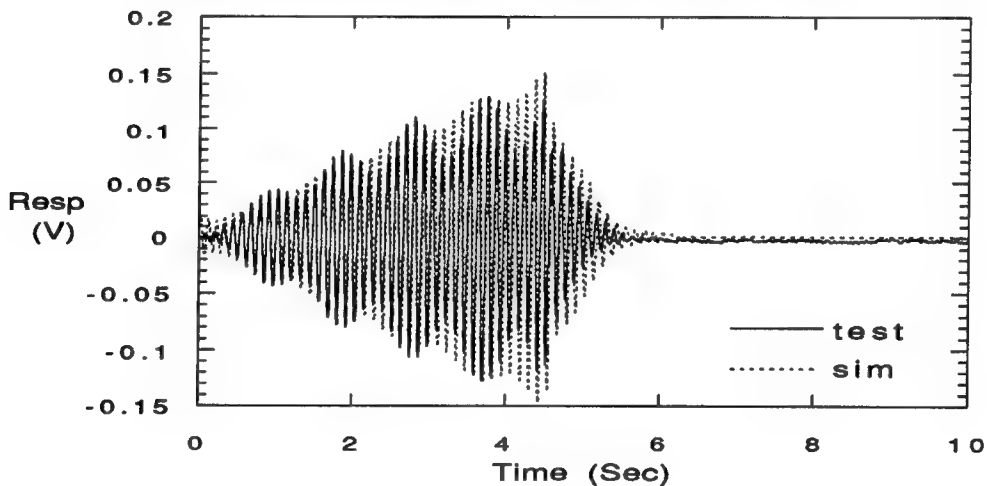
OPEN LOOP STRAIN GAGE RESPONSES



CONTROLLER DESIGNS - LQG

Linear quadratic gaussian (LQG) controller design is a model based technique. For this application, a system identification approach was taken. Three 30 second data sets were obtained, using a 15 Hz bandwidth random signal as input to the piezo struts, collocated strains as the output, and a 250 Hz sample rate. Using the Observer/Kalman Filter Identification (OKID) technique in the System/Observer/Controller Identification Toolbox (SOCIT) for MATLAB [15], a discrete 40 state, 2 input, 2 output model was obtained. A balanced model reduction was performed on this model to obtain a 10 state LQR design model. Using diagonal state weight ($W_x=10$) and control weight ($W_u=0.01$) matrices, LQR gains were obtained and coupled with the identified observer to form the LQG compensator. This controller was tested on the truss structure, with the damping of the first two modes increased to 7.25% and 6.7% respectively.

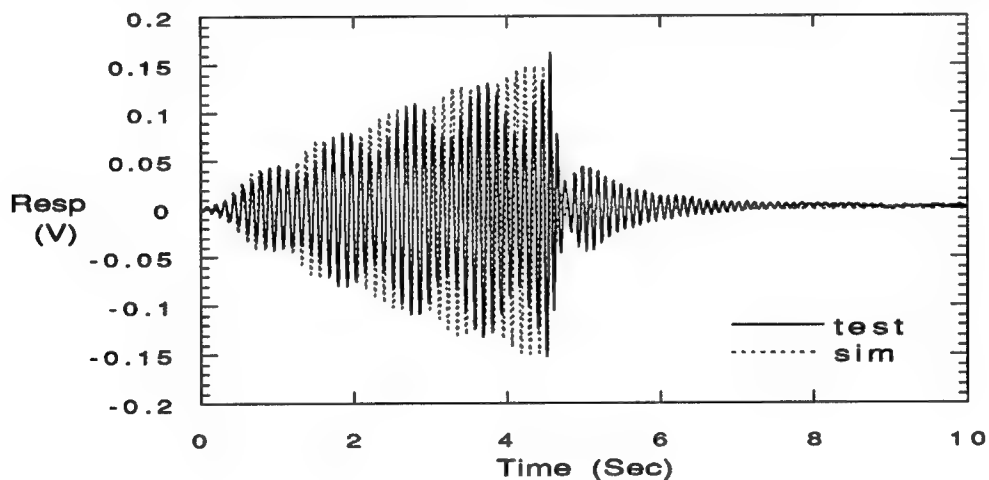
CLOSED LOOP STRAIN GAGE RESPONSES - LQG



CONTROLLER DESIGNS - SECOND ORDER DECENTRALIZED

A second order decentralized controller which digitally simulates a second order spring-mass-damper system at the piezoelectric strut/strain gage location was designed. With collocated actuators and sensors, this provides the necessary temporal phase shift to effect damping using strain measurements. The controllers were designed as SISO for each mode at each actuator/sensor pair. Test results are shown below.

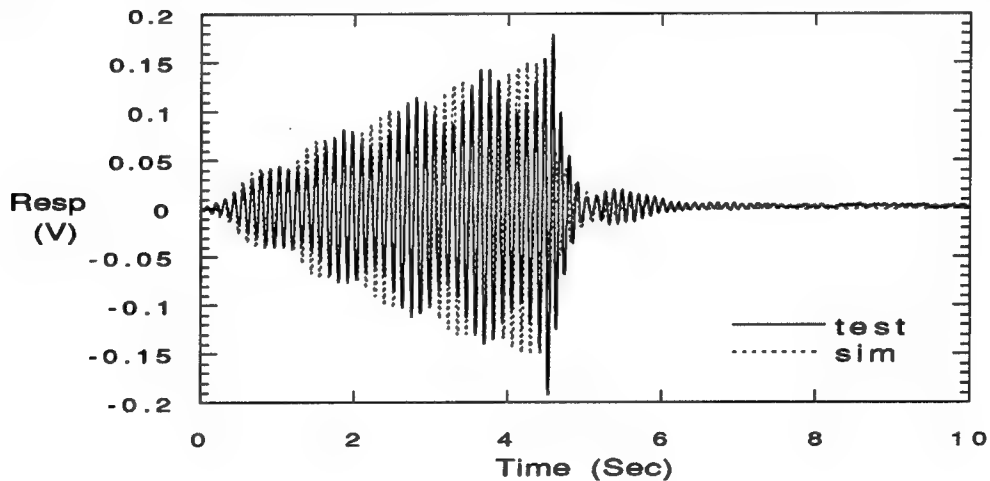
CLOSED LOOP STRAIN GAGE RESPONSES - 2ND ORDER DECENTRALIZED



CONTROLLER DESIGNS - DIRECT RATE FEEDBACK

Collocation of actuator and sensor pair implies that the output influence matrix is the transpose of the input influence matrix. A piezo film sensor is compatible with a piezo strut, and measures relative velocity if a current amplifier is used as a signal conditioner. Therefore, a piezo film/piezo actuator pair closes a direct rate feedback loop. The constant gain matrix, a positive definite diagonal matrix, results in a decentralized controller. When the damping matrix of the closed loop system is positive definite, the closed loop system is guaranteed to be stable [16]. The analytical and test results are shown below.

CLOSED LOOP STRAIN GAGE RESPONSES - DIRECT RATE FEEDBACK



SUMMARY

In this paper, an active truss structure using piezoelectric sensors and struts was modelled and tested. By comparing with the test data, the truncated finite element model obtained based on the modal mode model reduction scheme cannot predict the local stress concentration introduced by the forces applied by the piezo struts. Numerical results indicated that increasing either vibrational modes or nodal points on the active member did not improve the ability of the truncated model to predict the local effect. Combining static mode shapes with the dynamic modes adequately represents the deformations induced by the piezo struts. Closed loop tests using centralized and decentralized controllers demonstrated the ability to perform vibration suppression with piezoelectric devices on a truss structure.

- **Obtained practical experience in use of piezoelectric sensors and actuators**
- **Derived model of an active structure with piezoelectric devices**
- **Local stress concentration is observed due to the forces applied by the piezo strut**
- **Static mode shapes are used together with the vibrational mode shapes in the model reduction to emphasize the local effect**
- **Demonstrated ability to perform vibration suppression with these devices on a truss structure**

FUTURE WORK

With the experience obtained in this application of piezoelectric devices, several areas of future work are identified. In order to ensure sensor/actuator collocation, a piezoelectric strut with an integral strain gage sensor and/or piezoelectric film sensor will be built. On a large structure such as the Phase 2 CEM, it must be determined how many active struts are required to meet a performance objective, and what locations are best. This optimization process is currently underway. After piezo struts are installed in the Phase 2 structure, open and closed loop testing will be required to validate design methodologies. A final goal is creation of a "smart" structure, in which the structure, sensors, actuators, and controllers are integrated to form a total system.

- **Piezoelectric strut with built in piezoelectric sensor or strain gage to ensure sensor/actuator collocation**
- **Optimization of locations for sensors and actuators**
- **Open and closed loop testing on the more realistic testbeds**
- **Integration of structure/sensors/actuators/controller**

REFERENCES

- [1] C.-K. Lee, W.-W. Chiang and T.C. O'Sullivan, "Piezoelectric Modal Sensor/Actuator Pairs for Critical Active Damping Vibration Control," *Journal of the Acoustical Society of America*, 1989.
- [2] E.H. Anderson, J. Fanson, D. Moore, and M.A. Ealey, "2nd Generation Active Member," *Proceedings of the Fourth NASA/DOD Control/Structures Interaction Technology Conference*, Orlando, Florida, November 5-7, 1990.
- [3] C.C. Won, *Active Control of Smart Structures: Theory and Experiment*, Ph.D. Thesis, School of Aerospace Engineering, Georgia Institute of Technology, Atlanta, Georgia, December 1990.
- [4] C.-K Lee, T.C. O'Sullivan and W.-W. Chiang, "Piezoelectric Strain Rate Sensor and Actuator Designs for Active Vibration Control," *Proceedings of the 32nd Structures, Structural Dynamics, and Materials Conference*, Baltimore, MD, April 1991.
- [5] J.L. Fanson, C.-C. Chu, B.J. Lurie, and R.S. Smith, "Damping and Structural Control of the JPL Phase 0 Testbed Structure," *Journal of Intelligent Material Systems and Structures*, Vol.2, No.3, July 1991.
- [6] W.K. Belvin, K.E. Elliott, A. Bruner, J. Sulla, and J. Bailey, "The LaRC CSI Phase 0 Evolutionary Model Testbed: Design and Experimental Results," *Proceedings of the Fourth NASA/DOD Control/Structures Interaction Technology Conference*, Orlando, Florida, November 5-7, 1990.
- [7] W.P. Mason, Editor, *Physical Acoustics*, Vol.1, Part 1, Academic Press, 1964.
- [8] J.F. Nye, *Physical Properties of Crystals*, Oxford University Press, 1972.
- [9] H.F. Tiersten, *Linear Piezoelectric Plate Vibrations*, Plenum Press, 1969.
- [10] C.-K. Lee, and T.C. O'Sullivan, "Piezoelectric Strain Rate Gages," *Journal of the Acoustical Society of America*, 1990.

- [11] C.C. Won, J.-N. Juang, and C.K. Lee, "Shear Strain Rate Measurement Applied to Vibration Control of High-Rise Buildings," *Proceedings of the International Workshop on Intelligent Structures*, Taipei, Taiwan, July 1990.
- [12] C.A. Sandridge, and R.T. Haftka, "Accuracy of Eigenvalue Derivatives from Reduced-Order Structural Models," *Journal of Guidance, Control, and Dynamics*, Vol.12, No.6, Nov.-Dec. 1989.
- [13] C.A. Sandridge, and R.T. Haftka, "Modal Truncation, Ritz Vectors, and Derivatives of Closed-Loop Damping Ratios," *Journal of Guidance, Control, and Dynamics*, Vol.14, No.4, Jul.-Aug. 1991.
- [14] *Physik Instrumente Catalog*, GmbH & Co., Waldbronn, Germany , Dec. 1990.
- [15] J.-N. Juang, L.G. Horta, and M. Phan, " System/Observer/Controller Identification Toolbox", NASA TM-107566, Feb. 1992.
- [16] J.-N. Juang, and M. Phan, "Robust Controller Designs for Second-Order Dynamic Systems: A Virtual Passive Approach," *Proceedings of the 32nd Structures, Structural Dynamics & Materials Conference*, Baltimore, Maryland, April 1991.

REPORT DOCUMENTATION PAGE			Form Approved OMB No. 0704-0188
<p>Public reporting burden for this collection of information is estimated to average 1 hour per response, including the time for reviewing instructions, searching existing data sources, gathering and maintaining the data needed, and completing and reviewing the collection of information. Send comments regarding this burden estimate or any other aspect of this collection of information, including suggestions for reducing this burden, to Washington Headquarters Services, Directorate for Information Operations and Reports, 1215 Jefferson Davis Highway, Suite 1204, Arlington, VA 22202-4302, and to the Office of Management and Budget, Paperwork Reduction Project (0704-0188), Washington, DC 20503.</p>			
1. AGENCY USE ONLY (Leave blank)	2. REPORT DATE	3. REPORT TYPE AND DATES COVERED	
	February 1993	Conference Publication	
4. TITLE AND SUBTITLE	Fifth NASA/DoD Controls-Structures Interaction Technology Conference		5. FUNDING NUMBERS
6. AUTHOR(S)	Jerry R. Newsom, Compiler		590-14-41-01
7. PERFORMING ORGANIZATION NAME(S) AND ADDRESS(ES)	NASA Langley Research Center Hampton, VA 23681-0001		8. PERFORMING ORGANIZATION REPORT NUMBER
9. SPONSORING/MONITORING AGENCY NAME(S) AND ADDRESS(ES)	National Aeronautics and Space Administration Washington, DC 20546-0001 Department of Defense Washington, DC 20301		10. SPONSORING/MONITORING AGENCY REPORT NUMBER
11. SUPPLEMENTARY NOTES	NASA CP-3177, Part 1		
12a. DISTRIBUTION/AVAILABILITY STATEMENT	Unclassified-Unlimited Subject Category 18		12b. DISTRIBUTION CODE
<p>13. ABSTRACT (Maximum 200 words)</p> <p>This publication is a compilation of the papers presented at the Fifth NASA/DoD Controls-Structures Interaction (CSI) Technology Conference held in Lake Tahoe, Nevada, March 3-5, 1992. The conference, which was jointly sponsored by the NASA Office of Aeronautics and Space Technology and the Department of Defense, was organized by the NASA Langley Research Center. The purpose of this conference was to report to industry, academia, and government agencies on the current status of controls-structures interaction technology. The agenda covered ground testing, integrated design, analysis, flight experiments and concepts.</p>			
14. SUBJECT TERMS	Controls-structures interaction; Large space systems; Flexible structures		15. NUMBER OF PAGES
			435
17. SECURITY CLASSIFICATION OF REPORT	18. SECURITY CLASSIFICATION OF THIS PAGE	19. SECURITY CLASSIFICATION OF ABSTRACT	20. LIMITATION OF ABSTRACT
Unclassified	Unclassified		